Rocío Sáez Blázquez

DRESSING THE VACUUM:

Strong Light-Matter Coupling for Enhancing Photon Correlations and Exciton Transport

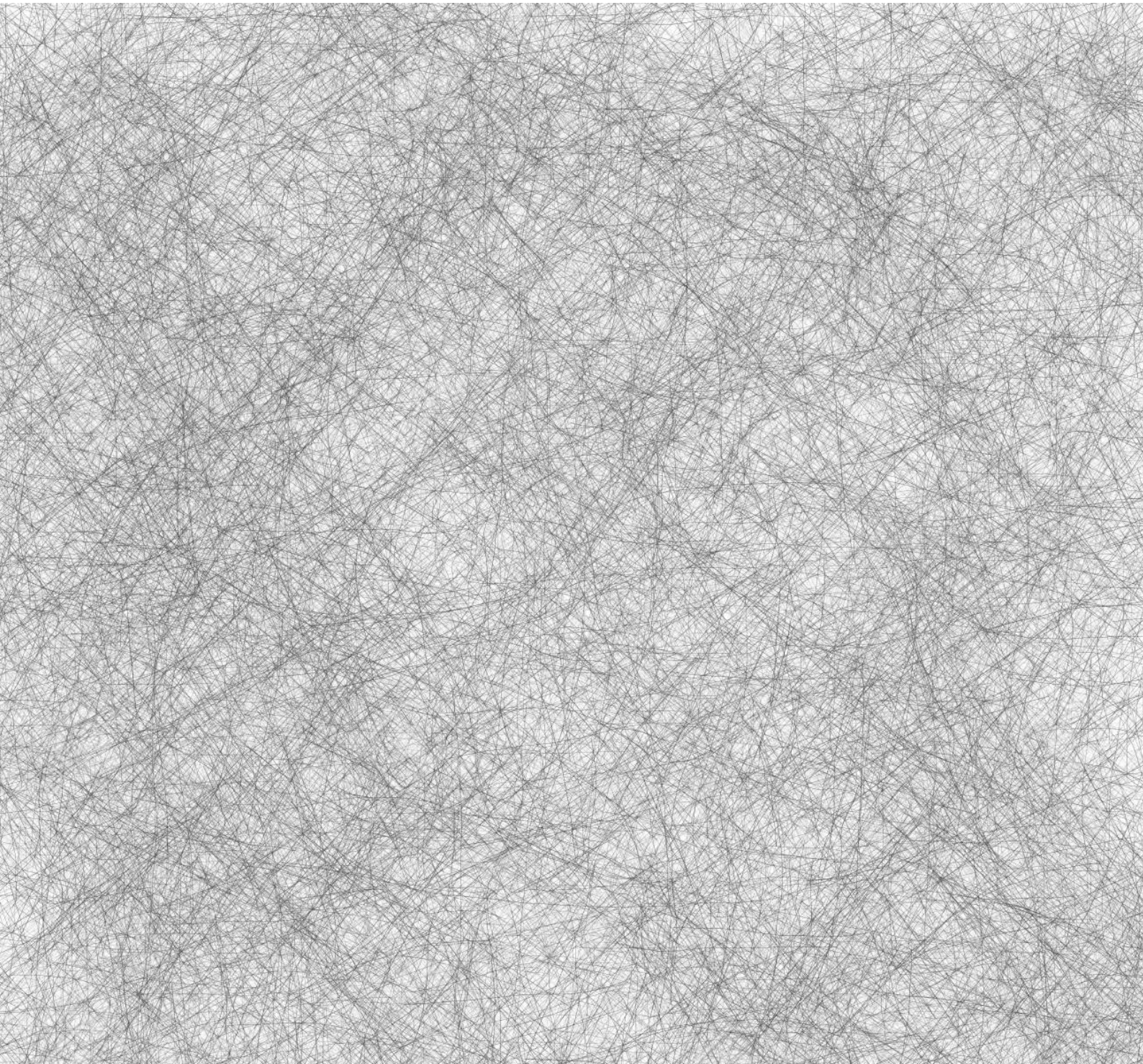

DRESSING THE VACUUM

STRONG LIGHT-MATTER COUPLING FOR ENHANCING
PHOTON CORRELATIONS AND EXCITON TRANSPORT

TESIS DOCTORAL
PRESENTADA EL 25 DE SEPTIEMBRE DE 2020 EN LA

UNIVERSIDAD AUTÓNOMA DE MADRID

PARA LA OBTENCIÓN DEL

TÍTULO DE DOCTOR

DENTRO DEL

PROGRAMA DE DOCTORADO EN FÍSICA DE LA
MATERIA CONDENSADA, NANOCIENCIA Y BIOFÍSICA

POR

ROCÍO SÁEZ BLÁZQUEZ

Y DIRIGIDA POR FRANCISCO J. GARCÍA VIDAL Y
ANTONIO I. FERNÁNDEZ DOMÍNGUEZ

DEPARTAMENTO DE FÍSICA TEÓRICA DE LA MATERIA CONDENSADA
FACULTAD DE CIENCIAS

UAM
Universidad Autónoma
de Madrid

Madrid, 2020

Tribunal:

Francesca Maria Marchetti (Presidenta)
Ferry Prins (Secretario)
Päivi Törmä (Vocal 1)
Inés de Vega (Vocal 2)
Said Rahimzadeh-Kalaleh Rodriguez (Vocal 3)

Vincenzo Giannini (Suplente 1)
Rubén Esteban (Suplente 2)

A mis padres, Ángel y Adita.

A mi hermana, Ruth.

A Eric.

El capvespre ha enrogit els arbres violeta.

La passió segons Renée Vivien,
Maria-Mercè Marçal

[*El atardecer ha enrojecido los árboles violetas.*]

RESUMEN

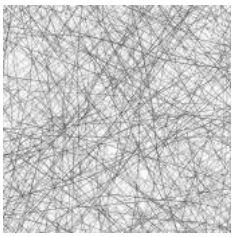

La comunidad científica ha prestado una gran atención a la interacción de la luz y la materia en el régimen de acoplamiento fuerte desde su primera realización experimental a finales de los años ochenta. Cuando fotones y excitones se acoplan fuertemente, aparecen unos nuevos estados, los polaritones, que se componen a la vez de luz y materia. Precisamente, es en esta naturaleza híbrida donde reside su gran potencial, que hace que los polaritones combinen propiedades de sus dos constituyentes: la coherencia de la luz y la interacción de la materia. Aparte del interés que despiertan por los fenómenos tan fascinantes que experimentan (tales como la dispersión estimulada, la formación de condensados o la posibilidad de funcionar como un láser), los polaritones son la base de numerosas aplicaciones, por ejemplo, en el campo de la información y comunicación cuánticas.

En el régimen de acoplamiento fuerte, los fotones y los excitones se benefician mutuamente, de forma que los polaritones pueden llegar a obtener mejores resultados que cualquiera de sus dos componentes sin la presencia del otro. En esta tesis se estudia el uso de la interacción entre la luz y la materia desde las dos posibles perspectivas: cuando los excitones modifican las características de la luz y cuando un campo electromagnético mejora la acción de los excitones.

FOTONES ayudados por excitones

Muchas aplicaciones requieren la generación bajo demanda de fotones individuales, lo que ha llevado al desarrollo de diferentes configuraciones para la creación de dichas fuentes de luz no clásica. En concreto, el acoplamiento fuerte entre luz y materia surgió como un nuevo paradigma en la generación de fotones uno a uno, donde el comportamiento no lineal que se precisa procede de la componente excitónica. Se observó que la anarmonicidad en la estructura de los niveles de energía propia de los sistemas en los que la luz y la materia están fuertemente acopladas daba lugar a fuertes correlaciones en los fotones emitidos. Este mecanismo fue estudiado para un número reducido de emisores, y se entendió que la presencia de un número mayor eliminaría el efecto deseado. En la primera parte de esta tesis, se estudian precisamente la coherencia de la luz emitida por un conjunto mesoscópico de emisores acoplados al campo electromagnético de una cavidad. En concreto, se estudian dos configuraciones experimentales: moléculas orgánicas acopladas a una nanocavidad plasmónica y puntos cuánticos embebidos en una microcavidad dieléctrica.

Nuestros resultados teóricos muestran un cambio en las correlaciones de los fotones emitidos cuando los emisores están acoplados a un modo de cavidad, de forma que el régimen de acoplamiento fuerte permite la creación de fuertes no linealidades incluso cuando el número de emisores es grande. Sorprendentemente, se obtiene un fuerte carácter no clásico como resultado de la interacción entre un subsistema bosónico (modo fotónico en una cavidad) y otro casi bosónico (un número mesoscópico de emisores). Por lo tanto, las correlaciones entre los fotones no solo se mantienen, sino que se incrementan debido a la interacción entre la luz y la materia. Esto reafirma el régimen de acoplamiento fuerte entre luz y materia como camino para la generación de luz no clásica más allá del caso de un solo emisor.

EXCITONES ayudados por fotones

Se ha demostrado que la modificación del entorno electromagnético de sistemas excitónicos mediante su colocación dentro de cavidades ópticas altera su acción de múltiples formas. Por ejemplo, se ha demostrado que en condiciones de acoplamiento fuerte se puede modificar el ritmo al que sucede una reacción química. Esto supuso el comienzo de un nuevo campo, cuyo objetivo es el control de diferentes propiedades químicas y materiales con la conveniente manipulación de las características de los polaritones. En este marco, se ha aprovechado también la formación de estados deslocalizados en el régimen de acoplamiento fuerte para aumentar el alcance y el ritmo del proceso de transporte de excitones en diferentes plataformas. En la segunda parte de esta tesis estudiamos este efecto, esto es, la modificación del proceso de transporte debido al acoplamiento de los excitones al campo electromagnético dentro de una cavidad. En concreto, hemos analizado dos sistemas: dos familias diferentes de moléculas orgánicas situadas en la misma cavidad y una unidad fotosintética típica presente en ciertas bacterias, también interaccionando con un modo fotónico.

Transferencia de energía a largas distancias entre dos conjuntos de moléculas ha sido obtenida experimentalmente considerando diferentes distribuciones de las partículas dentro de la cavidad. En nuestro trabajo proponemos una descripción teórica que arroja luz sobre el mecanismo físico responsable de este efecto. La formación de polaritones en el régimen de acoplamiento fuerte produce una mezcla de estados donadores y aceptadores que, junto con la presencia de vibraciones en las moléculas orgánicas, permiten que la transferencia de energía pueda tener lugar entre distancias más allá de la escala nanométrica.

También se ha analizado la modificación del transporte de excitones mediante el acoplamiento a un campo electromagnético en sistemas biológicos. Nuestros cálculos teóricos muestran que la dinámica de los excitones en la unidad fotosintética típica presente en ciertas bacterias se modifica en alto grado por su interacción con una cavidad óptica. El transporte de excitones se acelera en tres órdenes de magnitud, de forma que el complejo ubicado al final del proceso se puebla considerablemente sólo unos pocos femtosegundos después de la absorción inicial de la excitación. Nuestro modelo muestra el papel que juegan los polaritones, demostrando la robustez de este mecanismo frente a cambios en los parámetros del sistema.

Nuestros resultados teóricos en ambos sistemas presentan al acoplamiento fuerte entre luz y materia como una valiosa herramienta para la caracterización, ajuste y optimización de los mecanismos de transporte de excitones tanto en medios naturales como artificiales.

ABSTRACT

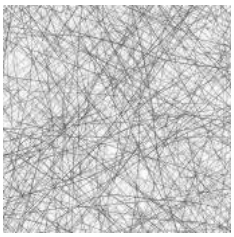

The interaction of light and matter in the strong coupling regime has been the focus of considerable research attention since its first experimental realization in the late 1980s. When photons and excitons are strongly coupled, new hybrid light-matter states arise, the so-called polaritons. Their huge potential and particular appeal lie precisely in their composite nature, as polaritons combine properties of their two constituents: the high coherence of light and the strong interaction of matter. Beyond their fundamental interest —mostly due to the intriguing phenomena they display, such as stimulated scattering, lasing, or condensation—, polaritons are in the basis of numerous applications. Not only are they valuable in the field of quantum information processing, but several polariton-based devices have emerged over these years.

In the strong coupling regime, both photons and excitons benefit from each other, and polaritons may outperform their separated constituents by themselves. In this thesis, we address the good of light-matter interaction from the two possible perspectives: the use of excitons to modify the light character, and the use of an electromagnetic field to improve the exciton performance.

PHOTONS taking advantage of excitons

The generation of single photons on demand is a prerequisite in numerous applications, thus leading to the development of several schemes for the creation of such nonclassical sources of light. In particular, strong light-matter coupling emerged as a new paradigm for the generation of photons one by one, where the required nonlinear behaviour comes from the excitonic component. The anharmonicity of the energy level structure in strongly coupled light-matter systems was found to give rise to photon correlations in the scattered field. This mechanism was explored for a reduced number of emitters, and it was understood that the presence of an increased number of them would remove the desired effect. In the first part of this thesis, we precisely study the coherence properties of the light scattered from a mesoscopic collection of emitters coupled to the electromagnetic field within a cavity. Specifically, two experimental configurations are explored, organic molecules coupled to plasmonic nanocavities and quantum dots embedded in dielectric microcavities.

Our theoretical results show that photon correlations become altered when emitters are coupled to a cavity mode, such that the strong coupling regime allows for large non-

linearities even when the number of emitters is large. Strong nonclassical features are surprisingly obtained as a result of the interaction between a purely bosonic subsystem (photonic mode in a cavity) and a quasi-bosonic one (mesoscopic emitter ensemble). Photon correlations are thus not only retained, but enhanced due to the light-matter interaction. This reinforces strong light-matter coupling as a route for the generation of nonclassical light beyond the single-emitter level.

EXCITONS taking advantage of photons

The modification of the electromagnetic environment of excitonic systems by placing them inside optical cavities has been shown to alter their performance in multiple ways. For instance, the rate of a chemical reaction was found to change under strong-coupling conditions. This opened up a new field, with the prospect of controlling chemical and material properties with the appropriate tailoring of the polaritonic characteristics. In this context, the formation of delocalized states in the strong-coupling regime has been also exploited for the enhancement of the spatial range and rate of exciton transport in diverse platforms. In the second part of this thesis we study this effect, that is, the modification of the transport process due to the coupling of excitons to the electromagnetic field within a cavity. In particular, two different systems are analyzed, distinct families of organic molecules hosted in the same optical cavity and an archetypal bacterial photosynthetic unit also interacting with a photonic mode.

Long-range energy transfer between two collections of molecules has been experimentally obtained considering different arrangements of the particles within the cavity. We provide a theoretical description which sheds light into the physical mechanism responsible for this effect. The formation of polaritons within the strong-coupling regime produces a mixing of donor and acceptor states which, together with the presence of vibrations in organic molecules, enable energy transfer to occur between distances beyond the nanometre scale.

Exciton transport in biological complexes has been also shown to be altered due to the coupling to an electromagnetic field. Our theoretical computations demonstrate that the exciton dynamics in an archetypal photosynthetic unit is greatly modified by its interaction with an optical cavity. Exciton transport is accelerated in three orders of magnitude, such that the complex at the end of the process is considerably populated within only a few femtoseconds after the initial absorption of the excitation. Our model reveals the role played by polaritons, showing the robustness of this mechanism against changes in the system parameters.

Our theoretical findings in both systems unveil strong light-matter coupling as an invaluable tool for the characterization, tailoring, and optimization of the mechanisms responsible for exciton transport in both natural and artificial systems.

Each one of these two parts is presented in a separated chapter, being these two preceded by an introductory part. Specifically, the text is organized as follows:

Chapter 1 | This first chapter provides an overview of the field that encompasses this thesis. As the work here developed falls within the area of cavity quantum electrodynamics, we start discussing some basic ideas related to the interaction of light and matter at the quantum level. The specifics of the strong coupling regime are thoroughly analyzed, summarizing the diverse experimental realizations and highlighting its applications. Then, we present an introduction to the use of light-matter coupling for the generation of single-photon sources (photons modified by excitons) and for the improvement of the exciton performance (excitons modified by photons). These two last sections are more clearly focused on the particular areas of our research activity.

Chapter 2 | The theoretical formalism used throughout this thesis is presented next, with the aim to give a detailed account of the equations and methods used for the description of hybrid systems and light-matter interactions. To this end, we review the standard formalism describing the dynamics of open quantum systems, introducing both the Lindblad and the Bloch–Redfield master equations. Next, we present the quantum description of light-matter systems, discussing the Jaynes–Cummings model in detail. After this introductory part, we focus on the description of the coherence properties displayed by a light beam, distinguishing the particular features associated with nonclassical light sources. Finally, the quantum description of organic molecules is presented, introducing the vibrational degrees of freedom in terms of a reservoir of harmonic oscillators to which the excitonic transition is coupled.

Chapter 3 | This chapter contains the first part of the original results of this thesis, concerned with the use of strong light-matter coupling for the modification of the statistics of the light coming from hybrid systems. In particular, we study photon correlations in mesoscopic ensembles of emitters coupled to a cavity resonance. The two procedures that lead to photon antibunching —namely, the photon blockade effect and destructive quantum interferences— are explored in two different experimental setups, highlighting the differences between them. Specifically, the analysis is carried out for a collection of organic molecules coupled to a plasmonic nanocavity and for a collection of quantum dots embedded in a dielectric microcavity.

Chapter 4 | The second part of the results is presented in this chapter, which focuses on the modification of the exciton performance due to the strong coupling to a cavity mode. The process of exciton transport is analyzed in two different systems, namely, two collections of molecules strongly coupled to a common cavity mode, and an archetypal bacterial photosynthetic unit. The modification of the exciton dynamics due to the interaction with the electromagnetic field within the cavity is analyzed, revealing the participation of the different polaritons in this mechanism, as well as the role played by vibrations.

Chapter 5 | In this brief final chapter, after summarizing the main results of this thesis, we present some general conclusions.

A series of Appendices are added at the end, which mainly expand the information discussed in Chapter 2 with the aim to make it more accessible and provide further details.

These correspond to part of the personal notes that I have been writing over these years, which may be helpful for the non-expert reader.

CONTENTS

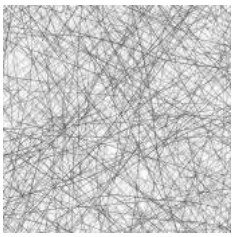

CHAPTER 1

INTRODUCTION

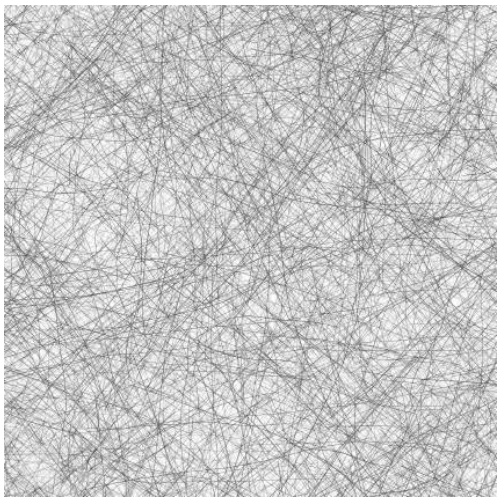

CHAPTER 1

INTRODUCTION

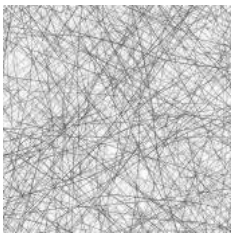

This thesis is devoted to different quantum phenomena emerging from the interaction of light and matter in the strong coupling regime —the modification of the statistics of the light coming from hybrid systems and the enhancement of exciton transport due to the coupling to a cavity mode. This introduction aims to give an overview of these areas, as well as to provide the key concepts that will appear throughout the text. Nonetheless, the more technical details and the theoretical formalism developed around these topics will be considered further in Chapter 2.

This chapter starts with some general insights into the issue of the interaction of light and matter in Section 1.1 (we elaborate on the strong coupling regime in Appendix A, giving an overview of the principal experimental realizations and its main applications). This first part of the chapter is conceived as an introductory section for these graduated in physics without specific knowledge in this field, hence we suggest the expert reader skip this preliminary section. In Section 1.2 we look at photons and the characteristics of the emitted light when modified by excitons, whereas in Section 1.3 the focus is on excitons, specifically on the modification of their properties by the coupling to a photonic mode.

1.1 Coupling light and matter

1.1.1 The field of cavity quantum electrodynamics

The interaction between matter and light, in the regime in which the quantum nature of light is revealed, is studied by the field of **quantum electrodynamics** (QED) [1]. Interesting phenomena arise in this regime, such as the quantum superposition of states and the presence of entanglement. Since the beginning of its formulation in the 1920s, a number of physical effects have been interpreted under the framework of this theory, as the case of the the Lamb shift [2] (the splitting in certain energy levels of the hydrogen atom is explained as the result of the interaction with vacuum energy fluctuations) or the Casimir effect [3] (the attractive force between two mirrors is described from the radiation

pressure of vacuum). Specifically, when light is presented in the form of electromagnetic modes confined in a cavity, we refer to **cavity quantum electrodynamics** (cavity QED for short) [4]. This theory is built on the basis of single quanta of light (**photons**) and single matter excitations (**excitons**). The interaction between photons and excitons is also the scope of this thesis.

An effect of the interaction of matter with the vacuum electromagnetic field is the phenomenon of **spontaneous emission** experienced by an emitter in its excited state. The possibility to enhance its radiation rate by modifying the electromagnetic environment was first noted by Purcell in 1946 [5]. In this context, the experimental observations of Drexhage in 1970 are remarkable [6]. The modification of the spontaneous emission rate of fluorophores when varying the distance from a mirror was reported, hence demonstrating the fact that the environment of the emitter clearly determines the properties of the emission. This idea about the manipulation of the electromagnetic environment of matter excitations started a broad field of research, mostly focused on the control of the natural lifetime and the emission pattern of emitters for the development of single-photon sources. When photons and excitons interact in this regime in which the intrinsic nature of both constituents is preserved, they are said to work within the **weak coupling regime**.

Photons and excitons are the building blocks of cavity QED, and both their strengths and weaknesses are identified. Photons are endowed with coherence, but barely interact. By contrast, excitons may interact strongly, although their action is limited to short distances and, worse still, they become defenceless against decoherence processes. Interestingly enough, when the coupling between matter and light is sufficiently strong so as to overcome any other decay or decoherence channel, new quasiparticles arise, the **polaritons**. These hybrid light-matter states combine characteristics of both constituents —they display coherence properties due to their photonic component as well as strong interactions due to their excitonic component. This regime in which both photons and excitons benefit from each other through the appearance of polaritons is known as the **strong coupling regime**.

New phenomena arise within the strong coupling regime, where either excitons benefit from their electromagnetic environment, or photons turn the presence of matter excitations to their advantage. Therefore, a number of applications exploit either the light or the matter part of these hybrid objects. In this thesis we deal with one specific problem of each area: we study the statistics of photons when modified by the presence of excitons, and analyze the energy-transfer process between excitons when interacting with a photonic mode.

1.1.2 Cavity QED ingredients

In the arena of light-matter coupling, many are the physical setups designed for the fruitful interaction of all kinds of excitons with some electromagnetic field at the quantum level. The important issue about cavities is that they increase the probability of the interaction of the emitter with the electromagnetic field, since the time that photons spend in the surroundings of the emitter is large in comparison to free space. Either as a response to restrictive external conditions or in the pursue of the observation of novel phenomena, a variety of physical configurations have been developed to meet specific requirements.

What follows is a closer look at the two main ingredients of cavity QED —optical cavities and quantum emitters.

Optical cavities

A specific arrangement that confines light is referred to as an **optical cavity**. The simplest models consist of two opposing mirrors, either flat or spherical. This is the case of the **Fabry–Pérot cavity**, composed of two flat, highly-reflecting mirrors separated by a certain distance. Standing waves are formed in between, such that the allowed wavelengths are those that commensurate the optical length of the cavity. All other electromagnetic modes are suppressed due to destructive interference, thus leading to a discrete energy spectrum. There also exist **optical resonators** in which travelling waves are guided and forced to interact with matter. There exist many structures capable of sustaining electromagnetic modes. Before summarizing the most popular optical cavities, we refer to some important quantities that characterize them:

- The **quality factor** Q of a cavity with a resonant mode of frequency ω_C is defined as:

$$Q \equiv \frac{\omega_C}{\gamma_C} , \tag{1.1}$$

  where γ_C represents the frequency width (the full width at half maximum) of the resonance. It should not be confused with the **finesse** F, the ratio between the separation of consecutive cavity resonances $\Delta\omega_C$ and the linewidth: $F \equiv \Delta\omega_C/\gamma_C$. This linewidth comes from the various decay channels that cavities present —they suffer from absorption, scattering by defects, interaction with the crystal lattice, etc. The quality factor can be taken as a measure of the **cavity lifetime**, $\tau_C = Q/\omega_C$, where $\tau_C = 1/\gamma_C$ represents the lifetime of an excitation within the cavity. Sometimes, complex frequencies are used, such that its imaginary part is related to the cavity linewidth through the expression: $\mathrm{Im}[\omega_C] = \gamma_C/2$.

- Another representative quantity is the **effective spatial volume** V_{eff} of the resonance supported by the cavity, which can be given in units of the **wavelength of the light** cubed, λ_C^3, or in terms of $(\lambda_0/n)^3$ if we consider the refractive index n characteristic of the material and the value of the wavelength in vacuum λ_0. By confining light in minute spatial volumes, the amplitude of the electric field increases significantly and thus, in turn, the coupling strength between light and matter. Actually, the **light-matter coupling constant** g behaves as:

$$g \propto \frac{1}{\sqrt{V_{\mathrm{eff}}}} ,$$

  hence small spatial volumes are required for achieving large values of the light-matter interaction (Equation 2.37).

Both quality factor and effective volume characterize cavities, being the ratio Q/V_{eff} a relevant parameter —this combination appears in the expression of the Purcell factor, as discussed below. Then, cavities with a high Q-factor and with small mode volumes are desired to observe quantum effects in the interaction of light and matter.

There exist several semiconductor, metallic, and dielectric structures used to confine

an electromagnetic mode, apart from the planar cavities consisting in two opposing mirrors previously mentioned. We now present a brief discussion of the different types of cavities with the help of some interesting references [7, 8], differentiating between semiconductor microcavities and plasmonic nanocavities.

Semiconductor microcavities Semiconductors are particularly appropriate materials since its characteristic structure of energy bands separated by gaps of forbidden energies allows for the finely-tuned control of electronic excitations. A semiconductor microcavity usually consists in a planar nanostructure made up of multiple layers with alternating values of the refractive index so as to produce the confinement of the light. Semiconductor microcavities are characterized by a high quality factor, ranging from a few thousands to more than a hundred million [9]. Among the various high-quality optical microcavities, three configurations are the most commonly used:

- **Planar configurations**: Many semiconductor cavities make use of planar surfaces, such as pillar or Bragg microcavities [10, 11]. Pillar (or micropost) cavities consist of a pair of distributed Bragg mirrors which provide the confinement of the light in the longitudinal direction. Thanks to total internal reflection, the light is also confined in the radial direction. Its design favours the positioning of quantum dots inside the cavity, as well as the manipulation of the emission coming out from one of the cavity extremes [12, 13]. The mode volume is usually around $(\lambda_0/n)^3$, and typical values of the Q-factor, usually limited by scattering loss, are around a few 1000s. These cavities usually operate at low frequencies, where absorption losses are small and, thus, large Q-factors can be achieved. For instance, micropillar cavities exhibiting quality factor values exceeding 20000 [14, 15] and even 150000 [16] have been reported.

- **Whispering-gallery resonators**: Semiconductor microdisks are an example of whispering-gallery mode cavities, where the wave travels along the border of the disk [17]. The confinement is produced due to total internal reflection at the curved boundary between two materials with different refractive indices. Typical values of the mode volume are around several $(\lambda_0/n)^3$. The Q-factor is usually of the order of 10000, limited by absorption losses (unless operating at low frequencies) and the surface roughness [18], although there are some examples with ultrahigh Q-factors in excess of a hundred million [9]. Apart from disk or toroidal configurations, there also exist spherical microresonators supporting whispering-gallery modes [19].

- **Photonic-crystal cavities**: These materials are composed of repeated regions of high and low dielectric constant [20]. This spatial pattern creates a spectral bandgap of forbidden frequencies for the light propagating through the crystal, called **photonic bandgap** (optical analogue of the forbidden energy bandgap for electrons in semiconductor materials). Photons with energies in the range of this photonic bandgap cannot travel through the material since waves reflected at the interfaces of regions with different dielectric constant interfere destructively. Nevertheless, the presence of some defects in the crystal may create localized photonic states within the gap. Thus photons with frequencies lying in the photonic bandgap cannot propagate through the crystal but be confined to defects, acting in turn as a microcavity. Actually, a point defect results in a microcavity, a line defect in a waveguide, and a

planar defect behaves as a perfect mirror [20, 21]. Through the radius and the type of the point defect, both the frequency and the symmetry of the localized photonic mode can be controlled [22]. Photonic-crystal cavities are characterized by high Q-factors, typically larger than 10^6, and mode volumes around $(\lambda_0/n)^3$ [23, 24, 25]. Purcell factors are really tunable in these cavities [26].

These solid implementations have the advantage of portability, as well as a fixed embedding. In comparison to cavities for atom systems, where emitters either move around or need trapping, quantum dots are usually grown directly in the resonant structure. This make easier to reduce the cavity volume and, in turn, reach higher values of the light-matter coupling. In solid-state platforms the control over the matter excitations is better, but they suffer from much higher decoherence by the coupling to the phononic modes of the semiconductor material.

Plasmonic nanocavities Metallic structures can support plasmonic modes characterized by a large sub-wavelength electromagnetic field. This interesting property has given rise to cavities built on the basis of plasmonic nanostructures, where plasmons display similar quantum phenomena than photons (such as interference effects and entanglement [27, 28]).

When metal nanostructures interact with light, the free electron gas of the metal particle can sustain oscillations of the charge density, called **plasmons**, with different resonance frequencies [29]. These collective excitations of the conduction electrons can be sustained within the bulk of the metal as well as confined at the interface between a metal and a dielectric medium. The latter are named **surface plasmons**, and we can differentiate two types based on the geometry of the interface under consideration:

- Flat metal surfaces support the propagation of **surface plasmon polaritons** (SPP) through the dielectric interface. They are propagating, dispersive electromagnetic waves coupled to the electron plasma of a conductor at a dielectric interface.
- Metal particles of dimensions smaller than the wavelength of the applied electromagnetic field sustain **localized surface plasmons** (LSP). They are non-propagating excitations of the conduction electrons of metallic nanostructures coupled to the applied electromagnetic field.

Additionally, we should mention **plasmonic surface lattice resonances** (PSLR), that is, collective resonances created in regular arrays of metallic nanoparticles [30]. These resonances arise as a result of the interaction between the localized plasmons associated with the nanoparticles and the light diffracted by the array. They are characterized by a very narrow spectral width (a few meVs), between one and two orders of magnitude lower than those associated with SPPs and LSPs. The excitation of plasmonic resonances can be done by direct illumination, while some momentum-matching techniques are required to excite propagating SPPs [31, 32].

The main properties of surface plasmons are the intense electromagnetic field enhancement and the sub-diffraction confinement of the modes. Plasmonic nanocavities with sub-wavelength mode volumes have been obtained down to $10^{-4}(\lambda_0/n)^3$ [33]. The price to pay for the large confinement is that these structures suffer from large dissipative

losses due to the high absorption of metals, reducing in turn the quality factor of the cavity (usually below 100). Nevertheless, they enable coupling strength values significantly larger than those associated with semiconductor cavities.

Several metallic configurations provide the platform to the generation of the different types of surface plasmons. Propagating plasmons have been generated in both flat and perforated metallic layers [34, 35], while different ensembles of nanoparticles and single nanostructures give rise to localized modes (involving spheres [36], cubes [37], triangular plates [38], particle-on-film systems [39, 40], bowtie configurations [41, 42], and some other dimers [43, 44]). More complex geometries give rise to both propagating and localized plasmons, including the previously mentioned arrays of metallic nanoparticles creating PSLRs [45, 46].

Quantum emitters

The matter component may involve a wide variety of emitters, ranging from atoms and molecules to quantum dots, NV-centres, or real spins in different solid state materials, as well as semiconductor circuits forming artificial atoms. Before summarizing their main features, we note some important quantities characterizing emitters in general:

- Emitters often present a preferential transition, which is the only one considered when working within the **two-level approximation** —the presence of other energy levels beyond the two states involved in that transition are not taken into account as long as they do not play an important role. Transitions between two states are characterized by the **transition frequency** and the **transition dipole moment**.

- Once emitters are excited, this energy can be dissipated either **radiatively** or **nonradiatively**, with associated **decay rates** γ_r and γ_{nr}, respectively. As mentioned above, these are not intrinsic to the emitter, but strongly dependent on its environment. Radiative transitions involve the emission of a photon, in contrast to nonradiative processes. Diverse dissipation channels are present depending on the case, such as vibrational relaxation, energy transfer to the environment, or quenching by other emitters. They may also suffer from **dephasing**, a loss of coherence due to the interaction with the environment.

- The lifetime of an excite state is the average time that the emitter stays in that state before relaxation to the ground state. The observed **lifetime** of an emitter is the inverse of the total **decay rate**: $\tau = 1/(\gamma_r + \gamma_{nr})$, where γ_r and γ_{nr} are the decay rates previously defined.

- The luminescence **quantum yield** $\mathcal{Q}$ associated with certain emitters is defined as the ratio of the number of photons emitted with respect to the number of photons absorbed. It can be given in terms of the previous decay rates as:

$$\mathcal{Q} = \frac{\gamma_r}{\gamma_r + \gamma_{nr}} \,. \tag{1.2}$$

  Fluophores, compounds that efficiently emit light once excited, present values of the quantum yield close to one.

There are several examples of quantum emitters that are used in the field of cavity QED, some of which are referred now:

- **Single atoms** and **ions**: Atoms and ions present a very clean two-level structure (their fluorescence emission lies in the optical and microwave regimes), with very narrow linewidths and practically without dephasing. Typical radiative lifetimes are around 30 ns, that corresponds to a linewidth of the order of 0.1 μeV. Both atoms and ions possess long coherence times [47], and usually operate at low temperature (although laser cooling is also used). As all atoms are exactly the same, atomic states are not only well-known, but completely reproducible.

- **Quantum dots**: Quantum dots are semiconductor particles with a discrete energy level structure which makes them similar to atoms. Their size is of the order of a few nanometres, and they are commonly grown in inorganic semiconductor microcavities. They present large electric dipole moments, larger than typical values of atomic transitions, and long relaxation and decoherence times. They can be engineered to have a wide range of optical properties, and these vary enormously with the specific material —their fluorescence emission may range from 250 to 1550 nm, and their radiative lifetimes may be from 0.1 to 10 ns [48]. Depending on the case, they can operate at room temperature, although they are commonly used at low temperature to diminish phononic dephasing and decoherence.

- **NV-center** in diamonds: The nitrogen-vacancy (NV) colour center in diamonds, NV-center for short, is a point defect that consists in the replacement of two neighbouring carbon atoms by one nitrogen atom and a vacancy [49, 50]. This pair can be charged with an additional electron (NV^-) or remain neutral (NV^0). The energy level structure of an NV-center is discretized and resembles that of an atom. Their fluorescence emission lies within the interval 640–720 nm, and the radiative lifetime is in the order of 10 ns. They can also operate at room temperature.

- Artificial atoms in single-layer and few-layer **2D materials**, such as transition metal dichalcogenides (**TMDC**): TMDCs are semiconductors composed of a layer of some transition metal (such as Mo, W...) placed between two layers of some chalcogen atom (such as S, Se, Te...) [51]. These atomically thin layered materials support localized excitons, whose optical emission exhibits narrow linewidths ($\sim 100\mu$eV) [52, 53, 54]. The main TMDCS presenting localized emission from quantum defects are tungsten diselenide (WSe_2) [55], molybdenum diselenide ($MoSe_2$) [56], and tungsten disulfide (WS_2) [57].

- **Organic molecules**: The more involved structure characteristic of organic molecules, presenting vibrational states on top of the electronic levels, translates to an increased broadening. Although typical values of the radiative lifetime are about a few nanoseconds, the associated linewidth is usually of some meV due to nonradiative broadening. It is precisely the large value of the dipole transition moment, usually around a few Debye, their main advantage. The fluorescence emission lies in the visible regime and they can operate at room temperature.

- **Molecular aggregates**: Molecular aggregates are collections of molecules gathering together due to non-covalent interactions [58]. An example of dye-molecule aggregates are the so-called **J-aggregates** [59], assemblies of fluorescent molecules

whose optical properties change importantly with respect to single molecules [60]. The absorption peak shifts to lower frequencies and becomes narrower when the aggregate is formed, and they present a narrow resonance emission band with a very small Stokes shift (that is, with hardly any difference between the peaks in absorption and emission spectra). In contrast, the absorption band in H-aggregates is shifted to longer frequencies with respect to the monomer absorption band, and they present low fluorescence.

Organic and inorganic platforms present Frenkel and Wannier–Mott excitons, respectively. An **exciton** is a an electron-hole pair which forms a bound state due to the electrostatic Coulomb force. The binding energy of an exciton is the energy of its ionization to a non-correlated electron-hole pair. **Frenkel excitons** are the ones formed in materials with a small relative permittivity ($\epsilon \sim 3$). Due to the strong Coulomb interaction within the electron-hole pair, these type of excitons tend to be small, of the order of the size of the unit cell, and present binding energies of the order of hundreds of meV. This is the case of organic materials, where there may be excitons located in a single molecule. Conversely, in semiconductor structures the hopping between lattice sites usually exceeds the Coulomb interaction, so excitons are delocalized, being extended over tens of unit cells. These are the so-called **Wannier–Mott excitons**, whose binding energies are typically of the order of a few meV. Apart from these two, other types of excitons may be defined. Advances in the technology related to the growth of semiconductor structures has led to the fabrication of confined systems that create potential wells for electrons and holes in an artificial manner.

In Chapter 3 we study the photon statistics of the light coming from two different configurations —quantum dots in semiconductor microcavities and organic molecules in plasmonic nanocavities. There, we will further explore the own peculiarities of these configurations, since the statistics of the emitted light is clearly influenced by the typical parameters associated with them.

1.1.3 Regimes of light-matter interaction

In the interaction of light and matter two different regimes are usually distinguished according to the balance between the coupling strength g and losses (either from the cavity, γ_C, or emitters, γ_{QE}), as we have introduced in Subsection 1.1.1:

- When the light-matter coupling remains weak, the system keeps within the so-called **weak coupling regime**. There, the principal feature consists in the modification of the spontaneous emission of emitters owing to its coupling to the resonant cavity, known as **Purcell effect**. The incoherent processes dominate this regime: $g \ll \gamma_C, \gamma_{QE}$.
- On the contrary, if the light-matter interaction becomes larger than any other dissipation channel, the system may enter the **strong coupling regime**. As a result of the rapid exchange of energy between cavity and emitters, the new eigenstates of the system turn out to be a quantum mixture of matter and light. These are referred to as **dressed states** or **polaritons**. The coherent term dominates this regime: $g \gg \gamma_C, \gamma_{QE}$.

Apart from these two, it has been recently explored the case in which the interaction becomes even stronger. This is called **ultra-strong coupling regime**, that takes place when the coupling strength is comparable to the transition frequencies in the system [61]. In the following, we summarize the main features of each one of these regimes.

Weak coupling regime

The **Purcell effect** refers to the variation of the spontaneous emission of a quantum emitter when placed inside a cavity, as we have already mentioned. The presence of the cavity alters the electromagnetic environment of the emitter, modifying in turn its emission rate.

Purcell factor An atom in its excited state experiences an irreversible exponential decay into the free space due to the interaction with the continuum of modes characterizing the vacuum. The rate of the transition can be computed form the Fermi's golden rule (Equation F.8), such that the rate is proportional to the **density of states in free space** ρ_{free} (vacuum density of states):

$$\rho_{\text{free}} = \frac{\omega_0^2}{\pi^2 c^3} \, .$$

This is the number of modes per unit volume with frequency ω_0. If we consider the dipole approximation for the interaction between the electromagnetic field and emitter (see Subsection 2.2.3), the vacuum density of states yields the following expression for the **spontaneous emission rate** of the emitter in free space [21]:

$$k_{\text{free}} = \frac{\omega_0^3 \, \mu_{\text{eg}}^2}{3\pi\epsilon_0 \hbar c^3} \, , \tag{1.3}$$

where μ_{eg} is the dipole moment of the transition and ϵ_0 is the vacuum permittivity. When the system is not in free space but located inside a cavity, the density of states changes. If we consider the simple case of a single-mode cavity, characterized by a frequency ω_{C} and radiative broadening γ_{C}, the density of states turns to:

$$\rho_{\text{cav}}(\omega) = \frac{\gamma_{\text{C}}}{2\pi V_{\text{eff}}} \frac{1}{(\gamma_{\text{C}}/2)^2 + (\omega - \omega_{\text{C}})^2} \, ,$$

where we have considered a Lorentzian profile associated with the cavity mode. There, V_{eff} is the effective volume of the cavity resonance. At resonance (that is, $\omega_{\text{C}} = \omega_0$) and considering a perfect matching between the field and the dipole orientation, the decay rate for the atom within the cavity reduces to:

$$k_{\text{cav}} = \frac{3}{4\pi^2} \left(\frac{\lambda_0}{n} \right)^3 \frac{Q}{V_{\text{eff}}} \, k_{\text{free}} \, , \tag{1.4}$$

where we have introduced the expression for the cavity Q-factor (Equation 1.1). The transition wavelength in vacuum is $\lambda_0 = 2\pi c/\omega_0$, and n is the refractive index. Therefore, there exists an enhancement of the spontaneous emission. As a consequence, the lifetime of an excited emitter is not an intrinsic property of the emitter, but depends on its electromagnetic environment. The **Purcell factor** is defined as the ratio $k_{\text{cav}}/k_{\text{free}}$, and from Equation 1.4 we have:

$$F_P = \frac{3}{4\pi^2} \left(\frac{\lambda_0}{n} \right)^3 \frac{Q}{V_{\text{eff}}} \, , \tag{1.5}$$

which is practically the ratio between the density of states within the cavity and at free space: $\rho_{\text{cav}}(\omega_0)/\rho_{\text{free}}$ (the missing factor 3 stems from not considering the dipole moment randomly oriented, but perfectly matching the cavity field [62]). This expression for the Purcell factor gives the maximum rate enhancement, and it takes place when the emitter fulfils: to be placed at the maximum of the field mode, to be at resonance with the cavity field, and to be oriented along the same direction as the field. That is, it requires both spectral and spatial overlaps between the emitter and the cavity. From this expression we learn that, in order to obtain large values of the Purcell factor, the Q-factor of the cavity should be large, while the mode volume should remain small. The ratio Q/V_{eff} is not easily enhanced in practice, since for smaller cavities the Q-factor attainable is limited.

The density of states within the cavity is larger than in free space if the emitter is resonant with the cavity mode, but the density of states seen by the dipole may be smaller if it is out of resonance. In that case, the spontaneous emission is not speed up, but suppressed, and the atom remains longer in its excited state. This effect was pointed out by Kleppner in 1981, who explored the inhibition of the spontaneous emission when there is no available states to which the atom can radiate [63]. This insists on the fact that the spontaneous emission is not an intrinsic property of emitters, but depends on the available electromagnetic states provided by the surrounding medium.

Experimental observation The experimental observation of the Purcell effect requires a high-quality cavity with dimensions around the value of the transition wavelength, which was not easily attainable by that time. After the experimental observations of Drexhage with dye molecules near dielectric surfaces [6], the enhancement of the emission rate of an atom inside a high-Q cavity was finally observed by Goy *et al.* in 1983, considering a Rydberg atom [64]. Afterwards, the inhibition of the emission rate was reported by Hulet *et al.* using Rydberg atoms as well [65]. Since then, both effects have been obtained not only for atoms but also in solid-state platforms [66, 67]. For instance, the control of the spontaneous emission thanks to semiconductor microcavities has been explored as a means to reduce the threshold of lasers [68, 69]. There exist various semiconductor structures engineered to build microcavity lasers, such as the vertical cavity surface emitting laser [70], where the light is confined between two Bragg reflectors. There are many other examples where quantum dots are placed in micropillars [71], microdisks [72], and in photonic crystals too [73], with the objective of manipulate its spontaneous emission. Plasmonic cavities have been also used to this end [74, 75].

Hence the effect of the electromagnetic field on the matter component when being within the weak coupling regime is the modification of its spontaneous decay rate. Within this regime, the role of the radiation can be thought of as a perturbation on the matter system. Indeed, the interaction can be treated with perturbation theory, and some classical analogues have been developed [76, 77]. In the preceding description, reabsorption has not been considered since its effect is weak: reabsorption produces an energy shift which is generally orders of magnitude smaller than the radiative broadening. Nevertheless, when placed inside a cavity, the probability of reabsorption of photons by the emitter increases. This rate can even overcome cavity losses, hence entering the strong coupling regime. The interaction with the cavity cannot be treated as a perturbation any more and a new description is required.

Strong-coupling regime

When the interaction between light and matter becomes so strong that overcomes the system losses, the system enters the strong coupling regime, as already explained. In contrast to the irreversible exponential decay that an excited atom suffers when being either in free space or within the weak-coupling regime, there exists a reversible exchange of energy between the emitter and the electromagnetic field at the so-called **Rabi frequency**. Single photons are repeatedly absorbed and emitted a few times before being irreversibly lost into the environment. This coherent exchange of energy, known as **vacuum Rabi oscillations**, is expected from the Jaynes–Cummings Hamiltonian [78]. This model describes, in fully quantum-mechanical terms, the system composed of a single two-level system interacting with a single mode of the electromagnetic field (see Subsection 2.2.4). In Figure 1.1 we represent the time evolution of the population associated with the excited state of a two-level system coupled to a resonant cavity mode. Three different values of the coupling constant g are considered. When the emitter is decoupled from the cavity ($g = 0$), it experiences the corresponding free-space exponential decay (purple line). For a low value of the coupling strength, the decay rate is enhanced as a result of the interaction with the cavity within the weak-coupling regime (turquoise line). Finally, when the value of g is large enough to overcome the system losses, the population of the emitter presents an oscillatory pattern, characteristic of the strong coupling regime (yellow line).

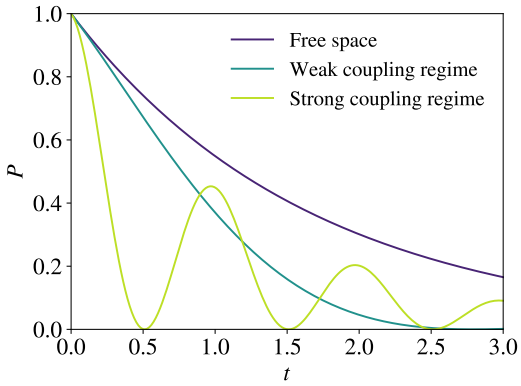

Figure 1.1. Dynamics of the population associated with the excited state of a two-level system interacting with an electromagnetic field. The population P is plotted as a function of time t for three different situations: when the emitter is completely decoupled from the cavity mode (purple line), and when the emitter interacts with the electromagnetic field within the weak (turquoise line) and strong (yellow line) coupling regimes.

Rabi oscillations manifest themselves in the spectrum as a splitting between the energies associated with the eigenmodes of the hybrid system —this energy gap is referred to as **Rabi splitting**, and it is determined by the frequency of the oscillations. As a result of the coherent exchange between cavity and emitters, the new eigenstates of the system are partly matter and partly light, the so-called **polaritons** [79]. The system composed of the electromagnetic field and the quantum emitters needs to be treated as a whole. Figure 1.2 depicts the first energy levels corresponding to the cavity (left) and to the emitter (right), where ω_0 and ω_{QE} are the respective transition frequencies. When being within the strong coupling regime (center), the **lower polariton** (LP) and the **upper polariton** (UP) are the new eigenstates, separated by the Rabi splitting Ω_{R}. The condition for strong coupling thus translates in the need for energy splitting values that exceed the linewidths of both the cavity mode and the emitter, so that the Rabi splitting is experimentally observable.

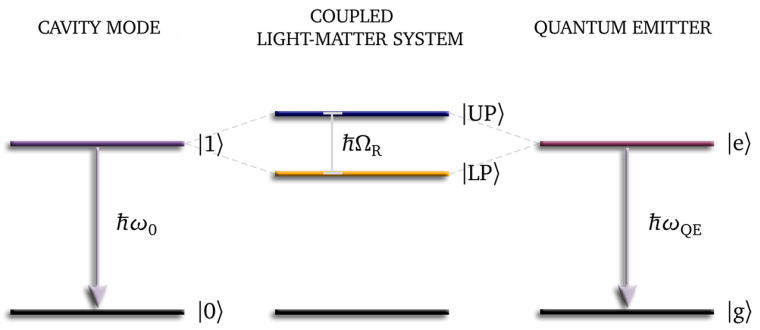

Figure 1.2. First energy levels corresponding to the cavity (left) and quantum emitter (right) for the uncoupled case, where the transition energies are $\hbar\omega_0$ and $\hbar\omega_{\mathrm{QE}}$, respectively. In the center, energy levels corresponding to the strongly-coupled system, where the new eigenstates of the first-excitation manifold correspond to the upper polariton (UP) and lower polariton (LP). The energy splitting between them is given by the Rabi frequency Ω_{R}.

The previous discussion corresponds to the case in which there is a single two-level system coupled to a single-mode cavity. Another manifestation of the splitting takes place in the anticrossing displayed by the dispersion relations of exciton and photon modes. When emitters and cavity are decoupled (or if the interaction lies within the weak-coupling regime), the spectroscopic features of the composed system (associated with exciton and photon modes) cross each other. Once the coupling is introduced, the two dispersion branches may not intersect. This energy separation is the so-called **anticrossing**, and it is a fingerprint of strong coupling. The new two branches of the dispersion relation correspond to the polaritons, and cannot be assigned to the exciton or the photon mode exclusively.

Experimental observation The presence of **Rabi oscillations** in a collection of two-level systems placed inside a cavity was first observed by Kaluzny *et al.* in 1983 [80], where the evolution of the excited state population of a collection of Rydberg atoms in a Fabry–Pérot cavity is shown. According to the Jaynes–Cummings model [78], the dynamics of the hybrid system is also characterized by the collapse and revival of coherence. These **coherence properties** were first pointed out by Cummings in 1965 [81], although only demonstrated for short times. It was in 1980 that Eberly *et al.* showed that those revivals remain at long times, and they occur periodically [82]. The persistence of the initial coherence, together with the discrete nature of the energy levels (which scale in energy as the square root of the total number of excitations in the system), are strictly a consequence of the quantum nature of the radiation field. Some experiments were developed to study the interaction of a single atom with a single mode of the electromagnetic field so as to illustrate the phenomena raising from the Jaynes–Cummings Hamiltonian. In particular, the **one-atom maser** was intensively used to this end [83, 84]. But it was not until 1987 that Rempe *et al.* observed the predicted quantum collapse and revival for the first time [85]. They used a Rydberg atom coupled to a single mode in a superconducting cavity, and measured the oscillation in the probability of finding the atom in the excited state. Since then, strong coupling has been experimentally obtained in many other configurations (although we now outline some of these realizations, see Appendix A, Section A.1, for a more detailed review).

After these first experiments aiming for the strong light-matter coupling with atoms in microwave cavities [85, 86], the first observation in the optical regime took place in 1989 [87]. Mode splitting with a **single atom** was first reported in 1992 by Thompson *et al.* [88], the same year in which strong coupling was achieved with a collection of semiconductor quantum wells in a dielectric microcavity by Weisbuch *et al.* These solid-

state platforms allows for Rabi splitting values of the order of 10 meV, as the cavity volume is considerably reduced. Strong coupling with a **single quantum emitter** was obtained in 2004 for various **semiconductor microcavities** structures [89, 90]. Due to the low binding energy of Wannier excitons in most semiconductors, these configurations usually require working at low temperatures. For this reason, **organic materials** emerged as a favourable platform: as we have mentioned, Frenkel excitons in organic semiconductors tend to present large binding energies that makes them more stable. Therefore, they are ideal for realizing strong light-matter coupling at **room temperature**. Apart from that, organic molecules display large dipole moments and high densities, hence leading to large values of the light-matter coupling. In particular, **J-aggregates** present small linewidths and large transition dipole strengths, making possible to achieve Rabi splitting values more than 10 times higher than the typical values within inorganic semiconductor cavities. Strong coupling using organic molecules was first observed by Lidzey *et al.* in 1998 [91], where a Rabi splitting value of 160 meV at room temperature was observed.

The development of **plasmonic nanostructures** able to confine light beyond the diffraction limit opened the possibility to reach even stronger coupling strengths than those provided by the previous semiconductor structures. Despite the substantial losses present in plasmonic structures, the large dipole moments and high densities displayed by organic molecules have helped to achieve the strong coupling regime in these setups. Strong-coupling was first reported using J-aggregates coupled to surface plasmon polaritons by Bellessa *et al.* in 2004, reaching a Rabi splitting value of 180 meV at room temperature [34] (300 meV in [92]). Strong coupling with a **single emitter** was first reported by using bowtie dimers by Santhosh *et al.* [93] and a nanoparticle-on-mirror cavity by Chikkaraddy *et al.* [94], both in 2016.

Properties and applications The interest raised by the strong coupling regime partly stems from the multiple phenomena exhibited by polaritons, such as stimulated polariton scattering [95, 96], parametric oscillation [97, 98], polariton lasing [99, 100], and condensation [101, 102] (see Appendix A, Section A.2, for a brief explanation of these effects and a relation of some others). Their hybrid light-matter composition lies behind some of these interesting features, as polaritons inherit characteristics from their two constituents: the distinctive **coherence** of light and the mutual **interactions** of excitons. Thus polaritons exhibit properties that neither light nor matter excitations hold themselves.

Strong coupling is also the basis for the creation of coherent **quantum superposition**. Cavity QED serves to explore the physics of open quantum systems and study diverse aspects connected to coherence and decoherence in quantum mechanics [103]. The understanding of light-matter interactions within the strong coupling regime leads to a better manipulation and control of quantum coherence and entanglement [104, 105]. The coherence properties associated with polaritons are of great interest in the field of quantum information processing [105], and the coherence present in polariton condensates are also useful in the development of quantum technologies [106, 107].

The unique properties exhibited by polaritons, as well as the increased understanding and control of light-matter interactions in the strong coupling regime, have led to the development of numerous applications. Apart from those in the field of quantum information processing, and the use of polaritons for quantum computation and simulation, several devices have their operating principle based on the formation of these hybrid

light-matter particles. For instance, the mechanism of stimulated scattering is behind the realization of low-threshold polariton lasers, ultrafast optical switches, and amplifiers. The advance in the use of new materials able to operate at room-temperature has been crucial for the development of practical applications. Several polariton-based devices have emerged, such as polariton light-emitting diodes [108, 109], switches [110], and transistors [111, 112]. Polaritons interactions are in the basis of the realization of polariton gates [113], where different implementations for usual operations are proposed [114, 115]. Some of these devices exploit the polarization bistability [116] or multistability [117, 118] of polaritons.

Therefore, strong coupling reveals itself as an invaluable tool to disclose new phenomena, and its clever use makes possible to develop original quantum optical devices. In particular, this thesis focuses on two possible applications of strong coupling that we have not mentioned so far—the modification of the **photon statistics** of a light source, and the enhancement of **exciton transport**. We further discuss these two aspects, but encompassed in a slightly broader context, in the second part of this chapter: we study the behaviour of photons when modified by excitons in Section 1.2, and the behaviour of excitons when modified by photons in Section 1.3.

1.2 Photons (modified by excitons)

Strong light-matter coupling emerged as a new paradigm for the realization of **single-photon sources**. The generation of photons one by one requires some sort of nonlinearity, and positively polaritons present a significant **nonlinear behaviour** inherited from their excitonic part. **Photon correlations** are altered when a collection of emitters are coupled to a cavity mode, and this is precisely the context of the work developed in Chapter 3. Hence, in this section, we discuss the realization of single-photon sources and the potential of strong light-matter coupling in this field.

1.2.1 Nonclassical light generation

Many applications involve the presence of single-photons sources, including secure quantum cryptography schemes or quantum computation using only linear optics and photodetection [119]. An **ideal single-photon source** emits one (and only one) photon in response to an external trigger, thus generating a (nonclassical) number state on demand. On the contrary, a coherent light beam or a thermal source do not generate Fock states, but their emission is characterized by a particular distribution around a mean number of photons [120].

Nonclassical light

The performance of tentative single-photon sources is assessed on the basis of the efficiency, defined as the fraction of photons generated per trigger, and the **second-order correlation function** $g^{(2)}(\tau)$ (see Subsection 2.3.3 for the precise definition and meaning of this magnitude). Its evolution as a function of the time delay τ gives the tendency of photons to arrive in groups, or *bunches*, as compared to coherent light. **Antibunching** takes place when $g^{(2)}(\tau) > g^{(2)}(0)$. Apart from being an explicit feature of a quantum field [121, 122], antibunching is a clear signature of single-photon sources: photons tend to be emitted equally spaced in time. Besides, the second-order correlation function at zero-time delay, $g^{(2)}(0)$, gives a measure of the statistics of the light. Specifically, it gives the probability of detecting two photons at the same time compared to the case of a coherent source. A **sub-Poissonian** light source is that with $g^{(2)}(0) < 1$, and it is also characteristic of single-photon sources: it barely emits two photons at the same time. As well as antibunching, sub-Poissonian emission is a signature of **nonclassical light** (both concepts are further discussed in Subsection 2.3.4).

The experimental observation that excited atoms emit single photons at a time, while undergoing quantum jumps, was reported by Kimble *et al.* in 1977 [123]. They studied photon statistics in the resonance fluorescence of a beam of sodium atoms excited with a laser field —specifically, the probability density $P_2(t, t+\tau)$, that represents the joint probability of photodetection at two times t and $t+\tau$. This probability density was found to increase with the time delay from $\tau = 0$, thus being the first direct measurement of **photon antibunching**. Apart from unambiguously demonstrating the nonclassical nature of radiation, this experiment constituted the first realization of a single-photon source.

Photon antibunching was later reported for a single ion stored in a radio-frequency trap [124]. Beyond atomic systems, the development of inorganic semiconductors led to the observation of photoluminescence on a single quantum dot at the beginning of the 1990s [125, 126]. Different solid-state platforms started being investigated as potential single-photon sources since then. Antibunching was first demonstrated with single dye molecules [127], NV-centers [128], and quantum dots [129] over that decade. A single-photon turnstile device that generated a train of single-photon pulses was subsequently reported by Michler *et al.* in 2000 [17]. Notice that, apart from emitting single photons, a mechanism in charge of the regulation of the excitation process is usually required in many applications.

Applications of single-photon sources

Single-photon sources present numerous applications in the field of quantum information processing and quantum computing and communication [130]. Optical quantum cryptography is based on the use of single-photon Fock states [131, 132], and practical realizations of quantum key distribution protocols use either true [133, 134] or pseudo-single-photon sources [135, 136]. The problem is that, in the latter case, the presence of more than one photon may lead to leakage towards an eavesdropper [137, 138]. In linear optical quantum computing [139], single photons are used as physical qubits [140, 141], and quantum memories able to work with single-photon Fock states have been also implemented [142, 143].

Some of the applications in this area involve two-photon interference, such as the ones related to quantum teleportation [144] or the generation of polarization-entangled photons [145]. These require single-photon sources emitting identical consecutive photons, that is, exhibiting mutual two-photon interference. Sources emitting indistinguishable photons have been obtained with a semiconductor quantum dot embedded in a pillar microcavity [146] or in a photonic crystal [147]. The optical microcavity is used to tailor the emission properties, and photons can be prepared into the same quantum state, namely, the same spatial mode an polarization [12].

The squeezed nature of single photons —so that they have less uncertainty in one quadrature than a coherent state— is useful in some other applications [148], as in the context of quantum metrology [149]. Their potential to reduce the level of fluctuations below the shot-noise limit translates to an increased precision of measurements [150, 151], specially for weak absorptions, where the shot noise is more problematic. Single-photon entangled pulses are also used in procedures related to positioning and clock synchronization [152], where electromagnetic pulses are repeatedly sent over a particular distance and the time of arrival is measured. Besides, the creation of specific entangled states from single photons allows for quantum optical lithography [153], where entanglement has been used to beat the diffraction limit.

Generation of single photons

Due to the broad variety of applications, the production of single photons on demand has focused great efforts. Different schemes have been developed to this end, including the generation of true and approximate single-photon emission. In a coherent light source, such as a laser, the photon number follows a Poissonian distribution [120]. **Attenuated laser signals** with an average photon number much less than one are approximately single-photon sources, although there always exists a non-zero probability of generating more than one photon. Nevertheless, faint laser pulses are sufficient in many applications, and they are widely used since true single-photon states are difficult to generate in practice. But there are some schemes which are not based on approximate but true single-photon Fock states. To this end, different configurations have been developed, such as atom-like sources or parametric downconversion [119, 154].

Atoms, or **atom-like systems** in general, can be arranged to emit single photons on demand via optical or electrical excitation [17, 155]. These structures are usually modelled as two-level systems [8], such that they only admit one excitation at a time —once excited due to the absorption of a single photon, they cannot absorb a second one. Then, single photons are generated via spontaneous emission. The two-level system emits a photon while returning to its ground state [123], hence it is no longer excited and thus unable to reemit (until it is excited again). Therefore, in the case of optical excitation, the atom-like system converts the incoming laser pulse, described by a coherent state, into a single-photon stream.

There exists a wide range of single quantum systems engineered to emit photons one by one, as the ones discussed in Subsection 1.1.2, that is, trapped ions and atoms [156, 157, 158], single molecules [127, 159, 160], NV-centers in diamonds and other color centers [161, 162], quantum wells [163], and semiconductor quantum dots [17,

164, 165]. The long lifetime exhibited by atomic transitions limits the rate of generation of single photons, a crucial point in many applications. Photostability and blinking are serious issues concerning fluorescent emission in organic molecules. In particular, quantum dots are specially interesting as single-photon sources since they present narrow spectral linewidths and rapid radiative decay rates [166], apart from their stability and the ease of the integration into structures such as inorganic microcavities [167, 168]. These hybrid platforms can be easily tailored to display excellent optical properties, as already mentioned. Diamond color centers are also excellent platforms to generate single photons, as they present photostable emission, room temperature operation, and long coherence times [169]. In the review by Buluta *et al.* [47], the different features displayed by natural and artificial atoms are thoroughly compared.

Nonlinear optical processes can be also used to create quantum light states, such as spontaneous **parametric downconversion** [170]. It consists in the generation of a pair a lower-energy photons (the so-called signal and idler photons) from one photon of higher energy (pump photon). This method produces highly correlated photons, hence it enables the preparation of entangled photon pairs [171, 172]. Alternatively, the second photon in the pair can be used to hearld the generation of a single photon [173]. While atom-like systems can be triggered to emit single photons on demand, parametric downconversion is a random process.

Finally, the use of **optical microcavities** has opened up new possibilities. First of all, they allow for the enhancement of the spontaneous emission rate due to the Purcell effect [167], as previously commented in Subsection 1.1.3. But more importantly, the operation within the strong coupling regime gives rise to nonlinearities which enable the generation of single photons in an alternative way. This is the topic of the following section, where the so-called photon blockade effect and single-photon emission via interference effects are discussed.

1.2.2 Using cavities in the generation of single photons

The coupling of single emitters to the electromagnetic field within a **cavity** provides multiple benefits concerning the generation of single photons [168, 166]. These hybrid platforms present higher repetition rates and higher quantum efficiencies, as well as an increased degree of indistinguishability [146, 174]. Besides, the cavity mode allows for a better control of the emission in terms of directionality and polarization, enabling the generation of one photon on demand into the desired mode [12, 146]. In the regime of **strong coupling** between a cavity and a collection of atoms, novel photon statistics was predicted [175] and observed [176]. In parallel, different realizations of single-photon sources consisting in single emitters strongly coupled to cavities were reported [156, 158, 177, 178], where the photon is generated as the result of a coherent process.

Within the strong coupling regime, the eigenstates of the Hamiltonian associated with a fixed number of excitations m are not degenerated, but present a splitting that depends on m. Within the Jaynes–Cummings model (see Subsection 2.2.4), the energy difference R_m between the two dressed states belonging to the mth-excitation manifold is given by (Equation 2.44): $R_m = 2\hbar g\sqrt{m}$, where g represents the light-matter coupling strength. Therefore, the energy gap between levels varies depending on the number of excitations

m, and the structure associated with the dressed states is then anharmonic. It is precisely this **anharmonicity** that leads to the photon blockade effect, a mechanism that allows for the generation of single photons in an alternative manner.

Photon blockade effect

Photon blockade is a quantum effect that prevents the injection of more than one photon into a nonlinear cavity mode, thus leading to antibunched emission. This phenomenon is known as photon blockade in analogy to the Coulomb blockade observed in small metallic and semiconductor devices, where the transport of charge through the device is carried out electron by electron [179, 180]. There, the presence of an electron can block the flow of another electron. In the case of photons, the transport of light through the optical system was thought to experience the same effect [181]. Nevertheless, the origin of both blocking processes are rather different: whereas the Coulomb blockade is produced via the direct interaction of electrons via the Coulomb repulsion, photon-photon interactions require the mediation of matter.

Mechanism The photon blockade effect arises within the regime of strong light-matter coupling due to the anharmonicity of the energy level structure. The resonant absorption of a photon of a particular frequency, which makes the coupled system reach the corresponding state in the first-excitation manifold, blocks the absorption of a second photon of this frequency because transitions to any state in the second-excitation manifold are detuned from resonance. Photon blockade manifests itself by the antibunching in the radiation field, and it allows for the realization of single-photon sources— the system is excited by an incident Poissonian stream of photons, while the emitted light presents antibunching. Notice that, in order to observe the photon blockade effect, the anharmonicity must be greater than the broadening of the energy levels.

This mechanism was first noted by Tian and Carmichael in 1992, as they showed that a cavity strongly coupled to an atom behaves as a two-level system as long as the system is excited near some resonance [182]. Through quantum trajectory simulations, they demonstrated that the presence of an excitation in the system blocked the absorption of a second photon, thus justifying the two-state approximation. This behaviour was pointed out to stem from the unequally spaced energy levels of the coupled system.

The analogy between electron transport in electronic devices and photon emission in strongly coupled optical devices was first suggested by Imamoğlu *et al.* in 1997 [181]. An effect equivalent to Coulomb blockade for electrons was suggested to occur for photons by using photon-photon interactions in a nonlinear optical cavity. According to the scheme proposed, a giant Kerr nonlinearity may be obtained by electromagnetically induced transparency [183]. This large nonlinearity would produce a stream of single photons in the transmitted field, that is, antibunching due to the photon blockade effect. A more accurate description of the photon-photon interactions was later offered [184, 185]. While some works further explored this scheme based on electromagnetically induced transparency [186, 187], there were other proposals to make feasible photon blockade, for instance, via localized surface plasmons [188].

Experimental observation The phenomenon of photon blockade in an atom-cavity system was first observed by Birnbaum *et al.* in 2005 [189]. They studied the photon statistics of the light transmitted by an optical cavity strongly coupled to a single trapped atom, and showed that the presence of an excitation in the composite system effectively blocks the transmission of a second photon. In particular, they measured the correlation function $g^{(2)}(\tau)$, obtaining both sub-Poissonian statistics and antibunching. Photon blockade was also investigated within the context of a photon turnstile device [190]. Apart from atomic systems, this mechanism was observed in a resonantly driven quantum dots embedded in a photonic-crystal cavity [191, 192] and also in the microwave regime with superconducting circuits [193, 194]. The observation of the photon blockade effect at significant detuning has been also reported [195]. Additionally, it has been proposed the polariton blockade effect, that is, that the presence of a single polariton can block the resonant injection of another [196].

The probability of absorption of a second photon once there is an excitation in the system can be studied as a function of the pumping frequency. The dropping in the probability is maximum when the pumping pulse is perfectly resonant with one of the two eigenstates of the first-excitation manifold [191, 192], signature of the photon blockade effect. On the contrary, an increase in the probability takes place when the probe is positioned between the two eigenstates [191]. When the laser is at resonance with the polariton eigenstates of the two-excitation manifold, photon bunching is observed [192]. This means that two photons of the same frequency are more likely to be transmitted through the cavity jointly than they would otherwise. **Photon correlation spectroscopy** was indeed proposed to analyze the higher-excited manifolds of strongly coupled systems [197, 198].

The anharmonicity of the energy structure of the cavity-atom system was then explored in the context of **two-photon processes** [199, 200], demonstrating that the hybrid system composed of a single atom strongly coupled to an optical cavity can absorb and emit resonant photons in pairs [199]. Thanks to the perfect tuning of the laser, a quantum state of the composite system containing two excitations was populated directly by means of a two-photon process. Likewise, the decay of the hybrid system leads to the emission of a pair of photons, thus converting the incoming coherent laser beam into a correlated stream of photon pairs.

Strong nonlinearities at the single-photon level In the photon blockade effect, nonlinearities at the single-photon level alter the quantum statistics of the emitted light from a cavity. Therefore, by exploiting the strong coupling regime, it is possible to generate strong **single-photon nonlinearities** [201]. These are crucial for the realization of photonic quantum technologies [202, 203], including the optical analogue of the Josephson interferometer (that is, two coherently driven linear optical cavities connected through a central cavity with a single-photon nonlinearity) [204] or a single-photon transistor (where the presence/absence of a single incident photon in a gate field is sufficient to allow/prevent the propagation of subsequent signal photons) [201]. The interaction of photons thus allows for all-optical devices in which one light signal controls another.

Strong photon-photon interactions allows for the study of interesting and potentially useful quantum phenomena that emerge in strongly-correlated optical systems. Optical systems exhibiting strongly correlated dynamics is achieved in arrays of coupled cavities

each containing a single two-level system in the photon-blockade regime [205, 206] or in nonlinear optical waveguides [207]. The formation of polaritons in these configurations led, for instance, to the prediction of a characteristic Mott insulator to superfluid quantum phase transition [205, 208, 206]. Arrays of cavities thus enable the implementation of the effective Bose-Hubbard model [209] and other Hamiltonians —photon hopping is allowed between neighbouring cavities, whereas the (either repulsive of attractive) force between two polaritons occupying the same site is generated by the large Kerr nonlinearity that arises when atoms with a specific level structure interact with light [208]. These photonic structures have then served as a basis for the proposal of different quantum many-body phenomena, such as the fermionization of photons [210] or the crystallization of polaritons in coupled array of cavities [211] in an array of driven dissipative nonlinear cavities.

A strong nonlinearity at the single quantum level is needed for all these realizations, as well as for the previously commented single-photon sources based on the photon blockade effect. A novel scheme was proposed by Liew and Savona [212], considering a configuration of coupled quantum modes that becomes strongly sensitive to changes in the number of excitations even if the nonlinear interaction is small. They numerically showed that strong photon antibunching was obtained with a weak Kerr nonlinearity in a resonantly driven photonic system composed of two coupled cavities. Although the photon blockade effect was argued to lie behind this antibunched emission, it was later shown by Bamba *et al.* that a destructive quantum interference effect was actually the responsible for the exhibited antibunching [213]. Prior to this case, a mechanism based on quantum interferences was already thought to explain the strong nonclassical effects in cavity systems with many atoms [175, 176], that we proceed to discuss in the following.

Interference-induced correlations

The generation of single-photon emission usually exploits the existence of some sort of nonlinearity in the photonic system. The presence of a large number of emitters would spoil this effect, as their collective response becomes approximately bosonic. Nevertheless, nonclassical features were still found, as demonstrated in two different studies published in 1991 [175, 176]. After having considered the single-atom case in a previous publication [214], Carmichael *et al.* computed the coincidence rate for photons transmitted by a weakly driven cavity containing a collection of identical two-level atoms interacting with a single cavity mode, all resonant with the driving field [175]. Nonclassical photon correlations were obtained even for large systems sizes, altough the emission does not present antibunching in the usual sense —the zeros in the correlation function $g^{(2)}(\tau)$ were not found at at $\tau = 0$ but at some finite delay. These nonclassical correlations were explained in terms of the interference of probability amplitudes and the collapse of the wavefunction. Rempe *et al.* studied the quantum statistical behaviour of the same system under strong coupling conditions both theoretical and experimentally [176], and correlations were interpreted as coming from interference effects as well. The presence of photon antibunching and sub-Poissonian statistics were reported when considering a collection of more than a hundred atoms, although the nonclassical signatures were not particularly significant. The important result is, however, that these features were observed to be largely independent of the number of atoms. Previously, Casagrande and Lugiato had

already predicted a subtle antibunching effect for a collection of emitters coupled to an optical cavity by solving a Fokker–Planck equation in the small noise approximation [215]. The results derived from the Fokker–Planck equation were later compared to the pure-state formalism, valid for weak driving fields, by Brecha *et al.* [216]. They performed a more complete study of the photon statistics of the transmitted field considering the same formalism as in Ref. [175]. Including the effects of dissipation, they realized that the nonclassical features were more prominent in the bad-cavity limit (in which the cavity decay rate is large compared to the spontaneous emission rate associated with the atom). All nonclassical effects were interpreted in terms of quantum interference of probability amplitudes.

Further experiments were performed aiming to explore different regimes and experimental conditions. For instance, it was studied the dependence of photon statistics on the intensity of the driving field when having a collection of ten emitters coupled to a single cavity mode [217]. The sub-Poissonian nature of the transmitted field at low-driving intensities was found to turn to super-Poissonian when increasing the pumping. Nevertheless, the field always exhibited antibunching. Photon correlations were also studied as a function of the detuning and the number of atoms [218, 219]. These experiments involving the measurement of correlations between pairs of photodetections were supplemented with squeezing experiments measuring the variation of the electromagnetic field amplitude [220, 221]. Nonclassical features were also reported following a combined procedure [222], studying the correlation of a photon detection with fluctuations of the electromagnetic field amplitude.

Therefore, contrary to expectations, quantum correlations were found when working with a reduced collection of particles due to quantum interference effects. As mentioned before, this can give rise to strong nonlinearities that enable the realization of strongly correlated photonic systems [213]. There have been a number of proposals for the implementation of a source of strongly sub-Poissonian light through this method based on destructive interference. For instance, it has been suggested a configuration composed of a single quantum dot simultaneously coupled to the two modes of a bimodal optical cavity [223]: when one mode of the cavity is resonantly pumped with a coherent source, the light transmitted by the cavity is shown to present a strongly sub-Poissonian character. This effect has been shown to vanish in the absence of cavity loss.

1.2.3 Computing photon correlations within the strong coupling regime

Much effort has been subsequently devoted to the analysis of the evolution of the quantum statistical properties of the light emitted by these hybrid systems for increasing number of emitters, assessing the possibility of generating nonclassical light with a mesoscopic ensemble. These two effects that lead to photon antibunching —namely, the photon blockade effect and destructive quantum interferences— have been equally addressed following several approaches. In this context, the Jaynes–Cummings model and its extensions have served as a basis for the description of the light-matter system and the associated interactions.

Quantum light-matter Hamiltonians

The most basic problem addressed in cavity QED is the interaction of a single emitter with a single mode of the electromagnetic field supported by a cavity. The electromagnetic field turns out to be formally equivalent to a collection of independent and uncoupled harmonic oscillators (see Appendix D, Section D.2), so the light component is easily tractable. The matter component, which might be atoms, molecules, or quantum dots, is usually described as two-level systems, although some other more complex models can be considered as well. In particular, this approximation is valid as long as there is just one relevant transition which is not disturbed by the presence of other energy levels. In this case, the state of the system can be properly represented by a two-dimensional Hilbert space.

For the purpose of studying the system within a completely quantum treatment, **Jaynes and Cummings** developed a model involving a two-level system coupled to a single quantized cavity mode [78], as we have already mentioned. The Jaynes–Cummings Hamiltonian is widely used in numerous fields since it successfully represents the quantum physics of that resonant interaction [224, 225]. This model was extended to an arbitrary number of emitters by **Tavis and Cummings** [226]. The resulting Hamiltonian is sometimes named after Dicke [227, 228], since he had already considered the coupling between a quantized cavity field and a large ensemble of two-level systems in his seminal work on superradiance [229]. These Hamiltonians, together with specific procedures to introduce the effect of losses, provide a successful theoretical description for a broad variety of configurations [61]. Nevertheless, the simplification of the electromagnetic field to a single (or few) quantized cavity modes is not always a good approximation and a more involved model thus needs to be introduced [230]. In our case, the Tavis–Cummings Hamiltonian is the starting point for the description of all quantum systems treated in this thesis.

Theoretical calculations of photon statistics

The desired nonclassical emission resulting from the interaction between quantum emitters and a photonic mode has been thoroughly investigated, comprising both semiconductor and plasmonic nanocavities [231, 232], as well as the coupling of cavity-emitter systems to waveguides [233, 234]. In light of the interest of the implementation of quantum technologies [202], the generation of nonclassical light on a chip has focused great efforts [195, 235]. In particular, the system composed of a single quantum dot embedded in a photonic crystal emerged as a promising configuration to this end [192] —due to their efficient coupling to waveguides [236], they can be easily integrated into optical circuits. Experimental realizations of nonclassical emission in these platforms, including those implementing a self-homodyne interferometric technique that reduces the characteristic large dissipation rates [237, 238], were often accompanied by numerical simulations of the photon statistics of the coupled system [195, 235], considering also higher-order photon correlations [239].

Most of these studies are performed for the single-emitter case [240], or involving just two [241, 242, 243] or a few particles [244, 245]. At the other extreme, the coherent emission of a large set of emitters was also discussed [246, 247], mainly in the context of superradiance [229, 248]. Numerical computations are performed using approximation

schemes, for instance, working in the framework of quantum trajectory theory [249]. Intensity fluctuations in steady-state superradiance [250] were studied by means of Monte Carlo simulations and semiclassical approximations [251, 252]. The transition to the subradiant regime was also explored with diverse techniques [253, 254]. Some other approximation schemes have been developed for the study of photon statistics with a large number of emitters, such as those based on the positive P representation [255, 256, 257] or those following different expansion procedures [258, 259, 260]. The coherence properties of the light generated under conditions of electromagnetically induced transparency in atomic media involving Rydberg atoms have been also analyzed [261, 262].

Therefore, detailed studies of the coherence properties of the light emitted by hybrid systems have been performed when having just a small number of emitters coupled to the cavity mode. The dimension of the Hilbert space grows exponentially with the number of emitters, which makes intractable the problem beyond some tens. This is the reason why the intermediate case of a mesoscopic ensemble has remained elusive. Our objective was thus the study of the photon statistics of the light emitted by these kind of configurations, and this is the work we present in Chapter 3. In particular, we consider both organic molecules coupled to plasmonic nanocavities [263] and quantum dots embedded in dielectric microcavities [264]. The two procedures that lead to photon antibunching —namely, the photon blockade effect and destructive quantum interferences— are there explored. Later, further studies have treated this mesoscopic regime [265, 266].

1.3 Excitons (modified by photons)

Apart from taking advantage of the composite nature of polaritons, strong coupling offers the possibility to alter the electromagnetic environment of excitonic systems and, in turn, vary the material performance. The appropriate tailoring of polaritonic characteristics has been shown to modify chemical reactions and material properties, as well as to enhance the spatial range and rate of exciton transport in organic platforms. This is precisely the topic of the work presented in Chapter 4. Hence, in this section, our discussion is focused on the process of exciton transport and the benefits to be gained from the strong coupling regime.

1.3.1 Modifying the exciton perfomance

The coupling of excitons to their electromagnetic environment has become a method to improve the performance of organic materials concerning a broad variety of aspects. Strong coupling has been shown to change their optical response [267, 268, 269] and also their chemical reactivity [270, 271, 272]. The rate of a photochemical reaction was first shown to change under strong coupling conditions by Hutchison *et al.* in 2012 [273]. Since then, **polaritonic chemistry** has become an active research field [274, 275] due to the potential of strong coupling to influence the chemical structure and chemical reactions

of organic species [276, 277]. Besides, material properties such as the work function [278], as well as the hysteresis of a phase transition [279], have been altered through the coupling to an electromagnetic field. The tailoring of chemical and material properties within the strong coupling regime is widely explored [280].

The ability to transform the electromagnetic environment has been also used to modify the **transport properties** of organic semiconductors [281, 282]. Energy transport in nanostructured materials and crystals occurs through the motion of excitons. The physical mechanism of **exciton transport** is present in a variety of phenomena, taking place in nature in the process of photosynthesis and also being crucial in the operation of several artificial devices. In **photosynthesis**, the sunlight absorbed by the light-harvesting complexes of an organism generates excitons that must be transported to the reaction center, where the conversion of the solar energy into chemical energy occurs (see Subsection 1.3.4). In turn, **organic solar cells** are equally engineered to efficiently move the excitons created under optical excitation to the interface where dissociation takes place [283, 284]. There are some other optoelectronic devices in which the process of exciton transport is crucial, such as light-emitting diodes [285] and excitonic transistors [286]. Understanding and controlling the mechanism responsible for the exciton transport is thus not only interesting from a fundamental standpoint, but it may lead to an optimization of these devices [287].

1.3.2 Incoherent exciton transport

Exciton transport mechanisms

Energy transfer takes place when the excitation placed in a molecule, named the **donor**, is transferred to another molecule, the **acceptor**, during the lifetime of the excited state. The motion of the excitation through nanostructured organic materials are produced by a sequence of shifts of the localized exciton from a particular position to a neighbouring place, in what is sometimes known as **random walk diffusion** [288, 289]. Depending on the electronic spin, the mechanism that controls this hopping is thought to be either the Förster energy transfer (if excitons are in the spin singlet state) or the Dexter energy transfer (if they are in the spin triplet state) [290]:

- **Förster energy transfer** consists in a resonant, near-field dipole-dipole interaction, which decreases with the sixth power of the separation between molecules [291]. It does not require direct contact between emitters, and the interaction distance is of the order of 5 – 10 nm.

- **Dexter energy transfer** consists in the simultaneous exchange of two electrons between nearest neighbours [292], and it requires direct contact between donor and acceptor molecules. The interaction decays exponentially with the separation between molecules, and energy transfer through this mechanism takes place over distances shorter than 1 nm.

Both Förster and Dexter mechanisms are **nonradiative processes**, and are the ones that prevail at **short distances**. When molecules are located far apart, transfer occurs via **radiative processes**, that is, involving the emission and absorption of a photon. This

interaction falls with the inverse of the separation between particles squared, so its range is longer [293]. Nevertheless, the probability of radiative transfer is generally low, so the directionality needs be controlled by external means [294, 295].

This nonradiative energy transfer process that takes place between molecules when their separation is of the order of a few nanometres was first described by Förster in 1948 [296]. The **Förster resonance energy transfer** (FRET), also known as fluorescence resonance energy transfer, takes place due to the near-field interaction produced between a couple of dipoles. According to Förster theory [291], the **energy transfer rate** k_{FRET} from donor to acceptor when the dipoles are separated a distance r is given by:

$$k_{\mathrm{FRET}} = \frac{1}{\tau_{\mathrm{D}}} \left(\frac{R_0}{r} \right)^6 ,$$

where τ_{D} is the donor lifetime (without the presence of any other emitter) and R_0 is the **Förster distance** for energy transfer. For a given donor-acceptor pair, the value R_0 is defined as the distance at which the energy transfer efficiency falls to 50 per cent. That **efficiency** η_{FRET} is given by the ratio of the energy transfer rate k_{FRET} with respect to the total rate of exciton relaxation:

$$\eta_{\mathrm{FRET}} = \frac{k_{\mathrm{FRET}}}{k_{\mathrm{FRET}} + \gamma_{\mathrm{r}} + \gamma_{\mathrm{nr}}} ,$$

where γ_{r} and γ_{nr} are the radiative and nonradiative decay rates associated with the donor when there is no acceptor in its surroundings. The variation of the efficiency as a function of the separation between donor and acceptor is given by:

$$\eta_{\mathrm{FRET}} = \frac{1}{1 + (r/R_0)^6} .$$

Due to the strong dependence of energy transfer on the separation between emitters, it is used to measure distances between sites in biological macromolecules [297, 298]. Energy transfer rates are important at short distances, but they decreases drastically when the separation becomes larger.

As viewed from the donor, the presence of another molecule supposes an additional decay channel, precisely the FRET relaxation rate k_{FRET}:

$$\gamma_{\mathrm{D}^*} = \gamma_{\mathrm{D}} + k_{\mathrm{FRET}} ,$$

where $\gamma_{\mathrm{D}} = \gamma_{\mathrm{r}} + \gamma_{\mathrm{nr}}$ is the donor decay rate when being alone, while γ_{D^*} stands for the decay rate in presence of the acceptor. The energy transfer rate through the Förster mechanism can be thus computed as the difference between the donor emission rate with and without the acceptor being around. As a consequence of energy transfer, the donor fluorescence gets reduced, so it can be thought of as a **quenching process**. Notice that energy transfer takes place through nonradiative processes, that is, the donor losses its excitation without the emission of a photon.

The **Förster distance** R_0 associated with a given donor-acceptor pair depends on the relative orientation between the dipoles corresponding to the donor emission and the acceptor absorption, the medium refractive index n, the quantum yield of the donor in absence of acceptor $\mathcal{Q}_{\mathrm{D}}$ (defined in Equation 1.2), and the overlap integral $J(\lambda)$ between

the donor emission and the acceptor absorption spectra [299]:

$$R_0^6 \propto \frac{\kappa^2 Q_D}{n^4} J(\lambda) ,$$

where κ^2 is a factor describing the relative orientation of dipoles. Typical values of R_0 are in the order of a few nanometres (typically, 3–6 nm), thus limiting the Förster energy transfer range to 10 nm. For this process to occur, not only the distance between molecules needs to be small, but the donor lifetime has to be sufficiently long. Besides, the donor emission spectrum should overlap with the acceptor absorption spectrum.

The mechanism of FRET is used in many applications related to medical diagnostics, DNA analysis, and optical imaging [300, 301]. The particular interest for biological research lies in its range of interaction, since the typical size of many biological elements is precisely a few nanometres. In general, the study of the energy transfer mechanism allows for the determination of molecular distances [302] and interactions [303], thus revealing information about conformational dynamics [304, 305]. Different nanosensors based on the FRET mechanism have been reported [306, 307, 308]. Some other applications are related to light emission [309, 310], such as the generation of color-converting systems [311, 312] and white-light-emitting structures [313], and photovoltaic devices [314, 315]. Indeed, exciton transport is intensively studied because of its relevance in the construction of synthetic light-harvesting structures [316, 317].

Enhancing the energy transfer performance at short distances

The process of FRET can be basically controlled by changing the distance between emitters, their spectral properties, or the relative orientation between dipoles [318, 319]. Several studies focused on the effect produced by the variation of different conditions [320]. For instance, energy transfer was found to be enhanced by two orders of magnitude when molecules are embedded in dielectric droplets [321, 322]. Much attention was also drawn to the effect that the **photonic environment** may have on this mechanism.

Theoretical works in the 1990s pointed out that the resonant dipole-dipole interaction becomes altered when interacting with a resonant mode in both cavities [323, 324] and periodic structures [325, 326]. An enhancement of the dipole-dipole interaction when emitters are placed in a cavity was effectively measured [327]. Subsequently, the Förster energy transfer was shown to be influenced by the cavity as well. Previous studies of fluorescence near interfaces had already shown the role of the photonic mode density —by placing the molecules in the surroundings on a metallic mirror, it was changed the number of photon modes to which the system could radiate [328]. In 2000, Andrew *et al.* demonstrated that the variation of the local photonic mode density within a cavity changes the donor emission rate and, in turn, the energy transfer process [329]. This insists on the idea of controlling the exciton performance by tailoring their electromagnetic environment within the **weak coupling regime**.

Some other works further explored this route, studying the variation of the energy transfer rate and efficiency by changing the spectral mode density with the use of different types of resonators [330, 331], nanoparticle arrays [332, 333], single metal nanoparticles [334, 335], and nanoantennas [336, 337]. Although some of them show that the transfer

rate depends linearly on the photonic mode density at the emission wavelength [329, 338], some others suggest a different result: the transfer efficiency does change with the density of states while the energy transfer rate remains independent [339, 340]. The complexity of the experimental setup and difficulties regarding the precise control of the position, orientation, and spectra of dipoles may be behind these contradictory results [341, 342].

Much theoretical effort was also devoted to this study of the FRET rate and efficiency in different environments [343, 344, 345]. A theoretical derivation within the Green-function formalism was performed considering emitters near a dispersing and absorbing media [346]. The existence of surface-guided waves in a planar interface was shown to modify both the short-range and the long-range dependences observed in free space (that is, the fall with the sixth and second power of the separation between molecules, respectively).

Enhancing the energy transfer performance at longer distances — radiative energy transfer

Although the modification of the electromagnetic environment may allow for the enhancement of the transfer rate, the range of the Förster mechanism is still below 10 nm. Interestingly, in 2004, Andrew *et al.* found that the range over which energy transfer occurs could be extended by coupling the molecules to a surface plasmon polariton mode formed on a metal film [294]. Donor and acceptor molecules were located on opposite sides of metallic films, such that the creation of **plasmonic excitations** involving both donor and acceptor layers served as a vehicle for the energy transfer. This variant of radiative transfer was shown to occur over distances up to 120 nm, while the range of the usual nonradiative Förster mechanism is of the order of a few nanometres. Metallic structures could thus provide the control over the directionality of the radiation by means of the confinement of the plasmonic excitations, and then produce efficient **radiative transfer** between emitters [295, 347]. This importantly increases the interaction range of FRET.

Apart from this, the enhancement of the rate of energy transfer by placing a metal particle near the pair of molecules was proposed in the mid 1980s [348, 349]. The observation of an improvement of the performance of energy transfer thanks to the use of metallic structures have been widely reported [350, 332, 351]. Nevertheless, as previously mentioned, whether energy-transfer rates and efficiencies can be modified by the photonic environment is still under debate [342].

Getting efficient energy transfer at even longer distances —long-range energy transfer

The **diffusion length** is defined as the mean displacement of an exciton over its lifetime. Excitons in organic materials usually suffer from large propagation losses due to decoherence and recombination, which translates to short propagation lengths. The connection between exciton transport and nanoscale **disorder** has been widely explored [75]. The process of exciton transport in molecular crystals starts with a period of random walk diffusion, followed by a subdiffusion stage when excitons get trapped. By increasing the

disorder, the transition to the subdiffusion period occurs earlier, diminishing in turn the exciton transport efficiency. As systems composed of organic molecules are disordered [352, 353], they possess large dissipation and dephasing rates, hence short propagation lengths. Apart from the study of the diffusion process in organic molecules [290, 354], exciton and charge transport in inorganic platforms have been also analyzed extensively [355, 356].

With the aim to improve the process of exciton transport, much effort has focused on the optimization of the nanoscale morphology of the material to increase the carrier mobility, as well as on finding ways to guide excitons to the desired place instead of relying on a random process. Alternatively, **strong coupling** has emerged as a means to circumvent the problem of the scattering induced by disorder in media. The formation of polaritons within this regime enables an alternative mechanism of exciton transport. As reported by Orgiu *et al.* in 2015, the conductance in organic semiconductors is enhanced when these materials are located in an optical cavity due to the strong coupling to the vacuum electromagnetic field [281]. Subsequent theoretical studies showed that strong coupling can enhance the efficiency of exciton transport in various orders of magnitude [282, 357], and a mechanism leading to charge conductivity enhancement under strong-coupling conditions was later proposed [358]. In this regime in which hybrid light-matter states are created, efficiency is not limited by the hopping between neighbouring molecules —transport occurs via the delocalized polariton modes, which extend over the spatial size of the optical field [359, 360]. Exciton transport in one dimensional molecular chains has been thoroughly explored since these initial works [361, 362], and exciton harvesting has been also demonstrated in an ensemble of quantum emitters strongly coupled to a localized surface plasmon [363].

The process of exciton transfer thus benefit from the coupling to an electromagnetic mode. Strong coupling enables excitation energy transfer to take place over distances beyond the nanometre scale —this is the so-called **long-range energy transfer**. In contrast to the Förster mechanism where incoherent excited states travel by means of random hops from one molecule to another, this is a coherent process mediated by polaritons. For this reason, it is also known as **polariton-mediated energy transfer**. Such coherent exciton transport mechanism is analyzed in the following.

1.3.3 Coherent exciton transport

Hybrid polaritons

A first step towards the achievement of long-range energy transfer was the creation of the so-called **hybrid polaritons**. They emerge when two distinct exciton species are simultaneously coupled to the same cavity mode, such that the resulting polaritons present contributions from both excitons as well as a photonic component. After being proposed by Agranovich *et al.* in 1997 [364], hybrid polaritons were experimentally obtained by strongly coupling two types of quantum wells to a semiconductor microcavity [365]. In this experimental realization, Wainstain *et al.* achieved a Rabi splitting value below 7 meV at 20 K.

The use of organic semiconductor microcavities led to the achievement of larger mode

splittings at room temperature. Specifically, hybrid polaritons displaying Rabi splitting values of 60 meV at room temperature were reported by Lidzey *et al.* in 2000 [366]. Two physically separated layers with different cyanine dyes were located in a planar microcavity, and hybrid polaritons arose from the hybridization of the cavity mode with the two molecular excitations. The photonic mode, in some sense, relates the two organic materials, otherwise disconnected. This was thought to serve as a pathway for the excitation to travel from one substance to the other.

Some other realizations of hybrid polaritons were performed through the coupling of Frenkel and Mott excitons in a hybrid organic-inorganic microcavity [367, 368], and also between different absorbing species spatially separated in photonic crystals [369].

Experimental realization

Energy transfer between two molecular species placed in a microcavity structure was first reported by Coles *et al.* in 2014 [370]. A blend of two types of cyanine dyes were located in a matrix between two metallic mirrors. When both species are strongly coupled to the cavity mode, energy transfer from donor to acceptor molecules is observed after non-resonant excitation. The process takes places thanks to the emergence of coherent excitations involving distinct molecular species, since polaritons are precisely the pathway for the excitation. The fingerprint of energy transfer is the reduction of the donor emission accompanied by the population of the acceptor excited state.

The change in the donor lifetime in the presence of the acceptor was first reported by Zhong *et al.* in 2016 [371], where two types of J-aggregated cyanine dyes were strongly coupled to the vacuum field of a cavity. From measurements of the decay lifetime outside and inside the cavity, the energy transfer rate was found to be increased by a factor of seven under strong coupling conditions (with respect to the situation outside the cavity). Shortly after, the same group reproduced this energy transfer mechanism when the two organic species were physically separated inside the cavity [372]. In this case, we can refer to **long-range energy transfer** properly, since the excitation once placed in the donor molecules is then transferred to acceptors, located more than one hundred nanometres away. A transfer efficiency of about 37 per cent was obtained, and the energy transfer process was shown to become independent of the distance between donor and acceptor molecules as long as the coupling strength is sustained. This is explained from the delocalized nature of polaritons, in charge of the excitation energy transfer [373]. Therefore, this has opened a way to obtain efficient energy transfer over distances beyond the nanometre scale. This energy transfer process has been also explored in plasmonic systems [374].

Theoretical description

By the time it was experimentally obtained, the underlying physical mechanism responsible for the long-range energy transfer was not well-understood, nor the role played by polariton coherence. Apart from being interesting from a fundamental point of view, a proper theoretical picture could lead to experimental configurations that are more appropriate for the enhancement of energy transfer through the polariton-mediated procedure. With this objective in mind, we provided a complete theoretical description of this mech-

anism through which the nonradiative energy transfer is extended over long distances [375]. This is the work we present in the first part of Chapter 4, in which the central role of the middle-polariton and molecular vibrations are disclosed.

The competition between the short-range dipole-dipole and the long-range polariton-mediated energy transfer mechanisms had been explored for a pair of emitters by using a simplified model [376]. There, no vibrations were included but for a three-level structure modelling the emitters. This computation based on rate equations pointed out the relevance of the relative detuning of the cavity with respect to the donor and acceptor molecules, which ultimately controls the polariton composition. A rate equation approach was also followed in other works [377]. Some other theoretical studies have tackled the role of vibrations in the process of exciton transport inside cavities [362] and a trapped-ion quantum simulator have been proposed to study vibrationally assisted energy transport in detail [378].

The potential of long-range energy transfer for different functionalities is being explored. For instance, molecular dynamics simulations have been carried out for a mixture of photoreactive and non-photoreactive molecules strongly coupled to the same confined light mode [379]. By varying the concentration of the different type of molecular species, the excitation can be swiftly localized in a single photoreactive molecule, thus collecting the energy necessary for its photochemical reaction.

1.3.4 Exciton transport in photosynthesis

Much research effort devoted to the study of exciton dynamics in organic molecules aims to gain a better understanding of the mechanism responsible for **photosynthesis** in biological complexes. Undoubtedly, exciton transport is a fundamental stage in this natural process: after solar photons are absorbed by the chromophores (light-sensitive molecules), the excitation energy needs to be rapidly transported to the reaction center [380, 381]. This process is known as **light harvesting**, and presents an efficiency close to one. The diverse light-harvesting complexes, together with the pathway followed by the excitation and the different time scales, are well-known. However, the ultimate mechanism responsible for this highly efficient energy transfer is not well understood, nor the extent to which quantum effects are involved.

The complete understanding of the dynamics of the excitation in photosynthetic systems, as well as the role played by the different elements, may lead to the optimization of artificial light-harvesting devices. Indeed, many configurations have been developed to perform the so-called artificial photosynthesis [382, 383], seeking to mirror this natural process [384]. As in photosynthetic systems, these devices need an efficient conversion of the harvested light. Beyond its practical application, fundamental research on natural light-harvesting compounds has been carried out. Apart from coherent excitation transport [385, 386], many other interesting phenomena have been observed, such as antibunched photon emission [387], or dephasing-assisted transport in ensembles of chromophores [388].

Light-harvesting dynamics

Photosynthetic organisms (such as plants and some types of bacteria and algae) present **light-harvesting complexes**, which are the responsible for the absorption of photons from the sunlight and the subsequent storage and funnelling of the created excitation to the reaction center [380, 381]. As we have indicated, this is the final step of the light-harvesting process, where charge separation takes place creating a transmembrane potential (which is the source of energy for all the following processes in the system). These light-harvesting complexes (also known as **light-harvesting antennas**) are composed of an ordered collection of **light-harvesting pigments** bound to proteins. These pigments are basically chlorophylls (Chl), bacteriochlorophylls (BChl), or phycocyanin, as the case may be.

Light harvesting in biological systems is conventionally explained within the **Förster mechanism** of energy transfer [291], through which the excitation in one antenna pigment hops to a nearby pigment as a result of the nonradiative dipole-dipole interaction [389]. This operation takes place incredibly fast and with an efficiency close to one, reason why some believed that a coherent excitation of assemblies of chromophores may be involved [390]. That being the case, exciton dynamics could not be described by the Förster mechanism. In fact, this simple model cannot be generally applied to photosynthetic systems due to the nanoscale packing of the pigments —the distance between sites is not sufficiently large so as to introduce the point-dipole approximation. Besides, both the antenna pigment which absorbs the excitation and the remaining parts responsible for exciton transport are formed by molecular aggregates. The fact that the excitation is not localized in a particular pigment, but delocalized over a number of them [390], was then added to the description.

Going a step further than Förster theory, Sumi [391, 392] and Scholes *et al.* [393, 394] incorporated the delocalized nature of excited states in the description of exciton dynamics. The Förster approach was later generalized to include multichromophoric situations [395, 396], providing an expression for the new FRET rate. While Förster theory neglects coherence effects, this more complete description includes coherence within donor and acceptor arrangements. Nevertheless, coherence between donor and acceptor states is not covered. Within this multichromophoric picture, the excitation delocalized over a set of chromophores is transferred to a nearby group through an incoherent hopping. This description is valid as long as the exciton states remain well-separated so as to not to get mixed [397, 398]. But this is not always the case, and a description including coherence in a broad sense is usually required.

In general, the dynamics of the excitation is studied according to two different regimes, based on the relation between the pigment-pigment interaction and the disorder [399]. The nanoscale dimensions of photosynthetic complexes (their sizes are in the region of 5 – 20 nm) usually leads to strong pigment-pigment interaction. On the other hand, the disorder may be caused by spectral inhomogeneity (static disorder) or by the electron-phonon interaction (dynamic disorder). These two extreme regimes are the following:

- When the excitonic couplings are small, exciton states are well-localized in individual chromophores. Then, energy transfer takes place due to successive incoherent hoppings between molecules, and **Förster theory** can be applied.

- When the excitonic couplings overcome disorder, exciton states are delocalized over a number of chromophores. In this case, we have to use the exciton basis and energy transfer occurs due to coherent phonon-induced relaxation between exciton levels. In this limit of strong electronic coupling, the **Redfield equations** describe the exciton dynamics. The Bloch–Redfield formalism [400, 401] used for describing the dynamics of a system weakly coupled to its environment is explained in Subsection 2.1.2.

In both cases the transfer rate can be computed using first-order perturbation theory, where the part of the Hamiltonian taken as a perturbation varies depending on the case: the excitonic coupling can be treated as a perturbation when the electronic interactions are weak, whereas it is the electron-phonon coupling that acts as a perturbation for strong electronic interactions [399]. Computing the dynamics in the intermediate regime in which the electronic coupling is comparable to the exciton-phonon coupling is a more involved task. A modified Redfield theory has been used [402, 403], in which multiphonon effects are taking into account [404]. This theory has some restrictions, and some other methods have been developed to incorporate diverse effects.

Quantum coherence

In the mid 1990s, researchers started thinking about the possible implication of coherence in the promotion of the efficiency in the first steps of photosynthesis. After being predicted [390, 405], and indirectly observed in the form of a quantum beating between exciton levels in a BChl protein [406], some studies effectively revealed coherence dynamics in different photosynthetic complexes in 2007. In particular, long-lasting quantum coherence between excitonic states ($>$ 660 fs) was found in the Fenna–Matthews–Olson (FMO) complex of the green sulphur bacteria by Engel *et al.* [385]. This means that energy transfer does not occur through incoherent hopping but there exists a wavelike coherent motion instead. Long-lasting coherence between two exciton states was also reported in the reaction center of a purple bacteria by Lee *et al.* [386]. The origin of such long-lived coherence was related to the protein environment, which preserves the electronic coherence and allow the excitation to move coherently in space. The excitation moves rapidly and reversibly in space, and the protection of coherence by the protein matrix would enhance the efficiency of the energy harvesting process.

Theoretical modelling of light-harvesting complexes

The theoretical description of photosynthetic complexes is thus carried out in terms of **exciton states** —the electronically excited states in these complexes are given by superpositions of molecular excited states. These exciton states serve as a basis for the description of the optical properties of light-harvesting complexes (the dipole moment of the optical transition associated with a particular exciton state would be expressed as a linear combination of molecular transition dipoles), as well as of the exciton dynamics [407]. Different theoretical models have been developed to determine the **site energies** and the **electronic coupling** between pigments, from which the associated Hamiltonian for the electronic excitations is built.

The electronic couplings between the transition dipoles of the pigments lead to the **excitonic couplings**. These interactions have been traditionally computed from the Förster theory, using the point-dipole approximation [389]. As we have commented, such approximation is generally no valid as these pigment-protein arrangements tend to be closely packed. Structural information provides valuable data to extract these interactions. The transition density cube method [408, 409] is commonly used to compute the excitonic couplings, but there are some other numerical methods developed to this end [410]. The effect of the protein matrix on the exciton couplings has been also explored [411, 412], since the presence of this environment may screen the Coulomb interaction.

The values of the **site energies** of the electronic transitions associated with the different chromophores need to be determined as well. These are the transition energies in absence of electronic couplings with other chromophores. In this case, precise information of the site energies cannot be extracted using only structructual information, as they are strongly affected by the protein environment and the long-range electrostatic interactions. Generally, these transition energies are determined by fitting to experimental data obtained in optical experiments.

Once the electronic Hamiltonian is built from the site energies and the electronic couplings, the effect of the environment needs to be included [413]. The coupling to the environment is the responsible for the exciton relaxation and play an important role in the exciton dynamics [388]. It is a common procedure to introduce the effect of the environment through the **spectral density**, which characterizes the strength of the coupling between chromophores and the continuum of bath modes (see Subsection 2.1.2). Each chromophore is considered to be interacting with its own phononic bath, which is uncorrelated from the rest. The spectral density is experimentally determined by using ultrafast nonlinear spectroscopic techniques.

This is the basis for the theoretical models aiming to describe the optical properties and the dynamics of the excitation energy transfer in photosynthetic complexes [414]. In our case, we were interested in studying the modification of the exciton dynamics due to the interaction with the electromagnetic field within an optical cavity. In Subsection 1.3.3, we discussed that the energy-transfer process between two collections of organic molecules benefits from the delocalization of polaritons. The creation of these hybrid light-matter states may also enhance the process of energy transfer in these photosynthetic complexes. In particular, we studied the cavity-modified exciton dynamics in the photosynthetic unit of purple bacteria [415], and this is the work we present in the second part of Chapter 4.

CHAPTER 2

THEORETICAL FRAMEWORK

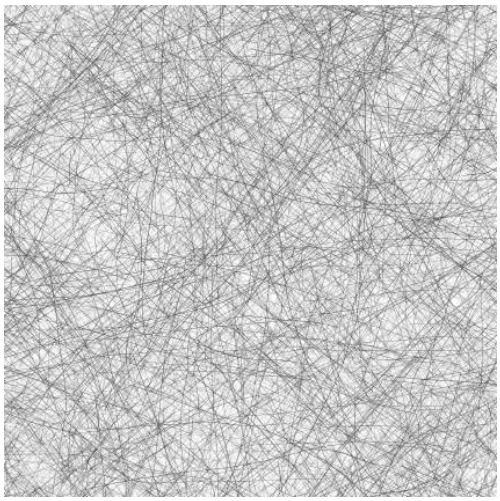

CHAPTER 2

THEORETICAL FRAMEWORK

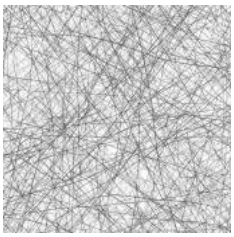

Powerful methods for the description of light-matter interaction have been developed over time. This introductory chapter is devoted to the theoretical formalism used throughout this thesis for the description of hybrid systems and some of their characteristics. With the aim to be self-contained, here we outline the most important concepts and equations which are the basis of the research work presented in the subsequent chapters. Therefore, we suggest the expert reader skip this part.

First, we introduce the density matrix formalism for the description of quantum systems in Section 2.1, where the equations governing their time evolution are also reviewed (some detailed derivations of different master equations are provided in Appendix C). Then, we study the quantum description of light-matter interaction in Section 2.2. After presenting the quantization of both the light and matter components, the Hamiltonian describing the light-matter coupling is discussed (some extensions of the information contained in this section are provided in Appendix D). In Section 2.3, the topic of optical fluctuations displayed by light sources is addressed, presenting the theoretical framework for the study of quantum coherence (the theory of classical coherence can be found in Appendix E). Finally, the focus is on matter, as the quantum description of organic molecules is analyzed in Section 2.4 (some extensions of this topic are located in Appendix F).

2.1 Quantum dynamics: master equation formalism

A quantum system is described through the associated Hamiltonian, the operator that comprises the energy of all its components. When considering closed quantum systems, the evolution takes place according to unitary transformations. But systems are not completely isolated from its surroundings, which requires the inclusion of incoherent processes in the formalism. The time dynamics of different hybrid systems interacting with their environment is precisely studied in this thesis. Here we overview the equations describing the time evolution of both closed and open quantum systems, referring to textbooks on this matter, such as Ref. [416, 417], for further reading.

2.1.1 Time-evolution of closed systems

A **closed system** is the one isolated from its environment, such that there is no interaction between them. The dynamics of the system is thus dictated by its Hamiltonian through a unitary (non-dissipative) transformation.

State vector description

Let us consider a closed quantum system described by the Hamiltonian $\hat{H}$ which, in general, will be time-dependent. The evolution of some state of the system $|\psi(t)\rangle$ is governed by the **Schrödinger equation**:

$$\frac{\mathrm{d}}{\mathrm{d}t}|\psi(t)\rangle = -\frac{\mathrm{i}}{\hbar}\hat{H}(t)\,|\psi(t)\rangle\ . \tag{2.1}$$

The time-evolution of that state can be expressed in terms of the **evolution operator** $\mathcal{U}(t,t_0)$ as:

$$|\psi(t)\rangle = \mathcal{U}(t,t_0)|\psi(t_0)\rangle\ ,$$

where $|\psi(t_0)\rangle$ is the initial state of the system. By introducing this expression into Equation 2.1, we obtain an equation for the evolution operator:

$$\frac{\mathrm{d}}{\mathrm{d}t}\mathcal{U}(t,t_0) = -\frac{\mathrm{i}}{\hbar}\hat{H}(t)\,\mathcal{U}(t,t_0)\ ,$$

whose formal solution is given by:

$$\mathcal{U}(t,t_0) = \mathrm{e}^{-\frac{\mathrm{i}}{\hbar}\hat{H}(t-t_0)}\ . \tag{2.2}$$

if the Hamiltonian is time-independent. Therefore, given the Hamiltonian describing the system, we can build the corresponding evolution operator and apply it to a particular state to know its time-evolution.

The Hamiltonian description is limited, since the state of the system may not be simply described by a ket $|\psi(t)\rangle$. In that case, it is required to work within the **density matrix formalism**, which is also useful when interested in the dynamics of only a small part of a larger system.

Density matrix formalism

When the state of the system can be described by some state vector $|\psi(t)\rangle$, the system is said to be in a **pure state**. The corresponding **density operator** $\hat{\rho}$ is easily built as the projector of that state:

$$\hat{\rho}(t) = |\psi(t)\rangle\langle\psi(t)|\ .$$

On the contrary, the system is said to be in a **mixed state** when it cannot be written as a simple ket. This is the situation, for instance, in which the system is in a mixture or ensemble of quantum states $|\psi_i\rangle$ (with $i = 1, 2\ldots$). The density operator is then built as:

$$\hat{\rho}(t) = \sum_i w_i|\psi_i(t)\rangle\langle\psi_i(t)|\ , \tag{2.3}$$

where w_i is the probability of finding the system in the state $|\psi_i\rangle$ (therefore, quantities w_i satisfy: $0 \leq w_i \leq 1$ and $\sum_i w_i = 1$). Note that this is just the sum of the projection operators over each component of the ensemble, $\hat{\mathbb{P}}_i = |\psi_i\rangle\langle\psi_i|$, weighted with the corresponding probability. In a density matrix, elements from its diagonal are called **populations**, while the off-diagonal elements are known as **coherences**. Apart from being Hermitian, density matrices are positive semi-definite (that is, $\langle\phi|\hat{\rho}|\phi\rangle \geq 0$ for any arbitrary state vector $|\phi\rangle$), and its trace is equal to one. Besides, $\mathrm{Tr}[\hat{\rho}^2] \leq 1$, and the equal takes place if and only if the density matrix represents a pure state.

In the density matrix formalism, the dynamics of the system is governed by the **Liouville–von Neumann equation**:

$$\frac{\mathrm{d}}{\mathrm{d}t}\hat{\rho}(t) = -\frac{\mathrm{i}}{\hbar}[\hat{H}(t), \hat{\rho}(t)] \,. \tag{2.4}$$

Alternatively, the time evolution of the density matrix $\hat{\rho}$ can be expressed in terms of a superoperator $\mathcal{L}$, the so-called **generalized Liouvillian**:

$$\frac{\mathrm{d}}{\mathrm{d}t}\hat{\rho}(t) = \mathcal{L}\hat{\rho}(t) \,.$$

If there exists no explicit time-dependence of the Liouvillian, the formal solution of this equation is given by:

$$\hat{\rho}(t) = \mathrm{e}^{\mathcal{L}(t-t_0)}\hat{\rho}(t_0) \,.$$

It can be now introduced the **generalized evolution operator** $\mathcal{V}(t, t_0)$, or propagator, which describes the time-evolution of the density matrix:

$$\hat{\rho}(t) = \mathcal{V}(t, t_0)\hat{\rho}(t_0) \,,$$

with:

$$\mathcal{V}(t, t_0) \equiv \mathrm{e}^{\mathcal{L}(t-t_0)} \,.$$

This density matrix formalism is mathematically equivalent to the formulation of quantum mechanics in terms of state vectors. Nonetheless, it provides a more general description as it considers that the system may be in a state that cannot be represented by a simple ket state. The density matrix formalism is also useful when the number of degrees of freedom comes to be large. The problem of solving the dynamics of the whole system becomes intractable, and other approaches need to be used. There, the density matrix is disclosed as a fundamental tool.

2.1.2 Time-evolution of open systems

There is no system completely isolated from its surroundings, as we have said before, so the theoretical framework presented for closed quantum systems needs to be extended. An **open quantum system** is the one that interacts with its environment, and this interaction induces changes in the dynamics of the system with respect to its closed counterpart. There may appear, for instance, loss of population or coherence as a result of the interaction. This makes it necessary to go beyond the unitary evolution displayed by closed systems and include the emerging incoherent processes in the dynamics.

In the derivation of the equations governing the dynamics of a system interacting with its environment, a possible approach could consist in the expansion of the definition of the system so as to include the environment itself. Since the composed system would be certainly closed, its dynamics will be described by the Liouville–von Neumann equation of motion. Nevertheless, the inclusion of all the degrees of freedom associated with the environment could make the problem unmanageable. Notice, however, that one is mainly interested in the dynamics of the original system, and not so much in the particular dynamics of its environment. As we will see now, the problem can be then reduced with the help of the density matrix formalism and the introduction of master equations for the description of the evolution of these open quantum systems.

System coupled to a reservoir

Let consider the system comprising all possible degrees of freedom so as to be considered as closed, hence the Liouville–von Neumann equation (Equation 2.4) gives the dynamics of the whole entity. Nevertheless, in most cases we are only interested in a part of the entire system (S), while considering the remaining as an environment o **reservoir** (R). The complete Hilbert space $\mathcal{H}$ can be expressed as the tensor product:

$$\mathcal{H} = \mathcal{H}_S \otimes \mathcal{H}_R \,,$$

where $\mathcal{H}_S$ and $\mathcal{H}_R$ stand for the Hilbert spaces associated with the system of interest and the reservoir, respectively. These two subsets in which the whole system is divided are usually not independent, but they are connected through an **interaction Hamiltonian** $\hat{H}_{int}$. Then, the general form of the complete Hamiltonian $\hat{H}$ can be written as sum of three parts:

$$\hat{H} = \hat{H}_S + \hat{H}_R + \hat{H}_{int} \,, \tag{2.5}$$

where $\hat{H}_S$ is Hamiltonian describing the system of interest, and $\hat{H}_R$ is the Hamiltonian associated with the reservoir. Each part acts on the corresponding Hilbert space, that is, $\hat{H}_S = \hat{H}_S \otimes \mathbb{1}_R$ is the part of the Hamiltonian acting only on S while $\hat{H}_R = \mathbb{1}_S \otimes \hat{H}_R$ acts only on the reservoir R. There, $\mathbb{1}_S$ and $\mathbb{1}_R$ are the identities in the corresponding Hilbert spaces.

The density matrix describing the state of the composite system $\hat{\rho}(t)$ evolves according to the Liouville–von Neumann equation (Equation 2.4). We are interested, by contrast, in the time-evolution of the reduced system S without requiring detailed information of the reservoir R. The density matrix corresponding to the small subset of interest can be obtained by tracing out the degrees of freedom of the environment:

$$\hat{\rho}_S(t) = \mathrm{Tr}_R[\hat{\rho}(t)] \,, \tag{2.6}$$

and it is known as the **reduced density matrix**. Our aim is to obtain an equation for $\hat{\rho}_S$ involving just the degrees of freedom of the system.

The Born–Markov master equation

Starting from the master equation that governs the dynamics of the whole system (Equation 2.4), we are interested in obtaining the one corresponding to the reduced density matrix. The Born–Markov approximation is the standard approach to this end (the complete derivation of the resulting master equation is given in Appendix C, Section C.1). First of all, it requires the transformation of Equation 2.4 to the interaction picture, yielding:

$$\frac{\mathrm{d}}{\mathrm{d}t}\tilde{\rho}(t) = -\frac{\mathrm{i}}{\hbar}[\tilde{H}_{\mathrm{int}}(t), \tilde{\rho}(t)] \,.$$

To simplify the notation, we drop the hats over operators from now on, and the tilde is used to indicate that operators are expressed in the interaction picture (see Appendix B for an overview of the different quantum representations). Notice that this equation is equivalent to that in the Schrödinger picture but involving the interaction Hamiltonian H_{int} instead. Some assumptions are then considered:

- When the coupling between system and reservoir is sufficiently weak, correlations between them remain negligible throughout the evolution. As a result, the density matrix describing the composite system can be considered separable at any time: $\tilde{\rho}(t) = \tilde{\rho}_{\mathrm{S}}(t) \otimes \tilde{\rho}_{\mathrm{R}}(t)$. Moreover, the reservoir is usually significantly larger than the system, and the state of the reservoir is practically not affected by its interaction with the system. Therefore, the reservoir can be taken as constant: $\tilde{\rho}_{\mathrm{R}}(t) \equiv B_0$. These two assumptions are known as the **Born approximation**, yielding together the following form for the density matrix describing the state of the composite system: $\tilde{\rho}(t) = \tilde{\rho}_{\mathrm{S}}(t) \otimes B_0$.
- The internal dynamics of the reservoir tends to be much faster than the dynamics of the system. In that case, bath correlations can be disregarded, as they are quickly lost in comparison with all relevant time-scales present in the system dynamics. This means considering a **Markovian environment**.

These assumptions are usually named together as the **Born–Markov approximation**, and the resulting master equation describing the dynamics of the reduced density matrix $\rho_{\mathrm{S}}(t)$ (Equation 2.6) in the interaction picture reads:

$$\frac{\mathrm{d}}{\mathrm{d}t}\tilde{\rho}_{\mathrm{S}}(t) = -\frac{1}{\hbar^2}\int_0^\infty \mathrm{Tr}_{\mathrm{R}}\left\{\left[\tilde{H}_{\mathrm{int}}(t), \left[\tilde{H}_{\mathrm{int}}(t-\tau), \tilde{\rho}_{\mathrm{S}}(t) \otimes B_0\right]\right]\right\} \mathrm{d}\tau \,, \tag{2.7}$$

where the trace is taken over all degrees of freedom associated with the reservoir.

The Bloch–Redfield master equation

The Born–Markov approximation is the standard approach for the derivation of the equation of motion of a system coupled to its environment (Equation 2.7), where H_{int} is the Hamiltonian describing their mutual interaction. From there, the **Bloch–Redfield formalism** provides a mechanism to introduce dissipation based on a microscopic model of the reservoir. The environment is usually considered as a large system in thermal equilibrium, and it is modelled as a continuum of oscillators. Then, dissipation arises from the coupling of the system to that thermal bath. Although outlined here, a more complete derivation of the Bloch–Redfield master equation can be found in Appendix C, Section C.2.

The derivation of the Bloch–Redfield formalism starts from Equation 2.7, once the Born–Markov approximation has been introduced. The **interaction Hamiltonian** H_{int} there involved can be expressed as the sum of products of operators:

$$H_{\text{int}} = \sum_j \mathcal{Q}_j \otimes \mathcal{R}_j \,, \tag{2.8}$$

where $\mathcal{Q}_j$ stand for operators in the Hilbert space of the subsystem S, and $\mathcal{R}_j$ for those acting on the Hilbert space of the reservoir R. When transformed to the interaction picture (see Appendix B), this Hamiltonian reads:

$$\tilde{H}_{\text{int}}(t) = \sum_j \tilde{\mathcal{Q}}_j(t) \otimes \tilde{\mathcal{R}}_j(t) \,,$$

where the tilde over operators indicate that they are expressed in the interaction picture. By substituting this form of the interaction Hamiltonian into Equation 2.7, and transforming the whole master equation into the Schrödinger picture, we arrive at:

$$\begin{aligned}\frac{\mathrm{d}}{\mathrm{d}t}\rho_{\text{S}}(t) = &-\frac{\mathrm{i}}{\hbar}\left[H_{\text{S}}, \rho_{\text{S}}(t)\right] \\ &-\frac{1}{\hbar^2}\sum_{j,k}\int_0^\infty \Big\{\Big(\mathcal{Q}_j\, \mathrm{e}^{-\frac{\mathrm{i}}{\hbar}H_{\text{S}}\tau}\, \mathcal{Q}_k\, \mathrm{e}^{\frac{\mathrm{i}}{\hbar}H_{\text{S}}\tau}\, \rho_{\text{S}}(t) - \mathrm{e}^{-\frac{\mathrm{i}}{\hbar}H_{\text{S}}\tau}\, \mathcal{Q}_k\, \mathrm{e}^{\frac{\mathrm{i}}{\hbar}H_{\text{S}}\tau}\, \rho_{\text{S}}(t)\, \mathcal{Q}_j\Big) \\ &\qquad \otimes \langle \tilde{\mathcal{R}}_j(t)\, \tilde{\mathcal{R}}_k(t-\tau)\rangle \\ &+\Big(\rho_{\text{S}}(t)\, \mathrm{e}^{-\frac{\mathrm{i}}{\hbar}H_{\text{S}}\tau}\, \mathcal{Q}_k\, \mathrm{e}^{\frac{\mathrm{i}}{\hbar}H_{\text{S}}\tau}\, \mathcal{Q}_j - \mathcal{Q}_j\, \rho_{\text{S}}(t)\, \mathrm{e}^{-\frac{\mathrm{i}}{\hbar}H_{\text{S}}\tau}\, \mathcal{Q}_k\, \mathrm{e}^{\frac{\mathrm{i}}{\hbar}H_{\text{S}}\tau}\Big) \\ &\qquad \otimes \langle \tilde{\mathcal{R}}_k(t-\tau)\, \tilde{\mathcal{R}}_j(t)\rangle\Big\}\, \mathrm{d}\tau \,.\end{aligned} \tag{2.9}$$

The first term corresponds to the coherent evolution governed by the system Hamiltonian, reproducing the Liouville–von Neumann equation (Equation 2.4). The other terms are related to the interaction with the environment, where correlation functions of reservoir operators get involved.

This master equation can be written in matrix form, for which we consider the basis composed of the eigenstates of the system Hamiltonian H_{S}:

$$H_{\text{S}}|\omega_n\rangle = \hbar\omega_n|\omega_n\rangle \,, \tag{2.10}$$

where $|\omega_n\rangle$ stands for the eigenstate of the Hamiltonian associated with the eigenvalue $\hbar\omega_n$. The ab-component of the matrix form of Equation 2.9 in this basis reads:

$$\begin{aligned}\frac{\mathrm{d}}{\mathrm{d}t}\rho_{ab}(t) = &-\mathrm{i}\omega_{ab}\, \rho_{ab}(t) \\ &-\frac{1}{\hbar^2}\sum_{j,k}\sum_{m,n}\int_0^\infty \Big\{\Big(\delta_{bn}\sum_o \mathcal{Q}^j_{ao}\mathcal{Q}^k_{om}\mathrm{e}^{-\mathrm{i}\omega_{om}\tau} - \mathcal{Q}^k_{am}\mathcal{Q}^j_{nb}\mathrm{e}^{-\mathrm{i}\omega_{am}\tau}\Big) \\ &\qquad \otimes \langle \tilde{\mathcal{R}}_j(t)\, \tilde{\mathcal{R}}_k(t-\tau)\rangle \\ &+\Big(\delta_{ma}\sum_o \mathcal{Q}^k_{no}\mathcal{Q}^j_{ob}\mathrm{e}^{-\mathrm{i}\omega_{no}\tau} - \mathcal{Q}^j_{am}\mathcal{Q}^k_{nb}\mathrm{e}^{-\mathrm{i}\omega_{nb}\tau}\Big) \\ &\qquad \otimes \langle \tilde{\mathcal{R}}_k(t-\tau)\, \tilde{\mathcal{R}}_j(t)\rangle\Big\}\, \rho_{mn}(t)\, \mathrm{d}\tau \,,\end{aligned}$$

where we have defined the components of the density matrix $\rho_{mn}(t) = \langle\omega_m|\rho_S(t)|\omega_n\rangle$, as well as the corresponding to the system operators $\mathcal{Q}^j_{mn} = \langle\omega_m|\mathcal{Q}_j|\omega_n\rangle$. Besides, we have introduced the following notation for the difference of frequencies: $\omega_{mn} = \omega_m - \omega_n$. At this point, we can introduce the **spectral density** (or **power spectrum**) associated with the bath:

$$\Theta_{jk}(\omega) = \frac{1}{2\pi}\int_{-\infty}^{\infty}\langle\tilde{\mathcal{R}}_j(t)\,\tilde{\mathcal{R}}_k(t+\tau)\rangle\,\mathrm{e}^{\mathrm{i}\omega\tau}\mathrm{d}\tau\,, \tag{2.11}$$

which is defined in terms of the correlation function of the reservoir operators $\tilde{\mathcal{R}}_j$ and $\tilde{\mathcal{R}}_k$ at times t and $t+\tau$ respectively (both concepts of correlation function and spectral density are studied in Appendix E, Section E.3). By considering this magnitude, the previous form of the master equation reduces to:

$$\frac{\mathrm{d}}{\mathrm{d}t}\rho_{ab}(t) = -\mathrm{i}\omega_{ab}\rho_{ab}(t) + \sum_{m,n}R_{abmn}\rho_{mn}(t)\,, \tag{2.12}$$

where we have introduced the so-called **Bloch–Redfield tensor**, which comprises all the incoherent processes:

$$\begin{aligned}R_{abmn} = -\frac{\pi}{\hbar^2}\sum_{j,k}\Bigg(&\delta_{bn}\sum_o \mathcal{Q}^j_{ao}\mathcal{Q}^k_{om}\Theta_{jk}(\omega_o-\omega_m) - \mathcal{Q}^k_{am}\mathcal{Q}^j_{nb}\Theta_{jk}(\omega_a-\omega_m)\\ &+\delta_{ma}\sum_o \mathcal{Q}^k_{no}\mathcal{Q}^j_{ob}\Theta^*_{jk}(\omega_o-\omega_n) - \mathcal{Q}^j_{am}\mathcal{Q}^k_{nb}\Theta^*_{jk}(\omega_b-\omega_n)\Bigg)\,.\end{aligned} \tag{2.13}$$

Therefore, the **Bloch–Redfield master equation** separates the time-evolution of the density matrix in two parts, when expressed in the Schrödinger picture. The first term corresponds to the coherent evolution, where the eigenfrequencies associated with the system Hamiltonian without interaction appear. Then, the second part accounts for all incoherent processes arising from the interaction with the reservoir. In this form of the master equation, the system-reservoir interaction is introduced by means of the reservoir spectral density Θ_{jk} and the operators $\mathcal{Q}_j$ through which the environment is coupled to the system.

Alternatively, the above equation for the components of the density matrix can be rewritten in terms of operators (Equation C.26), yielding:

$$\begin{aligned}\frac{\mathrm{d}}{\mathrm{d}t}\rho_S(t) = &-\frac{\mathrm{i}}{\hbar}\left[H_S,\rho_S(t)\right]\\ &-\frac{\pi}{\hbar^2}\sum_{j,k}\sum_{m,n}\Big\{\langle\omega_m|\mathcal{Q}_k|\omega_n\rangle\,\left(\mathcal{Q}_j|\omega_m\rangle\langle\omega_n|\rho_S(t) - |\omega_m\rangle\langle\omega_n|\rho_S(t)\mathcal{Q}_j\right)\\ &\qquad\qquad\Theta_{jk}(\omega_m-\omega_n)\\ &+\langle\omega_n|\mathcal{Q}_k|\omega_m\rangle\,\left(\rho_S(t)|\omega_n\rangle\langle\omega_m|\mathcal{Q}_j - \mathcal{Q}_j\rho_S(t)|\omega_n\rangle\langle\omega_m|\right)\\ &\qquad\qquad\Theta^*_{jk}(\omega_m-\omega_n)\,\Big\}\,.\end{aligned} \tag{2.14}$$

The Bloch–Redfield master equation will be used in Chapter 4 to introduce the coupling of organic molecules to their vibrational bath.

The Lindblad master equation

The equation governing the dynamics of the reduced density matrix ρ_S describing a system S interacting with a reservoir is thus given by Equation 2.9 when the interaction Hamiltonian is written as indicated in Equation 2.8. In particular, if we assume a rapid decay of correlations in the reservoir, we can take: $\langle \tilde{\mathcal{R}}_j(t)\, \tilde{\mathcal{R}}_k(t+\tau)\rangle \propto \delta(\tau)$. Therefore, the two correlation functions in Equation 2.9 can be written as follows:

$$\langle \tilde{\mathcal{R}}_j(t)\, \tilde{\mathcal{R}}_k(t-\tau)\rangle = \hbar^2 \lambda_{jk}\delta(\tau)\,,$$
$$\langle \tilde{\mathcal{R}}_k(t-\tau)\, \tilde{\mathcal{R}}_j(t)\rangle = \hbar^2 \lambda_{kj}\delta(\tau)\,,$$

where we have considered Equation C.23 and introduced the constant λ_{jk}. Considering this form for the correlation functions, Equation 2.9 reduces to:

$$\frac{\mathrm{d}}{\mathrm{d}t}\hat{\rho}_S(t) = -\frac{\mathrm{i}}{\hbar}\,[\hat{H}_S, \hat{\rho}_S(t)] - \sum_{j,k}\lambda_{jk}\left(\hat{\mathcal{Q}}_j^\dagger \hat{\mathcal{Q}}_k\, \hat{\rho}_S(t) + \hat{\rho}_S(t)\, \hat{\mathcal{Q}}_j^\dagger \hat{\mathcal{Q}}_k - 2\hat{\mathcal{Q}}_k \hat{\rho}_S(t) \hat{\mathcal{Q}}_j^\dagger\right)\,,$$

where we have recovered the hats over operators. The coefficient matrix $\lambda = (\lambda_{jk})$ can be diagonalized [416], yielding:

$$\frac{\mathrm{d}}{\mathrm{d}t}\hat{\rho}_S(t) = -\frac{\mathrm{i}}{\hbar}\,[\hat{H}_S, \hat{\rho}_S(t)] - \sum_{l}\frac{\gamma_l}{2}\left(\hat{\mathcal{O}}_l^\dagger \hat{\mathcal{O}}_l\, \hat{\rho}_S(t) + \hat{\rho}_S(t)\, \hat{\mathcal{O}}_l^\dagger \hat{\mathcal{O}}_l - 2\hat{\mathcal{O}}_l \hat{\rho}_S(t) \hat{\mathcal{O}}_l^\dagger\right)\,, \quad (2.15)$$

where γ_l are the non-negative eigenvalues and $\hat{\mathcal{O}}_l$ are the new set of operators. This is the so-called **Lindblad master equation**, and turns out to be the most general form of the (Markovian) evolution of a density matrix (that is, the most general completely positive and trace-preserving map of a density matrix onto the space of density matrices) [418, 419]. This master equation is usually written in terms of the functional $\mathcal{L}_{\hat{\mathcal{O}}}$, which acts on the density matrix as follows:

$$\mathcal{L}_{\hat{\mathcal{O}}}[\hat{\rho}] = 2\hat{\mathcal{O}}\hat{\rho}\hat{\mathcal{O}}^\dagger - \hat{\mathcal{O}}^\dagger\hat{\mathcal{O}}\hat{\rho} - \hat{\rho}\hat{\mathcal{O}}^\dagger\hat{\mathcal{O}}\,. \quad (2.16)$$

This is the **Lindblad term** associated with the operator $\hat{\mathcal{O}}$. Hence Equation 2.15 can be written in shorthand form as:

$$\frac{\mathrm{d}}{\mathrm{d}t}\hat{\rho}_S(t) = -\frac{\mathrm{i}}{\hbar}[\hat{H}_S, \hat{\rho}_S(t)] + \sum_{l}\frac{\gamma_l}{2}\mathcal{L}_{\hat{\mathcal{O}}_l}[\hat{\rho}_S]\,, \quad (2.17)$$

where $\hat{\mathcal{O}}_l$ are the operators through which the system is coupled to the environment, and γ_l are the associated rates. The Lindblad master equation is then composed of two parts. The first term is the **coherent part**, and corresponds to the unitary evolution of the system guided by its Hamiltonian (Equation 2.4). The second term is the **incoherent part** of the master equation, and represents the effective evolution induced by the environment. It comprises all incoherent processes arising from the coupling to the reservoir, and they may lead to a loss of population or coherence in the system. Since the system-reservoir coupling is weak so as to fulfil the Born–Markov approximation, this incoherent part represents just a small change in the unitary evolution of the system.

As with the Bloch–Redfield formalism, the Lindblad master equation describes the evolution of a system under the influence of a reservoir —the difference is the procedure

through which this effect is included. Within the Bloch–Redfield formalism, the master equation (Equation 2.12) is obtained from a microscopic model of the reservoir (with its noise-power spectrum getting ultimately involved). By contrast, Lindblad terms model the various incoherent processes in Equation 2.17. Operators $\hat{\mathcal{O}}_l$ try to reproduce the phenomenology of the dissipation mechanism, and the associated rates γ_l are free parameters, whose value is chosen according to the observed strength of the process. To some extent, the effect of the environment is introduced in the dynamics with certain insight into the nature of the specific source of dissipation, but there is not an underlying physical model for such processes.

2.2 Coupling light and matter

The interaction of light and matter in the quantum regime gives rise to interesting phenomena, since both excitons and photons are modified and their properties become altered as a result of this mutual influence. The research work presented in this thesis exploits this feature, and all the systems under study are composed of light and matter components interacting within the strong coupling regime. For this reason, we overview here the standard formalism for the description of the quantum light-matter interaction, paying special attention to the coupling of several quantum emitters to a single (quantized) cavity mode. Ref. [420, 120, 421] are specially recommended as an introduction to this topic.

2.2.1 Light: a collection of harmonic oscillators

Cavity QED deals with electromagnetic fields confined in a cavity, where **standing waves** or **running waves** are formed in keeping with the imposed conditions. For the simple case of a resonant cavity composed of two opposed parallel flat mirrors (Fabry–Pérot cavity), the longitudinal modes that survive are those such that the length of the cavity is equal to a multiple of half its wavelength, while all other wavelengths are suppressed due to destructive interference. A **single cavity mode** is generally singled out, not only in this case, and this mode is intended to be near the emitter resonance.

A single cavity mode

Bosonic creation and annihilation operators A single electromagnetic mode is formally equivalent to the one-dimensional harmonic oscillator, as shown in Appendix D, Section D.1. There, its quantization procedure is also explained. A cavity mode is thus described by the **creation** and **annihilation operators** $\hat{a}^\dagger$ and $\hat{a}$, fulfilling the **bosonic commutation relation** of Equation D.3, that is:

$$[\hat{a}, \hat{a}^\dagger] = 1 \, .$$

These operators act on the Fock state $|n\rangle$, representing the state with a fixed number n of excitations, as indicated in Equation D.6, that is:

$$\begin{aligned} a^\dagger|n\rangle &= \sqrt{n+1}\,|n+1\rangle\,, \\ a|n\rangle &= \sqrt{n}\,|n-1\rangle\,. \end{aligned} \tag{2.18}$$

They bring a state with n excitations to one with $n+1$ or $n-1$ excitations, respectively, so that they create or destroy a quantum $\hbar\omega$ of the excitation energy of the oscillator.

Hamiltonian The Hamiltonian corresponding to a single cavity mode of frequency ω_0 is given by Equation D.4, namely:

$$\hat{H}_\mathrm{C} = \hbar\omega_0\,\hat{a}^\dagger\hat{a}\,, \tag{2.19}$$

where we have removed the ground state energy (Equation D.5).

The (quantized) light component

The Hamiltonian corresponding to the quantized radiation field is equivalent to a collection of independent and uncoupled quantum harmonic oscillators, as discussed in Appendix D, Section D.2. There, the quantization of the free electromagnetic field is performed, both in a cavity and in infinite space. In particular, when we consider periodic boundary conditions in a three-dimensional cavity of side L and volume $V = L^3$, the **electric field operator** in the Schrödinger picture is given by Equation D.29, that is:

$$\hat{\boldsymbol{E}}(\boldsymbol{x}) = \sum_{\boldsymbol{k}}\sum_{\lambda}\sqrt{\frac{\hbar\omega_k}{2\epsilon_0 V}}\boldsymbol{\epsilon}_{\boldsymbol{k}\lambda}\left[\hat{a}_{\boldsymbol{k}\lambda}\mathrm{e}^{\mathrm{i}\boldsymbol{k}\cdot\boldsymbol{x}} + \hat{a}^\dagger_{\boldsymbol{k}\lambda}\mathrm{e}^{-\mathrm{i}\boldsymbol{k}\cdot\boldsymbol{x}}\right], \tag{2.20}$$

where the sum is performed over all possible wavevectors $\boldsymbol{k}$ compatible with the boundary conditions (Equation D.20), and over the two possible polarization values $\lambda = 1, 2$. The unit polarization vectors $\boldsymbol{\epsilon}_{\boldsymbol{k}\lambda}$ are both transverse (imposed by the Coulomb gauge, Equation D.13) and perpendicular to each other, obeying Equation D.21. Now, $\hat{a}^\dagger_{\boldsymbol{k}\lambda}$ and $\hat{a}_{\boldsymbol{k}\lambda}$ are the **creation** and **annihilation operators** associated with a mode with wavevector $\boldsymbol{k}$ and polarization λ, fulfilling the commutation rules in Equation D.27. Each mode of the field is thus described by an independent and uncoupled quantum-mechanical harmonic oscillator with associated frequency $\omega_k = c|\boldsymbol{k}|$. The **Hamiltonian operator** of the quantized radiation field is given by Equation D.31, or:

$$\hat{H}_\mathrm{rad} = \sum_{\boldsymbol{k}}\sum_{\lambda}\hbar\omega_k\hat{a}^\dagger_{\boldsymbol{k}\lambda}\hat{a}_{\boldsymbol{k}\lambda}\,, \tag{2.21}$$

when all zero-point energies (Equation D.32) are subtracted.

2.2.2 Matter: a collection of two-level systems

A **quantum emitter** is characterized by discrete energy levels, sometimes giving rise to very complex energy spectra. Although this energy structure is generally composed of multiple levels, most of the times emitters can be modelled as simple **two-level systems**,

with only one relevant transition. This comes from the fact that the energy separation between other levels is sufficiently large so as not to affect the transition of interest.

A single two-level system

Fermionic creation and annihilation operators Let $|g\rangle$ and $|e\rangle$ be the two available levels of a two-level system, that can be referred to as its ground state and first-excited state, respectively. Then, the **Hilbert space** associated with that two-level system is given by:

$$\mathscr{H}_2 = \{\alpha|g\rangle + \beta|e\rangle \mid \alpha, \beta \in \mathbb{C}\} \ .$$

These vectors forming the basis of the Hilbert space, $|g\rangle$ and $|e\rangle$, can be written in the canonical basis:

$$|g\rangle = \begin{pmatrix} 1 \\ 0 \end{pmatrix} , \qquad |e\rangle = \begin{pmatrix} 0 \\ 1 \end{pmatrix} .$$

We can think of them as the states representing left and right circular polarizations, or spin-up and spin-down. When working with this Hilbert space $\mathscr{H}_2$, observables can be expressed as $2x2$ (Hermitian) matrices. In particular, the quantum description of the system will be generally carried out in terms of the **σ-operators**, defined as:

$$\begin{aligned} \hat{\sigma}_{gg} \equiv |g\rangle\langle g| = \begin{pmatrix} 1 & 0 \\ 0 & 0 \end{pmatrix} , \qquad \hat{\sigma}_{ge} \equiv |g\rangle\langle e| = \begin{pmatrix} 0 & 1 \\ 0 & 0 \end{pmatrix} , \\ \hat{\sigma}_{eg} \equiv |e\rangle\langle g| = \begin{pmatrix} 0 & 0 \\ 1 & 0 \end{pmatrix} , \qquad \hat{\sigma}_{ee} \equiv |e\rangle\langle e| = \begin{pmatrix} 0 & 0 \\ 0 & 1 \end{pmatrix} . \end{aligned} \tag{2.22}$$

Specifically, $\hat{\sigma}_{eg}$ and $\hat{\sigma}_{ge}$ are known as the **creation** and **annihilation operators** associated with the quantum emitter, respectively:

$$\hat{\sigma}^\dagger \equiv |e\rangle\langle g| , \qquad \hat{\sigma} \equiv |g\rangle\langle e| . \tag{2.23}$$

The creation operator $\hat{\sigma}^\dagger$ shifts the system from the ground state to the excited state, while the annihilation operator $\hat{\sigma}$ brings the system from the excited to the ground state:

$$\hat{\sigma}^\dagger|g\rangle = |e\rangle , \qquad \hat{\sigma}|e\rangle = |g\rangle .$$

On the contrary, the reverse operations vanish:

$$\hat{\sigma}^\dagger|e\rangle = 0 , \qquad \hat{\sigma}|g\rangle = 0 .$$

An important property of the (fermionic) operators $\hat{\sigma}^\dagger$ and $\hat{\sigma}$ is that they fulfil the **anti-commutation algebra**:

$$[\hat{\sigma}, \hat{\sigma}^\dagger]_+ = \hat{\sigma}\hat{\sigma}^\dagger + \hat{\sigma}^\dagger\hat{\sigma} = \mathbb{1} .$$

This can be easily obtained from the closure theorem for a two level system, since the projection operators can be written as $|e\rangle\langle e| = \hat{\sigma}^\dagger\hat{\sigma}$ and $|g\rangle\langle g| = \hat{\sigma}\hat{\sigma}^\dagger$. The operator $\hat{\sigma}^z$ can be defined from them as:

$$\hat{\sigma}^z \equiv \frac{1}{2}(|e\rangle\langle e| - |g\rangle\langle g|) = \frac{1}{2}(\hat{\sigma}^\dagger\hat{\sigma} - \hat{\sigma}\hat{\sigma}^\dagger) , \tag{2.24}$$

acting on the ground and excited states as:

$$\hat{\sigma}^z|\mathrm{g}\rangle = -\frac{1}{2}\,|\mathrm{g}\rangle\,, \qquad \hat{\sigma}^z|\mathrm{e}\rangle = \frac{1}{2}\,|\mathrm{e}\rangle\,. \tag{2.25}$$

As we have mentioned, a two-level emitter can be thought as a spin-1/2 system, where $|\mathrm{g}\rangle$ and $|\mathrm{e}\rangle$ represents the spin-down and spin-up states. In this sense, the operator $\hat{\sigma}^z$ would be equivalent to a spin operator yielding the spin projection when applied to the system. The commutation relations that all these operators fulfil are the following:

$$[\hat{\sigma}^\dagger, \hat{\sigma}\,] = 2\hat{\sigma}^z\,, \qquad [\hat{\sigma}^z, \hat{\sigma}^\dagger] = \hat{\sigma}^\dagger\,, \qquad [\hat{\sigma}^z, \hat{\sigma}\,] = -\hat{\sigma}\,.$$

Hamiltonian The Hamiltonian $\hat{H}_{\mathrm{2LS}}$ describing a two-level system, characterized by the ground state $|\mathrm{g}\rangle$ with energy E_g and the excited state $|\mathrm{e}\rangle$ with energy E_e, is given by:

$$\hat{H}_{\mathrm{2LS}} = E_\mathrm{e}|\mathrm{e}\rangle\langle\mathrm{e}| + E_g|\mathrm{g}\rangle\langle\mathrm{g}| = E_\mathrm{e}\hat{\sigma}^\dagger\hat{\sigma} + E_g\hat{\sigma}\hat{\sigma}^\dagger\,,$$

where we have introduced their fermionic creation and annihilation operators $\hat{\sigma}^\dagger$ and $\hat{\sigma}$ defined in Equation 2.23. It is usual to define the **optical transition energy** as $\hbar\omega_{\mathrm{eg}} \equiv E_\mathrm{e} - E_g$, and set the ground state energy to zero, thus the Hamiltonian $\hat{H}_{\mathrm{2LS}}$ becomes:

$$\hat{H}_{\mathrm{2LS}} = \hbar\omega_{\mathrm{eg}}\hat{\sigma}^\dagger\hat{\sigma}\,. \tag{2.26}$$

Alternatively, one can subtract the constant quantity $\frac{1}{2}(E_\mathrm{e} + E_g)\mathbb{1}$ to $\hat{H}_{\mathrm{2LS}}$, such that we have the Hamiltonian written in terms of the $\hat{\sigma}^z$ operator:

$$\hat{H}_{\mathrm{2LS}} = \hbar\omega_{\mathrm{eg}}\hat{\sigma}^z\,. \tag{2.27}$$

The (quantized) matter component

Bright mode operators When working with a collection of N two-level systems, it is convenient to define the **bright mode operators** $\hat{S}^+$ and $\hat{S}^-$ as:

$$\hat{S}^+ \equiv \sum_{n=1}^{N}\hat{\sigma}_n^+ = \sum_{n=1}^{N}|\mathrm{e}_n\rangle\langle\mathrm{g}_n|\,, \qquad \hat{S}^- \equiv \sum_{n=1}^{N}\hat{\sigma}_n = \sum_{n=1}^{N}|\mathrm{g}_n\rangle\langle\mathrm{e}_n|\,, \tag{2.28}$$

where $|\mathrm{g}_n\rangle$ and $|\mathrm{e}_n\rangle$ are the ground and the excited states for the n-th emitter, and $\hat{\sigma}_n^\dagger$ and $\hat{\sigma}_n$ are the corresponding (fermionic) creation and annihilation operators. Besides, considering the operator $\hat{\sigma}_n^z$ for each emitter (Equation 2.24), we define:

$$\hat{S}^z \equiv \sum_{n=1}^{N}\hat{\sigma}_n^z = \frac{1}{2}\sum_{n=1}^{N}(|\mathrm{e}_n\rangle\langle\mathrm{e}_n| - |\mathrm{g}_n\rangle\langle\mathrm{g}_n|)\,. \tag{2.29}$$

These bright mode operators obey the following commutation relations:

$$[\hat{S}^+, \hat{S}^-] = 2\hat{S}^z\,, \qquad [\hat{S}^z, \hat{S}^+] = \hat{S}^+\,, \qquad [\hat{S}^z, \hat{S}^-] = \hat{S}^-\,,$$

hence the operator $\hat{S}^z$ can be also written as:

$$\hat{S}^z = \frac{1}{2}(\hat{S}^+\hat{S}^- - \hat{S}^-\hat{S}^+) \,. \tag{2.30}$$

Hamiltonian Let us consider now a collection of N two-level systems where $\hat{\sigma}_n^\dagger$ and $\hat{\sigma}_n$ are the creation and annihilation operators associated with the n-th emitter, and $\hbar\omega_n$ is its corresponding transition frequency. From Equation 2.26, the Hamiltonian of the complete system can be written as:

$$\hat{H}_{\text{mat}} = \sum_{n=1}^{N} \hbar\omega_n \, \hat{\sigma}_n^\dagger \hat{\sigma}_n \,,$$

Alternatively, if we consider Equation 2.27, the Hamiltonian can be expressed in terms of the $\hat{\sigma}^z$ operator:

$$\hat{H}_{\text{mat}} = \sum_{n=1}^{N} \hbar\omega_n \, \hat{\sigma}_n^z \,.$$

From this expression it is straightforward to express the Hamiltonian in terms of the bright mode operator $\hat{S}^z$, defined in Equation 2.29, when all quantum emitters are assumed to have the same transition frequency ω_{QE}:

$$\hat{H}_{\text{mat}} = \hbar\omega_{\text{QE}} \, \hat{S}^z \,.$$

2.2.3 Quantum description of light-matter interaction

In the present section, our analysis has been focused on the quantization of the radiation field when no matter is involved (Subsection 2.2.1), as well as on the description of quantum emitters in the absence of electromagnetic field (Subsection 2.2.2). Nevertheless, our real interest is the situation in which matter and light interact at the quantum level. We shall now proceed to the study of the interaction of the free electromagnetic field with non-relativistic matter.

The interaction Hamiltonian

The effect of the light-matter interaction is usually introduced in the theory by means of the minimal-coupling procedure, yielding the $\boldsymbol{p} \cdot \boldsymbol{A}$ form of the interaction Hamiltonian (Equation D.35). There, the light-matter coupling is carried out through the vector potential $\boldsymbol{A}$ of the field and the momentum $\boldsymbol{p}$ of the particle. Alternatively, this interaction can be expressed in terms of the electric field operator $\boldsymbol{E}$ and the position $\boldsymbol{r}$ of the particle, in the so-called $\boldsymbol{r} \cdot \boldsymbol{E}$ form of the interaction Hamiltonian (Equation D.43). Both procedures are summarized in Appendix D, Section D.3. Either way, the Hamiltonian $\hat{H}$ for the hybrid light-matter system can be ultimately separated in the contributions coming from the (non-interacting) radiation and matter components, $\hat{H}_{\text{rad}}$ and $\hat{H}_{\text{mat}}$, together with the part $\hat{H}_{\text{int}}$ accounting for the coupling between them:

$$\hat{H} = \hat{H}_{\text{rad}} + \hat{H}_{\text{mat}} + \hat{H}_{\text{int}} \,, \tag{2.31}$$

as shown in Equation D.36 and Equation D.44. In particular, the description of the light-matter interaction within the **electric-dipole approximation** (explained in Section D.3) is the procedure followed in this thesis. The resulting interaction Hamiltonian is in this case that of Equation D.43, namely:

$$\hat{H}_{\text{int}} = \hat{H}_{\text{ED}} = -\boldsymbol{d} \cdot \hat{\boldsymbol{E}} \ , \tag{2.32}$$

where the electric field operator is evaluated at the position of the dipole. Equation 2.32 is known as the **electric-dipole Hamiltonian**, and $\boldsymbol{d}$ stands for the **total electric-dipole moment** associated with the matter part. Although matter is essentially neutral due to the cancellation of the total charge on average, fluctuations in the electric charges give rise to a non-vanishing component of the electric field. It is through this electric component that matter couples to light. Specifically, through the dipolar fluctuations, the fairly dominant term when a multipolar expansion of the field is performed.

A two-level system interacting with the quantized electromagnetic field

Let us consider the simple case of a two-level system interacting with the quantized electromagnetic field, and derive the corresponding interaction Hamiltonian (within the electric-dipole approximation) in terms of creation and annihilation operators. First, we consider the non-interacting Hamiltonian $\hat{H}_0$, given by the sum of the matter part consisting in the two-level system (Equation 2.26) plus the radiation field expressed as a collection of uncoupled quantum-mechanical harmonic oscillators (Equation 2.21):

$$\hat{H}_0 = \hat{H}_{\text{2LS}} + \hat{H}_{\text{rad}} = \hbar\omega_0 \hat{\sigma}^\dagger \hat{\sigma} + \sum_{\boldsymbol{k}} \sum_{\lambda} \hbar\omega_k \hat{a}^\dagger_{\boldsymbol{k}\lambda} \hat{a}_{\boldsymbol{k}\lambda} \ , \tag{2.33}$$

where ω_0 is the transition frequency of the two-level system, and ω_k is the transition frequency associated with the radiation mode $\boldsymbol{k}$. Both the radiative and matter parts of the Hamiltonian are expressed in terms of the corresponding creation and annihilation operators. However, it is still pending this kind of description for the interaction Hamiltonian, given by Equation 2.32 when considering the electric-dipole approximation. To this end, we promote the transition dipole moment $\boldsymbol{d}$ associated with the two-level system to an operator, so the electric-dipole Hamiltonian reads:

$$\hat{H}_{\text{ED}} = -\hat{\boldsymbol{d}} \cdot \hat{\boldsymbol{E}} \ . \tag{2.34}$$

There, $\hat{\boldsymbol{d}}$ is now the **dipole operator**, related to the **transition dipole moment** of the two-level system, $\boldsymbol{d}_{\text{eg}}$, through the expression:

$$\hat{\boldsymbol{d}} = \boldsymbol{d}_{\text{eg}} |\text{e}\rangle\langle\text{g}| + \boldsymbol{d}_{\text{ge}} |\text{g}\rangle\langle\text{e}| \ . \tag{2.35}$$

That is, we have expressed the dipole operator in its matrix form, $\hat{\boldsymbol{d}} = \sum_{i,j} \boldsymbol{d}_{ij} |i\rangle\langle j|$ (with $i, j = \text{e}, \text{g}$), where the components are given by: $\boldsymbol{d}_{ij} = \langle i|\hat{\boldsymbol{d}}|j\rangle$. In our case, both components are related through:

$$\boldsymbol{d}^*_{\text{eg}} = \langle \text{e}|\hat{\boldsymbol{d}}|\text{g}\rangle^* = \langle \text{g}|\hat{\boldsymbol{d}}|\text{e}\rangle = \boldsymbol{d}_{\text{ge}} \ ,$$

and the diagonal components vanish: $\boldsymbol{d}_{gg} = 0$ and $\boldsymbol{d}_{ee} = 0$. Finally, if we consider the fermionic creation and annihilation operators $\hat{\sigma}^\dagger$ and $\hat{\sigma}$ corresponding to the two-level system (Equation 2.23), the dipole operator can be alternatively written as:

$$\hat{\boldsymbol{d}} = \boldsymbol{d}_{eg}(\hat{\sigma}^\dagger + \hat{\sigma}) \,, \tag{2.36}$$

where we have assumed that the transition dipole moment is real. By substituting this expression in the interaction Hamiltonian (Equation 2.34), as well as the expression of the electric field operator in the Schrödinger picture (Equation 2.20) at the origin of coordinates (recall that the electric field operator is evaluated at the position of the emitter within the electric-dipole approximation), we have:

$$\hat{H}_{ED} = \sum_{\boldsymbol{k}} \sum_{\lambda} \sqrt{\frac{\hbar\omega_{\boldsymbol{k}}}{2\epsilon_0 V}} \boldsymbol{\epsilon}_{\boldsymbol{k}\lambda} \cdot \boldsymbol{d}_{eg} (\hat{a}_{\boldsymbol{k}\lambda} + \hat{a}^\dagger_{\boldsymbol{k}\lambda})(\hat{\sigma}^\dagger + \hat{\sigma}) \,.$$

This expression can be simplified by defining the following quantity with dimensions of energy:

$$\hbar g_{\boldsymbol{k}\lambda} \equiv \sqrt{\frac{\hbar\omega_{\boldsymbol{k}}}{2\epsilon_0 V}} \boldsymbol{\epsilon}_{\boldsymbol{k}\lambda} \cdot \boldsymbol{d}_{eg} \,, \tag{2.37}$$

which gives a measure of the strength of the coupling. Then, the interaction Hamiltonian can be simply written as:

$$\hat{H}_{ED} = \sum_{\boldsymbol{k}} \sum_{\lambda} \hbar g_{\boldsymbol{k}\lambda} (\hat{a}_{\boldsymbol{k}\lambda} + \hat{a}^\dagger_{\boldsymbol{k}\lambda})(\hat{\sigma}^\dagger + \hat{\sigma}) \,. \tag{2.38}$$

Observe that two kind of processes are contained in this Hamiltonian: the terms $\hat{a}^\dagger\hat{\sigma}$ and $\hat{a}\sigma^\dagger$ conserve the number of excitations, but $\hat{a}^\dagger\hat{\sigma}^\dagger$ and $\hat{a}\hat{\sigma}$ do not (they involve the creation or annihilation of two particles at the same time). The contribution of these non-energy-conserving processes turns out to be negligible when the light-matter coupling is moderate ($|g_{\boldsymbol{k}\lambda}| \ll \omega_0$), hence they can be removed. These are fast-oscillating terms, as can be appreciated when working in the interaction picture (see Appendix B for an overview of quantum representations). Operators are transformed from the Schrödinger to the interaction picture by means of the unitary operator $\hat{\mathcal{U}}_0 = e^{-i\hat{H}_0 t/\hbar}$, where $\hat{H}_0$ is the non-interacting Hamiltonian of Equation 2.33. By applying this unitary transformation to $\hat{H}_{ED}$, the interaction Hamiltonian becomes:

$$\hat{H}^{(I)}_{ED}(t) = \sum_{\boldsymbol{k}} \sum_{\lambda} \hbar g_{\boldsymbol{k}\lambda} (\hat{a}_{\boldsymbol{k}\lambda} e^{-i\omega_k t} + \hat{a}^\dagger_{\boldsymbol{k}\lambda} e^{i\omega_k t})(\hat{\sigma}^\dagger e^{i\omega_0 t} + \hat{\sigma} e^{-i\omega_0 t}) \,.$$

The terms that do not conserve the number of excitations present a time evolution of the form $e^{\pm i(\omega_0+\omega_k)t}$, so they are negligible as long as $|g_{\boldsymbol{k}\lambda}| \ll \omega_0 + \omega_k$. Therefore, for moderate light-matter coupling, the terms $\hat{a}^\dagger\hat{\sigma}^\dagger$ and $\hat{a}\hat{\sigma}$ are usually disregarded. This is known as the **rotating wave approximation**, simplifying the Hamiltonian of Equation 2.38 to:

$$\hat{H}^{(RWA)}_{ED} = \sum_{\boldsymbol{k}} \sum_{\lambda} \hbar g_{\boldsymbol{k}\lambda} (\hat{a}_{\boldsymbol{k}\lambda} \hat{\sigma}^\dagger + \hat{a}^\dagger_{\boldsymbol{k}\lambda} \hat{\sigma}) \,, \tag{2.39}$$

working again in the Schrödinger picture. The first of these remaining terms corresponds to the absorption of a photon accompanied by the excitation of the two-level system from the ground to the excited state, while the second represents the emission of a photon while bringing the two-level system from the excited to the ground state.

Finally, we have arrived at an expression for the interaction Hamiltonian in terms of the creation and annihilation operators associated with both the matter and the radiation part. Therefore, the entire Hamiltonian is now expressed as desired. Notice that, the removal of the non-conserving terms considerably reduces the possible states of the system —as the interaction Hamiltonian conserves the number of excitations, the Hilbert space of the problem can be restricted to the number of excitations corresponding to the initial state.

2.2.4 Quantum light-matter Hamiltonians

All the parts involved in the complete Hamiltonian describing a general hybrid system (Equation 2.31) can be ultimately expressed in terms of the corresponding creation and annihilation operators: $\hat{\sigma}^\dagger$ and $\hat{\sigma}$ represent the fermionic creation and annihilation operators associated with two-level systems, while $\hat{a}^\dagger$ and $\hat{a}$ stand for the bosonic ones associated with cavity modes. In the following, we present some prominent examples of light-matter Hamiltonians, and the main features arising from the light-matter interaction.

Jaynes–Cummings Hamiltonian

One of the simplest problems consists in the coupling of a single atom to a single quantized cavity mode, which is described by the well-known **Jaynes–Cummings model**. The atom is modelled as a two-level system with transition frequency ω_{eg}, while the cavity mode is described as a quantum harmonic oscillator of frequency ω_0 (their corresponding non-interacting Hamiltonians are given in Equation 2.26 and Equation 2.19, respectively). The Jaynes–Cummings Hamiltonian reads:

$$\hat{H}_{\mathrm{JC}} = \hbar\omega_0 \hat{a}^\dagger \hat{a} + \hbar\omega_{\mathrm{eg}} \hat{\sigma}^\dagger \hat{\sigma} + \hbar g (a^\dagger \hat{\sigma} + \hat{a}\hat{\sigma}^\dagger) \,, \tag{2.40}$$

where the interaction Hamiltonian is given within the rotating-wave approximation (Equation 2.39) and g stands for the coupling strength ($g \ll \omega_0, \omega_{\mathrm{eg}}$).

Hilbert space The Jaynes–Cummings Hamiltonian acts on the Hilbert space of states that are tensor product of the two-dimensional space associated with the two-level system ($\mathscr{H}_{\mathrm{A}} = \{|s\rangle_{\mathrm{A}}\}$, where $s = \mathrm{g}, \mathrm{e}$ stands for the ground and excited states, respectively) and the infinite-dimensional space corresponding to the harmonic oscillator ($\mathscr{H}_{\mathrm{C}} = \{|n\rangle_{\mathrm{C}}\}$, where $n = 0, 1, 2\ldots$), namely:

$$\mathscr{H} = \mathscr{H}_{\mathrm{A}} \otimes \mathscr{H}_{\mathrm{C}} : \; \{|s\rangle_{\mathrm{A}} \otimes |n\rangle_{\mathrm{C}}\} \; .$$

These states can be represented in shorthand as $|s, n\rangle \equiv |s\rangle_{\mathrm{A}} \otimes |n\rangle_{\mathrm{C}}$, where the first position indicates the state of the atom whereas the second corresponds to the number of excitations in the cavity field. Within the rotating wave approximation, the Hamiltonian conserves the number of particles. The evolution of the system is thus restricted to a subspace with a fixed number of excitations m, and this value is determined by the initial

state. A basis for the associated two-dimensional Hilbert space is given by:

$$\mathscr{H}_m : \{|g, m\rangle, |e, m-1\rangle\} , \tag{2.41}$$

except for the case in which there is no excitations in the system ($m = 0$), where $\mathscr{H}_0 = |g, 0\rangle$. These Hilbert subspaces with a fixed number of excitations are usually known as the **rungs** of the **Jaynes–Cummings ladder**. Applying the creation or annihilation operators makes the system move up or down the ladder as it acquires or losses one excitation.

Energy spectrum Since the Hamiltonian does not mix subspaces with different number of excitations, its matrix representation is block diagonal with 2x2 blocks. The matrix corresponding to the m-rung reads:

$$\hat{H}_{\mathrm{JC}}^{(m)} : \begin{pmatrix} m\hbar\omega_0 & \hbar g\sqrt{m} \\ \hbar g\sqrt{m} & (m-1)\hbar\omega_0 + \hbar\omega_{\mathrm{eg}} \end{pmatrix} ,$$

in the basis given in Equation 2.41. The interaction term only couples these two states $|g, m\rangle$ and $|e, m-1\rangle$ belonging to the same manifold. The Hamiltonian can be diagonalized independently in each manifold, so the energy spectrum is also divided in subspaces with a fixed number of excitations. The two eigenenergies corresponding to the m-subspace read:

$$E_m^{(\pm)} = \frac{1}{2}\hbar(\omega_{\mathrm{eg}} - \omega_0) + m\hbar\omega_0 \pm \frac{1}{2}\sqrt{4\hbar^2 g^2 m + \hbar^2(\omega_{\mathrm{eg}} - \omega_0)^2} .$$

There, we can introduce the **detuning** Δ of the radiation frequency from the atomic resonance:

$$\Delta \equiv \omega_{\mathrm{eg}} - \omega_0 ,$$

and also the ***m*-photon Rabi frequency** Ω_m, which is related to the strength of the light-matter coupling:

$$\Omega_m \equiv 2g\sqrt{m} . \tag{2.42}$$

If we introduce these quantities and shift the origin of energies so as to remove the constant term, the eigenvalues $E_m^{(\pm)}$ reduces to:

$$E_m^{(\pm)} = m\hbar\omega_0 \pm \frac{1}{2}\hbar\sqrt{\Omega_m^2 + \Delta^2} . \tag{2.43}$$

There exists an energy gap of $\hbar\omega_0$ between consecutive subspaces, and the separation between the two energy levels belonging to the same manifold increases with m. For zero detuning ($\Delta = 0$) the energy splitting within a manifold is precisely the Rabi frequency:

$$R_m \equiv E_m^{(+)} - E_m^{(-)} = \hbar\Omega_m = 2\hbar g\sqrt{m} , \tag{2.44}$$

which is usually known as the **Rabi splitting** associated with the level with m excitations. Observe that the dependence on the manifold increases with $\sqrt{m}$ in that case. The structure of energy levels is depicted in Figure 2.1, which is characterized by the non-linear splitting. The $\sqrt{m}$ dependence of the splitting provides the non-linear behaviour of the system dynamics.

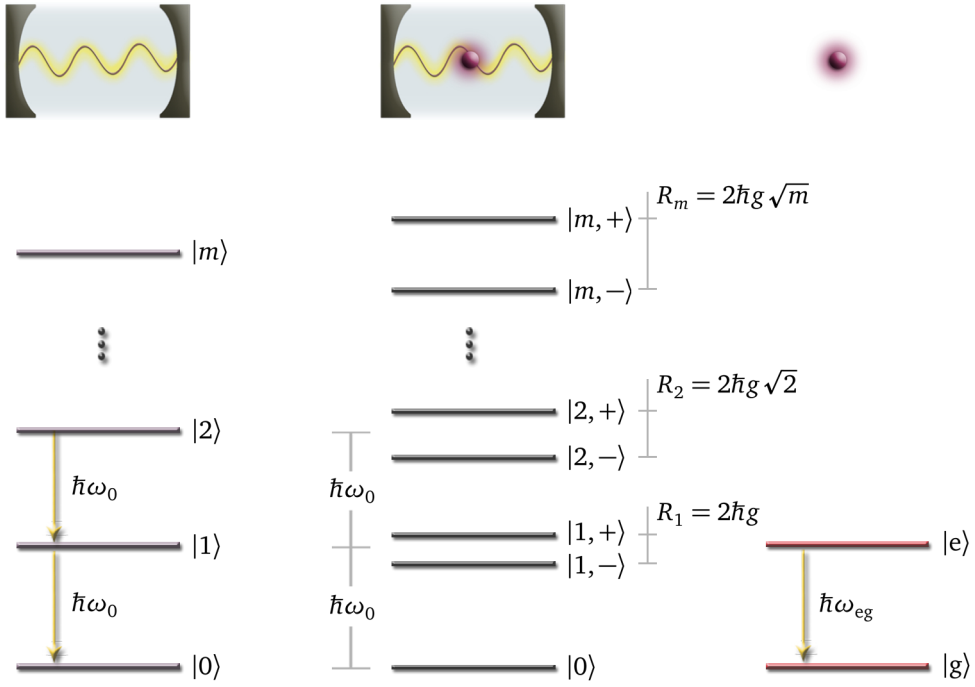

Figure 2.1. Jaynes–Cummings ladder. Energy levels for the different systems.

Polaritons The eigenvectors of the Jaynes–Cummings Hamiltonian associated with these energies $E_m^{(\pm)}$ are given by:

$$V_m^{(\pm)} = \left[\frac{-\Delta \pm \Theta_m}{\Omega_m}, 1\right],$$

in the basis given in Equation 2.41. There, we have defined the **generalized Rabi frequency** as $\Theta_m \equiv \sqrt{\Omega_m^2 + \Delta^2}$. These eigenstates can be rewritten as:

$$\begin{aligned} |m,+\rangle &= \cos\theta_m\,|g,m\rangle \;-\; \sin\theta_m\,|e,m-1\rangle\,, \\ |m,-\rangle &= \sin\theta_m\,|g,m\rangle \;+\; \cos\theta_m\,|e,m-1\rangle\,, \end{aligned} \tag{2.45}$$

where:

$$\cos\theta_m = \frac{\Theta_m - \Delta}{\sqrt{\Omega_m^2 + (\Theta_m - \Delta)^2}}\,, \qquad \sin\theta_m = \frac{\Omega_m}{\sqrt{\Omega_m^2 + (\Theta_m - \Delta)^2}}\,.$$

The eigenstates of the Hamiltonian, which we have denoted as $|m,\pm\rangle$, are known as **polaritons** or **dressed states**. They are linear combination of the **bare states** $|g,m\rangle$ and $|e,m-1\rangle$, as shown in Equation 2.45. The coefficients that give the transformation from the polariton to the bare basis are known as **Hopfield coefficients**. When written in terms of the **mixing angle** θ_m it is clear the property they obey: $\cos^2\theta_m + \sin^2\theta_m = 1$. The square of the Hopfield coefficient yields the fraction of the polariton made of either photon or exciton, as the case may be. It can be also thought as the probability to find the polariton in the one of the bare states. The Jaynes–Cummings Hamiltonian (Equation 2.40) is diagonalized in the polariton basis, and it can be written in terms of the polariton states as:

$$\hat{H}_{JC} = \sum_m \left[E_m^{(-)}|m,-\rangle\langle m,-| \;+\; E_m^{(+)}|m,+\rangle\langle m,+|\right].$$

In particular, $|m,-\rangle$ and $|m,+\rangle$ are usually named as **lower polariton** (LP) and **upper polariton** (UP). For the first manifold ($m=1$), where only one excitation is exchanged between the quantum emitter and the cavity mode, the eigenvectors at resonance are simply the following:

$$|1,\pm\rangle = \frac{1}{\sqrt{2}}(|\mathrm{e},0\rangle \pm |\mathrm{g},1\rangle)\,.$$

There exists a reversible exchange of the excitation between the quantum emitter and the cavity mode, which implies oscillations in the population dynamics of the bare states with frequency proportional to the Rabi splitting $R_1 = \hbar\Omega_1 = 2\hbar g$. That splitting R_1 is usually called **vacuum Rabi splitting**.

Dissipative Jaynes–Cummings model

The studied Jaynes–Cummings model is composed of a quantum emitter coupled to a electromagnetic mode in absence of any dissipation. Nevertheless, all components of the system suffer from losses, since they are unavoidably interacting with their environment. Therefore, we should include the dissipation processes associated with both the cavity and emitter, with decay rates γ_{C} and γ_{QE}, respectively.

All these incoherent processes can be introduced in the description in an approximate manner through an imaginary part in the frequencies, such that they transform to $\omega + \mathrm{i}\gamma/2$ (with γ being the associated decay rate). This leads to the so-called **dissipative Jaynes–Cummings Hamiltonian**, where the energy levels become modified. The energy of the dressed state $|m,\pm\rangle$, before given by Equation 2.43, now reads:

$$E_m^{(\pm)} = m\hbar\omega_0 - \frac{\Delta}{2} - \mathrm{i}\frac{(2m-1)\gamma_{\mathrm{C}}+\gamma_{\mathrm{QE}}}{4} \pm \sqrt{(\sqrt{m}g)^2 - \left(\frac{\gamma_{\mathrm{C}}-\gamma_{\mathrm{QE}}}{4} + \mathrm{i}\frac{\Delta}{2}\right)^2}\,.$$

Notice that the eigenenergies are now complex due to the dissipative part. The real part corresponds to the position of the energy while the imaginary part reflects the broadening of the transition.

Alternatively, the Lindblad formalism (see Subsection 2.1.2) can be introduced to account for dissipation in cavity and emitters. The processes that are commonly included in the dynamics through Lindblad terms (defined in Equation 2.16 for the general operator $\hat{\mathcal{O}}$) are the following:

- Radiative and nonradiative decay ($\hat{\mathcal{O}} = \hat{\sigma}, \hat{a}$): Loss of the excitation in the system due to radiative or nonradiative processes.
- Incoherent pumping ($\hat{\mathcal{O}} = \hat{\sigma}^\dagger, \hat{a}^\dagger$): Excitation due to the interaction with the reservoir, or the return of an excitation from the reservoir to the system as a result of its finite temperature.
- Pure dephasing ($\hat{\mathcal{O}} = \hat{\sigma}^\dagger\hat{\sigma}$): Loss of coherence in the emitter without altering the populations, which usually comes from the coupling to vibrational baths.

Collective strong coupling

The previous discussion corresponds to the case in which a single emitter is coupled to the cavity mode. A particular feature emerges when there is a collection of emitters interacting with the electromagnetic field within the cavity. In that case, the ensemble of emitters may be collectively coupled to the cavity resonance, such that the ensemble as a whole behaves as a single super-emitter. The collective coupling of the emitter ensemble to the cavity mode scales with the total number of emitters N as: $G = g\sqrt{N}$, and this variation in the coupling translates into the corresponding change in the energy splitting [422, 87]. The strong coupling regime is frequently attained by exploiting this collective interaction, as the dipole moment associated with the single emitter may be small to reach large values of the light-matter coupling. This is known as **collective strong coupling**.

In this regime of collective strong coupling, the cavity mode only couples to some specific collective state of the ensemble of emitters (that describing the super-emitter). Therefore, there are some other collective states of the emitter ensemble that do not coupled to light, which are referred to as **dark states**. These are superpositions of matter excitations. In the single-excitation manifold, the coupling of a collection of N emitters with a cavity mode leads to the appearance of two polaritons, as previously mentioned, and a collection of $N-1$ dark states.

2.2.5 Coherent driving

Sometimes the system is pumped by means of a beam of coherent light of a specific frequency. In doing so, the system is probed, in the sense that different transitions are favoured in accordance with the excitation energy. In Chapter 3 we will consider that coherent driving of the system, as well as in some cases studied in Chapter 4 (although the initialization of the system in a particular state will be also explored).

Hamiltonian for the coherent driving

The presence of this **coherent driving** is incorporated in the formalism through the addition of an extra term in the Hamiltonian of Equation 2.31 accounting for the **laser field** pumping the system:

$$\hat{H} = \hat{H}_{\text{rad}} + \hat{H}_{\text{mat}} + \hat{H}_{\text{int}} + \hat{H}_{\text{L}} \, .$$

As the excitation of the system is produced by a monochromatic classical electromagnetic field of energy $\hbar\omega_{\text{L}}$, the associated Hamiltonian is given by:

$$\hat{H}_L = \hat{\Omega}_L^\dagger \, \mathrm{e}^{-\mathrm{i}\omega_L t} + \hat{\Omega}_L \, \mathrm{e}^{\mathrm{i}\omega_L t} \, ,$$

which is clearly time-dependent. The laser field may pump either the cavity mode or the two level system, leading to the corresponding term. These are respectively given by:

$$\hat{\Omega}_L^\dagger = \Omega_L \hat{a}^\dagger \, , \qquad \hat{\Omega}_L^\dagger = \Omega_L \hat{\sigma}^\dagger \, ,$$

where $\hat{a}^\dagger$ is the creation operator for the cavity mode, and $\hat{\sigma}^\dagger$ is the fermionic creation operator associated with the two-level system. Notice that the laser field is treated clas-

sically whereas the cavity field is quantized. The **pumping strength** Ω_L is given by the electric-dipole interaction:

$$\Omega_L = \boldsymbol{d} \cdot \boldsymbol{E}_L \tag{2.46}$$

where $\boldsymbol{d}$ is the dipole moment and $\boldsymbol{E}_L$ represents the amplitude of the laser field. This magnitude is assumed to be real, and it is a measure of the coupling strength between the laser and the cavity or the two-level system.

Transforming to a rotating frame

The introduction of the coherent driving term in the Hamiltonian makes it time-dependent. A very useful tool when working with this kind of Hamiltonians consists in the transformation to a **rotating frame**. This transformation is specifically tailored such that the new Hamiltonian does not possess an explicit dependence on time, hence the study becomes easier. The transformation to the rotating frame is performed in Appendix D, Section D.4, for various Hamiltonians of interest. Let us consider here the case in which the system is composed of a cavity mode (with transition frequency ω_0 and creation and annihilation operators $\hat{a}^\dagger$ and $\hat{a}$) and a collection of N quantum emitters (with transition frequency ω_n and fermionic operators $\hat{\sigma}_n^\dagger$ and $\hat{\sigma}_n$ associated with the n-th emitter). The Hamiltonian of the entire system in the Schrödinger picture is given by:

$$\begin{aligned}\hat{H} = \hbar\omega_0 \hat{a}^\dagger \hat{a} + \sum_{n=1}^{N} \hbar\omega_n \sigma_n^\dagger \sigma_n + \sum_{n=1}^{N} \hbar\lambda_n (\hat{a}^\dagger \sigma_n + \hat{a}\sigma_n^\dagger) \\ + \hbar\Omega_0 (\hat{a}^\dagger \, e^{-\mathrm{i}\omega_L t} + \hat{a} \, e^{\mathrm{i}\omega_L t}) + \sum_{n=1}^{N} \hbar\Omega_n (\hat{\sigma}_n^\dagger \, e^{-\mathrm{i}\omega_L t} + \hat{\sigma}_n \, e^{\mathrm{i}\omega_L t}) \, ,\end{aligned}$$

where λ_n is the coupling constant between the n-th quantum emitter and the cavity mode, and Ω_0 and Ω_n are the coupling of the laser to the cavity mode and the n-th quantum emitter, respectively. We observe that the Hamiltonian is time-dependent due to the term associated with the coherent pumping. In order to change to a rotating frame, we consider the unitary operator $\mathcal{U}(t) = \mathrm{e}^{-\frac{\mathrm{i}}{\hbar}\hat{A}t}$ (Equation D.45), with the following Hermitian operator $\hat{A}$:

$$\hat{A} = \hbar\omega_L \hat{a}^\dagger \hat{a} + \sum_{n=1}^{N} \hbar\omega_L \hat{\sigma}_n^\dagger \hat{\sigma}_n \, .$$

From the transformation given in Equation D.47, the new Hamiltonian in the rotating frame reads:

$$\begin{aligned}\hat{H}_{\mathrm{RF}} = \hbar(\omega_0 - \omega_L)\hat{a}^\dagger \hat{a} + \sum_{n=1}^{N} \hbar(\omega_n - \omega_L)\hat{\sigma}_n^\dagger \hat{\sigma}_n + \sum_{n=1}^{N} \hbar\lambda_n (\hat{a}^\dagger \hat{\sigma}_n + \hat{a}\hat{\sigma}_n^\dagger) \\ + \hbar\Omega_0 (\hat{a}^\dagger + \hat{a}) + \sum_{n=1}^{N} \hbar\Omega_n (\hat{\sigma}_n^\dagger + \hat{\sigma}_n) \, ,\end{aligned} \tag{2.47}$$

where we observe that, effectively, the time-dependence has disappeared. Notice that, in turn, the transformation means an effective shift in the energies. This will be the Hamiltonian we consider in Chapter 3, where a collection of emitters is coupled to the cavity mode supported by either a plasmonic or a semiconductor cavity. This will be used in the same part of Chapter 4 as well, when two collections of organic molecules is coupled to the same electromagnetic mode inside the cavity.

2.3 Light: Optical fluctuations and coherence

Light sources may display a wide range of photon statistics based on their coherence properties. The first part of this thesis is devoted to the study of both amplitude and intensity correlations of the radiation field emitted by different hybrid quantum systems. For this reason, we overview here the quantum theory of coherence, and introduce those magnitudes and concepts that will be used later in Chapter 3. Textbooks in Ref. [120, 423] are widely used as an introduction to the coherence properties of light, and we partially follow them in our discussion.

2.3.1 Light sources: spectral density and optical fluctuations

Valuable information can be extracted from the study of the radiation coming out from a system. Optical interference experiments provide information about the temporal fluctuations of a light source. Before studying the quantum-mechanical theory of optical fluctuations and coherence, we should visit the corresponding classical theory as a preliminary, so as to understand the physical concepts and to identify the quantum nature of properties that some light sources may exhibit. In Appendix E, Section E.1, the classical radiation field $E(t)$ is first described as a stationary and ergodic random process. The **autocorrelation function** of that field at times t and $t+\tau$ can be then defined as indicated in Equation E.1, namely:

$$\Gamma(\tau) = \langle E^*(t)\, E(t+\tau)\rangle \,,$$

which only depends on the time delay τ. The classical theory of optical fluctuations is summarized in Appendix E, Section E.2.

Light sources are also characterized by its spectrum, which gives the frequency distribution of the radiation field. Ordinary spectroscopy is another source of information, from which we obtain the transitions taking place within the system: their frequencies and their corresponding broadenings. The lineshape of the emission is precisely discussed in Appendix E, Section E.3. There the connection between the emitted spectrum and the first-order coherence is shown, where the **spectral density** $S(\omega)$ associated with the electric field $E(t)$ is defined as indicated in Equation E.12, that is:

$$S(\omega) = \frac{1}{2\pi}\int_{-\infty}^{\infty} \Gamma(\tau)\, \mathrm{e}^{\mathrm{i}\omega\tau}\mathrm{d}\tau \,.$$

2.3.2 Intensity of the quantum radiation field

The quantum version of the classical coherence expressions given in Section E.2 can be practically obtained by promoting the vector field to an operator, although some comments concerning the detection of light, and the subsequent definition of the intensity, are convenient.

Quantum radiation field: the electric field operator

When working within the quantum formalism, the radiation field is described through the electric and magnetic field operators. If we consider periodic boundary conditions in a three-dimensional cavity of volume V, the expression of the electric field operator in terms of normal modes is the one given in Equation 2.20. If the light beam is assumed to be linearly polarized, we can work with the scalar operator:

$$\hat{E}(\boldsymbol{x},t)=\sum_{\boldsymbol{k}}\sqrt{\frac{\hbar\omega_k}{2\epsilon_0 V}}\left[\hat{a}_{\boldsymbol{k}}\mathrm{e}^{\mathrm{i}(\boldsymbol{k}\cdot\boldsymbol{x}-\omega_k t)}+\hat{a}_{\boldsymbol{k}}^{\dagger}\mathrm{e}^{-\mathrm{i}(\boldsymbol{k}\cdot\boldsymbol{x}-\omega_k t)}\right],$$

where the dependence of the creation and annihilation operators on the polarization has been removed. Notice that we have used the Heisenberg picture so as to make the time dependence explicit. The electric field operator can be split in its **positive** and **negative frequency** parts as follows:

$$\hat{E}(\boldsymbol{x},t)=\hat{E}^{(+)}(\boldsymbol{x},t)+\hat{E}^{(-)}(\boldsymbol{x},t),$$

where:

$$\begin{aligned}\hat{E}^{(+)}(\boldsymbol{x},t)&\equiv\sum_{\boldsymbol{k}}E_{0\boldsymbol{k}}\hat{a}_{\boldsymbol{k}}\mathrm{e}^{\mathrm{i}(\boldsymbol{k}\cdot\boldsymbol{x}-\omega_k t)},\\ \hat{E}^{(-)}(\boldsymbol{x},t)&\equiv\sum_{\boldsymbol{k}}E_{0\boldsymbol{k}}\hat{a}_{\boldsymbol{k}}^{\dagger}\mathrm{e}^{-\mathrm{i}(\boldsymbol{k}\cdot\boldsymbol{x}-\omega_k t)}.\end{aligned}\tag{2.48}$$

There, we have defined the amplitude of the field: $E_{0\boldsymbol{k}}\equiv\sqrt{\hbar\omega_{\boldsymbol{k}}/(2\epsilon_0 V)}$. As done when explaining the classical theory, we restrict our explanation to stationary light sources.

Intensity

The operator associated with the light intensity can be obtained by considering the **Poynting vector** $\boldsymbol{S}_L$, which gives the intensity of an electromagnetic field within the classical theory:

$$\boldsymbol{S}_L=\epsilon_0 c^2\boldsymbol{E}(\boldsymbol{r},t)\times\boldsymbol{B}(\boldsymbol{r},t).$$

There, $\boldsymbol{E}$ and $\boldsymbol{B}$ are the classical electric and magnetic fields. From the Poynting vector, the associated quantum operator for the intensity can be defined as:

$$\hat{\boldsymbol{I}}(\boldsymbol{r},t)=\epsilon_0 c^2[\hat{\boldsymbol{E}}^{(-)}(\boldsymbol{r},t)\times\hat{\boldsymbol{B}}^{(+)}(\boldsymbol{r},t)-\hat{\boldsymbol{B}}^{(-)}(\boldsymbol{r},t)\times\hat{\boldsymbol{E}}^{(+)}(\boldsymbol{r},t)],$$

where we have considered the positive and negative frequency parts of both the electric and the magnetic field operators. For a polarized parallel light beam, the intensity operator reduces to:

$$\hat{I}(\boldsymbol{r},t)=2\epsilon_0 c\hat{\boldsymbol{E}}^{(-)}(\boldsymbol{r},t)\hat{\boldsymbol{E}}^{(+)}(\boldsymbol{r},t).$$

Therefore, given the electric field operator $\hat{E}(\boldsymbol{r},t)$ split in the positive and negative frequency parts as indicated in Equation 2.48, the light **intensity** at a given point, $I(\boldsymbol{r})$, is computed as:

$$I(\boldsymbol{r})=\langle\hat{E}^{(-)}(\boldsymbol{r},t)\,\hat{E}^{(+)}(\boldsymbol{r},t)\rangle,\tag{2.49}$$

which does not depend on time since the light source is considered stationary. This magnitude offers a measure of the quantity of photons arriving at the detector. Notice that angle brackets stand for quantum expectation values, calculated from the density operator according to Equation B.4.

2.3.3 Quantum correlation functions

The study of correlations between light beams has been performed within the classical framework in Appendix E, Section E.2. In that case, there exists a close connection with interference experiments. Nevertheless, correlations also correspond to a measure defined quantum mechanically, and we proceed now to their study.

Quantum first-order correlation function

The quantum **first-order correlation function** $g^{(1)}(\boldsymbol{r}_1, t_1; \boldsymbol{r}_2, t_2)$ of the electric operator $\hat{E}(\boldsymbol{r}, t)$ at positions $\boldsymbol{r}_1$ and $\boldsymbol{r}_2$ at times t_1 and t_2, respectively, is given by:

$$G^{(1)}(\boldsymbol{r}_1, \boldsymbol{r}_2; \tau) = \langle \hat{E}^{(-)}(\boldsymbol{r}_1, t)\, \hat{E}^{(+)}(\boldsymbol{r}_2, t+\tau) \rangle \,,$$

where we have introduced the time delay $\tau = t_2 - t_1$, and its positive and negative frequency parts of the electric field operator are given in Equation 2.48. Normalizing this expression, we arrive at the **degree of first-order coherence** :

$$g^{(1)}(\boldsymbol{r}_1, \boldsymbol{r}_2; \tau) = \frac{\langle \hat{E}^{(-)}(\boldsymbol{r}_1, t)\, \hat{E}^{(+)}(\boldsymbol{r}_2, t+\tau) \rangle}{\sqrt{I(\boldsymbol{r}_1)\, I(\boldsymbol{r}_2)}} \,,$$

where the intensity is defined in Equation 2.49. If we consider correlations at the same spatial position, we have the **degree of first-order temporal coherence**:

$$g^{(1)}(\tau) = \frac{\langle \hat{E}^{(-)}(t)\, \hat{E}^{(+)}(t+\tau) \rangle}{\langle \hat{E}^{(-)}(t)\, \hat{E}^{(+)}(t) \rangle} \,,$$

where we have explicitly written the expression for the intensity in the denominator. We observe that these definitions are equivalent to the classical ones (see Equation E.5 and Equation E.6), where the electric field variable has been substituted by the corresponding (positive or negative frequency part of the) electric field operator.

Light can be also named according to the degree of first-order coherence as indicated in the classical case (Equation E.8), so we can have incoherent ($|g^{(1)}(\tau)| = 0$), partially coherent ($0 < |g^{(1)}(\tau)| < 1$), and first-order coherent ($|g^{(1)}(\tau)| = 1$) light beams.

Quantum second-order correlation function

The physical meaning of the quantum coherence is the same as that of its classical version —second-order coherence measures correlations in the light intensity. This can be measured with the help of photodetectors, since the transition rate of the absorption of a photon by the detector is proportional to the light intensity. Then, the second-order

correlation function gives the probability of a joint absorption by the detectors at two space-time points.

The quantum **second-order correlation function** between the electric field operator $\hat{E}(\boldsymbol{r},t)$ at two space-time positions $(\boldsymbol{r}_1,t_1)$ and $(\boldsymbol{r}_2,t_2)$ is defined as:

$$G^{(2)}(\boldsymbol{r}_1,\boldsymbol{r}_2;\tau)=\langle\hat{E}^{(-)}(\boldsymbol{r}_1,t)\,\hat{E}^{(-)}(\boldsymbol{r}_2,t+\tau)\,\hat{E}^{(+)}(\boldsymbol{r}_2,t+\tau)\,\hat{E}^{(+)}(\boldsymbol{r}_1,t)\rangle\ ,$$

where $\tau=t_2-t_1$, and the positive and negative frequency parts of the scalar operator are given in Equation 2.48. From that, the quantum **degree of second-order coherence** is obtained by normalizing with the intensity (Equation 2.49):

$$g^{(2)}(\boldsymbol{r}_1,\boldsymbol{r}_2;\tau)=\frac{\langle\hat{E}^{(-)}(\boldsymbol{r}_1,t)\,\hat{E}^{(-)}(\boldsymbol{r}_2,t+\tau)\,\hat{E}^{(+)}(\boldsymbol{r}_2,t+\tau)\,\hat{E}^{(+)}(\boldsymbol{r}_1,t)\rangle}{I(\boldsymbol{r}_1)\,I(\boldsymbol{r}_2)}\ .$$

This magnitude is related to the probability of detecting a photon in the detector placed at $\boldsymbol{r}_2$ at time t_2 once a photon has reached the detector placed at $\boldsymbol{r}_1$ at time t_1. In particular, if we consider correlations at the same position, we have the **degree of second-order temporal coherence**:

$$g^{(2)}(\tau)=\frac{\langle\hat{E}^{(-)}(t)\,\hat{E}^{(-)}(t+\tau)\,\hat{E}^{(+)}(t+\tau)\,\hat{E}^{(+)}(t)\rangle}{\langle\hat{E}^{(-)}(t)\,\hat{E}^{(+)}(t)\rangle^2}\ . \tag{2.50}$$

This is basically a measure of the correlation of the intensity of a light beam at two different times t and $t+\tau$. It is related to the probability of detecting a photon in the detector at time $t+\tau$ once a photon has reached the detector at time t. Hence a large value of the $g^{(2)}(\tau)$ function means that the probability is high, while a small value means that the probability is low. In the next section, we will show in which sense the degree of second-order coherence offers information about the non-classical character of a field.

2.3.4 Nonclassical light

Whereas classical and quantum theory yield the same results for some kinds of light, there exist some others whose properties cannot be described from the classical theory —these are named **nonclassical light sources**. They exhibit some features that cannot be described from the classical statistical theory, and the quantum nature of light needs to be incorporated.

In Section E.2 we showed the properties satisfied by the classical degree of second-order coherence. In the quantum case, since expectation values are positive, from Equation 2.50 we have:

$$0\leq g^{(2)}(\tau)\leq\infty\ .$$

This is the same expression as the one obtained for the classical $g^{(2)}(\tau)$, given in Equation E.10. Nevertheless, it cannot be obtained a relation equivalent to Equation E.9 for the quantum version of $g^{(2)}(0)$, nor is it possible to find an inequality similar to that in Equation E.11, which relates the values of $g^{(2)}(\tau)$ at zero and non-zero time delays. These two inequalities that are different within classical and quantum theory lead to two distinct characterizations of light sources:

- While $g^{(2)}(\tau) \leq g^{(2)}(0)$ for a classical light source, this is not necessarily true within the quantum formalism. The relative value of $g^{(2)}(\tau)$ with respect to the value at zero-time delay leads to the definition of photon bunching and photon antibunching.

- While $g^{(2)}(0) \geq 1$ for a classical light source, there are quantum states of light which present values of $g^{(2)}(0)$ below one. The value of $g^{(2)}(0)$ characterizes the statistics of the emitted light, which can be Poissonian, super-Poissonian, or sub-Poissonian.

Light lying beyond the classical limits is called **nonclassical light**. In the following, we will study each of these characterizations of light that allow us to differentiate purely quantum light states.

Photon bunching and photon antibunching

For stationary light sources, the degree of second-order temporal coherence (Equation 2.50) does not depend on the time t but just in the time interval τ. When we set this lapse to zero, this magnitude is related to the probability of detecting two photons at the same time. This is known as the **zero-delay second-order coherence degree**, $g^{(2)}(0)$.

The relative value of $g^{(2)}(\tau)$ with respect to its value at zero-time delay yields the following classification:

- If $g^{(2)}(\tau) \leq g^{(2)}(0)$, photons are said to be **bunched**. The sun or a gas discharge lamp produce this kind of light. The probability of detecting two photons at the same time is greater than that of a coherent source. This means that photons are arranged in groups, or bunches. Bunching is then a signature of multiphoton processes.

- If $g^{(2)}(\tau) = g^{(2)}(0) = 1$, photons are said to be **coherent**, which is the case of a classical laser field.

- If $g^{(2)}(\tau) \geq g^{(2)}(0)$, photons are said to be **antibunched**. The probability of detecting two photons at the same time is lower than that of a coherent source. In this case, photons tend to be distributed equally spaced, hence it is a characteristic of single photon emitters.

In Figure 2.2 we represent pictorially these three cases. A light source is emitting photons that eventually reach the detector. Above the corresponding lines are depicted various detections as a function of time, mimicking the emission from three different light sources. The central line corresponds to a coherent light source, where photons appear completely uncorrelated from each other. The lower line reproduces the emission from a bunched light source, where photons show a tendency to come together in groups. Finally, the upper line corresponds to an antibunched light source. There, photons are distributed almost equally spaced, reaching the detector practically one by one. When using antibunched light, the probability of having two detections at the same time is lower than that for the two other cases: the detection of a photon decreases the probability of a second detection.

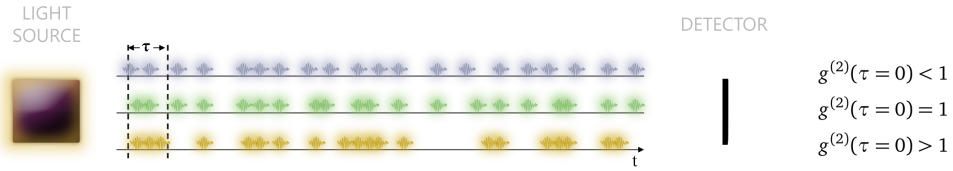

Figure 2.2. Representation of several detections over time corresponding to three different light sources. The statistics of the emitted light is related to the value of the $g^{(2)}(0)$ function: the upper line corresponds to bunching ($g^{(2)}(0) > 1$), the central line to coherent light ($g^{(2)}(0) = 1$), and the lower line to antibunching ($g^{(2)}(0) < 1$).

Bunching is characteristic of classical light sources, since the classical inequality of Equation E.11 is satisfied. Nevertheless, antibunched light does not follow the classical relation, thus it is a signature of quantum processes.

Photon statistics

Photon statistics refers to the probability distribution of detecting n photons within some time interval. In general, the distribution $p(n,\lambda)$ represents the probability of some event happening a number of times n in a certain interval, once the average number of events in that interval, λ, is specified. In this case, the **event rate** (or rate parameter) is given by the mean photon number, that is, $\lambda \equiv \langle n \rangle$. **Coherent states** represent the state of a laser field, and they possess a **Poissonian probability distribution** for the photon number probability, that is:

$$p(n,\lambda) = e^{-\lambda}\frac{\lambda^n}{n!}\,,$$

whose variance is $(\Delta n)^2 = \langle n \rangle$. This is a distinct characteristic of a coherent light field. Therefore, light sources for which the photon-number variance is equal to the mean photon number are coherent sources, which present **Poissonian statistics**. But one may find light sources exhibiting sub-Poissonian or super-Poissonian statistics. Three types of light sources can be thus distinguished based on the statistical distribution, where the defining feature is the relation between the variance $(\Delta n)^2$ of the probability distribution and the average number of photons $\langle n \rangle$:

- If $(\Delta n)^2 > \langle n \rangle$, the light source presents **super-Poissonian statistics**. Chaotic light is an example of light with this kind of statistics, where the variance for (single-mode) chaotic light is given by $(\Delta n)^2 = \langle n \rangle + \langle n \rangle^2$. There is an extra contribution to the $\langle n \rangle$ term characterizing coherent light, which represents additional fluctuations. Thermal light, following a Bose-Einstein distribution, is another example of light with sub-Poissonian statistics.

- If $(\Delta n)^2 = \langle n \rangle$, the light source is coherent and exhibits **Poissonian statistics**.

- If $(\Delta n)^2 < \langle n \rangle$, the variance of the photon-number distribution lies below the value for coherent light, and the light source presents **sub-Poissonian statistics**. This is the case of Fock states, where $(\Delta n)^2 = 0$ since there is no uncertainty in the photon number, and single-mode light fields, for which $(\Delta n)^2 = \langle n \rangle - \langle n \rangle^2$.

The statistical properties of a light source can be alternatively characterized by the so-called **Q-parameter**, defined as:

$$Q = \frac{(\Delta n)^2 - \langle n \rangle}{\langle n \rangle} = \langle n \rangle \left(g^{(2)}(0) - 1 \right)\,.$$

This expression explicitly shows the connection between the probability distribution of a light source and the degree of second-order coherence at zero-time delay. The **zero-delay second-order coherence degree** $g^{(2)}(0)$ thus gives information about the statistics of the emitted light. According to this value, light can be classified in the groups listed above:

- If $g^{(2)}(0) > 1$, light presents **super-Poissonian statistics**. For instance, $g^{(2)}(0) = 2$ for chaotic or thermal light.
- If $g^{(2)}(0) = 1$, the light source is coherent and exhibits **Poissonian statistics**.
- If $g^{(2)}(0) < 1$, light presents **sub-Poissonian statistics**. This is characteristic of quantum light sources. The one-photon state represents the limiting case $g^{(2)}(0) = 0$ and, in general, $g^{(2)}(0) = 1 - 1/n$ for the Fock state $|n\rangle$ (with $n \geq 1$).

Within the classical theory, we obtained $g^{(2)}(0) \geq 1$ (Equation E.9), but Fock states do not fulfil this constraint. There exists a range of values for the quantum second-order coherence at zero-time delay that is not accessible from a classical source: $0 \leq g^{(2)}(0) \leq 1$. The reason lies in the quantum nature of these states, without classical counterpart. Sub-Poissonian statistics is a purely quantum effect that cannot be reproduced from any classical theory. In this sense, $g^{(2)}(0)$ is said to offer a measure of the classicality of the light. Coherent and thermal states present their classical analogues, so their behaviour can be explained from a classical theory and they are subject to the properties derived within the classical formalism.

Notice that the range of values of $g^{(2)}(0)$ associated with nonclassical light corresponds to $-1 \leq Q < 0$ and $0 \leq (\Delta n)^2 \leq \langle n \rangle$. Then, these are different observables that can be used to determine the nonclassicality of a light source. While Poissonian and super-Poissonian statistics can be described by a semiclassical theory, light exhibiting sub-Poissonian statistics requires a purely quantum formalism, where the electromagnetic field is also quantized.

Antibunching and sub-Poissonian statistics are often associated. They are, nevertheless, distinct properties and need not necessarily be simultaneously observed [424, 124].

2.4 Matter: Quantum description of organic molecules

Quantum emitters are commonly described as two-level systems, where the only two relevant energy levels are the ones corresponding to the ground and first-excited states. Nevertheless, when working with organic molecules this model becomes insufficient. The more involved energy structure displayed by organic molecules requires the inclusion of nuclear degrees of freedom in the description. Vibrational and rotational modes thus arise, enriching the dynamics.

In this section, we overview the theory of Franck–Condon transitions between potential energy surfaces, and present the vibrational Hamiltonian obtained from the displaced

harmonic oscillator model. The presence of vibronic transitions leaves a fingerprint the absorption spectrum that is also analyzed. Two interesting textbooks on this matter are Ref. [425, 426], and we refer to them for a more detailed study.

2.4.1 Hamiltonian for organic molecules

Due to these internal structure characteristic of organic molecules, they cannot be described as simple two-level systems. On the contrary, the energy structure have to be refined by the inclusion of nuclear degrees of freedom: on top of the electronic states, there are vibrational and rotational modes that enrich the dynamics. Firstly, we study the Hamiltonian associated with organic molecules, accounting for both electronic and vibrational energies, within the displaced harmonic oscillator model.

Displaced harmonic oscillator model

Organic molecules present several electronic states, between which transitions can occur. In Appendix F, Section F.1, we outline the main processes that may appear, involving rather different time scales (see Figure F.1). In our discussion we consider just the first two electronic states, the ground state $|g\rangle$ and the first excited (singlet) state $|e\rangle$. As we have mentioned, nuclear degrees of freedom need to be included in the description, but these can be treated separately by considering the Born–Oppenheimer approximation. This leads to a picture based on nuclei moving in the effective potentials created by electrons, as explained in Appendix F, Section F.2.

The energy of the electronic states of a molecule depends on the specific nuclear configuration. This is usually described through **potential energy curves** representing the energy at each electronic energy level as a function of the nuclear coordinate q. The most simplified model considers the curves associated with the ground and the first-excited electronic states as identical harmonic oscillator potentials whose equilibrium positions are displaced from one another a quantity d along the nuclear coordinate q. It is known as the **displaced harmonic oscillator (DHO) model**, and its scheme is shown in Figure 2.3. The origin of this displacement between the potential minima is the fact that the equilibrium position of the nucleus corresponding to the excited molecule is shifted with respect to its position in the ground state.

The DHO model is frequently used to describe transitions involving changes in both electronic and vibrational states, that are known as **vibronic transitions**. The two parameters characterising this model are then the vibrational mode frequency ω_v and the distance d between the minimum of the ground and first-excited potential energy curves. As we will see, this offset will be larger as the electron-phonon interaction strengthen, and is relevant in the profiles of the emission and absorption spectra.

Energies within the DHO model

Let us consider just two states of a molecule, $|\mathcal{G}\rangle$ and $|\mathcal{E}\rangle$, where their associated electronic states are the ground state $|g\rangle$ and the excited state $|e\rangle$, respectively. Within the

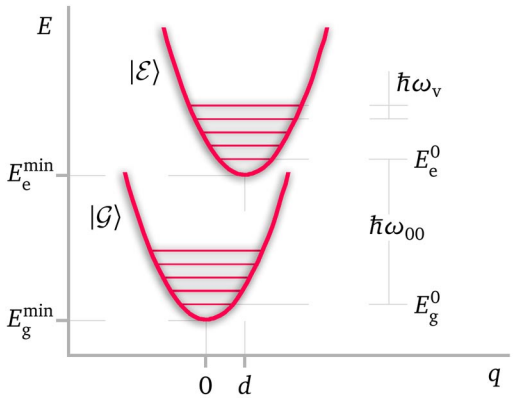

Figure 2.3. Harmonic potentials giving the vibrational modes of frequency $\hbar\omega_v$ associated with the ground and first-excited electronic states $|g\rangle$ and $|e\rangle$. Their minima are located at E_g^{min} and E_e^{min}, and are displaced a quantity d along the nuclear coordinate q. There, $|\mathcal{G}\rangle$ and $|\mathcal{E}\rangle$ stand for two molecular states.

DHO model, their corresponding vibrational potentials will be described through identical harmonic oscillators of mass m and frequency ω_v (hence both possess the same eigenmodes) but whose minima are displaced a quantity d along the nuclear coordinate q, as shown in Figure 2.3. The energy of these two states can be thus written as:

$$\begin{aligned} E_{\mathcal{G}} &= E_g^{min} + \frac{p^2}{2m} + \frac{1}{2}m\omega_v^2 q^2 \,, \\ E_{\mathcal{E}} &= E_e^{min} + \frac{p^2}{2m} + \frac{1}{2}m\omega_v^2 (q-d)^2 \,, \end{aligned} \tag{2.51}$$

where E_g^{min} and E_e^{min} are the minima of the vibrational potentials for the electronic ground and excited states, respectively. We set $E_g^{min} = 0$ and introduce the energy associated with the **pure electronic transition** (or **zero-phonon vibronic transition**), that is, the one that does not involve phonon excitations:

$$E_e^{min} - E_g^{min} = E_e^0 - E_g^0 \equiv \hbar\omega_{00} \,. \tag{2.52}$$

Here, E_g^0 and E_e^0 stand for the ground vibrational states of the respective quantum harmonic oscillators.

Hamiltonian within the DHO model

The Hamiltonian describing the organic molecule, composed of the state $|\mathcal{G}\rangle$ with energy $E_{\mathcal{G}}$ and the state $|\mathcal{E}\rangle$ with energy $E_{\mathcal{E}}$, is given by:

$$H = E_{\mathcal{G}}|\mathcal{G}\rangle\langle\mathcal{G}| + E_{\mathcal{E}}|\mathcal{E}\rangle\langle\mathcal{E}| \,, \tag{2.53}$$

where the energies $E_{\mathcal{G}}$ and $E_{\mathcal{E}}$ are given in Equation 2.51. Recall that the Born–Oppenheimer approximation implies that the state of the system can be written as a product state from its nuclear and electronic components. Therefore, the states of the molecule $|\mathcal{G}\rangle$ and $|\mathcal{E}\rangle$ can be expressed in terms of their nuclear and electronic states separately, namely: $|\mathcal{G}\rangle = |g\rangle \otimes |\chi_g\rangle$ and $|\mathcal{E}\rangle = |e\rangle \otimes |\chi_e\rangle$, where $|g\rangle$ and $|e\rangle$ are the electronic ground and first-excited states, while $|\chi_g\rangle$ and $|\chi_e\rangle$ stands for their corresponding vibrational components.

The Hamiltonian corresponding to the vibrational contribution can be quantized as shown in Section D.1. First, the nuclear coordinate q and the momentum p are promoted to the quantum operators $\hat{q}$ and $\hat{p}$, and then these are written in terms of the creation and

annihilation operators $\hat{b}^\dagger$ and $\hat{b}$:

$$\hat{q} = \sqrt{\frac{\hbar}{2m\omega_\mathrm{v}}}\,(\hat{b} + \hat{b}^\dagger)\,, \qquad \hat{p} = -\mathrm{i}\sqrt{\frac{\hbar m\omega_\mathrm{v}}{2}}\,(\hat{b} - \hat{b}^\dagger)\,, \tag{2.54}$$

equivalently to Equation D.2. These bosonic operators $\hat{b}^\dagger$ and $\hat{b}$ (which fulfils the corresponding commutation relation $[\hat{b}, \hat{b}^\dagger] = 1$) describe, respectively, the creation and annihilation of a vibrational mode of frequency ω_v. By substituting these expressions into Equation 2.51, and considering also the contribution from the electronic part (Equation 2.26), the quantum Hamiltonian becomes:

$$\hat{H} = \hbar\omega_{00}\hat{\sigma}^\dagger\hat{\sigma} + \hbar\omega_\mathrm{v}\left(\frac{1}{2} + \hat{b}^\dagger\hat{b}\right) + \frac{1}{2}m\omega_\mathrm{v}^2 d^2\hat{\sigma}^\dagger\hat{\sigma} + \hbar\omega_\mathrm{v}\sqrt{\frac{m\omega_\mathrm{v}}{2\hbar}}d\,(\hat{b} + \hat{b}^\dagger)\,\hat{\sigma}^\dagger\hat{\sigma}\,,$$

where $\hat{\sigma}^\dagger$ and $\hat{\sigma}$ are the fermionic creation and annihilation operators associated with the electronic transition (defined in Equation 2.23). A shift in the energies can be performed so as to remove the constant term $\hbar\omega_\mathrm{v}/2$. Additionally, we can define the **Huang-Rhys parameter** D as:

$$D \equiv \frac{m\omega_\mathrm{v}}{2\hbar}d^2\,, \tag{2.55}$$

hence the previous Hamiltonian becomes:

$$\hat{H} = \hbar\omega_{00}\hat{\sigma}^\dagger\hat{\sigma} + \hbar\omega_\mathrm{v}\hat{b}^\dagger\hat{b} + \hbar\omega_\mathrm{v}D\hat{\sigma}^\dagger\hat{\sigma} + \hbar\omega_\mathrm{v}\sqrt{D}\,(\hat{b} + \hat{b}^\dagger)\,\hat{\sigma}^\dagger\hat{\sigma}\,. \tag{2.56}$$

From the last term it is clear that this dimensionless parameter D represents the strength of the coupling between nuclear and electronic degrees of freedom. We can also introduce other two related parameters whose precise physical meaning will be unveiled later, the **vibronic coupling** λ, defined as:

$$\lambda \equiv \omega_\mathrm{v}\sqrt{D}\,, \tag{2.57}$$

and the **reorganization energy** Λ, defined as:

$$\Lambda \equiv \frac{1}{2}m\omega_\mathrm{v}^2 d^2 = \hbar\omega_\mathrm{v}D\,. \tag{2.58}$$

Written in terms of these parameters, the molecular Hamiltonian of Equation 2.56 reads:

$$\hat{H} = (\hbar\omega_{00} + \Lambda)\hat{\sigma}^\dagger\hat{\sigma} + \hbar\omega_\mathrm{v}\hat{b}^\dagger\hat{b} + \hbar\lambda(\hat{b} + \hat{b}^\dagger)\,\hat{\sigma}^\dagger\hat{\sigma}\,.$$

Alternatively to the frequency of the zero-phonon vibronic transition ω_{00}, we can consider the **vertical Franck–Condon transition frequency** ω_eg, defined as:

$$\hbar\omega_\mathrm{eg} \equiv \hbar\omega_{00} + \Lambda\,, \tag{2.59}$$

such that the molecular Hamiltonian finally reads:

$$\hat{H} = \hbar\omega_\mathrm{eg}\hat{\sigma}^\dagger\hat{\sigma} + \hbar\omega_\mathrm{v}\hat{b}^\dagger\hat{b} + \hbar\lambda(\hat{b} + \hat{b}^\dagger)\,\hat{\sigma}^\dagger\hat{\sigma}\,. \tag{2.60}$$

This Hamiltonian represents the coupling of the electronic vertical transition of energy $\hbar\omega_\mathrm{eg}$ with the vibrational mode of frequency ω_v.

The two molecular states $|\mathcal{G}\rangle$ and $|\mathcal{E}\rangle$ previously introduced in Equation 2.53 are usu-

ally not independent, but they are connected through the interaction term arising as a consequence of the external field pumping the system. The Hamiltonian describing the pumped system is studied in Appendix F, Section F.3.

Vertical transition energy

Nuclear displacements are negligible during electronic transitions given the reduced time over which they take place. This assumption is the Franck–Condon principle, which implies that the most likely vibronic transitions are those which connect states with similar equilibrium positions of nuclei (see Appendix F, Section F.2). These correspond to vertical lines in a diagram as the one in Figure 2.3, reason why they are also known as **vertical transitions**.

The **vertical transition energy** $\Delta_{\mathcal{EG}}$ is given by the energy difference between the molecular states $|\mathcal{G}\rangle$ and $|\mathcal{E}\rangle$ at a certain nuclear coordinate q:

$$\Delta_{\mathcal{EG}} \equiv E_{\mathcal{E}} - E_{\mathcal{G}} \,,$$

where the energies $E_{\mathcal{G}}$ and $E_{\mathcal{E}}$ are given in Equation 2.51. Notice that for $q = 0$, the energy gap reduces to:

$$\Delta_{\mathcal{EG}} = \hbar\omega_{00} + \frac{1}{2} m\omega_{\mathrm{v}}^2 d^2 = \hbar\omega_{00} + \Lambda \,, \tag{2.61}$$

where we have considered the definition of reorganization energy given in Equation 2.58. Notice that this is nothing but the vertical Franck–Condon transition energy $\hbar\omega_{\mathrm{eg}}$ defined in Equation 2.59. Therefore, the **reorganization energy** Λ can be thought as the vibrational energy that can be liberated in the electronic excited state after a vertical transition from the electronic ground state with no vibrational excitations.

2.4.2 Harmonic oscillator reservoir for vibrations

Coupling to a set of vibrational modes

So far the discussion has been focused on the coupling of an electronic transition with a single vibrational mode, whose Hamiltonian is given in Equation 2.60. Nevertheless, there usually exists a whole set of modes κ to which the electronic transition is coupled. In that case, the Hamiltonian reads:

$$\hat{H} = \hbar\omega_{\mathrm{eg}} \hat{\sigma}^\dagger \hat{\sigma} + \sum_\kappa \hbar\omega_\kappa \hat{b}_\kappa^\dagger \hat{b}_\kappa + \sum_\kappa \hbar\lambda_\kappa (\hat{b}_\kappa + \hat{b}_\kappa^\dagger)\, \hat{\sigma}^\dagger \hat{\sigma} \,, \tag{2.62}$$

where $\hat{b}_\kappa^\dagger$ and $\hat{b}_\kappa$ are the bosonic creation and annihilation operators associated with the vibrational mode of frequency ω_κ. There, λ_n is the coupling strength between the electronic transition and the vibrational mode κ (**exciton-phonon coupling**), which can be parametrized through the Huang-Rhys parameter D_κ according to Equation 2.57, that is:

$$\lambda_\kappa = \omega_\kappa \sqrt{D_\kappa} \,. \tag{2.63}$$

The electronic transition may even be coupled to a quasi-continuum of vibrational modes, which is commonly referred to as a **vibrational bath**. In that case, it is convenient to introduce the function $J(\omega)$, defined as:

$$J(\omega) = \sum_{\kappa} \hbar^2 \lambda_\kappa^2 \, \delta(\omega - \omega_\kappa) = \sum_{\kappa} \hbar^2 \omega_\kappa^2 D_\kappa \, \delta(\omega - \omega_\kappa) \, . \tag{2.64}$$

This function is usually named **spectral density** (or **power spectrum**), just as the Fourier transform of the time-correlation function (see, for example, Equation 2.11 or Equation F.24). Nevertheless, we will see later that these two are intimately connected (Equation 2.68). The power spectrum defined in Equation 2.64 is a continuum of modes of frequency ω_κ (modelled as a delta function centered at the frequency of the oscillator) with associated strengths $\lambda_\kappa = \omega_k \sqrt{D_\kappa}$. Instead, we can consider Lorentzian functions associated with some homogeneous broadening γ, so that:

$$J(\omega) = \sum_{\kappa} \hbar^2 \lambda_\kappa^2 \frac{1}{\pi} \frac{\gamma}{(\omega - \omega_\kappa)^2 + \gamma^2} \, .$$

The response of the system to the excitation is encoded in the spectral density modelling the vibrational bath. The interaction of the electronic transition with the vibrational bath modifies the spectrum associated with the molecule.

Spectral density and correlation function

That vibrational bath to which the electronic transition is coupled can be treated within the formalism for open quantum systems explained in Subsection 2.1.2. The system of interest is here composed of the electronic transition experienced by the organic molecule, while the nuclear degrees of freedom would be introduced in the description through a harmonic oscillator reservoir. From the Hamiltonian in Equation 2.62, we observe that the reservoir operator $\hat{\mathcal{R}}$ (when the interaction Hamiltonian is expressed as in Equation 2.8) would be given by:

$$\hat{\mathcal{R}} = \sum_{\kappa} \hbar \lambda_\kappa (\hat{b}_\kappa^\dagger + \hat{b}_\kappa) \, , \tag{2.65}$$

while the system operator would correspond to $\hat{\mathcal{Q}} = \hat{\sigma}^\dagger \hat{\sigma}$. For simplicity, we have considered just one molecule coupled to its own vibrational bath, so we have just one term in the interaction Hamiltonian. The dynamics of the open quantum system, governed by the Bloch–Redfield master equation (Equation 2.12), involves the time-correlation function of these reservoir operators $\hat{\mathcal{R}}(t)$. Actually, they appear in the description through the spectral density $S(\omega)$, defined as:

$$S(\omega) = \frac{1}{2\pi} \int_{-\infty}^{\infty} \langle \tilde{\mathcal{R}}(t) \, \tilde{\mathcal{R}}(t+\tau) \rangle \, \mathrm{e}^{\mathrm{i}\omega\tau} \mathrm{d}\tau \, , \tag{2.66}$$

equivalent to the expression in Equation 2.11 when having only one reservoir operator ($S(\omega) \equiv \Theta_{jj}(\omega)$). Notice that the spectral density $S(\omega)$ in Equation 2.66 is nothing but the Fourier transform of the time-correlation function $\mathcal{C}(t) \equiv \langle \tilde{\mathcal{R}}(t) \, \tilde{\mathcal{R}}(t+\tau) \rangle$. Some general relations between these two magnitudes can be found in Appendix F, Section F.5. When considering the operator in Equation 2.65, the spectral density $S(\omega)$ becomes (Equa-

tion F.35):

$$S(\omega) = \sum_{\kappa} \hbar^2 \lambda_\kappa^2 \left(n(\omega_\kappa)\, \delta(\omega + \omega_\kappa) + [1 + n(\omega_\kappa)]\, \delta(\omega - \omega_\kappa) \right), \tag{2.67}$$

where $n(\omega)$ is the Bose-Einstein distribution function at certain temperature T:

$$n(\omega) = \frac{1}{e^{\hbar\omega/k_B T} - 1} .$$

The detailed derivation of this result can be found in Subsection F.5.2. It is obtained by considering the correlation function $C(t)$ as the average over all vibrational modes in thermal equilibrium with an environment at temperature T (Equation F.23). Taking into account the definition of $J(\omega)$ given in Equation 2.64, the spectral density from Equation 2.67 can be alternatively written as (Equation F.37):

$$S(\omega) = [1 + n(\omega)][J(\omega) - J(-\omega)] . \tag{2.68}$$

CHAPTER 3

PHOTONS MODIFIED BY EXCITONS

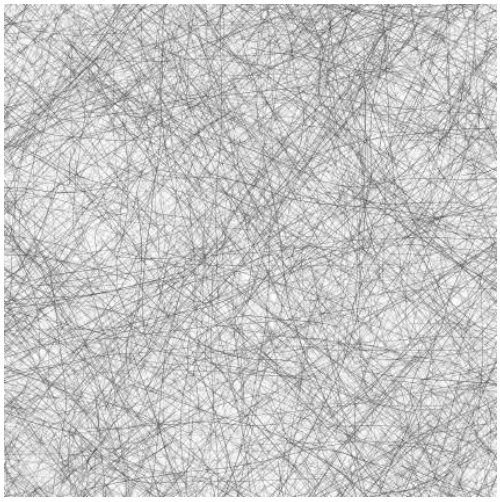

CHAPTER 3

PHOTONS MODIFIED BY EXCITONS

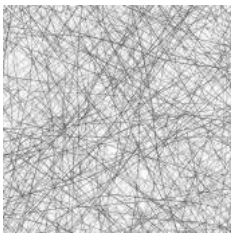

The study of the photon statistics of the light emitted by a quantum system has been a central theme in the field of quantum optics. The simplest case of the light resonantly scattered by a single emitter has focused great efforts, as interesting phenomena derive from that interaction. Apart from displaying a characteristic spectrum [427, 428], resonance fluorescence in atoms was shown to exhibit photon antibunching and sub-Poissonian statistics [121, 123] (see Subsection 2.3.4 for the theoretical description of these two concepts). Nonclassical light emission was later reported in different solid-state platforms. As explained in the introductory chapter (Section 1.2), the prospect of a better control of the characteristics of the emission, as well as of an improved performance as single-photon sources, led to the placement of these emitters into cavities and consider the light emerging from the composite system.

The coherence properties displayed by the photons leaking out of the cavity become modified by the coupling to excitons. While the hybrid system receives an incoming stream of coherent photons (when pumped by a laser), the resulting emission may present strong (either positive or negative) photon correlations. In this context of nonclassical light generation (see Subsection 1.2.1), the regime of strong light-matter interactions opened up new possibilities (see Subsection 1.2.2). The nonlinearities that arise due to the formation of polaritons are the responsible for the photon-blockade effect, where the presence of a photon in the strongly-coupled system prevents the absorption of a second one. Apart from this mechanism of generation of single photons, destructive interferences can lead to antibunching and sub-Poissonian statistics as well.

These two effects have been theoretically analyzed (see Subsection 1.2.3), mainly for the single-atom case or considering just a small number of emitters. The exponential scaling of the Hilbert space makes this problem intractable when dealing with large emitter ensembles. At the same time, the coupling of a macroscopic collection of emitters to a single cavity mode has been discussed in the context of superradiance, where different approximations need to be introduced. In our work, the focus is precisely in this intermediate regime of a mesoscopic number of emitters (up to a hundred). In particular, we study intensity correlations in the light emitted by a collection of emitters when coupled to the photonic mode supported by a cavity. Our findings reveal that photon correlations are not only maintained but enhanced due to the light-matter interaction. This coupling

allows for large nonlinearities even when the number of emitters is large. Strong coupling is thus reinforced as a route for generating nonclassical light beyond the single-emitter level.

The chapter is organized as follows. First, we consider the specific experimental setup of a collection of organic molecules hosted in a plasmonic nanocavity in Section 3.1. The resulting picture is compared to the case of quantum dots coupled to a semiconductor microcavity in Section 3.2, revealing the importance of losses and the role played by the closed/open character of the cavity. Finally, in Section 3.3, we explore those configurations leading to sub-Poissonian statistics in detail, distinguishing between correlations produced via the photon-blockade effect to those coming from interference mechanisms.

3.1 Photon statistics in plasmonic nanocavities

There is an increasing scientific and technological interest in the design and implementation of nanoscale sources of quantum light [429], as commented above. The ability to engineer the light-matter interaction at the nanoscale allows for a wide range of experiments, focused for instance on the control of the spontaneous emission or the enhancement of interactions at the single-photon level [203]. Plasmonic nanocavities present a promising prospect in this context, as light is confined in the nanoscale and the resulting small effective volumes lead to strong light-matter interactions [430].

Here, we investigate the quantum statistics of the light scattered from a plasmonic nanocavity coupled to a mesoscopic ensemble of emitters under low coherent pumping. The main results of this work have been published as: *R. Sáez-Blázquez, J. Feist, A. I. Fernández-Domínguez, and F. J. García-Vidal, "Enhancing photon correlations through plasmonic strong coupling," Optica* **4***, 1363–1367 (2017)*.

3.1.1 The system: a collection of quantum emitters within a plasmonic nanocavity

In this first analysis, the system is thus a collection of organic molecules interacting with the electromagnetic field supported by a plasmonic nanocavity. The whole system is driven by a coherent laser, and the resulting emission is examined. In the first place, all molecules are considered identical, as well as their couplings to the plasmonic mode. Nevertheless, the effects introduced due to the inhomogeneous broadening in the emitter ensemble and the spatial inhomogeneity of the plasmon near-field will be discussed later.

Model and theoretical description

Hamiltonian The system under study is composed of N identical **quantum emitters** (QE) with transition dipole moment $\boldsymbol{\mu}_{\mathrm{QE}}$ and frequency ω_{QE} interacting with the near-

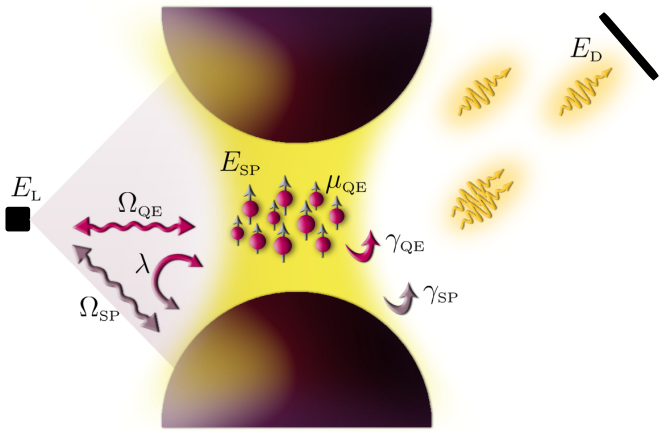

Figure 3.1. Scheme of the system, composed of an ensemble of quantum emitters coupled to a generic plasmonic nanocavity. The whole system is coherently pumped by a laser field.

field $\boldsymbol{E}_{\mathrm{SP}}$ (which is considered the same for all emitters) of a single **surface plasmon** (SP) mode of energy ω_{SP} supported by a generic nanocavity. Both the ensemble of quantum emitters and the plasmonic mode are coherently driven by a **laser** field $\boldsymbol{E}_{\mathrm{L}}$ of frequency ω_L. A scheme of the setup is depicted in Figure 3.1, in which the main parameters characterizing the system are displayed. According to Subsection 2.2.4, the **Tavis–Cummings Hamiltonian** could be used to describe the system, as we have a collection of two-level systems interacting with a single bosonic mode. Considering the parameters characterizing our model, the Hamiltonian reads ($\hbar = 1$):

$$\hat{H} = \Delta_{\mathrm{SP}}\hat{a}^\dagger\hat{a} + \Delta_{\mathrm{QE}}\hat{S}_z + \lambda(\hat{S}^+\hat{a} + \hat{S}^-\hat{a}^\dagger) + \Omega_{\mathrm{SP}}(\hat{a}^\dagger + \hat{a}) + \Omega_{\mathrm{QE}}(\hat{S}^+ + \hat{S}^-)\,, \tag{3.1}$$

where $\hat{a}^\dagger$ and $\hat{a}$ are the bosonic creation and annihilation operators associated with the plasmonic mode (Equation 2.18), while and $\hat{S}^+$ and $\hat{S}^-$ are the bright mode operators defined in Equation 2.28 (with $\hat{S}_z = [\hat{S}^+, \hat{S}^-]/2$ according to Equation 2.30). The **detuning** with respect to the laser frequency, $\Delta_{\mathrm{QE/SP}} \equiv \omega_{\mathrm{QE/SP}} - \omega_{\mathrm{L}}$ for the emitter and the plasmon resonances respectively, appears as a result of the transformation to the rotating frame (Equation 2.47). Notice that the **light-matter coupling** term of the Hamiltonian is written within the rotating wave approximation (Equation 2.39), and $\lambda \equiv \boldsymbol{E}_{\mathrm{SP}} \cdot \boldsymbol{\mu}_{\mathrm{QE}}$ in accordance to the electric-dipole approximation (Equation 2.37). The two last terms in the Hamiltonian correspond to the coupling to the laser, where the **pumping strengths** are given by $\Omega_{\mathrm{QE}} \equiv \boldsymbol{E}_{\mathrm{L}} \cdot \boldsymbol{\mu}_{\mathrm{QE}}$ and $\Omega_{\mathrm{SP}} \equiv \boldsymbol{E}_{\mathrm{L}} \cdot \boldsymbol{\mu}_{\mathrm{SP}}$ according to Equation 2.46. There, $\boldsymbol{\mu}_{\mathrm{SP}}$ is the effective surface plasmon dipole moment.

Time dynamics Both subsystems undergo **radiative** (r) and **non-radiative** (nr) **damping**, as represented in Figure 3.2. The total decay rate is thus given by $\gamma_{\mathrm{QE/SP}} = \gamma^{\mathrm{r}}_{\mathrm{QE/SP}} + \gamma^{\mathrm{nr}}_{\mathrm{QE/SP}}$ for the emitters and the surface plasmon resonance, respectively. We consider emitters in which pure dephasing is negligible, as this process would suppress quantum correlations in the emitted photons. The dynamics of the density matrix $\hat{\rho}$ describing the hybrid system is governed by the **Liouville–von Neumann master equation** (Equation 2.17):

$$\frac{\mathrm{d}}{\mathrm{d}t}\hat{\rho} = -\mathrm{i}\,[\hat{H}, \hat{\rho}] + \frac{\gamma_{\mathrm{SP}}}{2}\mathcal{L}_{\hat{a}}[\hat{\rho}] + \frac{\gamma^{\mathrm{r}}_{\mathrm{QE}}}{2}\mathcal{L}_{\hat{S}^-}[\hat{\rho}] + \sum_{n=1}^{N}\frac{\gamma^{\mathrm{nr}}_{\mathrm{QE}}}{2}\mathcal{L}_{\hat{\sigma}_n}[\hat{\rho}]\,, \tag{3.2}$$

Figure 3.2. Two-level system modelling the quantum emitter [**Left**] and plasmon resonance [**Right**] with their associated decay rates.

where the **Lindblad term** $\mathcal{L}_{\hat{\mathcal{O}}}[\hat{\rho}]$ accounts for the losses associated with the operator $\hat{\mathcal{O}}$, which is defined in Equation 2.16. While all plasmon losses are included in the term $\mathcal{L}_{\hat{a}}$, two different terms have to be added for the emitters: radiative losses are described through the bright mode operator $\hat{S}^{-}$ (corresponding to the assumption that emitters are at sub-wavelength distances and thus radiate like a collective dipole), but nonradiative losses are assigned to single emitters. Therefore, it is the single-atom annihilation operator $\hat{\sigma}_n$ for the n-th emitter that is involved in the latter case (Equation 2.23).

Exact numerical solutions to Equation 3.2 can be obtained for the strong coupling regime, but such calculations are only possible for configurations involving very small quantum emitter ensembles [244], even far from the emitter saturation regime [431]. In order to circumvent this limitation and explore photon statistics in mesoscopic ensembles, we make use of an effective non-Hermitian Hamiltonian [432].

Effective Hamiltonian In the regime of sufficiently low driving intensity, the contribution of the so-called **refilling** or **feeding terms** $\mathcal{O}\rho\mathcal{O}^{\dagger}$ appearing in the Lindblad superoperators (Equation 2.16) remains negligible. When they are removed, the Lindblad master equation (Equation 3.2) becomes equivalent to the Schrödinger equation $\mathrm{d}|\psi\rangle/\mathrm{d}t = -\mathrm{i}\hat{H}_{\mathrm{eff}}|\psi\rangle$, governing the time evolution of the state of the system $|\psi\rangle$ (Equation 2.1), with an **effective Hamiltonian**:

$$\hat{H}_{\mathrm{eff}} = \hat{H} - \mathrm{i}\frac{\gamma_{\mathrm{SP}}}{2}\hat{a}^{\dagger}\hat{a} - \mathrm{i}\frac{\gamma^{\mathrm{r}}_{\mathrm{QE}}}{2}\hat{S}^{+}\hat{S}^{-} - \mathrm{i}\frac{\gamma^{\mathrm{nr}}_{\mathrm{QE}}}{2}\hat{S}^{z}\,, \tag{3.3}$$

where $\hat{H}$ is the Hamiltonian of Equation 3.1. Notice that only bright mode operators appear in this effective Hamiltonian. Within this approach, the dark states of the ensemble (superpositions of the quantum emitter excitations that do not couple to the cavity or the external light) can thus be disregarded without further approximation. This corresponds to a drastic reduction in the Hilbert space when considering a large number N of emitters: instead of having to consider N and $N(N-1)$ states in the one- and two-excitation manifold, respectively, only one **singly-excited bright state** and one **doubly-excited bright state** play a role. These are written as $\sum_{n=1}^{N}\hat{\sigma}_n^{\dagger}|0\rangle/\sqrt{N}$ and $\sum_{n,m=1}^{N}\hat{\sigma}_n^{\dagger}\hat{\sigma}_m^{\dagger}|0\rangle/\sqrt{N(N-1)}$ (with $n \neq m$), respectively.

Steady state solution and computation of coherence properties

Steady state In this low-pumping regime, one can solve perturbatively the Schrödinger equation $\hat{H}_{\mathrm{eff}}|\psi\rangle = 0$ to find the **steady-state solution** (equivalent to computing the steady state density matrix from the master equation $\mathrm{d}\hat{\rho}/\mathrm{d}t = 0$). Considering the incident laser amplitude E_L as the small parameter, the effective Hamiltonian of Equation 3.3

can be split as $\hat{H}_{\text{eff}} = \hat{H}_0 + E_L\hat{V}$, where the second term is the driving, that is:

$$E_L\hat{V} = \Omega_{\text{SP}}(\hat{a}^\dagger + \hat{a}) + \Omega_{\text{QE}}(\hat{S}^+ + \hat{S}^-) \, .$$

The remaining terms are thus:

$$\hat{H}_0 = \Delta_{\text{SP}}\hat{a}^\dagger\hat{a} + \Delta_{\text{QE}}\hat{S}_z + \lambda(\hat{S}^+\hat{a} + \hat{S}^-\hat{a}^\dagger) - \mathrm{i}\frac{\gamma_{\text{SP}}}{2}\hat{a}^\dagger\hat{a} - \mathrm{i}\frac{\gamma_{\text{QE}}^{\text{r}}}{2}\hat{S}^+\hat{S}^- - \mathrm{i}\frac{\gamma_{\text{QE}}^{\text{nr}}}{2}\hat{S}^z \, . \tag{3.4}$$

The steady state $|\psi\rangle$ can be also expanded in a power series of E_L, such that it becomes:

$$|\psi\rangle = \sum_{k=0} E_L^k |\psi_k\rangle \, . \tag{3.5}$$

Substituting these expansions into the equation $\hat{H}_{\text{eff}}|\psi\rangle = 0$ and grouping terms for each power of E_L, we arrive at a set of linear equations. The zeroth-order equation leads simply to $|\psi_0\rangle = |0\rangle$ (that is, the ground state, which represents no excitations in the system) whereas the kth-order equation turns out to be $\hat{H}_0|\psi_k\rangle + \hat{V}|\psi_{k-1}\rangle = 0$. These equations can be successively solved so that the steady state is finally obtained from this **perturbative approach**.

First- and second-order correlation functions Once the steady-state density matrix is known, the first- and second-order correlation functions can be calculated from the (negative-frequency part of the) **scattered far-field operator** at the detector:

$$\hat{\boldsymbol{E}}_{\text{D}}^{(-)} \propto \boldsymbol{\mu}_{\text{SP}}\hat{a}^\dagger + \boldsymbol{\mu}_{\text{QE}}\hat{S}^+ \, , \tag{3.6}$$

where we have considered the emission coming from both the surface plasmon mode (Equation 2.48) and the collection of quantum emitters. Note that we have taken advantage of the sub-wavelength dimensions of the system to neglect the differences between the electromagnetic Green's function describing the emission from the different subsystems in the far-field at the detector $\hat{\boldsymbol{E}}_{\text{D}}$. The correlation functions can be evaluated by considering the perturbative solution for the steady state of the system (Equation 3.5). The **scattering intensity** I (defined in Equation 2.49) and the **normalized zero-delay second-order correlation function** $g^{(2)}(0)$ (defined in Equation 2.50 for a general value of the time delay τ) in the steady state are thus computed as:

$$I = \langle\psi_1|\hat{\boldsymbol{E}}_{\text{D}}^{(-)}\hat{\boldsymbol{E}}_{\text{D}}^{(+)}|\psi_1\rangle \tag{3.7}$$

$$g^{(2)}(0) = \langle\psi_2|\hat{\boldsymbol{E}}_{\text{D}}^{(-)}\hat{\boldsymbol{E}}_{\text{D}}^{(-)}\hat{\boldsymbol{E}}_{\text{D}}^{(+)}\hat{\boldsymbol{E}}_{\text{D}}^{(+)}|\psi_2\rangle/I^2 \, . \tag{3.8}$$

From these equations, it follows that our perturbative calculations can be restricted to second order, and we can truncate the Hilbert space at the two-excitation manifold. For the computation of the **second-order correlation function** $g^{(2)}(\tau)$, the evolution operator $\mathcal{U}(t) = \exp[-\mathrm{i}\hat{H}_{\text{eff}}t]$ has to be introduced:

$$\begin{aligned} g^{(2)}(\tau) &= \langle\hat{\boldsymbol{E}}_{\text{D}}^{(-)}(0)\,\hat{\boldsymbol{E}}_{\text{D}}^{(-)}(\tau)\,\hat{\boldsymbol{E}}_{\text{D}}^{(+)}(\tau)\,\hat{\boldsymbol{E}}_{\text{D}}^{(+)}(0)\rangle/I^2 \\ &= \langle\psi|\hat{\boldsymbol{E}}_{\text{D}}^{(-)}\,\mathcal{U}^\dagger(\tau)\,\hat{\boldsymbol{E}}_{\text{D}}^{(-)}\hat{\boldsymbol{E}}_{\text{D}}^{(+)}\,\mathcal{U}(\tau)\,\hat{\boldsymbol{E}}_{\text{D}}^{(+)}|\psi\rangle/I^2 \, , \end{aligned} \tag{3.9}$$

where $\hat{\boldsymbol{E}}_{\text{D}}^{(-)} \equiv \hat{\boldsymbol{E}}_{\text{D}}^{(-)}(0)$, and the perturbative solution of $|\psi\rangle$ up to second order is also used in the calculation.

Parameters

The parameters modelling the single surface plasmon resonance and the collection of quantum emitters are in accordance with the values they present in typical experimental setups. The energy of the surface plasmon resonance is set to $\omega_{SP} = 3$ eV, with a total decay rate $\gamma_{SP} = 0.1$ eV. The associated effective dipole moment is chosen as $\mu_{SP} = 19$ e·nm [433]. The two-level systems modelling the quantum emitters present a transition frequency $\omega_{QE} = 3$ eV, and the nonradiative and radiative decay rates are set to $\gamma_{QE}^{nr} = 15$ meV and $\gamma_{QE}^{r} = 6$ μeV, respectively. The former value corresponds to a transition dipole moment $\mu_{QE} = 1$ e·nm according to Equation 1.3. These values are typical of organic molecules with a very low quantum yield, in which collective strong coupling has been already reported [434, 435]. As we show later, this type of emitters favours the generation of photon correlations. For a practical realization of our findings with organic emitters, note that the experiments should be carried out at low temperature in order to avoid pure dephasing processes.

Only low laser intensities are considered, so as to work within the perturbative regime. Therefore, we study quantum correlations far from the pumping regime in which the emitter saturation becomes relevant. For simplicity, we assume the plasmonic near-field $\boldsymbol{E}_{SP}$ parallel to the laser field $\boldsymbol{E}_{L}$ (which corresponds, for instance, to particle-on-mirror cavities [94]). Moreover, we only consider the optimum configuration for strong coupling, in which the transition dipole moment of the emitters $\boldsymbol{\mu}_{QE}$ is aligned with the plasmonic field $\boldsymbol{E}_{SP}$.

3.1.2 Coherence properties: uncoupled and strongly-coupled subsystems

Before investigating photon correlations under strong-coupling conditions, we consider both subsystems uncoupled first. The light emitted by the plasmonic resonance is sketched in Figure 3.3 [Left]. When computing the second-order correlation function at zero time delay for the plasmonic mode, we find that it is equal to one regardless the frequency of the laser. In Figure 3.3 [Right], we plot this magnitude $g^{(2)}(0)$ as a function of the detuning of the laser with respect to the plasmon frequency, Δ_{SP}. This result is expected from the inherent bosonic character of plasmons.

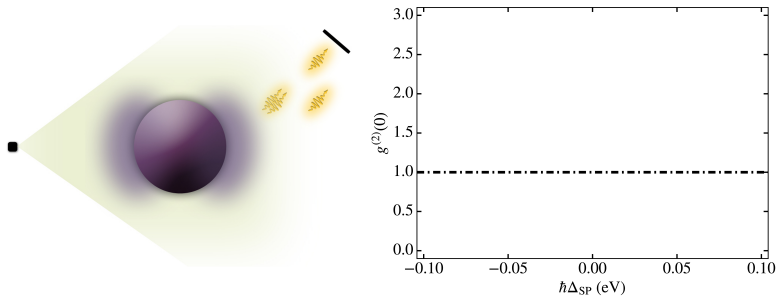

Figure 3.3. **[Left]** Scheme of a surface plasmon resonance emitting light, which is measured in the far-field by a detector. **[Right]** Normalized second-order correlation function at zero-time delay, $g^{(2)}(0)$, as a function of the laser detuning Δ_{SP} for an empty plasmonic cavity.

The light emitted by a collection of N quantum emitters driven by a laser is considered next, as represented in Figure 3.4 [Left]. We plot the second-order correlation function at zero-time delay in Figure 3.4 [Center]. Ensembles of different number of

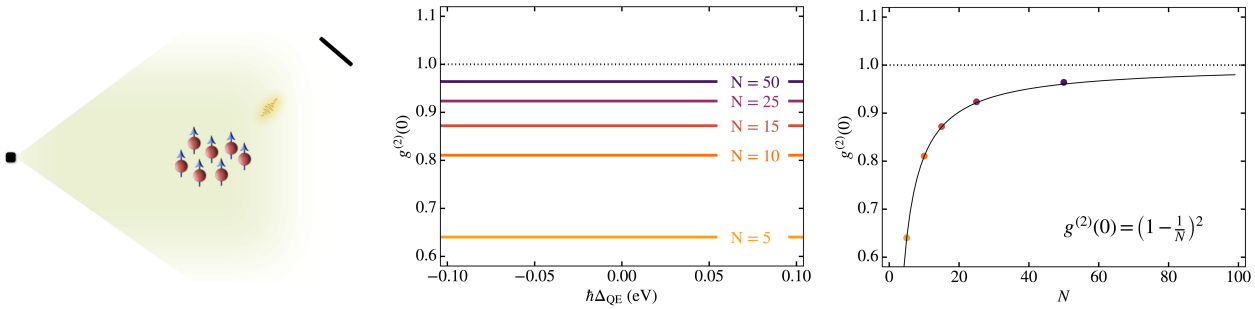

Figure 3.4.
[Left] Scheme of a collection of quantum emitters driven by a laser, whose far-field radiation is measured by a detector. **[Center]** Normalized second-order correlation function $g^{(2)}(0)$ as a function of the laser detuning Δ_{QE}. Different emitter ensemble sizes are considered, ranging from $N = 5$ (yellow) to $N = 50$ (purple). **[Right]** Value of $g^{(2)}(0)$ as a function of the number of emitters N. Coloured dots indicate the values previously shown in [Center], while the continuous black line represents the function $g^{(2)}(0) = (1-1/N)^2$.

emitters are considered, ranging from $N = 5$ (in yellow) to $N = 50$ (in purple). Again, this magnitude does not depend on the frequency of the laser: $g^{(2)}(0)$ is the same for all values of the detuning of the laser from the emitter frequency, Δ_{QE}. We observe that the second-order coherence degree is always below one, hence it corresponds to sub-Poissonian photon statistics. Nevertheless, it decreases rapidly with the ensemble size —notice, for instance, that $g^{(2)} = 0.96$ when having 50 emitters. As the number of emitters increases, the system bosonizes and the quantum character of the scattered light is lost. This is clearly observed in Figure 3.4 [Right], where the $g^{(2)}(0)$ values associated with the previous five cases are plotted versus N. Additionally, we represent the function $g^{(2)}(0) = |1-1/N|^2$, as this is the law governing the coherence degree for an ensemble of emitters.

As a last step, we consider these two **subsystems strongly coupled** while pumped by a coherent laser. An scheme of the configuration is shown in Figure 3.5 [Left]. We consider a coupling strength $\lambda = 17$ meV as an example, and plot the $g^{(2)}(0)$ value as a function of the laser detuning Δ_L in Figure 3.5 [Right]. Different coloured lines stand for different ensemble sizes, corresponding to the same cases considered in Figure 3.4 [Center] in absence of cavity. We observe that both sub-Poissonian and super-Poissonian statistics take place in the strong coupling regime, and photon correlations are enhanced even when the the number of emitters is large. The light coming from the hybrid system possesses truly different coherence characteristics as compared to the two subsystems uncoupled (see Figure 3.3 [Right] and Figure 3.4 [Center]).

This is precisely the main result of our work, namely, collective plasmonic strong coupling can significantly enhance photon correlations in mesoscopic systems (in comparison to the uncoupled subsystems). Therefore, contrary to what is expected, plasmonic

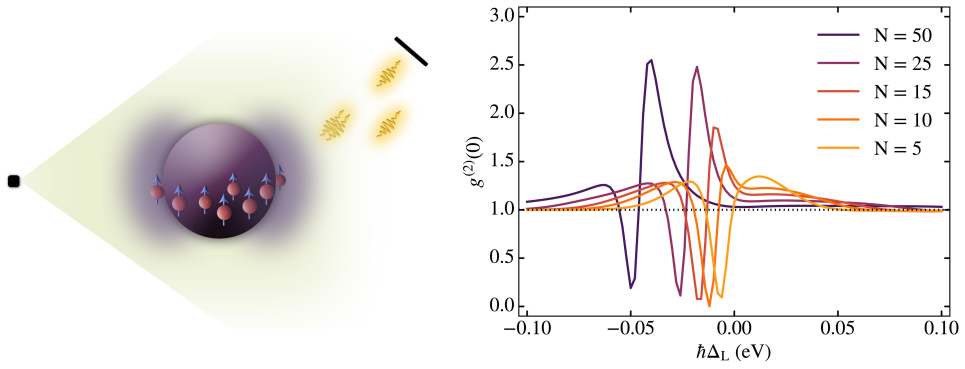

Figure 3.5. **[Left]** Scheme of a collection of quantum emitters coupled to a plasmon resonance, while the whole system is driven by a laser. The far-field radiation is measured by a detector. **[Center]** Normalized second-order correlation function $g^{(2)}(0)$ as a function of the laser detuning Δ_L. Different emitter ensemble sizes are considered, ranging from $N = 5$ (yellow) to $N = 50$ (purple).

nanocavities allow photon correlations to survive in emitter ensembles of considerable size. Indeed, these correlations are not only retained but enhanced when the number of emitters increases. In the following, we will explore these configurations and the coherence properties of the emitted light in more detail.

3.1.3 Intensity and coherence

Considering the parameters before indicated, in this section we study the quantum statistics of the photons scattered by a plasmonic nanocavity strongly coupled to a mesoscopic emitter ensemble under coherent pumping. The two-level systems modelling the emitters are at resonance with the plasmonic mode, such that $\omega_0 \equiv \omega_{\mathrm{QE}}, \omega_{\mathrm{SP}}$. Figure 3.6 shows the **scattering intensity** I (top row) and the **zero-delay second-order correlation function** $g^{(2)}(0)$ (bottom row) for three different collections of emitters: $N = 1$ (a), 5 (b), and 25 (c). Both magnitudes are plotted as a function of the laser detuning $\omega_L - \omega_0$ and the coupling strength λ, which is expressed in units of the cavity decay rate $\gamma_{\mathrm{C}} \equiv \gamma_{\mathrm{SP}}$.

Intensity

The intensity maps are plotted in Figure 3.6 [Top], where two scattering maxima are observed. These correspond to the **polariton energies** within the strong coupling regime—that is, the eigenenergies of the dressed states in the one-excitation manifold (the first-rung of the Tavis–Cummings ladder). For each value of the coupling strength we find two intensity peaks at laser frequencies that match the lower polariton (LP) and upper polariton (UP) energies. These energies are obtained by diagonalizing the corresponding block of the unperturbed Hamiltonian H_0 (Equation 3.4). The dispersion curves are plotted in Figure 3.6 [Top] with dotted lines overlapping the maps, so that the correspondence is easily observed. Note that these two maxima branches are also apparent within the weak coupling regime, so their presence here cannot be regarded as an energy splitting. Actually, these double maxima have their origin in a **Fano-like interference**, taking place when two signals with very different linewidths interact [436, 437, 438]. The pronounced minimum in the scattering intensity is, in this case, produced by the destructive interference between the cavity and emitter emission.

Apart from the explained structure, we observe that there exists an **asymmetry** between the two intensity maxima branches: the one corresponding to the UP is distinctly brighter than the associated with the LP. Note that the emission coming from each polariton can be described from either the parallel (UP) or antiparallel (LP) superposition of the dipole moments associated with the plasmon and the bright mode of the emitter ensemble. Since the dipole moment corresponding to the UP is larger, its emission is more intense. This difference in the effective dipole moment between the two polaritons grows as N increases, as a consequence of the greater collective dipole moment of the ensemble. Hence the contrast between branches should become more pronounced for larger ensemble sizes, as observed.

From the **analytical results** obtained thanks to the perturbative approach described before, we can get a better understanding of the emission pattern. First, we have to compute the steady-solution (Equation 3.5) up to second order. The expression for the

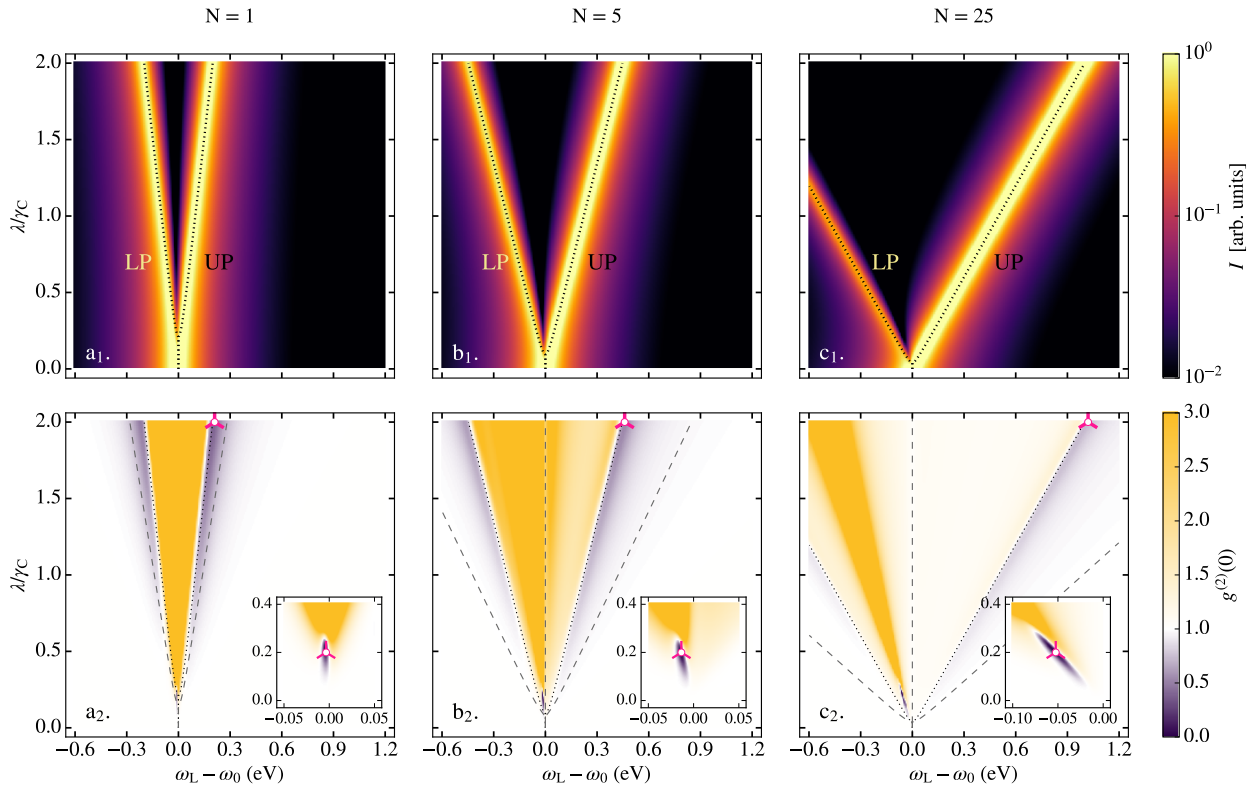

Figure 3.6.
Scattering intensity I (top row) and correlation function $g^{(2)}(0)$ (bottom row) versus laser detuning and coupling strength (in units of the cavity decay rate γ_C) for a system of $N = 1$ (a), 5 (b) and 25 (c) quantum emitters coupled to a plasmonic nanocavity. In these panels, dotted (dashed) lines plot the polariton frequencies (half-frequencies) in the one-excitation (two-excitation) manifold. Insets zoom into the low coupling region. Magenta marks indicate points whose $g^{(2)}(\tau)$ is plotted in Figure 3.22 (a_1).

scattered intensity I is then computed from Equation 3.7, yielding:

$$I \propto \left| \frac{\tilde{\Delta}_{SP}\mu_{QE}^2 + \tilde{\Delta}_{QE}\mu_{SP}^2/N - 2\lambda\mu_{SP}\mu_{QE}}{\tilde{\Delta}_{SP}\tilde{\Delta}_{QE}/N - \lambda^2} \right|^2 , \tag{3.10}$$

where the detunings of the laser frequency from both the surface plasmon, Δ_{SP}, and the emitters, Δ_{QE}, are redefined so as to introduce the associated losses:

$$\begin{aligned} \tilde{\Delta}_{SP} &\equiv \Delta_{SP} - i\gamma_{SP}/2 , \\ \tilde{\Delta}_{QE} &\equiv \Delta_{QE} - i(\gamma_{QE}^{nr} + N\gamma_{QE}^{r})/2 . \end{aligned} \tag{3.11}$$

This expression confirms the origin of the intensity maxima: the condition for which the denominator vanishes, $\lambda^2 = \tilde{\Delta}_{SP}\tilde{\Delta}_{QE}/N$. This gives us the dispersion curves associated with the LP and UP. Notice that a $\sqrt{N}$ dependence appears, which is the characteristic scaling of the collective coupling. Additionally, this expression sheds light into the asymmetry in the polariton branches. When the losses from both cavity and emitters are neglected, the intensity behaves as:

$$I \propto \left(1 \mp \sqrt{N}\,\frac{\mu_{QE}}{\mu_C}\right)^2 ,$$

where the upper sign corresponds to the LP, and the lower sign to the UP. Therefore, as the number of emitters grows, the UP branch becomes brighter.

Coherence

The coherence maps are plotted in Figure 3.6 [Bottom], where areas of super-Poissonian (yellow coloured) as well as sub-Poissonian (blue coloured) statistics are found for all ensembles sizes. Our attention is first focused in the **single-emitter case** ($N = 1$). There, we observe a main super-Poissonian area located between the LP and UP energies (again depicted as dotted lines) for all coupling values. Close to these polariton frequencies, but still far from the two-excitation eigenenergies (depicted as dashed lines), regions of sub-Poissonian light are found, being more pronounced as the coupling strengthens. These correspond to the well-known **photon blockade** effect, where the presence of an excitation in the system prevents the absorption of a second photon at certain frequencies due to the anharmonicity of the energy ladder. Apart from these two stripes, we find another area of sub-Poissonian emission that is enlarged in the corresponding inset. It lies around the resonant frequency $\omega_L = \omega_0$. The mechanism that lies behind is the destructive interference among possible decay paths that produces the suppression of two-photon processes and hence the drop of $g^{(2)}(0)$ below one [213]. Although this mechanism is sometimes referred to as **unconventional antibunching**, here we use the term **interference-induced correlations**. In Subsection 3.3.1, these two different types of sub-Poissonian light are discussed in further detail.

The main statistical features emerging at the single-emitter level are also present when having a collection of emitters. This is observed in Figure 3.6 [Bottom], in the panels corresponding to $N = 5$ (b_2) and $N = 25$ (c_2). The area of bunched light remains between the one-excitation eigenenergies, although it tends to approach the LP branch when the number of emitters increases. This tilt is also observed for the interference-induced correlation area: the region of negative correlations shifts towards the LP energy, while values for the function $g^{(2)}(0)$ below one are still achieved within the same coupling range as for the single-emitter case. This is better observed in Figure 3.7, where the $g^{(2)}(0)$ values are plotted for $N = 1$ (a), 5 (b), 25 (c) and 50 (d) emitters in a reduced area. In this case, the light-matter coupling strength is expressed through the **single-emitter cooperativity** C:

$$C \equiv \frac{2\lambda^2}{\gamma_{\rm QE}\gamma_{\rm SP}} \,. \tag{3.12}$$

Notice that the upper limit $C = 2$, which corresponds to $\lambda = 0.03$ eV, is well below the collective ultra-strong coupling regime. We observe that up to 25 quantum emitters, photon emission is sub-Poissonian within a narrow frequency window located at $C \lesssim 1$.

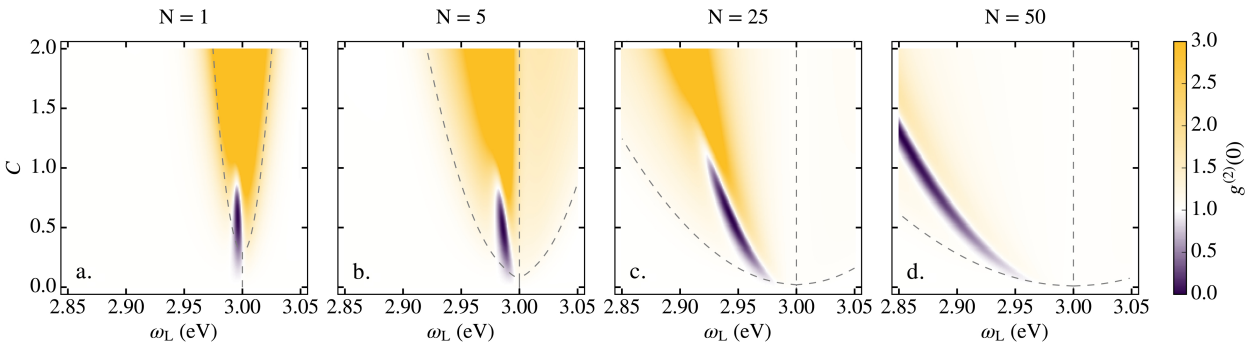

Figure 3.7. (a)-(d) Correlation function $g^{(2)}(0)$ versus laser frequency $\omega_{\rm L}$ and single-emitter cooperativity C for various hybrid systems. In the upper (lower) panels dotted (dashed) lines plot the polariton frequencies (half-frequencies) in the one-excitation (two-excitation) manifold.

This implies that the single-emitter cooperativity can be taken as a parameter determining photon correlations in ensembles containing up to several tens of emitters. Remarkably, there are still a spectral window displaying strong correlations ($g^{(2)}(0) \approx 0$) even for $N = 50$, whereas the emission from the uncoupled emitter ensemble is essentially classical (see Figure 3.4 [Center]). Note that by increasing further the number of emitters, the system eventually bosonizes (that is, $g^{(2)}(0) = 1$) and the quantum character of the emitted light is then lost. Focusing now on the region associated with the photon-blockade effect, in Figure 3.6 [Bottom] we observe that the minimum following the UP branch is deeper than the LP one. Nevertheless, it is noticeable how both fade for larger sizes of the emitter ensemble. Indeed, for $N = 25$ there are a wide range of coupling strengths where this effect is not observable. On the contrary, for moderate values of the coupling the dip corresponding to interference effects is not only present, but becomes quite pronounced.

Finally, from our perturbative approach we can obtain the **analytical expression** for the correlation function $g^{(2)}(0)$ as well. Considering again the perturbative solution for the steady state (Equation 3.5), we compute the degree of second-order coherence from Equation 3.8:

$$g^{(2)}(0) = \left| 1 - \frac{1}{N} \left(\frac{\tilde{\Delta}_{\mathrm{SP}}\mu_{\mathrm{QE}} - \lambda\mu_{\mathrm{SP}}}{\tilde{\Delta}_{\mathrm{SP}}\mu_{\mathrm{QE}}^2 + \tilde{\Delta}_{\mathrm{QE}}\mu_{\mathrm{SP}}^2/N - 2\lambda\mu_{\mathrm{SP}}\mu_{\mathrm{QE}}} \right)^2 \frac{(\tilde{\Delta}_{\mathrm{QE}} + iN\gamma^{\mathrm{r}}_{\mathrm{QE}}/2)[\tilde{\Delta}_{\mathrm{SP}}\tilde{\Delta}_{\mathrm{QE}}\mu_{\mathrm{QE}}^2 + (\tilde{\Delta}_{\mathrm{SP}}\mu_{\mathrm{QE}} - \lambda\mu_{\mathrm{C}})^2 - N\lambda^2\mu_{\mathrm{QE}}^2]}{(\tilde{\Delta}_{\mathrm{QE}} + i\gamma^{\mathrm{r}}_{\mathrm{QE}}/2)(\tilde{\Delta}_{\mathrm{SP}}^2 + \tilde{\Delta}_{\mathrm{SP}}\tilde{\Delta}_{\mathrm{QE}} - N\lambda^2) - \tilde{\Delta}_{\mathrm{SP}}(N-1)\lambda^2} \right|^2, \tag{3.13}$$

where we have made use of the redefined detunings $\tilde{\Delta}_{\mathrm{SP}}$ and $\tilde{\Delta}_{\mathrm{QE}}$ of Equation 3.11. We observe that, as expected, $g^{(2)}(0) \to 1$ when N tends to infinity for a fixed value of the coupling strength —hence the expression does recover the bosonization limit. Notice also that the denominator of the first term coincides with the numerator of the analytical expression for the intensity (Equation 3.10), and the vanishing condition for the denominator of the second term yields the polariton energies of the second-rung of the Tavis–Cummings ladder.

3.1.4 Degree of bunching and antibunching

In order to obtain a general view of the **degree of photon correlations** attainable through light-matter coupling, we evaluate Equation 3.13 at its spectral maxima and minima. Figure 3.8 shows these extreme values of $g^{(2)}(0)$ as a function of the number of emitters N and cooperativity C (Equation 3.12). Figure 3.8 (b) renders Max$[g^{(2)}(0)]$ (top, in yellow) and Min$[g^{(2)}(0)]$ (bottom, in purple). Cuts of these maps at particular values of the cooperativity are plotted in the corresponding panels of Figure 3.8 (a), ranging from $C = 0.1$ (yellow) to $C = 2$ (purple). According to the statistics of the scattered photons, three domains can be identified:

- For small emitter ensembles and large C, only positive correlations take place, as observed in Figure 3.7 (a)-(c) for $C > 1$. In this regime, Max$[g^{(2)}(0)]$ grows when the coupling strength increases, and it develops a maximum around $N \sim 10$ for all cooperativity values.

- For very large emitter ensembles, polaritons bosonize ($g^{(2)}(0) = 1$). Observe that, according to Equation 3.13, the $1/N$ factor governs the degree of second-order coherence $g^{(2)}(0)$. This yields that both maxima and minima approach 1 monotonically as the number of emitters increases.

- At intermediate N and C, both bunched and antibunched emission takes place, although within different spectral windows.

In this third domain, positive correlations decay monotonically with N, whereas negative correlations are enhanced. Observe, for instance, the lines corresponding to $C = 1$ (dark blue) and $C = 2$ (purple) in Figure 3.8 (a_2). Min$[g^{(2)}(0)]$ starts diminishing with N until it reaches a minimum value —this corresponds to the lowest $g^{(2)}(0)$ achievable for a given C. Alternatively, we can think in the lowest $g^{(2)}(0)$ achievable for a given number of emitters. If we focus on $N = 40$, for instance, we observe that negative correlations increases as the light-matter coupling strengthens only up to a point, from which an increase in the cooperativity produces a sharp fall in the correlations.

Therefore, the degree of second-order coherence $g^{(2)}(0)$ presents a minimum at a particular number of emitters for a given coupling strength (or, alternatively, it presents a minimum at a certain coupling strength for a given number of emitters). It can be proven that this minimum coincides with a sharp dip in the population of the plasmon state (written as a linear combination of polariton states) in the two-excitation manifold.

The three areas of differentiated photon statistics are schematized in Figure 3.9, where the dashed line indicates the cooperativity value at which the minimum value of the $g^{(2)}(0)$ is reached for a specific number of emitters. In the limit of $\mu_{SP} \gg \mu_{QE}$, which is a good approximation for our problem at small N, this condition simplifies to:

$$C = \frac{\gamma_{QE} + \gamma_{SP}}{2\gamma_{SP}} \simeq \frac{1}{2}$$

Effectively, in Figure 3.9 we observe that the minimum is attained around $C \sim 0.5$ for a reduced number of emitters. Figure 3.8 (a_2) also shows this minimum developing with increasing cooperativity at $N \sim 10$ and reaching $g^{(2)}(0) = 0$ at $C = 0.5$. Remarkably,

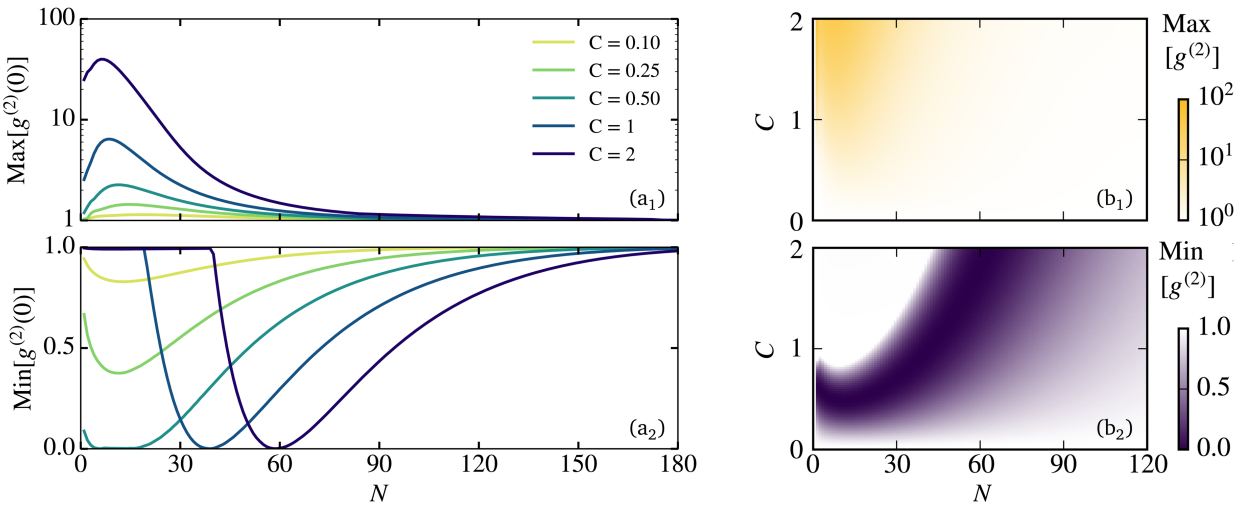

Figure 3.8. **(a)** Maximum (top) and minimum (bottom) value of the correlation function $g^{(2)}(0)$ as a function of the number of molecules N for several values of the single emitter cooperativity C. **(b)** Map of photon positive (top) and negative (bottom) correlations as a function of N and C.

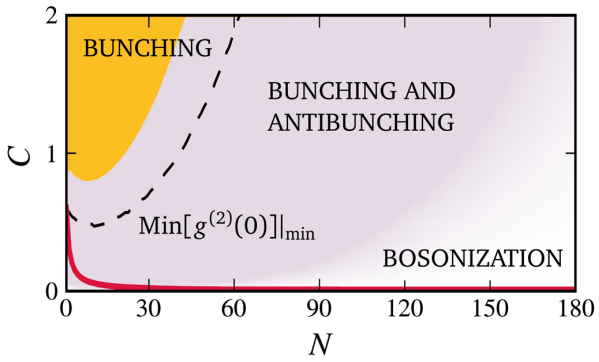

Figure 3.9. Division of the NC-map according to photon statistics: parametric regions presenting only bunching (yellow), both bunching and antibunching (lilac), and neither bunching nor antibunching (white). For each number N, the dashed black line indicates the cooperativity C at which the value of Min$[g^{(2)}(0)]$ is minimum (that is, this curve corresponds to the minimum of the function depicted in Figure 3.8(b$_2$))

this zero in $g^{(2)}(0)$ shifts to larger N for higher cooperativity, yielding strong photon antibunching at ensemble sizes as large as 100 quantum emitters. Therefore, as anticipated in Figure 3.7 (d), plasmonic strong coupling leads to the emergence of strong quantum nonlinearities in large excitonic systems, which would present $g^{(2)}(0) \simeq 1$ when not coupled to the plasmonic nanocavity (Figure 3.4 [Center]).

3.1.5 Varying the parameters

Although the quantitative results shown in Figure 3.6 depend on the specifics of the system, we have checked that our findings and their fundamental implications remain valid for a wide range of realistic configurations. In the following, we show the impact of different changes of the parameters on the preceding results. In particular, we first test the effective Hamiltonian approach in the low pumping (perturbative) regime against full Liouvillian calculations. Then, we analyze the case in which the surface plasmon field is considered spatially inhomogeneous and when inhomogeneous broadening is introduced for the quantum emitters. Note that emitters cannot be formally described through a single bright state in these two cases, but must be treated individually. The effect of plasmonic losses and the non-radiative decay of emitters on the second-order correlation function is also studied. Next, dipole-dipole interactions among emitters are introduced, exploring the sensitivity of photon correlations against these interactions. Finally, we discuss the impact of the open/closed character of the cavity. All the calculations in this section are carried out for hybrid systems involving five quantum emitters ($N = 5$).

Effective Hamiltonian versus full Liouvillian

The effective non-Hermitian Hamiltonian $\hat{H}_{\text{eff}}$ in Equation 3.3 is obtained by taking the low-pumping limit in the full master equation. The refilling terms in the Lindblad superoperators describing the radiative and nonradiative damping associated with the plasmonic mode and emitters can be neglected in this limit. Although these terms ensure the normalization of the steady-state density matrix $\hat{\rho}$, this condition can be relaxed in the low-pumping regime. There, the population concentrates at the ground state $|0\rangle$ (no excitations in the system), hence we can set $\text{Tr}\{\hat{\rho}\} \simeq \langle 0|0\rangle = 1$ and approximate the Lindblad super-operators (defined in Equation 2.16) by:

$$\mathcal{L}_{\hat{\mathcal{O}}}[\hat{\rho}] \simeq -\hat{\mathcal{O}}^{\dagger}\hat{\mathcal{O}}\hat{\rho} - \hat{\rho}\hat{\mathcal{O}}^{\dagger}\hat{\mathcal{O}} = -\{\hat{\mathcal{O}}^{\dagger}\hat{\mathcal{O}}, \hat{\rho}\}\ . \tag{3.14}$$

where $\hat{\mathcal{O}}$ stands for a general operator. The subtraction of the refilling terms from the Lindblad super-operators not only enables the description of the steady-state of the system in terms of an effective Hamiltonian, but, more importantly, it also removes its dependence on the dark states of the emitter ensemble.

This approach yields exact results for low enough intensities of the laser field E_{L}. This is shown in Figure 3.10 for the particular case of $N = 5$, where all parameters remain the same as in the preceding section. This figure shows the intensity (top) and the photon correlations (bottom) as a function of the laser frequency ω_L for five different values of the single-emitter cooperativity C. While color solid lines plot the results derived from a full Liouvillian treatment, black dotted lines result from effective Hamiltonian calculations. The former were obtained from the numerical solution of the equation for the steady state density matrix $\hat{\rho}$ (Equation 3.2), computing the intensity I and the second-order correlation function $g^{(2)}(0)$ according to the density matrix formalism, that is:

$$I = \mathrm{Tr}\left[\hat{\rho}\hat{\boldsymbol{E}}_{\mathrm{D}}^{(-)}\hat{\boldsymbol{E}}_{\mathrm{D}}^{(+)}\right],$$
$$g^{(2)}(0) = \mathrm{Tr}\left[\hat{\rho}\hat{\boldsymbol{E}}_{\mathrm{D}}^{(-)}\hat{\boldsymbol{E}}_{\mathrm{D}}^{(-)}\hat{\boldsymbol{E}}_{\mathrm{D}}^{(+)}\hat{\boldsymbol{E}}_{\mathrm{D}}^{(+)}\right]/I^2,$$

where $\hat{\boldsymbol{E}}_{\mathrm{D}}^{(-)}$ is the far-field electric operator given in Equation 3.6 . The pumping parameters were set to $\Omega_{\mathrm{SP}} = 19$ meV and $\Omega_{\mathrm{QE}} = 1$ meV, and the steady-state density matrix was calculated up to the three-excitation manifold. In all cases, both solutions are in perfect agreement. Note that a rather moderate number of emitters was chosen as the Liouvillian calculations become cumbersome for larger ensemble sizes.

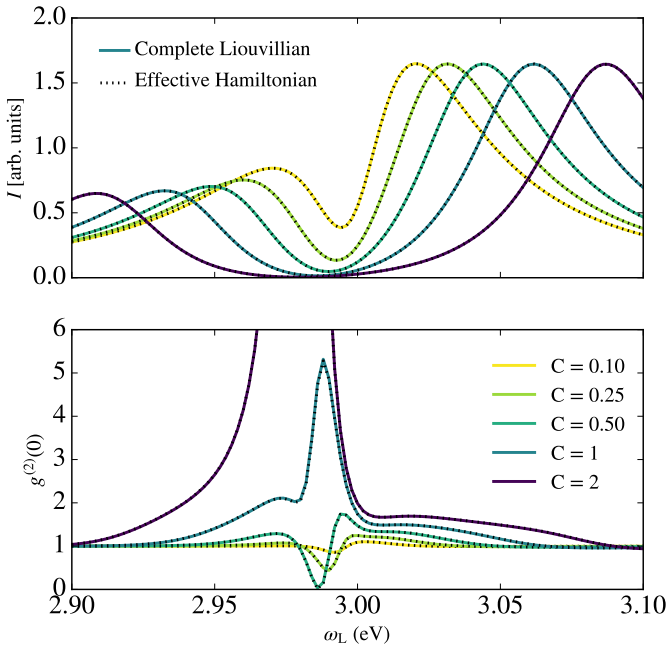

Figure 3.10. Scattering intensity (top) and zero-delay second-order correlation function $g^{(2)}(0)$ (bottom) versus laser frequency for $N = 5$ emitters coupled to a plasmonic cavity for various cooperativity values, ranging from $C = 0.1$ (yellow) to $C = 2$ (purple). Solid color lines stand for the full Liouvillian computations, where black dotted lines corresponds to the effective Hamiltonian approach.

Spatial inhomogeneity of the plasmon near-field

Second, we analyze the effect that the introduction of spatial inhomogeneity in the surface plasmon near-field has on the scattering intensity and photon correlations for strongly

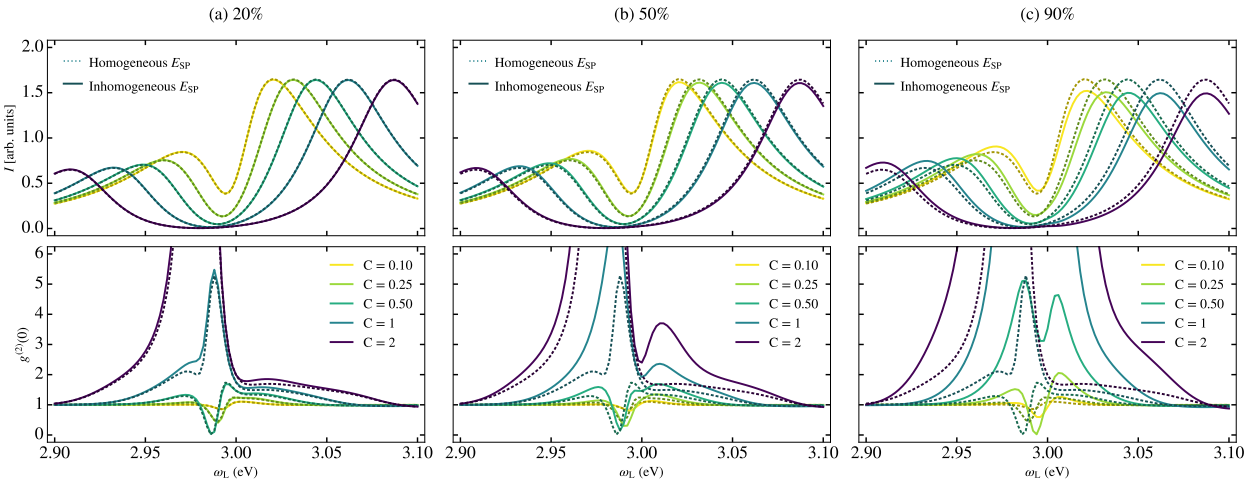

Figure 3.11. Scattering intensity I (top) and zero-delay second-order correlation function $g^{(2)}(0)$ (bottom) versus laser frequency ω_L for various C-values. Solid lines correspond to spatially inhomogeneous plasmon near-fields with 20 (a), 50 (b) and 90 % (c) variation in $E_{SP\|}$ within the emitter ensemble. Dotted lines render homogeneous (uniform $E_{SP\|}$) results, and are the same in all cases.

coupled emitter ensembles. A spatially dependent surface plasmon field, $\boldsymbol{E}_{SP} = \boldsymbol{E}_{SP}(\boldsymbol{r})$, would lead to a coupling strength varying across the emitter ensemble as:

$$\lambda_n = \boldsymbol{E}_{SP}(\boldsymbol{r}_n) \cdot \boldsymbol{\mu}_{QE,n} = E_{SP\|}(\boldsymbol{r}_n)\mu_{QE}, \tag{3.15}$$

where $\boldsymbol{r}_n$ denotes the position of the n-th emitter, and $E_{SP\|}(\mathbf{r}_n)$ stands for the electric field component parallel to the emitter dipole moment at this position. For simplicity, we assume that all the emitter dipole moments $\boldsymbol{\mu}_{QE,n}$ are parallel and present the same magnitude μ_{QE}. Besides, this helps us to better explore the spatial dependence of the plasmonic near-field. In contrast to Equation 3.1, the Hamiltonian describing the coherent dynamics now has the form:

$$\hat{H} = \Delta_{SP}\hat{a}^\dagger\hat{a} + \Delta_{QE}\hat{S}_z + \sum_{n=1}^{N}\lambda_n(\hat{\sigma}_n^\dagger\hat{a} + \hat{\sigma}_n\hat{a}^\dagger) + \Omega_{SP}(\hat{a}^\dagger + \hat{a}) + \Omega_{QE}(\hat{S}^+ + \hat{S}^-), \tag{3.16}$$

Under low-pumping conditions, the full Liouvillian describing the steady-state density matrix for a hybrid system, in which the light-matter coupling is given by Equation 3.15, can still be mapped into an effective non-Hermitian Hamiltonian as in Equation 3.3. The Lindblad terms can be still approximated in the form of Equation 3.14. Nevertheless, calculating the steady-state for this Hamiltonian requires accounting for not only the bright state of the emitter ensemble but also all the dark states (due to the presence of the single-atom operators $\hat{\sigma}_n$ in Equation 3.16). This makes its computation much heavier, despite the fact that the perturbative treatment explained above remains valid.

Figure 3.11 plots the scattering intensity I (top) and zero-delay second-order correlation function $g^{(2)}(0)$ (bottom) for the coupled system with five different single-emitter cooperativities, ranging from $C = 0.1$ (yellow) to $C = 2$ (purple). While dotted lines correspond to plasmonic cavities with a uniform (homogeneous) electric near-field across the ensemble, solid lines render I and $g^{(2)}(0)$ for various degrees of spatial inhomogeneity in $E_{SP\|}$: 20 (a), 50 (b) and 90% (c). Note that these percentages indicate the relative deviation of the extremal values of λ_n. In order to make a meaningful comparison between different systems, the collective coupling strength is kept constant in all cases (for

a given single-emitter cooperativity); that is, we impose the condition:

$$\sum_{n=1}^{N} \lambda_n^2 = N\gamma_{\mathrm{SP}}\gamma_{\mathrm{QE}}C/2.$$

The top panels of Figure 3.11 demonstrate that the far-field intensity is very robust to variations in the individual coupling λ_n. In top panels (a) and (b), homogeneous and inhomogeneous calculations virtually overlap. Only at 90% plasmonic inhomogeneity, appreciable deviations between both sets of data take place. Note that the contrast between UP and LP peaks decreases with spatial inhomogeneity. The bottom panels of Figure 3.11 show that photon correlations are more sensitive to spatial inhomogeneities of the plasmonic near-field. We can observe that a non-uniform electric near-field leads to two main effects on $g^{(2)}(0)$:

- For large values of the cooperativity, the bunching maxima broaden and their height increases. This removes regions of moderate antibunching that emerge for intermediate cooperativity (C=0.5) in the homogeneous case.
- At lower values of the cooperativity, the deep antibunching minima shift towards higher laser frequencies ω_{L}, but the minimum in $g^{(2)}(0)$ presents a similar depth. In fact, the correlation minima at $C = 0.1$ and $C = 0.25$ are still slightly deeper in the inhomogeneous calculations.

Despite these differences, Figure 3.11 proves that plasmon spatial inhomogeneities do not lead to qualitative changes neither in the intensity nor in photon correlations.

Inhomogeneous broadening in the emitter ensemble

Next, we focus on how the inhomogeneous broadening of the emitter transition frequencies may affect the photon correlations in the hybrid system. In contrast to Equation 3.1, the Hamiltonian accounting for these effects has the form:

$$\hat{H} = \Delta_{\mathrm{SP}}\hat{a}^{\dagger}\hat{a} + \sum_{n=1}^{N} \Delta_{\mathrm{QE},n}\hat{\sigma}_n^{\dagger}\hat{\sigma}_n + \lambda(\hat{S}^{+}\hat{a} + \hat{S}^{-}\hat{a}^{\dagger}) + \Omega_{\mathrm{SP}}(\hat{a}^{\dagger} + \hat{a}) + \Omega_{\mathrm{QE}}(\hat{S}^{+} + \hat{S}^{-}),$$

where $\Delta_{\mathrm{QE},n} \equiv \omega_{\mathrm{QE},n} - \omega_{\mathrm{L}}$, and $\omega_{\mathrm{QE},n}$ is the transition frequency for the n-th quantum emitter. The description of radiative and nonradiative damping remains the same as in Equation 3.14. Nevertheless, like in the previous section, obtaining the steady-state solution for this Hamiltonian requires considering the dark states of the emitter ensemble, even in its perturbative treatment.

Figure 3.12 displays $g^{(2)}(0)$ versus laser frequency ω_L and cooperativity C for inhomogeneously broaden emitter ensembles ($N = 5$). All the parameters remain the same as in Figure 3.7 (b), except for the emitter transition frequencies: they are now uniformly distributed around $\omega_0 = \omega_{\mathrm{SP}} = 3$ eV. The minimum and maximum values of the ratio $|\omega_{\mathrm{QE},n} - \omega_0|/\gamma_{\mathrm{QE}}^{\mathrm{nr}}$ are indicated by the percentages above each panel. Panels (a) and (b) show that photon correlations are not affected by differences in the emission frequencies if these are smaller than or comparable to $\gamma_{\mathrm{QE}}^{\mathrm{nr}} = 15$ meV. In panel (c), the spectral

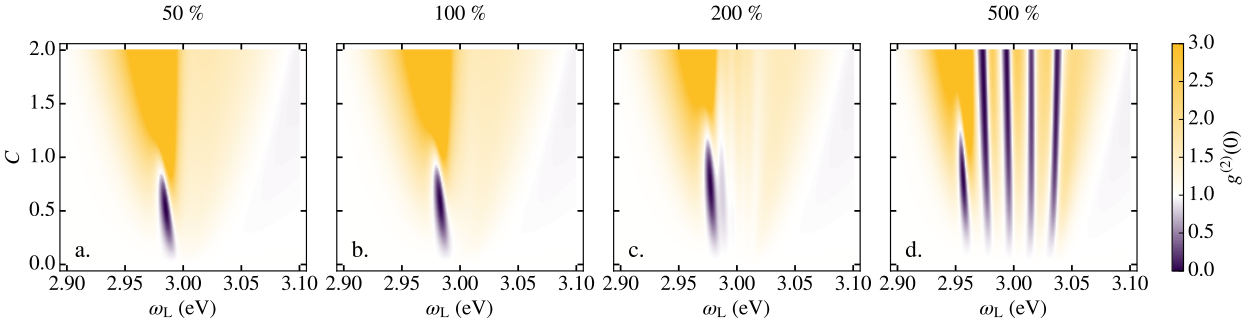

Figure 3.12. Second-order correlation function $g^{(2)}(0)$ versus laser frequency ω_L and cooperativity C for a emitter ensembles with $\gamma_{QE}^{nr} = 15$ meV. The emitter transition frequencies are uniformly distributed around ω_{SP}. The percentages indicate the extremal values of the ratio in each panel.

broadening is twice larger than the nonradiative decay rate, and we can observe that the region of antibunching is slightly distorted and extents into larger values of the cooperativity. Finally, five well defined spectral lines (as many as emitters in the ensemble) yielding $g^{(2)}(0) < 1$ are apparent in panel (d). In this case, $|\omega_{QE,n} - \omega_0|$ is up to five times larger than γ_{QE}^{nr} and the photon correlation maps are qualitatively different from those obtained for identical emitters. Thus, Figure 3.12 shows that a large emitter nonradiative decay rate (low quantum yield) increases the robustness of the hybrid system against inhomogeneous broadening effects.

Effect of plasmon losses and emitter nonradiative decay

Now, we investigate the effect of the plasmon damping and the emitter nonradiative decay on the correlations of the photon scattered by these hybrid systems. Here, we neglect spectral inhomogeneities in the ensemble, and focus on emitters with identical characteristics (that is, with the same transition frequency ω_{QE} and decay rate γ_{QE}).

In the first place, we explore the variation of the plasmon losses. Figure 3.13 displays photon correlation maps for values of the damping rate γ_{SP} ranging from 500 meV to 10 meV. In order to allow the comparison between different systems, the coupling strength is expressed in terms of the coupling strength λ, instead of the single-emitter cooperativity C (Equation 3.12). Notice that panel (c) corresponds to the case before considered (see Figure 3.7 (b)). Panels (a) and (b) show that the regions yielding strong photon correlations widen significantly (both in λ and ω_L) by increasing plasmon losses. This broadening is accompanied by a slight shift towards higher coupling strengths. On the contrary, bunching and antibunching take place at sharper spectral windows and smaller couplings

Figure 3.13. Zero-delay second-order correlation function $g^{(2)}(0)$ versus laser frequency ω_L and coupling strength λ for emitter ensembles coupled to plasmonic cavities with four different decay rates γ_{SP}.

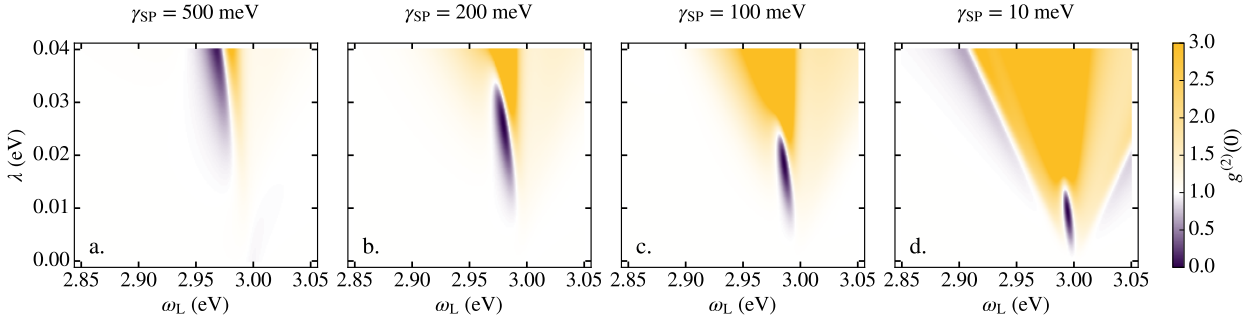

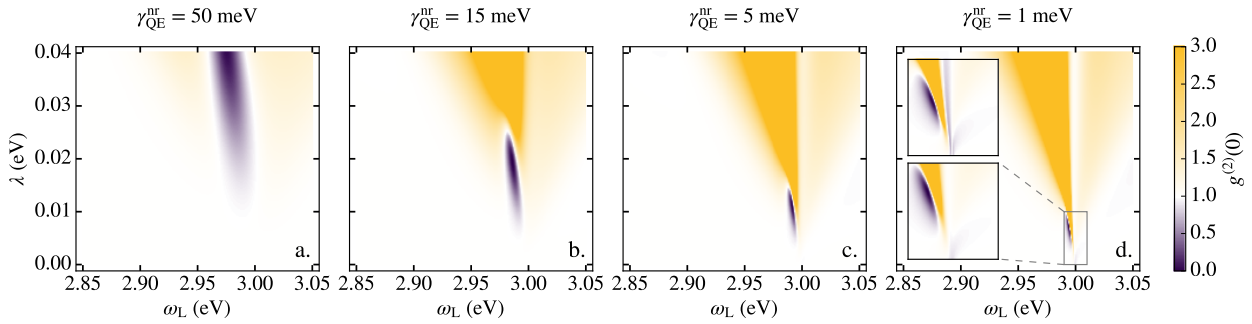

Figure 3.14. Zero-delay second-order correlation function $g^{(2)}(0)$ versus laser frequency ω_L and coupling strength λ for emitter ensembles coupled to a plasmonic cavities with four different emitter nonradiative decay rates.

for lower plasmon damping, as shown in panel (d). The comparison against panel (c) indicates that the asymmetry in $g^{(2)}(0)$ around the resonant condition $\omega_L = \omega_{QE/SP}$ diminishes with decreasing γ_{SP}. More interestingly, for larger λ, the system develops a rather spectrally symmetric correlation function maximum (strong bunching) centered at $\omega_{QE/SP}$. This is accompanied by two $g^{(2)}(0)$ minimum side bands, associated with the photon-blockade effect later discussed.

Figure 3.14 renders $g^{(2)}(0)$ as a function of the laser frequency ω_L and the coupling strength λ for identical quantum emitters with different values of the nonradiative decay γ_{QE}^{nr}. Panel (b) is taken as a reference, since it is equivalent to Figure 3.7 (b) and corresponds to emitters with very low quantum yield ($\mathcal{Q} = 7 \cdot 10^{-5}$). By increasing γ_{QE}^{nr}, the region of antibunching widens in ω_L and moves to higher values of the cooperativity, as shown in panel (a). On the contrary, panel (c) shows that, by reducing the emitter nonradiative decay rate, $g^{(2)}(0) < 1$ takes place into narrower spectral windows at lower coupling strengths. As expected, this phenomenology is very similar to the one shown in Figure 3.13, as both emitter and plasmon decay rates contribute in the same way to the polariton linewidth. Panel (d) displays photon correlations for emitters with a quantum yield $\mathcal{Q} = 10^{-3}$, showing the same trend as panels (a)-(c). The bottom inset zooms into the antibunching region. The top inset renders $g^{(2)}(0)$ within the same window but for emitters with a quantum yield $\mathcal{Q} = 0.5$ ($\gamma_{QE}^{nr} = \gamma_{QE}^{r} = 6\mu$eV). The correlation functions for both systems only present a slight difference within this region. Note that the latter develops an extremely narrow and rather shallow antibunching band close to the condition $\omega_L = \omega_{QE/SP}$.

Therefore, the parametric studies presented in Figure 3.13 and Figure 3.14 show that the significant nonradiative losses inherent to organic molecules and plasmonic cavities allow for the generation of robust photon correlations in hybrid systems.

Impact of emitter-emitter interactions

Finally, we explore how photon correlations are altered when dipole-dipole interactions within the emitter ensemble are taken into account. These are described by adding new terms to the Hamiltonian $\hat{H}$ of Equation 3.1. The new Hamiltonian $\hat{H}'$ acquires the form:

$$\hat{H}' = \hat{H} + \frac{1}{2}\sum_{i \neq j} V_{ij}[\hat{\sigma}_i^\dagger \hat{\sigma}_j + \hat{\sigma}_j^\dagger \hat{\sigma}_i],$$

where indices i and j run from 1 to N, and V_{ij} stand for the interaction strength between the corresponding emitters (with $i \neq j$). The implementation of this Hamiltonian requires considering a specific configuration of the hybrid system. For simplicity, we assume that all emitters are placed along a ring of radius R, and that their dipole moments are all parallel and normal to the ring plane. In this configuration, the interaction strength is given by [282]:

$$V_{ij} = \frac{\mu_{\mathrm{QE}}^2}{4\pi\epsilon_0 |\boldsymbol{r}_i - \boldsymbol{r}_j|^3} \tag{3.17}$$

where $\boldsymbol{r}_i$ represents the position corresponding to the i-th emitter. Note that all emitters are identical and are coupled with the same strength λ to the plasmonic cavity. Previous theoretical studies on single-particle and dimer nanocavities [433, 439] have shown that the coupling λ scales with the inverse of the volume of the system, in a similar way as Equation 3.17. Therefore, increasing the radius of the emitter distribution does not alter the ratio V_{ij}/λ.

In Figure 3.15, we explore the effect of dipole-dipole interactions. Panels (a) and (b) plot $g^{(2)}(0)$ versus laser frequency for ensembles of $N = 5$ emitters distributed in rings with $R = 9$ (yellow-green), 10 (turquoise), and 12 (purple) nm. The nanocavity is modelled as a silver nanosphere with radius of 6 nm in the center of the emitter ring. The coupling strength for the dipolar plasmon mode supported by the system is computed according to Delga *et al.* [433], obtaining $\lambda = 37$, 27, and 16 meV for $R = 9$, 10, and 12 nm, respectively. In these panels, dotted lines render the values of $g^{(2)}(0)$ obtained within the non-interacting emitter approximation. Notice that these spectra correspond to cuts at single-emitter cooperativities C equal to 1.80 (green), 0.98 (turquoise) and 0.35 (purple) in Figure 3.7 (b). The three values of the radii have been chosen so that the smallest yields a broad bunching maxima and the largest a narrow antibunching dip, with an intermediate configuration in between.

Solid lines in the left panel of Figure 3.15 plot $g^{(2)}(0)$ for interacting emitters evenly distributed along the ring (2π radians). We can observe that the impact of dipole-dipole interactions in photon correlations is moderate for the three emitter ensembles, with the smallest effect in the case showing antibunching ($R = 12$ nm). As the ratio V_{ij}/λ is the same for all values of R, we can infer that there is another energy scale that affects the sensitivity of the system to emitter interactions. Solid lines in the central panel of Figure 3.15 show photon correlation spectra for an ensemble that spreads only within 0.88π radians along the ring (see insets). By varying the angular extent of the emitter arrangement, all the parameters except for V_{ij} remain the same as in the left panel. Specifically, the nearest-neighbour interaction strength is enhanced by a factor 9.7 for all ring radii,

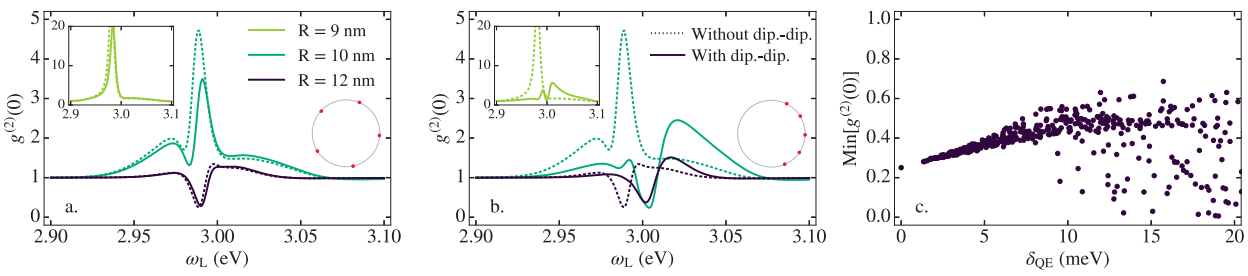

Figure 3.15. Zero-delay second-order correlation function $g^{(2)}(0)$ versus laser frequency ω_L for $N = 5$ emitters evenly distributed along three rings of different radii R. In (a), the ensembles are evenly spread along the whole ring perimeter (2π radians), whereas in (b), the emitter ensemble ranges only over an arc of 0.88π radians. In all cases, solid (dotted) lines correspond to interacting (non-interacting) quantum emitters. (c) The minimum value of $g^{(2)}(0)$ for a large number of random distributions of emitters on the ring with $R = 12$ nm, plotted as a function of δ_{QE}, the maximum energy shift induced by dipole-dipole interactions.

leading to a more significant impact of dipole-dipole interactions on $g^{(2)}(0)$. Interestingly, we again find that while bunching (observed at $R = 9$ and 10 nm) is severely impacted by interactions, the antibunching observed at $R = 12$ nm is quite robust —notice that $g^{(2)}(0)$ shows almost the same shape but shifted in energy compared to the non-interacting case.

In order to explore this in more detail, the right panel of Figure 3.15 shows the minimum value of $g^{(2)}(0)$ obtained for a large number of completely random configurations of emitters along the ring, plotted as a function of δ_{QE}, the largest energy shift obtained by diagonalizing just the emitter-emitter interaction. This shows that the degree of antibunching in the system is quite robust against emitter-emitter interactions and only slowly decreases as the interaction-induced shifts increase. Once the interactions become comparable to the emitter linewidth $\gamma_{\mathrm{QE}} = 15$ meV, a similar regime is entered, which is similar to the case of large inhomogeneous broadening (see Figure 3.12). The plasmon then does not couple collectively to all emitters, but almost independently to different energetically resolved superpositions of emitters. This leads to an effective interaction with fewer QEs, and thus even more pronounced antibunching in some cases.

Open and closed cavities

Plasmonic nanocavities are referred to as **open cavities** in the sense that emitters are driven by the external laser field, and their emission is received at the detector. On the contrary, a closed configuration is typical of inorganic semiconductor microcavities, where only the photonic mode is pumped by the laser, and the emission coming from the cavity is the only field measured at the detector. Considering the same cavity and emitter parameters that we have used so far, we can explore the changes introduced when quantum emitters are not directly pumped by the laser and only the radiation coming from the cavity is registered, thus mimicking the setup of a **closed cavity** with a plasmonic nanocavity.

Results for the intensity I and the correlation function $g^{(2)}(0)$ for different values of the coupling strength λ are shown in Figure 3.16 for these two situations: with (a) and without (b) considering both the pumping and the emission associated with the emitter ensemble. To make the comparison, we present the particular case of a collection of $N = 5$ quantum emitters. Therefore, the lines appearing in the left-hand column of Figure 3.16 correspond to cuts of the maps (b_1) and (b_2) of Figure 3.6 at four particular values of the coupling strength.

First, in Figure 3.16 [Top row] we notice that the asymmetry in the two intensity peaks is removed when considering only the emission from the cavity. As commented before, for an open cavity the effective dipole moment of the LP and the UP are, respectively, the parallel and antiparallel superpositions of those of the cavity and the quantum emitters. This makes the emission of the UP brighter, and it also introduces a clear dependence on the number of emitters. On the contrary, in the closed configuration both polaritons radiate with the same associated dipole moment (corresponding to the cavity, which is the same regardless the ensemble size). The associated emission is thus identical. Notice also that the positions of the intensity peaks are the same for open and closed configurations, as the polariton energies do not change.

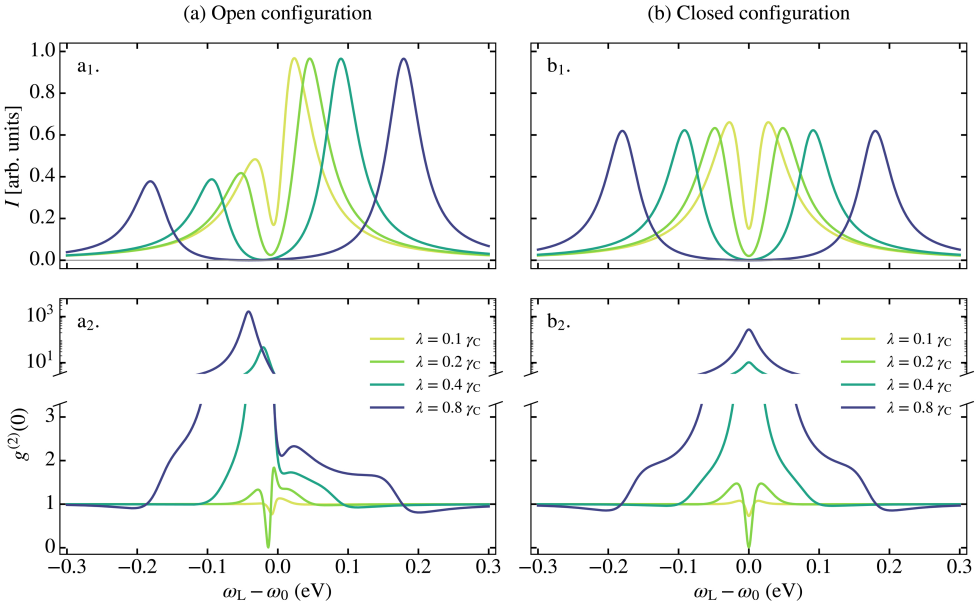

Figure 3.16. Scattering intensity I (top row) and correlation function $g^{(2)}(0)$ (bottom row) versus laser detuning $\omega_L - \omega_0$ for a system of $N = 5$ quantum emitters coupled to a plasmonic nanocavity for various coupling strengths with (a) and without (b) considering the pumping to and the emission from the quantum emitters.

The symmetry observed in the intensity patterns for the closed configuration is also kept in the correlation function $g^{(2)}(0)$ (Figure 3.16 [Bottom row]). Apart from this difference, the main features concerning the statistics of the emission are kept, namely: first, around the zero value of the laser detuning ($\omega_L = \omega_0$) there exists a dip for reduced values of the coupling strength, whereas a maximum is developed as the interaction increases; and, second, for frequencies near the one-excitation polaritons, the photon blockade effect is observable. Looking at Figure 3.16 (a_2), we confirm that the minimum following the UP branch is the deepest.

3.2 Photon statistics in semiconductor microcavities

The demand for macroscopic quantum light sources is driving a growing interest in the properties of the light generated by all kinds of hybrid systems, including those involving a mesoscopic number of emitters. In Section 3.1 we discussed the potential of plasmonic nanocavities in this context, as they enable strong photon correlations even when the number of emitters is large. But there exist many other physical implementations in which antibunched emission could be obtained thanks to this procedure based on strong light-matter coupling. Semiconductor microcavities reveal themselves as an excellent platform to this end due to the wide variety of available experimental realizations. Analyzing the particularities of each system in the generation of single photons would help us to take the most of each configuration.

Here, we investigate the quantum statistics of the light scattered from a semiconductor microcavity coupled to a mesoscopic ensemble of quantum dots under low coherent pumping, comparing the results with those obtained in the previous section for a col-

lection of organic molecules coupled to a plasmonic nanocavity. This content is part of the work published as: *R. Sáez-Blázquez, J. Feist, F. J. García-Vidal, and A. I. Fernández-Domínguez, "Photon statistics in collective strong coupling: Nanocavities and microcavities" Phys. Rev A* **98***, 013839 (2018)*.

3.2.1 The system: a collection of emitters either in a plasmonic nanocavity or in a semiconductor microcavity

In this section, the system under study is a collection of quantum dots embedded in a semiconductor microcavity. With the aim to make the comparison with the situation studied in Section 3.1, we consider the general case of N quantum emitters located in a cavity and highlight the differences.

Model and theoretical description

The modelling of the system is thus the same as the one performed in the previous section: we have collection of N two-level systems coupled to a single cavity mode supported by an optical cavity. The **Hamiltonian** is then equivalent to that in Equation 3.1, that is:

$$\hat{H} = \Delta_{\mathrm{C}}\hat{a}^{\dagger}\hat{a} + \Delta_{\mathrm{QE}}\hat{S}_z + \lambda(\hat{S}^{+}\hat{a} + \hat{S}^{-}\hat{a}^{\dagger}) + \Omega_{\mathrm{C}}(\hat{a}^{\dagger} + \hat{a}) + \Omega_{\mathrm{QE}}(\hat{S}^{+} + \hat{S}^{-}) \, ,$$

where we have substituted the subscript *SP* in the parameters referring to the surface plasmon mode for a *C*, as we now deal with a generic cavity. Every emitter is coupled to a quantized single cavity mode through the electric-dipole interaction, and they are considered not to interact among them apart from through the cavity mode. A laser field coherently pumps the system, and the emitted light is collected in a detector located in the far-field.

An illustration of the system is depicted in Figure 3.17, where the two cases of a nanocavity (left) and a microcavity (right) are distinguished. Both the pumping and the emission varies according to the corresponding open or closed character: whereas for nanocavities the entire system is pumped and the radiation from both the quantum emitters and the cavity is observed (**open configuration**), in microcavities the coupling to the outside mode is mediated by the mirrors, such that only the cavity mode is pumped and only its emission is received at the detector (**closed configuration**). Apart from this fundamental distinction, the size and characteristic losses are also differentiating features between these two types of cavities. By nanocavities, we are referring to plasmonic cavities, where the spatial dimensions are reduced to the nanometre scale and cavity losses are substantial (~ 0.1 eV) [440]. In contrast, by microcavities we refer here to photonic crystals and other semiconductor structures with sizes of the order of micrometres and whose absorption is much lower (~ 0.1 meV) [7].

The theoretical description of the **time dynamics** is also equivalent to that performed in Subsection 3.1.1, so we refer to that part for all necessary details. Once the **steady state** is known from the perturbative procedure there described, the correlation properties of the emitted light are calculated. Nevertheless, the negative-frequency part of the **scattered far-field operator** at the detector, $\boldsymbol{E}_{\mathrm{D}}^{(-)}$ depends on the type of cavity we consider:

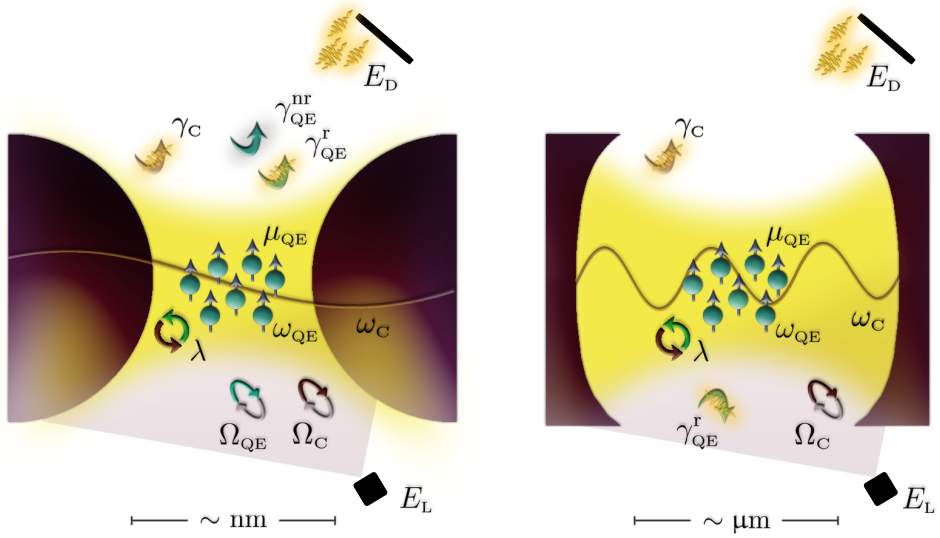

Figure 3.17. Scheme of the systems, composed of a collection of quantum emitters coupled to an electromagnetic mode supported by either a nano- (left) or a micro- (right) cavity. The set of parameters characterising the system are sketched.

while for nanocavities the radiation from both cavity and quantum emitters is taken into account (Equation 3.6), $\boldsymbol{E}_{\mathrm{D}}^{(-)} \propto \boldsymbol{\mu}_{\mathrm{C}}\hat{a}^{\dagger} + \boldsymbol{\mu}_{\mathrm{QE}}\hat{S}^{+}$, for microcavities just the emission coming from the cavity is detected, $\boldsymbol{E}_{\mathrm{D}}^{(-)} \propto \boldsymbol{\mu}_{\mathrm{C}}\hat{a}^{\dagger}$. This reflects the open/closed character of each type of cavity. Note that the differences between the electromagnetic Green's function describing the emission from the cavity and the various emitters in these cavities can be neglected due to their deeply subwavelength dimensions.

Parameters

As in Section 3.1, our attention is focused on resonant coupling, setting $\omega_{\mathrm{C}}, \omega_{\mathrm{QE}} \equiv \omega_0 = 3$ eV in all cases. Beyond that, we have to consider a specific set of parameters for each system. The dissipation rate associated with the **semiconductor microcavity** is taken to be $\gamma_{\mathrm{C}} = 66$ μeV (16 GHz) [191], which corresponds to the spontaneous decay rate of a dipole moment $\mu_C = 3.1$ e·nm [21]. On the contrary, substantial nonradiative losses are a distinctive feature of plasmonic nanocavities [29, 441], hence we set $\gamma_C = 0.1$ eV (24 THz) for the nanocavity. This value also incorporates the radiative losses corresponding to a dipole with $\mu_C = 19$ e·nm, which mimics the cavity emission [363].

Regarding the **emitters** , we consider those typically used in the experimental setups involving each cavity. First, the quantum emitters usually located inside dielectric cavities are characterized by negligible nonradiative losses, thus $\gamma_{\mathrm{QE}}^{\mathrm{nr}} = 0$. In particular, we choose semiconductor **quantum dots** with a dipole moment $\mu_{QE} = 0.25$ e·nm, which corresponds to a radiative decay rate $\gamma_{\mathrm{QE}}^{\mathrm{r}} = 0.41$ μeV (0.10 GHz) [191]. Conversely, the quantum emitters interacting with plasmonic nanocavities were considered to be **organic molecules** with $\mu_{\mathrm{QE}} = 1$ e·nm, and presenting very low quantum yield (Equation 1.2). The specific rates chosen for these emitters are $\gamma_{\mathrm{QE}}^{\mathrm{nr}} = 15$ meV (3.6 THz) and $\gamma_{\mathrm{QE}}^{\mathrm{r}} = 6$ μeV (1.5 GHz). Note that a rather large nonradiative decay rate was considered in order to account for the quantum-yield reduction experienced by organic molecules arranged in dense ensembles [434].

In our study, we assume that both open and closed cavities operate at low temperature,

which diminishes greatly the impact of pure-dephasing processes in the dynamics of both quantum dots [442] and organic molecules [443]. Accordingly, we have not included this decoherence mechanism in our theoretical model. Besides, we consider again that the external laser field $\boldsymbol{E}_{\mathrm{L}}$ is parallel to both the cavity and the quantum emitters dipole moments. Note that this turns out to be the optimal configuration to enter the strong coupling regime.

3.2.2 Intensity and coherence

In Section 3.1 we studied the plasmonic nanocavity, where the light reaching the detector comes from both the quantum emitters and the cavity itself. Now we focus on the typical configuration of **dielectric microcavities**, where only the cavity mode is pumped and direct emission from the emitters is not considered (**closed configuration**). A study similar to the previous section is carried out, determining the intensity I and the zero-delay second-order correlation function $g^{(2)}(0)$. The results are shown in Figure 3.18 for the same three cases considered in Figure 3.18, that is: $N = 1$ (a), 5 (b), and 25 (c) quantum emitters coupled to the cavity.

Intensity

The intensity panels are plotted in Figure 3.18 [Top], which reveal again the presence of the two **polariton branches** when entering the strong coupling regime. The energies corresponding to the dressed states in the one-excitation manifold are plotted in dotted lines, and they overlap the intensity peaks. Nevertheless, in contrast to the nanocavity configuration, these two intensity maxima are symmetric and barely vary their height as the number of emitters increases. As previously commented, this is due to the fact that only the emission from the cavity is registered, so the effective radiating dipole moment is always the same.

This underlying symmetry is also revealed in the **analytical expression** of the intensity, computed from the perturbative approach. First, we determine the steady-state solution (Equation 3.5) up to second order, from which the scattered intensity I is obtained (Equation 3.7):

$$I \propto \left| \frac{\tilde{\Delta}_{\mathrm{QE}} \mu_{\mathrm{C}}^2 / N}{\tilde{\Delta}_{\mathrm{C}} \tilde{\Delta}_{\mathrm{QE}} / N - \lambda^2} \right|^2 .$$

There, $\tilde{\Delta}_{\mathrm{C}}$ and $\tilde{\Delta}_{\mathrm{QE}}$ are the detunings redefined equivalently to Equation 3.11, that is:

$$\begin{aligned} \tilde{\Delta}_{\mathrm{C}} &\equiv \Delta_{\mathrm{C}} - \mathrm{i}\gamma_{\mathrm{C}}/2 \,, \\ \tilde{\Delta}_{\mathrm{QE}} &\equiv \Delta_{\mathrm{QE}} - \mathrm{i}(\gamma_{\mathrm{QE}}^{\mathrm{nr}} + N\gamma_{\mathrm{C}}^{\mathrm{r}})/2 \,. \end{aligned}$$

The expression for the intensity can be reproduced from that corresponding to nanocavities (Equation 3.10) just by considering the limit $\mu_{\mathrm{QE}} \to 0$. We observe that the denominator remains unchanged, so its vanishing condition give us again the energy dispersion for the polaritons and hence the position of the intensity maxima.

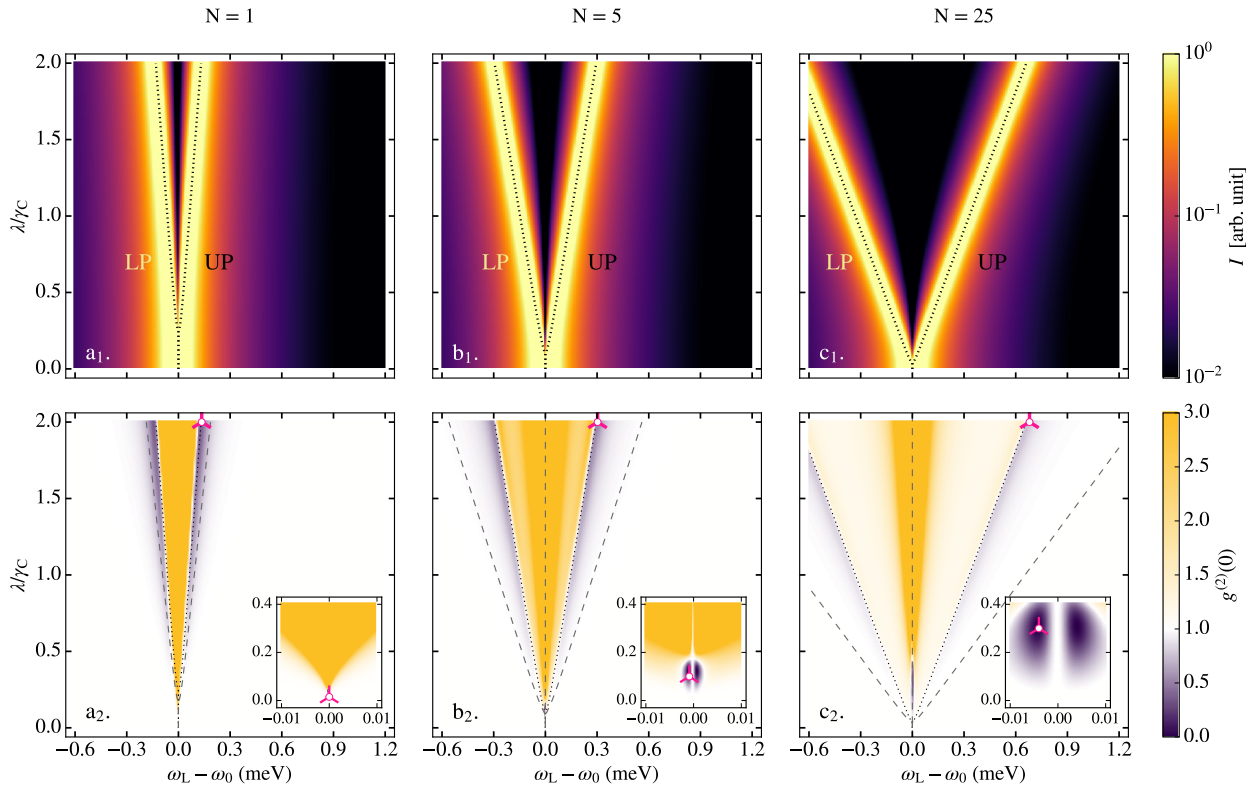

Figure 3.18. Scattering intensity I (top row) and correlation function $g^{(2)}(0)$ (bottom row) versus laser detuning and coupling strength (in units of the cavity decay rate γ_C) for a system of $N = 1$ (a), 5 (b) and 25 (c) quantum emitters coupled to a dielectric microcavity. In these panels, dotted (dashed) lines plot the polariton frequencies (half-frequencies) in the one-excitation (two-excitation) manifold. Insets zoom into the low coupling region. Magenta marks indicate points whose $g^{(2)}(\tau)$ is plotted in Figure 3.22 (b_1).

Coherence

The results for the correlation function $g^{(2)}(0)$ depicted in the bottom row of Figure 3.18 show a similar pattern to the ones found for nanocavities (Figure 3.6), although incorporating the symmetry already expected. Around the zero laser detuning ($\omega_L = \omega_0$) and for intermediate (or large) coupling strengths we find super-Poissonian statistics (yellow coloured). These panels also show the two types of sub-Poissonian emission (blue coloured) previously observed: the associated with the phenomenon of photon blockade, as well as that related to destructive interference. The position of the eigenenergies corresponding both to the one- and two-excitation manifolds are plotted in dotted and dashed lines, respectively, overlapping the correlation maps. The frequencies where the **photon blockade** effect occurs are easily relatable next to the dotted lines. Nevertheless, it is in the other area of sub-Poissonian emission —the one associated with **interference effects**— where the main difference between open and closed cavities appears. Apart from the spectral symmetry already discussed, the development of two dips instead of a single one is the most apparent feature. For lower values of the coupling strength, we find $g^{(2)}(0) = 1$ at zero detuning, while on both sides of this frequency, a window with sub-Poissonian emission is visible. The presence of this double dip pattern disappears when introducing nonradiative losses associated with the quantum emitters.

The evolution of correlations as the number of emitters increases differs from the open nanocavity case. Apart from the fact that symmetry modifies the laser frequencies at which the different regions are achieved (for a specific value of the coupling strength), the main variation concerns the sub-Poissonian emission caused by destructive interference. These areas are enlarged in the insets of Figure 3.18. As the ensemble size increases, the

parameter ranges in which we find $g^{(2)}(0) < 1$ clearly widen. Therefore, it is possible to obtain antibunched emission for a specific coupling strength just by increasing the number of emitters. Beyond a particular N, the system tends to reach the bosonization limit, where $g^{(2)}(0) = 1$. The onset of this regime depends on the coupling strength between cavity and emitters and, as seen in Figure 3.18 (c_2), for $N = 25$ we still find significant negative correlations for a wide interval of coupling values. Note that the photon blockade region does not endure so long and it practically disappears for a few emitters within this coupling range.

There exists a major aspect, not mentioned before, that should be highlighted: the range of laser detunings at which this non-classical behaviour is found is of the order of meV. Notice that the energy scale in Figure 3.18 differs in three orders of magnitude from the one corresponding to nanocavities (Figure 3.6). Therefore, the spectral robustness and accessibility of the antibunched regions is significantly different in open and closed cavities, specially in the case of interference-induced negative correlations.

Finally, to gain insight into the coherence properties discussed above, we present the analytical expression for the correlation function $g^{(2)}(0)$ following the same perturbative procedure as before:

$$g^{(2)}(0) = \left| 1 - \frac{1}{N} \left(\frac{\lambda}{\tilde{\Delta}_{\mathrm{QE}}/N} \right)^2 \frac{(\tilde{\Delta}_{\mathrm{QE}} + \mathrm{i}N\gamma^{\mathrm{r}}_{\mathrm{QE}}/2)\lambda^2}{(\tilde{\Delta}_{\mathrm{QE}} + \mathrm{i}\gamma^{\mathrm{r}}_{\mathrm{QE}}/2)(\tilde{\Delta}^2_{\mathrm{C}} + \tilde{\Delta}_{\mathrm{C}}\tilde{\Delta}_{\mathrm{QE}} - N\lambda^2) - \lambda^2\tilde{\Delta}_{\mathrm{C}}(N-1)} \right|^2 ,$$

which can be also obtained by taking $\mu_{\mathrm{QE}} \to 0$ in Equation 3.13. Again, this expression yields $g^{(2)}(0) = 1$ when $N \to \infty$, so the classical behaviour is recovered in this limit. Note as well that we find $g^{(2)}(0) = 1$ at the resonant frequency $\omega_L = \omega_0$ when all losses are neglected.

3.3 Exploring configurations with sub-Poissonian statistics

Two different configurations have been explored in the preceding sections as potential single-photon sources. Both organic molecules in plasmonic nanocavities (Section 3.1) and quantum dots in semiconductor microcavities (Section 3.2) have been shown to enhance photon correlations even when the number of emitters is large. Understanding the processes through which photon correlations are created, and identifying the role of the different factors involved, would help to take the most of each available configuration.

Here, we explore the two mechanisms leading to sub-Poissonian statistics —namely, the photon blockade effect and destructive interference processes. We also study the dependence of these two types of negative correlations on the spectral detuning between cavity and emitters, as well as its evolution as the time delay between photon detections increases. Throughout the discussion, the performance of plasmonic nanocavities and dielectric microcavities are compared.

3.3.1 Presence of two mechanisms leading to sub-Poissonian light

Studying the photon statistics of the light emitted by coupled systems, we have identified two types of sub-Poissonian emission appearing in both nanocavities and microcavities. In order to shed light into their different nature, we now proceed to examine their presence in more detail. We consider the same parameters as before, starting with the resonant case $\omega_C, \omega_{QE} \equiv \omega_0 = 3$ eV. In Figure 3.19, the focus is on the **photon blockade effect** —which takes place close to the polariton energies of the one-excitation manifold—, whereas in Figure 3.20 we study the sub-Poissonian emission associated with **destructive interference** —which appears for moderate coupling strength in the region of zero-detuning. The population, the intensity I, and the correlation functions $G^{(2)}(0)$ and $g^{(2)}(0)$ (see Subsection 2.3.3 for the definitions) are plotted as a function of the laser detuning $\omega_L - \omega_0$ for nano- (left-hand side panels) and micro- (right-hand side panels) cavities at specific coupling strengths to explore these processes.

Photon blockade

The sub-Poissonian emission due to the **photon blockade effect** originates from the anharmonicity of the Tavis–Cummings ladder, as we have commented before. When the laser has an energy close to that of one of the polaritons at the one-excitation manifold, the population of this particular hybrid state increases. In panels (a_1) and (b_1) of Figure 3.19, populations are plotted in the basis of the dressed states. There, the continuous coloured lines, corresponding to the population of the UP (dark pink) and the LP (light pink), experience an increase when the laser frequency is tuned to be in the vicinity of the corresponding polariton frequency (continuous vertical grey lines). Nevertheless, for these specific energies, the laser is out of resonance for promoting the state from the one- to the two-excitation manifold (dashed vertical grey lines depict these energy differences). This diminishes the probability of emission of two simultaneous photons, which in turn leads to sub-Poissonian statistics. These panels also show, in dashed coloured lines, the populations of the states belonging to the two-excitation manifold: two LPs (light pink), one LP and one UP (very light grey) and two UPs (dark pink). Note that the maxima of these curves are not located exactly at the polariton frequencies, but they are slightly shifted as a consequence of the energy differences between the one- and the two-excitation manifolds.

When the populations are expressed in terms of the cavity and emitter states, panels (a_2) and (b_2) of Figure 3.19, all curves belonging to the same subspace (continuous or dashed lines for the one- and two-excitation manifolds, respectively) seem to converge to the same value at the frequencies where the photon blockade phenomenon takes place (that is, near the polariton frequencies). Apart from that, we observe that there exist two clear minima in the population curves corresponding to the state with one (continuous dark blue line) and two (dashed dark blue line) excitations in the cavity. Each of them has a replica in one of the curves depicted in panels (a_3) and (b_3) of Figure 3.19. This is especially visible for the nanocavities where these two minima do not coincide. Indeed, the intensity (yellow line) and the $G^{(2)}(0)$ (ochre line) functions reproduce the form of the populations of the states with one and two excitations in the cavity mode, respectively. The origin of this correspondence is clear for the closed configuration (as only the emission

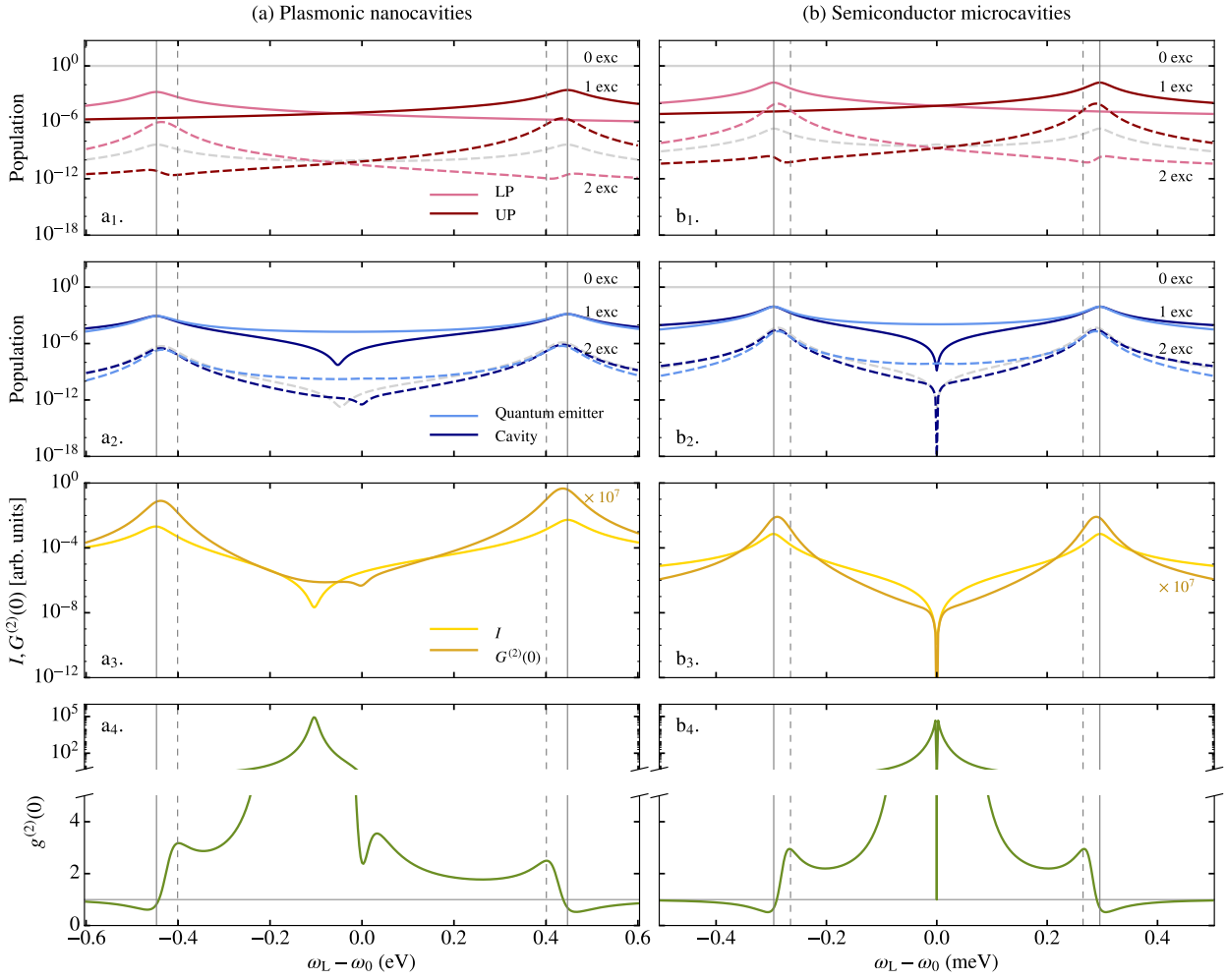

Figure 3.19.
Population [in the polariton basis (first row) and in the cavity-emitters basis (second row)], intensity I, and correlation functions $G^{(2)}(0)$ and $g^{(2)}(0)$ versus laser detuning for a system of $N = 5$ quantum emitters coupled to a nano- (a) and a micro- (b) cavity at coupling strength $\lambda/\gamma_C = 2$ (for which the photon blockade effect appears). In these panels, continuous vertical grey lines indicate the polariton frequencies in the one-excitation manifold, while the dashed ones represent the energy differences between the state of one LP and one UP (belonging to the two-excitation manifold) and the state with either one LP (left dashed line) or one UP (right dashed line).

from the cavity is detected). For the open one, it results from the fact that the dipole moment of the cavity is greater than the collective dipole of the emitter ensemble. Hence the former contributes the most to the emitted light (for a reduced number of emitters). Note that intensity accounts for one-photon processes, while $G^{(2)}(0)$ reflects two-photon processes instead (Equation 3.8).

The intensity plots reflect the presence of the polariton energies as well—each scattering peak coincides with a maximum in the polariton population and, naturally, with the position of the polariton energy. The intensity minima are certainly located between the two polariton energies, far from resonance. The fact that the maxima in $G^{(2)}(0)$ are shifted from those in the scattered intensity provokes the characteristic shape in the normalized second-order correlation function, shown in panels (a_4) and (b_4) of Figure 3.19. Values of the $g^{(2)}(0)$ function below one are located close to the polariton energies (vertical continuous grey lines), whereas there appear two relative maxima at laser frequencies that match energy differences between the one- and the two-excitation manifold (vertical dashed grey lines). For the nanocavity, the different positions of I and $G^{(2)}(0)$ minima in Figure 3.19 (a_3) leads to maxima and a minima in $g^{(2)}(0)$ near resonance, although the emission is always super-Poissonian in this frequency window.

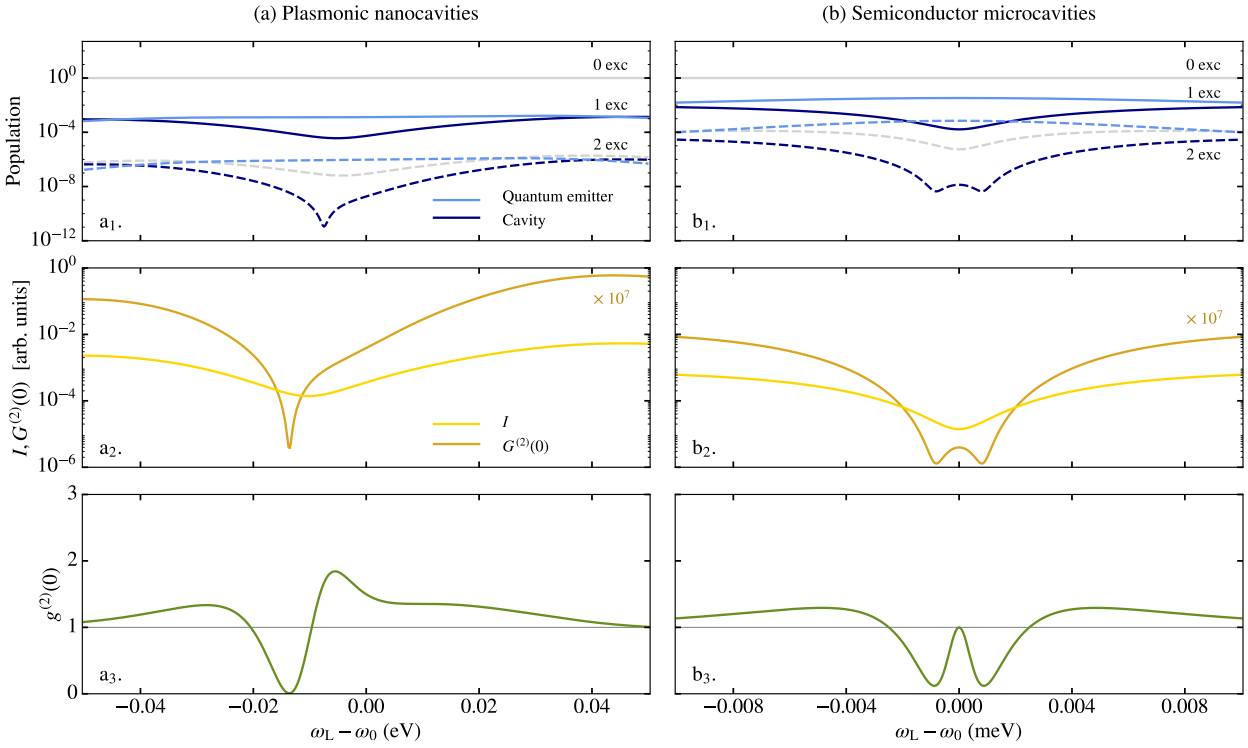

Figure 3.20. Population (in the cavity-emitters basis), intensity I, and correlation functions $G^{(2)}(0)$ and $g^{(2)}(0)$ versus laser detuning for a system of $N = 5$ quantum emitters coupled to a nano- (a) and a micro- (b) cavity at coupling strengths $\lambda/\gamma_C = 0.2$ and 0.1 respectively (for which the interference-induced correlations appear).

Interference-induced correlations

The decrease of $g^{(2)}(0)$ below one is referred to as unconventional photon blockade when its origin cannot be explained in terms of the energy levels as done for the (conventional) photon blockade effect. Actually, these negative correlations are produced due to the **destructive interference** between different available decay paths [212, 213].

The population curves, panels (a_1) and (b_1) in Figure 3.20, reveal that it is a decrease in the population of the state corresponding to two cavity-mode excitations (dashed dark blue lines) that produces the minimum in the $G^{(2)}(0)$ function. It is then transferred to the normalized $g^{(2)}(0)$ and, consequently, there appears sub-Poissonian statistics in the vicinity of this laser frequency. This correspondence between cavity population and correlations is observed in both types of cavities, although there exists a difference between them: whereas only one dip takes place in nanocavities, two of them emerge in the case of microcavities. Notice that this behaviour differs from the photon blockade mechanism, where a related fall in the population of the state with two cavity-mode excitations is not observed (on the contrary, as previously pointed out, all populations seem to converge to the same value).

The intensity and correlation function $G^{(2)}(0)$ are depicted in panels (a_2) and (b_2) in Figure 3.20. As in the previous case, these curves clearly follow the shape of the populations associated with the states corresponding to one (continuous dark blue lines) and two (dashed dark blue lines) excitations in the cavity mode, respectively. The different position of the minima for these two magnitudes is again responsible for the shape of the $g^{(2)}(0)$ function. Nevertheless, now values below one are reached (the interference-induced photon correlations). In Figure 3.19, the minimum in the $G^{(2)}$ did not lead to

sub-Poissonian statistics, although it did correspond to a minimum in $g^{(2)}(0)$. Note that this fall was not so abrupt when compared with the intensity dip.

3.3.2 Effect of detuning between cavity and emitters frequencies on the correlation function $g^{(2)}(0)$

Our discussion has been focused on the resonant case so far, in which cavity and emitters present the same frequency ω_0. We now explore the effect of the detuning on the correlation function $g^{(2)}(0)$. For the two emitter case, it has been shown that the parameter range in which sub-Poissonian statistics emerges can be enlarged by means of the introduction of detuning between cavity and emitters frequencies [243]: the spectral window becomes wider, and stronger couplings are required. This is the tendency we observe in Figure 3.21, where the correlation function $g^{(2)}(0)$ is plotted versus the laser detuning $\omega_L - \omega_C$ and the coupling strength λ for various values of the **cavity-emitter detuning** $\Theta \equiv \omega_{QE} - \omega_C$. There, the emitter frequencies ω_{QE} vary while the cavity mode resonance is always fixed to be $\omega_C = \omega_0 \equiv 3$ eV. The case considered is that composed of $N = 5$ quantum emitters coupled to either a nano- (top row) or a micro- (bottom row) cavity, hence these would correspond to panels (b_2) from Figure 3.6 and Figure 3.18, respectively, if no detuning were present (that is, $\Theta = 0$).

Figure 3.21 shows that, effectively, for both types of cavities the region with **interference-induced correlations** spreads as the difference in energy between cavity and emitters increases, although this effect is more pronounced in microcavities. Via detuning, the range of laser frequencies for which sub-Poissonian emission is attainable broadens —it extends over a frequency window with a width of almost half the detuning. Focusing now on the vertical axis, we observe that for a particular value of the coupling strength, it is possible to have $g^{(2)}(0) < 1$ near the resonant frequency just by increasing the detuning between cavity and emitters. Furthermore, note that the introduction of detuning makes it possible to achieve lower values of $g^{(2)}(0)$, whereby improving the quantum character of the emitted light. This is also true for the **photon blockade effect** following the UP—since this is the dressed state with a greater emitter contribution in this case—, which deepens. For a better visualization, the energies corresponding to the eigenvalues of the dressed states are plotted in dotted (one-excitation manifold) and dashed (two-excitation manifold) lines in all panels. For both nano- and microcavities, the photon blockade effect reinforces near the UP, whereas it fades at the LP. For instance, when $\Theta = 3\gamma_C$ the photon blockade effect following the lower branch disappears—no sub-Poissonian emission takes place in its surroundings. Note that varying the sign of the detuning, the roles of UP and LP are exchanged.

Regarding the region with interference-induced correlations, there exists a particularity for the microcavity that is worth mentioning: now we only observe one prevailing dip, instead of two (as it was for the zero detuning case, $\Theta = 0$). As a consequence of the loss of symmetry, the dip closer to the emitter frequency becomes narrower, and the other one widens, when the detuning increases. This makes the patterns observed for $g^{(2)}(0)$ at a specific detuning Θ quite similar for nano- and microcavities. Nevertheless, the energy range is very different—note that the coupling strength λ is given in units of the decay rate γ_C, and the values corresponding to plasmonic ($\gamma_C \sim 0.1$ eV) and dielectric ($\gamma_C \sim 0.1$

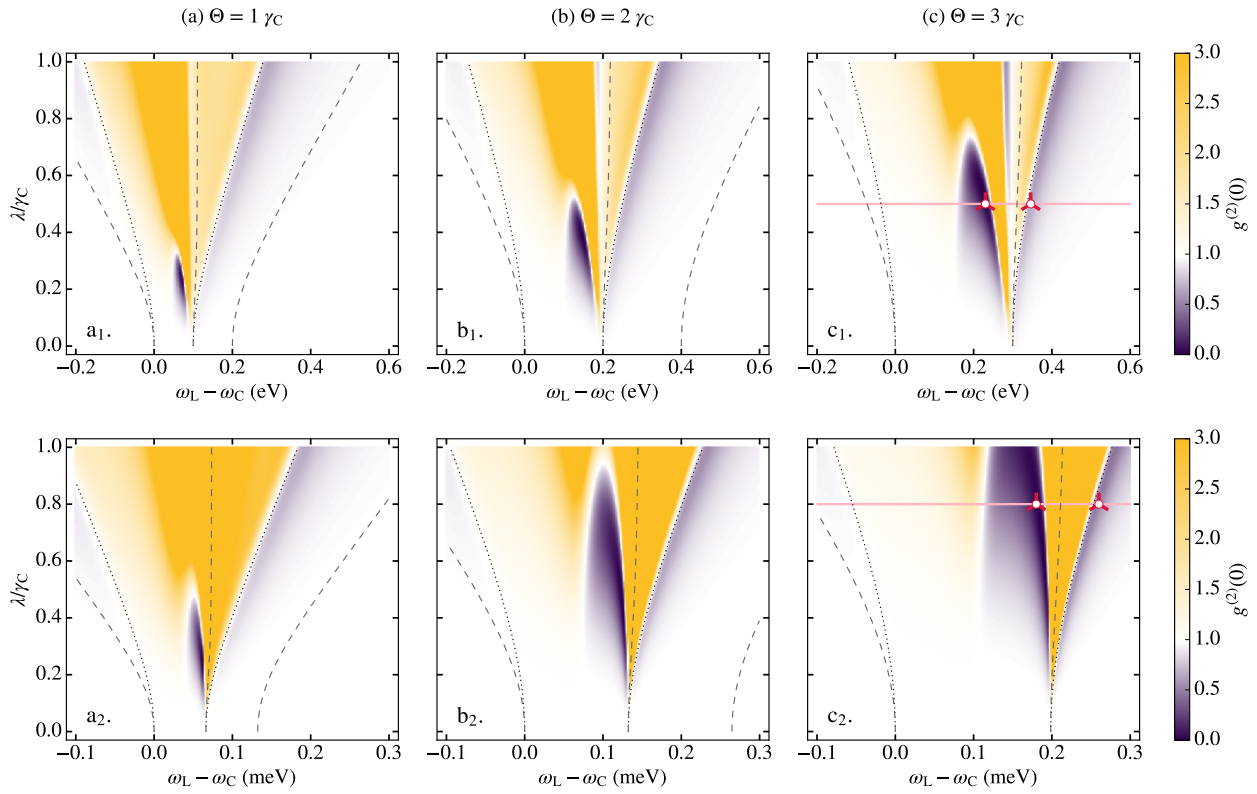

Figure 3.21. Correlation function $g^{(2)}(0)$ versus laser detuning and coupling strength (in units of the cavity decay rate γ_C) for a system of $N = 5$ quantum emitters coupled to a nano- (top row) and a micro- (bottom row) cavity for various values of the detuning between cavity and emitters, $\Theta = 1\ \gamma_C$ (a), $2\ \gamma_C$ (b), and $3\ \gamma_C$ (c). In these panels, dotted (dashed) lines plot the polariton frequencies (half-frequencies) in the one-excitation (two-excitation) manifold. Horizontal pink lines and magenta marks in (c) panels indicate points whose $g^{(2)}(0)$ is plotted in Figure 3.23.

meV) cavities differ by around three orders of magnitude (as do the laser detunings).

3.3.3 Dependence of the correlation function $g^{(2)}(\tau)$ on the time delay τ

Finally, we study the behaviour of the second-order correlation function $g^{(2)}(\tau)$ at non-zero time delays τ for various configurations displaying sub-Poissonian statistics ($g^{(2)}(0) < 1$). This helps us to resolve whether the emitted light is actually antibunched ($g^{(2)}(0) < g^{(2)}(\tau)$). In top panels of Figure 3.22, we plot $g^{(2)}(\tau)$ as a function of τ (in units of the cavity lifetime $1/\gamma_C$) for an ensemble of N quantum emitters interacting with either a nano- (a) or a microcavity (b) when there is no detuning between them ($\Theta = 0$). We consider three ensemble sizes $N = 1$ (yellow lines), 5 (green lines), and 25 (blue lines), and select two different configurations for each case: one belonging to the photon blockade area (continuous lines) and the another displaying sub-Poissonian statistics due to quantum interference effects (dotted lines). All configurations are indicated in Figure 3.6 and Figure 3.18 through magenta marks.

Focusing first on the continuous lines (**photon blockade**), we observe that the correlation function approaches one almost monotonically as the time interval τ increases, hence we can talk properly of photon antibunching. Nevertheless, there exist some oscillations whose amplitude diminishes as the ensemble size increases. Remarkably, there is practically no difference between the behaviour for nano- and microcavities once the time scale is normalized by the cavity decay time $1/\gamma_C$ —in both cases, the time evolution follows the same tendency, and the degree of correlation reached from both effects is similar. Note that all configurations have been chosen for a coupling strength $\lambda/\gamma_C = 2$ for both

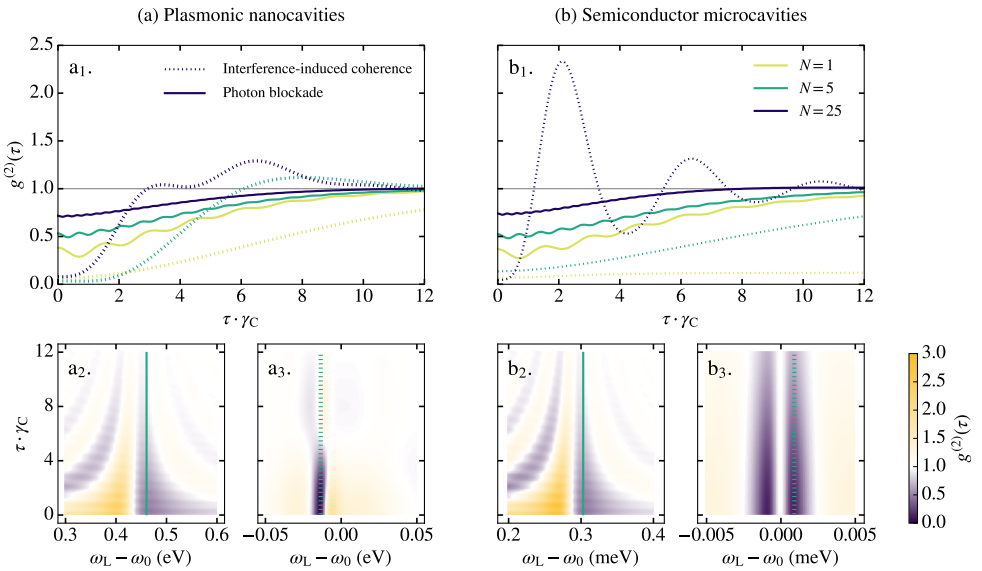

Figure 3.22. Correlation function $g^{(2)}(\tau)$ for N quantum emitters interacting with either a nano- (a) or a micro- (b) cavity at resonance ($\Theta = 0$). In top panels, $g^{(2)}(\tau)$ is plotted versus the time delay τ (in units of the cavity time $1/\gamma_C$) for three different ensemble sizes ($N = 1$, 5 and 25). Two different configurations (which correspond to the points indicated in Figure 3.6 and Figure 3.18) are selected. Continuous lines are used for the antibunching related to the photon blockade effect while dotted lines are used for interference-induced correlations. In bottom panels, $g^{(2)}(\tau)$ is plotted versus laser detuning $\omega_L - \omega_0$ and time delay θ (also in units of $1/\gamma_C$) for an ensemble of $N = 5$ emitters and selecting two different coupling strengths in each case: $\lambda = 2\gamma_C$ (a_2) and 0.2 γ_C (a_3) for plasmonic nanocavities and $\lambda = 2\gamma_C$ (b_2) and 0.1 γ_C (b_3) for dielectric microcavities. In these bottom panels, vertical green lines correspond to the curves for $N = 5$ depicted at the top.

types of cavities, although the laser detuning varies in order to consider the minimum of the $g^{(2)}(0)$ attainable at this coupling. These two sets of curves also highlight that the degree of coherence is quickly lost when increasing the number of emitters.

Dotted lines show instead the evolution for configurations displaying **interference-induced correlations**. We first observe that the degree of coherence at $\tau = 0$ reached from this effect is stronger than the associated with the photon blockade mechanism, although the couplings are smaller: for the nanocavity, $\lambda/\gamma_C = 0.2$, while for the microcavity it takes the values $\lambda/\gamma_C = 0.04$, 0.1, and 0.3 for $N = 1$, 5, and 25 respectively. Oscillations in the τ-evolution of the function $g^{(2)}(\tau)$ are observed as N increases, although we still have antibunched light since $g^{(2)}(0) < g^{(2)}(\tau)$. When comparing nanocavities and microcavities, we observe that oscillations in the latter are more pronounced. Moreover, note again the difference in γ_C, which translates into the fact that the temporal evolution is significantly faster in the plasmonic nanocavity (a direct consequence of the spectrally broad character of photon correlations in the system).

A more general picture is shown in the bottom row of Figure 3.22, where $g^{(2)}(\tau)$ is plotted as a function of the laser detuning $\omega_L - \omega_0$ and the time delay τ (again in units of the cavity time $1/\gamma_C$). We consider a collection of $N = 5$ emitters interacting with either a nanocavity (a) or a microcavity (b) for specific coupling strengths (see figure caption). The particular values of the laser detuning marked with vertical green lines (continuous for photon blockade and dotted for interference-induced correlations) correspond to the ones depicted in (a_1) and (b_1) for $N = 5$. These contour plots show that oscillatory patterns are also present for configurations displaying super-Poissonian statistics at zero time delay.

We have thus found that sub-Poissonian statistics is accompanied by antibunched light in the zero-detuning configurations explored in Figure 3.22. Although $g^{(2)}(\tau)$ approaches one as the time delay increases, its evolution is far from monotonous for interference-induced correlations —they present an oscillatory pattern taking values above and below one before reaching the coherent limit. This also happens when detuning between the

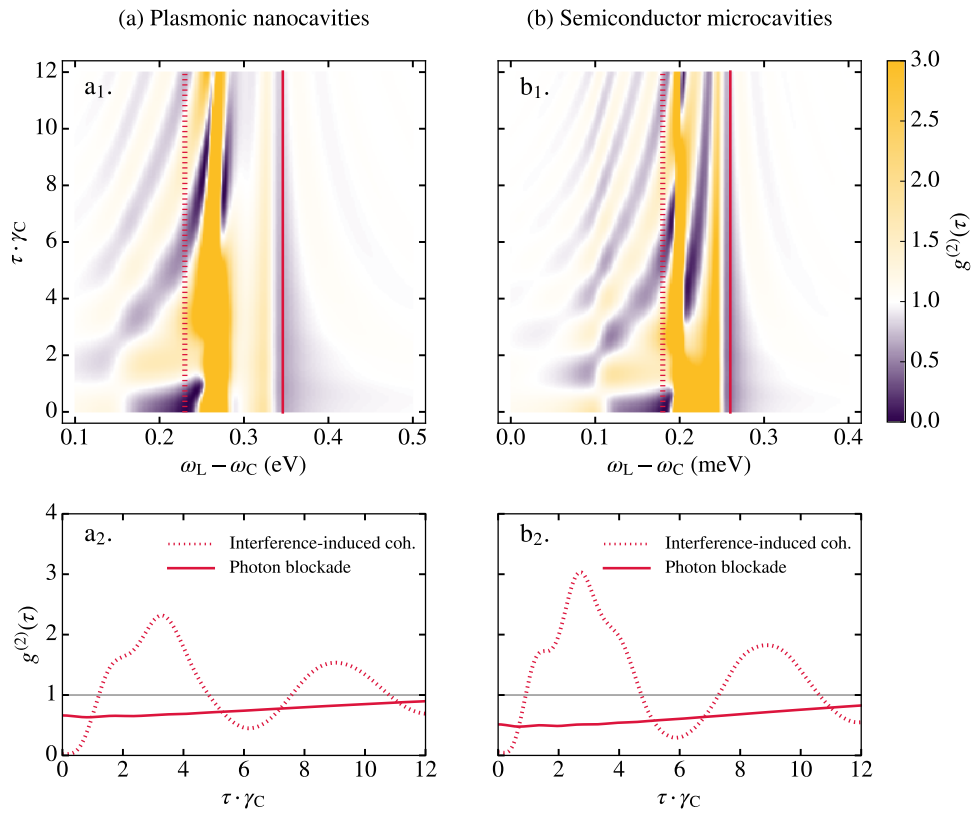

Figure 3.23. Correlation function $g^{(2)}(\tau)$ for an ensemble of $N = 5$ quantum emitters interacting with either a nanocavity (a) or a microcavity (b) when $\Theta = 3\gamma_C$. In top panels, $g^{(2)}(\tau)$ is plotted versus laser detuning $\omega_L - \omega_C$ and time interval τ (in units of the cavity time $1/\gamma_C$) for coupling strength $\lambda = 0.5\gamma_C$ in (a) and $\lambda = 0.8\gamma_C$ in (b). The cuts at $\tau = 0$ correspond to the continuous pink lines depicted in Figure 3.21 (c). Bottom panels show cuts of the contour plots on top at laser detunings yielding two minima in the $g^{(2)}(0)$ function. These specific configurations are indicated by red lines in the top panels and by red markers in Figure 3.21 (c).

cavity frequency and the emitters is introduced. An example is shown in the top row of Figure 3.23, where the function $g^{(2)}(\tau)$ is plotted for a particular coupling strength as a function of laser detuning $\omega_L - \omega_C$ and the time delay τ (in units of $1/\gamma_C$) for $N = 5$ quantum emitters interacting with either a nanocavity (a) or a microcavity (b). Here, we have considered a detuning $\Theta = 3\gamma_C$, so these plots corresponds to horizontal cuts in the panels of the third column of Figure 3.21 (indicated by horizontal pink lines), at $\lambda/\gamma_C = 0.5$ for plasmonic nanocavities and $\lambda/\gamma_C = 0.8$ for dielectric microcavities. In these panels, for most laser detunings, the correlation function develops an oscillatory pattern as τ increases for both sub- and super-Poissonian statistics at $\tau = 0$. Again, the close similarity between the patterns for both cavities is remarkable (once the delay time is expressed in units of $1/\gamma_C$).

We observe that there exists a significant difference in the temporal dependence of negative correlations also once detuning between cavity and emitters is introduced. This is evident in the bottom panels of Figure 3.23, where two specific values of $\omega_L - \omega_C$ are considered (indicated in Figure 3.21 with magenta marks) in order to select configurations that displays sub-Poissonian statistics due to interference effects (dotted line) and photon blockade (continuous line). These plots of $g^{(2)}(\tau)$ versus the time delay correspond to vertical cuts in the associated panels (a_1) and (b_1) of Figure 3.23 (see vertical red lines). In the case of photon blockade, $g^{(2)}(\tau)$ approaches one monotonically as the delay increases. In contrast, quantum interference leads to an oscillatory pattern in correlations. Both retain a temporal evolution similar to the one obtained at $\Theta = 0$ in Figure 3.22. Note that even the temporal slope and pitch of oscillations remain the same. Therefore, by detuning cavity and emitters, the opportunity to obtain sub-Poissonian light

improves (as we have mentioned before, the parameter regions widen) without altering qualitatively its evolution with time delay between photon detections. Again, the phenomenology for nanocavities and microcavities coincide, given that the values of laser detuning and time delay, both normalized to the cavity losses, are the same.

3.4 Conclusions

In Section 3.1, we have investigated the complex photon statistics phenomenology that emerges from the strong coupling of a mesoscopic ensemble of quantum emitters and a single plasmon mode supported by a generic nanocavity. We have presented an analytical method describing the optical response of these systems under low-intensity coherent illumination. Our approach provides insights into the role that both the polariton ladder and its tuning through the single-emitter cooperativity play in the emission of strongly correlated (either bunched or antibunched) light. The presence of two different mechanisms leading to sub-Poissonian statistics has been noted, displaying distinguishable features. Finally, our results have demonstrated the robustness of these compound systems against bosonization effects, predicting strong intensity correlations at considerable ensemble sizes. Our theoretical findings demonstrate the feasibility and establish experimental guidelines towards the realization of nanoscale nonclassical light sources operating beyond the single-emitter level.

In Section 3.2, we have discussed the statistical properties of the light generated by a collection of quantum dots coupled to the single electromagnetic mode supported by a semiconductor microcavity. Theoretical computations based on an effective Hamiltonian approach have been carried out to describe the response of this system in comparison to the previously studied in Section 3.1. Special attention has been focused on exploring the impact that the distinct open/closed character of these two types of cavities has on the scattered light. For both cavity configurations, sub-Poissonian emission has been observed not only at the single-emitter level, but also for mesoscopic ensembles involving several tens of emitters. Our results show the two different mechanisms that yield significant negative correlations in the interaction between an emitter ensemble and a cavity: photon blockade and destructive interference. The former takes place at high coupling strengths (comparable to or larger than the cavity decay rate), while the latter becomes relevant for weaker cavity-emitter interactions. Despite their distinct open/closed character and the largely different physical parameters describing nanocavities and microcavities, the photon statistics phenomenology for both systems is remarkably similar (once normalized to the cavity losses).

In Section 3.3, photon correlations in both plasmonic nanocavities and dielectric microcavities have been further analyzed following the same perturbative procedure as in the preceding sections. The particularities of the two mechanisms leading to negative correlations have been highlighted. We have also shown that the parameter range yielding antibunched light can be enlarged thanks to the cavity-emitter spectral detuning. The

exploration of the evolution of the second-order correlation function has revealed the slow fading of photon blockade antibunching, in contrast to the fast fading of the correlations due to destructive interference. Despite the distinct energy scales and the differences introduced by their respectively open and closed character, the photon statistics phenomenology presents remarkable similarities in both types of cavities. Our findings may serve as guidance for the optimization of quantum optical phenomena for specific applications through the appropriate choice of material parameters for their implementation.

CHAPTER 4

EXCITONS MODIFIED BY PHOTONS

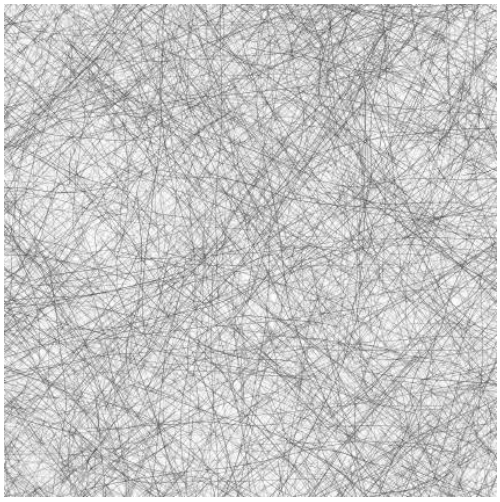

CHAPTER 4

EXCITONS MODIFIED BY PHOTONS

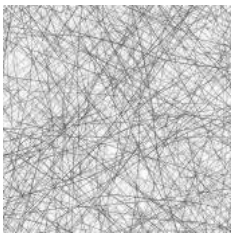

One of the most interesting effects that arise under the strong coupling regime is the feasibility of collectively coupling a macroscopic number of molecules to a single cavity mode (up to ca. 10^5 molecules [444]). The hybrid light-matter states that are formed extend over distances comparable to the wavelength of the light [359, 360], hence distances much larger than the scale of the localized molecular excitation. Thankfully, the formation of these delocalized states is possible even with highly disordered organic materials [445, 352]. As explained in the introductory chapter (Section 1.3), the delocalized nature of polaritons, together with the participation of multiple material excitations, have been exploited for the modification of the transport properties in different platforms.

The electromagnetic environment of excitonic systems becomes altered when these are placed inside an optical cavity, thus enabling the control of their performance through the light-matter interaction. Within the strong coupling regime, diverse material properties can be controlled through the manipulation of the polaritonic characteristics (see Subsection 1.3.1). Since the first experimental demonstration of the modification of the rate of a photochemical reaction through strong light-matter coupling [273], polaritonic chemistry has become a very active research field. Apart from their potential to manipulate the chemical structure and reactions, the formation of these delocalized states also enables the enhancement of the spatial range and rate of exciton transport in organic platforms. A related process, energy transfer, may also benefit from this polariton-based mechanism.

Energy transfer between molecules has been traditionally obtained through the Förster mechanism, a near-field dipole-dipole interaction which decreases with the sixth power of the separation. This makes energy transfer inefficient for distances beyond a few nanometres. Diverse procedures were followed with the aim to extend this range, as well as to improve the energy transfer performance (see Subsection 1.3.2). The coupling of molecules to the electromagnetic field within a cavity started being considered to this end, where the exploration of the strong coupling regime marked a qualitative leap forward (see Subsection 1.3.3). The coherent and delocalized character of polaritons allowed for energy transfer beyond the nanometre range, where the time scale of the process is set by the Rabi frequency and the operative distance is determined by the wavelength of the photonic mode. Although experimentally obtained, the underlying physical mechanism

responsible for the long-range energy transfer were not well-understood, nor the role played by polariton coherence. Here, we present a theoretical description of this process, unveiling the importance of the mixing of both donor and acceptor molecules in the polaritonic states as well as the role played by vibrations.

Exciton dynamics is also thoroughly explored within biological systems (see Subsection 1.3.4), due to its importance in the mechanism responsible for photosynthesis —the excitation needs to be transported from the complexes responsible for the absorption of solar photons to the place where charge separation occurs. Here, we demonstrate that the exciton dynamics in a photosynthetic unit belonging to archetypal purple bacteria can be greatly modified by its interaction with an optical cavity. In this way, we apply the concepts learnt from organic semiconductor microcavities to these new systems, highlighting the benefits that strong light-matter coupling may bring to this field.

This chapter, devoted to the modification of the exciton transport mechanism thanks to the coupling to a cavity mode, is thus organized in two clearly differentiated parts. First, we consider the realization of long-range energy transfer between ensembles of molecules in Section 4.1, where we discuss the physical mechanism behind this polariton-mediated process. Then, we move to the problem of exciton dynamics between photosynthetic complexes in Section 4.2, focusing on the modification of the dynamics when these systems are coupled to a common cavity mode.

4.1 Cavity-modified energy transfer between two collections of organic molecules

As previously mentioned, much research attention has been focused on exploring the opportunities that the phenomenon of collective strong coupling brings into material science. In particular, we are interested in the process of energy transfer. Experimental studies have demonstrated that the appropriate tailoring of polaritonic characteristics in ensembles of organic molecules coupled to the confined electromagnetic field within a cavity yields a large enhancement of the efficiency and spatial range of energy transfer. In this context, two experimental realizations are worth emphasising. First, the realization carried out by Coles *et al.*, in which energy transfer between organic dyes in a strongly coupled optical microcavity was first obtained [370]. There, donor and acceptor molecules were blended within the cavity. Later, this process of energy transfer mediated by polaritons was carried out when the two families of molecules were kept physically separated by Zhong *et al.* [372].

Here, we investigate the polariton-mediated mechanism behind this long-range energy transfer process for these two different configurations, namely, donor and acceptor molecules that are either intermixed or physically separated. The main results of this work have been published as: *R. Sáez-Blázquez, J. Feist, A. I. Fernández-Domínguez, and F. J. García-Vidal, "Organic polaritons enable local vibrations to drive long-range energy transfer," Phys. Rev. B* **97***, 241407 (R) (2018)* [375].

4.1.1 The system: two collections of organic molecules within a cavity

With the aim to study the process of cavity-modified energy transfer between two collections of organic molecules, we consider the two paradigmatic experimental realizations previously mentioned. These are represented in Figure 4.1, where donor and acceptor molecules are either intermixed (left) or physically separated (right) inside the cavity. The first configuration tries to mimic the experimental setup considered by Coles *et al.* [370], while the second arrangement of molecules matches the experimental configuration reported by Zhong *et al.* [372].

Model and theoretical description

The system under study is thus composed of two collections of quantum emitters, N_{D} **donors** (blue) and N_{A} **acceptors** (red), between which the transfer of energy is sought. Both donors and acceptors are modelled as identical two-level systems with transition frequencies ω_{D} and ω_{A}, respectively, as shown in Figure 4.2. They are placed, either blended or separated by a wall of width d, inside an **optical cavity** which supports a mode of frequency ω_{C}. In the first configuration (Figure 4.1 [Left]), the coupling g_ι between the ι-th molecule and the electromagnetic mode is assumed to follow the spatial profile of the fundamental cavity mode. In the second scenario (Figure 4.1 [Right]), g_ι presents a dependence dictated by the second cavity mode (note that the coupling strength profile exhibits a node at the position of the dividing barrier).

Hamiltonian The Hamiltonian describing these two hybrid systems includes the excitation of the cavity mode (Equation 2.19), as well as the excitation of each one of the donor and acceptor molecules (Equation 2.27):

$$\hat{H}_{\mathrm{S}} = \omega_{\mathrm{C}}\,\hat{a}^\dagger\hat{a} + \sum_{\iota=1}^{N_{\mathrm{D}}}\omega_{\mathrm{D}}\hat{\sigma}_\iota^z + \sum_{\iota=1}^{N_{\mathrm{A}}}\omega_{\mathrm{A}}\hat{\sigma}_\iota^z + \sum_{\iota=1}^{N_{\mathrm{D}}+N_{\mathrm{A}}} g_\iota(\hat{a}^\dagger\hat{\sigma}_\iota + \hat{a}\hat{\sigma}_\iota^\dagger)\,. \tag{4.1}$$

There, $\hat{a}^\dagger$ and $\hat{a}$ are the bosonic creation and annihilation operators for the cavity mode (Equation 2.18), and $\hat{\sigma}_\iota^\dagger$ and $\hat{\sigma}_\iota$ are the fermionic creation and annihilation operators corresponding to the ι-th molecule (Equation 2.23), with $\hat{\sigma}_\iota^z \equiv [\hat{\sigma}_\iota^\dagger, \hat{\sigma}_\iota]/2$. The last term of the Hamiltonian represents the coupling of the cavity mode to each molecule, with coupling strength g_ι, where the rotating wave approximation has been introduced (Equa-

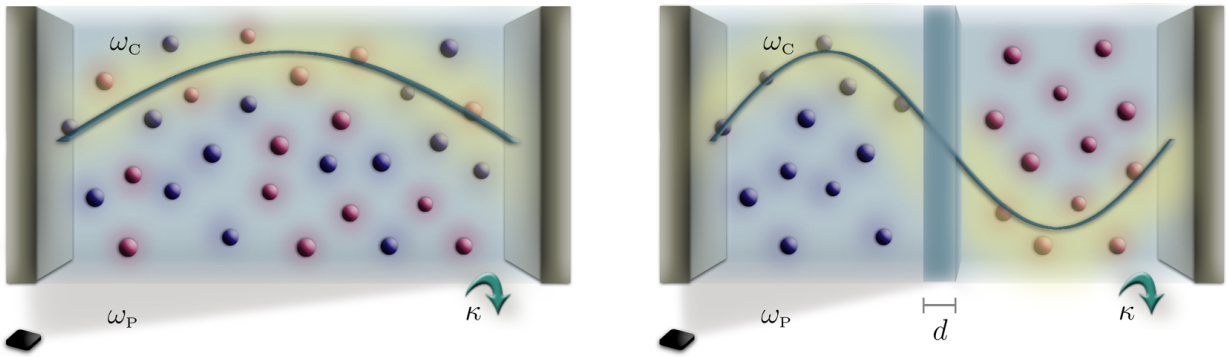

Figure 4.1. Scheme of the configurations under study, where the molecules are placed in the cavity either intermixed [left] or separated by a dividing wall [right], with the set of parameters characterizing the model.

tion 2.39). Notice that, within this approach, we disregard dipole-dipole coupling between molecules as its contribution to exciton transport is negligible when the polariton-mediated mechanism is fully operative [282].

With the aim to study polariton-mediated energy transfer in these systems, the optical cavity is coherently pumped by a laser of frequency ω_{P} and driving strength Ω_{P}. The new term to be added to the Hamiltonian accounting for this **coherent pumping** reads ($\hbar = 1$):

$$\hat{H}_{\mathrm{P}} = \Omega_{\mathrm{P}}(\hat{a}^{\dagger} \mathrm{e}^{-\mathrm{i}\omega_{\mathrm{P}} t} + \hat{a}\mathrm{e}^{\mathrm{i}\omega_{\mathrm{P}} t}) \, .$$

The complete Hamiltonian $\hat{H} = \hat{H}_{\mathrm{S}} + \hat{H}_{\mathrm{P}}$ can be expressed in the **rotating frame** (see Subsection 2.2.5), thus yielding:

$$\begin{aligned} \hat{H} = (\omega_{\mathrm{C}} - \omega_{\mathrm{P}})\, \hat{a}^{\dagger}\hat{a} + \sum_{\iota=1}^{N_{\mathrm{D}}} (\omega_{\mathrm{D}} - \omega_{\mathrm{P}})\, \hat{\sigma}_{\iota}^{z} + \sum_{\iota=1}^{N_{\mathrm{A}}} (\omega_{\mathrm{A}} - \omega_{\mathrm{P}})\, \hat{\sigma}_{\iota}^{z} \\ + \sum_{\iota=1}^{N_{\mathrm{D}}+N_{\mathrm{A}}} g_{\iota}(\hat{a}^{\dagger}\hat{\sigma}_{\iota} + \hat{a}\hat{\sigma}_{\iota}^{\dagger}) + \Omega_{P}(\hat{a}^{\dagger} + \hat{a}) \, . \end{aligned} \tag{4.2}$$

The time dependence has been removed from the Hamiltonian, and now we have the detunings with respect to the laser frequency instead of the transition frequencies.

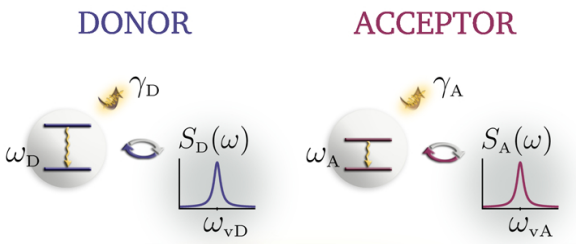

Figure 4.2. Scheme of the two-level systems modelling both donor [Left] and acceptor [Right] molecules, with the set of parameters characterizing the different dissipation channels.

Time dynamics The dynamics of the system is described through the **master equation formalism** for open quantum systems (see Subsection 2.1.2 for a review of this topic), since various dissipative mechanisms are present. The different dissipation channels experienced by molecules are depicted in Figure 4.2. Radiative losses associated with donors and acceptors (with decay rates γ_{D} and γ_{A}, respectively), as well as cavity dissipative losses (with decay rate κ), can be introduced in the description through the associated **Lindblad terms** $\mathcal{L}_{\hat{\mathcal{O}}}$ (defined in Equation 2.16). There, the operator $\hat{\mathcal{O}}$ responsible for the losses is either the cavity $\hat{a}$ or the n-th molecule $\hat{\sigma}_n$ annihilation operators, as the case may be. Besides, we describe the dissipation experienced by molecular excitations due to their internal vibronic structure by means of the general **Bloch–Redfield formalism** (see Appendix C, Section C.2, for an overview of this approach). This requires the inclusion of **spectral densities** $\Theta_{jk}(\omega)$, defined in Equation 2.11, characterising the local vibrational reservoir of each molecule. Since each molecule is considered to be coupled to its local independent bath, only the densities $\Theta_{jk}(\omega)$ with $j = k$ are present, thus the spectral density associated with the ι-th molecule is given by $S_{\iota}(\omega) \equiv \Theta_{\iota\iota}(\omega)$. The operator $\mathcal{Q}_{\iota}$ appearing in the interaction Hamiltonian of Equation 2.8 (and thus in the Bloch–Redfield tensor of Equation 2.13) is here given by $\mathcal{Q}_{\iota} = \hat{\sigma}_{\iota}^{\dagger}\hat{\sigma}_{\iota}$. This $\mathcal{Q}_{\iota}$ stands for the operator through which the system is coupled to the reservoir, and its specific form stems from the interaction term of the Hamiltonian given in Equation 2.60, which describes the coupling of the electronic transition of a molecule to a vibrational mode.

Considering the different dissipation channels and their corresponding descriptions (Equation 2.15 for the Lindblad formalism and Equation 2.14 for the Bloch–Redfield formalism), the **master equation** that governs the evolution of the density matrix $\hat{\rho}$ describing the system reads:

$$\frac{\mathrm{d}}{\mathrm{d}t}\hat{\rho}(t) = -\mathrm{i}[\hat{H},\hat{\rho}(t)] + \frac{\kappa}{2}\mathcal{L}_{\hat{a}}[\hat{\rho}] + \sum_{\iota=1}^{N_\mathrm{D}}\frac{\gamma_\mathrm{D}}{2}\mathcal{L}_{\hat{\sigma}_\iota}[\hat{\rho}] + \sum_{\iota=1}^{N_\mathrm{A}}\frac{\gamma_\mathrm{A}}{2}\mathcal{L}_{\hat{\sigma}_\iota}[\hat{\rho}]$$
$$-\pi\sum_{\iota=1}^{N_\mathrm{D}+N_\mathrm{A}}\sum_{m,n}\{\langle\omega_m|\mathcal{Q}_\iota|\omega_n\rangle\ (\mathcal{Q}_\iota|\omega_m\rangle\langle\omega_n|\rho(t) - |\omega_m\rangle\langle\omega_n|\rho(t)\mathcal{Q}_\iota)\ S_\iota(\omega_m-\omega_n) + \mathrm{h.c.}\}\ , \tag{4.3}$$

where the Hamiltonian $\hat{H}$ is the one given in Equation 4.2. There, introduced the polariton eigenbasis, that is, the basis composed of the Hamiltonian eigenstates: $\hat{H}|\omega_n\rangle = \omega_n|\omega_n\rangle$ (Equation 2.10). Hence, in the master equation, while the subindex ι runs over the number of molecules, either donor (D) or acceptor (A) molecules, subindices m and n stand for all the Hamiltonian eigenstates.

Parameters

Our numerical computations are firstly performed by the configuration in which donor and acceptor molecules are separated within the optical cavity (Figure 4.1 [Right]), following the experimental setup previously mentioned [372]. The different physical magnitudes are thus parametrized in accordance to those there reported. In our numerical computations, a simplified system is considered, where $N_\mathrm{D} = 16$ donors and $N_\mathrm{A} = 16$ acceptors are extended over a length of 100 nm and separated by a wall of $d = 10$ nm. The **transition frequencies** associated with donor and acceptor molecules are $\omega_\mathrm{D} = 2.1$ eV and $\omega_\mathrm{A} = 1.88$ eV, respectively, and the cavity mode is tuned to be at resonance with the former ones. The **coupling** of molecules to the cavity field is characterized by a Rabi splitting $\Omega_\mathrm{R} = 0.16$ eV, with g_ι following the spatial profile of the second cavity mode. The total **losses** of the cavity are set to $\kappa = 0.01$ eV (which corresponds to a lifetime of 60 fs, including both non-radiative and radiative channels). The radiative losses of the molecules are $\gamma_\mathrm{D}, \gamma_\mathrm{A} = 1.3$ μeV (corresponding to 500 ps), which are typical values for organic molecules. The **spectral densities** mimicking the molecular vibrational reservoirs are taken as two Lorentzian-like profiles vanishing at zero frequency (so that only transitions to states of lower energy are promoted):

$$S_\iota(\omega) = \gamma_\phi\frac{\omega}{\omega_{\mathrm{v}\iota}}\frac{\xi^2}{(\omega-\omega_{\mathrm{v}\iota})^2+\xi^2}\ , \tag{4.4}$$

where $\iota = \mathrm{D}, \mathrm{A}$ stand for donors and acceptors, respectively. Spectral densities are considered the same for all molecules within the same family, and this form corresponds to the simple case of a single vibrational mode of frequency $\omega_{\mathrm{v}\iota}$ and width ξ. As we aim to show the role of vibrations in the energy-transfer process, the resonant vibrational frequencies ω_D and ω_A are not fixed (their values are of the order of 0.1 eV). The strength of the exciton-phonon coupling is parametrized by γ_ϕ, which determines the phonon-induced transition rate on resonance. In our calculations we set $\gamma_\phi = 0.013$ eV, that corresponds to the relatively small exciton-phonon coupling present in J-aggregates. This value would be

greater if considering monomeric chromophores that present larger values of the Stokes shift. Regarding the linewidth of these vibrational modes, we consider a large value, $\xi = 0.01$ eV, in order to account for the effective broadening of the resonances due to cavity losses ($\xi \approx \kappa$).

4.1.2 Energy level structure

Before studying the process of energy transfer, we examine the energy-level structure associated with the system. Notice that, as our focus is on the strong coupling regime, the description needs to be performed in terms of the new emerging eigenstates of the Hamiltonian. In the hybrid system composed of a single quantum emitter interacting with a single cavity mode (see Jaynes–Cummings Hamiltonian in Subsection 2.2.4), two polaritons arise: the **lower polariton** (LP) and the **upper polariton** (UP), whose energies are separated by the **Rabi splitting** energy $\hbar\Omega_R$. This structure of energy levels is depicted in Figure 4.3 [Right]. When having a collection of molecules instead of only one, apart from the two previous polaritons, a set of (degenerated) **dark states** appear. These are states that do not couple to light, and consist in superpositions of molecular excited states. In Figure 4.3 [Center] we plot this situation, where the energy associated with dark states (that is, the corresponding to the molecular excitations) is indicated with a dashed grey line, lying between the UP and LP energies. Finally, if the cavity hosts two types of molecules, apart from the UP and the LP, a third polariton arises: the **middle polariton** (MP). Besides, there are two collections of dark states, each one associated with one type of molecules (and thus degenerated at the corresponding energy). This level structure is represented in Figure 4.3 [Left], where the sets of dark states are plotted in dashed grey lines again.

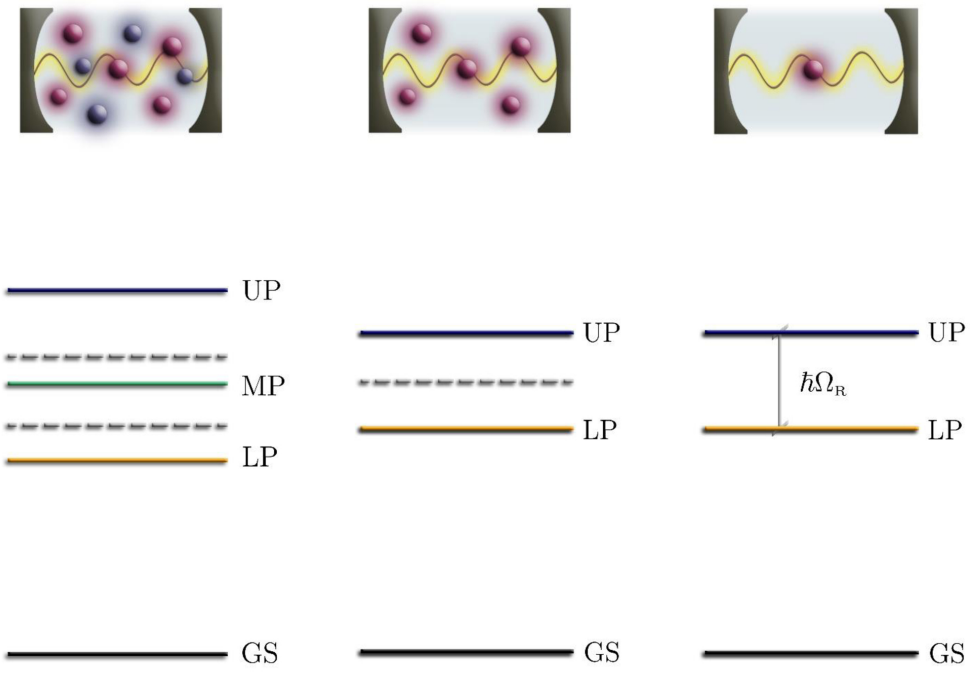

Figure 4.3. Sketch and energy levels associated with three distinct configurations: a single molecule [Right], a collection of molecules [Center], and a collection of two types of molecules [Left] interacting with a single cavity mode. The energy levels corresponding to the upper (UP), middle (MP), and lower (LP) polaritons, as well as to the ground state (GS), are represented with continuous lines, while the set of dark states are indicated with grey dashed lines. The energy distance $\hbar\Omega_R$ stands for the Rabi splitting.

This latter situation is precisely the one corresponding to our setup: two types of emitters, donor and acceptor molecules, are coupled to the same cavity mode. The level structure is thus composed of three polaritons and two sets of dark states. Considering the parameters before indicated, we compute the **eigenenergies** of the system by diagonalizing the Hamiltonian of Equation 4.1. These are plotted as a function of the Rabi frequency Ω_R in Figure 4.4 (a), where this magnitude is defined in terms of the donor molecules as $\Omega_R \equiv \left(\sum_{\iota=1}^{N_D} g_\iota^2\right)^{1/2}$. Effectively, three **polaritons** arise within the strong coupling regime: the UP (blue), the MP (green), and the LP (yellow). Together with them, there are two sets of **dark states**: $N_D - 1$ superpositions of donor states and $N_A - 1$ superpositions of acceptor states. These constitute the $\mathcal{D}$ and $\mathcal{A}$ dark subspaces, degenerated at the energies of the bare donor (grey dash-dotted line) and bare acceptor (grey dashed line) molecules, respectively. It is important to note that the eigenenergies depicted in Figure 4.4 (a) only depend on Ω_R and not on the particular set of couplings g_ι, hence this result is valid for both the intermixed and the physically-separated molecular arrangements.

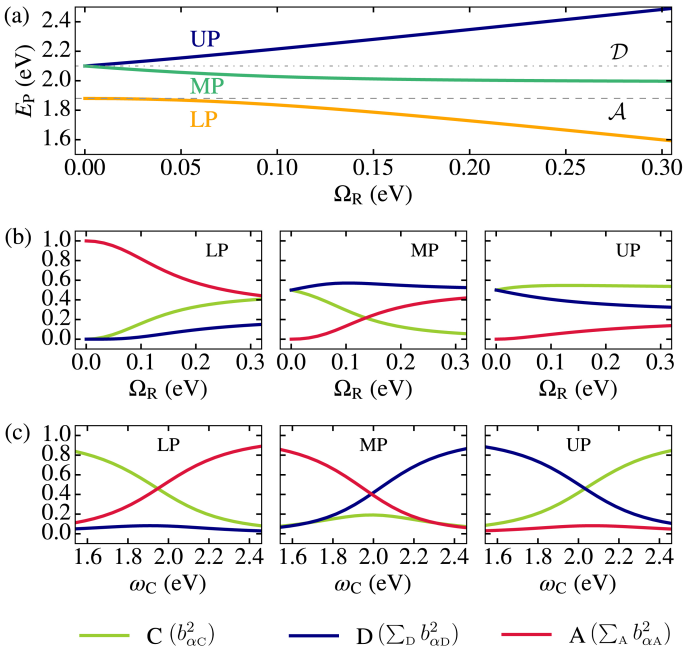

Figure 4.4. (a) Energies corresponding to the upper (UP), middle (MP), and lower (LP) polaritons are depicted as a function of the Rabi frequency Ω_R in blue, green, and yellow, respectively. Dash-dotted and dashed lines stand for the donor and acceptor energies and their associated dark states $\mathcal{D}$ and $\mathcal{A}$. (b-c) Coefficients representing the cavity (green), donor (blue), and acceptor (red) components of the LP (left), MP (center), and UP (right) as a function of the Rabi frequency Ω_R for $\omega_C = 2.1$ eV in (b), and as a function of the cavity frequency ω_C for $\Omega_R = 0.16$ eV in (c).

Polaritons are hybrid states, partly light and partly matter. The **Hopfield coefficient** $b_{\alpha\iota}$ (where ι = C, D, or A) describes the content of cavity (C), donor (D), or acceptor (A) corresponding to the state α belonging to the polariton basis (where α = UP, MP, or LP). The cavity and matter components of each polariton are plotted in Figure 4.4 as a function of the Rabi splitting Ω_R (panels b) and the cavity frequency ω_C (panels c). There, the cavity component is depicted in yellow green, while the donor and acceptor components are shown in blue and red, respectively. For the set of parameters considered, the UP branch mainly results from the hybridization of cavity and donor molecules, while the LP branch is composed mostly of acceptor states mixed with the optical field. As a result, UP and LP can be essentially identified with donor and acceptor molecules, respectively, although the presence of other components should not be overlooked. For instance, for large coupling strengths, we observe that there is a not insignificant contribution of acceptor molecules in the UP, as well as a contribution of donor molecules in the LP. Concerning the MP branch, it contains a mixture of states in which both types of molecules have similar weights for certain parameter ranges.

4.1.3 Energy-transfer process

Once the structure of energy levels has been determined, we proceed to the study of the process of energy transfer from donor to acceptor molecules when the two families are strongly coupled to the same cavity mode. The excitation thus needs to be placed at the donor molecules. To this end, the **driving laser** is tuned to pump the cavity at the UP frequency, so that all the excitation is placed in this polariton and, consequently, mainly in the donor molecules.

Transfer efficiency

The energy transfer process can be theoretically quantified in a way similar to experiments, where the light emission at the LP frequency is measured. Hence we define the **transfer efficiency** T as the ratio between the emission from the LP and the total light leaking from the cavity under coherent pumping, that is:

$$T = \frac{b_{\mathrm{LC}}^2 P_{\mathrm{L}}}{b_{\mathrm{LC}}^2 P_{\mathrm{L}} + b_{\mathrm{MC}}^2 P_{\mathrm{M}} + b_{\mathrm{UC}}^2 P_{\mathrm{U}}} \,. \tag{4.5}$$

There, P_α stands for the population of polariton α (with $\alpha = \mathrm{U}$, M, or L, corresponding to the UP, MP, and LP, respectively), whose cavity content is given by the Hopfield coefficient $b_{\alpha\mathrm{C}}$ previously defined.

As the pumping is tuned to be at the UP resonance, composed mostly of acceptors, all the excitation is initially placed in this state. Should vibrational baths for emitters not exist, the excitation would remain in the UP while fading away due to cavity losses. Nonetheless, given the complex vibrational structure exhibited by molecules, the excitation eventually ends at the LP state, which entails the excitation of the acceptor molecules —hence energy transfer from donors to acceptors takes place. In our computations we consider coherent pumping and determine the steady state of the system from Equation 4.3. Then, the transfer efficiency T can be computed from Equation 4.5 by considering the Hopfield coefficients associated with the specific configuration.

With the aim to investigate the role of vibrations in the transfer of the excitation from the UP to the LP, we fix all the parameters of the model except for the spectral densities S_{D} and S_{A} (given in Equation 4.4). These mimic the molecular vibrational reservoirs associated with donor and acceptor molecules, respectively. In particular, we compute the transfer efficiency T as a function of the two **resonant vibrational frequencies** ω_{vD} and ω_{vA}, associated with donor and acceptor molecules, respectively. The result is plotted in Figure 4.5 [Left], where a darker color means a higher transfer efficiency. The relevant energy differences between eigenstates are indicated in the margins of this panel with coloured arrows. The contour plot reveals the configurations for which the T is enhanced:

- We observe a vertical line at $\omega_{\mathrm{vA}} \sim 0.42$ eV, which originates from the resonant tuning of the spectral density $S_{\mathrm{A}}(\omega)$ with the transition from the UP to the $\mathcal{A}$-states. This feature cannot be attributed to an energy-transfer process, since it is the acceptor component of the UP that directly produces it. This enhancement of exciton transport mediated by polaritons has already been predicted [282, 363].

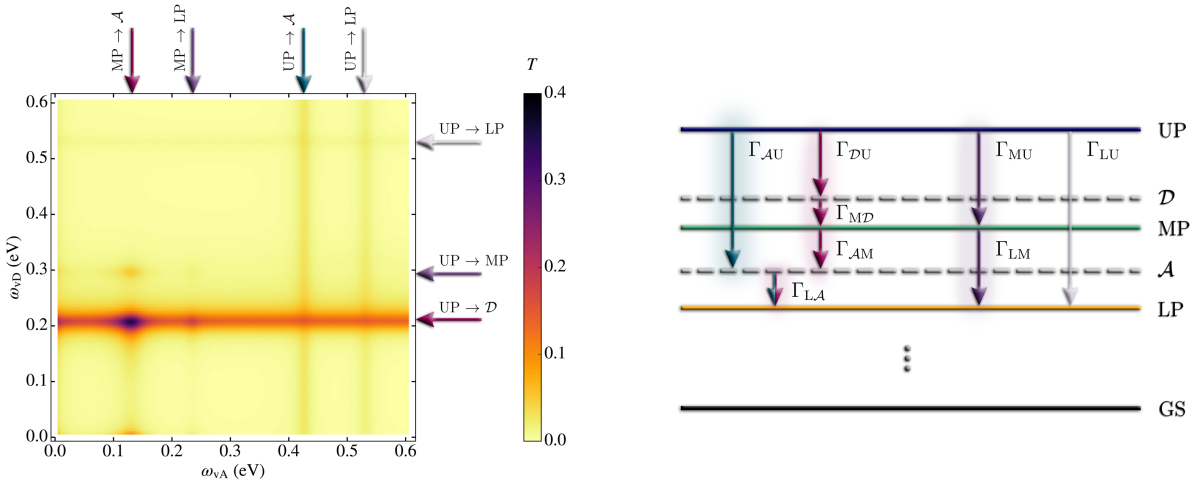

Figure 4.5.
[Left] Transfer efficiency, T, for $N_D = 16$ donors and $N_A = 16$ acceptors, coupled such that the Rabi splitting is $\Omega_R = 0.16$ eV, when varying the center frequencies of the Lorentzians representing the thermal bath associated with donor and acceptor molecules, respectively. The corresponding transitions are marked by arrows on the top and right edges. **[Right]** Level scheme of the polaritons (as well as the two sets of dark states $\mathcal{D}$ and $\mathcal{A}$) showing various paths of decay,which are labelled with their corresponding rates .

- There are also two equivalent lines of high transfer efficiency at $\omega_{v\iota} \sim 0.53$ eV (with $\iota = D, A$), one horizontal and one vertical. This vibrational frequency corresponds to the energy gap between the UP and the LP. Therefore, vibrations promote the direct transition from the UP to the LP to some extent.

- Apart from those, the more pronounced enhancement of the transfer efficiency takes place when the spectral density associated with donor molecules, $S_D(\omega)$, peaks at the frequency that equals the energy gap between the UP and the $\mathcal{D}$-states. Importantly, T is maximum at a single point along this horizontal line. This maximum emerges when the spectral density associated with acceptor molecules, ω_{vA}, also matches the energy difference between the MP and the $\mathcal{A}$-states.

All the possible processes that lead the population from the UP to the LP are shown in Figure 4.5 [Right]. There, the horizontal coloured lines stand for the UP (blue), MP (green), LP (yellow) energies, and the dark subspaces $\mathcal{D}$ and $\mathcal{A}$ are represented with dashed grey lines. The direct decay of the UP into $\mathcal{A}$-states is indicated in green, while the channels involving only polaritons are the purple and grey routes. Nevertheless, our numerical results reveal that the main pathway that leads to energy transfer from donor to acceptor molecules corresponds to the red route. There, the population is carried from the UP to the LP through the MP thanks to local exciton-vibration interactions. The mixed composition of the MP, which combines donor and acceptor molecule populations in similar proportions, is crucial for this boost of the energy transfer. Notice that this requires both donor and acceptor molecules to be strongly coupled to the cavity mode, and the achievable enhancement is strongly reduced when only one of the collections becomes hybridized [377].

Importantly, we have verified that the general picture offered by Figure 4.5 [Left] on the link between energy transfer and molecular vibrations is not altered, even at the quantitative level, when donor and acceptor molecules are intermixed, as long as the Rabi splitting remains the same. This demonstrates that Ω_R is the only key parameter describing the effect of light-matter coupling in the process of energy transfer, which is independent of aspects such as the actual molecular arrangement or the spatial dependence of the cavity mode, in agreement with experimental results [372].

Therefore, when donor molecules are excited in experiments, the energy is first stored in the UP. Then, promoted by local exciton-vibration interactions in the donor molecules, the excitation reaches MP. Finally, local excitation-vibration interactions in the acceptor molecules lead this excitation energy to the LP. This process is represented in Figure 4.5.

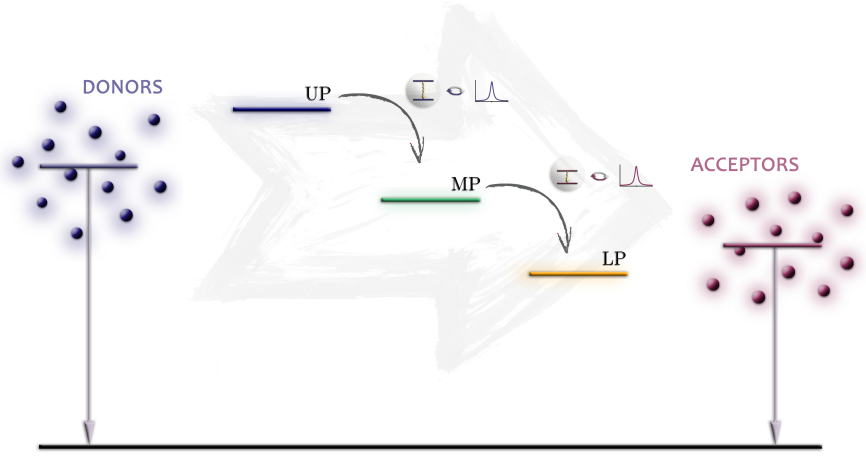

Figure 4.6. Mechanism responsible for the long-range energy transfer.

Analytical expressions for the transition rates

An additional check can be performed in the previous analysis of the transfer efficiency. In the computation of the steady-state solution from Equation 4.3, our numerical results show that terms coupling the off-diagonal (coherences) and diagonal (populations) elements of the density matrix can be disregarded in the Bloch–Redfield master equation. Under this approximation, we can now restrict our attention to the **transition rates** Γ connecting eigenstates of the coupled system, either polaritonic or dark states (as the ones depicted in Figure 4.5 [Right]). This greatly simplifies the numerical treatment, making the theoretical study of systems involving a much larger number of donor and acceptor molecules feasible. Moreover, we can obtain analytical expressions for the relevant decay rates, expressed only in terms of the Hopfield coefficients $b_{\alpha\iota}$ and the vibronic spectral densities S_{D} and S_{A}. We recall that $b_{\alpha\iota}$ (where ι = C, D, or A) describes the content of cavity (C), donor (D), or acceptor (A) corresponding to the polariton state α (where α = U, M, or L).

Starting from the general expression of the Bloch–Redfield tensor (Equation 2.13), the only relevant components are those of the form R_{aamm}. If we consider our particular case, in which $\Theta_{\iota\iota}(\omega) \equiv S_\iota(\omega)$ and $\mathcal{Q}_\iota = \hat{\sigma}_\iota^\dagger \hat{\sigma}_\iota$, the component of the Bloch–Redfield tensor (with $a \neq m$) reduces to:

$$R_{aamm} = 2\pi \sum_\iota |\langle \omega_a | \hat{\sigma}_\iota^\dagger \hat{\sigma}_\iota | \omega_m \rangle|^2 S_\iota(\omega_a - \omega_m) \,. \tag{4.6}$$

Depending on the nature of the states involved in the transition, we can thus identify three different sets of decay rates:

- First, those three transitions connecting two polariton states, α and β, are given by:

$$\Gamma_{\alpha\beta} = \sum_{\iota=\mathrm{D,A}} b_{\beta\iota}^2 b_{\alpha\iota}^2 S_\iota(\omega_\beta - \omega_\alpha)\,,$$

  where $\alpha, \beta =$ UP, MP, or LP. Notice that the dependence of the Hopfield coefficients $b_{\alpha\iota}$ (where $\iota = \mathrm{D, A}$) on the number of molecules is of the form $b_{\alpha\iota} \sim 1/\sqrt{N_\iota}$, yielding $\Gamma_{\alpha\beta} \sim 1/N_{\mathrm{A,D}}$. Therefore, Γ_{MU}, Γ_{LM} and Γ_{LU} vanish as the number of molecules increases, and the contribution to the energy transfer from the purple and grey routes in Figure 4.5 [Right] are negligible in very large systems.

- Second, the rates associated with the decay of the dark subspaces $\mathcal{D}$ and $\mathcal{A}$ to a polariton state of lower energy are given by:

$$\Gamma_{\mathrm{M}\mathcal{D}} = \frac{1}{N_\mathrm{D}} \sum_\mathrm{D} b_{\mathrm{MD}}^2\, S_\mathrm{D}(\omega_\mathrm{D} - \omega_\mathrm{M}),$$
$$\Gamma_{\mathrm{L}\mathcal{D}} = \frac{1}{N_\mathrm{D}} \sum_\mathrm{D} b_{\mathrm{LD}}^2\, S_\mathrm{D}(\omega_\mathrm{D} - \omega_\mathrm{L}),$$
$$\Gamma_{\mathrm{L}\mathcal{A}} = \frac{1}{N_\mathrm{A}} \sum_\mathrm{A} b_{\mathrm{LA}}^2\, S_\mathrm{A}(\omega_\mathrm{A} - \omega_\mathrm{L}).$$

  We observe that these rates present the same $1/N_{\mathrm{A,D}}$ dependence as the decay rates between polaritonic states. However, in contrast to decay from polariton states (which decay efficiently by cavity leakage of their photonic contribution), the competing decay paths due to bare-molecule radiative and nonradiative decay are typically on the order of nanoseconds for high-quantum-yield emitters. Consequently, even slow decay from the dark states efficiently populates the lower-lying polaritons.

- Finally, the transition rates from polariton states to dark subspaces that have lower energies have the form:

$$\Gamma_{\mathcal{D}\mathrm{U}} = \frac{N_\mathrm{D} - 1}{N_\mathrm{D}} \sum_\mathrm{D} b_{\mathrm{UD}}^2\, S_\mathrm{D}(\omega_\mathrm{U} - \omega_\mathrm{D}),$$
$$\Gamma_{\mathcal{A}\mathrm{U}} = \frac{N_\mathrm{A} - 1}{N_\mathrm{A}} \sum_\mathrm{A} b_{\mathrm{UA}}^2\, S_\mathrm{A}(\omega_\mathrm{U} - \omega_\mathrm{A}),$$
$$\Gamma_{\mathcal{A}\mathrm{M}} = \frac{N_\mathrm{A} - 1}{N_\mathrm{A}} \sum_\mathrm{A} b_{\mathrm{MA}}^2\, S_\mathrm{A}(\omega_\mathrm{M} - \omega_\mathrm{A}).$$

  There, the $N_\iota - 1$ term reflects the (large) number of dark states to which polaritons can decay. The dependence of these rates on the number of molecules is thus $\Gamma_{\mathcal{D}\mathrm{U}} \sim (N_\mathrm{D} - 1)/N_\mathrm{D}$ and $\Gamma_{\mathcal{A}\mathrm{U}}, \Gamma_{\mathcal{A}\mathrm{M}} \sim (N_\mathrm{A} - 1)/N_\mathrm{A}$. Therefore, these three decay rates do not decrease as the number of molecules increases, as the other six rates do. This gives analytical support to our Bloch–Redfield numerical results that showed the prevalence of the red route in the decay of the excitation from the UP to the LP.

Our analytical results not only explain the numerical findings previously discussed but also serve as a guideline to **optimize** the long-range energy transfer mediated by strong coupling. In order to enhance the transfer efficiency, the vibration-driven decay $\Gamma_{\mathcal{D}\mathrm{U}}$ ($\Gamma_{\mathcal{A}\mathrm{M}}$) from the upper (middle) polariton to the $\mathcal{D}$ ($\mathcal{A}$) dark states has to be comparable or faster than its decay $b_{UC}^2\kappa$ ($b_{MC}^2\kappa$) due to cavity losses. This can be achieved

most straightforwardly by using cavities with very low losses. However, for given cavity losses, optimization relies on minimizing the cavity component of the upper and middle polaritons while maximizing the donor component of the UP, as well as the acceptor component of the MP. Both these conditions favour low cavity frequencies, as observed in Figure 4.4 (c). In addition, the vibration-driven decay can be enhanced by bringing the energy detuning between UP and $\mathcal{D}$ (MP and $\mathcal{A}$) into resonance with the main vibronic frequency of the donor (acceptor) molecules. Another way to enhance both $\Gamma_{\mathcal{D}\mathrm{U}}$ and $\Gamma_{\mathcal{A}\mathrm{M}}$ is to employ organic molecules with a large γ_ϕ, as these decay rates are proportional to the spectral densities. Our model envisages that transfer efficiencies close to 100% can be reached under the conditions $\Gamma_{\mathcal{D}\mathrm{U}} \gg b_{U\mathrm{C}}^2\kappa$ and $\Gamma_{\mathcal{A}\mathrm{M}} \gg b_{M\mathrm{C}}^2\kappa$.

Assessing the energy-transfer process

From the previous analytical expressions for the transition rates, we can extract valuable information about the process of energy transfer regarding its dependence on the cavity frequency ω_C and the coupling strength (encoded in the Rabi frequency Ω_R). As we have seen, the decay rates are given exclusively in terms of the Hopfield coefficients $b_{\alpha\iota}$ (with $\iota = \mathrm{C}$, D, or A, and $\alpha = \mathrm{U}$, M, or L) and the vibronic spectral densities S_D and S_A. We now focus on the part of the rates that do not depend on the spectral densities, but just on the coefficients preceding them. This would correspond to the case in which the vibrational frequencies associated with donor and acceptor molecules are optimized so as to reach the higher possible value of the transfer efficiency, or if spectral densities are taken as constant.

Efficiency The efficiency of the process E can be computed as the sum of the efficiency associated with the red and green paths in Figure 4.5 [Right], that are those that prevail:

$$E \equiv \frac{\Gamma_{\mathcal{A}U}}{\Gamma_{\mathcal{A}U} + \Gamma_{\mathcal{D}U} + \Gamma_{\mathrm{D}U}} + \frac{\Gamma_{\mathcal{D}U}}{\Gamma_{\mathcal{A}U} + \Gamma_{\mathcal{D}U} + \Gamma_{\mathrm{D}U}} \frac{\Gamma_{\mathcal{A}M}}{\Gamma_{\mathcal{A}M} + \Gamma_{\mathrm{D}M}} .$$

There, $\Gamma_{\mathrm{D}U} = \kappa\ b_{U\mathrm{C}}^2$ and $\Gamma_{\mathrm{D}M} = \kappa\ b_{U\mathrm{M}}^2$ represent the losses due to the cavity component of the corresponding polariton. In this expression we have taken the effectivity of the transitions from the dark states to the lower-lying polaritons as unity, since as we have mentioned there are no other dissipation channels for them. In Figure 4.7 [Left] the effective efficiency $E_\mathrm{eff} = b_{U\mathrm{D}}^2 b_{L\mathrm{A}}^2 E$ is plotted as a function of the cavity frequency ω_C and the Rabi splitting Ω_R. The bare efficiency has to be weighted with the donor component of the UP and the acceptor component of the LP so as to consider the real transfer from donors to acceptors. Notice that, as shown in Figure 4.4 (c), the donor character of the UP diminishes as the cavity frequency grows, and the acceptor component of the LP diminishes as the cavity frequency decreases. The result is that the maximum effective efficiency takes place for cavity frequencies located in the middle of the transition frequencies of donors and acceptors. The reason why the efficiency decreases as the coupling strengthen is that the cavity components of the LP and UP rise, as seen in Figure 4.4 (b), and losses due to the cavity thus increase.

Reaction rate Another way to assess the energy-transfer process is through the reaction rate R, defined as the sum of the reaction rates corresponding to each one of the steps from the UP to the LP. The path displaying the fastest rate is the red one in Figure 4.5

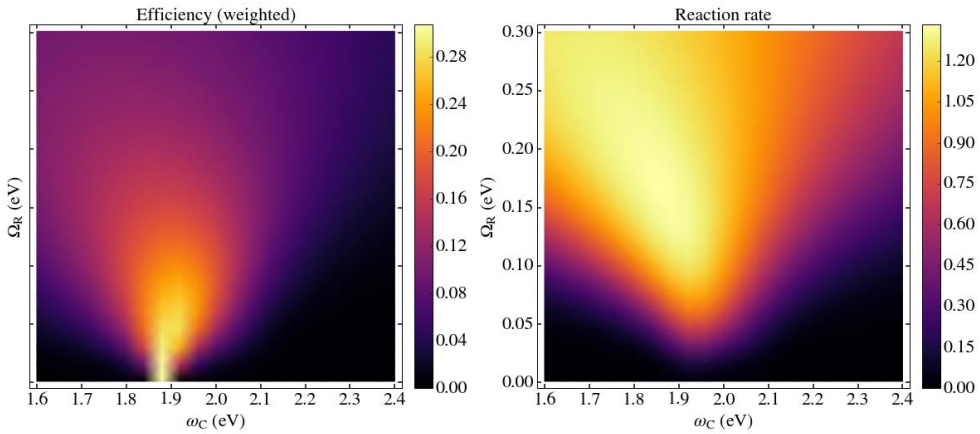

Figure 4.7. **[Left]** Efficiency E and **[Right]** reaction rate R as a function of the cavity frequency ω_C and the Rabi splitting Ω_R for $N_D = 16$ donor and $N_A = 16$ acceptor molecules.

[Right]), as this is the prevailing process meaning actual energy transfer from donors to acceptors. If we consider this route, the reaction rate becomes:

$$R \equiv \left(\frac{1}{\Gamma_{\mathcal{D}U}} + \frac{1}{\Gamma_{M\mathcal{D}}} + \frac{1}{\Gamma_{\mathcal{A}M}} + \frac{1}{\Gamma_{L\mathcal{A}}} \right)^{-1} .$$

In Figure 4.7 [Right] we plot the reaction rate R as a function of the cavity frequency ω_C and the Rabi splitting Ω_R. Again, the advantageous cavity frequencies are those located between the donor and acceptor transition frequencies, and the reaction rate grows as the Rabi splitting increases.

4.2 Cavity-modified exciton dynamics in a photosynthetic unit

Plasmonic nanostructures have been shown to modify the optical properties of different photosynthetic complexes [387, 446, 447]. Moreover, there exists experimental evidence of collective strong coupling in ensembles of living bacteria [448], giving rise even to the concept of *living polaritons* [449]. Coles et al. reported a Rabi splitting of around 150 meV [370], which implies that about one thousand chlorosomes present in green sulfur bacteria are coherently coupled to a cavity photon.

Here, we demonstrate that the exciton dynamics in an archetypal purple bacterial photosynthetic unit is greatly modified by its interaction with an optical cavity. The main results of this work have been published as: *R. Sáez-Blázquez, J. Feist, E. Romero, A. I. Fernández-Domínguez, and F. J. García-Vidal, "Cavity-modified exciton dynamics in photosynthetic units," J. Phys. Chem. Lett.* **10**, *4252–4258 (2019)* [415].

4.2.1 The system: an archetypal purple bacterial photosynthetic unit

Photosynthetic purple bacteria have been widely studied since their structure is considerably less complex than that of algae and higher plants [450]. The **photosynthetic unit** of these bacteria is composed of a reaction center and two types of light-harvesting antennas: one core light-harvesting complex 1 (named **LH1**), and some peripheral light-harvesting complexes 2 (named **LH2**). The structure and function of the photosynthetic apparatus of purple bacteria have been described in several reviews [451, 452]. Here, we present the main components of their photosynthetic unit, and outline the process of exciton dynamics from the peripheral antennas to the reaction center.

Structure of the photosynthetic unit

The **photosynthetic unit** of purple bacteria is basically composed of a LH1 complex embracing the reaction center and a collection of LH2 antennas surrounding them. Nevertheless, the specific arrangement and distribution of both complexes within the bacterial membrane depends on the particular ambient and light intensity conditions. While the function of LH2 antennas is mainly the capture of solar light, the LH1 is responsible for handing the excitation over to the reaction center. The high-resolution structure of some photosynthetic complexes are available, from the first images of the FMO complex of green bacteria [453, 454, 455]. There, the structural disposition of bacteriochlorophylls (BChl) pigments is displayed, all accompanied by carotenoids and a matrix of proteins:

- **LH2 antenna**. The structure of the LH2 complex of the *Rhodopseudomonas (Rps.) acidophila* at 2.5 Å resolution [456] and the *Rhodospirillum (Rs.) molischianum* at 2.4 Å resolution [457] are known. Figure 4.8 represents a top view of the structure of the *Rps. acidophila*, the one chosen for this work. The complex is a nonameric circular pigment-protein aggregate, where each subunit is composed of three BChls and two carotenoid molecules (in orange). In particular, the BChl pigments are organized in two concentric rings: an outer ring of 9 weakly interacting BChl molecules (in blue), the so-called **B800 ring**, and an inner ring of 18 strongly interacting BChl molecules (in green), the so-called **B850 ring**. These BChl molecules are named according to their associated absorption maxima, around 800 nm and 850 nm, respectively. Actually, this last spectral band is found at some point between 820 nm and 850 nm depending on the bacterial species. The inner B850 ring is arranged in twos, such that each pair contains one BChla (light green) and one BChlb (dark green).

- **LH1 antenna**. The high-resolution structure of the LH1 complex belonging to several species have been published, including the *Rs. rubrum* (at 8.5 Å resolution) [458], the *Rps. viridis* [459], and the *Rps. palustris* (at 4.8 Å resolution) [460]. The BChl pigments in this complex form either a ring with 16-fold symmetry (two bound BChl molecules in each subunit) with the reaction center placed inside [458, 459] or an open circle composed of 30 BChl molecules [460]. The LH1 antenna is characterized by single absorption band in the near infrared, located around 875 nm.

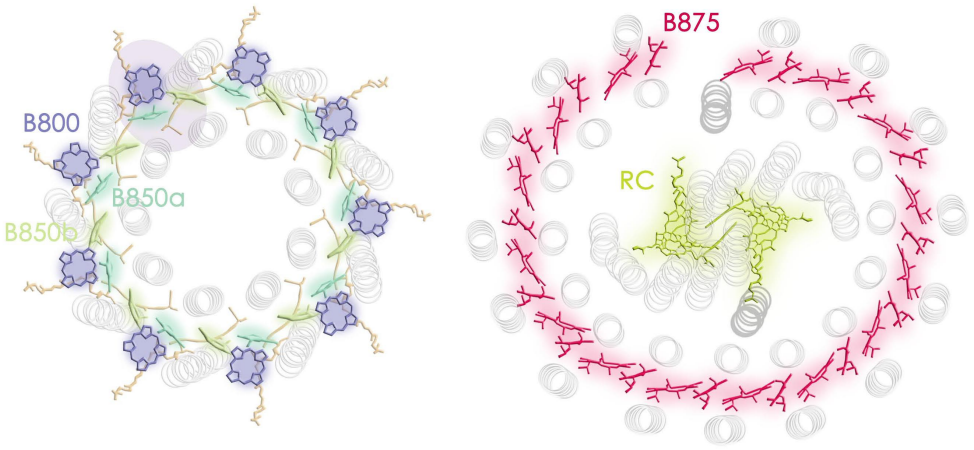

Figure 4.8. **Left** Sketch of the LH2 antenna, composed of nine BChl molecules in the B800 ring, and eighteen molecules in the B850 ring. **Right** Sketch of the LH1 antenna, composed of thirty BChl molecules in the B875 ring.

Carotenoids are pigments that also contribute in the light-harvesting process, since they cover a region of the visible spectrum not accessible by the BChl pigments (specifically, they absorb between 450 and 550 nm). Besides, carotenoids protect against excessive light through the mechanism of quenching [461].

Exciton states and transitions within the LH2 antenna

The pigments in the B800 ring are well separated from any other molecule, so the excitation is quite **localized**. On the contrary, the B850 ring is densely packed: the average distance between nearest-neighbour pigments is about 9 Å. This gives rise to strong pigment-pigment interactions and, in turn, a **delocalization** of the exciton state over some molecules. Many theoretical and experimental efforts have been devoted to the determination of the extent of such delocalization. The exciton in the B850 ring was first shown to be extended over approximately four pigments [462], but some other results have been reported [463, 464]. In fact, exciton delocalization has been shown to vary with multiple factors [465], so different values can be obtained depending on the experimental conditions and the theoretical assumptions (as well as on the definition of delocalization itself). Besides, the delocalization varies with time: the excitation is thought to be delocalized over the whole ring at the moment of excitation, while localized in approximately four pigments after a few femtoseconds [399].

The entire LH2 antenna is thus characterized by a collection of exciton states, comprising collective excitations with a high degree of delocalization as well as other excitations more localized due to the presence of weakly coupled pigments. In general, these exciton states are coupled to a continuum of low-frequency **phonons** (pigment vibrations). These phonons are precisely the responsible for energy transfer since they enable the transmission of the excitation between exciton states belonging to the same or different spectral bands. Then, the excitation initially absorbed by the B800 ring is subsequently transferred from higher-energy to lower-energy states, eventually reaching the reaction center. Therefore, phonons are crucial for the process of energy transfer in photosynthetic complexes, similarly to the process of long-range energy transfer between collections of

organic molecules previously discussed in Section 4.1.

Apart from the **homogeneous broadening** due to the coupling of electronic excitations to pigment vibrations, electronic transitions also present **inhomogeneous broadening** due to ensemble averaging. The associated linewidths are determined by hole-burning and fluorescence line-narrowing measurements. For the LH1 complex, homogeneous and inhomogeneous linewidths of 235 cm^{-1} and 530 cm^{-1}, respectively, have been reported at room temperature for the *Rhodobacter sphaeroides* [466]. In the same experiment, respective values of 188 cm^{-1} and 390 cm^{-1} have been found for the homogeneous and inhomogeneous linewidths in the absorption line associated with the B850 component of the LH2 complex. Nevertheless, some other results have been reported for the same transition, for instance, a homogeneous width of 210 cm^{-1} at the band center [467], and a total linewidth of 300 cm^{-1} [468]. From these experimental results, the Franck–Condon factors corresponding to the dominant electronic transition can be extracted. These parameters give the strength of the coupling between chromophores and the continuum of vibrational modes, modelling the associated spectral density (see Subsection 2.4.1).

Time-scales of the exciton dynamics within the photosynthetic unit

Thanks to time-resolved (sub-100 fs) nonlinear techniques and theoretical modelling, the energy transfer pathway and the time-scales associated with each step are known. The dynamics is usually described from an exciton model, where the exciton relaxation occurs due to the coupling to the exciton-phonon environment modelled through the Redfield theory. Several works have focused on the energy transfer dynamics in the photosynthetic purple bacteria, carrying out sub-picosencond absorption and fluorescence spectroscopy at room and low temperatures.

The excitation is initially created in the B800 ring after the absorption of a solar photon, under the most likely scenario. That excitation is subsequently distributed among the other B800 pigments, and also delivered to the B850 ring with similar associated time-scales [469]. In particular, the B800-to-B850 transfer is determined to take about 0.5–1 ps at room temperature [470, 471, 469] (and 2.5 ps at 77 K for the *Rb. sphaeroides* [470]). Once in the B850 molecules, the excitation passes from the LH2 to the LH1 complex, process that is reported to last around 3 ps at room temperature for the *Rb. sphaeroides* (and 5 ps at 77 K) [471]. The last step consists in the trapping of the excitation by the reaction center. This operation is slow, and it has been estimated to take around 35 ps for the *Rs. rubrum* [472]. This value is considerably larger than the associated with the other stages, hence the whole energy-transfer process is limited by the trapping rate. This time can be explained by the relatively long distance that exists between the reaction center and pigments forming the LH1. At the same time, this larger rate prevents the photo-oxidation of the pigments as a result of an excessively fast process. These pigments serve, in this sense, as a photo protection.

4.2.2 Exciton dynamics within a single LH2 antenna

First, the exciton dynamics is analyzed within a single LH2 complex, as a preliminary study of the effect that the coupling to a cavity mode may cause.

A single LH2 antenna: model and theoretical description

The study is carried out for the typical **LH2 complex** present in the *Rps. acidophila*, whose structure has been outlined in Subsection 4.2.1. An sketch of the system is depicted in Figure 4.9, where the collection of $N_{\text{LH2}} = 27$ pigments is distributed in a double-ring structure. The B800 ring is composed of nine weakly interacting BChl molecules (blue dots), while the B850 ring involves nine (closely-packed) dimers of two BChl molecules each (light and dark green).

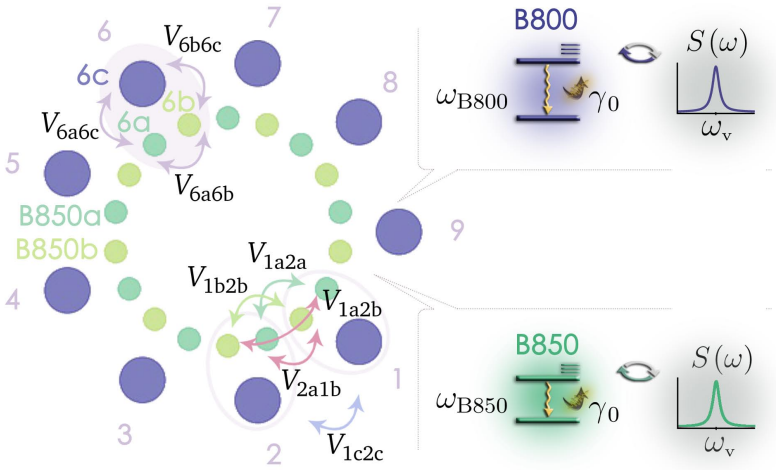

Figure 4.9. Sketch of the LH2 antenna, composed of nine BChl molecules in the B800 ring, and eighteen molecules in the B850 ring.

Hamiltonian All pigments are modelled as two-level systems, where $\hat{\sigma}_i^\dagger$ and $\hat{\sigma}_i$ are the creation and annihilation operators associated with the i-th molecular excitation, and ω_i is the corresponding energy. The **Hamiltonian** $\hat{H}_{\text{LH2}}$ describing the LH2 complex reads ($\hbar = 1$):

$$\hat{H}_{\text{LH2}} = \sum_{i=1}^{N_{\text{LH2}}} \omega_i \hat{\sigma}_i^\dagger \hat{\sigma}_i + \sum_{i,j=1}^{N_{\text{LH2}}} V_{ij} \{\hat{\sigma}_i^\dagger \hat{\sigma}_j + \hat{\sigma}_j^\dagger \hat{\sigma}_i\}, \tag{4.7}$$

where V_{ij} is the coupling strength between molecules i and j (with $i \neq j$). When this system is coupled to a cavity mode of frequency ω_{C}, with creation and annihilation operators $\hat{a}^\dagger$ and $\hat{a}$, the Hamiltonian becomes:

$$\hat{H}_{\text{LH2+C}} = \omega_{\text{C}} \hat{a}^\dagger \hat{a} + \hat{H}_{\text{LH2}} + \sum_{i=1}^{N_{\text{LH2}}} g_i (\hat{\sigma}_i^\dagger \hat{a} + \hat{\sigma}_i \hat{a}^\dagger), \tag{4.8}$$

where $\hat{H}_{\text{LH2}}$ is the Hamiltonian associated with the LH2 complex (Equation 4.7). Notice that the rotating wave approximation has been introduced in the coupling term, where

g_i is the coupling strength between the cavity mode and the i-th pigment.

Time dynamics The dynamics of the system is described through the **master equation formalism** for open quantum systems (see Subsection 2.1.2). First, the relaxation process associated with each pigment i is introduced through the corresponding **Lindblad term** $\mathcal{L}_{\hat{\sigma}_i}$, given by Equation 2.16. There, the operator involved is the pigment annihilation operator $\hat{\sigma}_i$, and the associated decay rate is γ_0 (the same for all BChls). The dissipation associated with the cavity is also described through the Lindblad formalism, where $\mathcal{L}_{\hat{a}}$ involves the cavity annihilation operator $\hat{a}$, and κ stands for the corresponding decay rate. Apart from the previous relaxation processes, BChl pigments experience vibrational dissipation and incoherent interactions. These can be introduced in the description through the **Bloch–Redfield approach** (see Appendix C, Section C.2, for an overview of this approach). According to this procedure, the incoherent dissipation emerging from the interaction with a reservoir is described by means of the **reservoir spectral density**.

The resulting master equation is thus composed of a coherent part describing the unitary evolution governed by the Hamiltonian of Equation 4.8, and a second term accounting for all incoherent processes arising from the interaction with the reservoir (Equation 2.15 describes the evolution within the Lindblad formalism while Equation 2.14 gives the dynamics within Bloch–Redfield formalism). The **master equation** that governs the evolution of the density matrix $\hat{\rho}$ describing the hybrid system reads ($\hbar = 1$):

$$\frac{\mathrm{d}}{\mathrm{d}t}\hat{\rho}(t) = -\mathrm{i}[\hat{H}_{\mathrm{LH2+C}}, \hat{\rho}(t)] + \frac{\kappa}{2}\mathcal{L}_{\hat{a}}[\hat{\rho}] + \sum_{i=1}^{N_{\mathrm{LH2}}} \frac{\gamma_0}{2}\mathcal{L}_{\hat{\sigma}_i}[\hat{\rho}]$$
$$- \pi \sum_{i=1}^{N_{\mathrm{LH2}}} \sum_{m,n} \{\langle\omega_m|\mathcal{Q}_i|\omega_n\rangle \ (\mathcal{Q}_i|\omega_m\rangle\langle\omega_n|\rho(t) - |\omega_m\rangle\langle\omega_n|\rho(t)\mathcal{Q}_i) \ S_i(\omega_m - \omega_n) + \mathrm{h.c.}\} \ , \tag{4.9}$$

where $H_{\mathrm{LH2+C}}$ is the Hamiltonian in Equation 4.8. The index i runs over all BChl pigments present in the LH2 (comprising both the B800 and the B850 rings), while the indexes m and n refer to the Hamiltonian eigenstates: $\hat{H}_{\mathrm{LH2+C}}|\omega_n\rangle = \omega_n|\omega_n\rangle$ (Equation 2.10). There, each pigment is considered to be coupled to its local independent bath, such that $S_i(\omega) \equiv \Theta_{ii}(\omega)$ stands for the spectral density associated with the i-th molecule. In the last term of the master equation, $\mathcal{Q}_i$ stands for the operator through which the system is coupled to the reservoir, here given by $\mathcal{Q}_i = \hat{\sigma}_i^\dagger \hat{\sigma}_i$ (as derived from the interaction term of the Hamiltonian given in Equation 2.60, which describes the coupling of the electronic transition of a molecule to a vibrational mode).

Parameters The site energies associated with the BChl pigments are set to $\omega_{\mathrm{B800}} = 1.549$ eV and $\omega_{\mathrm{B850a,b}} = 1.520$ eV. Let us parametrize the interactions within the subunit composed of one B800 and two B850 pigments first, as the one within the shaded area in Figure 4.9. These molecules are labelled as 6a, 6b, and 6c, where the number corresponds to the subunit index and a, b, and c stand for the B850a, B850b, and B800 BChls, respectively. The interaction between chromophores belonging to the same subunit are $V_{\mathrm{1a1c}} = 1.6$ meV, $V_{\mathrm{1b1c}} = 0.4$ meV, and $V_{\mathrm{1a1b}} = -33.8$ meV. The interactions between molecules belonging to nearest-neighbour subunits, for instance between those belonging to the subunits 1 and 2, are $V_{\mathrm{1c2c}} = 3.1$ meV within the B800 ring, and $V_{\mathrm{1a2a}} = 6.2$ meV, $V_{\mathrm{1b2b}} = 4.5$ meV, $V_{\mathrm{1b2a}} = -36.1$ meV, and $V_{\mathrm{1a2b}} = -1.5$ meV within the B850 ring.

Besides, $V_{1c2a} = -3.3$ meV. These parameters have been taken from the studies of Sauer *et* al. [468] and Tretiak *et* al. [473].

The cavity decay rate is set to $\kappa = 13\,\mu$eV, which corresponds to a lifetime of 50 ps and a quality factor $Q = \omega_C/2\kappa \simeq 6 \cdot 10^4$, parameters similar to those recently reported in deeply subwavelength dielectric cavities [474]. The decay rate associated with BChl pigments is taken as $\gamma_0 = 1\ \mu$eV. This value stems from the lifetime associated with the molecules within the LH2 complex, which is about 1 nanosecond. Note that the exciton width introduced in the cross section calculation is about 10^4 times larger than this value.

Finally, the vibrational spectral density of the pigments is parametrized using the Franck–Condon factors given by Zazubovic *et al.* [475], together with a thermal line broadening in agreement with De Caro *et al.* [476]. The same spectral density is considered for all molecules, which is depicted in Figure 4.10 [Right].

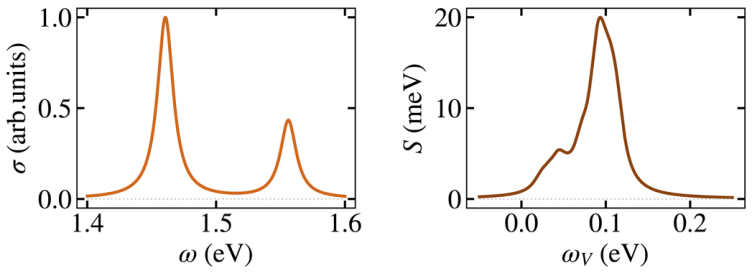

Figure 4.10. [**Left**] Absorption spectrum σ of a single LH2 complex, including disorder and inhomogeneous broadening. [**Right**] Vibrational spectral density S for all LH2 pigments.

Absorption spectrum

Once the parameters have been fixed according to the available literature, we check our model by computing the **absorption spectrum** for a single, isolated LH2 antenna. To this end, the transition matrix element of the total **dipole moment operator** $\hat{M}$ is built as:

$$\hat{M} = \sum_{i=1}^{N_{\mathrm{LH2}}} \mu_i \hat{\sigma}_i^\dagger \,,$$

where $\mu_{\mathrm{B800}} = \mu_{\mathrm{B850}} = 6.13$ D [477] for the excitonic eigenstates of our model. The absorption spectrum is built as a sum of Lorentzian contributions centered at the excitonic energies and weighted by the square of the corresponding matrix element of the dipole moment operator. Their width is set to 15 meV for B800 and B850 excitons, in order to take into account the disorder and inhomogeneous broadening inherent to the measurements performed on ensembles of LH2 complexes [478]. The spectrum, thus computed, is depicted in Figure 4.10 [Left] , which reproduces the double-peaked absorption profile reported experimentally [478, 479], with maxima around 1.44 eV (860 nm) and 1.55 eV (800 nm).

Polariton structure

First of all, we explore the different eigenstates that arise when the LH2 complex is strongly coupled to the cavity mode. In order to gain a general picture of the composition of these states, we make use of the sketch of the LH2 antenna shown in Figure 4.9. There, different coloured circles represent the BChl molecules: B800 molecules are depicted in

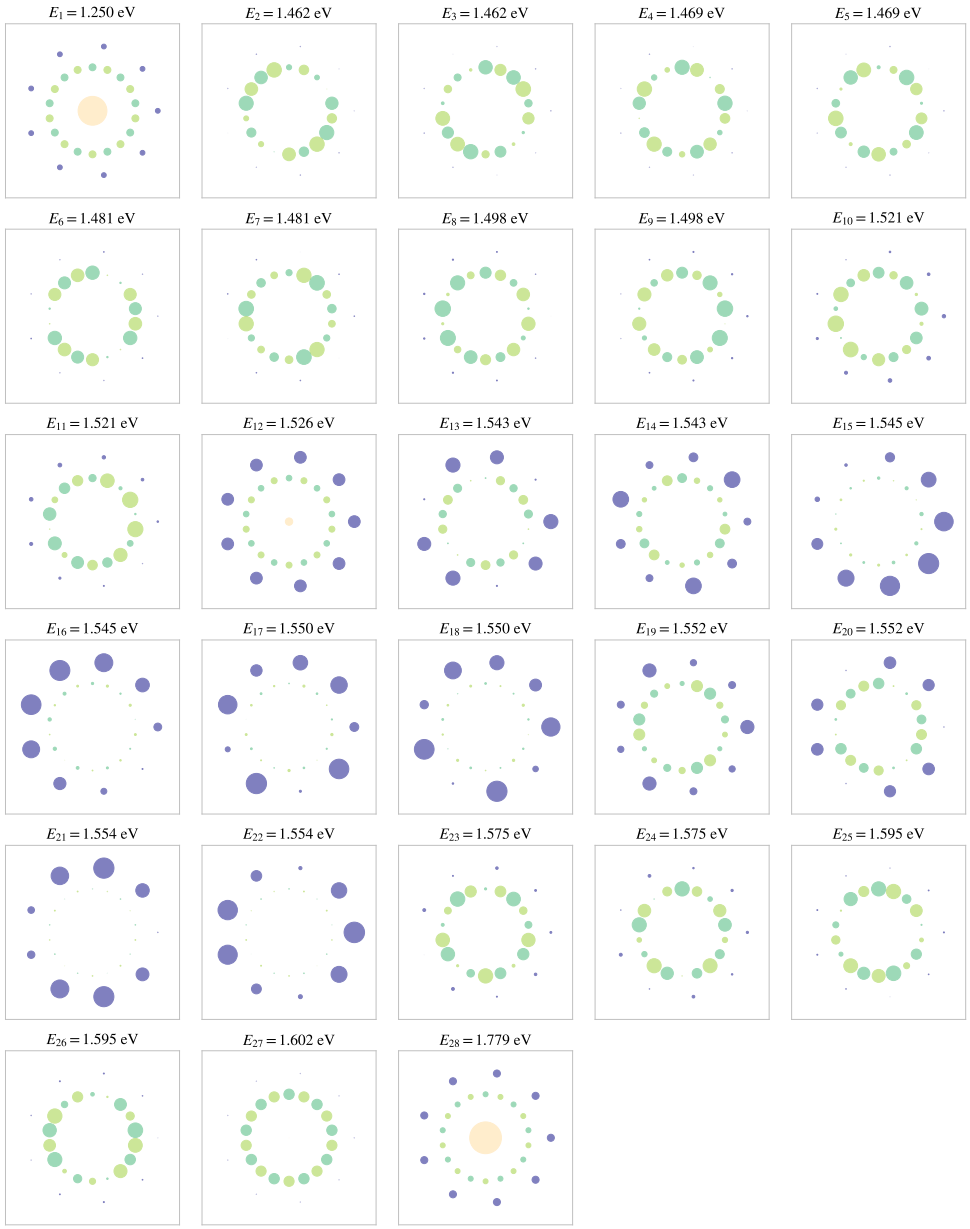

Figure 4.11. Sketch of the eigenstates of the coupled system for $g_0 = 9$ meV, where the radius of the circle representing each molecule is proportional to its population. B800 and B850 BChls are represented in blue and green, respectively, while the cavity content is depicted with a yellow circle in the center of the arrangement.

blue, while B850 molecules are in green (either light or dark so as to differentiate the two B850 BChls within the same protomer). In Figure 4.11, the eigenstates of the coupled system are represented following this sketch, where the radius of the circle representing each molecule is proportional to its population. Additionally, the cavity content is represented with a yellow circle in the center of the arrangement. These states are computed by diagonalizing the Hamiltonian in Equation 4.8 for a coupling strength $g_0 = 5$ meV. As a result of the interaction between molecules and cavity, three **polaritons** arise, corresponding to the states labelled as 1, 12, and 28 in Figure 4.11. These are the states that present cavity content. The remaining states are named **dark states**, and they are linear combinations of electronic excitations within the B800 and B850 molecules that do not couple to the cavity mode. We observe that there are eigenstates that are exclusively composed of one type of molecules, while other present an admixture of both (for instance, the states labelled as 12, 13, and 14).

Exciton dynamics

The exciton dynamics within a LH2 complex becomes modified due to its interaction with an optical cavity. We consider the initial state in which all B800 molecules are coherently excited, and compute the time evolution of the density matrix representing the coupled system by solving Equation 4.9. In Figure 4.12, the population associated with the B800 (blue) and B850 (green) molecules is plotted as a function of time, together with the occupation of the cavity (yellow) and the ground state (black). In Figure 4.12(a), the results correspond to the uncoupled case, where the B850 molecules are barely excited in the first 300 fs after the excitation of the B800 molecules. On the contrary, when the whole system is coupled to a cavity mode, these B850 pigments are fast populated, as observed in Figure 4.12(b). There, we plot the evolution of the population when the coupling strength is set to $g_0 = 15$ meV, and for the cavity frequency $\omega_C = 1.5$ eV. For instance, notice that B850 molecules present an occupation larger than 20% within only a few femtoseconds after the initial excitation of the B800 pigments.

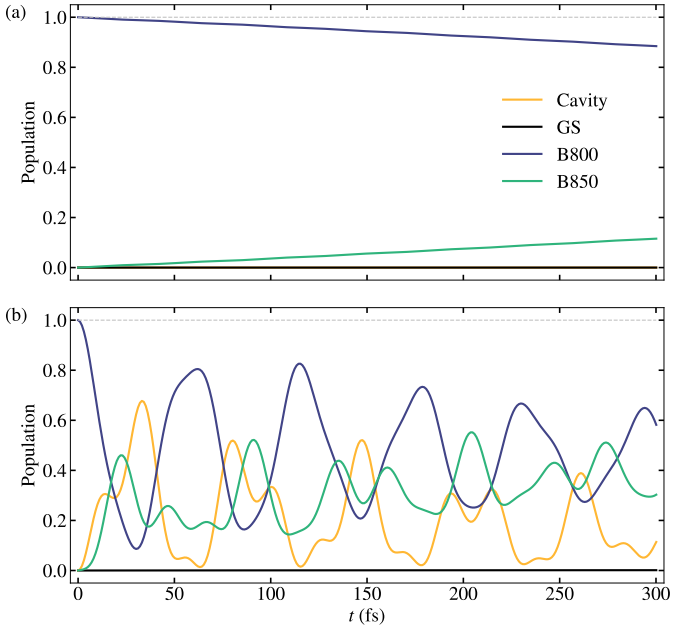

Figure 4.12. Exciton population dynamics for the LH2 complex from an initial state given by the superposition of excited B800 molecules where the system is either uncoupled from the cavity (a) or coupled to the cavity with $g_0 = 15$ meV (b).

4.2.3 Exciton dynamics within a photosynthetic unit

Once the exciton dynamics in a single LH2 complex has been studied, we consider the complete photosynthetic unit, whose structure has been previously analyzed (see Subsection 4.2.1).

A photosynthetic unit: model and theoretical description

The archetypal **photosynthetic unit** configuration consists in a ring of six LH2 antennas surrounding a single LH1 complex, as depicted in Figure 4.13. The LH1 antenna (red circle) is taken as the final stage of the exciton transfer mechanism, since our interest is focused on the excitation reaching this stage.

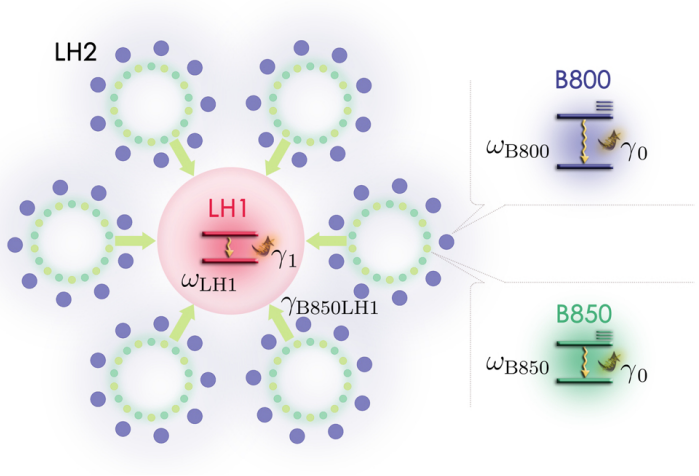

Figure 4.13. Sketch of the photosynthetic unit considered in this work: six LH2 antennas (comprising 9 B800 and 18 B850 molecules each) surrounding a single LH1 complex. The insets show the two-level system exciton model of B-molecules and LH1, which experience both radiative and vibrational decay.

Hamiltonian The dynamics within the LH1 complex is not considered, so it is modelled as a simple two-level system with transition frequency ω_{LH1}. Although being composed of a collection of B875 pigments, this simplified model for the LH1 complex is valid in the low population regime. The LH2 antennas are described as in Subsection 4.2.2, that is, a collection of $N_{\text{LH2}} = 27$ pigments are distributed in a double-ring structure. The outer ring is composed of nine B800 molecules (blue dots), while the inner ring comprises nine dimers made up of a B850a and a B850 molecule each (dark and light green dots, respectively). The **Hamiltonian** $\hat{H}_{\text{PSU}}$ describing the whole photosynthetic unit is thus given by ($\hbar = 1$):

$$\hat{H}_{\text{PSU}} = \omega_{\text{LH1}} \hat{\sigma}^{\dagger}_{\text{LH1}} \hat{\sigma}_{\text{LH1}} + \sum_{n=1}^{6} \hat{H}_{\text{LH2},n} \tag{4.10}$$

where $\hat{\sigma}^{\dagger}_{\text{LH1}}$ and $\hat{\sigma}_{\text{LH1}}$ are the fermionic creation and annihilation operators associated with the LH1 complex (Equation 2.23). The Hamiltonian $\hat{H}_{\text{LH2},n}$ associated with the n-th LH2 complex is given by Equation 4.7.

The photosynthetic unit previously modelled is placed within a **cavity** which supports a resonant mode, as shown in Figure 4.14. Starting from the previous Hamiltonian describing the photosynthetic unit (Equation 4.10), some terms need to be added so as to include the action of the cavity. Apart from the excitation of the cavity mode of frequency ω_{C}, we have to consider the coherent coupling of each BChl molecule to the radiation. The **Hamiltonian** $\hat{H}$ of the entire system reads ($\hbar = 1$):

$$\begin{aligned}\hat{H}_{\text{PSU+C}} = \omega_{\text{C}} \hat{a}^{\dagger}\hat{a} + \omega_{\text{LH1}} \hat{\sigma}^{\dagger}_{\text{LH1}} \hat{\sigma}_{\text{LH1}} + \sum_{n=1}^{6} \hat{H}_{\text{LH2},n} + \\ + g_0 \left[\eta(\hat{\sigma}^{\dagger}_{\text{LH1}} \hat{a} + \hat{\sigma}_{\text{LH1}} \hat{a}^{\dagger}) + \sum_{n=1}^{6} \sum_{i=1}^{N_{\text{LH2}}} (\hat{\sigma}^{\dagger}_{n,i} \hat{a} + \hat{\sigma}_{n,i} \hat{a}^{\dagger}) \right],\end{aligned}$$

where $\hat{a}^{\dagger}$ and $\hat{a}$ are the bosonic creation and annihilation operators for the cavity mode (Equation 2.18), and g_0 is the coupling strength between the cavity mode and some molecule within the LH2 complex. There, η stands for the dipole moment of the LH1 complex normalized to μ_{B800}. The Hamiltonian $\hat{H}_{\text{LH2},n}$ of the n-th LH2 antenna is given in Equation 4.7, and $\hat{\sigma}^{\dagger}_{n,i}$ and $\hat{\sigma}_{n,i}$ stand for the creation and annihilation operators associated with the pigment i belonging to the n-th LH2 antenna.

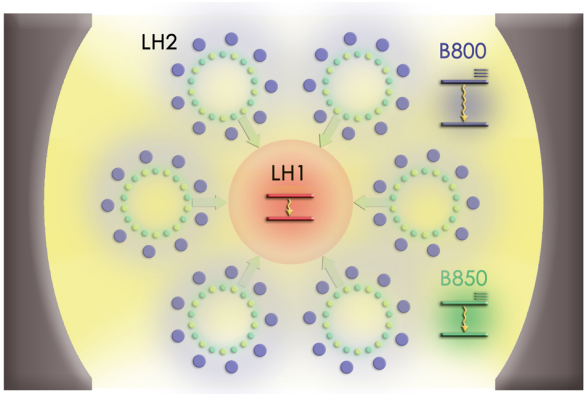

Figure 4.14. Photosynthetic unit placed inside a cavity.

Time dynamics The master equation for the whole photosynthetic unit is arranged in blocks, corresponding to the six LH2 antennas and the core LH1 complex. These blocks are connected through Lindblad terms accounting for the incoherent interaction between the LH1 complex and each one of the LH2 antennas (through those pigments in the B850 ring closest to the LH1 complex, pigments labelled as $i = 1$), specifically:

$$\frac{\gamma_{\text{B850LH1}}}{2}\mathcal{L}_{\hat{\sigma}^{\dagger}_{\text{LH1}}\hat{\sigma}_{n,1}}[\hat{\rho}]\,,$$

whose explicit form is that of Equation 2.16. There, γ_{B850LH1} represents the associated rate. The operators involved in the Lindblad term are the annihilation operator $\hat{\sigma}_{n,1}$ associated with the molecule labelled as $i = 1$ within the B850 ring of the n-th LH2 antenna, and the creation operator $\hat{\sigma}^{\dagger}_{\text{LH1}}$ associated with the LH1 complex.

The different dissipation mechanisms within the LH2 antennas are introduced in the master equation as performed in Subsection 4.2.2, where the relaxation processes are included through the corresponding Lindblad terms while the vibrational dissipation is described within the Bloch–Redfield formalism (see Equation 4.9). Finally, cavity losses are described through the Lindblad formalism, where the term $\mathcal{L}_{\hat{a}}$ involves the annihilation operator associated with the cavity mode and κ represents the associated rate.

Parameters The LH2 complexes are parametrized as in Subsection 4.2.2, so we refer to that part for the specific values of each magnitude. The transition frequency associated with the two-level system modelling the LH1 complex is set to $\omega_{\text{LH1}} = 1.417$ eV [480], and the associated decay rate is taken as $\gamma_1 = 0$ so as to avoid the decay of the LH1 excitations into the ground state (as we have mentioned, our interest is precisely focused on the excitation reaching the LH1 complex). The parameter describing the incoherent interaction between the LH1 complex and each one of the LH2 antennas is set to $\gamma_{\text{B850LH1}} = 2$ meV, which yields LH2-LH1 transition rates in agreement with experiments [481]. The dipole moment of the LH1 complex normalized to μ_{B800} is taken as $\eta = 3.8$ [482].

Energy level structure

First of all, we study the energy level structure associated with the whole system, composed of the photosynthetic unit coupled to the cavity mode. The eigenstates of the hybrid system are computed by diagonalizing the associated Hamiltonian (Equation 4.11). As a result of the strong light-matter interaction between molecules and cavity, several hy-

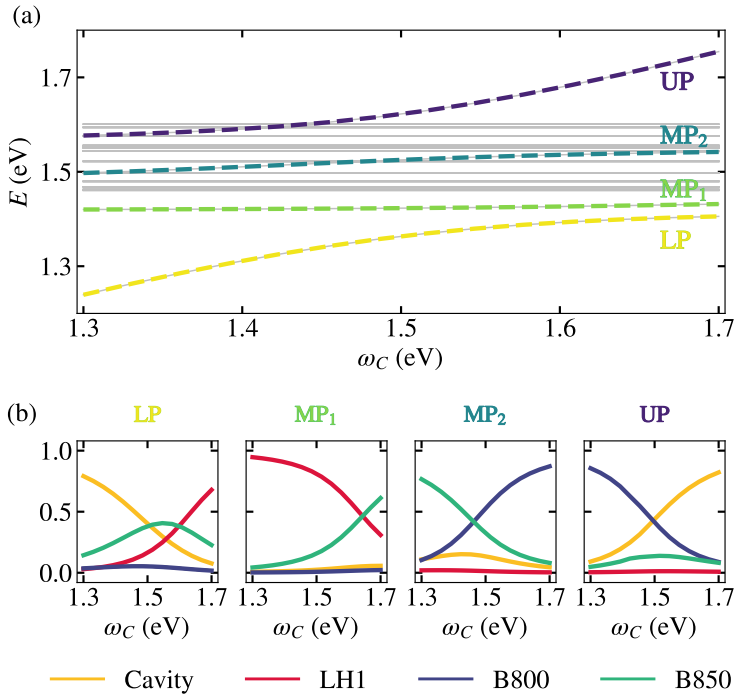

Figure 4.15. (a) Energies of the lower (LP, yellow), middle (MP1, green,and MP2, turquoise), and upper (UP, purple) polaritons as a function of the cavity frequency ω_C for a coupling strength value $g_0 = 9$ meV. (b) Coefficients representing the cavity (yellow), LH1 (red), B800 (blue), and B850 (green) content of the four polaritons (from left to right, LP, MP_1, MP_2, and UP) as a function of the cavity frequency ω_C.

brid light-matter states arise. In particular, due to the characteristics of the system, four **polaritons** appear, together with the set of the so-called **dark states**. These states are linear combinations of electronic excitations within the LH1 and LH2 complexes that do not couple to the cavity mode.

In Figure 4.15 (a), the energies of the eigenstates of the system are plotted as a function of the frequency of the cavity mode ω_C, where we have considered a light-matter strength $g_0 = 9$ meV (which introduces the system in the strong coupling regime). Effectively, four polariton branches are observed: the lower polariton (LP) in yellow, the middle polaritons MP_1 and MP_2 in green and turquoise respectively, and the upper polariton (UP) in purple. Besides, dark states are represented with continuous grey lines, which effectively remain uncoupled from the cavity field. Notice that, as $g_0 = \mu_{B800}\sqrt{\omega_C/2\epsilon_0 V_{eff}}$ (Equation 2.37), the value g_0 that we have considered corresponds to an effective volume $V_{eff} = (15\,\text{nm})^3$ for the cavity at $\omega_C = 1.6$ eV. This is attainable not only in plasmonic, but also in available dielectric cavities [483].

Figure 4.15 (b) shows, from left to right, the square of the **Hopfield coefficients** for the LP, MP_1, MP_2, and UP as a function of the cavity frequency ω_C. This yields the cavity (yellow), LH1 (red), B800 (blue), and B850 (green) components corresponding to each polariton. Note that the polariton character can be strongly modified by changing the cavity frequency. For this specific value of the coupling strength, only the LP and the UP present a substantial cavity content, but only at low and high cavity frequencies, respectively. Far from these region, LP is mostly LH1 (the element with lower energy) while UP is mostly B800 (the pigment with higher energy). In contrast, both MPs present a moderate cavity component, but combine excitonic contents coming from different pigments: MP_1 is a mixture of LH1 and B800, whereas MP_2 presents contributions from the two types of LH2 pigments. As we have seen in Section 4.1, it is precisely the hybrid character of these states (especially evident for MP_2 at $\omega_C \simeq 1.4$ eV, where B800

and B850 coefficients become similar) that may promote population transfer through the polariton-assisted mechanism [375].

Excitation dynamics (I): Uncoupled photosynthetic unit

The aim of this work is the study of the modification of the exciton dynamics in an archetypal purple bacterial photosynthetic unit due to the interaction with an optical cavity. For this reason, we explore the exciton dynamics within an uncoupled photosynthetic unit first, so as to make the comparison. The **population dynamics** for a freestanding photosynthetic unit is considered in Figure 4.16, where the initial state corresponds to the coherent superposition of excitations in all the B800 pigments. This mimics the experimental setup in which the photosynthetic unit is pumped by an ultrashort laser pulse centered around 800 nm.

We observe that the population in the B800 molecules (blue line) decays within approximately 3 ps, being transferred to the B850 molecules (green line). The excitation is then carried from the B850 molecules to the LH1 complex (red line), whose population grows within a time scale of about 20 ps after the initial excitation. Note that the time interval is much shorter than γ_0^{-1}, thus the ground state (black line) is negligibly populated in the whole exciton transfer process.

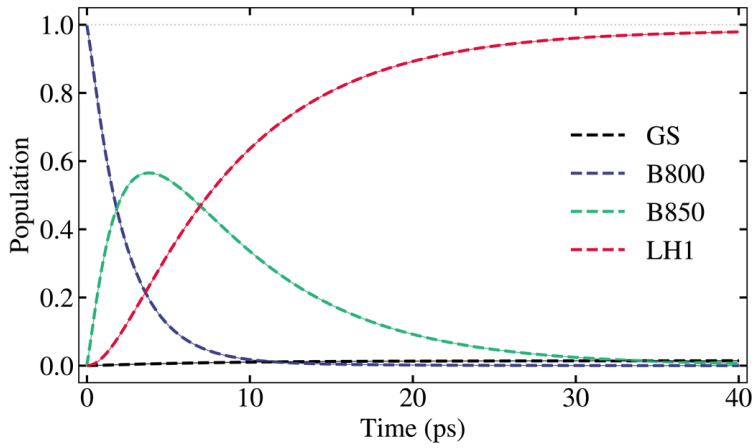

Figure 4.16. Exciton population dynamics for the photosynthetic unit from an initial state given by the superposition of excited B800 molecules in the six LH2 antennas.

Excitation dynamics (II): Photosynthetic unit within a cavity

After presenting the results for the dynamics of the freestanding complex obtained from our parametrization of the system, we discuss the exciton dynamics when the photosynthetic unit is strongly coupled to the electromagnetic field supported by the cavity. With the aim to perform a meaningful comparison against the freestanding photosynthetic unit, we set the initial state as the coherent superposition of equally excited B800 molecules, as in Figure 4.16. In particular, we choose $\omega_C = 1.6$ eV and $g_0 = 9$ meV. For this configuration, Figure 4.15 (b) shows that the LP is composed of LH1 excitations mostly, which allows us to set the final stage of the polariton-assisted energy transfer mechanism at the LH1 complex.

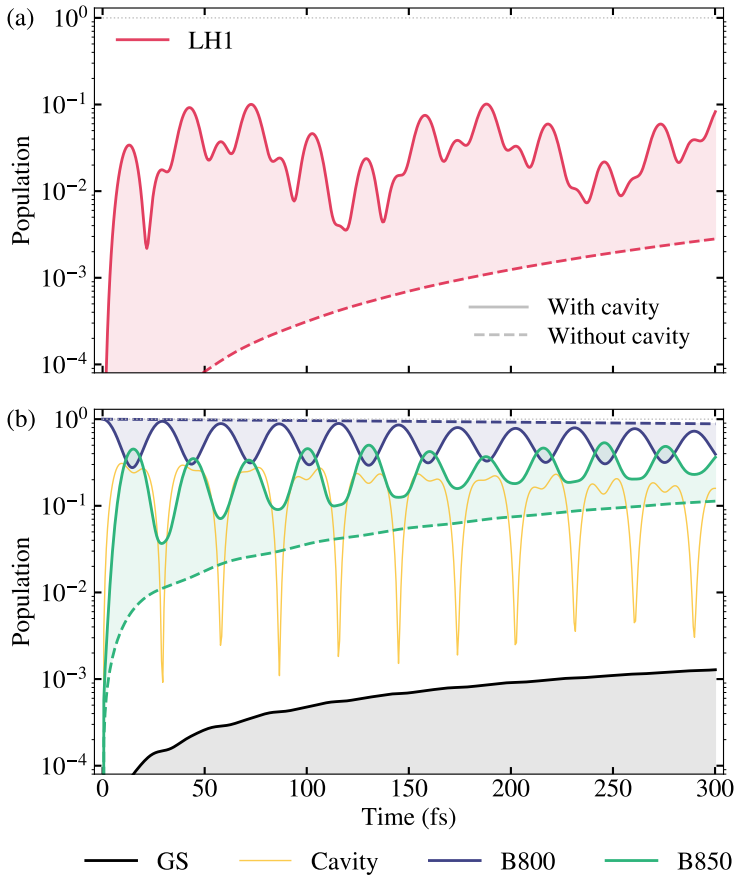

Figure 4.17. Exciton dynamics for the photosynthetic unit in Figure 4.13. (a) LH1 population versus time after the initial excitation of the B800 molecules for the PSU isolated (dashed line) and coupled to an optical cavity with $\omega_C = 1.6$ eV and $g_0 = 9$ meV (solid line). (b) Temporal evolution of the ground state (black), B800 (blue), and B850 (green) populations with (solid line) and without (dashed line) cavity. The cavity population is shown in the yellow solid line. The differences between populations have been shaded in all cases to highlight the effect of strong coupling.

Figure Figure 4.17 displays the comparison between the population dynamics for the photosynthetic unit in isolation (dashed lines) and interacting with the cavity mode (solid lines). Figure 4.17(a) shows that exciton-photon strong coupling in the photosynthetic unit gives rise to an extremely fast occupation of the LH1 complex, which acquires a significant population ($\sim$ 10%) within only a 20 fs delay. In absence of the cavity, the LH1 population is negligible in this time scale, and becomes comparable only after a few ps, see Figure 4.16. This is the main result of this work, namely, the polariton-assisted reduction in population transfer times taking place in photosynthetic units by three orders of magnitude.

Figure 4.17(b) plots the evolution of the population corresponding to the B800 (blue) and B850 (green) molecules, both exhibiting more regular Rabi oscillations than the LH1. The occupation associated with B800 pigments remains constant and close to unity for the freestanding photosynthetic unit, but the occurrence of strong coupling gives rise to a coherent energy exchange that feeds population into the other molecular and cavity (yellow line) states. Black lines correspond to the ground state, whose population is larger in the strong-coupling regime. This is a consequence of the short lifetime of the cavity relative to the antenna pigments ($\kappa \sim \gamma_0/20$). Nevertheless, this loss channel can be mitigated by using nanocavities with higher quality factors.

Varying the coupling strength The study of the population dynamics has been performed for a specific value of the light-matter coupling g_0. In Figure 4.18 we consider the same computation as in Figure 4.17, but for slightly different values of this magnitude,

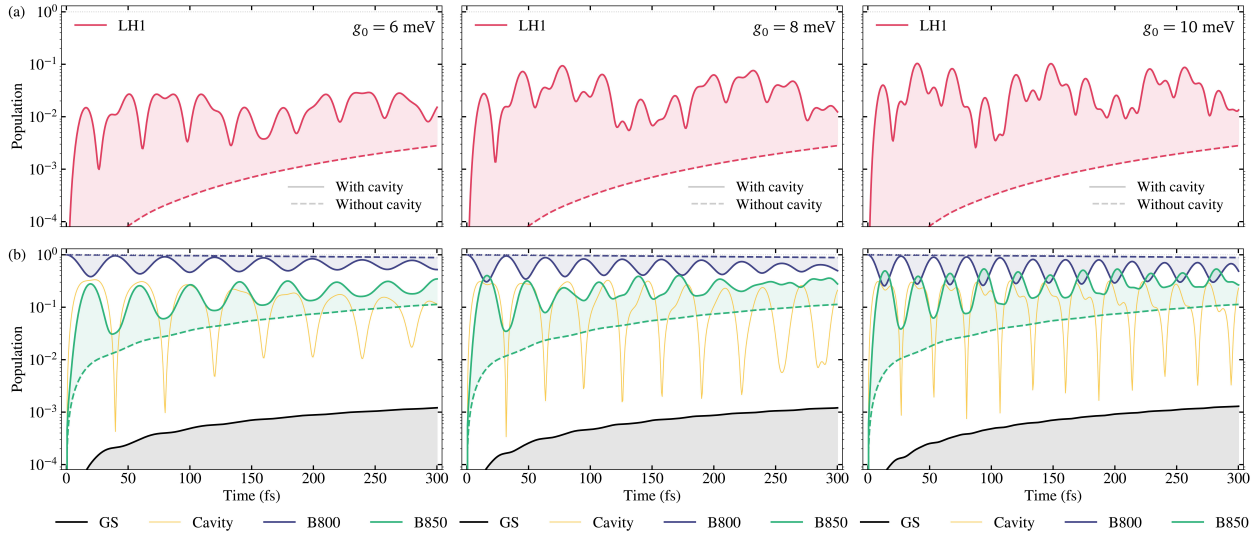

Figure 4.18.
Exciton dynamics equivalent to Figure 4.17, where $g_0 = 6$ meV [Left], $g_0 = 8$ meV [Center], and $g_0 = 10$ meV [Right]

specifically $g_0 = 6$ meV [Left], $g_0 = 8$ meV [Center], and $g_0 = 10$ meV [Right]. In all cases, the cavity frequency is set to $\omega_C = 1.6$ eV. We observe that the results are qualitatively the same. The LH1 complex is swiftly populated, and only becomes comparable to the uncoupled case after some time. Rabi oscillations in the population of the B800 and B850 molecules are also observed. Thus strong light matter coupling also leads to an extremely fast occupation of the B850 molecules after excitation of the B800 pigments.

Introducing different light-matter couplings Note that the time evolution has been always calculated assuming the same coupling strength for all the B800 and B850 pigments in the photosynthetic unit (see Equation 4.11). Importantly, our findings hold beyond this approximation, as long as the Rabi frequency remains the same as in the uniform description [375]. In order to show that, for a given Rabi frequency, we consider the case in which the couplings of all B800 and B850 molecules to the cavity mode are randomized. This would correspond to the case in which pigments are no longer aligned, thus accounting for their different orientations with respect to the cavity field.

In Figure 4.19 we plot the exciton dynamics for the photosynthetic unit coupled to a cavity mode of frequency $\omega_C = 1.6$ eV. Two different values of the light-matter coupling are considered: $g_0 = 9$ meV [Left] and $g_0 = 15$ meV [Right]. Again, panels (a) plot the population in the LH1 complex (red), while panels (b) plot the occupation in the B800 (blue) and B850 (green) molecules, together with the associated with the cavity (yellow) and the ground state (black). In this figure, the situation in which the couplings of all B800 and B850 molecules to the cavity mode are the same (continuous lines) is plotted against the case where the coupling is different for each pigment in the photosynthetic unit (dashed lines). In particular, we consider five implementations, where the coupling of the B800 and B850 molecules to the cavity mode is randomized. Specifically, we have multiplied each coupling term by a random number following a normal distribution centered at zero and with standard deviation of value 0.2, imposing the same collective coupling strength as in the uniform configuration. Notice that the solid lines in left panels ($g_0 = 9$ meV) correspond to the data in Figure 4.17.

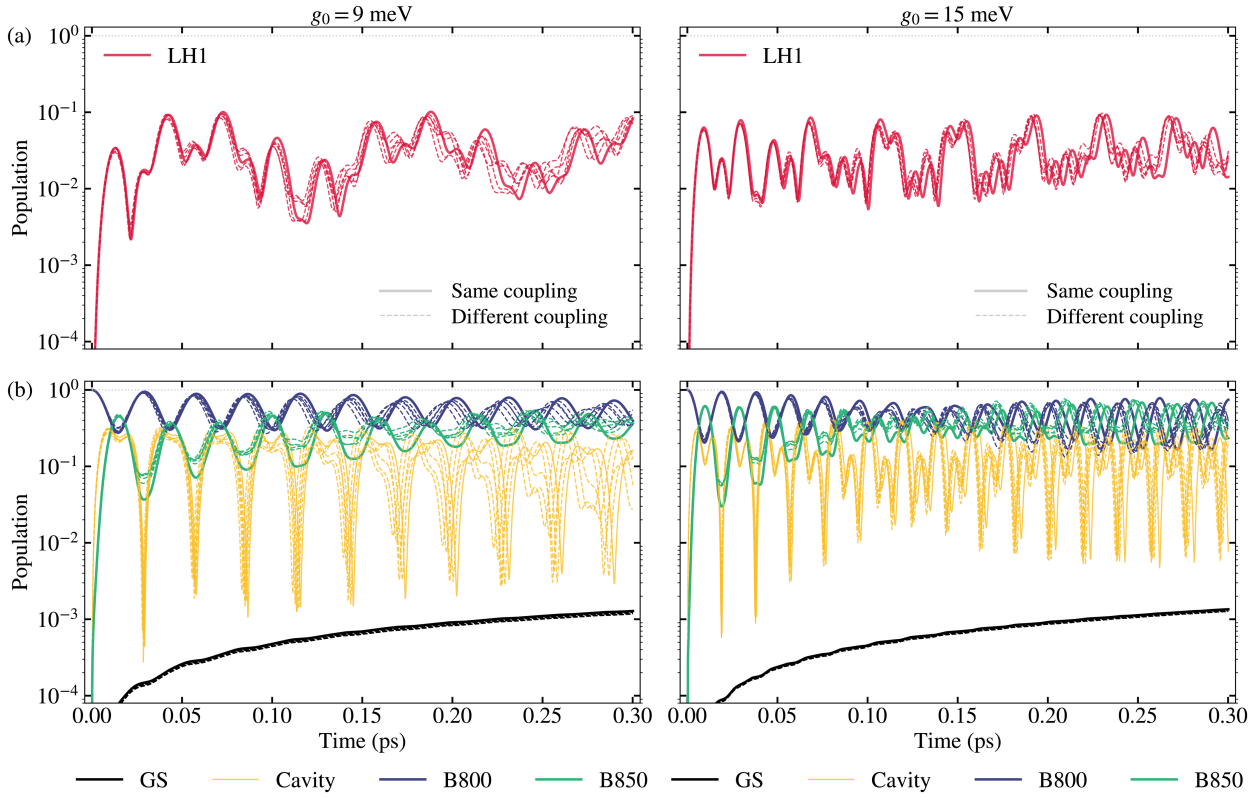

Figure 4.19.
Exciton dynamics for the photosynthetic unit coupled to an optical cavity with $\omega_C = 1.6$ eV and two different values of the light-matter coupling: $g_0 = 9$ meV [Left] and $g_0 = 15$ meV [Right]. Two situations are considered: when the couplings of all B800 and B850 molecules to the cavity mode are assumed to be the same (continuous lines) and when they are randomized (five different implementations are plotted with dashed lines). In all cases, the Rabi frequency (collective coupling strength) is the same.

For the two collective couplings considered in Figure 4.19, we observe that the exciton dynamics is only slightly modified when the pigments are no longer aligned. Therefore, we conclude that our findings are robust against variations in the couplings of each pigment in the photosynthetic unit to the cavity mode.

Varying the initial state The initial state has been always set as the coherent superposition of equally excited B800 molecules. This choice has allowed us to perform a meaningful comparison of the exciton dynamics in the photosynthetic unit with and without being coupled to the cavity. It could be argued that a more realistic initial state would consist in the excitation of the cavity mode. For this reason, we explore the population dynamics in this situation in Figure 4.20. There, we plot the exciton dynamics for a cavity frequency $\omega_C = 1.6$ eV and considering three different values of the coupling strength: $g_0 = 5$ meV [Left], $g_0 = 9$ meV [Center] , and $g_0 = 15$ meV [Right]. Panels (a) plot the occupation associated with the LH1 antenna, showing that the fast population of this complex also takes place for this initial state. Effectively, the LH1 occupation reaches a value $\sim 10\%$ within a few fs delay after the initial excitation of the cavity mode. Panels (b) plot the temporal evolution of the cavity (yellow), B800 (blue), B850 (green), and ground (black) states.

Up to this point, we have thus shown that the exciton dynamics in a photosynthetic unit is greatly modified due to the interaction with a cavity mode, regardless the excitation configuration or small changes in the coupling of each antenna pigment to the cavity mode.

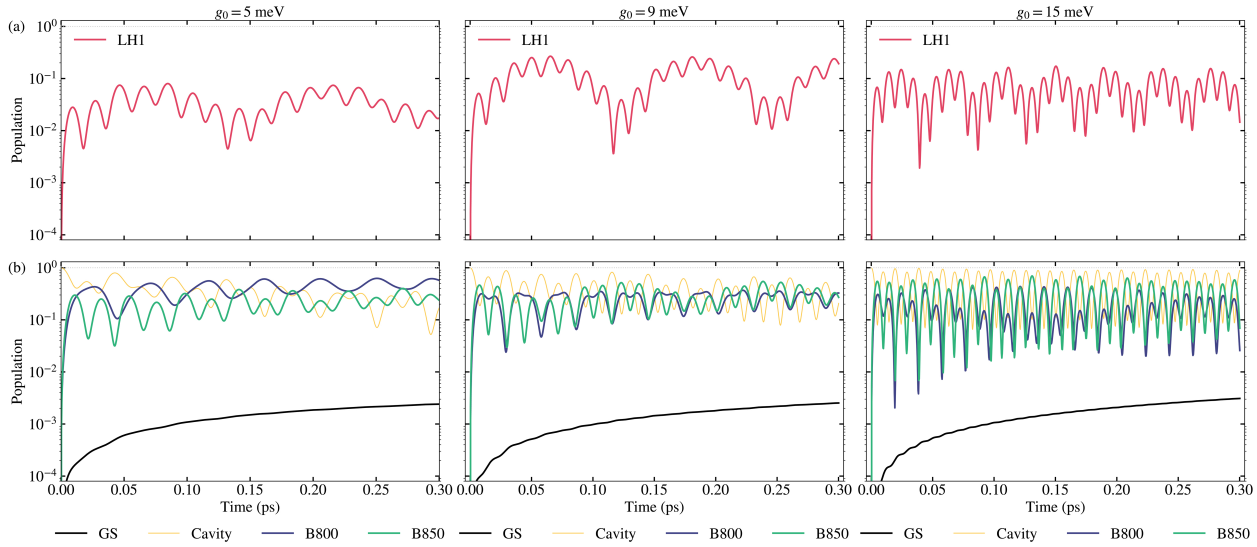

Figure 4.20.
Exciton dynamics for the photosynthetic unit coupled to the cavity mode with $\omega_C = 1.6$ eV when considering the excitation of the cavity as an initial state. Three different values of the coupling strength are considered: $g_0 = 5$ meV [Left], $g_0 = 9$ meV [Center] , and $g_0 = 15$ meV [Right]. (a) Temporal evolution of the LH1 population. (b) Temporal evolution of the ground state (black), B800 (blue), and B850 (green) populations.

LH1 population

In Section 4.1, we studied the process of energy transfer between two collection of molecules coupled to a single cavity mode. There, we showed that the phenomenon of exciton transport is mediated by the polaritons that emerge when being within the strong coupling regime. This mechanism is also present in the case here studied, where the excitation first located in the B800 molecules eventually ends in the LH1 complex thanks to the formation of polaritons. As already observed in Figure 4.15, the character of polaritons varies strongly with the frequency of the cavity which, in turn, may influence the exciton transport process. In the following, we explore the dependence of the excitation transfer from the B800 molecules to the LH1 complex on the two parameters set by the optical cavity, ω_C and g_0, and its connection with the polaritonic content of B800 and LH1 excitations.

A coherent superposition of equally excited B800 molecules is taken as the initial state, and we are interested in the population in the LH1 complex. Figure 4.21(a) displays a contourplot of the LH1 population averaged over the first 300 fs after the excitation of the B800 molecules (the time span in Figure 4.17). This magnitude is plotted as a function of the cavity frequency ω_C and the coupling strength g_0. Note that the temporal averaging naturally removes peak effects related to the irregular Rabi oscillations apparent in panels (a) of Figure 4.17 and Figure 4.18. We observe a distinct behaviour when varying each parameter. By increasing the exciton-photon coupling g_0 (that is, reducing the cavity mode volume), the LH1 population grows. Nevertheless, this enhancement is not produced in a purely monotonic fashion, but small oscillations are apparent. On the contrary, the dependence on the cavity frequency ω_C is much weaker. This is a surprising result, given the strong dependence of the Hopfield coefficients, and therefore the polariton character, on the cavity frequency (see Figure 4.15 (b)).

With the aim to understand the pattern observed for the LH1 population, we explore the character of polaritons within this region of parameters. Inspired by the work discussed in Section 4.1, we consider the combination of content of B800 and LH1 excitations

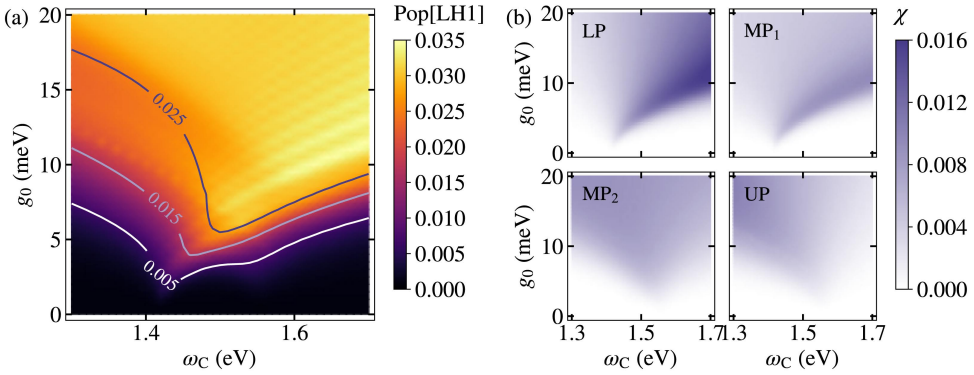

Figure 4.21. (a) LH1 population averaged over the first 300 fs after the excitation of the LH2 B800 pigments versus the cavity frequency ω_C and the photon-exciton coupling strength g_0. Color solid lines render contours of the magnitude χ (Equation 4.11). **(b)** Polariton component of B800 and LH1 excitations, encoded in the magnitude $\chi_\alpha \equiv |\langle\alpha|\text{LH1}\rangle|^2|\langle\alpha|\text{B800}\rangle|^2$, with α=LP, MP1, MP2, and UP.

on the various polaritons α. To this end, we define the magnitude χ_α as:

$$\chi_\alpha \equiv |\langle\alpha|\text{LH1}\rangle|^2|\langle\alpha|\text{B800}\rangle|^2 \,, \tag{4.11}$$

which can be simply expressed in terms of the Hopfield coefficients as: $\chi_\alpha = b^2_{\alpha\text{B800}} b^2_{\alpha\text{LH1}}$. Figure 4.21(b) plots this magnitude χ_α as a function of the cavity frequency ω_C and the coupling strength g_0 for the four polaritons: α = LP, MP$_1$, MP$_2$, and UP. We observe that, as expected, χ_α grows with g_0 in all cases, as the light-matter hybridization increases with this parameter. However, the B800 and LH1 projections over the different polaritons varies differently with respect to ω_C. For large couplings ($g_0 > 10$ meV), χ_{LP} dominates LH1 excitations for blue-detuned cavities, whereas χ_{MP_2} and χ_{UP} are the largest contributions for red-detuned ones. On the other hand, for modest couplings ($g_0 \lesssim 10$ meV), χ_{LP} and χ_{MP_1} are largest for red-detuned cavities, while χ_{MP_2} and χ_{UP} present a maximum within the spectral window between 1.5 and 1.6 eV. In order to establish a comparison between this magnitude defined in Equation 4.11 and the population in the LH1 complex, the contour lines in Figure 4.21(a) render $\sum_\alpha \chi_\alpha$. The coincidence between these lines and the pattern in the averaged LH1 population indicate that the interplay among the different polaritons play a crucial role in the fast population transfer from B800 molecules to the LH1 complex in the studied photosynthetic units.

Finally, we determine the occupation of the LH1 complex at long times. Figure 4.22 displays the LH1 population evaluated 40 ps after the initial B800 excitation. This corresponds to the maximum time displayed in Figure 4.16, when practically all the excitation

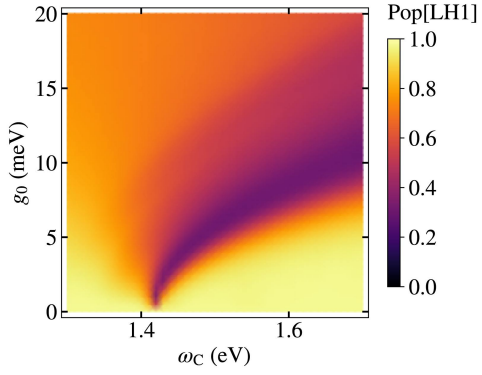

Figure 4.22. LH1 population 40 ps after the initial excitation of the system as a function of omega and g

is located in the LH1 complex for the freestanding photosynthetic unit. By comparing Figure 4.21(a) and Figure 4.22, we observe that the region where the LH1 population is maximum at short times virtually overlaps the region where the LH1 population is minimum at long times. In particular, the cavity parameters used in Figure 4.17 (namely, $\omega_C = 1.6$ eV and $g_0 = 9$ meV) maximize the LH1 population at short times as observed in Figure 4.21(a). Nevertheless, for these values, the LH1 occupation at long times is approximately 50% lower than the value reached for the freestanding photosynthetic unit (see Figure 4.16).

The origin of this low occupation of the LH1 state at long times can be found in Figure 4.15(b). Note that the Hopfield coefficients for the LP reveal that the lowest energy level in the hybrid system has only a 50% content on the LH1 state at $\omega_C = 1.6$ eV. However, the comparison between Figure 4.21(a) and Figure 4.22 proves that a compromise between populations at short and long times can be achieved at large coupling strengths ($g_0 > 10$ meV) and intermediate cavity frequencies ($\omega_C \simeq 1.5$ eV).

4.3 Conclusions

In Section 4.1, we have investigated the phenomenon of long-range energy transfer between two sets of molecules either intermixed or separated by a distance in the nanometre scale. We have presented both a numerical treatment based on the Bloch–Redfield formalism and an analytical approach to underpin the physics of this mechanism mediated by collective strong coupling. We have demonstrated the key role played by the delocalized character of the middle polariton in this process as it enables the vibrations to transfer the excitation from donor to acceptor molecules. Importantly, this non-local energy transfer is dominated by the Rabi frequency and do not depend on the particular arrangement of the molecules inside the cavity or the electromagnetic mode spatial profile. Therefore, as long as collective strong coupling is achieved, our theoretical results predict that there is no limit in the physical separation attainable between donor and acceptor molecules. Not only we have been able to unveil the physical mechanism behind vibration-driven long-range energy transfer, but our analytical approach has allowed us to deliver specific recipes to optimize the phenomenon.

In Section 4.2, we have studied the exciton dynamics within an archetypal purple bacterial photosynthetic unit, comprising six LH2 antennas surrounding a single LH1 complex. In particular, we have explored the impact that the interaction with an optical cavity has on the efficiency of exciton transport taking place in these systems. To this end, we have developed a Bloch–Redfield master equation approach that accounts for the interplay between the B800 and B850 BChl molecules within each LH2 antenna, as well as their interactions with the central LH1 complex. Using a realistic parametrization of both photosynthetic unit and optical cavity, we have investigated the formation of polaritons in the system, revealing that these can be tuned to accelerate its exciton dynamics. Specifically, our computations show that strong coupling in realistic cavities

can accelerate exciton dynamics in a photosynthetic unit in three orders of magnitude. The LH1 complex, the stage immediately prior to the reaction center, is considerably populated within only a few femtoseconds after the initial excitation of the B800 pigments present in the LH2 antenna. Besides, our model reveals the contribution of the different polaritonic states to this fast population transfer, and the dependence of the process on the frequency of the cavity mode and its effective volume (or pigment-photon coupling strength). Our theoretical findings unveil polaritonic phenomena as a promising route for the characterization, tailoring, and optimization of light-harvesting mechanisms in natural and artificial photosynthetic processes.

CHAPTER 5

CONCLUSIONS

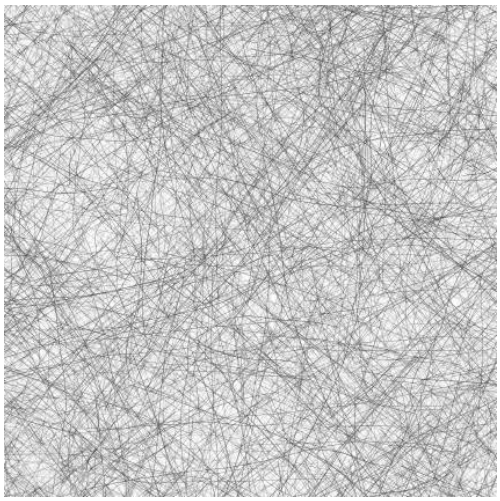

CHAPTER 5

CONCLUSIONS

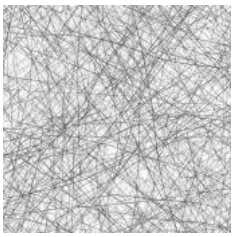

Strong light-matter coupling enables the creation of mixed light-matter states, the so-called polaritons, whose hybrid character has been used to achieve new functionalities. As it has been repeatedly stated, polaritons inherit characteristics from their two constituents, such that they present coherence due to their light component and may interact due to their excitonic part. In this thesis we have focused on two specific problems where either photons or excitons benefit from strong light-matter interactions.

PHOTONS

In the first part of the thesis, we have investigated the complex photon statistics phenomenology that emerges from the coupling of a mesoscopic ensemble of quantum emitters to the electromagnetic field within a cavity. Two different experimental setups have been explored, namely, a collection of organic molecules coupled to a plasmonic nanocavity and a collection of quantum dots embedded in a dielectric microcavity.

From our results, we have concluded that both plasmonic and dielectric cavities enable photon correlations in mesoscopic ensembles involving several tens of emitters. The presence of negative correlations is robust against the variation of the system parameters. This makes strong light-matter coupling a promising route for the generation of nonclassical light beyond the single-emitter level.

EXCITONS

In the second part of the thesis, we have analyzed the modification of the exciton dynamics due to the coupling to the electromagnetic field within a cavity. The formation of delocalized states within the strong-coupling regime allows for the enhancement of the spatial range and rate of exciton transport in diverse platforms.

First, we have studied the phenomenon of long-range energy transfer between two collections of molecules. In accordance with actual experimental realizations, two different arrangements of donor and acceptor molecules within the cavity have been considered —they are either intermixed or physically separated by a dividing barrier. Our numerical and analytical results show that energy transfer from donor to acceptor molecules takes place with the participation of the middle polariton. Its delocalized character and

mixed composition (involving both donor and acceptor states) are crucial aspects in this mechanism, which allows for energy transfer beyond the nanometre scale.

Second, the exciton dynamics in an archetypal bacterial photosynthetic unit has been considered. We have demonstrated that the exciton dynamics within these complexes is greatly modified by its interaction with a cavity mode: this process is accelerated by three orders of magnitude. This yields a significant occupation of the complex at the end of the energy-transfer process.

Therefore, the formation of hybrid light-matter states within the strong coupling regime enhances the exciton-transport mechanism in these two systems. Our theoretical models provide physical insights into the phenomenon of polariton-mediated energy transfer, which would help to optimize the exciton-transport process in diverse natural and artificial systems.

CONCLUSIONES

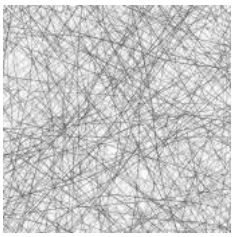

La interacción fuerte entre la luz y la materia permite la creación de estados compuestos de luz y materia a la vez, los llamados polaritones, cuyo carácter híbrido ha sido empleado para lograr nuevas funcionalidades. Tal y como hemos comentado en repetidas ocasiones, los polaritones heredan características de sus dos constituyentes, de forma que presentan coherencia debido a su componente de luz y pueden interaccionar debido a su parte excitónica. En esta tesis nos hemos centrado en dos problemas específicos donde o bien lo fotones o bien los excitones se benefician de las interacciones fuertes entre luz y materia.

FOTONES

En la primera parte de esta tesis hemos investigado la compleja fenomenología que aparece en la estadística de los fotones como resultado del acoplamiento de un conjunto mesoscópico de emisores cuánticos al campo electromagnético de una cavidad. En particular, hemos considerado dos montajes experimentales diferentes: un conjunto de moléculas orgánicas acopladas a una cavidad plasmónica y un conjunto de puntos cuánticos embebidos en una microcavidad dieléctrica.

A partir de los resultados de nuestra investigación, hemos determinado que tanto las cavidades plasmónicas como las dieléctricas pemiten la generación de correlaciones en los fotones en conjuntos mesoscópicos de varias decenas de emisores. La presencia de correlaciones negativas es robusta frente a la variación de los parámetros. Esto hace del régimen de acoplamiento fuerte entre luz y materia un camino prometedor en el campo de la generación de luz no clásica más allá del caso de un solo emisor.

EXCITONES

En la segunda parte de esta tesis hemos analizado la modificación de la dinámica de los excitones como resultado del acoplamiento al campo electromagnético dentro de una cavidad. La formación de estados deslocalizados en el régimen de acoplamiento fuerte permite aumentar tanto el alcance como el ritmo del transporte de excitones en diversas plataformas.

Primero, hemos estudiado el fenómeno de transferencia de energía a largas distancias entre dos conjuntos de moléculas. De acuerdo a las realizaciones experimentales

disponibles, hemos considerado dos distribuciones diferentes de las moléculas donadoras y aceptadoras dentro de la cavidad: éstas se encuentran entremezcladas o separadas físicamente por una barrera divisora. Nuestros resultados, tanto analíticos como numéricos, muestran que la transferencia de energía entre las moléculas donadoras y aceptadoras tiene lugar con la participación del polaritón intermedio. Su carácter deslocalizado y su composición mixta (la cual involucra estados donadores y aceptadores) son aspectos cruciales en este mecanismo, que permite la transferencia de energía más allá de la escala nanométrica.

En segundo lugar, hemos considerado la dinámica de excitones en una unidad fotosintética típica de ciertas bacterias. Hemos demostrado que la dinámica de los excitones entre los diferentes compuestos se modifica en alto grado como resultado de su interacción con un modo de cavidad: el proceso se acelera en tres órdenes de magnitud. Esto hace que el compuesto situado al final del proceso de transferencia de energía se vea significativamente poblado.

Por lo tanto, la formación de estados híbridos de luz y materia en el régimen de acoplamiento fuerte mejora el mecanismo de transporte de excitones en estos dos sistemas analizados. Nuestros modelos teóricos ofrecen una explicación física de este fenómeno de transferencia de energía mediado por polaritones, los cuales podrían ayudar a optimizar el proceso de transporte de excitones en sistemas diversos.

APPENDICES

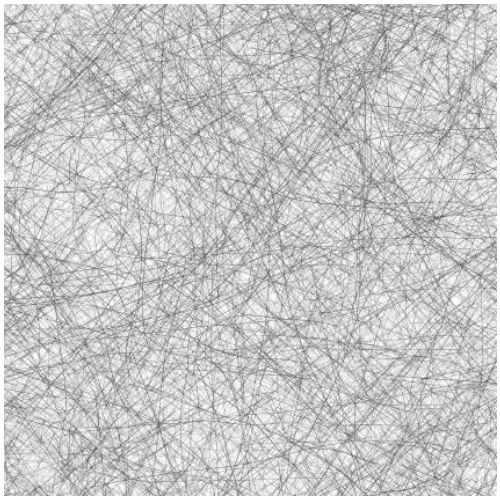

APPENDIX A

POLARITONS: WORKING WITHIN THE STRONG COUPLING REGIME

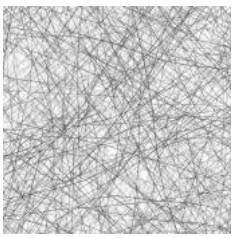

The interest raised by the strong coupling regime stems from the multiple phenomena exhibited by polaritons, which are otherwise impossible to observe. The distinctive characteristics inherited from their two constituents enable polaritons to present features that neither light nor matter excitations hold themselves. These singular properties are translated into practical applications, with the design of polaritonic devices and the prospect of new quantum optical systems. Besides, the strong coupling regime offers the possibility to explore light-matter interactions, hence its importance from a fundamental point of view as well. In this Appendix, we review the first experimental realizations of strong coupling (Section A.1), followed by the main properties of polaritons and their potential applications (Section A.2). There exist interesting reviews that focus on the strong coupling regime in both semiconductor [484, 485] and plasmonic [430] cavities, and also devoted to the ultrastrong coupling regime [61].

A.1 Experimental realizations of strong coupling

Atoms in cavities

The first experiments aiming for the strong coupling of matter excitations with a cavity mode were performed with atoms in microwave cavities. In particular, they were originally carried out with **Rydberg atoms** [83, 84], where one-atom maser experiments tried to reproduce the quantum phenomena emerging from the Jaynes–Cummings Hamiltonian [486]. These atoms benefit from a large electric dipole moment between neighbouring energy levels (leading to large values of the coupling to the radiation field), where the resonant frequency lies in the microwave domain. This also facilitates its physical implementation in large-size cavities, where atoms need to be kept in the same position (with

a constant and precise value of the coupling strength) for a relatively long time. At the same time, these systems are characterized by large mode volumes, which is detrimental to the achievement of large values of the light-matter coupling. Rydberg atoms present low spontaneous emission rate, and the preferential transition is not perturbed by others, thus constituting ideal realizations of two-level systems [83].

The strong coupling was first observed for a single Rydberg atom in a **microwave cavity** by Rempe *et al.* in 1987 [85], soon followed by the work of Brune *et al.* [86]. The first observation of strong coupling in the **optical regime** took place in 1989, when Raizen *et al.* obtained the characteristic mode splitting for a collection of atoms interacting with a single-mode of an optical cavity [87]. This experiment was followed by others, where the associated photon statistics was also explored [487, 176]. Rabi splitting with a **single atom** was first reported in 1992 by Thompson *et al.* [88]. Since then, different configurations have been explored, including the trapping of individual atoms in the strong coupling regime [488, 489].

Inorganic semiconductor microcavities

Advances in **semiconductor microcavities** led to the detection of strong coupling in various solid-state platforms, reaching Rabi splitting values of the order of 10 meV. In contrast to atoms, the use of **quantum dots** embedded in these solid implementations offers the possibility to reach smaller cavity volumes, meeting in turn larger coupling strengths. The tight confinement of light is combined with the important electric dipole moments displayed by quantum dots (larger than typical values of atomic transitions), making this setup an ideal candidate for the observation of strong coupling. Besides, solid-state platforms are free from the elaborated experimental techniques demanded by single atoms, associated with their trapping and cooling. The control of the spatial overlap between emitters and cavity mode, as well as the possibility to tune the frequency of both emitters and resonant mode of the cavity, are important advantages. As a counterpart, solid-state systems present phonon interactions that make the transition broader, a problem that is not present when dealing with perfectly isolated atomic systems.

Since the first experimental realization of strong coupling with quantum wells excitons in 1992 by Weisbuch *et al.* [490], inorganic semiconductor microcavities have been widely used. Anticrossing between the exciton and the photon modes [491] and vacuum Rabi oscillations [492] were soon reported. In these experiments, several Wannier excitons supported by semiconductor quantum wells are coupled to the electromagnetic mode confined in a monolithic solid-state system. Although strong coupling in microcavities containing inorganic materials is usually observed at low temperatures, strong coupling fingerprints were also found at room temperature by Houdré *et al.* in 1994 [493]. Strong coupling with a **single quantum emitter** was first obtained in 2004 for various semiconductor microcavities structures: in planar micropillars by Reithmaier *et al.* [89], in whispering-gallery microdisks by Peter *et al.* [494], and also with a photonic crystal cavity mode by Yoshie *et al.* [90]. All these experiments were performed at low temperatures, around 30 K. These experiments were followed by many other realizations in different setups.

Organic semiconductor microcavities

In the way of achieving stronger light-matter interactions, **organic semiconductor microcavities** appeared as a great opportunity. Organic molecules display large dipole moments and high densities, thus leading to large values of the light-matter coupling. In particular, **J-aggregates** present small linewidths and large transition dipole strengths, making possible to achieve Rabi splitting values more than 10 times higher than the typical values within inorganic semiconductor cavities. Apart from the prospect of having Rabi splitting values of the order of 100 meV, organic materials offer a platform for realizing strong coupling at **room temperature**. Unlike Wannier excitons in inorganic semiconductors, whose associated low binding energies usually require cryogenic temperatures, Frenkel excitons in organic semiconductors tend to present large binding energies that makes them more stable.

Strong coupling using **organic molecules** was first observed by Lidzey *et al.* in 1998 [91]. There, a Rabi splitting value of 160 meV at room temperature was observed in a planar microcavity containing a porphyrin dye as the optically active material. Soon after, strong coupling was also reported using J-aggregates of a cyanine dye, showing Rabi splitting values of the order of 80 meV [495, 496]. Besides these particles, diverse organic materials are used to provide the matter excitations, such as other dye molecules or **organic crystals** [497]. Strong coupling was also obtained between a cavity photon and multiple vibronic transitions in a single material [498] and with molecular vibrational modes of the electronic ground state [499, 500], due to the absorption features displayed by organic compounds (see Section 2.4 and Appendix F). Organic semiconductor microcavities also provide a suitable platform to reach the ultra-strong coupling regime [434, 501], where Rabi splitting values of the order of 1 eV have been observed.

Not only dielectric microcavities, but also all-metal microcavities (in which the tighter confinement of the field favours the coupling to the matter component) have been used with organic semiconductors, where a Rabi splitting value in excess of 300 meV is achieved at room temperature [502]. Indeed, excitons in organic materials are coupled to all kinds of electromagnetic modes, not only to cavity photons but also to localized surface plasmons or surface plasmons polaritons, as well as to surface lattice resonances.

Organic molecules in plasmonic cavities

The development of plasmonic nanostructures able to confine light beyond the diffraction limit has opened the possibility to reach even stronger coupling strengths than those provided by the previous semiconductor structures. Despite the substantial losses present in plasmonic structures, the large dipole moments and high densities displayed by organic molecules have helped to achieve the strong coupling regime in these setups. Different configurations have served as a basis to build **plasmonic nanocavities**, adequately prepared for hosting both organic and inorganic emitters.

Strong-coupling was first reported using J-aggregates coupled to surface plasmon polaritons by Bellessa *et al.* in 2004, reaching a Rabi splitting value of 180 meV at room temperature [34] (300 meV in [92]). This experiment was soon followed by many other realizations involving J-aggregates coupled to plasmonic resonances on nanostructured

surfaces [35, 503] and metallic nanorods assemblies [504]. The observation of coherent Rabi oscillations was also reported [505]. Apart from J-aggregates, some other organic molecules have been used —coupled to both surface plasmon polaritons [506, 507] and to plasmonic surface lattice resonances [508, 509]—, as well as excitons in inorganic materials [510, 511]. Strong coupling has been also obtained with organic excitons coupled to localized surface plasmons formed in diverse nanostructures, such as in nanoshells [512], in single metallic dimers [513], or in a single silver nanoprism [38]. Strong coupling with a single emitter was first reported by using bowtie dimers by Santhosh *et al.* [93] and a nanoparticle-on-mirror cavity by Chikkaraddy *et al.* [94], both in 2016.

Plasmonic cavities provide tiny mode volumes because of the confinement of the electromagnetic field beyond the diffraction limit. On the other hand, the high metal losses makes them to present very low values of the Q-factor. Many configurations have been studied to increase the Q/V ratio. The development of **hybrid cavities** composed of different material systems seems to be a promising route. They combine the benefits of both plasmonic and photonic elements. For instance, metal nanoparticles are assembled to a dielectric photonic crystal cavity, yielding quality factors close to 1000 [514]. Other structures are fabricated by coating the surface of a dielectric or semiconducting core with a thin metal layer [515, 516]. There are many examples where hybrid cavities are used to reach the strong coupling regime.

Other systems

Trapped ions and artificial atoms, such as excitons in 2D materials and NV-centers, should be also mentioned as other types of emitters used in this field. **Trapped ions** are also demonstrated to reach the strong coupling regime [517]. Their drawback is that the dimension of the cavity is not smaller enough to achive large values of the light-matter coupling, so that many ions are necessary.

Excitons in **TMDCs** are ideal candidates to reach the strong coupling regime at room temperature [518], since they present high biding energies (up to several hundreds of meVs [519, 520]) and large oscillator strengths [521]. Strong coupling of different TMDCs have been obtained in dielectric microcavities since 2014, mainly in Fabry–Perot resonators in which the active layer is kept between two distributed Bragg reflectors. For instance, a Rabi splitting of 46 meV was obtained by embedding a monolayer of MoS_2 inside a dielectric microcavity at room temperature [522], a splitting of 20 meV by embedding a monolayer of $MoSe_2$ at cryogenic temperatures [523], and a splitting of 40 meV by embedding a monolayer of WS_2 at an intermediate temperature (110-230 K) [524]. Strong coupling has been also reported with different TMDC monolayers embedded in dielectric distributed Bragg reflectors recovered with a thin metallic cap [525], where the Tamm plasmon states arise [526, 527]. Nevertheless, splittings at room temperature are barely resolved and on the order of thermal energies, so larger values of the energy gap are required. The use of metallic Fabry–Pérot cavities has led to larger values of the Rabi splitting, reaching values of about 100 meV with WS_2 monolayers [528, 529]. Room temperature strong coupling has been also pursued in different plasmonic structures, including lattice resonances in ordered arrays of metallic nanostructures [530] and localized surface plasmons (for instance, in metallic nanoprisms [531] and in nanoparticle-on-mirror

cavities [532]).

NV-centers are able to achieve the regime of strong coupling when placed inside a microwave cavity. Unlike atoms, NV-centers do not require trapping techniques nor large magnetic fields to reach the resonance frequency. This makes them attractive systems to couple to the microwave photons trapped in superconducting circuits [533], together with the long coherence time that they exhibit [534]. Strong coupling was observed for a collection of NV-centers in a superconducting resonator [535, 536], as well as also for ensembles of spins in other solid state materials [537].

Strong coupling has been also achieved in **mechanical resonators**. It has been observed the normal mode splitting when a mechanical resonator is coupled to an optical cavity [538]. Apart from these mechanical systems, **superconducting circuits** also provide a platform to reach the strong coupling regime, where the coherent interaction of a superconducting two-level system with a single microwave photon has been reported [539]. These superconducting devices have been also shown to behave as artificial atoms, where quantum optical effects have been observed for a single superconducting macroscopic two-level system [540]. Superconducting devices that behave as an artificial atom and can be developed as qubits in quantum information processing applications. These macroscopic superconducting devices can be integrated in electronic circuits and help in the development quantum optical systems on a chip.

A.2 Properties of polaritons and applications of strong coupling

The hybrid light-matter composition of polaritons makes them combine properties inherited from each constituent, namely, polaritons present the distinctive **coherence** of light and the mutual **interactions** displayed by excitons. This gives rise to a number of new interesting phenomena and applications as well, which will be outlined in the following.

Bosonic character First of all, we should mention the type of statistics followed by our subject matter. Composed of two fermions, excitons exhibit bosonic properties at low densities [541, 542]. Nevertheless, as they are **composite bosons**, rather than pure bosons, their composite constitution may become relevant for higher densities [543]. Polaritons, as a mixture of photons and excitons, thus behave as bosons as well [544, 545] —the Pauli exclusion principle does not apply, and large occupations of the same state are allowed. This fact is precisely in the basis of a variety of phenomena displayed by polaritons.

Multiple **nonlinear effects** are observed in polaritons, resulting from the interaction between their excitonic component. In particular, polariton-polariton interactions in semiconductor microcavities lie behind effects such as stimulated scattering, polariton condensation, or superfluidity, to name a few.

Bottleneck effect In semiconductor microcavities, different optical wavevectors are attained by varying the angle of the light with respect to the axis of the cavity. This results in the familiar shape of the **dispersion relations** within the strong coupling regime, which give the energy of the polaritons as a function of the angle (or, alternatively, the wavevector $\boldsymbol{k}$). An example is shown in Figure A.1, where the energies of the non-interacting cavity and exciton are depicted in dashed lines. There exists an energy minimum at $k = 0$, which corresponds to light travelling along the cavity axis. The dispersion relations associated with the lower polariton (LP) and the upper polariton (UP) are depicted in purple and green respectively. Notice that the dispersion relation associated with the LP branch is exciton-like for large values of the (in-plane) wavevector, while it is photon-like at small wavevector values. Indeed, around $k \simeq 0$, it presents the parabolic dispersion relation that is characteristic of photons. The modification of the dispersion curves with the formation of polaritons lead to the so-called **bottleneck effect** [546, 547], namely, the relaxation from large wavevector states towards $k \simeq 0$ is very slow [548]. However, it was found possible to overcome such obstacle and obtain large occupation numbers in the LP final state through the process of stimulated scattering [549].

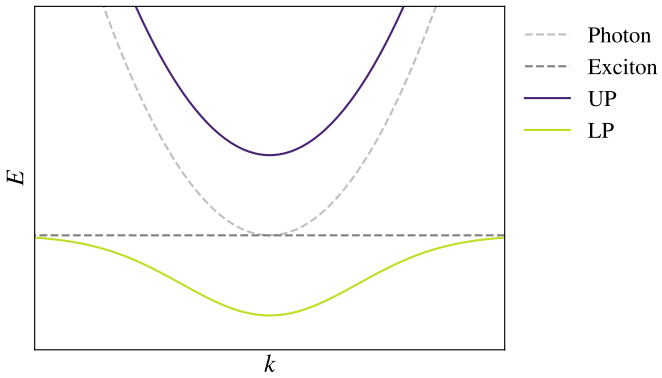

Figure A.1. Dispersion relation corresponding to the LP (yellow) and the UP (purple) as a function of the in-plane momentum k. The energies of the non-interacting exciton and cavity field are shown in dashed lines.

Stimulated polariton scattering Various photoluminescence experiments involving strong coupling in semiconductor microcavities reported a **nonlinear behaviour** in the emission in the late 1990s [550, 551], explained as a stimulating effect [544]. In the pump-probe experiment carried out by Savvidis *et al.* [95], a pump pulse excites resonantly polaritons in the LP branch carrying the wavevector $\boldsymbol{k}$ that corresponds to the particular angle of incidence of the laser. A probe pulse is set at normal incidence ($k = 0$), and its reflected spectrum is measured. For a critical angle, a pair of pump polaritons scatter to produce a (signal) polariton with $k = 0$ —which genererates some gain— together with a second (idler) polariton with a higher wavevector (such that both energy and momentum are conserved). **Stimulated scattering** is evidenced by an enormous peak in the probe signal, displaying an optical gain approaching 100. This experiment was soon followed by others [552, 553], showing final-state stimulation even at high temperature [554]. A theory for polariton amplification was proposed by Ciuti *et al.* [96]. Stimulated scattering leads to the concentration of polaritons in two specific states, with final-state occupancies close to one.

Parametric oscillation Once a reservoir of identical polaritons is created through a pumping pulse, a scattering mechanism is needed to transfer some of these reservoir polaritons to the ground state. Pure bosons without charge do not present such a mech-

anism, but polaritons do [545]. It is precisely their excitonic part that allows for the parametric process in which, above a pump strength threshold, a couple of pump polaritons scatter to produce both signal and idler modes such that the energy and momentum are conserved (polariton-polariton parametric scattering) [96, 555]. Apart form the **parametric amplification** previously mentioned [95, 556], **parametric oscillation** can be also produced, where a coherent population in the signal mode appears without the presence of a probe pulse [97, 98]. The process of parametric conversion allows for the generation of twin or entangled photons, used in quantum optics applications such as quantum crypography. Since the signal and idler modes present a frequency shifted with respect the pump pulse, it would also serve to access spectral regions difficult to reach with available devices. The analogy between polaritons and optical parametric oscillators has been thoroughly explored [557], pointing out new effects that strongly-coupled systems may exhibit [558, 559]. The polarization characteristics and the spin dynamics of these polaritons have been intensively studied both theoretical [560, 561] and experimentally [562, 563].

Polariton lasing The phenomenon of stimulated scattering may lead to a macroscopic occupation of the ground-state polariton. Due to the leakage of the photonic component of these polaritons, **coherent light** starts to be emitted. This process led to the development of a new type of coherent light source —the **polariton laser**. The creation of a polariton condensate able to emit coherent laser light was first discussed by Imamoğlu *et al.* in 1996 [99, 564], and experimentally pursued from then on. After some initial attempts [565, 566] that were finally interpreted within standard lasing [567], polariton lasing was first achieved by Deng *et al.* in 2003 [100]. In photon lasing, photons are the particles that develop coherence through stimulating emission. On the contrary, in this new source, the coherence comes from polaritons —the coherent emission is simply photon emission from the coherent, condensed state. Polaritons decay mainly due to its photonic component, and those photons than scape the cavity keep some information of the initial polariton state, such as energy, momentum, spin, and phase [568]. Another difference between photon and polariton lasing is connected to the origin of such stimulated emission: while it is the photon emission itself that is stimulated in the photon laser, stimulation and emission are separated processes in a polariton laser. There, the stimulated process is the polariton scattering to the high-density state. This allows for a coherent emission without the requirement of population inversion (that is, the requirement of having more population in an excited state than in the ground state), that translates into the prospect of very low threshold coherent sources [569, 570].

Polariton condensation Given the bosonic character of polaritons, one could expect a phase transition from the incoherent reservoir of polaritons to a coherent ground state [571]. Below a critical temperature (or, equivalently, above a critical density), polaritons would spontaneously occupy the ground state forming a **Bose–Einstein condensate** (BEC). Light mass particles favour the formation of the condensate, and this is precisely one of the main characteristics of polaritons in semiconductor cavities. They possess an effective mass four orders of magnitude lighter than the exciton mass, and nine orders of magnitude if compared to rubidium atoms (for which BEC was observed at temperatures below 200 nK [572]). This means that a macroscopically occupied polariton state could take place in these solid-state platforms at standard cryogenic temperatures. After the report of some evidences of spontaneous coherence [573], **polariton condensation**

was first observed by Kasprzak *et al.* in 2006 [101], showing a massive occupation of the ground-state polariton, with an increase of both temporal and spatial coherence. Soon after, Balili *et al.* reported condensation of polaritons in a trap [102]. These first realizations were obtained in a state of non-equilibrium, given the typically short lifetime associated with polaritons (comparable to thermalization times). Nevertheless, the observation of polariton condensation in thermal equilibrium was finally achieved [574].

Experiments involving CdTe-based [101] or GaAs-based [102, 575] microcavities require temperatures of about 10 K to obtain the condensation of polaritons. The use of new **inorganic materials**, such as GaN [576] and ZnO [577], have allowed for polariton condensation at higher temperatures [578]. Indeed, there have been several **room-temperature realizations** of polariton lasing and polariton condensation in these inorganic platforms [579, 580]. This is an important issue for device applications, together with the possibility of exciting by electric injection rather than by an optical source — electrons and holes are injected separately before relaxing and forming polariton states [581]. Different realizations of an electrically pumped polariton laser have been already reported [582, 583]. Although we have only referred to polaritons in inorganic cavities so far, polariton lasing have been also found in organic microcavities [584] and in plasmonic structures [435]. **Organic materials** provide higher critical temperatures, although the shorter polariton lifetimes and the weaker nonlinearities displayed by organic polaritons makes them less favourable to the observation of some other resonant nonlinear processes. Polariton lasing and polariton condensation at room-temperature have been reported in several organic systems [585, 586], such that a broad range of wavelengths are spanned [587].

Superfluidity and other effects Polariton condensation can lead to some other related phenomena, including superfluidity, vortex formation, and Berezinskii–Kosterlitz–Thouless and Bardeen–Cooper–Schrieffer physics [588, 589]. **Superfluidity** consists in the possibility to flow without friction [590], and it is a manifestation of macroscopic coherence. Theoretical works pointed out a superfluid regime for polaritons in a microcavity [591, 592], and some experimental evidences were found by Amo *et al.* in 2009 [593, 594]. Room-temperature superfluidity has been also reported [595]. One of the features of superfluidity is the appearance of **quantum vortices** [596]. The formation of quantized vortices in the condensed phase of a polariton fluid have been experimentally observed [597, 598, 599], and also theoretically studied [600]. The optical spin Hall effect in the polaritons generated in a semiconductor microcavity is another phenomenon observed in this platform [601, 602]. Some efforts are devoted to the observation of proper quantum effects in polaritonic systems.

Quantum coherence The coherence properties inherited by polaritons lie behind some interesting features they display [603], as the ones that we have previously mentioned. The phenomenon of polariton lasing manifests the macroscopic coherence created from the stimulated polariton scattering process, and the condensate of polaritons implies coherence of many particles that occupy the same macroscopic state. Long-range spatial coherence is effectively found in these compounds [604, 605]. But beyond that, strong coupling is the basis for the creation of coherent **quantum superposition**. Quantum coherence refers to the quantum superposition of quantum states, so it is inherently involved in strong coupling. Cavity QED serves to explore the physics of open quantum

systems and study diverse aspects connected to coherence and decoherence in quantum mechanics [103]. The understanding of light-matter interactions within the strong coupling regime leads to a better manipulation and control of quantum coherence and entanglement [104, 105]. The coherence properties associated with polaritons are of great interest in the field of quantum information processing [105], and the coherence present in polariton condensates are also useful in the development of quantum technologies [106, 107].

Quantum information processing The field of quantum information technology has benefited from the strong coupling regime in various cavity QED implementations — different information processing tasks can be realized when two-level systems are strongly coupled to a cavity mode [105]. The preparation and coherent manipulation of entangled states form the basis of this area. Atomic systems have been widely used in quantum computation [606], where a complete isolation from the environment is required. Information is encoded in the quantum state of a two-level system, referred to as a qubit, and any dissipation of energy over the quantum computation process may ruin the operation. The high degree of quantum coherence displayed by atoms have led to their use in the implementation of quantum logic [607], where the large optical nonlinearities attainable in cavity QED are exploited. The implementation of scalable photonic quantum computation has been also carried out in these platforms [608, 609]. Trying to face the problem of scalability, solid-state platforms started receiving great attention [610, 611]. The quantum nature of the system composed of a quantum dot and a cavity in the strong-coupling regime was confirmed [612], thus enabling its use in quantum information applications. Cavity QED systems have been also considered in the implementation of distributed quantum networks [613].

APPENDIX B

QUANTUM PICTURES

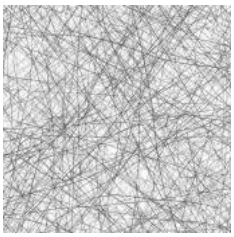

There exist various representations of states and operators when working within the quantum formalism —these are known as **quantum pictures**. These different formulations of quantum mechanics are all equivalent, since operators and states in a particular picture are related by a change of basis (that is, a unitary transformation) to the same operators and states in some other picture. Nevertheless, a specific way to represent them may be more convenient according to the problem to solve. In this Appendix, we provide a brief summary of the three different quantum pictures and the form of the corresponding equations that govern the time dynamics: the Schrödinger picture (Section B.1), the Heisenberg picture (Section B.2), and the interaction or Dirac picture (Section B.3)

B.1 Schrödinger picture

In the **Schrödinger picture**, the time-evolution of the quantum system is carried entirely by the states representing the system. On the contrary, operators present no time-dependence.

- States evolve in time: $|\psi(t)\rangle$, $\hat{\rho}(t)$.
- Operators are constant: $\hat{A}$.

Notice that, although operators in the Schrödinger picture do not evolve in time, they can be explicitly time-dependent due to an applied external field varying in time. The same is valid for the specific case of the Hamiltonian, which can be explicitly time-dependent: $\hat{H} = \hat{H}(t)$.

States and operators in the Schrödinger picture

States Let the system be described by a certain vector state $|\psi(t)\rangle$. The **evolution operator** $\mathcal{U}(t, t_0)$ transforms the state at some initial time t_0 to the state at time t:

$$|\psi(t)\rangle = \mathcal{U}(t, t_0)|\psi(t_0)\rangle \ . \tag{B.1}$$

When the Hamiltonian $\hat{H}$ describing the system is time-independent, the evolution operator reads:

$$\mathcal{U}(t, t_0) = \mathrm{e}^{-\frac{\mathrm{i}}{\hbar}\hat{H}(t-t_0)} \,. \tag{B.2}$$

If the state of the system is alternatively described by the **density matrix operator** $\hat{\rho}$, its evolution can be also expressed in terms of the density matrix at some initial time t_0 through the evolution operator $\mathcal{U}(t, t_0)$:

$$\hat{\rho}(t) = \mathcal{U}(t, t_0)\, \hat{\rho}(t_0)\, \mathcal{U}^{\dagger}(t, t_0) \,. \tag{B.3}$$

For instance, if the state of the system is given by Equation 2.3, we can verify that the density matrix transforms as mentioned:

$$\begin{aligned}
\hat{\rho}(t) = \sum_i w_i \, |\psi_i(t)\rangle\langle\psi_i(t)| &= \sum_i w_i \, \mathcal{U}(t, t_0)|\psi_i(t_0)\rangle\langle\psi_i(t_0)|\mathcal{U}^{\dagger}(t, t_0) \\
&= \mathcal{U}(t, t_0)\left(\sum_i w_i \, |\psi_i(t_0)\rangle\langle\psi_i(t_0)|\right)\mathcal{U}^{\dagger}(t, t_0) \\
&= \mathcal{U}(t, t_0)\, \hat{\rho}(t_0)\, \mathcal{U}^{\dagger}(t, t_0) \,.
\end{aligned}$$

Observables Although observables themselves do not evolve in time, the evolution of the state is transferred to the evolution of the expectation value of any observable $\hat{A}$:

$$\langle\hat{A}\rangle(t) = \langle\psi(t)|\, \hat{A}\, |\psi(t)\rangle = \langle\psi(t_0)|\, \mathcal{U}^{\dagger}(t, t_0)\, \hat{A}\, \mathcal{U}(t, t_0)\, |\psi(t_0)\rangle \,.$$

Within the density matrix formalism, the expectation value of an observable $\hat{A}$ is computed as:

$$\langle\hat{A}\rangle(t) = \mathrm{Tr}[\hat{\rho}(t)\, \hat{A}] \,. \tag{B.4}$$

Time-evolution equations

The time-evolution of some state of the system $|\psi(t)\rangle$ is governed by the **Schrödinger equation**:

$$\frac{\mathrm{d}}{\mathrm{d}t}|\psi(t)\rangle = -\frac{\mathrm{i}}{\hbar}\hat{H}|\psi(t)\rangle \,, \tag{B.5}$$

where $\hat{H}$ is the (time-independent) Hamiltonian describing the system. By substituting Equation B.1 into the Schrödinger equation, we observe that the Hamiltonian also guides the time-evolution of $\mathcal{U}(t, t_0)$:

$$\frac{\mathrm{d}}{\mathrm{d}t}\mathcal{U}(t, t_0) = -\frac{\mathrm{i}}{\hbar}\hat{H}(t)\, \mathcal{U}(t, t_0) \,. \tag{B.6}$$

Alternatively, when working within the density matrix formalism, the evolution of the density matrix operator $\hat{\rho}(t)$ is given by the **Liouville–von Neumann equation**:

$$\frac{\mathrm{d}}{\mathrm{d}t}\hat{\rho}(t) = -\frac{\mathrm{i}}{\hbar}\left[\hat{H}, \hat{\rho}(t)\right] \,, \tag{B.7}$$

since the derivation of Equation B.3 leads to:

$$\begin{aligned}\frac{\mathrm{d}}{\mathrm{d}t}\hat{\rho}(t) &= \frac{\mathrm{d}\,\mathcal{U}(t,t_0)}{\mathrm{d}t}\,\hat{\rho}(t_0)\,\mathcal{U}^\dagger(t,t_0) + \mathcal{U}(t,t_0)\,\hat{\rho}(t_0)\,\frac{\mathrm{d}\,\mathcal{U}^\dagger(t,t_0)}{\mathrm{d}t} \\ &= -\frac{\mathrm{i}}{\hbar}\hat{H}\,\mathcal{U}(t,t_0)\,\hat{\rho}(t_0)\,\mathcal{U}^\dagger(t,t_0) + \frac{\mathrm{i}}{\hbar}\,\mathcal{U}(t,t_0)\,\hat{\rho}(t_0)\,\mathcal{U}^\dagger(t,t_0)\hat{H} \\ &= -\frac{\mathrm{i}}{\hbar}\hat{H}\hat{\rho}(t) + \frac{\mathrm{i}}{\hbar}\hat{\rho}(t)\hat{H}\,.\end{aligned}$$

There, we have considered the time-evolution of the operator $\mathcal{U}(t,t_0)$ given by Equation B.6 and the time evolution of the density matrix operator $\hat{\rho}(t)$ given by Equation B.3.

B.2 Heisenberg picture

In the **Heisenberg picture**, it is the operators that capture the time-evolution of the quantum system, whereas states remain constant in time:

- States are constant: $|\psi_\mathrm{H}\rangle$, $\hat{\rho}_\mathrm{H}$.
- Operators evolve in time: $\hat{A}_\mathrm{H}(t)$.

States and operators in the interaction picture

States States in the Heisenberg picture coincide with the corresponding states in the Schrödinger picture at time t_0:

$$|\psi_\mathrm{H}\rangle = |\psi(t_0)\rangle\,.$$

It is the same for the density matrix operator, which also remains time-independent:

$$\hat{\rho}_\mathrm{H} = \hat{\rho}(t_0)\,.$$

Operators An operator in the Heisenberg picture is defined in terms of the evolution operator $\mathcal{U}(t,t_0)$ as:

$$\hat{A}_\mathrm{H}(t) = \mathcal{U}^\dagger(t,t_0)\,\hat{A}\,\mathcal{U}(t,t_0)\,. \tag{B.8}$$

We can check that the expectation value of an operator $\hat{A}$ in this picture is equal to its respective value in the Schrödinger picture:

$$\langle\hat{A}\rangle = \langle\psi(t)|\,\hat{A}\,|\psi(t)\rangle = \langle\psi(t_0)|\,\mathcal{U}^\dagger(t,t_0)\,\hat{A}\,\mathcal{U}(t,t_0)\,|\psi(t_0)\rangle = \langle\psi_\mathrm{H}|\,\hat{A}_\mathrm{H}(t)\,|\psi_\mathrm{H}\rangle = \langle\hat{A}(t)\rangle_\mathrm{H}\,,$$

and when working within the density matrix formalism:

$$\begin{aligned}\langle\hat{A}\rangle = \mathrm{Tr}[\hat{\rho}(t)\,\hat{A}] &= \mathrm{Tr}[\mathcal{U}(t,t_0)\,\hat{\rho}(t_0)\,\mathcal{U}^\dagger(t,t_0)\,\hat{A}\,\mathcal{U}(t,t_0)\,\mathcal{U}^\dagger(t,t_0)] \\ &= \mathrm{Tr}[\mathcal{U}(t,t_0)\,\hat{\rho}_\mathrm{H}\,\hat{A}_\mathrm{H}(t)\,\mathcal{U}^\dagger(t,t_0)] = \mathrm{Tr}[\hat{\rho}_\mathrm{H}\,\hat{A}_\mathrm{H}(t)] = \langle\hat{A}(t)\rangle_\mathrm{H}\,.\end{aligned}$$

Time-evolution equations

The time-evolution of an operator $\hat{A}_{\mathrm{H}}(t)$ in the Heisenberg picture is given by the **Heisenberg equation** of motion:

$$\frac{\mathrm{d}}{\mathrm{d}t}\hat{A}_{\mathrm{H}}(t) = -\frac{\mathrm{i}}{\hbar}[\hat{A}_{\mathrm{H}}(t), \hat{H}_{\mathrm{H}}(t)] + \left(\frac{\partial \hat{A}}{\partial t}\right)_{\mathrm{H}} , \tag{B.9}$$

where ∂ stands for the partial derivative. There, we have introduced the following definition:

$$\left(\frac{\partial \hat{A}}{\partial t}\right)_{\mathrm{H}} = \mathcal{U}^{\dagger}(t, t_0)\, \frac{\partial \hat{A}}{\partial t}\, \mathcal{U}(t, t_0) \equiv \frac{\partial \hat{A}_{\mathrm{H}}(t)}{\partial t} .$$

The equation of motion for operators in the Heisenberg picture can be obtained by deriving Equation B.8:

$$\begin{aligned}
\frac{\mathrm{d}}{\mathrm{d}t}\hat{A}_{\mathrm{H}}(t) &= \frac{\partial \mathcal{U}^{\dagger}(t, t_0)}{\partial t}\, \hat{A}\, \mathcal{U}(t, t_0) + \mathcal{U}^{\dagger}(t, t_0)\, \frac{\partial \hat{A}}{\partial t}\, \mathcal{U}(t, t_0) + \mathcal{U}^{\dagger}(t, t_0)\, \hat{A}\, \frac{\partial \mathcal{U}(t, t_0)}{\partial t} \\
&= \frac{\mathrm{i}}{\hbar}\, \mathcal{U}^{\dagger}(t, t_0)\, \hat{H}\, \hat{A}\, \mathcal{U}(t, t_0) + \mathcal{U}^{\dagger}(t, t_0)\, \frac{\partial \hat{A}}{\partial t}\, \mathcal{U}(t, t_0) - \frac{\mathrm{i}}{\hbar}\, \mathcal{U}^{\dagger}(t, t_0)\, \hat{A}\, \hat{H}\, \mathcal{U}(t, t_0) \\
&= \frac{\mathrm{i}}{\hbar}\, \hat{H}_{\mathrm{H}}(t)\, \hat{A}_{\mathrm{H}}(t) - \frac{\mathrm{i}}{\hbar}\, \hat{A}_{\mathrm{H}}(t)\, \hat{H}_{\mathrm{H}}(t) + \mathcal{U}^{\dagger}(t, t_0)\, \frac{\partial \hat{A}}{\partial t}\, \mathcal{U}(t, t_0) \\
&= -\frac{\mathrm{i}}{\hbar}\, [\hat{A}_{\mathrm{H}}(t), \hat{H}_{\mathrm{H}}(t)] + \frac{\partial \hat{A}_{\mathrm{H}}(t)}{\partial t} ,
\end{aligned}$$

where we have made use of the equation for the time evolution of $\mathcal{U}$ (Equation B.6) and the definition of Equation B.8.

B.3 Interaction picture

An intermediate case between the Schrödinger and the Heisenberg pictures is the so-called interaction (or Dirac) picture, where the time-evolution is shared between states and operators. That is, in the **interaction picture**, both states and operators evolve in time:

- States evolve in time: $|\psi_{\mathrm{I}}(t)\rangle$, $\hat{\rho}_{\mathrm{I}}(t)$.
- Operators evolve in time: $\hat{A}_{\mathrm{I}}(t)$.

The interaction picture is useful when having time-dependent Hamiltonians, where the complete Hamiltonian $\hat{H}$, expressed in the Schrödinger picture, can be split as:

$$\hat{H}(t) = \hat{H}_0 + \hat{H}_{\mathrm{int}}(t) .$$

The time-independent $\hat{H}_0$ comprises the energies of the components of the system when the interaction among them is ignored, whereas $\hat{H}_{\mathrm{int}}$ describes the interaction. This is the part that carries the explicit time-dependence, and can be usually treated as a perturbation of $\hat{H}_0$. Since the non-interacting Hamiltonian is normally a solvable problem, the eigenstates of $\hat{H}_0$ are used to describe the dynamics induced by the time-dependent part, as long as the interaction Hamiltonian is small enough.

States and operators in the interaction picture

States Apart from the evolution operator involving the complete Hamiltonian $\hat{H}$ (Equation B.2), two other evolution operators can be defined from its two constituents:

$$\begin{aligned}\mathcal{U}_0(t,t_0) &= \mathrm{e}^{-\frac{\mathrm{i}}{\hbar}\hat{H}_0(t-t_0)}\,,\\ \mathcal{U}_{\mathrm{int}}(t,t_0) &= \mathrm{e}^{-\frac{\mathrm{i}}{\hbar}\hat{H}_{\mathrm{int}}(t-t_0)}\,.\end{aligned}$$

Given the vector $|\psi(t)\rangle$ in the Schrödinger picture, the corresponding state in the interaction picture is defined through:

$$\begin{aligned}|\psi_{\mathrm{I}}(t)\rangle &= \mathcal{U}_0^{\dagger}(t,t_0)\,|\psi(t)\rangle\,,\\ &= \mathcal{U}_0^{\dagger}(t,t_0)\,\mathcal{U}(t,t_0)|\psi(t_0)\rangle = \mathcal{U}_{\mathrm{int}}(t,t_0)|\psi(t_0)\rangle\,.\end{aligned}$$

Density matrix The density matrix operator $\hat{\rho}(t)$, given in the Schrödinger picture, transforms to the interaction picture as:

$$\hat{\rho}_{\mathrm{I}}(t) = \mathcal{U}_0^{\dagger}(t,t_0)\;\hat{\rho}(t)\,\mathcal{U}_0(t,t_0)\,. \tag{B.10}$$

For instance, when the density matrix is built from a ket state, we have:

$$\hat{\rho}_{\mathrm{I}}(t) = |\psi_{\mathrm{I}}(t)\rangle\langle\psi_{\mathrm{I}}(t)| = \mathcal{U}_0^{\dagger}(t,t_0)|\psi(t)\rangle\langle\psi(t)|\mathcal{U}_0(t,t_0) = \mathcal{U}_0^{\dagger}(t,t_0)\;\hat{\rho}(t)\,\mathcal{U}_0(t,t_0)\,.$$

Operators Some operator $\hat{A}$ in the Schrödinger picture is transformed to the interaction picture as:

$$\hat{A}_{\mathrm{I}}(t) = \mathcal{U}_0^{\dagger}(t,t_0)\;\hat{A}\,\mathcal{U}_0(t,t_0)\,. \tag{B.11}$$

Note that for the specific case of the operator $\hat{H}_0$, the interaction picture and the Schrödinger picture coincide:

$$\hat{H}_{0,\mathrm{I}}(t) = \mathcal{U}_0^{\dagger}(t,t_0)\;\hat{H}_0\,\mathcal{U}_0(t,t_0) = \hat{H}_0\,,$$

but this is not true for the interaction Hamiltonian $\hat{H}_{\mathrm{int}}$:

$$\hat{H}_{\mathrm{int,I}}(t) = \mathcal{U}_0^{\dagger}(t,t_0)\;\hat{H}_{\mathrm{int}}(t)\,\mathcal{U}_0(t,t_0)\,.$$

We can check that the expectation value of some operator $\hat{A}$ in the interaction picture remains the same as in the Schrödinger picture:

$$\begin{aligned}\langle\hat{A}(t)\rangle_{\mathrm{I}} &= \langle\psi_{\mathrm{I}}(t)|\;\hat{A}_{\mathrm{I}}(t)\;|\psi_{\mathrm{I}}(t)\rangle\\ &= \langle\psi(t)|\;\mathcal{U}_0(t,t_0)\,\hat{A}_{\mathrm{I}}(t)\,\mathcal{U}_0^{\dagger}(t,t_0)\;|\psi(t)\rangle = \langle\psi(t)|\;\hat{A}\;|\psi(t)\rangle = \langle\hat{A}\rangle\,,\end{aligned}$$

and when working within the density matrix formalism:

$$\langle\hat{A}(t)\rangle_{\mathrm{I}} = \mathrm{Tr}[\hat{\rho}_{\mathrm{I}}(t)\,\hat{A}_{\mathrm{I}}(t)] = \mathrm{Tr}[\mathcal{U}_0^{\dagger}(t,t_0)\;\hat{\rho}(t)\,\hat{A}\,\mathcal{U}_0(t,t_0)] = \mathrm{Tr}[\hat{\rho}(t)\,\hat{A}] = \langle\hat{A}\rangle\,.$$

Note The interaction picture becomes a half-way point between the Schrödinger and the Heisenberg pictures: while states evolve according to $\hat{H}_{\mathrm{int}}$, operators evolve under $\hat{H}_0$. Notice that:

- When $\hat{H}_0 = 0$, then $\hat{H} = \hat{H}_{\text{int}}$, and the Schrödinger picture is recovered.
- When $\hat{H}_{\text{int}} = 0$, then $\hat{H} = \hat{H}_0$, and the Heisenberg picture is recovered.

Time-evolution equations

States. The time-evolution for a state in the interaction picture is given by:

$$\frac{\mathrm{d}}{\mathrm{d}t}|\psi_{\mathrm{I}}(t)\rangle = -\frac{\mathrm{i}}{\hbar}\hat{H}_{\text{int,I}}(t)|\psi_{\mathrm{I}}(t)\rangle \ .$$

Indeed, if we start from the Schrödinger equation (Equation B.5) and take into account the relations between states and operators in both pictures, we have:

$$\begin{aligned}
\frac{\mathrm{d}}{\mathrm{d}t}|\psi(t)\rangle &= -\frac{\mathrm{i}}{\hbar}\hat{H}|\psi(t)\rangle \\
\frac{\mathrm{d}}{\mathrm{d}t}\left(\mathcal{U}_0|\psi_{\mathrm{I}}(t)\rangle\right) &= -\frac{\mathrm{i}}{\hbar}\,\mathcal{U}_0\,\hat{H}_{\mathrm{I}}(t)\,\mathcal{U}_0^{\dagger}\,\mathcal{U}_0|\psi_{\mathrm{I}}(t)\rangle \\
-\frac{\mathrm{i}}{\hbar}\hat{H}_0\,\mathcal{U}_0|\psi_{\mathrm{I}}(t)\rangle + \mathcal{U}_0\frac{\mathrm{d}}{\mathrm{d}t}|\psi_{\mathrm{I}}(t)\rangle &= -\frac{\mathrm{i}}{\hbar}\,\mathcal{U}_0\,\left(\hat{H}_0 + \hat{H}_{\text{int,I}}(t)\right)|\psi_{\mathrm{I}}(t)\rangle \\
\frac{\mathrm{d}}{\mathrm{d}t}|\psi_{\mathrm{I}}(t)\rangle &= -\frac{\mathrm{i}}{\hbar}\hat{H}_{\text{int,I}}(t)|\psi_{\mathrm{I}}(t)\rangle \ .
\end{aligned}$$

Note that this is nothing but the Schrödinger equation for the state in the interaction picture where only the interaction Hamiltonian dictates the time-evolution (expressed in the interaction picture as well).

Operators. In the interaction picture, operators evolve in time with the Hamiltonian $\hat{H}_0$, so:

$$\frac{\mathrm{d}}{\mathrm{d}t}\hat{A}_{\mathrm{I}}(t) = -\frac{\mathrm{i}}{\hbar}[\hat{A}_{\mathrm{I}}(t), \hat{H}_0]$$

Notice that it has the form of the Heisenberg equation (Equation B.9) for the operator expressed in the interaction picture where the total Hamiltonian $\hat{H}$ has been replaced by the unperturbed Hamiltonian $\hat{H}_0$.

Density matrix. The density matrix in the interaction picture evolves according to the equation:

$$\frac{\mathrm{d}}{\mathrm{d}t}\hat{\rho}_{\mathrm{I}}(t) = -\frac{\mathrm{i}}{\hbar}[\hat{H}_{\text{int,I}}(t), \hat{\rho}_{\mathrm{I}}(t)] \ ,$$

Indeed, if we start from the Liouville–von Neumann equation (Equation B.7):

$$\begin{aligned}
\frac{\mathrm{d}}{\mathrm{d}t}\hat{\rho}(t) &= -\frac{\mathrm{i}}{\hbar}[\hat{H}, \hat{\rho}(t)] \\
\frac{\mathrm{d}}{\mathrm{d}t}\left(\mathcal{U}_0\,\hat{\rho}_{\mathrm{I}}(t)\,\mathcal{U}_0^{\dagger}\right) &= -\frac{\mathrm{i}}{\hbar}\mathcal{U}_0\,[\hat{H}_{\mathrm{I}}(t), \hat{\rho}_{\mathrm{I}}(t)]\,\mathcal{U}_0^{\dagger} \\
-\frac{\mathrm{i}}{\hbar}\hat{H}_0\mathcal{U}_0\rho_{\mathrm{I}}(t)\mathcal{U}_0^{\dagger} + \frac{\mathrm{i}}{\hbar}\mathcal{U}_0\rho_{\mathrm{I}}(t)\hat{H}_0\mathcal{U}_0^{\dagger} + \mathcal{U}_0\frac{\mathrm{d}\hat{\rho}_{\mathrm{I}}(t)}{\mathrm{d}t}\mathcal{U}_0^{\dagger} &= -\frac{\mathrm{i}}{\hbar}\mathcal{U}_0\,[\hat{H}_{0,\mathrm{I}} + \hat{H}_{\text{int,I}}(t), \hat{\rho}_{\mathrm{I}}(t)]\,\mathcal{U}_0^{\dagger} \\
-\frac{\mathrm{i}}{\hbar}[\hat{H}_0, \rho_{\mathrm{I}}(t)] + \frac{\mathrm{d}\hat{\rho}_{\mathrm{I}}(t)}{\mathrm{d}t} &= -\frac{\mathrm{i}}{\hbar}[\hat{H}_0 + \hat{H}_{\text{int,I}}(t), \hat{\rho}_{\mathrm{I}}(t)] \\
\frac{\mathrm{d}}{\mathrm{d}t}\hat{\rho}_{\mathrm{I}}(t) &= -\frac{\mathrm{i}}{\hbar}[\hat{H}_{\text{int,I}}(t), \rho_{\mathrm{I}}(t)] \ ,
\end{aligned}$$

where we have considered the relations between states and operators in the Schrödinger and interaction pictures.

APPENDIX C

QUANTUM MASTER EQUATIONS

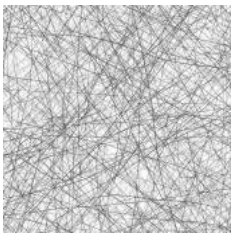

In this Appendix, we provide some extensions of the topics discussed in Section 2.1, dealing with the description of the dynamics of open quantum systems. In particular, we derive the Born–Markov master equation (Section C.1) and spell out the steps leading to the Bloch–Redfield master equation (Section C.2).

C.1 Master equation in the Born–Markov approximation

The **Liouville–von Neumann equation** (Equation 2.4) governs the dynamics of the density matrix $\hat{\rho}$ describing the whole system:

$$\frac{\mathrm{d}}{\mathrm{d}t}\hat{\rho}(t) = -\frac{\mathrm{i}}{\hbar}[\hat{H}(t), \hat{\rho}(t)] \,. \tag{C.1}$$

When dealing with open quantum systems, the total Hamiltonian $\hat{H}$ can be expressed as sum of the parts describing the system of interest S, the reservoir R, and their mutual interaction, that is, $\hat{H} = \hat{H}_\mathrm{S} + \hat{H}_\mathrm{R} + \hat{H}_\mathrm{int}$ (Equation 2.5). We are interested in the evolution of the **reduced density matrix** $\hat{\rho}_\mathrm{S}$ (describing the subsystem S and defined in Equation 2.6) without requiring detailed information of the reservoir. The standard approach for the derivation of the corresponding master equation consists in the introduction of the Born–Markov approximation. Although it can be found in many textbooks (such as those in Ref. [416, 614]), we reproduce here the derivation in detail. To simplify the notation, we drop the hats over operators in this section.

Transforming into the interaction picture. The first step is to consider the Liouvillian equation for the complete system (Equation C.1), and express it in the interaction picture (see Appendix B for an overview of the different quantum pictures). From now on, the tilde over operators are used to indicate that they are expressed in the interaction picture.

First of all, according to Equation B.10, the transformed density matrix $\tilde{\rho}$ reads:

$$\tilde{\rho}(t) = \mathcal{U}_0^\dagger(t,t_0)\,\rho(t)\,\mathcal{U}_0(t,t_0)\,,$$

where $\mathcal{U}_0(t,t_0) = \exp[-\mathrm{i}H_0(t-t_0)/\hbar]$. There, H_0 stands for the Hamiltonian without interactions, that is, $H_0 = H_\mathrm{S} + H_\mathrm{R}$. From now on, we will consider $t_0 = 0$ as the initial time, thus:

$$\tilde{\rho}(t) = \mathrm{e}^{\frac{\mathrm{i}}{\hbar}H_0 t}\,\rho(t)\,\mathrm{e}^{-\frac{\mathrm{i}}{\hbar}H_0 t}\,.$$

By deriving this expression with respect to time, we arrive at an equation connecting the time derivative of the density matrix expressed in the Schrödinger and in the interaction picture:

$$\dot{\tilde{\rho}}(t) = \mathrm{e}^{\frac{\mathrm{i}}{\hbar}H_0 t}\dot{\rho}(t)\,\mathrm{e}^{-\frac{\mathrm{i}}{\hbar}H_0 t} + \frac{\mathrm{i}}{\hbar}[H_0,\tilde{\rho}(t)]\,, \tag{C.2}$$

where the dot represents time derivative. There, we can substitute $\dot{\rho}(t)$ by the Lindblad-Von Neumann equation for the total Hamiltonian $H = H_0 + H_\mathrm{int}$ (Equation C.1):

$$\begin{aligned}\dot{\tilde{\rho}}(t) &= \mathrm{e}^{\frac{\mathrm{i}}{\hbar}H_0 t}\left(-\frac{\mathrm{i}}{\hbar}[H_0+H_\mathrm{int},\rho(t)]\right)\mathrm{e}^{-\frac{\mathrm{i}}{\hbar}H_0 t} + \frac{\mathrm{i}}{\hbar}[H_0,\tilde{\rho}(t)] = \\ &= -\frac{\mathrm{i}}{\hbar}[H_0,\tilde{\rho}(t)] - \frac{\mathrm{i}}{\hbar}[\tilde{H}_\mathrm{int}(t),\tilde{\rho}(t)] + \frac{\mathrm{i}}{\hbar}[H_0,\tilde{\rho}(t)] = -\frac{\mathrm{i}}{\hbar}[\tilde{H}_\mathrm{int}(t),\tilde{\rho}(t)]\,,\end{aligned}$$

where we have considered the transformation of operators from the Schrödinger to the interaction picture (Equation B.11). Note that the non-interacting Hamiltonian has the same expression in both pictures, $H_0 = \tilde{H}_0$, while the interaction Hamiltonian now acquires an explicit dependence on time: $\tilde{H}_\mathrm{int}(t) = \mathrm{e}^{\frac{\mathrm{i}}{\hbar}H_0 t}H_\mathrm{int}\,\mathrm{e}^{-\frac{\mathrm{i}}{\hbar}H_0 t}$. We have arrived at the well-known equation for the dynamics of the density matrix in the interaction picture, which is equivalent to that in the Schrödinger picture (Equation 2.4) but involving the interaction Hamiltonian H_int:

$$\dot{\tilde{\rho}}(t) = -\frac{\mathrm{i}}{\hbar}[\tilde{H}_\mathrm{int}(t),\tilde{\rho}(t)]\,. \tag{C.3}$$

This equation can be formally integrated, yielding:

$$\tilde{\rho}(t) = \tilde{\rho}(0) - \frac{\mathrm{i}}{\hbar}\int_0^t [\tilde{H}_\mathrm{int}(t'),\tilde{\rho}(t')]\mathrm{d}t'\,.$$

The substitution of this expression into Equation C.3 leads to an integro-differential equation for the density matrix describing the complete system:

$$\begin{aligned}\dot{\tilde{\rho}}(t) &= -\frac{\mathrm{i}}{\hbar}\left[\tilde{H}_\mathrm{int}(t),\left(\rho(0) - \frac{\mathrm{i}}{\hbar}\int_0^t \left[\tilde{H}_\mathrm{int}(t'),\tilde{\rho}(t')\right]\mathrm{d}t'\right)\right] \\ &= -\frac{\mathrm{i}}{\hbar}\left[\tilde{H}_\mathrm{int}(t),\rho(0)\right] - \frac{\mathrm{i}}{\hbar}\left[\tilde{H}_\mathrm{int}(t),-\frac{\mathrm{i}}{\hbar}\int_0^t \left[\tilde{H}_\mathrm{int}(t'),\tilde{\rho}(t')\right]\mathrm{d}t'\right]\,,\end{aligned}$$

where we have introduced the fact that $\tilde{\rho}(0) = \rho(0)$. Finally, extracting the integral from the commutator, we have:

$$\dot{\tilde{\rho}}(t) = -\frac{\mathrm{i}}{\hbar}[\tilde{H}_\mathrm{int}(t),\rho(0)] - \frac{1}{\hbar^2}\int_0^t \left[\tilde{H}_\mathrm{int}(t),\left[\tilde{H}_\mathrm{int}(t'),\tilde{\rho}(t')\right]\right]\mathrm{d}t'\,. \tag{C.4}$$

Tracing out the bath degrees of freedom. As our goal is an equation for the reduced density matrix ρ_S (Equation 2.6), we trace out the degrees of freedom of the environment R in Equation C.4:

$$\mathrm{Tr}_R\left\{\dot{\tilde{\rho}}(t)\right\} = -\frac{i}{\hbar}\mathrm{Tr}_R\left\{\left[\tilde{H}_{int}(t), \rho(0)\right]\right\} - \frac{1}{\hbar^2}\int_0^t \mathrm{Tr}_R\left\{\left[\tilde{H}_{int}(t), \left[\tilde{H}_{int}(t'), \tilde{\rho}(t')\right]\right]\right\} dt' \,.$$

Supposing that there are no correlations between the system S and the reservoir R at time $t = 0$, the initial state of the system can be factorized as $\rho(0) = \rho_S(0) \otimes B_0$ (where B_0 is the density matrix for the reservoir), and:

$$\mathrm{Tr}_R\left\{\left[\tilde{H}_{int}(t), \rho(0)\right]\right\} = \mathrm{Tr}_R\left\{\left[\tilde{H}_{int}(t), \rho_S(0) \otimes B_0\right]\right\} = 0 \,.$$

That is, the first term of the right hand side of previous equation is zero, yielding:

$$\mathrm{Tr}_R\left\{\dot{\tilde{\rho}}(t)\right\} = -\frac{1}{\hbar^2}\int_0^t \mathrm{Tr}_R\left\{\left[\tilde{H}_{int}(t), \left[\tilde{H}_{int}(t'), \tilde{\rho}(t')\right]\right]\right\} dt' \,. \tag{C.5}$$

Born approximation. When the coupling between system and reservoir is sufficiently weak and the reservoir is considerably larger than the system of interest, there exist two approximations that can be performed. First, there is practically no effect of the system on the reservoir, so we can take the bath as constant: $\tilde{\rho}_R(t) \equiv B_0$. Second, as correlations between the system and the bath remain negligible throughout the evolution, the density matrix can be considered separable at any time: $\tilde{\rho}(t) = \tilde{\rho}_S(t) \otimes \tilde{\rho}_R(t)$. These two assumptions are known as the **Born approximation**, yielding together the following form for the density matrix describing the state of the composite system:

$$\tilde{\rho}(t) = \tilde{\rho}_S(t) \otimes B_0 \,,$$

that is, $\tilde{\rho}(t)$ can be always written as the product of two parts, one corresponding to the system of interest and the other associated with the bath (which turns out to be constant). Inserting this expression into Equation C.5, we have:

$$\dot{\tilde{\rho}}_S(t) = -\frac{1}{\hbar^2}\int_0^t \mathrm{Tr}_R\left\{\left[\tilde{H}_{int}(t), \left[\tilde{H}_{int}(t'), \tilde{\rho}_S(t') \otimes B_0\right]\right]\right\} dt' \,. \tag{C.6}$$

Therefore, we have finally achieved an expression for the evolution of the reduced density matrix $\tilde{\rho}_S$.

Markov approximation. From Equation C.6 we observe that the state at time t depends on the state of the system in all previous times (note that it appears the integration of $\rho_S(t')$ over t'). Therefore, this equation is said to be **non-Markovian** as the evolution of the system depends not only on its present state but on its past history. The replacement of $\rho_S(t')$ by $\rho_S(t)$ is known as the **Markov approximation**, and Equation C.6 becomes:

$$\dot{\tilde{\rho}}_S(t) = -\frac{1}{\hbar^2}\int_0^t \mathrm{Tr}_R\left\{\left[\tilde{H}_{int}(t), \left[\tilde{H}_{int}(t'), \tilde{\rho}_S(t) \otimes B_0\right]\right]\right\} dt' \,,$$

known as **Redfield equation**. Nevertheless, there still exists an implicit dependence on the past, so this master equation is still non-Markovian. To overcome this issue, we can

perform the substitution $t' \to t - t'$ in the integrand:

$$\dot{\tilde{\rho}}_S(t) = -\frac{1}{\hbar^2}\int_0^t \mathrm{Tr}_R\left\{\left[\tilde{H}_{int}(t),\left[\tilde{H}_{int}(t-t'),\tilde{\rho}_S(t)\otimes B_0\right]\right]\right\}\mathrm{d}t' \,,$$

where the integration limits do not change since $\mathrm{d}t' \to \mathrm{d}(t-t') = -\mathrm{d}t'$, and $t' \in \{0, t\}$ now corresponds to $t - t' \in \{t-0, t-t\} = \{t, 0\}$. We can replace the time parameter t' by τ to help us to understand this variable as an indicator of the lapse of time (with respect to the present) in which we have to take into account memory effects from the bath. If τ_R stands for the reservoir correlation time (that is, the time over which correlations in the bath decay), the integrand becomes negligible for times $\tau \gg \tau_R$ as bath correlations do not remain long in comparison with all relevant time-scales of the system dynamics. Therefore, we can extend the upper integration limit to infinity:

$$\dot{\tilde{\rho}}_S(t) = -\frac{1}{\hbar^2}\int_0^\infty \mathrm{Tr}_R\left\{\left[\tilde{H}_{int}(t),\left[\tilde{H}_{int}(t-\tau),\tilde{\rho}_S(t)\otimes B_0\right]\right]\right\}\mathrm{d}\tau \,.$$

This equation is now Markovian. These two approximations are often named together as the **Born–Markov approximation**. Correlations in the bath are considered short-lived in the sense that the dynamics of the bath is much faster than the dynamics of the system.

C.2 The Bloch–Redfield master equation

The **Bloch–Redfield formalism** provides a procedure to introduce the influence of the reservoir in the dynamics of open systems. The different incoherent processes arising as a result of the interaction with the reservoir are derived from a microscopic description, thus the master equation is obtained from a more fundamental way. In this section, we provide the derivation of the Bloch–Redfield master equation, briefly outlined in the main text and which can be also found in Ref. [614, 615].

Master equation in the Born–Markov approximation The derivation of the Bloch–Redfield master equation starts from the Redfield equation after introducing the Born–Markov approximation (Equation 2.7), that is:

$$\dot{\tilde{\rho}}_S(t) = -\frac{1}{\hbar^2}\int_0^\infty \mathrm{Tr}_R\left\{\left[\tilde{H}_{int}(t),\left[\tilde{H}_{int}(t-\tau),\tilde{\rho}_S(t)\otimes B_0\right]\right]\right\}\mathrm{d}\tau \,. \tag{C.7}$$

This equation gives the evolution of the reduced density matrix ρ_S under the influence of a reservoir, where B_0 is the density matrix describing the constant state of that reservoir. There, H_{int} is the interaction Hamiltonian, and the tilde over operators indicate that they are expressed in the interaction picture (see Appendix B). On the other hand, the non-interacting Hamiltonian is given by $H_0 = H_S + H_R$, that is, the sum of the Hamiltonian corresponding to the system of interest H_S, and the one associated with the reservoir H_R.

Expression for the interaction Hamiltonian The interaction Hamiltonian H_{int} can be expressed as the sum of products of operators:

$$H_{\text{int}} = \sum_j \mathcal{Q}_j \otimes \mathcal{R}_j \,, \tag{C.8}$$

where $\mathcal{Q}_j$ stand for operators in the Hilbert space of the subsystem S, and $\mathcal{R}_j$ for those acting on the Hilbert space of the reservoir R. Notice that, when written in the interaction picture, these operators present an explicit dependence on time (Equation B.11):

$$\tilde{\mathcal{Q}}_j(t) = \mathrm{e}^{\frac{\mathrm{i}}{\hbar}H_{\text{S}}t}\ \mathcal{Q}_j\ \mathrm{e}^{-\frac{\mathrm{i}}{\hbar}H_{\text{S}}t}\,, \qquad \tilde{\mathcal{R}}_j(t) = \mathrm{e}^{\frac{\mathrm{i}}{\hbar}H_{\text{R}}t}\ \mathcal{R}_j\ \mathrm{e}^{-\frac{\mathrm{i}}{\hbar}H_{\text{R}}t}\,. \tag{C.9}$$

Then, the Hamiltonian of Equation C.8 transformed to the interaction picture reads:

$$\begin{aligned}\tilde{H}_{\text{int}}(t) &= \sum_j \mathrm{e}^{\frac{\mathrm{i}}{\hbar}(H_{\text{S}}+H_{\text{R}})t}(\mathcal{Q}_j \otimes \mathcal{R}_j)\ \mathrm{e}^{-\frac{\mathrm{i}}{\hbar}(H_{\text{S}}+H_{\text{R}})t} \\ &= \sum_j \left(\mathrm{e}^{\frac{\mathrm{i}}{\hbar}H_{\text{S}}t}\mathcal{Q}_j\ \mathrm{e}^{-\frac{\mathrm{i}}{\hbar}H_{\text{S}}t}\right) \otimes \left(\mathrm{e}^{\frac{\mathrm{i}}{\hbar}H_{\text{R}}t}\mathcal{R}_j\ \mathrm{e}^{-\frac{\mathrm{i}}{\hbar}H_{\text{R}}t}\right) = \sum_j \tilde{\mathcal{Q}}_j(t) \otimes \tilde{\mathcal{R}}_j(t)\,.\end{aligned}$$

By substituting this form of the interaction Hamiltonian into the master equation in the Born–Markov approximation (Equation C.7), we have:

$$\dot{\tilde{\rho}}_{\text{S}}(t) = -\frac{1}{\hbar^2}\int_0^\infty \mathrm{Tr}_{\text{R}}\left\{\left[\sum_j \tilde{\mathcal{Q}}_j(t)\ \otimes \tilde{\mathcal{R}}_j(t),\right.\right. \left.\left.\left[\sum_k \tilde{\mathcal{Q}}_k(t-\tau)\otimes\tilde{\mathcal{R}}_k(t-\tau), \tilde{\rho}_{\text{S}}(t)\otimes B_0\right]\right]\right\}\mathrm{d}\tau\,,$$

and writing out the commutators in full:

$$\begin{aligned}\dot{\tilde{\rho}}_{\text{S}}(t) &= -\frac{1}{\hbar^2}\sum_{j,k}\int_0^\infty \mathrm{Tr}_{\text{R}}\left\{\left[\tilde{\mathcal{Q}}_j(t)\otimes\tilde{\mathcal{R}}_j(t),\ \left(\tilde{\mathcal{Q}}_k(t-\tau)\,\tilde{\rho}_{\text{S}}(t)\otimes\tilde{\mathcal{R}}_k(t-\tau)\,B_0\right.\right.\right. \\ &\qquad \left.\left.\left. -\tilde{\rho}_{\text{S}}(t)\,\tilde{\mathcal{Q}}_k(t-\tau)\otimes B_0\,\tilde{\mathcal{R}}_k(t-\tau)\right)\right]\right\}\mathrm{d}\tau \\ &= -\frac{1}{\hbar^2}\sum_{j,k}\int_0^\infty \left\{\tilde{\mathcal{Q}}_j(t)\,\tilde{\mathcal{Q}}_k(t-\tau)\,\tilde{\rho}_{\text{S}}(t)\ \ \otimes \mathrm{Tr}_{\text{R}}\left\{\tilde{\mathcal{R}}_j(t)\,\tilde{\mathcal{R}}_k(t-\tau)\,B_0\right\}\right. \\ &\qquad -\tilde{\mathcal{Q}}_j(t)\,\tilde{\rho}_{\text{S}}(t)\,\tilde{\mathcal{Q}}_k(t-\tau)\ \otimes\ \mathrm{Tr}_{\text{R}}\left\{\tilde{\mathcal{R}}_j(t)\,B_0\,\tilde{\mathcal{R}}_k(t-\tau)\right\} \\ &\qquad -\tilde{\mathcal{Q}}_k(t-\tau)\,\tilde{\rho}_{\text{S}}(t)\,\tilde{\mathcal{Q}}_j(t)\ \otimes\ \mathrm{Tr}_{\text{R}}\left\{\tilde{\mathcal{R}}_k(t-\tau)\,B_0\,\tilde{\mathcal{R}}_j(t)\right\} \\ &\qquad \left.+\,\tilde{\rho}_{\text{S}}(t)\,\tilde{\mathcal{Q}}_k(t-\tau)\,\tilde{\mathcal{Q}}_j(t)\ \otimes\ \mathrm{Tr}_{\text{R}}\left\{B_0\,\tilde{\mathcal{R}}_k(t-\tau)\,\tilde{\mathcal{R}}_j(t)\right\}\right\}\mathrm{d}\tau\,.\end{aligned} \tag{C.10}$$

In the last step, we have considered that the trace is taken over the reservoir degrees of freedom. Notice that if $\mathcal{O}$ is an operator in the Hilbert space of R, its expectation value is given by:

$$\langle\mathcal{O}\rangle = \mathrm{Tr}_{\text{S}\otimes\text{R}}[\mathcal{O}\rho(t)] = \mathrm{Tr}_{\text{R}}[\mathcal{O}\mathrm{Tr}_{\text{S}}[\rho(t)]] = \mathrm{Tr}_{\text{R}}[\mathcal{O}\rho_{\text{R}}(t)] = \mathrm{Tr}_{\text{R}}[\mathcal{O}B_0]\,, \tag{C.11}$$

where $\rho(t)$ is the density matrix describing the entire system, composed of the system of interest and the reservoir. In this derivation, we have substituted the expression of the reduced density matrix for the reservoir $\rho_{\text{R}}(t) = \mathrm{Tr}_{\text{S}}[\rho(t)]$ which, in this case, is given by the constant density matrix B_0. Therefore, considering Equation C.11, all the previous

traces in Equation C.10 can be rewritten as correlation functions:

$$\mathrm{Tr_R}\{\tilde{\mathcal{R}}_k(t-\tau)\,B_0\,\tilde{\mathcal{R}}_j(t)\} = \mathrm{Tr_R}\{\tilde{\mathcal{R}}_j(t)\,\tilde{\mathcal{R}}_k(t-\tau)\,B_0\} = \langle\tilde{\mathcal{R}}_j(t)\,\tilde{\mathcal{R}}_k(t-\tau)\rangle\,,$$
$$\mathrm{Tr_R}\{\tilde{\mathcal{R}}_j(t)\,B_0\,\tilde{\mathcal{R}}_k(t-\tau)\} = \mathrm{Tr_R}\{B_0\,\tilde{\mathcal{R}}_k(t-\tau)\,\tilde{\mathcal{R}}_j(t)\} = \langle\tilde{\mathcal{R}}_k(t-\tau)\,\tilde{\mathcal{R}}_j(t)\rangle\,.$$

There, we have taken into account that the trace is invariant under cyclic permutation, that is, $\mathrm{Tr}[ABC] = \mathrm{Tr}[BCA] = \mathrm{Tr}[CAB]$, where A, B, and C are operators. Introducing these expressions for the traces, the Equation C.10 results in:

$$\begin{aligned}\dot{\tilde{\rho}}_\mathrm{S}(t) = -\frac{1}{\hbar^2}\sum_{j,k}\int_0^\infty \Big\{\big(\tilde{\mathcal{Q}}_j(t)\,\tilde{\mathcal{Q}}_k(t-\tau)\,\tilde{\rho}_\mathrm{S}(t) - \tilde{\mathcal{Q}}_k(t-\tau)\,\tilde{\rho}_\mathrm{S}(t)\,\tilde{\mathcal{Q}}_j(t)\big) \\ \otimes\,\langle\tilde{\mathcal{R}}_j(t)\,\tilde{\mathcal{R}}_k(t-\tau)\rangle \\ + \big(\tilde{\rho}_\mathrm{S}(t)\,\tilde{\mathcal{Q}}_k(t-\tau)\,\tilde{\mathcal{Q}}_j(t) - \tilde{\mathcal{Q}}_j(t)\,\tilde{\rho}_\mathrm{S}(t)\,\tilde{\mathcal{Q}}_k(t-\tau)\big) \\ \otimes\,\langle\tilde{\mathcal{R}}_k(t-\tau)\,\tilde{\mathcal{R}}_j(t)\rangle\Big\}\,\mathrm{d}\tau\,.\end{aligned} \tag{C.12}$$

Going back to the Schrödinger picture Our intention is to transform this master equation into the Schrödinger picture. In Equation C.2 we obtained a relation between the time derivative of the density matrix in the Shrödinger and in the interaction picture. Now, we are interested in a similar expression but considering just the density matrix associated with the subsystem S. According to Equation B.10, the density matrix in the Schrödinger picture is related to the one in the interaction picture through:

$$\rho_\mathrm{S}(t) = \mathrm{e}^{-\frac{\mathrm{i}}{\hbar}H_\mathrm{S}t}\,\tilde{\rho}_\mathrm{S}(t)\,\mathrm{e}^{\frac{\mathrm{i}}{\hbar}H_\mathrm{S}t}\,. \tag{C.13}$$

If we derive this expression with respect to time, we get:

$$\begin{aligned}\dot{\rho}_\mathrm{S}(t) &= \left(-\frac{\mathrm{i}}{\hbar}\,H_\mathrm{S}\right)\mathrm{e}^{-\frac{\mathrm{i}}{\hbar}H_\mathrm{S}t}\tilde{\rho}_\mathrm{S}(t)\,\mathrm{e}^{\frac{\mathrm{i}}{\hbar}H_\mathrm{S}t} \;+\; \mathrm{e}^{-\frac{\mathrm{i}}{\hbar}H_\mathrm{S}t}\dot{\tilde{\rho}}_\mathrm{S}(t)\,\mathrm{e}^{\frac{\mathrm{i}}{\hbar}H_\mathrm{S}t} \;+\; \mathrm{e}^{-\frac{\mathrm{i}}{\hbar}H_\mathrm{S}t}\tilde{\rho}_\mathrm{S}(t)\,\mathrm{e}^{\frac{\mathrm{i}}{\hbar}H_\mathrm{S}t}\left(\frac{\mathrm{i}}{\hbar}H_\mathrm{S}\right) \\ &= -\frac{\mathrm{i}}{\hbar}\,[H_\mathrm{S},\rho_\mathrm{S}(t)] + \mathrm{e}^{-\frac{\mathrm{i}}{\hbar}H_\mathrm{S}t}\dot{\tilde{\rho}}_\mathrm{S}(t)\,\mathrm{e}^{\frac{\mathrm{i}}{\hbar}H_\mathrm{S}t}\,,\end{aligned}$$

so the time-evolution of the density matrix in the Schrödinger picture is given by the coherent evolution guided by the system Hamiltonian H_S plus some other terms:

$$\dot{\rho}_\mathrm{S}(t) = -\frac{\mathrm{i}}{\hbar}\,[H_\mathrm{S},\rho_\mathrm{S}(t)] + \mathrm{e}^{-\frac{\mathrm{i}}{\hbar}H_\mathrm{S}t}\dot{\tilde{\rho}}_\mathrm{S}(t)\,\mathrm{e}^{\frac{\mathrm{i}}{\hbar}H_\mathrm{S}t}\,.$$

There, we can now substitute the expression of the time derivative $\dot{\tilde{\rho}}_\mathrm{S}(t)$ given in Equation C.12:

$$\begin{aligned}\dot{\rho}_\mathrm{S}(t) = -\frac{\mathrm{i}}{\hbar}\,[H_\mathrm{S},\rho_\mathrm{S}(t)] \\ -\frac{1}{\hbar^2}\sum_{j,k}\int_0^\infty \mathrm{e}^{-\frac{\mathrm{i}}{\hbar}H_\mathrm{S}t}\Big\{\big(\tilde{\mathcal{Q}}_j(t)\tilde{\mathcal{Q}}_k(t-\tau)\tilde{\rho}_\mathrm{S}(t) - \tilde{\mathcal{Q}}_k(t-\tau)\tilde{\rho}_\mathrm{S}(t)\tilde{\mathcal{Q}}_j(t)\big) \\ \otimes\,\langle\tilde{\mathcal{R}}_j(t)\tilde{\mathcal{R}}_k(t-\tau)\rangle \\ + \big(\tilde{\rho}_\mathrm{S}(t)\tilde{\mathcal{Q}}_k(t-\tau)\tilde{\mathcal{Q}}_j(t) - \tilde{\mathcal{Q}}_j(t)\tilde{\rho}_\mathrm{S}(t)\tilde{\mathcal{Q}}_k(t-\tau)\big) \\ \otimes\,\langle\tilde{\mathcal{R}}_k(t-\tau)\tilde{\mathcal{R}}_j(t)\rangle\Big\}\,\mathrm{e}^{\frac{\mathrm{i}}{\hbar}H_\mathrm{S}t}\mathrm{d}\tau\,.\end{aligned} \tag{C.14}$$

All the terms within the integral should be expressed in the Schrödinger picture. By taking into account the transformation of the operators $\tilde{\mathcal{Q}}_j$ shown in Equation C.9, as well as the transformation of the density matrix of Equation C.13, we obtain the transformation of each term separately:

$$\begin{aligned}
\tilde{\mathcal{Q}}_j(t)\tilde{\mathcal{Q}}_k(t-\tau)\tilde{\rho}_S(t) &= e^{\frac{i}{\hbar}H_S t}\,\mathcal{Q}_j\,e^{-\frac{i}{\hbar}H_S t}e^{\frac{i}{\hbar}H_S(t-\tau)}\,\mathcal{Q}_k\,e^{-\frac{i}{\hbar}H_S(t-\tau)}\,e^{\frac{i}{\hbar}H_S t}\,\rho_S(t)\,e^{-\frac{i}{\hbar}H_S t}\\
&= e^{\frac{i}{\hbar}H_S t}\,\mathcal{Q}_j\,e^{-\frac{i}{\hbar}H_S \tau}\,\mathcal{Q}_k\,e^{\frac{i}{\hbar}H_S \tau}\,\rho_S(t)\,e^{-\frac{i}{\hbar}H_S t}\,,\\
\tilde{\mathcal{Q}}_k(t-\tau)\tilde{\rho}_S(t)\tilde{\mathcal{Q}}_j(t) &= e^{\frac{i}{\hbar}H_S(t-\tau)}\,\mathcal{Q}_k\,e^{-\frac{i}{\hbar}H_S(t-\tau)}\,e^{\frac{i}{\hbar}H_S t}\,\rho_S(t)\,e^{-\frac{i}{\hbar}H_S t}\,e^{\frac{i}{\hbar}H_S t}\,\mathcal{Q}_j\,e^{-\frac{i}{\hbar}H_S t}\\
&= e^{\frac{i}{\hbar}H_S(t-\tau)}\,\mathcal{Q}_k\,e^{\frac{i}{\hbar}H_S \tau}\,\rho_S(t)\,\mathcal{Q}_j\,e^{-\frac{i}{\hbar}H_S t}\,,\\
\tilde{\rho}_S(t)\tilde{\mathcal{Q}}_k(t-\tau)\tilde{\mathcal{Q}}_j(t) &= e^{\frac{i}{\hbar}H_S t}\,\rho_S(t)\,e^{-\frac{i}{\hbar}H_S t}\,e^{\frac{i}{\hbar}H_S(t-\tau)}\,\mathcal{Q}_k\,e^{-\frac{i}{\hbar}H_S(t-\tau)}e^{\frac{i}{\hbar}H_S t}\,\mathcal{Q}_j\,e^{-\frac{i}{\hbar}H_S t}\\
&= e^{\frac{i}{\hbar}H_S t}\,\rho_S(t)\,e^{-\frac{i}{\hbar}H_S \tau}\,\mathcal{Q}_k\,e^{\frac{i}{\hbar}H_S \tau}\,\mathcal{Q}_j\,e^{-\frac{i}{\hbar}H_S t}\,,\\
\tilde{\mathcal{Q}}_j(t)\tilde{\rho}_S(t)\tilde{\mathcal{Q}}_k(t-\tau) &= e^{\frac{i}{\hbar}H_S t}\,\mathcal{Q}_j\,e^{-\frac{i}{\hbar}H_S t}\,e^{\frac{i}{\hbar}H_S t}\,\rho_S(t)\,e^{-\frac{i}{\hbar}H_S t}\,e^{\frac{i}{\hbar}H_S(t-\tau)}\,\mathcal{Q}_k\,e^{-\frac{i}{\hbar}H_S(t-\tau)}\\
&= e^{\frac{i}{\hbar}H_S t}\,\mathcal{Q}_j\,\rho_S(t)\,e^{-\frac{i}{\hbar}H_S \tau}\,\mathcal{Q}_k\,e^{-\frac{i}{\hbar}H_S(t-\tau)}\,.
\end{aligned}$$

If we now substitute these terms expressed in the Schrödinger picture into Equation C.14, the master equation becomes:

$$\begin{aligned}
\dot{\rho}_S(t) = &-\frac{i}{\hbar}\,[H_S,\rho_S(t)]\\
&-\frac{1}{\hbar^2}\sum_{j,k}\int_0^\infty \Big\{\Big(\mathcal{Q}_j\,e^{-\frac{i}{\hbar}H_S\tau}\,\mathcal{Q}_k\,e^{\frac{i}{\hbar}H_S\tau}\,\rho_S(t) - e^{-\frac{i}{\hbar}H_S\tau}\,\mathcal{Q}_k\,e^{\frac{i}{\hbar}H_S\tau}\,\rho_S(t)\,\mathcal{Q}_j\Big)\\
&\qquad\otimes\langle\tilde{\mathcal{R}}_j(t)\tilde{\mathcal{R}}_k(t-\tau)\rangle\\
&\quad+\Big(\rho_S(t)\,e^{-\frac{i}{\hbar}H_S\tau}\,\mathcal{Q}_k\,e^{\frac{i}{\hbar}H_S\tau}\,\mathcal{Q}_j - \mathcal{Q}_j\,\rho_S(t)\,e^{-\frac{i}{\hbar}H_S\tau}\,\mathcal{Q}_k\,e^{\frac{i}{\hbar}H_S\tau}\Big)\\
&\qquad\otimes\langle\tilde{\mathcal{R}}_k(t-\tau)\tilde{\mathcal{R}}_j(t)\rangle\Big\}\,d\tau\,.
\end{aligned}\tag{C.15}$$

Writing it in matrix form In order to obtain a matrix expression for the master equation, we consider the eigenstates of the system Hamiltonian H_S, that is:

$$H_S|\omega_n\rangle = \hbar\omega_n|\omega_n\rangle\,,$$

where $|\omega_n\rangle$ stands for the eigenstate of the Hamiltonian associated with the eigenvalue $\hbar\omega_n$. The coherent term of Equation C.15 can be easily written in this basis:

$$\begin{aligned}
[H_S,\rho_S(t)] = H_S\rho_S(t) - \rho_S(t)H_S &= \sum_{m,r,n}|\omega_m\rangle\langle\omega_m|H_S|\omega_r\rangle\langle\omega_r|\rho_S(t)|\omega_n\rangle\langle\omega_n|\\
&\quad-\sum_{m,r,n}|\omega_m\rangle\langle\omega_m|\rho_S(t)|\omega_r\rangle\langle\omega_r|H_S|\omega_n\rangle\langle\omega_n|\\
&= \sum_{m,r,n}\hbar\omega_r|\omega_m\rangle\langle\omega_m|\omega_r\rangle\langle\omega_n|\,\rho_{rn}(t) - \sum_{m,r,n}\hbar\omega_n|\omega_m\rangle\langle\omega_r|\omega_n\rangle\langle\omega_n|\,\rho_{mr}(t)\\
&= \sum_{m,r,n}\hbar\omega_r\delta_{mr}|\omega_m\rangle\langle\omega_n|\,\rho_{rn}(t) - \sum_{m,r,n}\hbar\omega_n\delta_{rn}|\omega_m\rangle\langle\omega_n|\,\rho_{mr}(t)\\
&= \sum_{m,n}\hbar(\omega_m-\omega_n)|\omega_m\rangle\langle\omega_n|\,\rho_{mn}(t)\,,
\end{aligned}$$

where we have introduced the following notation for the matrix element of the density matrix: $\rho_{mn}(t) = \langle\omega_m|\rho_S(t)|\omega_n\rangle$. Instead of considering the complete matrix expression, we focus on the ab-component, which in this case reads:

$$\langle\omega_a|[H_S, \rho_S(t)]|\omega_b\rangle = \hbar(\omega_a - \omega_b)\,\rho_{ab}(t)\,. \tag{C.16}$$

Making use of the closure relation $\mathbb{1} = \sum_m |\omega_m\rangle\langle\omega_m|$, all the other terms belonging to the incoherent part of the master equation can be expressed in this basis. For example, the ab-component of the first of these terms reads:

$$\begin{aligned}
\langle\omega_a|\mathcal{Q}_j e^{-\frac{i}{\hbar}H_S\tau}\mathcal{Q}_k e^{\frac{i}{\hbar}H_S\tau}\rho_S(t)|\omega_b\rangle &= \langle\omega_a|\mathcal{Q}_j\left(\sum_m|\omega_m\rangle\langle\omega_m|\right)e^{-\frac{i}{\hbar}H_S\tau}\left(\sum_p|\omega_p\rangle\langle\omega_p|\right)\\
&\qquad \mathcal{Q}_k\left(\sum_n|\omega_n\rangle\langle\omega_n|\right)e^{\frac{i}{\hbar}H_S\tau}\left(\sum_q|\omega_q\rangle\langle\omega_q|\right)\rho_S(t)|\omega_b\rangle\\
&= \sum_{m,p,n,q}|\omega_l\rangle\langle\omega_l|\mathcal{Q}_j|\omega_m\rangle\langle\omega_m|e^{-\frac{i}{\hbar}H_S\tau}|\omega_p\rangle\langle\omega_p|\mathcal{Q}_k|\omega_n\rangle\langle\omega_n|e^{\frac{i}{\hbar}H_S\tau}|\omega_q\rangle\langle\omega_q|\rho_S(t)|\omega_b\rangle\\
&= \sum_{m,p,n,q}\mathcal{Q}^j_{am}\mathcal{Q}^k_{pn}\langle\omega_m|e^{-i\omega_p\tau}|\omega_p\rangle\langle\omega_n|e^{i\omega_q\tau}|\omega_q\rangle\,\rho_{qb}(t)\\
&= \sum_{m,p,n,q}\mathcal{Q}^j_{am}\mathcal{Q}^k_{pn}e^{-i(\omega_p-\omega_q)\tau}\delta_{m,p}\delta_{n,q}\,\rho_{qb}(t)\\
&= \sum_{m,n}\mathcal{Q}^j_{am}\mathcal{Q}^k_{mn}e^{-i(\omega_m-\omega_n)\tau}\,\rho_{nb}(t)\,,
\end{aligned} \tag{C.17}$$

where $\mathcal{Q}^j_{mn} = \langle\omega_m|\mathcal{Q}_j|\omega_n\rangle$ denotes the matrix elements of the system operators. We perform the same calculation for the remaining terms, yielding:

$$\begin{aligned}
&\langle\omega_a|e^{-\frac{i}{\hbar}H_S\tau}\mathcal{Q}_k e^{\frac{i}{\hbar}H_S\tau}\rho_S(t)\mathcal{Q}_j|\omega_b\rangle\\
&\qquad = \sum_{p,q,m,n}\langle\omega_a|e^{-\frac{i}{\hbar}H_S\tau}|\omega_p\rangle\langle\omega_p|\mathcal{Q}_k|\omega_q\rangle\langle\omega_q|e^{\frac{i}{\hbar}H_S\tau}|\omega_m\rangle\langle\omega_m|\rho_S(t)|\omega_n\rangle\langle\omega_n|\mathcal{Q}_j|\omega_b\rangle\\
&\qquad = \sum_{m,n}\mathcal{Q}^k_{am}\mathcal{Q}^j_{nb}e^{-i(\omega_a-\omega_m)\tau}\,\rho_{mn}(t)\,,
\end{aligned} \tag{C.18}$$

$$\begin{aligned}
&\langle\omega_a|\rho_S(t)e^{-\frac{i}{\hbar}H_S\tau}\mathcal{Q}_k e^{\frac{i}{\hbar}H_S\tau}\mathcal{Q}_j|\omega_b\rangle\\
&\qquad = \sum_{m,p,n,q}\langle\omega_a|\rho_S(t)|\omega_m\rangle\langle\omega_m|e^{-\frac{i}{\hbar}H_S\tau}|\omega_p\rangle\langle\omega_p|\mathcal{Q}_k|\omega_n\rangle\langle\omega_n|e^{\frac{i}{\hbar}H_S\tau}|\omega_q\rangle\langle\omega_q|\mathcal{Q}_j|\omega_b\rangle\\
&\qquad = \sum_{m,n}\mathcal{Q}^k_{mn}\mathcal{Q}^j_{nb}e^{-i(\omega_m-\omega_n)\tau}\,\rho_{am}(t)\,,
\end{aligned} \tag{C.19}$$

$$\begin{aligned}
&\langle\omega_a|\mathcal{Q}_j\rho_S(t)e^{-\frac{i}{\hbar}H_S\tau}\mathcal{Q}_k e^{\frac{i}{\hbar}H_S\tau}|\omega_b\rangle\\
&\qquad = \sum_{m,p,n,q}\langle\omega_a|\mathcal{Q}_j|\omega_m\rangle\langle\omega_m|\rho_S(t)|\omega_p\rangle\langle\omega_p|e^{-\frac{i}{\hbar}H_S\tau}|\omega_n\rangle\langle\omega_n|\mathcal{Q}_k|\omega_q\rangle\langle\omega_q|e^{\frac{i}{\hbar}H_S\tau}|\omega_b\rangle\\
&\qquad = \sum_{m,n}\mathcal{Q}^j_{am}\mathcal{Q}^k_{nb}e^{-i(\omega_n-\omega_b)\tau}\,\rho_{mn}(t)\,.
\end{aligned} \tag{C.20}$$

We now turn to Equation C.15 and write the ab-component of the matrix form associated with the complete master equation:

$$\begin{aligned}\dot{\rho}_{ab}(t) = &-\frac{\mathrm{i}}{\hbar}\langle\omega_a|[H_{\mathrm{S}},\rho_{\mathrm{S}}(t)]|\omega_b\rangle \\ &-\frac{1}{\hbar^2}\sum_{j,k}\int_0^\infty \Big\{\Big(\langle\omega_a|\mathcal{Q}_j\,\mathrm{e}^{-\frac{\mathrm{i}}{\hbar}H_{\mathrm{S}}\tau}\,\mathcal{Q}_k\,\mathrm{e}^{\frac{\mathrm{i}}{\hbar}H_{\mathrm{S}}\tau}\,\rho_{\mathrm{S}}(t)|\omega_b\rangle \\ &\qquad -\langle\omega_a|\mathrm{e}^{-\frac{\mathrm{i}}{\hbar}H_{\mathrm{S}}\tau}\,\mathcal{Q}_k\,\mathrm{e}^{\frac{\mathrm{i}}{\hbar}H_{\mathrm{S}}\tau}\,\rho_{\mathrm{S}}(t)\,\mathcal{Q}_j|\omega_b\rangle\Big)\otimes\langle\tilde{\mathcal{R}}_j(t)\tilde{\mathcal{R}}_k(t-\tau)\rangle \\ &\quad +\Big(\langle\omega_a|\rho_{\mathrm{S}}(t)\,\mathrm{e}^{-\frac{\mathrm{i}}{\hbar}H_{\mathrm{S}}\tau}\,\mathcal{Q}_k\,\mathrm{e}^{\frac{\mathrm{i}}{\hbar}H_{\mathrm{S}}\tau}\,\mathcal{Q}_j|\omega_b\rangle \\ &\qquad -\langle\omega_a|\mathcal{Q}_j\,\rho_{\mathrm{S}}(t)\,\mathrm{e}^{-\frac{\mathrm{i}}{\hbar}H_{\mathrm{S}}\tau}\,\mathcal{Q}_k\,\mathrm{e}^{\frac{\mathrm{i}}{\hbar}H_{\mathrm{S}}\tau}|\omega_b\rangle\Big)\otimes\langle\tilde{\mathcal{R}}_k(t-\tau)\tilde{\mathcal{R}}_j(t)\rangle\Big\}\,\mathrm{d}\tau\,.\end{aligned}$$

There we substitute the components previously obtained in Equation C.16 for the coherent part, and from Equation C.17 to Equation C.20 for the incoherent terms:

$$\begin{aligned}\dot{\rho}_{ab}(t) = &-\mathrm{i}\omega_{ab}\,\rho_{ab}(t) \\ &-\frac{1}{\hbar^2}\sum_{j,k}\int_0^\infty\Bigg\{\Bigg(\sum_{m,n}\mathcal{Q}^j_{am}\mathcal{Q}^k_{mn}\mathrm{e}^{-\mathrm{i}\omega_{mn}\tau}\,\rho_{nb}(t)-\sum_{m,n}\mathcal{Q}^k_{am}\mathcal{Q}^j_{nb}\mathrm{e}^{-\mathrm{i}\omega_{am}\tau}\rho_{mn}(t)\Bigg) \\ &\qquad\otimes\langle\tilde{\mathcal{R}}_j(t)\tilde{\mathcal{R}}_k(t-\tau)\rangle \\ &\quad+\Bigg(\sum_{m,n}\mathcal{Q}^k_{mn}\mathcal{Q}^j_{nb}\mathrm{e}^{-\mathrm{i}\omega_{mn}\tau}\,\rho_{am}(t)-\sum_{m,n}\mathcal{Q}^j_{am}\mathcal{Q}^k_{nb}\mathrm{e}^{-\mathrm{i}\omega_{nb}\tau}\rho_{mn}(t)\Bigg) \\ &\qquad\otimes\langle\tilde{\mathcal{R}}_k(t-\tau)\tilde{\mathcal{R}}_j(t)\rangle\Big\}\,\mathrm{d}\tau \\ = &-\mathrm{i}\omega_{ab}\,\rho_{ab}(t) \\ &-\frac{1}{\hbar^2}\sum_{j,k}\int_0^\infty\Bigg\{\Bigg(\sum_{m,n}\delta_{bm}\sum_o\mathcal{Q}^j_{ao}\mathcal{Q}^k_{on}\mathrm{e}^{-\mathrm{i}\omega_{on}\tau}\rho_{nm}(t)-\sum_{m,n}\mathcal{Q}^k_{am}\mathcal{Q}^j_{nb}\mathrm{e}^{-\mathrm{i}\omega_{am}\tau}\rho_{mn}(t)\Bigg) \\ &\qquad\otimes\langle\tilde{\mathcal{R}}_j(t)\tilde{\mathcal{R}}_k(t-\tau)\rangle \\ &\quad+\Bigg(\sum_{m,n}\delta_{na}\sum_o\mathcal{Q}^k_{mo}\mathcal{Q}^j_{ob}\mathrm{e}^{-\mathrm{i}\omega_{mo}\tau}\rho_{nm}(t)-\sum_{m,n}\mathcal{Q}^j_{am}\mathcal{Q}^k_{nb}\mathrm{e}^{-\mathrm{i}\omega_{nb}\tau}\rho_{mn}(t)\Bigg) \\ &\qquad\otimes\langle\tilde{\mathcal{R}}_k(t-\tau)\tilde{\mathcal{R}}_j(t)\rangle\Big\}\,\mathrm{d}\tau\,,\end{aligned}$$

where we have introduced the following notation for the frequency difference: $\omega_{mn}\equiv\omega_m-\omega_n$. Interchanging the subindices m and n in two of these terms so as to have the

component ρ_{mn} in common, we finally have:

$$\begin{aligned}\dot{\rho}_{ab}(t) = &-\mathrm{i}\omega_{ab}\,\rho_{ab}(t)\\ &-\frac{1}{\hbar^2}\sum_{j,k}\sum_{m,n}\int_0^\infty\Bigg\{\Bigg(\delta_{bn}\sum_o \mathcal{Q}^j_{ao}\mathcal{Q}^k_{om}\mathrm{e}^{-\mathrm{i}\omega_{om}\tau} - \mathcal{Q}^k_{am}\mathcal{Q}^j_{nb}\mathrm{e}^{-\mathrm{i}\omega_{am}\tau}\Bigg)\\ &\qquad\otimes\langle\tilde{\mathcal{R}}_j(t)\tilde{\mathcal{R}}_k(t-\tau)\rangle\\ &+\Bigg(\delta_{ma}\sum_o \mathcal{Q}^k_{no}\mathcal{Q}^j_{ob}\mathrm{e}^{-\mathrm{i}\omega_{no}\tau} - \mathcal{Q}^j_{am}\mathcal{Q}^k_{nb}\mathrm{e}^{-\mathrm{i}\omega_{nb}\tau}\Bigg)\\ &\qquad\otimes\langle\tilde{\mathcal{R}}_k(t-\tau)\tilde{\mathcal{R}}_j(t)\rangle\Bigg\}\;\rho_{mn}(t)\,\mathrm{d}\tau\;,\end{aligned} \tag{C.21}$$

Correlation functions Given two (complex) stationary functions, $z_j(t)$ and $z_k(t)$, the two-time correlation function is defined as:

$$\Gamma_{jk}(\tau) = \langle z_j^*(t)\, z_k(t+\tau)\rangle = \langle z_j^*(0)\, z_k(\tau)\rangle\;, \tag{C.22}$$

where we have taken into account that the correlation function does not depend on time t, but just on the time delay τ. Its complex conjugate will be given by:

$$\Gamma^*_{jk}(\tau) = \langle z_j^*(0)\, z_k(\tau)\rangle^* = \langle z_k^*(\tau)\, z_j(0)\rangle = \langle z_k^*(0)\, z_j(-\tau)\rangle = \Gamma_{kj}(-\tau)\;.$$

Equivalently, the two correlation functions appearing in the master equation can be expressed as:

$$\begin{aligned}&\langle\tilde{\mathcal{R}}_j(t)\,\tilde{\mathcal{R}}_k(t-\tau)\rangle = \langle\tilde{\mathcal{R}}_j(0)\,\tilde{\mathcal{R}}_k(-\tau)\rangle = \Gamma_{jk}(-\tau)\\ &\langle\tilde{\mathcal{R}}_k(t-\tau)\,\tilde{\mathcal{R}}_j(t)\rangle = \langle\tilde{\mathcal{R}}_k(-\tau)\,\tilde{\mathcal{R}}_j(0)\rangle = \langle\tilde{\mathcal{R}}_k(0)\,\tilde{\mathcal{R}}_j(\tau)\rangle = \Gamma_{kj}(\tau) = \Gamma^*_{jk}(-\tau)\;,\end{aligned} \tag{C.23}$$

so Equation C.21 can be rewritten as:

$$\begin{aligned}\dot{\rho}_{ab}(t) = &-\mathrm{i}\omega_{ab}\,\rho_{ab}(t)\\ &-\frac{1}{\hbar^2}\sum_{j,k}\sum_{m,n}\int_0^\infty\Bigg\{\Bigg(\delta_{bn}\sum_o \mathcal{Q}^j_{ao}\mathcal{Q}^k_{om}\mathrm{e}^{-\mathrm{i}\omega_{om}\tau} - \mathcal{Q}^k_{am}\mathcal{Q}^j_{nb}\mathrm{e}^{-\mathrm{i}\omega_{am}\tau}\Bigg)\otimes\Gamma_{jk}(-\tau)\\ &+\Bigg(\delta_{ma}\sum_o \mathcal{Q}^k_{no}\mathcal{Q}^j_{ob}\mathrm{e}^{-\mathrm{i}\omega_{no}\tau} - \mathcal{Q}^j_{am}\mathcal{Q}^k_{nb}\mathrm{e}^{-\mathrm{i}\omega_{nb}\tau}\Bigg)\otimes\Gamma^*_{jk}(-\tau)\Bigg\}\;\rho_{mn}(t)\,\mathrm{d}\tau\;.\end{aligned} \tag{C.24}$$

Spectral density From the two-point correlation function $\Gamma_{jk}(\tau)$ given in Equation C.22, the spectral density (or power spectrum) is then defined as:

$$\Theta_{jk}(\omega) = \frac{1}{2\pi}\int_{-\infty}^{\infty}\Gamma_{jk}(\tau)\,\mathrm{e}^{\mathrm{i}\omega\tau}\mathrm{d}\tau\;,$$

whose complex conjugate will be given by:

$$\begin{aligned}\Theta^*_{jk}(\omega) = \frac{1}{2\pi}\int_{-\infty}^{\infty}\Gamma^*_{jk}(\tau)\,\mathrm{e}^{-\mathrm{i}\omega\tau}\mathrm{d}\tau &= \frac{1}{2\pi}\int_{-\infty}^{\infty}\Gamma_{kj}(-\tau)\,\mathrm{e}^{-\mathrm{i}\omega\tau}\mathrm{d}\tau\\ &= \frac{1}{2\pi}\int_{-\infty}^{\infty}\Gamma_{kj}(\tau)\,\mathrm{e}^{\mathrm{i}\omega\tau}\mathrm{d}\tau = \Theta_{kj}(\omega)\;.\end{aligned}$$

Additionally, it can be shown that the half integral of the correlation function is given by:

$$\frac{1}{2\pi}\int_0^\infty \Gamma_{jk}(\tau)\, \mathrm{e}^{\mathrm{i}\omega\tau}\mathrm{d}\tau = \frac{1}{2}\Theta_{jk}(\omega) + \mathrm{i}\chi_{jk}(\omega)\,,$$

where χ_{jk} entails a (complex) shift in the frequency. Then, the integral in Equation C.24 can be solved by introducing the corresponding spectral density. Two types of terms appear, that are computed as follows:

$$\begin{aligned}\int_0^\infty \mathrm{e}^{-\mathrm{i}(\omega_o-\omega_m)\tau}\Gamma_{jk}(-\tau)\,\mathrm{d}\tau &= \pi\Theta_{jk}(\omega_o-\omega_m)\\ \int_0^\infty \mathrm{e}^{-\mathrm{i}(\omega_n-\omega_o)\tau}\Gamma^*_{jk}(-\tau)\,\mathrm{d}\tau = \int_0^\infty \mathrm{e}^{\mathrm{i}(\omega_o-\omega_n)\tau}\Gamma_{kj}(\tau)\,\mathrm{d}\tau &= \pi\Theta_{kj}(\omega_o-\omega_n)\\ &= \pi\Theta^*_{jk}(\omega_o-\omega_n)\,,\end{aligned}$$

where we have neglected the energy shift (otherwise some other extra terms appear [615]). By introducing these expressions in Equation C.24, the master equation reduces to:

$$\begin{aligned}\dot\rho_{ab}(t) = &-\mathrm{i}\omega_{ab}\;\rho_{ab}(t)\\ &-\frac{\pi}{\hbar^2}\sum_{j,k}\sum_{m,n}\;\Big(\delta_{bn}\sum_o \mathcal{Q}^j_{ao}\mathcal{Q}^k_{om}\Theta_{jk}(\omega_o-\omega_m) - \mathcal{Q}^k_{am}\mathcal{Q}^j_{nb}\Theta_{jk}(\omega_a-\omega_m)\\ &\quad+\delta_{ma}\sum_o \mathcal{Q}^k_{no}\mathcal{Q}^j_{ob}\Theta^*_{jk}(\omega_o-\omega_n) - \mathcal{Q}^j_{am}\mathcal{Q}^k_{nb}\Theta^*_{jk}(\omega_b-\omega_n)\Big)\;\rho_{mn}(t)\;.\end{aligned} \tag{C.25}$$

This equation for the components of the density matrix can be rewritten in terms of operators, as $\rho_\mathrm{S} = \sum_{a,b}\rho_{ab}|\omega_a\rangle\langle\omega_b|$, yielding:

$$\begin{aligned}\dot\rho_\mathrm{S}(t) = &-\frac{\mathrm{i}}{\hbar}\,[H_\mathrm{S},\rho_\mathrm{S}(t)]\\ &-\frac{\pi}{\hbar^2}\sum_{j,k}\sum_{m,n}\Big\{\langle\omega_m|\mathcal{Q}_k|\omega_n\rangle\left(\mathcal{Q}_j|\omega_m\rangle\langle\omega_n|\rho_\mathrm{S}(t) - |\omega_m\rangle\langle\omega_n|\rho_\mathrm{S}(t)\mathcal{Q}_j\right)\Theta_{jk}(\omega_m-\omega_n)\\ &\quad+\langle\omega_n|\mathcal{Q}_k|\omega_m\rangle\left(\rho_\mathrm{S}(t)|\omega_n\rangle\langle\omega_m|\mathcal{Q}_j - \mathcal{Q}_j\rho_\mathrm{S}(t)|\omega_n\rangle\langle\omega_m|\right)\Theta^*_{jk}(\omega_m-\omega_n)\Big\}\,.\end{aligned} \tag{C.26}$$

Therefore, we have finally obtained an expression for the time-evolution of the density matrix in the Schrödinger picture where the incoherent part is given in term of the spectral function of the reservoir.

Bloch–Redfield tensor The master equation given in Equation C.25 can be expressed in shorthand as:

$$\dot\rho_{ab}(t) = -\mathrm{i}\omega_{ab}\;\rho_{ab}(t) + \sum_{m,n} R_{abmn}\;\rho_{mn}(t)\;,$$

where we have defined the so-called **Bloch–Redfield tensor** comprising all the incoherent part of the master equation:

$$R_{abmn} = -\frac{\pi}{\hbar^2}\sum_{j,k}\Bigg(\delta_{bn}\sum_{o}\mathcal{Q}^j_{ao}\mathcal{Q}^k_{om}\Theta_{jk}(\omega_o-\omega_m) - \mathcal{Q}^k_{am}\mathcal{Q}^j_{nb}\Theta_{jk}(\omega_a-\omega_m) \\ +\delta_{ma}\sum_{o}\mathcal{Q}^k_{no}\mathcal{Q}^j_{ob}\Theta^*_{jk}(\omega_o-\omega_n) - \mathcal{Q}^j_{am}\mathcal{Q}^k_{nb}\Theta^*_{jk}(\omega_b-\omega_n)\Bigg)\,. \tag{C.27}$$

Secular approximation Additionally, fast oscillating terms (in the interaction picture) can be disregarded as their contribution is small. This is known as **secular approximation**, through which all terms that correspond to transition frequencies much smaller than the characteristic frequencies of the system can be neglected.

APPENDIX D

QUANTUM DESCRIPTION OF LIGHT-MATTER INTERACTION

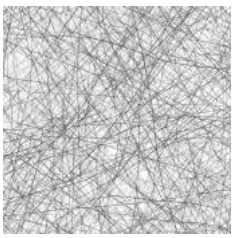

In this Appendix we provide some extensions of the topics discussed in Section 2.2, dealing with the quantum description of light-matter interaction. First, we discuss the canonical quantization of the free electromagnetic field: we start with the quantum-mechanical harmonic oscillator (Section D.1) and, then, discuss the standard quantization procedure of the electromagnetic field in infinite volume and within a cavity (Section D.2). Then, the light-matter interaction Hamiltonian is derived considering the minimal-coupling procedure and, later, performing the electric-dipole approximation (Section D.3). The procedure of the transformation to the rotating frame is finally discussed (Section D.4), which is convenient when dealing with time-dependent Hamiltonians.

D.1 The quantum-mechanical harmonic oscillator

Let us consider a (one-dimensional) **harmonic oscillator** of mass m and force constant κ, whose classical Hamiltonian is given by:

$$H = \frac{p^2}{2m} + \frac{1}{2}m\omega^2 q^2 \,,$$

where $\omega = \sqrt{\kappa/m}$ is the frequency of the different modes. From the **correspondence principle**, the classical position and momentum variables q and p can be promoted to Hermitian operators, and the classical Hamiltonian gives way to its quantum version $\hat{H}$:

$$\hat{H} = \frac{\hat{p}^2}{2m} + \frac{1}{2}m\omega^2\hat{q}^2 \,. \tag{D.1}$$

The position and momentum operators $\hat{p}$ and $\hat{q}$ obey the commutation relation $[\hat{q}, \hat{p}] = i\hbar$. From them, the non-Hermitian **ladder operators** $\hat{a}^\dagger$ and $\hat{a}$ are defined as:

$$\begin{aligned} \hat{a}^\dagger &= \frac{1}{\sqrt{2m\hbar\omega}}(m\omega\hat{q} - i\hat{p}) \,, \\ \hat{a} &= \frac{1}{\sqrt{2m\hbar\omega}}(m\omega\hat{q} + i\hat{p}) \,, \end{aligned} \tag{D.2}$$

also known as the creation and annihilation operators, respectively. These satisfy the commutation relation:

$$[\hat{a}, \hat{a}^\dagger] = \hat{a}\hat{a}^\dagger - \hat{a}^\dagger\hat{a} = 1 \,. \tag{D.3}$$

In terms of the ladder operators $\hat{a}^\dagger$ and $\hat{a}$, the harmonic oscillator Hamiltonian (Equation D.1) reads:

$$\hat{H} = \hbar\omega\left(\frac{1}{2} + \hat{a}^\dagger\hat{a}\right) \,. \tag{D.4}$$

Let $|n\rangle$ be the eigenstates of the system with associated eigenvalue E_n, that is, $\hat{H}|n\rangle = E_n|n\rangle$. When solving the Schrödinger equation for the harmonic oscillator Hamiltonian of Equation D.4, it is found that the **energy spectrum** is given by:

$$E_n = \left(\frac{1}{2} + n\right)\hbar\omega \,, \tag{D.5}$$

where $n = 0, 1, 2\ldots$ The lowest energy level ($n = 0$) correspond to the **ground state**, also known as **vacuum state**, whose energy is given by: $E_0 = \frac{1}{2}\hbar\omega$. Above this state, the spectrum of the harmonic oscillator consist of equally-spaced energy levels separated by an amount $\hbar\omega$. The index n thus represents the number of quanta or excitations of energy $\hbar\omega$. Since states $|n\rangle$ are eigenstates of the product $\hat{a}^\dagger\hat{a}$ with:

$$\hat{a}^\dagger\hat{a}\ |n\rangle = n\ |n\rangle \,,$$

the operator $\hat{n} \equiv \hat{a}^\dagger\hat{a}$ is known as the **number operator** —when applied to a state, it yields its number of excitations. In the same way, states $|n\rangle$ are named **number states** or **Fock states**, because they represent states with a fixed number of excitations. The ladder operators $\hat{a}^\dagger$ and $\hat{a}$ act on number states as follows:

$$\begin{aligned} a^\dagger|n\rangle &= \sqrt{n+1}\ |n+1\rangle \,, \\ a|n\rangle &= \sqrt{n}\ |n-1\rangle \,, \end{aligned} \tag{D.6}$$

that is, they respectively move a step up or down in the energy ladder, bringing a state with n excitations to one with $n+1$ or $n-1$ excitations, as applicable. Therefore, they create or destroy a quantum $\hbar\omega$ of the excitation energy of the oscillator. For these reason, $\hat{a}^\dagger$ and $\hat{a}$ are commonly known as the **creation** and **annihilation operators**, respectively.

The ground state $|0\rangle$ is defined such that $\hat{a}|0\rangle = 0$. This corresponds to the state with no particles, thus it is also called **vacuum state**, as already mentioned. Notice that we can obtain all the other states from the vacuum by applying the creation operator successively:

$$|n\rangle = \frac{(\hat{a}^\dagger)^n}{\sqrt{n!}}|0\rangle \,,$$

where the factor in the denominator ensures the normalization of the state.

D.2 Quantization of the free electromagnetic field

The quantization of the electromagnetic field is performed from the classical equations, with the eventual promotion of the classical variables to quantum operators. The equations of the classical theory should be first put into a suitable form where the electromagnetic field is described as a collection of harmonic oscillators. From that, the replacement from a classical to a quantum oscillator is easily carried out. The canonical quantization of the free electromagnetic field can be found in many textbooks (see for instance Ref. [1, 616])

D.2.1 The classical radiation field

The electromagnetic field in a medium

In the framework of classical electrodynamics, the **electric field** $\boldsymbol{E}$ and the **magnetic field** $\boldsymbol{B}$ in presence of the electric charge density ρ and the electric current density $\boldsymbol{J}$ are governed by the **Maxwell equations**:

$$\nabla \cdot \boldsymbol{E} = \frac{\rho}{\epsilon_0} , \qquad \text{(D.7)} \qquad\qquad \nabla \cdot \boldsymbol{B} = 0 , \qquad \text{(D.8)}$$

$$\nabla \times \boldsymbol{E} + \frac{\partial \boldsymbol{B}}{\partial t} = 0 , \qquad \text{(D.9)} \qquad\qquad \nabla \times \boldsymbol{B} - \frac{1}{c^2}\frac{\partial \boldsymbol{E}}{\partial t} = \mu_0 \boldsymbol{J} , \qquad \text{(D.10)}$$

written in the SI convention. All these variables are functions of position $\boldsymbol{x}$ and time t, although it is not explicitly written so as to simplify the notation. In these equations, ∂ represents the partial derivative and ∇ is the nabla operator (the three-dimensional gradient operator). The speed of light c is connected to the vacuum permittivity ϵ_0 and the vacuum permeability μ_0 through: $c = 1/\sqrt{\epsilon_0 \mu_0}$. Both the electric and the magnetic fields can be expressed in terms of the **vector potential** $\boldsymbol{A}$ and the **scalar potential** ϕ as:

$$\boldsymbol{E} = -\frac{\partial \boldsymbol{A}}{\partial t} - \nabla \phi , \qquad \boldsymbol{B} = \nabla \times \boldsymbol{A} , \qquad \text{(D.11)}$$

which makes Equation D.8 and Equation D.9 be satisfied identically. The substitution of fields thus expressed in Equation D.7 and Equation D.10 yields:

$$\begin{aligned} -\frac{\partial}{\partial t}(\nabla \cdot \boldsymbol{A}) - \nabla^2 \phi &= \frac{\rho}{\epsilon_0} , \\ \nabla \times \nabla \times \boldsymbol{A} + \frac{1}{c^2}\frac{\partial^2 \boldsymbol{A}}{\partial t^2} + \frac{1}{c^2}\frac{\partial}{\partial t}(\nabla \phi) &= \mu_0 \boldsymbol{J} , \end{aligned} \qquad \text{(D.12)}$$

where we can make use of the vector identity: $\nabla \times \nabla \times \boldsymbol{A} \equiv \nabla(\nabla \cdot \boldsymbol{A}) - \nabla^2 \boldsymbol{A}$.

The transversality condition

Potentials in Equation D.11 are not unique, since Maxwell equations are invariant under the **gauge transformation**:

$$\begin{aligned}\phi &\rightarrow \phi' = \phi - \frac{\partial \Lambda}{\partial t}\,,\\ \boldsymbol{A} &\rightarrow \boldsymbol{A}' = \boldsymbol{A} + \nabla\Lambda\,,\end{aligned}$$

where Λ is an arbitrary scalar function depending on position and time as well. A specific gauge can be selected by imposing some condition on ϕ and $\boldsymbol{A}$. In particular, the **Coulomb gauge** reads:

$$\nabla\cdot\boldsymbol{A} = 0\,, \tag{D.13}$$

also known as the transversality condition (a transverse field is that whose divergence is zero). By introducing the Coulomb gauge, Equation D.12 get reduced to:

$$-\nabla^2\phi = \frac{\rho}{\epsilon_0}\,, \tag{D.14}$$

$$-\nabla^2\boldsymbol{A} + \frac{1}{c^2}\frac{\partial^2\boldsymbol{A}}{\partial t^2} + \frac{1}{c^2}\frac{\partial}{\partial t}(\nabla\phi) = \mu_0\boldsymbol{J}\,. \tag{D.15}$$

The second of these equations can be further simplified by considering the decomposition of the current density $\boldsymbol{J}$ in its transverse (T) and longitudinal (L) components, $\boldsymbol{J} = \boldsymbol{J}_\mathrm{T} + \boldsymbol{J}_\mathrm{L}$, such that $\nabla\cdot\boldsymbol{J}_\mathrm{T} = 0$ and $\nabla\times\boldsymbol{J}_\mathrm{L} = 0$ (see Helmholtz's theorem). Then, Equation D.15 can be split in its longitudinal and transverse parts:

$$\begin{aligned}\frac{1}{c^2}\frac{\partial}{\partial t}(\nabla\phi) &= \mu_0\boldsymbol{J}_\mathrm{L}\,,\\ -\nabla^2\boldsymbol{A} + \frac{1}{c^2}\frac{\partial^2\boldsymbol{A}}{\partial t^2} &= \mu_0\boldsymbol{J}_\mathrm{T}\,,\end{aligned} \tag{D.16}$$

since the vector potential $\boldsymbol{A}$ is transverse (Equation D.13) and $\nabla\phi$ is a longitudinal field (from the identity $\nabla\times\nabla\phi \equiv 0$, for any scalar field ϕ). Similarly, the electric field $\boldsymbol{E}$ (Equation D.11) can be also separated into its longitudinal (L) and transverse (T) parts:

$$\boldsymbol{E}_\mathrm{L} = -\nabla\phi\,, \qquad \boldsymbol{E}_\mathrm{T} = -\frac{\partial\boldsymbol{A}}{\partial t}\,, \tag{D.17}$$

while the magnetic field $\boldsymbol{B}$ is wholly transverse according to Equation D.8.

The electromagnetic field in vacuum

The starting point for the quantization of the electromagnetic field in **free space** (that is, where there is no matter to interact with the radiation) is the Maxwell equations in vacuum, without charges ($\rho = 0$) nor currents ($\boldsymbol{J} = 0$). In that case, Equation D.16 reduces to:

$$\nabla^2\boldsymbol{A} = \frac{1}{c^2}\frac{\partial^2\boldsymbol{A}}{\partial t^2}\,, \tag{D.18}$$

where $\boldsymbol{A}$ satisfies the Coulomb gauge condition (Equation D.13). We enclose the electromagnetic field within a cubic box of side L, where periodic boundary conditions are assumed. The general solution for the **vector potential** $\boldsymbol{A}$ can be written as the superposition of modes with associated **wavevector** $\boldsymbol{k}$ and **polarization** λ:

$$\boldsymbol{A}(\boldsymbol{x},t) = \sum_{\boldsymbol{k}}\sum_{\lambda}\left[\boldsymbol{\epsilon}_{\boldsymbol{k}\lambda}a_{\boldsymbol{k}\lambda}(t)\,\mathrm{e}^{\mathrm{i}\boldsymbol{k}\cdot\boldsymbol{x}} + \boldsymbol{\epsilon}^*_{\boldsymbol{k}\lambda}a^*_{\boldsymbol{k}\lambda}(t)\,\mathrm{e}^{-\mathrm{i}\boldsymbol{k}\cdot\boldsymbol{x}}\right]\,, \tag{D.19}$$

where $\sum_{\boldsymbol{k}} \equiv \sum_{n_x}\sum_{n_y}\sum_{n_z}$ stands for the sum over all possible wavevectors compatible with the boundary conditions, namely:

$$k_x = \frac{2\pi}{L} n_x \,, \qquad k_y = \frac{2\pi}{L} n_y \,, \qquad k_z = \frac{2\pi}{L} n_z \,, \tag{D.20}$$

with $n_x, n_y, n_z = 0, \pm 1, \pm 2, \ldots$ In Equation D.19, the coefficients $a_{\boldsymbol{k}\lambda}$ and $a^*_{\boldsymbol{k}\lambda}$ are the (complex) **amplitudes** of the modes, and the subindex λ runs over the two possible polarization values (that is, $\lambda = 1, 2$). The (unit) **polarization vectors** $\boldsymbol{\epsilon}_{\boldsymbol{k}\lambda}$ are both transverse (imposed by the Coulomb gauge) and perpendicular to each other, so they obey:

$$\begin{aligned} \boldsymbol{k} \cdot \boldsymbol{\epsilon}_{\boldsymbol{k}\lambda} &= 0 \,, \\ \boldsymbol{\epsilon}^*_{\boldsymbol{k}\lambda} \cdot \boldsymbol{\epsilon}_{\boldsymbol{k}\lambda'} &= \delta_{\lambda\lambda'} \,, \end{aligned} \tag{D.21}$$

where $\delta_{\lambda\lambda'}$ is the Kronecker delta (it is equal to one when the two indices are identical and is zero otherwise). Therefore, given a wavevector $\boldsymbol{k}$, the polarization vectors $\boldsymbol{\epsilon}_{\boldsymbol{k}1}$ and $\boldsymbol{\epsilon}_{\boldsymbol{k}2}$ are chosen such that $(\boldsymbol{\epsilon}_{\boldsymbol{k}1}, \boldsymbol{\epsilon}_{\boldsymbol{k}2}, \boldsymbol{k}/|\boldsymbol{k}|)$ forms an orthonormal basis. All mode components in Equation D.19 are independent from each other, so they separately obey Equation D.18. This leads to the following equation of motion for the coefficients:

$$\frac{\partial^2 a_{\boldsymbol{k}\lambda}(t)}{\partial t^2} + \omega_k^2 a_{\boldsymbol{k}\lambda}(t) = 0 \,,$$

where we have defined the **mode frequency** $\omega_k = c|\boldsymbol{k}|$. The solution of this equation reads:

$$a_{\boldsymbol{k}\lambda}(t) = a_{\boldsymbol{k}\lambda} \mathrm{e}^{-\mathrm{i}\omega_k t},$$

and substituting this time evolution for the coefficients in Equation D.19, the vector potential finally becomes:

$$\boldsymbol{A}(\boldsymbol{x}, t) = \sum_{\boldsymbol{k}} \sum_{\lambda} \left[\boldsymbol{\epsilon}_{\boldsymbol{k}\lambda} a_{\boldsymbol{k}\lambda} \mathrm{e}^{\mathrm{i}(\boldsymbol{k}\cdot\boldsymbol{x} - \omega_k t)} + \boldsymbol{\epsilon}^*_{\boldsymbol{k}\lambda} a^*_{\boldsymbol{k}\lambda} \mathrm{e}^{-\mathrm{i}(\boldsymbol{k}\cdot\boldsymbol{x} - \omega_k t)} \right] . \tag{D.22}$$

According to Equation D.11 and Equation D.17, the transverse **electric field** $\boldsymbol{E}_{\mathrm{T}}$ and the **magnetic field** $\boldsymbol{B}$ in the Coulomb gauge are given in terms of the vector potential $\boldsymbol{A}$ as follows:

$$\boldsymbol{E}_{\mathrm{T}} = -\frac{\partial \boldsymbol{A}}{\partial t} \,, \qquad \boldsymbol{B} = \nabla \times \boldsymbol{A} \,.$$

By substituting the general solution for the vector potential given in Equation D.19, we have:

$$\begin{aligned} \boldsymbol{E}_{\mathrm{T}}(\boldsymbol{x}, t) &= \mathrm{i}\omega_{\boldsymbol{k}} \sum_{\boldsymbol{k}} \sum_{\lambda} \boldsymbol{\epsilon}_{\boldsymbol{k}\lambda} \left[a_{\boldsymbol{k}\lambda} \mathrm{e}^{\mathrm{i}(\boldsymbol{k}\cdot\boldsymbol{x} - \omega_k t)} - a^*_{\boldsymbol{k}\lambda} \mathrm{e}^{-\mathrm{i}(\boldsymbol{k}\cdot\boldsymbol{x} - \omega_k t)} \right] , \\ \boldsymbol{B}(\boldsymbol{x}, t) &= \mathrm{i} \sum_{\boldsymbol{k}} \sum_{\lambda} [\boldsymbol{k} \times \boldsymbol{\epsilon}_{\boldsymbol{k}\lambda}] \left[a_{\boldsymbol{k}\lambda} \mathrm{e}^{\mathrm{i}(\boldsymbol{k}\cdot\boldsymbol{x} - \omega_k t)} - a^*_{\boldsymbol{k}\lambda} \mathrm{e}^{-\mathrm{i}(\boldsymbol{k}\cdot\boldsymbol{x} - \omega_k t)} \right] , \end{aligned} \tag{D.23}$$

where we have assumed real polarization vectors. The total **energy of the electromagnetic field** within the box is given by:

$$\mathscr{E}_{\mathrm{rad}} = \frac{1}{2} \int_{\mathrm{box}} \mathrm{d}V \left[\epsilon_0 \, \boldsymbol{E}_{\mathrm{T}}(\boldsymbol{x}, t) \cdot \boldsymbol{E}_{\mathrm{T}}(\boldsymbol{x}, t) + \frac{1}{\mu_0} \boldsymbol{B}(\boldsymbol{x}, t) \cdot \boldsymbol{B}(\boldsymbol{x}, t) \right] . \tag{D.24}$$

This integral can be evaluated by substituting the electric and magnetic fields from Equa-

tion D.23, arriving at:

$$\mathscr{E}_{\text{rad}} = 2\epsilon_0 V \sum_{\boldsymbol{k}} \sum_{\lambda} \omega_k^2 a_{\boldsymbol{k}\lambda}^* a_{\boldsymbol{k}\lambda} \,, \tag{D.25}$$

where $V = L^3$ is the volume of the box. The contribution of each mode resembles the Hamiltonian associated with a quantum mechanical oscillator (Equation D.4), once the ground state contribution is removed. In fact, we can define the variables $q_{\boldsymbol{k}\lambda}$ and $p_{\boldsymbol{k}\lambda}$ as follows:

$$\begin{aligned} a &= \frac{1}{2\omega_k \sqrt{\epsilon_0 V m}} (m\omega_k q_{\boldsymbol{k}\lambda} + \mathrm{i} p_{\boldsymbol{k}\lambda}) \,, \\ a^* &= \frac{1}{2\omega_k \sqrt{\epsilon_0 V m}} (m\omega_k q_{\boldsymbol{k}\lambda} - \mathrm{i} p_{\boldsymbol{k}\lambda}) \,, \end{aligned}$$

such that Equation D.25 becomes:

$$\mathscr{E}_{\text{rad}} = \sum_{\boldsymbol{k}} \sum_{\lambda} \left[\frac{1}{2} m\omega_k^2 q_{\boldsymbol{k}\lambda}^2 + \frac{p_{\boldsymbol{k}\lambda}^2}{2m} \right] .$$

Then, $q_{\boldsymbol{k}\lambda}$ and $p_{\boldsymbol{k}\lambda}$ can be seen as the canonical position and momentum variables. Therefore, the electromagnetic field can be thought of as a collection of independent and uncoupled harmonic oscillators (characterized by the wavevector $\boldsymbol{k}$ and the polarization λ), whose quantization can be performed as done in Section D.1.

D.2.2 The quantum radiation field

Quantization within a box

In the previous section we have considered the classical electromagnetic field confined in a cubic box of side L (and volume $V = L^3$), such that the general solution for the vector potential $\boldsymbol{A}$ was given by Equation D.22. The quantization procedure involves the substitution of the classical vector fields by the corresponding quantum-mechanical operators. By comparing the classical electromagnetic energy written as in Equation D.25 with the quantum Hamiltonian corresponding to the harmonic oscillator (Equation D.4), we can introduce the following identification:

$$\begin{aligned} a_{\boldsymbol{k}\lambda} \quad &\to \quad \sqrt{\frac{\hbar}{2\epsilon_0 V \omega_k}}\, \hat{a}_{\boldsymbol{k}\lambda} \,, \\ a_{\boldsymbol{k}\lambda}^* \quad &\to \quad \sqrt{\frac{\hbar}{2\epsilon_0 V \omega_k}}\, \hat{a}_{\boldsymbol{k}\lambda}^\dagger \,. \end{aligned}$$

By carrying out these replacements in Equation D.22, the **vector potential operator** $\hat{A}$ is written as:

$$\hat{\boldsymbol{A}}(\boldsymbol{x}, t) = \sum_{\boldsymbol{k}} \sum_{\lambda} \sqrt{\frac{\hbar}{2\epsilon_0 V \omega_k}} \boldsymbol{\epsilon}_{\boldsymbol{k}\lambda} \left[\hat{a}_{\boldsymbol{k}\lambda} \mathrm{e}^{\mathrm{i}(\boldsymbol{k}\cdot\boldsymbol{x} - \omega_k t)} + \hat{a}_{\boldsymbol{k}\lambda}^\dagger \mathrm{e}^{-\mathrm{i}(\boldsymbol{k}\cdot\boldsymbol{x} - \omega_k t)} \right] , \tag{D.26}$$

where the sum is performed over all possible wavevectors $\boldsymbol{k}$ compatible with the boundary conditions (Equation D.20), and over the two possible polarization values $\lambda = 1, 2$. Now, $\hat{a}_{\boldsymbol{k}\lambda}^\dagger$ and $\hat{a}_{\boldsymbol{k}\lambda}$ are the **creation** and **annihilation operators** associated with a mode with

wavevector $\boldsymbol{k}$ and polarization λ. They fulfil the following commutation rules:

$$\begin{aligned}
&[\hat{a}_{\boldsymbol{k}\lambda}, \hat{a}_{\boldsymbol{k}'\lambda'}] = 0 \,, \\
&[\hat{a}^{\dagger}_{\boldsymbol{k}\lambda}, \hat{a}^{\dagger}_{\boldsymbol{k}'\lambda'}] = 0 \,, \\
&[\hat{a}_{\boldsymbol{k}\lambda}, \hat{a}^{\dagger}_{\boldsymbol{k}'\lambda'}] = \delta_{\lambda\lambda'}\delta_{\boldsymbol{k}\boldsymbol{k}'} \,,
\end{aligned} \tag{D.27}$$

that is, the different modes are independent and their corresponding creation and annihilation operators commute. As in Equation D.6, we have:

$$\begin{aligned}
\hat{a}^{\dagger}_{\boldsymbol{k}\lambda}|n_{\boldsymbol{k}\lambda}\rangle &= \sqrt{n_{\boldsymbol{k}\lambda}+1}\;|n_{\boldsymbol{k}\lambda}+1\rangle \,, \\
\hat{a}_{\boldsymbol{k}\lambda}|n_{\boldsymbol{k}\lambda}\rangle &= \sqrt{n_{\boldsymbol{k}\lambda}}\;|n_{\boldsymbol{k}\lambda}-1\rangle \,.
\end{aligned}$$

There, $n_{\boldsymbol{k}\lambda}$ represents the number of photons excited in the mode $\boldsymbol{k}\lambda$, and $|n_{\boldsymbol{k}\lambda}\rangle$ is the state with such a fixed number of excitations (known as **Fock state** or **photon-number state**). These are eigenstates of the **number operator** $\hat{n}_{\boldsymbol{k}\lambda} \equiv \hat{a}^{\dagger}_{\boldsymbol{k}\lambda}\hat{a}_{\boldsymbol{k}\lambda}$ with associated eigenvalue $n_{\boldsymbol{k}\lambda}$:

$$\hat{n}_{\boldsymbol{k}\lambda}|n_{\boldsymbol{k}\lambda}\rangle = n_{\boldsymbol{k}\lambda}|n_{\boldsymbol{k}\lambda}\rangle \,.$$

The ground-state of the field is the **vacuum state** $|\{0\}\rangle$, defined such that $\hat{a}_{\boldsymbol{k}\lambda}|\{0\}\rangle = 0$ for all $\boldsymbol{k}$ and λ. This is the state in which there is no photons excited in any of the modes $\boldsymbol{k}\lambda$, so $n_{\boldsymbol{k}\lambda} = 0$ for all wavevector $\boldsymbol{k}$ and polarization λ.

By considering the same substitution of the classical amplitudes $a_{\boldsymbol{k}\lambda}$ and $a^{*}_{\boldsymbol{k}\lambda}$ by the corresponding quantum operators $\hat{a}_{\boldsymbol{k}\lambda}$ and $\hat{a}^{\dagger}_{\boldsymbol{k}\lambda}$ in Equation D.23, the **electric** and **magnetic quantum operators** take the form:

$$\begin{aligned}
\hat{\boldsymbol{E}}_{\mathrm{T}}(\boldsymbol{x},t) &= \mathrm{i}\sum_{\boldsymbol{k}}\sum_{\lambda}\sqrt{\frac{\hbar\omega_k}{2\epsilon_0 V}}\boldsymbol{\epsilon}_{\boldsymbol{k}\lambda}\left[\hat{a}_{\boldsymbol{k}\lambda}\mathrm{e}^{\mathrm{i}(\boldsymbol{k}\cdot\boldsymbol{x}-\omega_k t)} - \hat{a}^{\dagger}_{\boldsymbol{k}\lambda}\mathrm{e}^{-\mathrm{i}(\boldsymbol{k}\cdot\boldsymbol{x}-\omega_k t)}\right] \,, \\
\hat{\boldsymbol{B}}(\boldsymbol{x},t) &= \mathrm{i}\sum_{\boldsymbol{k}}\sum_{\lambda}\sqrt{\frac{\hbar}{2\epsilon_0 V\omega_k}}[\boldsymbol{k}\times\boldsymbol{\epsilon}_{\boldsymbol{k}\lambda}]\left[\hat{a}_{\boldsymbol{k},\lambda}\mathrm{e}^{\mathrm{i}(\boldsymbol{k}\cdot\boldsymbol{x}-\omega_k t)} - \hat{a}^{\dagger}_{\boldsymbol{k}\lambda}\mathrm{e}^{-\mathrm{i}(\boldsymbol{k}\cdot\boldsymbol{x}-\omega_k t)}\right] \,.
\end{aligned} \tag{D.28}$$

Notice that $\hat{\boldsymbol{E}}(\boldsymbol{x},t)$ and $\hat{\boldsymbol{B}}(\boldsymbol{x},t)$ are expressed in the Heisenberg picture, where operators carry the time-dependence (see Appendix B for an overview of the quantum pictures). Nevertheless, it is convenient to transform the electric field operator to the Schrödinger picture for future derivations:

$$\hat{\boldsymbol{E}}_{\mathrm{T}}(\boldsymbol{x}) = \sum_{\boldsymbol{k}}\sum_{\lambda}\sqrt{\frac{\hbar\omega_k}{2\epsilon_0 V}}\boldsymbol{\epsilon}_{\boldsymbol{k}\lambda}\left[\hat{a}_{\boldsymbol{k}\lambda}\mathrm{e}^{\mathrm{i}\boldsymbol{k}\cdot\boldsymbol{x}} + \hat{a}^{\dagger}_{\boldsymbol{k}\lambda}\mathrm{e}^{-\mathrm{i}\boldsymbol{k}\cdot\boldsymbol{x}}\right] \,, \tag{D.29}$$

where we have introduced a $\pi/2$ phase shift and removed the time dependences. We observe that the amplitude of the electric field inside the cavity is given by: $E_{0\boldsymbol{k}} = \sqrt{\hbar\omega_k/(2\epsilon_0 V)}$.

In analogy to Equation D.24, the **Hamiltonian operator** of the quantized radiation field can be taken as:

$$\hat{H}_{\mathrm{rad}} = \frac{1}{2}\int_{\mathrm{V}}\mathrm{d}^3\boldsymbol{x}\left[\epsilon_0\,\hat{\boldsymbol{E}}_{\mathrm{T}}(\boldsymbol{x},t)\cdot\hat{\boldsymbol{E}}_{\mathrm{T}}(\boldsymbol{x},t) + \frac{1}{\mu_0}\hat{\boldsymbol{B}}(\boldsymbol{x},t)\cdot\hat{\boldsymbol{B}}(\boldsymbol{x},t)\right] \,. \tag{D.30}$$

As expected, the substitution of the electric and magnetic field operators from Equa-

tion D.28 yields:

$$\hat{H}_{\text{rad}} = \sum_{\boldsymbol{k}} \sum_{\lambda} \hbar\omega_{\boldsymbol{k}} \left(\frac{1}{2} + \hat{a}^{\dagger}_{\boldsymbol{k}\lambda} \hat{a}_{\boldsymbol{k}\lambda} \right) , \tag{D.31}$$

that is, the energy associated with a collection of independent and uncoupled quantum harmonic oscillators (see Equation D.4). Each mode $\boldsymbol{k}\lambda$ of the field is in this sense associated with a quantum-mechanical harmonic oscillator. There, we could subtract the sum of all zero-point energies:

$$E_0 = \frac{1}{2} \sum_{\boldsymbol{k}} \sum_{\lambda} \hbar\omega_{\boldsymbol{k}} , \tag{D.32}$$

that is, the sum of the energies corresponding to the ground state.

Quantization in infinite volume

Once the quantization of the electromagnetic field has been carried out within a cubic box, the case of the infinite volume is straightforwardly obtained. The difference lies merely in the allowed values for the wavevector $\boldsymbol{k}$ —while this magnitude is discretized for the cavity, for the infinite volume they form a continuum.

When considering a cubic region of side L, the allowed values for the wavelength λ is restricted according to the imposed boundary conditions. When these are periodic, the length of the cavity needs to fit an integer number of wavelengths, so the allowed values are $\lambda = L/n$ (with $n = 1, 2, \ldots$). Since $k = |\boldsymbol{k}| = 2\pi/\lambda$, this entails the constraint in the wavevector previously indicated in Equation D.20. In k-space, the volume associated with each value of k is $(2\pi/L)^3$. As a consequence, the transformation from the cavity to the infinite volume can be performed through the change:

$$\begin{aligned} \sum_{\boldsymbol{k}} &\rightarrow \left(\frac{L}{2\pi} \right)^3 \int \mathrm{d}\boldsymbol{k}^3 \\ \hat{a}_{\boldsymbol{k}\lambda} &\rightarrow \sqrt{\left(\frac{2\pi}{L} \right)^3} \hat{a}_{\lambda}(\boldsymbol{k}) \end{aligned}$$

Directly from Equation D.26, the **vector potential operator** $\hat{A}$ for the free electromagnetic field in infinite space is written as:

$$\hat{\boldsymbol{A}}(\boldsymbol{x}, t) = \sum_{\lambda} \int \mathrm{d}^3\boldsymbol{k} \sqrt{\frac{\hbar}{(2\pi)^3 2\epsilon_0 \omega_k}} \left[\boldsymbol{\epsilon}_{\lambda}(\boldsymbol{k}) \hat{a}_{\lambda}(\boldsymbol{k}) \mathrm{e}^{\mathrm{i}(\boldsymbol{k}\cdot\boldsymbol{x} - \omega_k t)} + \boldsymbol{\epsilon}^{*}_{\lambda}(\boldsymbol{k}) \hat{a}^{\dagger}_{\lambda}(\boldsymbol{k}) \mathrm{e}^{-\mathrm{i}(\boldsymbol{k}\cdot\boldsymbol{x} - \omega_k t)} \right] .$$

We have again the creation and annihilation operators $\hat{a}^{\dagger}_{\lambda}(\boldsymbol{k})$ and $\hat{a}_{\lambda}(\boldsymbol{k})$ associated with a mode $\boldsymbol{k}\lambda$, obeying in this case the commutation relation:

$$[\hat{a}_{\lambda}(\boldsymbol{k}), \hat{a}^{\dagger}_{\lambda'}(\boldsymbol{k}')] = \delta_{\lambda\lambda'} \delta^{(3)}(\boldsymbol{k} - \boldsymbol{k}') .$$

In contrast to Equation D.27, now we have the Dirac delta $\delta^{(3)}(\boldsymbol{k} - \boldsymbol{k}')$ associated with the wavevectors. The corresponding **electric** and **magnetic quantum operators** are now

given by:

$$\hat{\boldsymbol{E}}(\boldsymbol{x},t) = \mathrm{i}\sum_{\lambda}\int \mathrm{d}^3\boldsymbol{k}\,\sqrt{\frac{\hbar\omega_k}{(2\pi)^3 2\epsilon_0}}\boldsymbol{\epsilon}_\lambda(\boldsymbol{k})\left[\hat{a}_\lambda(\boldsymbol{k})\mathrm{e}^{\mathrm{i}(\boldsymbol{k}\cdot\boldsymbol{x}-\omega_k t)} - \hat{a}^\dagger_\lambda(\boldsymbol{k})\mathrm{e}^{-\mathrm{i}(\boldsymbol{k}\cdot\boldsymbol{x}-\omega_k t)}\right],$$

$$\hat{\boldsymbol{B}}(\boldsymbol{x},t) = \mathrm{i}\sum_{\lambda}\int \mathrm{d}^3\boldsymbol{k}\,\sqrt{\frac{\hbar}{(2\pi)^3 2\epsilon_0\omega_k}}[\boldsymbol{k}\times\boldsymbol{\epsilon}_\lambda(\boldsymbol{k})]\left[\hat{a}_\lambda(\boldsymbol{k})\mathrm{e}^{\mathrm{i}(\boldsymbol{k}\cdot\boldsymbol{x}-\omega_k t)} - \hat{a}^\dagger_\lambda(\boldsymbol{k})\mathrm{e}^{-\mathrm{i}(\boldsymbol{k}\cdot\boldsymbol{x}-\omega_k t)}\right].$$

After the substitution of these expressions in Equation D.30, the Hamiltonian of the electromagnetic radiation reads:

$$\hat{H}_{\mathrm{rad}} = \sum_{\lambda}\int \mathrm{d}^3\boldsymbol{k}\;\hbar\omega_k\;\hat{a}^\dagger_\lambda(\boldsymbol{k})\hat{a}_\lambda(\boldsymbol{k})\,.$$

There, we have subtracted the **zero-point energy** or **vacuum energy** E_0, that is, the energy contribution corresponding to the vacuum state:

$$E_0 = \frac{1}{2}\sum_{\lambda}\int \mathrm{d}^3\boldsymbol{k}\;\hbar\omega_k = \int \mathrm{d}^3\boldsymbol{k}\;\hbar\omega_k\,.$$

D.3 Quantum description of light-matter interaction

The effect of the light-matter interaction is usually introduced in the theory by means of the minimal-coupling procedure, leading to the so-called $p\cdot A$ Hamiltonian. Alternatively, the interaction Hamiltonian can be derived within the electric-dipole approximation, resulting the $r\cdot E$ Hamiltonian. Although many textbooks address this issue in-depth (for instance, see Ref. [1, 120]), a brief review of these two approaches are presented in the following.

The vector potential Hamiltonian

Let us consider a charged particle with momentum $\boldsymbol{p}$ at position $\boldsymbol{r}$ interacting with an electromagnetic field with vector potential $\boldsymbol{A}$. According to the **minimal-coupling principle**, the interaction is introduced by transforming the momentum of the particle as $\boldsymbol{p}\to\boldsymbol{p}-e\boldsymbol{A}(\boldsymbol{r})$, hence the kinetic energy term becomes:

$$\frac{\boldsymbol{p}^2}{2m} \quad\to\quad \frac{(\boldsymbol{p}^2 - e\boldsymbol{A}(\boldsymbol{r}))^2}{2m}\,,$$

where m and e are the mass and the charge of the particle, respectively. Observe that the vector potential is evaluated at the position of the particle. If we now turn to a quantum description and consider a collection of particles of mass m_j and charge e_j located at $\boldsymbol{r}_j$ with momentum $\hat{\boldsymbol{p}}_j$, the complete quantum Hamiltonian can be written in the Coulomb

gauge (Equation D.13) as:

$$\hat{H}_{\text{mc}} = \hat{H}_{\text{rad}} + \frac{1}{2}\int \mathrm{d}\boldsymbol{r}\ \rho(\boldsymbol{r})\phi(\boldsymbol{r}) + \sum_j \frac{1}{2m_j}\left(\hat{\boldsymbol{p}}_j - e_j\hat{\boldsymbol{A}}(\boldsymbol{r}_j)\right)^2 , \tag{D.33}$$

which is known as the **minimal-coupling Hamiltonian**. The first term is the Hamiltonian describing the free electromagnetic field, given by Equation D.30. The second term corresponds to the electrostatic energy associated with the charge distribution, where $\phi(\boldsymbol{r})$ is the scalar potential created by the particles, and $\rho(\boldsymbol{r})$ is the charge density. In this case, $\rho(\boldsymbol{r}) = \sum_j e_j \delta^{(3)}(\boldsymbol{r} - \boldsymbol{r}_j)$, and thus $\phi(\boldsymbol{r}) = (1/4\pi\epsilon_0)\sum_j e_j/|\boldsymbol{r} - \boldsymbol{r}_j|$ according to Equation D.14. The electrostatic energy, together with the kinetic energy contribution $\hat{\boldsymbol{p}}_j^2/(2m_j)$, form the matter Hamiltonian:

$$\hat{H}_{\text{mat}} \equiv \frac{1}{2}\int \mathrm{d}\boldsymbol{r}\ \rho(\boldsymbol{r})\phi(\boldsymbol{r}) + \sum_j \frac{\hat{\boldsymbol{p}}_j^2}{2m_j} , \tag{D.34}$$

since these depends only on the variables of the particles. The remaining part of the Hamiltonian in Equation D.33 makes up the **interaction Hamiltonian**:

$$\hat{H}_{\text{int}} \equiv -\sum_j \frac{e_j}{m_j}\hat{\boldsymbol{p}}\cdot\hat{\boldsymbol{A}}(\boldsymbol{r}_j) + \frac{e_j^2}{2m_j}\hat{\boldsymbol{A}}^2(\boldsymbol{r}_j) , \tag{D.35}$$

which is known as the ***p* · *A* form** of the interaction Hamiltonian. The Hamiltonian describing the whole interacting system can be thus written as the sum of three parts:

$$\hat{H}_{\text{mc}} = \hat{H}_{\text{rad}} + \hat{H}_{\text{mat}} + \hat{H}_{\text{int}} . \tag{D.36}$$

The introduction of the light-matter interaction through the minimal-coupling procedure yields the $\boldsymbol{p}\cdot\boldsymbol{A}$ form of the interaction Hamiltonian. Nevertheless, sometimes it is more convenient to transform the Hamiltonian such that the light-matter coupling is carried out through the electric field operator rather than through the vector potential. This leads to the $\boldsymbol{r}\cdot\boldsymbol{E}$ form of the Hamiltonian, that will be studied now.

The electric-dipole Hamiltonian

Starting from the minimal-coupling interaction, we aim for a Hamiltonian expressed in terms of the electric and magnetic field operators rather than involving the vector potential operator. This can be accomplished by performing the unitary transformation to the minimal-coupling Hamiltonian $\hat{H}_{\text{mc}}$ (Equation D.33) defined by the operator $\hat{\Lambda}$:

$$\hat{\Lambda} = \exp\left[\frac{\mathrm{i}}{\hbar}\int \mathrm{d}^3\boldsymbol{r}\ \hat{\boldsymbol{P}}(\boldsymbol{r})\cdot\hat{\boldsymbol{A}}(\boldsymbol{r})\right] . \tag{D.37}$$

The resulting Hamiltonian $\hat{H}' = \hat{\Lambda}^{-1}\hat{H}_{\text{mc}}\hat{\Lambda}$ is the so-called **Power-Zienau-Woolley Hamiltonian** [617, 618, 619]. In this new formulation, the system of particles (characterized by the charge density ρ and the electric current density $\boldsymbol{J}$) is described by the **polarization density** $\boldsymbol{P}$ and the **magnetization density** $\boldsymbol{M}$:

$$\rho(\boldsymbol{r}) = -\nabla\cdot\boldsymbol{P}(\boldsymbol{r}) , \qquad \boldsymbol{J}(\boldsymbol{r}) = \dot{\boldsymbol{P}}(\boldsymbol{r}) + \nabla\times\boldsymbol{M}(\boldsymbol{r}) ,$$

where the ∇ is the nabla operator and the dot stands for time derivative. These magnitudes can be written in terms of the system parameters as:

$$\boldsymbol{P}(\boldsymbol{r}) = \sum_j \int_0^1 \mathrm{d}\zeta \; e_j \boldsymbol{r}_j \delta(\boldsymbol{r} - \zeta \boldsymbol{r}_j) \,, \qquad \boldsymbol{M}(\boldsymbol{r}) = \sum_j \int_0^1 \mathrm{d}\zeta \; \zeta e_j \boldsymbol{r}_j \times \dot{\boldsymbol{r}}_j \;\; \delta(\boldsymbol{r} - \zeta \boldsymbol{r}_j) \,,$$

where $\boldsymbol{r}_j$ is the position of the j-th particle, with charge e_j. From the classical theory of atom-radiation interaction, the **electric potential energy** of the system of particles in the transverse electric field $\boldsymbol{E}_\mathrm{T}$ is defined as:

$$V_\mathrm{E} = -\int \mathrm{d}^3\boldsymbol{r} \; \boldsymbol{P}(\boldsymbol{r}) \cdot \boldsymbol{E}_\mathrm{T}(\boldsymbol{r}) \,, \tag{D.38}$$

while the **magnetic potential energy** in the magnetic field $\boldsymbol{B}$ is given by:

$$V_\mathrm{M} = -\int \mathrm{d}^3\boldsymbol{r} \; \boldsymbol{M}(\boldsymbol{r}) \cdot \boldsymbol{B}(\boldsymbol{r}) \,. \tag{D.39}$$

The quantum version of these magnitudes appear when performing the above transformation, such that the interaction between particles and radiation in the Power–Zienau–Woolley Hamiltonian can be written in the form of an expansion in the electric and magnetic multipole moments.

In the following, we consider each term of the minimal-coupling Hamiltonian of Equation D.36 separately, and study its transformation through the unitary operator $\hat{\Lambda}$ (Equation D.37). First, the radiation component $\hat{H}_\mathrm{rad}$ transforms to the same free-field Hamiltonian (given in Equation D.30) plus two extra contributions:

$$\hat{H}'_\mathrm{rad} = \hat{H}_\mathrm{rad} - \int \mathrm{d}^3\boldsymbol{r} \; \boldsymbol{P}(\boldsymbol{r}) \cdot \hat{\boldsymbol{E}}_\mathrm{T}(\boldsymbol{r}) + \frac{1}{2\epsilon_0} \int \mathrm{d}^3\boldsymbol{r} \; \boldsymbol{P}^2_\mathrm{T}(\boldsymbol{r}) \,.$$

The second term is the quantum version of the electric potential energy V_E (Equation D.38), and it comes from the electric component of the radiative energy. Additionally, we have a last term that only depends on the matter variables (there, $\boldsymbol{P}_\mathrm{T}$ stands for the transverse part of the polarization). Next, the matter Hamiltonian of Equation D.34 turns out to remain unaltered in the transformation:

$$\hat{H}'_\mathrm{mat} = \hat{H}_\mathrm{mat} \,.$$

Finally, the transformation of the interaction part of the Hamiltonian (Equation D.35) leads to the appearance of the quantum version of the magnetic potential energy V_M (Equation D.39) together with some other nonlinear magnetic contributions:

$$\hat{H}'_\mathrm{int} = -\int \mathrm{d}^3\boldsymbol{r} \; \boldsymbol{M}(\boldsymbol{r}) \cdot \hat{\boldsymbol{B}}(\boldsymbol{r}) + \sum_j \frac{e_j^2}{2m_j} \left[\int_0^1 \mathrm{d}\zeta \; \zeta \; \boldsymbol{B}(\zeta \boldsymbol{r}_j) \times \boldsymbol{r}_j \right]^2 \,. \tag{D.40}$$

The complete transformed Hamiltonian H' can be rearranged so as to have the same contributions as in Equation D.36, that is:

$$H' = \hat{H}^\mathrm{PZW}_\mathrm{rad} + \hat{H}^\mathrm{PZW}_\mathrm{mat} + \hat{H}^\mathrm{PZW}_\mathrm{int} \,,$$

where $\hat{H}^{\mathrm{PZW}}_{\mathrm{rad}}$ and $\hat{H}^{\mathrm{PZW}}_{\mathrm{mat}}$ represent the (non-interacting) radiation and matter components, respectively, and $\hat{H}^{\mathrm{PZW}}_{\mathrm{int}}$ is the interaction Hamiltonian. The radiation part is simply $\hat{H}^{\mathrm{PZW}}_{\mathrm{rad}} = \hat{H}_{\mathrm{rad}}$, with the Hamiltonian of the free electromagnetic field given in Equation D.30. The matter part reads:

$$\hat{H}^{\mathrm{PZW}}_{\mathrm{mat}} = \hat{H}_{\mathrm{mat}} + \frac{1}{2\epsilon_0}\int \mathrm{d}^3\boldsymbol{r}\ \boldsymbol{P}^2_{\mathrm{T}}(\boldsymbol{r})\,,$$

where $\hat{H}_{\mathrm{mat}}$ is the expression in Equation D.34. The last part only introduces a change in the energy levels, and will be disregarded. The interaction Hamiltonian is thus composed of the following terms:

$$\hat{H}^{\mathrm{PZW}}_{\mathrm{int}} = -\int \mathrm{d}^3\boldsymbol{r}\ \boldsymbol{P}(\boldsymbol{r})\cdot\hat{\boldsymbol{E}}_{\mathrm{T}}(\boldsymbol{r}) - \int \mathrm{d}^3\boldsymbol{r}\ \boldsymbol{M}(\boldsymbol{r})\cdot\hat{\boldsymbol{B}}(\boldsymbol{r}) + \sum_j \frac{e_j^2}{2m_j}[Q]^2\,, \tag{D.41}$$

where we have named as Q the expression in brackets in Equation D.40. The first two terms can be written as a sum of terms describing the interaction of the **multipole electric and magnetic moments** of the system of charges with the electromagnetic field. By performing a Taylor expansion, the quantum version of the electric potential energy of Equation D.38 can be expressed as the following sum of multipole moments of the atomic charge distribution:

$$-\int \mathrm{d}^3\boldsymbol{r}\ \boldsymbol{P}(\boldsymbol{r})\cdot\hat{\boldsymbol{E}}_{\mathrm{T}}(\boldsymbol{r}) = -\sum_j e_j\left\{1+\frac{1}{2!}(\boldsymbol{r}_j\cdot\nabla)+\frac{1}{3!}(\boldsymbol{r}_j\cdot\nabla)^2+\ldots\right\}\boldsymbol{r}_j\cdot\hat{\boldsymbol{E}}_{\mathrm{T}}(0)\,.$$

In the multipole expansion, the electric field is precisely evaluated in the origin of coordinates (the electromagnetic field barely varies over the dimension of an atom). The first term of the expansion gives the **electric-dipole interaction**:

$$V^{(\mathrm{d})}_{\mathrm{E}} = -\sum_j e_j\boldsymbol{r}_j\cdot\hat{\boldsymbol{E}}_{\mathrm{T}}(0)\,. \tag{D.42}$$

Then, we have the quadrupole term and higher-order multipoles, but these contributions turn out to be much smaller than the electric-dipole potential energy. Equivalently, the same Taylor expansion can be performed for the quantum version of the magnetic potential energy of Equation D.39:

$$-\int \mathrm{d}^3\boldsymbol{r}\ \boldsymbol{M}(\boldsymbol{r})\cdot\hat{\boldsymbol{B}}(\boldsymbol{r}) = -\sum_j \frac{e_j}{m_j}\left\{\frac{1}{2!}+\frac{2}{3!}(\boldsymbol{r}_j\cdot\nabla)+\frac{3}{4!}(\boldsymbol{r}_j\cdot\nabla)^2+\ldots\right\}m_j(\boldsymbol{r}_j\times\dot{\boldsymbol{r}}_j)\cdot\hat{\boldsymbol{B}}(0)\,.$$

However, all these terms, including the magnetic-dipole potential energy, are also smaller than the leading electric-dipole term of Equation D.42.

The **electric-dipole approximation** consists in keeping just the dominant electric-dipole contribution (Equation D.42), while disregarding the higher-order terms in the expansion of the electrical potential energy, as well as all the magnetic multipoles and non-linear terms. As a result, the interaction Hamiltonian of Equation D.41 reduces to the **electric-dipole Hamiltonian**:

$$\hat{H}^{\mathrm{PZW}}_{\mathrm{int}} \approx \hat{H}_{\mathrm{ED}} \equiv -\boldsymbol{d}\cdot\hat{\boldsymbol{E}}\,. \tag{D.43}$$

which is also known as the ***r* · *E* form** of the interaction Hamiltonian. There, we have

defined the **total electric-dipole moment** of the charge distribution as:

$$\boldsymbol{d} \equiv \sum_j e_j \boldsymbol{r}_j \ ,$$

that can be easily upgraded to an operator, as will see later.

Therefore, the total Hamiltonian of the interacting system can be finally written as the sum of three parts:

$$\hat{H} = \hat{H}_{\text{rad}} + \hat{H}_{\text{mat}} + \hat{H}_{\text{ED}} \ . \tag{D.44}$$

Notice that this new version of the Hamiltonian, expressed only in terms of the electric and magnetic field operators, is exactly the same as the minimal-coupling Hamiltonian (Equation D.36) except for the interaction term. In both cases, $\hat{H}_{\text{rad}}$ stands for the Hamiltonian of the free electromagnetic field (Equation D.30), while $\hat{H}_{\text{mat}}$ represents the Hamiltonian describing the matter part without interaction (Equation D.34).

D.4 Transformation to a rotating frame

When working with time-dependent Hamiltonians, the transformation to a **rotating frame** is a common procedure. This transformation allows us to change to a reference system in which the Hamiltonian becomes time-independent. In this Appendix, we perform the transformation to the rotating frame for various Hamiltonians of interest.

Transformation to a rotating frame

Starting from the Hamiltonian written in the Schrödinger picture, we will perform a **unitary transformation** [620]:

$$\mathcal{U}(t) = \mathrm{e}^{-\frac{\mathrm{i}}{\hbar}\hat{A}t} \ , \tag{D.45}$$

where $\hat{A}$ is an arbitrary Hermitian operator. The state in this new frame $|\tilde{\psi}\rangle$ is related to that in the Schrödinger picture $|\psi\rangle$ according to:

$$|\tilde{\psi}(t)\rangle = \mathcal{U}^\dagger(t)|\psi(t)\rangle \ . \tag{D.46}$$

We want this transformed state $|\tilde{\psi}\rangle$ to obey the Schrödinger equation (Equation 2.1) for the corresponding transformed Hamiltonian $\hat{H}_{\text{RF}}$:

$$\frac{\mathrm{d}}{\mathrm{d}t}|\tilde{\psi}(t)\rangle = -\frac{\mathrm{i}}{\hbar}\hat{H}_{\text{RF}}|\tilde{\psi}(t)\rangle \ .$$

By substituting the transformation of Equation D.46 in the previous Schrödinger equation, we have:

$$\begin{aligned}
\frac{\mathrm{d}}{\mathrm{d}t}|\tilde{\psi}(t)\rangle = \frac{\mathrm{d}}{\mathrm{d}t}\left(\mathcal{U}^\dagger(t)|\psi(t)\rangle\right) &= \mathcal{U}^\dagger(t)\frac{\mathrm{d}|\psi(t)\rangle}{\mathrm{d}t} + \frac{\mathrm{d}\mathcal{U}^\dagger(t)}{\mathrm{d}t}|\psi(t)\rangle \\
&= -\frac{\mathrm{i}}{\hbar}\,\mathcal{U}^\dagger(t)\hat{H}|\psi(t)\rangle + \frac{\mathrm{i}}{\hbar}\hat{A}\mathcal{U}^\dagger(t)|\psi(t)\rangle \\
&= -\frac{\mathrm{i}}{\hbar}\left(\mathcal{U}^\dagger(t)\hat{H}\mathcal{U}(t) - \hat{A}\right)\mathcal{U}^\dagger(t)|\psi(t)\rangle = -\frac{\mathrm{i}}{\hbar}\hat{H}_{\text{RF}}|\tilde{\psi}(t)\rangle \ .
\end{aligned}$$

Therefore, the expression of the transformed Hamiltonian $\hat{H}_{\text{RF}}$ in terms of $\hat{H}$ is given by:

$$\hat{H}_{\text{RF}} = \mathcal{U}^{\dagger}(t)\hat{H}\mathcal{U}(t) - \hat{A}\,. \tag{D.47}$$

Useful operator identities First of all, let us introduce some useful operator identities that we will need at some point in the derivations carried out the present Appendix. Let $|\phi\rangle$ and $|\chi\rangle$ be two orthogonal states and ξ be a parameter. Then it can be proved the following identities [620]:

- Identity 1:
$$e^{\xi|\phi\rangle\langle\phi|}|\chi\rangle = |\chi\rangle\,,$$
$$\langle\chi|e^{\xi|\phi\rangle\langle\phi|} = \langle\chi|\,.$$

- Identity 2:
$$e^{\xi|\phi\rangle\langle\phi|}|\phi\rangle = e^{\xi}|\phi\rangle\,,$$
$$\langle\phi|\,e^{\xi|\phi\rangle\langle\phi|} = \langle\phi|\,e^{\xi}\,.$$

- Identity 3:
$$e^{\xi\hat{a}^{\dagger}\hat{a}}\;\hat{a}\;e^{-\xi\hat{a}^{\dagger}\hat{a}} = \;e^{-\xi}\;\hat{a}\,,$$

  where $\hat{a}^{\dagger}$ and $\hat{a}$ are the bosonic creation and annihilation operators associated with some cavity mode.

One cavity mode driven by a laser

Let us consider first the case of a cavity mode of frequency ω_0 driven by a laser of frequency ω_L. The complete Hamiltonian in the Schrödinger picture is given by:

$$\hat{H} = \hbar\omega_0\;\hat{a}^{\dagger}\hat{a} + \hbar\Omega_0(a^{\dagger}\;e^{-i\omega_L t} + \hat{a}\;e^{i\omega_L t})\,,$$

where $\hat{a}^{\dagger}$ and $\hat{a}$ are the creation and annihilation operators for the cavity mode and Ω_0 is the coupling constant between the cavity mode and the laser field. In order to transform the description to a rotating frame and remove the explicit time-dependence, we consider the unitary operator U given in Equation D.45, with the Hermitian operator $\hat{A}$:

$$\hat{A} = \hbar\omega_L\hat{a}^{\dagger}\hat{a}\,.$$

From Equation D.47, the Hamiltonian $\tilde{\hat{H}}$ corresponding to the rotating frame can be computed:

$$\begin{aligned}
\hat{H}_{\text{RF}} &= U^{\dagger}(t)\hat{H}U(t) - \hat{A} \\
&= e^{i\omega_L\hat{a}^{\dagger}\hat{a}t}\left\{\hbar\omega_0\;\hat{a}^{\dagger}\hat{a} + \hbar\Omega_0(\hat{a}^{\dagger}\;e^{-i\omega_L t} + \hat{a}\;e^{i\omega_L t})\right\}e^{-i\omega_L\hat{a}^{\dagger}\hat{a}t} - \hbar\omega_L\hat{a}^{\dagger}\hat{a} \\
&= \hbar(\omega_0-\omega_L)\;\hat{a}^{\dagger}\hat{a} + \hbar\Omega_0\left\{e^{-i\omega_L t}e^{i\omega_L\hat{a}^{\dagger}\hat{a}t}\;\hat{a}^{\dagger}\;e^{-i\omega_L\hat{a}^{\dagger}\hat{a}t} + e^{i\omega_L t}e^{i\omega_L\hat{a}^{\dagger}\hat{a}t}\;\hat{a}\;e^{-i\omega_L\hat{a}^{\dagger}\hat{a}t}\right\} \\
&= \hbar(\omega_0-\omega_L)\;\hat{a}^{\dagger}\hat{a} + \hbar\Omega_0\left\{e^{-i\omega_L t}e^{i\omega_L t}\hat{a}^{\dagger} + e^{i\omega_L t}e^{-i\omega_L t}\hat{a}\right\} \\
&= \hbar(\omega_0-\omega_L)\;\hat{a}^{\dagger}\hat{a} + \hbar\Omega_0(\hat{a}^{\dagger} + \hat{a})\,,
\end{aligned}$$

where we have used the operator properties showed at the beginning of this Appendix.

One quantum emitter driven by a laser

If we consider now a system in which one quantum emitter of frequency ω_{QE} is driven by a laser of frequency ω_L, the Hamiltonian in the Schrödinger picture reads:

$$\hat{H} = \hbar\omega_{QE}\hat{\sigma}^\dagger\hat{\sigma} + \hbar\Omega_{QE}(\hat{\sigma}^\dagger e^{-i\omega_L t} + \hat{\sigma}e^{i\omega_L t}) ,$$

where $\hat{\sigma}^\dagger$ and $\hat{\sigma}$ are the fermionic creation and annihilation operators for the two-level system and Ω_{QE} represents the coupling strength to the laser field. To perform the transformation to the rotating frame, we consider the unitary operator of Equation D.45, where $\hat{A}$ is given by:

$$\hat{A} = \hbar\omega_L\hat{\sigma}^\dagger\hat{\sigma} .$$

The Hamiltonian $\hat{H}_{\text{RF}}$ corresponding to the rotating frame is computed from the relation of Equation D.47:

$$\begin{aligned}
\hat{H}_{\text{RF}} &= U^\dagger(t)\hat{H}U(t) - \hat{A} \\
&= e^{i\omega_L\hat{\sigma}^\dagger\hat{\sigma}t}\left\{\hbar\omega_{QE}\hat{\sigma}^\dagger\hat{\sigma} + \hbar\Omega_{QE}(\hat{\sigma}^\dagger e^{-i\omega_L t} + \hat{\sigma}e^{i\omega_L t})\right\} e^{-i\omega_L\hat{\sigma}^\dagger\hat{\sigma}t} - \hbar\omega_L\hat{\sigma}^\dagger\hat{\sigma} \\
&= \hbar(\omega_{QE} - \omega_L)\hat{\sigma}^\dagger\hat{\sigma} + \hbar\Omega_{QE}\left\{e^{-i\omega_L t}e^{i\omega_L\hat{\sigma}^\dagger\hat{\sigma}t}\sigma^\dagger e^{-i\omega_L\hat{\sigma}^\dagger\hat{\sigma}t} + e^{i\omega_L t}e^{i\omega_L\hat{\sigma}^\dagger\hat{\sigma}t}\hat{\sigma}e^{-i\omega_L\hat{\sigma}^\dagger\sigma t}\right\} \\
&= \hbar(\omega_{QE} - \omega_L)\hat{\sigma}^\dagger\hat{\sigma} + \hbar\Omega_{QE}\left\{e^{-i\omega_L t}e^{i\omega_L|e\rangle\langle e|t}|e\rangle\langle g|e^{-i\omega_L|e\rangle\langle e|t} + e^{i\omega_L t}e^{i\omega_L|e\rangle\langle e|t}|g\rangle\langle e|e^{-i\omega_L|e\rangle\langle e|t}\right\} \\
&= \hbar(\omega_{QE} - \omega_L)\sigma^\dagger\sigma + \hbar\Omega_{QE}\left\{e^{-i\omega_L t}e^{i\omega_L t}|e\rangle\langle g| + e^{i\omega_L t}|g\rangle\langle e|\ e^{-i\omega_L t}\right\} \\
&= \hbar(\omega_{QE} - \omega_L)\hat{\sigma}^\dagger\hat{\sigma} + \hbar\Omega_{QE}(\hat{\sigma}^\dagger + \hat{\sigma}) ,
\end{aligned}$$

where, again, we have also used the operator properties shown at the beginning of this Appendix.

N quantum emitters driven by a laser

When the system is composed of N quantum emitters of frequency ω_n, all of them driven by a laser of frequency ω_L, the Hamiltonian in the Schrödinger picture is given by:

$$\hat{H} = \sum_{n=1}^{N}\hbar\omega_n\hat{\sigma}_n^\dagger\hat{\sigma}_n + \sum_{n=1}^{N}\hbar\Omega_n(\hat{\sigma}_n^\dagger e^{-i\omega_L t} + \hat{\sigma}_n e^{i\omega_L t}) ,$$

where $\hat{\sigma}_n^\dagger$ and $\hat{\sigma}_n$ are the fermionic creation and annihilation operators for the n-th quantum emitter and Ω_n is the coupling constant between the n-th quantum emitter and the laser field. The operator $\hat{A}$ to use in this case is given by:

$$\hat{A} = \sum_{n=1}^{N}\hbar\omega_L\hat{\sigma}_n^\dagger\hat{\sigma}_n ,$$

yielding the following transformed Hamiltonian:

$$\hat{H}_{\text{RF}} = \sum_{n=1}^{N}\hbar(\omega_n - \omega_L)\,\hat{\sigma}_n^\dagger\hat{\sigma}_n + \sum_{n=1}^{N}\hbar\Omega_n(\hat{\sigma}_n^\dagger + \hat{\sigma}_n) .$$

One cavity mode and N quantum emitters driven by a laser

In the Schrödinger picture, the Hamiltonian of the total system involving the excitation of both the cavity mode (with transition frequency ω_0 and creation and annihilation operators $\hat{a}^\dagger$ and $\hat{a}$) and the collection of N quantum emitters (with transition frequency ω_n and fermionic operators $\hat{\sigma}_n^\dagger$ and $\hat{\sigma}_n$) is given by:

$$\begin{aligned}\hat{H} = \hbar\omega_0\hat{a}^\dagger\hat{a} + \sum_{n=1}^{N}\hbar\omega_n\sigma_n^\dagger\sigma_n + \sum_{n=1}^{N}\hbar\lambda_n(\hat{a}^\dagger\sigma_n + \hat{a}\sigma_n^\dagger)\\ +\hbar\Omega_0(\hat{a}^\dagger\, e^{-i\omega_L t} + \hat{a}\, e^{i\omega_L t}) + \sum_{n=1}^{N}\hbar\Omega_n(\hat{\sigma}_n^\dagger\, e^{-i\omega_L t} + \hat{\sigma}_n\, e^{i\omega_L t})\,,\end{aligned}$$

where λ_n is the coupling constant between the n-th quantum emitter and the cavity mode and Ω_0 and Ω_n are the coupling to the laser of the cavity mode and the n-th quantum emitter respectively. By considering the operator $\hat{A}$:

$$\hat{A} = \hbar\omega_L\hat{a}^\dagger\hat{a} + \sum_{n=1}^{N}\hbar\omega_L\hat{\sigma}_n^\dagger\hat{\sigma}_n\,,$$

in the unitary operator of Equation D.45, this Hamiltonian will be transformed to the rotating frame:

$$\begin{aligned}\hat{H}_{\mathrm{RF}} &= U^\dagger(t)\hat{H}U(t) - \hat{A}\\
&= e^{i\omega_L\hat{a}^\dagger\hat{a}t}\prod_{n=1}^{N}e^{i\omega_L\hat{\sigma}_n^\dagger\hat{\sigma}_n t}\left\{\hbar\omega_0\hat{a}^\dagger\hat{a} + \sum_{n=1}^{N}\hbar\omega_n\hat{\sigma}_n^\dagger\hat{\sigma}_n + \sum_{n=1}^{N}\hbar\lambda_n(\hat{a}^\dagger\hat{\sigma}_n + \hat{a}\hat{\sigma}_n^\dagger)\right.\\
&\quad\left.+\hbar\Omega_0(\hat{a}^\dagger\, e^{-i\omega_L t} + \hat{a}\, e^{i\omega_L t}) + \sum_{n=1}^{N}\hbar\Omega_n(\hat{\sigma}_n^\dagger\, e^{-i\omega_L t} + \hat{\sigma}_n\, e^{i\omega_L t})\right\}e^{-i\omega_L\hat{a}^\dagger\hat{a}t}\prod_{n=1}^{N}e^{-i\omega_L\hat{\sigma}_n^\dagger\hat{\sigma}_n t}\\
&\quad-\hbar\omega_L\hat{a}^\dagger\hat{a} - \sum_{n=1}^{N}\hbar\omega_L\hat{\sigma}_n^\dagger\hat{\sigma}_n\\
&= \hbar(\omega_0-\omega_L)\hat{a}^\dagger\hat{a} + \sum_{n=1}^{N}\hbar(\omega_n-\omega_L)\hat{\sigma}_n^\dagger\hat{\sigma}_n\\
&\quad+ e^{i\omega_L\hat{a}^\dagger\hat{a}t}\prod_{n=1}^{N}e^{i\omega_L\hat{\sigma}_n^\dagger\hat{\sigma}_n t}\left\{\sum_{n=1}^{N}\hbar\lambda_n(\hat{a}^\dagger\hat{\sigma}_n + \hat{a}\hat{\sigma}_n^\dagger)\right\}e^{-i\omega_L\hat{a}^\dagger\hat{a}t}\prod_{n=1}^{N}e^{-i\omega_L\hat{\sigma}_n^\dagger\hat{\sigma}_n t}\\
&\quad+ e^{i\omega_L\hat{a}^\dagger\hat{a}t}\left\{\hbar\Omega_0(\hat{a}^\dagger\, e^{-i\omega_L t} + \hat{a}\, e^{i\omega_L t})\right\}e^{-i\omega_L\hat{a}^\dagger\hat{a}t}\\
&\quad+\prod_{n=1}^{N}e^{i\omega_L\hat{\sigma}_n^\dagger\hat{\sigma}_n t}\left\{\sum_{n=1}^{N}\hbar\Omega_n(\hat{\sigma}_n^\dagger\, e^{-i\omega_L t} + \hat{\sigma}_n\, e^{i\omega_L t})\right\}\prod_{n=1}^{N}e^{-i\omega_L\hat{\sigma}_n^\dagger\hat{\sigma}_n t}\\
&= \hbar(\omega_0-\omega_L)\hat{a}^\dagger\hat{a} + \sum_{n=1}^{N}\hbar(\omega_n-\omega_L)\hat{\sigma}_n^\dagger\hat{\sigma}_n + \sum_{n=1}^{N}\hbar\lambda_n(\hat{a}^\dagger\hat{\sigma}_n + \hat{a}\hat{\sigma}_n^\dagger)\\
&\quad+\hbar\Omega_0(\hat{a}^\dagger + \hat{a}) + \sum_{n=1}^{N}\hbar\Omega_n(\hat{\sigma}_n^\dagger + \hat{\sigma}_n)\,,\end{aligned}$$

where we observe that, effectively, the time-dependence has been removed.

APPENDIX E

LIGHT: THE CLASSICAL RADIATION FIELD

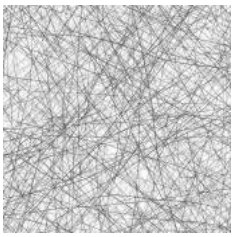

This Appendix is mainly devoted to the description and analysis of the classical radiation field. First, we present the description of the classical radiation field as a stationary and ergodic random process (Section E.1), which serves us to introduce the definition of the autocorrelation function in terms of time and ensemble averages. The most important part of this Appendix is the discussion of classical coherence (Section E.2), while the quantum counterparts of the magnitudes here presented are treated in the main text (specifically, in Subsection 2.3.2 and Subsection 2.3.3).

E.1 Classical radiation field: stationary and ergodic random process

Field as a random variable The radiation field coming from a light source is characterized by a certain frequency ω_0 and some broadening arisen as a result of different processes. This situation is equivalent to having an ensemble of quasi-monochromatic signals centered at that frequency. The electromagnetic field can be hence taken as a **random function** of position and time, such that every time it is measured we obtain a value of the field according to the associated probability distribution. As a consequence, the field can be treated in statistical terms, where every measurement corresponds to an element of all possible realizations of the field.

Stationary light source The statistical properties of a light source are said to be **stationary** when those processes that cause the fluctuations do not change with time. In this case, the probability distribution and the different magnitudes monitoring the coherence do not depend on time. However, although the probability distribution is constant in time, the value of the field amplitude obtained in a measurement is still a random variable, whose value fluctuates precisely according to that probability distribution.

Ensemble average Given a (complex) random function $z(t)$, the ensemble average at time t is the average over the ensemble of all realizations $z^{(k)}(t)$:

$$\langle z(t)\rangle_{\mathrm{e}} = \lim_{N\to\infty} \frac{1}{N}\sum_{k=1}^{N} z^{(k)}(t)\,.$$

There, the angle brackets $\langle\cdot\rangle_{\mathrm{e}}$ denote ensemble average. The (two-time) autocorrelation function of this process at times t_1 and t_2 is given by:

$$\Gamma(t_1,t_2) \equiv \langle z^*(t_1)\, z(t_2)\rangle_{\mathrm{e}}\,.$$

This function gives information about how long correlations extend in the variable t. If the process $z(t)$ is stationary, all the ensemble averages are independent of the origin of time. The expectation value of any function which is statistically stationary is invariant under a time translation. Therefore, the mean $\langle z(t)\rangle_{\mathrm{e}}$ and the autocorrelation function $\Gamma(t_1,t_2)$ are invariant under time translations. As a consequence, $\Gamma(t_1,t_2)$ does not depend on the specific values t_1 and t_2, but just on the time difference $\tau = t_2 - t_1$, so it can be written as:

$$\Gamma(t_2-t_1) \equiv \Gamma(\tau) = \langle z^*(t)\, z(t+\tau)\rangle_{\mathrm{e}}\,,$$

where we have renamed the time variables as $t_1 \to t$ and $t_2 \to t+\tau$. Notice that, although on average the signal does not depend on time, every realization $z^{(k)}(t)$ does vary in time.

Time average Given a particular realization k of the stationary random process $z(t)$, its time average over a certain time interval T is given by:

$$\overline{z^{(k)}} \equiv \lim_{T\to\infty} \frac{1}{T}\int_{t-T/2}^{t+T/2} z^{(k)}(t')\mathrm{d}t'$$

where the bar over the variable stands for time average. This does not depend on time t nor the interval T but, in general, it may depend on the specific realization k of the ensemble.

Ergodicity If the different time averages $\overline{z^{(k)}}$ are all equal and coincide with the ensemble average $\langle z(t)\rangle_{\mathrm{e}}$, the stationary random process $z(t)$ is said to be an ergodic process [423]. In general, a stationary random process is ergodic as long as correlations of the random process vanish quickly enough in time. In this case, a single realization of the random process can be divided into shorter parts which are uncorrelated between each other, obtaining in that way an ensemble of realizations. Then it is easy to see that average over time would be equivalent to averaging over an ensemble of realizations.

Autocorrelation function As is the time average, the temporal (two-time) autocorrelation function is invariable under time translations if $z(t)$ is a stationary process. As a consequence, this magnitude does not depend on the specific values t_1 and t_2 between which correlations are studied, but on the time difference $\tau = t_2 - t_1$:

$$\Gamma^{(k)}(t_2-t_1) = \Gamma^{(k)}(\tau) = \langle z^{(k)*}(t)\, z^{(k)}(t+\tau)\rangle_{\mathrm{t}} = \lim_{T\to\infty}\frac{1}{T}\int_{-T/2}^{T/2} z^{(k)*}(t)\, z^{(k)}(t+\tau)\,\mathrm{d}t\,,$$

where we have considered a specific realization of the ensemble $z^{(k)}(t)$. In the case of having an ergodic process, ensemble and time averages are equivalent, so the autocorrelation function $\Gamma(\tau)$ of the stationary process $z(t)$ can be simply written as:

$$\Gamma(\tau) = \langle z^*(t)\, z(t+\tau)\rangle \,. \tag{E.1}$$

For any complex stationary random process $z(t)$, the autocorrelation function $\Gamma(\tau)$ presents the following properties [423]:

- From the definition of Equation E.1, the equal time correlation function is given by $\Gamma(0) = \langle |z(t)|^2\rangle$, so:

  $$\Gamma(0) \geq 0 \,,$$

  where the equal takes place only in the trivial case in which $z(t)$ is zero for all times.

- It is Hermitian:

  $$\Gamma(-\tau) = \Gamma^*(\tau) \,, \tag{E.2}$$

  since $\Gamma(\tau) = \langle z^*(t)\, z(t+\tau)\rangle = \langle z^*(t-\tau)\, z(t)\rangle = \langle z^*(t)\, z(t-\tau)\rangle^* = \Gamma^*(-\tau)$.

- It cannot exceed the value at $\tau = 0$:

  $$|\Gamma(\tau)| \leq \Gamma(0) \,, \tag{E.3}$$

  since $|\Gamma(\tau)|^2 = |\langle z^*(t)\, z(t+\tau)\rangle|^2 \leq \langle z^*(t)\, z(t)\rangle\langle z^*(t+\tau)\, z(t+\tau)\rangle = \Gamma^2(0)$. There, we have made use of the Schwarz inequality: $|\langle u, v\rangle|^2 \leq \langle u, u\rangle\langle v, v\rangle$.

E.2 Classical coherence

Let us consider a classical electromagnetic field emitted by a light source. If we ignore its polarizability, the radiation field received at certain position $\boldsymbol{r}$ at time t can be represented by a complex scalar function $E(\boldsymbol{r}, t)$. For any realistic light source, that amplitude of the electric field presents fluctuation on time. There are many sources contributing to these fluctuations. Notice, for example, that the total radiation field is usually the superposition of the contribution of a large number of emitters which are, in principle, independent of each other. The field is thus assumed to be represented by a random variable.

The concept of coherence

The concept of coherence can be understood as the degree of knowledge that one has about the field at some (spatial, temporal) point when knowing its value in another (spatial, temporal) point. And this idea is also valid when talking about two different fields: we may wonder about our degree of knowledge of some field knowing some information about another field. In particular, we are interested in the electromagnetic field $E(t)$ coming out from a light source, and the coherence with itself.

The measure of coherence in a field is given mathematically by correlations: given the value of the electromagnetic field at some time $t = t_0$, the knowledge of that field at another time t is related to the average $\langle E(t_0)E(t)\rangle$. Then, if the field is coherent, there will be some relation between the values of the field $E(t_0)$ and $E(t)$ and the average will yield some fixed value. On the contrary, the average will vanish if values at these times are not related to each other.

Intensity

Given the complex variable $E(\boldsymbol{r},t)$ representing the amplitude of the radiation field, the **instantaneous intensity** $I(\boldsymbol{r},t)$ at point $\boldsymbol{r}$ and time t can be defined as:

$$I(\boldsymbol{r},t) = E^*(\boldsymbol{r},t)E(\boldsymbol{r},t)\ .$$

From this expression of the intensity, we can compute its average over many realizations of the field. The **ensemble averaged intensity** of the light at position $\boldsymbol{r}$ and time t is given by:

$$\langle I(\boldsymbol{r},t)\rangle_{\mathrm{e}} = \langle E^*(\boldsymbol{r},t)E(\boldsymbol{r},t)\rangle_{\mathrm{e}} = \lim_{N\to\infty}\frac{1}{N}\sum_{k=1}^{N}E^*_{(k)}(\boldsymbol{r},t)E_{(k)}(\boldsymbol{r},t)\ ,$$

where $\langle\cdot\rangle_{\mathrm{e}}$ denotes ensemble average. Alternatively, we can compute the **time averaged intensity**:

$$\langle I(\boldsymbol{r},t)\rangle_{\mathrm{t}} = \langle E^*(\boldsymbol{r},t)E(\boldsymbol{r},t)\rangle_{\mathrm{t}} = \lim_{T\to\infty}\frac{1}{2T}\int_{-T}^{T}E^*(\boldsymbol{r},t)E(\boldsymbol{r},t)\,\mathrm{d}t\ ,$$

where $\langle\cdot\rangle_{\mathrm{t}}$ denotes time average. These quantities may actually not be the same. Nevertheless, we will assume that our light field $E(\boldsymbol{r},t)$ is stationary (so expectation values do not depend on t) and ergodic (the time average of their properties is equal to the average over realizations). Since time and ensemble averages are thus equivalent, we can omit the subscript t or e in the previous angle brackets and maintain the definition. Then, the **intensity** I of the electric field $E(\boldsymbol{r},t)$ at certain point $\boldsymbol{r}$ is simply defined as:

$$I(\boldsymbol{r}) = \langle E^*(\boldsymbol{r},t)E(\boldsymbol{r},t)\rangle\ . \tag{E.4}$$

It is worth mentioning that in most cases ensemble averaging is performed directly since the radiation coming out from a light source is the combination of the radiation from many emitters, whose emission is independent from each other. Moreover, detectors perform themselves a time averaging, since their resolution time is of the order of 10^{-12} s while fluctuations are of the order of 10^{-15} s. Therefore, the rapid optical variations of the field are not measured, but just the time average over an interval long compared to the characteristic time scales of the fluctuations.

From now on, we will restrict our discussion to light with stationary statistics and ergodic properties. Time averaging is thus equivalent to ensemble averaging and expectation values do not depend on time.

Classical first-order coherence

Given the electric field $E(\boldsymbol{r},t)$, the **first-order correlation function** between the field amplitude at positions $\boldsymbol{r}_1$ and $\boldsymbol{r}_2$ at times t_1 and t_2, respectively, is given by:

$$G^{(1)}(\boldsymbol{r}_1,\boldsymbol{r}_2;\tau) = \langle E^*(\boldsymbol{r}_1,t)E(\boldsymbol{r}_2,t+\tau)\rangle \,, \tag{E.5}$$

where we have introduced the time delay variable $\tau = t_2 - t_1$. This is nothing but the autocorrelation function defined in Equation E.1 when generalized to include the spatial variable. Notice also that $G^{(1)}(\boldsymbol{r},\boldsymbol{r};\tau=0)$ represents the intensity at point $\boldsymbol{r}$.

The correlation function $G^{(1)}$ is usually normalized in order to eliminate the dependence on the absolute value of the field, thus arriving at the definition of **degree of first-order coherence**:

$$g^{(1)}(\boldsymbol{r}_1,\boldsymbol{r}_2;\tau) = \frac{\langle E^*(\boldsymbol{r}_1,t)E(\boldsymbol{r}_2,t+\tau)\rangle}{\sqrt{\langle E^*(\boldsymbol{r}_1,t)E(\boldsymbol{r}_1,t)\rangle\langle E^*(\boldsymbol{r}_2,t+\tau)E(\boldsymbol{r}_2,t+\tau)\rangle}} \,.$$

In the denominator there appear the intensity at positions $\boldsymbol{r}_1$ and $\boldsymbol{r}_2$, that are supposed to be different from zero. Since intensity does not vary with time for stationary light sources (Equation E.4), we can simply write:

$$g^{(1)}(\boldsymbol{r}_1,\boldsymbol{r}_2;\tau) = \frac{\langle E^*(\boldsymbol{r}_1,t)E(\boldsymbol{r}_2,t+\tau)\rangle}{\sqrt{I(\boldsymbol{r}_1)\,I(\boldsymbol{r}_2)}} \,.$$

In particular, if we consider coherence at the same spatial position, the expression reduces to:

$$g^{(1)}(\tau) = \frac{\langle E^*(t)E(t+\tau)\rangle}{\langle E^*(t)E(t)\rangle} \,, \tag{E.6}$$

what is specifically named as **degree of first-order temporal coherence**. There, it is involved the correlation between the fields at the same position but at different times. This quantity satisfies the following properties:

- For $\tau = 0$:
$$g^{(1)}(0) = 1 \,.$$
- From the Hermiticity property of the autocorrelation function (Equation E.2):
$$g^{(1)}(-\tau) = [g^{(1)}(\tau)]^* \,. \tag{E.7}$$
- Since $g^{(1)}(\tau) = \Gamma(\tau)/\Gamma(0)$, the inequality of Equation E.3 leads:
$$0 \leq |g^{(1)}(\tau)| \leq 1 \,.$$

The degree of first order coherence is measured in experiments with interferometers (such as the Michelson or the Mach–Zehnder interferometers), where the light beam is first split in two parts and then these two beams are forced to interact after introducing a time delay between them. When the output intensity is recorded, there appears an interference pattern, where the **visibility** $\mathcal{V}$ is defined from the maximum and minimum values of the intensity in that pattern: $\mathcal{V} = (I_{\text{max}} - I_{\text{min}})/(I_{\text{max}} + I_{\text{min}})$. The visibility turns

to be the modulus of the first-order coherence degree:

$$\mathcal{V} = |g^{(1)}(\tau)| \, .$$

In this sense, the degree of first-order coherence offers a measure of the facility to obtain interference fringes when light is superposed. This magnitude can take values from zero (for an **incoherent field**) to one (for a fully **coherent field**). Between these two extreme cases, we have **partially coherent light**. Then, according to the degree of first-order coherence, light can be denoted as follows:

$$\begin{aligned} |g^{(1)}(\tau)| &= 0 && \text{complete incoherence} \\ 0 < |g^{(1)}(\tau)| &< 1 && \text{partial coherence} \\ |g^{(1)}(\tau)| &= 1 && \text{complete first-order coherence} \end{aligned} \tag{E.8}$$

When the analytical expression for the modulus of the degree of first-order temporal coherence is known —this is the case, for instance, of chaotic light with a Lorentzian or Gaussian frequency spectrum [120]—, the **coherence time** τ_c may be defined as:

$$\tau_c \equiv \int_{-\infty}^{\infty} |g^{(1)}(\tau)|^2 \, \mathrm{d}\tau \, .$$

This is a measure of the time over which correlations of the radiation field persist. For chaotic light, correlations vanish for values of τ much longer than the coherence time, that is, $g^{(1)}(\tau) \to 0$ for $\tau \gg \tau_c$. On the contrary, for a classical wave propagating along the z-direction with frequency ω_0 and wavenumber $k = \omega_0/c$, whose electric field is thus given by $E(z,t) = E_0 \mathrm{e}^{-\mathrm{i}(kz-\omega_0 t)}$, the degree of first-order temporal coherence is $g^{(1)}(\tau) = \mathrm{e}^{-\mathrm{i}\omega_0\tau}$. Therefore, $|g^{(1)}(\tau)| = 1$ and the light is first-order coherent for all values of τ.

Classical second-order coherence

Apart from correlations in the amplitude of electric fields, expressed by the degree of first-order coherence, correlations in their intensity can be also measured. This is done, for instance, in the Hanbury Brown and Twiss experiment, which provides a measurement of intensity fluctuations. These are higher-order interference effects that arise from the interference of two intensities, and they can be expressed in terms of the degree of second-order coherence. Given an electric field $E(\boldsymbol{r}, t)$, we will consider two-time measurements of the intensity at a fixed time delay τ and study intensity fluctuations.

The **second-order correlation function** between the electric field $E(\boldsymbol{r}, t)$ at two space-time positions $(\boldsymbol{r}_1, t_1)$ and $(\boldsymbol{r}_2, t_2)$ is given by:

$$G^{(2)}(\boldsymbol{r}_1, \boldsymbol{r}_2, \tau) = \langle E^*(\boldsymbol{r}_1, t) E^*(\boldsymbol{r}_2, t+\tau) E(\boldsymbol{r}_2, t+\tau) E(\boldsymbol{r}_1, t) \rangle \, ,$$

where we have considered the time delay variable $\tau = t_2 - t_1$. The normalization of this expressions yields the **degree of second-order coherence**:

$$g^{(2)}(\boldsymbol{r}_1, \boldsymbol{r}_2, \tau) = \frac{\langle E^*(\boldsymbol{r}_1, t) E^*(\boldsymbol{r}_2, t+\tau) E(\boldsymbol{r}_2, t+\tau) E(\boldsymbol{r}_1, t) \rangle}{\langle E^*(\boldsymbol{r}_1, t) E(\boldsymbol{r}_1, t) \rangle \langle E^*(\boldsymbol{r}_2, t+\tau) E(\boldsymbol{r}_2, t+\tau) \rangle} \, ,$$

which can be written in terms of the intensity (Equation E.4) as:

$$g^{(2)}(\boldsymbol{r}_1, \boldsymbol{r}_2, \tau) = \frac{\langle E^*(\boldsymbol{r}_1, t) E^*(\boldsymbol{r}_2, t+\tau) E(\boldsymbol{r}_2, t+\tau) E(\boldsymbol{r}_1, t) \rangle}{I(\boldsymbol{r}_1, t) I(\boldsymbol{r}_2, t+\tau)} \, .$$

Notice that, for stationary light sources, these intensities are constant in time. When considering coherence at the same spatial position, the above expression reduces to:

$$g^{(2)}(\tau) = \frac{\langle E^*(t) E^*(t+\tau) E(t+\tau) E(t) \rangle}{\langle E^*(t) E(t) \rangle^2} \, ,$$

which is known as the **degree of second-order temporal coherence**. This quantity presents the following properties:

- It is symmetric:
$$g^{(2)}(-\tau) = g^{(2)}(\tau) \, .$$
- From Cauchy's inequality (that states that $2I_1 I_2 \leq I_1^2 + I_2^2$ for any pair of real numbers I_1 and I_2), it follows:
$$1 \leq g^{(2)}(0) \leq \infty \, , \tag{E.9}$$
but, nevertheless, it does not apply for $\tau \neq 0$, so:
$$0 \leq g^{(2)}(\tau) \leq \infty \, . \tag{E.10}$$
- It cannot exceed the value at $\tau = 0$:
$$g^{(2)}(\tau) \leq g^{(2)}(0) \tag{E.11}$$

Equivalently to the definition of first-order coherence, the light is said to be **second-order coherent** if $|g^{(1)}(\tau)| = 1$ and, additionally, $g^{(2)}(\tau) = 1$. In particular, the electric field described by the wave $E(z,t) = E_0 \mathrm{e}^{-\mathrm{i}(kz - \omega_0 t)}$ of frequency ω_0 and wavenumber $k = \omega_0 / c$, is second-order coherent —not only $|g^{(1)}(\tau)| = 1$, but also $g^{(2)}(\tau) = 1$ for all values of τ. On the contrary, it can be shown that chaotic light presents $g^{(2)}(0) = 2$, and $g^{(2)}(\tau) \to 1$ for $\tau \gg \tau_c$.

Correlations in the intensity are related to **joint probabilities**. Once a signal is detected at time t, the probability of detecting a signal at time $t + \tau$ is given by the joint probability $P_2(t, t+\tau)$, which is proportional to the correlation function $\langle I(t) I(t+\tau) \rangle$. Therefore, the existence of **intensity correlations** means that if we obtain a detection in one point at some time, it is more probable to detect a signal in another point at another time with respect to the random case (or uncorrelated sources). This is what is known as **bunching**, since the different detections seem to be arranged in groups or bunches. We will study this in more detail in the next section, dealing with quantum coherence.

E.3 Lineshape of the emission

The spectrum of a particular stationary random process is the strength of the fluctuations associated with a particular component of the Fourier decomposition of that field. Light sources are also characterized by its spectrum, which gives the frequency distribution of the radiation field. There exists a connection between the first-order coherence and the emitted spectrum. As we will see, the spectral density of a random process and its autocorrelation function form a Fourier transform pair.

Spectral density Let us consider the radiation field $E(t)$ emitted by a statistically stationary light source. Its first-order autocorrelation function is given in Equation E.5, that we will simply denote it as $\Gamma(\tau)$ in accordance to Equation E.1 (where we dealt with the autocorrelation function of a general stationary and ergodic random process):

$$\Gamma(\tau) = \langle E^*(t)E(t+\tau)\rangle \ .$$

From this function, the spectral density $S(\omega)$ associated with the electric field $E(t)$ is defined as:

$$S(\omega) = \frac{1}{2\pi}\int_{-\infty}^{\infty} \Gamma(\tau)\, \mathrm{e}^{\mathrm{i}\omega\tau}\mathrm{d}\tau \ , \tag{E.12}$$

which is also known as power spectrum. The integration of this expression over frequencies yields the correlation function at zero-time delay:

$$\begin{aligned}\int_{-\infty}^{\infty} S(\omega)\,\mathrm{d}\omega &= \frac{1}{2\pi}\int_{-\infty}^{\infty}\mathrm{d}\omega\int_{-\infty}^{\infty}\mathrm{d}\tau\ \Gamma(\tau)\,\mathrm{e}^{\mathrm{i}\omega\tau} \\ &= \frac{1}{2\pi}\int_{-\infty}^{\infty}\mathrm{d}\tau\ \Gamma(\tau)\int_{-\infty}^{\infty}\mathrm{d}\omega\ \mathrm{e}^{\mathrm{i}\omega\tau} = \int_{-\infty}^{\infty}\mathrm{d}\tau\ \Gamma(\tau)\delta(\tau) = \Gamma(0)\ ,\end{aligned}$$

where we have made use of the integral representation of the delta function:

$$\delta(\omega-\omega') = \frac{1}{2\pi}\int_{-\infty}^{\infty}\mathrm{e}^{\mathrm{i}(\omega-\omega')t}\ \mathrm{d}t \ . \tag{E.13}$$

Normalized spectrum The spectral density $S(\omega)$ can be normalized by the division of Equation E.12 by the previous integral:

$$N(\omega) = \frac{S(\omega)}{\int_{-\infty}^{\infty} S(\omega)\,\mathrm{d}\omega} = \frac{1}{2\pi}\frac{1}{\Gamma(0)}\int_{-\infty}^{\infty}\Gamma(\tau)\,\mathrm{e}^{\mathrm{i}\omega\tau}\mathrm{d}\tau \ , \tag{E.14}$$

so, effectively: $\int_{-\infty}^{\infty} N(\omega)\,\mathrm{d}\omega = 1$. Observe that there appears the degree of first-order coherence, defined as $g^{(1)}(\tau) = \Gamma(\tau)/\Gamma(0)$ according to Equation E.6, so the normalized spectrum becomes:

$$N(\omega) = \frac{1}{2\pi}\int_{-\infty}^{\infty} g^{(1)}(\tau)\,\mathrm{e}^{\mathrm{i}\omega\tau}\mathrm{d}\tau \ . \tag{E.15}$$

This is nothing but the Fourier transform of the degree of first-order coherence, and it is also known as the lineshape of the emission. From the Hermiticity property of the first-order coherence degree (Equation E.7), the normalized spectrum can be alternatively

written as:

$$N(\omega) = \frac{1}{\pi}\,\mathrm{Re}\int_0^\infty g^{(1)}(\tau)\,\mathrm{e}^{\mathrm{i}\omega\tau}\mathrm{d}\tau\ ,$$

where the integration is carried out just over the positive values of the delay.

The expression in Equation E.15 gives a formal connection between the spectrum of the light (determined in spectroscopic experiments) and its coherence properties (obtained through time-dependent measurements of its fluctuations). Experimentally, the spectral density is obtained by counting the number of photons arriving with a particular energy, so we have the decomposition of the field in terms of the different frequency components. The spectral density gives the strength associated to each Fourier component, as we will show next.

Strength of the Fourier components The definition given before for the spectral density (Equation E.12) is, effectively, related to the strength of a particular component of the Fourier decomposition. The radiation field can be decomposed in its harmonic components by considering the Fourier integral:

$$E(t) = \int_{-\infty}^{\infty} \tilde{E}(\omega)\,\mathrm{e}^{-\mathrm{i}\omega t}\mathrm{d}\omega\ .$$

Each one of the Fourier components $\tilde{E}(\omega)$ can be written in turn as:

$$\tilde{E}(\omega) = \frac{1}{2\pi}\int_{-\infty}^{\infty} E(t)\,\mathrm{e}^{\mathrm{i}\omega t}\mathrm{d}t\ .$$

The spectral density could be defined simply as $S(\omega) = |\tilde{E}(\omega)|^2$, since this gives the strength of a particular component. Nevertheless, this definition is disregarded as it presents technical problems for some functions [423]. Since $\tilde{E}(\omega)$ is also a random process, we may ask about the expectation value of the product $\tilde{E}(\omega)\tilde{E}(\omega')$ instead:

$$\begin{aligned}
\langle\tilde{E}^*(\omega)\tilde{E}(\omega')\rangle =& \frac{1}{(2\pi)^2}\int_{-\infty}^{\infty}\mathrm{d}t\int_{-\infty}^{\infty}\mathrm{d}t'\ \langle E^*(t)E(t')\rangle\ \mathrm{e}^{\mathrm{i}(\omega' t'-\omega t)}\\
=& \frac{1}{(2\pi)^2}\int_{-\infty}^{\infty}\mathrm{d}t\int_{-\infty}^{\infty}\mathrm{d}t'\ \ \Gamma(t'-t)\,\mathrm{e}^{\mathrm{i}\omega'(t'-t)}\mathrm{e}^{\mathrm{i}(\omega'-\omega)t}\\
=& \frac{1}{(2\pi)^2}\int_{-\infty}^{\infty}\mathrm{d}t\ \mathrm{e}^{\mathrm{i}(\omega'-\omega)t}\int_{-\infty}^{\infty}\mathrm{d}\tau\ \ \Gamma(\tau)\,\mathrm{e}^{\mathrm{i}\omega'\tau}\\
=& \frac{1}{2\pi}\int_{-\infty}^{\infty}\mathrm{d}t\ \mathrm{e}^{\mathrm{i}(\omega'-\omega)t}\tilde{\Gamma}(\omega')\ ,
\end{aligned}$$

where we have substituted the correlation function $\langle E^*(t)E(t')\rangle = \Gamma(t'-t)$ and we have also considered the Fourier transform of the correlation function:

$$\tilde{\Gamma}(\omega) = \frac{1}{2\pi}\int_{-\infty}^{\infty}\mathrm{d}\tau\ \ \Gamma(\tau)\,\mathrm{e}^{\mathrm{i}\omega\tau}\ .$$

By considering the integral representation of the delta function (Equation E.13), the previous expectation value can be simply written as:

$$\langle\tilde{E}^*(\omega)\tilde{E}(\omega')\rangle = \tilde{\Gamma}(\omega)\delta(\omega-\omega')\ .$$

From this expression we can regard $\tilde{\Gamma}(\omega)$ as a measure of the strength of the fluctuations of the Fourier component at frequency ω. This is precisely the meaning of the spectral density, thus $\tilde{\Gamma}(\omega)$ is identified with the spectral density $S(\omega)$. Then, we can rewrite the previous expectation value as:

$$\langle \tilde{E}^*(\omega)\tilde{E}(\omega')\rangle = S(\omega)\delta(\omega-\omega') \,,$$

and write the spectral density as the Fourier transform of the autocorrelation function:

$$S(\omega) \equiv \tilde{\Gamma}(\omega) = \frac{1}{2\pi}\int_{-\infty}^{\infty} \Gamma(\tau)\, \mathrm{e}^{\mathrm{i}\omega\tau}\, \mathrm{d}\tau \,.$$

This expression for the spectral density is in accordance to the definition given before (Equation E.12). Inversely, we can write:

$$\Gamma(\tau) = \int_{-\infty}^{\infty} S(\omega)\, \mathrm{e}^{-\mathrm{i}\omega\tau}\, \mathrm{d}\tau$$

These two expressions are generally referred to as the Wiener–Khintchine theorem, that states that the spectral density of a stationary random process and its correlation function form a **Fourier transform pair**. Equation E.15 is an alternative form of that theorem, since it links the spectral density and the degree of first-order coherence.

APPENDIX F

MATTER: ORGANIC MOLECULES

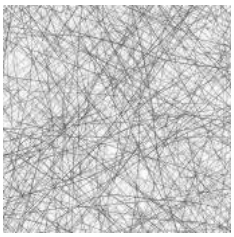

In this Appendix, we provide some extensions of the topics discussed in Section 2.4, which deals with the quantum description of organic molecules. First, we describe different types of **electronic transitions** present in organic molecules (Section F.1) before focusing on the first two electronic states: the ground and the first-excited electronic states. The description of the molecule energy structure in terms of energy surfaces after introducing the **Born–Oppenheimer approximation** is discussed next (Section F.2). The Hamiltonian describing organic molecules is here completed with the addition of the **coherent pumping term** (Section F.3). Absorption experiments show the richness of the inner level structure of organic molecules —the absorption spectrum reveals interesting characteristics of their vibrational structure. In this Appendix we obtain some expressions related to the absorption spectrum of organic molecules, such as the **transition rate** and the **lineshape function** (Section F.4), as well as the **correlation function** and the **spectral density** (Section F.5). Finally, we study the characteristic profile of the **absorption spectrum** associated with organic molecules, and analyze the imprint left by the different relevant quantities of the displaced harmonic oscillator model on it (Section F.6). Some interesting books are those in Ref. [425, 426], which are partially followed in the discussion.

F.1 Electronic transitions

Organic molecules present different electronic states that can be either singlets or triplets depending on its spin multiplicity*. The four main electronic states are the ground state S_0, and the three excited states S_1, S_2, and T_1 (where S and T stand for singlet and triplet states, respectively). Different transitions between these electronic states can occur according to various selection rules. The **spin selection rule** states that only those transitions connecting states with the same spin multiplicity are allowed. As a consequence, spin-allowed transitions will be more likely than spin-forbidden ones. Nevertheless, spin-

*The spin multiplicity is given by $2S+1$, where S is the total spin angular momentum. For singlets the total spin is $S=0$, while for triplets, $S=1$.

orbit coupling (that is, the interaction between the spin angular momentum and the orbital angular momentum) allows for the change in spin multiplicity, such that when this term is large, the probability of spin-forbidden transitions increases.

Luminescence refers, in general, to the spontaneous emission of light from any substance. When this emission takes place as a result of the previous absorption of a photon, then it is called **photoluminescence**. The absorption of a photon leads to the promotion of an electron from the ground electronic state to an excited electronic state of the same spin multiplicity, in a process that lasts $1-10$ fs. When being at an excited electronic state, different transitions can occur, distinguishing between radiative and nonradiative processes [426].

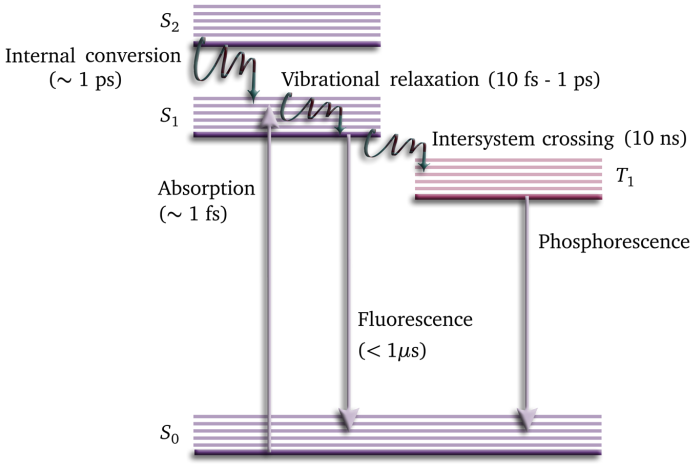

Figure F.1. Sketch of the first four electronic states typically present in organic molecules: the ground state S_0 and the three excited states S_1, S_2, and T_1, where S and T stand for singlet and triplet states, respectively. Different transitions are represented with arrows together with their associated lifetimes, where we distinguish between radiative (straight lines) and nonradiative (wavy lines) transitions.

Radiative transitions

Radiative processes are those that involve the absorption or emission of a photon. Depending on the excited electronic state from which the transition starts, we have:

- **Absorption**: absorption of a photon such that the system goes from the ground state to an excited electronic state with the same spin multiplicity (for instance, $S_0 \to S_1$). The average lifetime of these transitions is on the order of 1 fs.

- **Fluorescence**: emission of a photon from an excited electronic state with the same spin multiplicity as the ground electronic state (for instance, $S_1 \to S_0$). These transitions are spin-allowed, and the average lifetimes of the excited states are typically less than 1 μs.

- **Phosphorescence**: emission of a photon from a triplet excited state to the singlet ground state (for instance, $T_1 \to S_0$). These transitions are spin-forbidden, and the associated lifetimes range from 1 μs to 10 s.

Since the average lifetime of the excited state is much longer for phosphorescence than fluorescence, this is the way in which these two processes are distinguished in the emission bands.

Nonradiative processes

Non-radiative transitions are those that do not involve the emission nor the absorption of a photon. Different kinds of nonradiative transitions can take place in molecules:

- **Vibrational relaxation**: when being at an excited vibrational level, relaxation to the lowest vibrational level of the same electronic state. This process occurs on a time scale ranging from 10 fs to 1 ps, so it is faster than luminescence.

- **Internal conversion**: relaxation to a lower singlet excited state from another singlet state (for instance, $S_2 \rightarrow S_1$), so the same spin multiplicity remains. The associated lifetime is about 1 ps.

- **Intersystem crossing**: relaxation between excited states with different spin multiplicities (for instance, $S_1 \rightarrow T_1$). This process occurs on a time scale of 10 ns.

- **Nonradiative de-excitation**: when being at an excited electronic state, nonradiative relaxation to the ground electronic state through the release of thermal energy (for instance, phonons in crystals are responsible for nonradiative de-excitation processes). Although the amount of released heat cannot be experimentally measured in general, this kind of processes are known to be present due to the quenching of luminescence.

F.2 Franck–Condon transitions between potential energy surfaces

Born–Oppenheimer approximation

Widely used in molecular physics and quantum chemistry, the **Born–Oppenheimer approximation** provides a description of molecules in which nuclear and electronic degrees of freedom can be treated separately. This is possible due to the different energy scales associated with these two subsystems: around 100 meV for nuclear and 2 eV for electronic states. As electrons move faster than nuclei, their disposition is adjusted adiabatically to nuclear motions, reason why this assumption is also called **adiabatic approximation**.

Within this approximation, the total state of the molecule ($|\psi\rangle$) can be written in terms of its electronic ($|\phi\rangle$) and nuclear ($|\chi\rangle$) components:

$$|\psi(x,R)\rangle = |\phi(x,R)\rangle \otimes |\chi(R)\rangle \ ,$$

where x and R stand for electronic and nuclear degrees of freedom, respectively. The state of the molecule will be the solution to the Schrödinger equation: $H|\psi(x,R)\rangle = E|\psi(x,R)\rangle$, where the Hamiltonian H comprises the kinetic terms for both nuclei and electrons, as well as the effective nuclei-electron and internuclear interactions. There, E

represents the energy of the state. This equations is now solved in two stages:

Step 1. First, the nuclear kinetic energy T_n is removed from the complete Hamiltonian H, and the nuclei positions are introduced into the electronic part as mere parameters. Solving the Schrödinger equation for the electronic Hamiltonian $H_e = H - T_n$, one obtains the electronic eigenstates $|\phi_k\rangle$ for each value of the nuclear positions R:

$$H_e(x,R)\,|\phi_k(x,R)\rangle = E_k(R)\,|\phi_k(x,R)\rangle\ ,$$

where E_k is the associated energy. A general state can be now expressed as lineal superposition of the calculated eigenstates: $|\psi(x,R)\rangle = \sum_k |\phi_k(x,R)\rangle \otimes |\chi_k(R)\rangle$.

Step 2. The previously disregarded term T_n is now considered together with the electronic eigenenergies $E_k(R)$, so that the Schrödinger equation for the nuclear motion can be solved at this point. Terms coupling different electronic eigenstates, $|\chi_k\rangle$ and $|\chi_{k'}\rangle$, can be neglected if their corresponding electronic energies, E_k and E'_k, are adequately separated. Hence we end up with a set of uncoupled differential equations:

$$(T_n + E_k(R))\,|\chi_k^l(R)\rangle = E_l\,|\chi_k^l(R)\rangle\ , \tag{F.1}$$

one for each electronic eigenstate k. As a consequence, the state of the molecule can be written as a product of single electronic and nuclear states: $|\psi_k^l(x,R)\rangle = |\phi_k(x,R)\rangle \otimes |\chi_k^l(R)\rangle$. Notice that energies E_l correspond to the total energy of the molecule, including not only the electronic part, but also the contribution from nuclei (vibrations, rotations and translations of the whole molecule).

All in all, the Born–Oppenheimer approximation leads to a picture based on nuclei moving in the effective potentials created by electrons. Solving first the electronic Schrödinger equation we get a set of independent energy surfaces on which nuclei move, the so-called **potential energy surfaces**. Then, for each electronic surface, the nuclear dynamics is resolved, which corresponds to rotational or vibrational nuclear excitation.

Potential energy surfaces

In the following, we will only refer to the first two electronic states, the ground state $|g\rangle$ and the first (electronically) excited state $|e\rangle$. Their energies as a function of the nuclear configuration will be given by their corresponding potential energy surfaces (or **potential energy curves** when considering just one nuclear degree of freedom), as shown in Figure F.2 [Left]. Modulated by these energy potentials, there would appear different vibrational modes within the same electronic state, corresponding to the nuclear movement.

In general, models including these phononic modes approximate these potential energy curves by harmonic potentials that is a good compromise near the potential minimum. In Figure F.2 [Right], it is shown the harmonic approximation (red line) to the ground and first-excited state potential energy curves (black line). There, different vibrational levels are depicted.

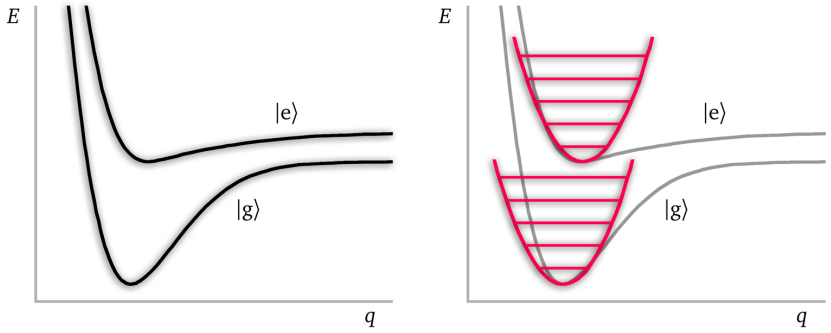

Figure F.2. [**Left**] Potential energy curves for the ground state $|g\rangle$ and the first (electronically) excited state $|e\rangle$ as a function of the nuclear degree of freedom q. [**Right**] Harmonic approximation around the minima of the first two potential energy curves.

Franck–Condon transitions

The absorption of light takes place within a time scale of some femtoseconds, time over which nuclei can be considered to be frozen in a good approximation. The **Franck–Condon principle** is the assumption that nuclear displacements are negligible during electronic transitions. According to this rule, those vibronic transitions that connect states with similar equilibrium distances are the only ones that eventually take place. When looking at energy level diagrams depicted as a function of the nuclear coordinate, only vibronic transitions described by vertical lines occur since the nuclear coordinate cannot vary during this process. For this reason, these are also known as **vertical transitions**.

In fact, the probability P of the occurrence of a vibronic transition between two states is proportional to the square of the overlap of their corresponding vibrational components $|\chi_{\text{initial}}\rangle$ and $|\chi_{\text{final}}\rangle$:

$$P \propto |\langle \chi_{\text{initial}} | \chi_{\text{final}} \rangle|^2 \,, \tag{F.2}$$

which is known as the **Franck–Condon factor**. Hence, the intensity of a vibronic transition is consequently given by this overlap.

F.3 Coherently pumped organic molecule

The two molecular states $|\mathcal{G}\rangle$ and $|\mathcal{E}\rangle$ involved in the Hamiltonian of Equation 2.53 are usually not independent, but they are connected through the interaction term arising as a consequence of the external field pumping the system. The Hamiltonian describing the pumped system $\hat{H}$ can be generally written as:

$$\begin{aligned} \hat{H} &= \hat{H}_{\mathcal{G}} + \hat{H}_{\mathcal{E}} + \hat{H}_{\mathcal{GE}} \\ &= E_{\mathcal{G}} |\mathcal{G}\rangle\langle\mathcal{G}| + E_{\mathcal{E}} |\mathcal{E}\rangle\langle\mathcal{E}| + V_{\text{eg}} |\mathcal{E}\rangle\langle\mathcal{G}| + V_{\text{ge}} |\mathcal{G}\rangle\langle\mathcal{E}| \,, \end{aligned} \tag{F.3}$$

where $E_{\mathcal{G}}$ and $E_{\mathcal{E}}$ are the energies corresponding to the molecular states $|\mathcal{G}\rangle$ and $|\mathcal{E}\rangle$, that is, $\hat{H}_{\mathcal{G}}|\mathcal{G}\rangle = E_{\mathcal{G}}|\mathcal{G}\rangle$ and $\hat{H}_{\mathcal{E}}|\mathcal{E}\rangle = E_{\mathcal{E}}|\mathcal{E}\rangle$. These energies are given by Equation 2.51 within the DHO model. The interaction term V_{eg} can be written in the electric-dipole approximation (Equation 2.32) as:

$$V_{\text{eg}}(t) = -\boldsymbol{E}_L(t) \cdot \boldsymbol{\mu}_{\text{eg}} \,, \tag{F.4}$$

where $\boldsymbol{\mu}_{\text{eg}}$ is the dipole moment associated with the electronic transition $|\text{e}\rangle \rightarrow |\text{g}\rangle$. The interaction term possesses an explicit time-dependency due to the electric field $\boldsymbol{E}_L(t)$ pumping the system. This external electric field is taken to be monochromatic of frequency ω_L: $\boldsymbol{E}_L(t) = \boldsymbol{E}_0 \text{e}^{-\text{i}\omega_L t} + \boldsymbol{E}_0^* \text{e}^{\text{i}\omega_L t}$, and it is treated semiclassically. Due to this time-dependency, it is convenient to reorganize the Hamiltonian of Equation F.3 as $\hat{H}(t) = \hat{H}_0 + \hat{H}_1(t)$, where $\hat{H}_0$ is just a shift in the ground state energy:

$$\begin{aligned}\hat{H}_0 \quad &= \hbar\omega_L |\mathcal{G}\rangle\langle\mathcal{G}| \,, \\ \hat{H}_1(t) &= (E_\mathcal{G} - \hbar\omega_L)|\mathcal{G}\rangle\langle\mathcal{G}| + E_\mathcal{E}|\mathcal{E}\rangle\langle\mathcal{E}| - \boldsymbol{E}_L(t)\cdot\boldsymbol{\mu}_{\text{eg}}|\mathcal{E}\rangle\langle\mathcal{G}| - \boldsymbol{E}_L(t)\cdot\boldsymbol{\mu}_{\text{eg}}^*|\mathcal{G}\rangle\langle\mathcal{E}| \,.\end{aligned}$$

The interaction picture (see Appendix B) can be then introduced, where operators are transformed by considering the relation $\hat{H}^{(\text{I})}(t) = \mathcal{U}_0^\dagger(t)\, \hat{H}\, \mathcal{U}_0(t)$, with $\mathcal{U}_0(t) = e^{-\frac{\text{i}}{\hbar}\hat{H}_0 t} = e^{-\text{i}\omega_L t|\mathcal{G}\rangle\langle\mathcal{G}|}$. Therefore, the time-dependent Hamiltonian $\hat{H}_1$, when transformed to the interaction picture, reads:

$$\begin{aligned}\hat{H}_1^{(\text{I})}(t) = (E_\mathcal{G} - \hbar\omega_L)\text{e}^{\text{i}\omega_L t}|\mathcal{G}\rangle\langle\mathcal{G}|\text{e}^{-\text{i}\omega_L t} + E_\mathcal{E}|\mathcal{E}\rangle\langle\mathcal{E}| \\ - (\boldsymbol{E}_0\text{e}^{-\text{i}\omega_L t} + \boldsymbol{E}_0^*\text{e}^{\text{i}\omega_L t})\boldsymbol{\mu}_{\text{eg}}|\mathcal{E}\rangle\langle\mathcal{G}|\text{e}^{-\text{i}\omega_L t} - (\boldsymbol{E}_0\text{e}^{-\text{i}\omega_L t} + \boldsymbol{E}_0^*\text{e}^{\text{i}\omega_L t})\boldsymbol{\mu}_{\text{eg}}^*\text{e}^{\text{i}\omega_L t}|\mathcal{G}\rangle\langle\mathcal{E}| \,,\end{aligned}$$

since $\mathcal{U}_0^\dagger|\mathcal{G}\rangle = \text{e}^{\text{i}\omega_L t}|\mathcal{G}\rangle$ and $\mathcal{U}_0^\dagger|\mathcal{E}\rangle = |\mathcal{E}\rangle$. Rewriting this expression, we observe that the Hamiltonian $\hat{H}_1^{(\text{I})}(t)$ presents a time-independent part and another one that oscillates at twice the field frequency ω_L:

$$\begin{aligned}\hat{H}_1^{(\text{I})}(t) \;&= (E_\mathcal{G} - \hbar\omega_L)|\mathcal{G}\rangle\langle\mathcal{G}| + E_\mathcal{E}|\mathcal{E}\rangle\langle\mathcal{E}| \\ &\quad - \boldsymbol{E}_0^*\boldsymbol{\mu}_{\text{eg}}|\mathcal{E}\rangle\langle\mathcal{G}| - \boldsymbol{E}_0\boldsymbol{\mu}_{\text{eg}}\text{e}^{-2\text{i}\omega_L t}|\mathcal{E}\rangle\langle\mathcal{G}| - \boldsymbol{E}_0\boldsymbol{\mu}_{\text{eg}}^*|\mathcal{G}\rangle\langle\mathcal{E}| - \boldsymbol{E}_0^*\boldsymbol{\mu}_{\text{eg}}^*\text{e}^{2\text{i}\omega_L t}|\mathcal{G}\rangle\langle\mathcal{E}| \,.\end{aligned}$$

Neglecting these high-frequency oscillations, procedure known as the **rotating wave approximation**, we arrive at a time-independent Hamiltonian:

$$\hat{H}_1^{(\text{I})} = (E_\mathcal{G} - \hbar\omega_L)|\mathcal{G}\rangle\langle\mathcal{G}| + E_\mathcal{E}|\mathcal{E}\rangle\langle\mathcal{E}| - \boldsymbol{E}_0^*\boldsymbol{\mu}_{\text{eg}}|\mathcal{E}\rangle\langle\mathcal{G}| - \boldsymbol{E}_0\boldsymbol{\mu}_{\text{eg}}^*|\mathcal{G}\rangle\langle\mathcal{E}| \,. \tag{F.5}$$

Condon approximation In general, the dipole operator associated to a specific electronic transition is a function of the nuclear degrees of freedom q, that is, $\hat{\boldsymbol{\mu}} = \hat{\boldsymbol{\mu}}(q)$. This function can be expanded around the equilibrium configuration q_0:

$$\hat{\boldsymbol{\mu}}(q) = \hat{\boldsymbol{\mu}}(q_0) + \frac{\partial\hat{\boldsymbol{\mu}}(q)}{\partial q}(q - q_0) + \dots \,,$$

and it can be approximated by its equilibrium value (as long as it does not vanish due to symmetries):

$$\hat{\boldsymbol{\mu}}(q) \approx \hat{\boldsymbol{\mu}}(q_0) \equiv \hat{\boldsymbol{\mu}}_{\text{eg}} \,.$$

This is known as the **Condon approximation**, which states that the transition dipole moment operator $\hat{\boldsymbol{\mu}}$ does not depend on the nuclear coordinates, so we can write:

$$\hat{\boldsymbol{\mu}}_{\text{eg}} = \mu_{\text{eg}}|e\rangle\langle g| + \mu_{\text{ge}}|\text{g}\rangle\langle\text{e}| = \mu_{\text{eg}}(\hat{\sigma}^\dagger + \hat{\sigma}) \,,$$

where μ_{eg} is then the dipolar momentum of the electronic transition, as done in Equation 2.36.

F.4 Transition rate and lineshape function

The absorption spectrum depends on the transition rate at which the system is promoted from the ground to the excited state due to the absorption of a photon. This rate can be estimated through the Fermi's Golden rule, and expressed in terms of the lineshape function. In this section we will see how the Franck–Condon factor appears in the expression of the transition rate, as well as the correlation function of the transition dipole moment.

F.4.1 Transition rate

Let us consider two molecular states $|\mathcal{G}_\iota\rangle$ and $|\mathcal{E}_\kappa\rangle$ expressed in terms of their electronic and vibrational components as $|\mathcal{G}_\iota\rangle \equiv |\mathrm{g}\rangle \otimes |\chi_{\mathrm{g}}^{\iota}\rangle$ and $|\mathcal{E}_\kappa\rangle \equiv |\mathrm{e}\rangle \otimes |\chi_{\mathrm{e}}^{\kappa}\rangle$ when working within the adiabatic approximation (see Section F.2). There, $|\mathrm{g}\rangle$ and $|\mathrm{e}\rangle$ stand for the electronic ground and first-excited states respectively, while $\{|\chi_{\mathrm{g}}^{\iota}\rangle\}_\iota$ and $\{|\chi_{\mathrm{e}}^{\kappa}\rangle\}_\kappa$ denote their corresponding Hilbert spaces for vibrational excitations (hence states $|\chi_{\mathrm{g}}^{\iota}\rangle$ and $|\chi_{\mathrm{e}}^{\kappa}\rangle$ denote those with ι and κ vibrational modes excited).

The Hamiltonian describing the system is given by Equation F.3, which can be rewritten by taking into account the electronic and nuclear components of the molecular states:

$$\begin{aligned}\hat{H} &= \hat{H}_{\mathcal{G}} + \hat{H}_{\mathcal{E}} + \hat{H}_{\mathcal{G}\mathcal{E}} \\ &= \sum_{\iota} E_{\mathcal{G}_\iota} |\mathcal{G}_\iota\rangle\langle\mathcal{G}_\iota| + \sum_{\kappa} E_{\mathcal{E}_\kappa} |\mathcal{E}_\kappa\rangle\langle\mathcal{E}_\kappa| + \sum_{\iota,\kappa} V_{\kappa\iota} |\mathcal{E}_\kappa\rangle\langle\mathcal{G}_\iota| + \sum_{\iota,\kappa} V_{\iota\kappa} |\mathcal{G}_\iota\rangle\langle\mathcal{E}_\kappa| \,,\end{aligned} \tag{F.6}$$

where sums run over all possible vibrational states ι and κ appearing on top of the ground and excited electronic states, respectively. The coupling term $V_{\kappa\iota}$ is given by Equation F.4 within the electric-dipole approximation ($V_{\kappa\iota} = V_{\mathrm{eg}}$), and $E_{\mathcal{G}_\iota}$ and $E_{\mathcal{E}_\kappa}$ are the energies of each molecular state, namely:

$$\begin{aligned}\hat{H}_{\mathcal{G}} |\mathcal{G}_\iota\rangle &= E_{\mathcal{G}_\iota} |\mathcal{G}_\iota\rangle \,, \\ \hat{H}_{\mathcal{E}} |\mathcal{E}_\kappa\rangle &= E_{\mathcal{E}_\kappa} |\mathcal{E}_\kappa\rangle \,.\end{aligned} \tag{F.7}$$

Transition rate from Fermi's golden rule

The transition rate from the excited state $|\mathcal{E}_\kappa\rangle$ to the lower-lying state $|\mathcal{G}_\iota\rangle$ can be computed through the **Fermi's golden rule**, so we have:

$$\mathrm{K}_{\mathcal{E}_\kappa \mathcal{G}_\iota} = \mathrm{K}_{\mathcal{E}_\kappa \to \mathcal{G}_\iota} = \frac{2\pi}{\hbar} |V_{\iota\kappa}|^2 \delta(E_{\mathcal{E}_\kappa} - E_{\mathcal{G}_\iota}) \,, \tag{F.8}$$

where $V_{\iota\kappa}$ is the coupling term present in the Hamiltonian describing the system (Equation F.6), and $E_{\mathcal{G}_\iota}$ and $E_{\mathcal{E}_\kappa}$ are the energies of each molecular state. If instead of just considering the transition between two particular states $|\mathcal{G}_\iota\rangle$ and $|\mathcal{E}_\kappa\rangle$ we contemplate all possible vibrational states $\{|\chi_{\mathrm{g}}^{\iota}\rangle\}_\iota$ present in the final state, the transition rate reads:

$$\mathrm{K}_{\mathcal{E}_\kappa \mathcal{G}} = \sum_{\iota} \mathrm{K}_{\mathcal{E}_\kappa \mathcal{G}_\iota} = \frac{2\pi}{\hbar} \sum_{\iota} |V_{\iota\kappa}|^2 \delta(E_{\mathcal{E}_\kappa} - E_{\mathcal{G}_\iota}) \,,$$

where we perform the sum over all vibrational states accessible from the initial state.

The system is sometimes considered to be in thermal equilibrium with an environment at certain temperature T. Therefore, the initial state would be a superposition of vibrational modes following a **thermal distribution**:

$$f(E_\alpha) = \frac{\mathrm{e}^{-E_\alpha/k_\mathrm{B}T}}{\sum_{\alpha'} \mathrm{e}^{-E_{\alpha'}/k_\mathrm{B}T}} \,, \tag{F.9}$$

where k_B is the Boltzmann constant. Then transitions are not produced from just a specific vibrational state $|\chi_\mathrm{e}^\kappa\rangle$, but from a thermalized initial state $|\tilde{\mathcal{E}}\rangle$. Since $f(E_\alpha)$ gives the probability of finding the system in the vibrational state $|\alpha\rangle$, the transition rate from the thermalized initial state $|\tilde{\mathcal{E}}\rangle$ is given by:

$$\mathrm{K}_{\tilde{\mathcal{E}}\mathcal{G}} = \sum_\kappa f(E_{\mathcal{E}_\kappa}) \mathrm{K}_{\mathcal{E}_\kappa \mathcal{G}} = \frac{2\pi}{\hbar} \sum_{\kappa,\iota} f(E_{\mathcal{E}_\kappa}) |V_{\iota\kappa}|^2 \, \delta(E_{\mathcal{E}_\kappa} - E_{\mathcal{G}_\iota}) \,,$$

where the sum runs over all vibrational states associated with both the ground and the excited electronic states.

Absorption rate from a state in thermal equilibrium

The previous expression is also valid for the reverse process, the transition rate from the thermalized ground state $|\tilde{\mathcal{G}}\rangle$ to all possible vibrational states in the first-excited electronic state:

$$\mathrm{K}_{\tilde{\mathcal{G}}\mathcal{E}} = \frac{2\pi}{\hbar} \sum_{\iota,\kappa} f(E_{\mathcal{G}_\iota}) |V_{\kappa\iota}|^2 \, \delta(E_{\mathcal{G}_\iota} - E_{\mathcal{E}_\kappa}) \,.$$

The transition rate resulting from the absorption of a photon of energy $\hbar\omega$ will be given by:

$$\mathrm{K}_{\tilde{\mathcal{G}}\mathcal{E}} = \frac{2\pi}{\hbar} \sum_{\iota,\kappa} f(E_{\mathcal{G}_\iota}) |\langle \mathcal{E}_\kappa | \boldsymbol{E}_0^* \hat{\boldsymbol{\mu}}_\mathrm{eg} | \mathcal{G}_\iota \rangle|^2 \, \delta(\hbar\omega + E_{\mathcal{G}_\iota} - E_{\mathcal{E}_\kappa}) \,,$$

where we have substituted the matrix element $V_{\kappa\iota} = \langle \mathcal{E}_\kappa | \boldsymbol{E}_0^* \hat{\boldsymbol{\mu}}_\mathrm{eg} | \mathcal{G}_\iota \rangle$ considering the expression of the coupling term in the rotating frame (Equation F.5). The transition dipole operator $\hat{\boldsymbol{\mu}}_\mathrm{eg}$ can be considered to have the same orientation as the laser field, so: $|\langle \mathcal{E}_\kappa | \boldsymbol{E}_0^* \hat{\boldsymbol{\mu}}_\mathrm{eg} | \mathcal{G}_\iota \rangle|^2 = E_0^2 \, |\langle \mathcal{E}_\kappa | \hat{\mu}_\mathrm{eg} | \mathcal{G}_\iota \rangle|^2$. This matrix element can be further simplified by introducing the **Condon approximation**, which states that the dipole operator does not depend on the nuclear degrees of freedom and, therefore, it can be taken out from the matrix element:

$$|V_{\kappa\iota}|^2 = E_0^2 \, |\langle \mathcal{E}_\kappa | \hat{\mu}_\mathrm{eg} | \mathcal{G}_\iota \rangle|^2 = E_0^2 \, |\langle \mathrm{e}, \chi_\mathrm{e}^\kappa | \Big(\mu_\mathrm{eg} |\mathrm{e}\rangle\langle \mathrm{g}| + \mu_\mathrm{eg}^* |\mathrm{g}\rangle\langle \mathrm{e}| \Big) | \mathrm{g}, \chi_\mathrm{g}^\iota \rangle|^2 = E_0^2 \mu_\mathrm{eg}^2 \, |\langle \chi_\mathrm{e}^\kappa | \chi_\mathrm{g}^\iota \rangle|^2 \,,$$

where we have introduced the expression for the dipole operator: $\hat{\mu}_\mathrm{eg} = \mu_\mathrm{eg} |\mathrm{e}\rangle\langle \mathrm{g}| + \mu_\mathrm{ge} |\mathrm{g}\rangle\langle \mathrm{e}|$ according to Equation 2.35. Therefore, the transition rate finally reads:

$$\mathrm{K}_{\tilde{\mathcal{G}}\mathcal{E}} = \frac{2\pi}{\hbar} \, E_0^2 \mu_\mathrm{eg}^2 \sum_{\iota,\kappa} f(E_{\mathcal{G}_\iota}) |\langle \chi_\mathrm{e}^\kappa | \chi_\mathrm{g}^\iota \rangle|^2 \, \delta(\hbar\omega + E_{\mathcal{G}_\iota} - E_{\mathcal{E}_\kappa}) \,. \tag{F.10}$$

In this expression we recognize the **Franck–Condon factor** $F_{\kappa\iota} \equiv |\langle \chi_\mathrm{e}^\kappa | \chi_\mathrm{g}^\iota \rangle|^2$, that stands for the overlap between the vibrational wavefunctions of the two states (Equation F.2). Therefore, we observe that the rate of some vibronic transition does depend on the overlap of the vibrational components.

Vibrational equilibrium statistical operator

Notice that the denominator of the thermal distribution $f(E_{\mathcal{G}_\iota})$, whose expression is given in Equation F.9, can be expressed as the trace over all initial states associated with the electronic ground state:

$$f(E_{\mathcal{G}_\iota}) = \frac{e^{-E_{\mathcal{G}_\iota}/k_B T}}{\sum_{\iota'} e^{-E_{\mathcal{G}_\iota'}/k_B T}} = \frac{e^{-E_{\mathcal{G}_\iota}/k_B T}}{\mathrm{Tr}_g[e^{-\hat{H}_\mathcal{G}/k_B T}]} , \tag{F.11}$$

since:

$$\sum_{\iota'} e^{-E_{\mathcal{G}_{\iota'}}/k_B T} = \sum_{\iota'} e^{-E_{\mathcal{G}_{\iota'}}/k_B T} \langle \mathcal{G}_{\iota'}|\mathcal{G}_{\iota'}\rangle = \sum_{\iota'} \langle \mathcal{G}_{\iota'}| e^{-E_{\mathcal{G}_{\iota'}}/k_B T} |\mathcal{G}_{\iota'}\rangle$$
$$= \sum_{\iota'} \langle \mathcal{G}_{\iota'}| e^{-\hat{H}_\mathcal{G}/k_B T} |\mathcal{G}_{\iota'}\rangle = \mathrm{Tr}_g[e^{-\hat{H}_\mathcal{G}/k_B T}] .$$

There, we have taken into account that energy $E_{\mathcal{G}_{\iota'}}$ is an eigenvalue of the Hamiltonian $\hat{H}_\mathcal{G}$ according to Equation F.7, and $\mathrm{Tr}_g[\hat{\mathcal{O}}]$ denotes the trace of operator $\hat{\mathcal{O}}$ over all vibrational states associated with the electronic ground state:

$$\mathrm{Tr}_g[\hat{\mathcal{O}}] = \sum_\iota \langle \mathcal{G}_\iota|\hat{\mathcal{O}}|\mathcal{G}_\iota\rangle .$$

Considering the expression in Equation F.11 for the thermal distribution $f(E_{\mathcal{G}_\iota})$, we have:

$$\sum_\iota f(E_{\mathcal{G}_\iota}) \langle \mathcal{G}_\iota|\hat{\mathcal{O}}|\mathcal{G}_\iota\rangle = \sum_\iota \frac{e^{-E_{\mathcal{G}_\iota}/k_B T}}{\mathrm{Tr}_g[e^{-\hat{H}_\mathcal{G}/k_B T}]} \langle \mathcal{G}_\iota|\hat{\mathcal{O}}|\mathcal{G}_\iota\rangle = \sum_\iota \langle \mathcal{G}_\iota| \frac{e^{-E_{\mathcal{G}_\iota}/k_B T}}{\mathrm{Tr}_g[e^{-\hat{H}_\mathcal{G}/k_B T}]} \hat{\mathcal{O}}|\mathcal{G}_\iota\rangle$$
$$= \sum_\iota \langle \mathcal{G}_\iota| \frac{e^{-\hat{H}_\mathcal{G}/k_B T}}{\mathrm{Tr}_g[e^{-\hat{H}_\mathcal{G}/k_B T}]} \hat{\mathcal{O}}|\mathcal{G}_\iota\rangle = \sum_\iota \langle \mathcal{G}_\iota|\hat{W}_g \hat{\mathcal{O}}|\mathcal{G}_\iota\rangle = \mathrm{Tr}_g[\hat{W}_g\, \hat{\mathcal{O}}] ,$$

where we have defined the vibrational equilibrium statistical operator for the electronic ground state $\hat{W}_g$:

$$\hat{W}_g \equiv \frac{1}{\mathcal{Z}} e^{-\hat{H}_\mathcal{G}/k_B T} = \frac{e^{-\hat{H}_\mathcal{G}/k_B T}}{\mathrm{Tr}_g[e^{-\hat{H}_\mathcal{G}/k_B T}]} . \tag{F.12}$$

Taking into account the definition of the average value of an operator, the sum over the subindex ι can be thus expressed in these different forms:

$$\sum_\iota f(E_{\mathcal{G}_\iota}) \langle \mathcal{G}_\iota|\hat{\mathcal{O}}|\mathcal{G}_\iota\rangle = \mathrm{Tr}_g[\hat{W}_g\, \hat{\mathcal{O}}] = \langle \hat{\mathcal{O}}\rangle_g . \tag{F.13}$$

F.4.2 Two expressions for the absorption rate

Absorption rate as a function of the dipole correlator

Let us consider the previous transition rate $\mathrm{K}_{\vec{\mathcal{G}}\mathcal{E}}$ before introducing the Condon approximation, that is:

$$\mathrm{K}_{\vec{\mathcal{G}}\mathcal{E}} = \frac{2\pi}{\hbar} E_0^2 \sum_{\iota,\kappa} f(E_{\mathcal{G}_\iota}) |\langle \mathcal{E}_\kappa|\hat{\mu}_{eg}|\mathcal{G}_\iota\rangle|^2 \, \delta(\hbar\omega + E_{\mathcal{G}_\iota} - E_{\mathcal{E}_\kappa}) ,$$

where $|\langle\mathcal{E}_\kappa|\hat{\mu}_{\text{eg}}|\mathcal{G}_\iota\rangle|^2 = \langle\mathcal{G}_\iota|\hat{\mu}_{\text{eg}}|\mathcal{E}_\kappa\rangle\langle\mathcal{E}_\kappa|\hat{\mu}_{\text{eg}}|\mathcal{G}_\iota\rangle$. Taking into account the Fourier representation of the delta function (Equation E.13):

$$\delta(\hbar\omega) = \frac{1}{2\pi\hbar}\int_{-\infty}^{\infty} \mathrm{e}^{\mathrm{i}\omega t}\mathrm{d}t \ , \tag{F.14}$$

the transition rate can be alternatively expressed as:

$$\begin{aligned}\mathrm{K}_{\tilde{\mathcal{G}}\mathcal{E}} =& \frac{2\pi}{\hbar}\frac{1}{2\pi\hbar}E_0^2\sum_{\iota,\kappa}\int_{-\infty}^{\infty}\mathrm{d}t\ f(E_{\mathcal{G}_\iota})\ \langle\mathcal{G}_\iota|\hat{\mu}_{\text{eg}}|\mathcal{E}_\kappa\rangle\langle\mathcal{E}_\kappa|\hat{\mu}_{\text{eg}}|\mathcal{G}_\iota\rangle\ \mathrm{e}^{\mathrm{i}[\omega-(E_{\mathcal{E}_\kappa}-E_{\mathcal{G}_\iota})/\hbar]t} \\ =& \frac{E_0^2}{\hbar^2}\sum_{\iota,\kappa}\int_{-\infty}^{\infty}\mathrm{d}t\ \mathrm{e}^{\mathrm{i}\omega t}\ f(E_{\mathcal{G}_\iota})\ \langle\mathcal{G}_\iota|\mathrm{e}^{\mathrm{i}E_{\mathcal{G}_\iota}t/\hbar}\hat{\mu}_{\text{eg}}\mathrm{e}^{-\mathrm{i}E_{\mathcal{E}_\kappa}t/\hbar}|\mathcal{E}_\kappa\rangle\langle\mathcal{E}_\kappa|\hat{\mu}_{\text{eg}}|\mathcal{G}_\iota\rangle \ .\end{aligned}$$

Now, let us introduce the Hamiltonian $\hat{H}_o = \hat{H}_{\mathcal{G}} + \hat{H}_{\mathcal{E}}$, composed of the non-interacting part of the complete Hamiltonian of Equation F.6. The eigenvalue problem of Equation F.7 can be rewritten in terms of H_o as: $\hat{H}_o|\mathcal{G}_\iota\rangle = E_{\mathcal{G}_\iota}|\mathcal{G}_\iota\rangle$ and $\hat{H}_o|\mathcal{E}_\kappa\rangle = E_{\mathcal{E}_\kappa}|\mathcal{E}_\kappa\rangle$. Therefore, the energies $E_{\mathcal{G}_\iota}$ and $E_{\mathcal{E}_\kappa}$ can be replaced by the Hamiltonian $\hat{H}_o$ in the expression of the transition rate:

$$\mathrm{K}_{\tilde{\mathcal{G}}\mathcal{E}} = \frac{E_0^2}{\hbar^2}\sum_{\iota,\kappa}\int_{-\infty}^{\infty}\mathrm{d}t\ \mathrm{e}^{\mathrm{i}\omega t}\ f(E_{\mathcal{G}_\iota})\ \langle\mathcal{G}_\iota|\mathrm{e}^{\mathrm{i}\hat{H}_o t/\hbar}\hat{\mu}_{\text{eg}}\mathrm{e}^{-\mathrm{i}\hat{H}_o t/\hbar}|\mathcal{E}_\kappa\rangle\langle\mathcal{E}_\kappa|\hat{\mu}_{\text{eg}}|\mathcal{G}_\iota\rangle \ .$$

The time evolution of the dipole operator $\hat{\mu}_{\text{eg}}$ is given by Equation B.11 when considering the transformation from the Schrödinger to the interaction picture, hence: $\hat{\mu}_{\text{eg}}(t) = \mathrm{e}^{\mathrm{i}\hat{H}_o t/\hbar}\hat{\mu}_{\text{eg}}\mathrm{e}^{-\mathrm{i}\hat{H}_o t/\hbar}$, and $\hat{\mu}_{\text{eg}}(0) = \hat{\mu}_{\text{eg}}$. Introducing these expressions, the transition rate reads:

$$\mathrm{K}_{\tilde{\mathcal{G}}\mathcal{E}} = \frac{E_0^2}{\hbar^2}\sum_{\iota,\kappa}\int_{-\infty}^{\infty}\mathrm{d}t\ \mathrm{e}^{\mathrm{i}\omega t}\ f(E_{\mathcal{G}_\iota})\ \langle\mathcal{G}_\iota|\hat{\mu}_{\text{eg}}(t)|\mathcal{E}_\kappa\rangle\langle\mathcal{E}_\kappa|\hat{\mu}_{\text{eg}}(0)|\mathcal{G}_\iota\rangle \ .$$

The completeness relation for the final states, $\sum_\kappa|\mathcal{E}_\kappa\rangle\langle\mathcal{E}_\kappa| = \mathbb{1}$, simplifies the previous expression to:

$$\mathrm{K}_{\tilde{\mathcal{G}}\mathcal{E}} = \frac{E_0^2}{\hbar^2}\sum_{\iota}\int_{-\infty}^{\infty}\mathrm{d}t\ \mathrm{e}^{\mathrm{i}\omega t}\ f(E_{\mathcal{G}_\iota})\ \langle\mathcal{G}_\iota|\hat{\mu}_{\text{eg}}(t)\hat{\mu}_{\text{eg}}(0)|\mathcal{G}_\iota\rangle \ . \tag{F.15}$$

Within the integral there appears the thermal average over all initial states, hence the sum over the index ι can be expressed as a correlation function:

$$\mathrm{K}_{\tilde{\mathcal{G}}\mathcal{E}} = \frac{E_0^2}{\hbar^2}\int_{-\infty}^{\infty}\mathrm{d}t\ \mathrm{e}^{\mathrm{i}\omega t}\ \langle\hat{\mu}_{\text{eg}}(t)\hat{\mu}_{\text{eg}}(0)\rangle_{\text{g}} \ ,$$

where the subindex g indicates that the average is performed over all states with $|\text{g}\rangle$ as electronic component (Equation F.13). Finally, if we denote the **correlation function** of the dipole operator as:

$$\mathcal{C}_\mu(\tau) \equiv \langle\hat{\mu}_{\text{eg}}(\tau)\hat{\mu}_{\text{eg}}(0)\rangle_{\text{g}} \ , \tag{F.16}$$

the transition rate from the thermalized ground state $|\tilde{\mathcal{G}}\rangle$ to all the accessible excited states $|\mathcal{E}_\kappa\rangle$ as a result of the absorption of a photon of energy $\hbar\omega$ becomes:

$$\mathrm{K}_{\tilde{\mathcal{G}}\mathcal{E}}(\omega) = \frac{E_0^2}{\hbar^2}\int_{-\infty}^{\infty}\mathrm{d}\tau\ \mathrm{e}^{\mathrm{i}\omega\tau}\mathcal{C}_\mu(\tau) \ , \tag{F.17}$$

where we have made explicit the dependence on the frequency of the photon.

Absorption rate as a function of some other correlator

Let us start from the expression of the absorption rate in Equation F.10. By considering the Fourier representation of the delta function (Equation F.14), the absorption rate $\mathrm{K}_{\tilde{\mathcal{G}}\mathcal{E}}$ becomes:

$$\mathrm{K}_{\tilde{\mathcal{G}}\mathcal{E}} = \frac{E_0^2\mu_{\mathrm{eg}}^2}{\hbar^2} \sum_{\iota,\kappa} \int_{-\infty}^{\infty} \mathrm{d}t \; f(E_{\mathcal{G}_\iota}) |\langle \chi_{\mathrm{e}}^{\kappa} | \chi_{\mathrm{g}}^{\iota} \rangle|^2 \; \mathrm{e}^{\mathrm{i}[\omega - (E_{\mathcal{E}_\kappa} - E_{\mathcal{G}_\iota})/\hbar]t} \; .$$

The term with the overlap of the vibrational wavefunctions can be rewritten as $|\langle \chi_{\mathrm{g}}^{\iota} | \chi_{\mathrm{e}}^{\kappa} \rangle|^2 = \langle \chi_{\mathrm{g}}^{\iota} | \chi_{\mathrm{e}}^{\kappa} \rangle \langle \chi_{\mathrm{e}}^{\kappa} | \chi_{\mathrm{g}}^{\iota} \rangle$, hence the last part of the integrand becomes:

$$\begin{aligned} |\langle \chi_{\mathrm{g}}^{\iota} | \chi_{\mathrm{e}}^{\kappa} \rangle|^2 \; \mathrm{e}^{-\mathrm{i}(E_{\mathcal{E}_\kappa} - E_{\mathcal{G}_\iota})t/\hbar} &= \langle \chi_{\mathrm{g}}^{\iota} | \mathrm{e}^{\mathrm{i}E_{\mathcal{G}_\iota} t/\hbar} \mathrm{e}^{-\mathrm{i}E_{\mathcal{E}_\kappa} t/\hbar} | \chi_{\mathrm{e}}^{\kappa} \rangle \langle \chi_{\mathrm{e}}^{\kappa} | \chi_{\mathrm{g}}^{\iota} \rangle \\ &= \langle \chi_{\mathrm{g}}^{\iota} | \mathrm{e}^{\mathrm{i}\hat{H}_{\mathcal{G}} t/\hbar} \mathrm{e}^{-\mathrm{i}\hat{H}_{\mathcal{E}} t/\hbar} | \chi_{\mathrm{e}}^{\kappa} \rangle \langle \chi_{\mathrm{e}}^{\kappa} | \chi_{\mathrm{g}}^{\iota} \rangle \; , \end{aligned}$$

where we have considered the eigenvalue problem of Equation F.7. The substitution of this expression into the absorption rate yields:

$$\begin{aligned} \mathrm{K}_{\tilde{\mathcal{G}}\mathcal{E}} &= \frac{E_0^2\mu_{\mathrm{eg}}^2}{\hbar^2} \sum_{\iota,\kappa} \int_{-\infty}^{\infty} \mathrm{d}t \; \mathrm{e}^{\mathrm{i}\omega t} \; f(E_{\mathcal{G}_\iota}) \langle \chi_{\mathrm{g}}^{\iota} | \mathrm{e}^{\mathrm{i}\hat{H}_{\mathcal{G}} t/\hbar} \mathrm{e}^{-\mathrm{i}\hat{H}_{\mathcal{E}} t/\hbar} | \chi_{\mathrm{e}}^{\kappa} \rangle \langle \chi_{\mathrm{e}}^{\kappa} | \chi_{\mathrm{g}}^{\iota} \rangle \\ &= \frac{E_0^2\mu_{\mathrm{eg}}^2}{\hbar^2} \sum_{\iota} \int_{-\infty}^{\infty} \mathrm{d}t \; \mathrm{e}^{\mathrm{i}\omega t} \; f(E_{\mathcal{G}_\iota}) \langle \chi_{\mathrm{g}}^{\iota} | \mathrm{e}^{\mathrm{i}\hat{H}_{\mathcal{G}} t/\hbar} \mathrm{e}^{-\mathrm{i}\hat{H}_{\mathcal{E}} t/\hbar} | \chi_{\mathrm{g}}^{\iota} \rangle \; , \end{aligned}$$

where we have introduced the completeness relation for the vibrational states associated with the electronic first-excited state, that is, $\sum_\kappa |\chi_{\mathrm{e}}^{\kappa}\rangle\langle\chi_{\mathrm{e}}^{\kappa}| = \mathbb{1}$. Taking into account Equation F.13, we can write the summation over the vibrational index ι as a trace:

$$\mathrm{K}_{\tilde{\mathcal{G}}\mathcal{E}} = \frac{E_0^2\mu_{\mathrm{eg}}^2}{\hbar^2} \int_{-\infty}^{\infty} \mathrm{d}t \; \mathrm{e}^{\mathrm{i}\omega t} \; \mathrm{Tr}_{\mathrm{g}}\left[\hat{W}_{\mathrm{g}} \mathrm{e}^{\mathrm{i}\hat{H}_{\mathcal{G}} t/\hbar} \mathrm{e}^{-\mathrm{i}\hat{H}_{\mathcal{E}} t/\hbar} \right] .$$

where $\hat{W}_{\mathrm{g}}$ is the vibrational equilibrium statistical operator for the electronic ground state, defined in Equation F.12. We can also define the following thermal average over the vibrational eigenstates associated with the electronic ground state:

$$\mathcal{F}(t) \equiv \langle \mathrm{e}^{\mathrm{i}\hat{H}_{\mathcal{G}} t/\hbar} \mathrm{e}^{-\mathrm{i}\hat{H}_{\mathcal{E}} t/\hbar} \rangle_{\mathrm{g}} = \mathrm{Tr}_{\mathrm{g}}\left[\hat{W}_{\mathrm{g}} \mathrm{e}^{\mathrm{i}\hat{H}_{\mathcal{G}} t/\hbar} \mathrm{e}^{-\mathrm{i}\hat{H}_{\mathcal{E}} t/\hbar} \right] , \tag{F.18}$$

so the absorption rate can be simply written as:

$$\mathrm{K}_{\tilde{\mathcal{G}}\mathcal{E}}(\omega) = \frac{E_0^2\mu_{\mathrm{eg}}^2}{\hbar^2} \int_{-\infty}^{\infty} \mathrm{d}t \; \mathrm{e}^{\mathrm{i}\omega t} \; \mathcal{F}(t) \; . \tag{F.19}$$

F.4.3 Lineshape function

Relation between the transition rate and the lineshape function

Within the Condon approximation, the transition rate $\mathrm{K}_{\tilde{\mathcal{G}}\mathcal{E}}$ (Equation F.10) is composed of an electronic factor multiplied by the overlap integral of the vibrational wavefunctions.

This can be explicitly noted by writing it in the form:

$$\mathrm{K}_{\tilde{\mathcal{G}}\mathcal{E}} = \frac{2\pi}{\hbar}\, E_0^2 \mu_{\mathrm{eg}}^2\, \mathcal{A}(\omega), \tag{F.20}$$

with:

$$\mathcal{A}(\omega) = \sum_{\iota,\kappa} f(E_{\mathcal{G}_\iota}) |\langle \chi_{\mathrm{e}}^{\kappa} | \chi_{\mathrm{g}}^{\iota} \rangle|^2\, \delta(\hbar\omega + E_{\mathcal{G}_\iota} - E_{\mathcal{E}_\kappa})\,.$$

This last part is commonly known as the **lineshape function** $\mathcal{A}(\omega)$, or Franck–Condon-weighted density of states, and it is the responsible for the dependence of the absorption rate on the frequency. Taking into account the Fourier representation of the delta function (Equation F.14), the lineshape function $\mathcal{A}(\omega)$ can be alternatively written as:

$$\mathcal{A}(\omega) = \frac{1}{2\pi\hbar} \sum_{\iota,\kappa} \int_{-\infty}^{\infty} \mathrm{d}t\; f(E_{\mathcal{G}_\iota}) |\langle \chi_{\mathrm{e}}^{\kappa} | \chi_{\mathrm{g}}^{\iota} \rangle|^2\, \mathrm{e}^{\mathrm{i}[\omega - (E_{\mathcal{E}_\kappa} - E_{\mathcal{G}_\iota})/\hbar]t}$$

From the expression of the absorption rate in Equation F.19, the lineshape function can be also expressed in terms of the terms of $\mathcal{F}(t)$:

$$\mathcal{A}(\omega) = \frac{1}{2\pi\hbar} \int_{-\infty}^{\infty} \mathrm{d}t\; \mathrm{e}^{\mathrm{i}\omega t}\; \mathcal{F}(t)\,, \tag{F.21}$$

where $\mathcal{F}(t)$ is defined in Equation F.18.

Absorption rate as a function of the dipole correlator

The relation between the lineshape function and the transition rate is defined in Equation F.20. If we consider the expression of the transition rate $\mathrm{K}_{\tilde{\mathcal{G}}\mathcal{E}}$ in terms of the correlation function $\mathcal{C}(\tau)$ given in Equation F.17, the lineshape function can be written as:

$$\mathcal{A}(\omega) = \frac{\hbar}{2\pi} \frac{1}{E_0^2 \mu_{\mathrm{eg}}^2} \mathrm{K}_{\tilde{\mathcal{G}}\mathcal{E}} = \frac{1}{2\pi\hbar} \frac{1}{\mu_{\mathrm{eg}}^2} \int_{-\infty}^{\infty} \mathrm{d}\tau\; \mathrm{e}^{\mathrm{i}\omega\tau} \mathcal{C}_\mu(\tau)\,.$$

Notice that there appears the Fourier transform of the correlation function. According to the Condon approximation, the dipole operator $\hat{\mu}_{\mathrm{eg}}$ does not depend on the nuclear degrees of freedom, so the correlation function (Equation F.16) for zero-time delay becomes:

$$\mathcal{C}_\mu(0) = \langle \hat{\mu}_{\mathrm{eg}}(0) \hat{\mu}_{\mathrm{eg}}(0) \rangle_{\mathrm{g}} = \langle \hat{\mu}_{\mathrm{eg}} \hat{\mu}_{\mathrm{eg}} \rangle_{\mathrm{g}} = \mu_{\mathrm{eg}}^2\,.$$

As a consequence, the lineshape function could be written as:

$$\mathcal{A}(\omega) = \frac{1}{2\pi\hbar} \frac{1}{\mathcal{C}_\mu(0)} \int_{-\infty}^{\infty} \mathrm{d}\tau\; \mathrm{e}^{\mathrm{i}\omega\tau} \mathcal{C}_\mu(\tau)\,, \tag{F.22}$$

and we recover the expression given for the normalized spectrum in Equation E.14 (in that case, we had the correlation function of the electric field operator $\Gamma(\tau)$). The lineshape function $\mathcal{A}(\omega)$ is then nothing but the normalized spectral density.

F.5 Correlation function and spectral density

The lineshape function characterizing the absorption spectrum of some molecule can be written in terms of the correlation function of the dipole operator, as shown in Equation F.22. We study now a more convenient form to express that correlation function for some interesting cases.

F.5.1 General expression for the time correlation function

Let us consider a generic quantum correlation function $\mathcal{C}(t)$ corresponding to some some thermal average as the one shown in Equation F.13, that is:

$$\mathcal{C}(t) = \langle \hat{A}(t)\hat{A}(0)\rangle = \sum_{\alpha} f(E_\alpha)\ \langle \alpha|\hat{A}(t)\hat{A}(0)|\alpha\rangle\ , \tag{F.23}$$

where $\hat{A}$ is a generic quantum operator and the average is performed over all vibrational modes α in thermal equilibrium with an environment at certain temperature T. There, $f(E_\alpha)$ stand for the probability of the state α according to the thermal distribution of Equation F.9.

Fourier transform of the correlation function

Starting from the generic correlation function presented in Equation F.23, its Fourier transform will be denoted as $S(\omega)$:

$$S(\omega) \equiv \tilde{\mathcal{C}}(\omega) = \frac{1}{2\pi}\int_{-\infty}^{\infty} \mathcal{C}(t)\ \mathrm{e}^{\mathrm{i}\omega t}\ \mathrm{d}t\ . \tag{F.24}$$

In general, $\mathcal{C}(t)$ will be a complex function, but obeying the relation $\mathcal{C}(-t) = \mathcal{C}^*(t)$ as already noted in Equation E.2. This implies that its Fourier transform $S(\omega)$ is real, and it can be also shown that $S(\omega) \geq 0$. It is convenient to decompose $\mathcal{C}(t)$ into its real and imaginary parts, such that $\mathcal{C}(t) = \mathcal{C}_{\mathrm{R}}(t) + \mathcal{C}_{\mathrm{I}}(t)$, with:

$$\begin{aligned} \mathcal{C}_{\mathrm{R}}(t) &= (\mathcal{C}(t) + \mathcal{C}^*(t))/2\ , \\ \mathcal{C}_{\mathrm{I}}(t) &= (\mathcal{C}(t) - \mathcal{C}^*(t))/2\ . \end{aligned}$$

Due to the time symmetry previously noted, these functions coincide with the symmetric and antisymmetric components of $\mathcal{C}(t)$, that is, $\mathcal{C}_{\mathrm{R}}(-t) = \mathcal{C}_{\mathrm{R}}(t)$ and $\mathcal{C}_{\mathrm{I}}(-t) = -\mathcal{C}_{\mathrm{I}}(t)$. Likewise, we consider the Fourier transform of each of these components:

$$\begin{aligned} S_{\mathrm{S}}(\omega) &= \frac{1}{2\pi}\int_{-\infty}^{\infty} \mathrm{d}t\ \mathrm{e}^{\mathrm{i}\omega t}\ \mathcal{C}_{\mathrm{R}}(t) = (S(\omega) + S(-\omega))/2\ , \\ S_{\mathrm{A}}(\omega) &= \frac{1}{2\pi}\int_{-\infty}^{\infty} \mathrm{d}t\ \mathrm{e}^{\mathrm{i}\omega t}\ \mathcal{C}_{\mathrm{I}}(t) = (S(\omega) - S(-\omega))/2\ , \end{aligned} \tag{F.25}$$

obeying that $S(\omega) = S_{\mathrm{S}}(\omega) + S_{\mathrm{A}}(\omega)$. Notice that both inherit the defined symmetry, that is, $S_{\mathrm{S}}(\omega)$ is symmetric while $S_{\mathrm{A}}(\omega)$ is antisymmetric with respect to the frequency ω.

Property of the Fourier transform of the correlation function

Now, consider the explicit expression of the correlation function given in Equation F.23 so as to express the complete expression for its Fourier transform:

$$S(\omega) = \frac{1}{2\pi} \sum_{\alpha} \int_{-\infty}^{\infty} f(E_\alpha)\ \langle \alpha | \hat{A}(t) \hat{A}(0) | \alpha \rangle\ \mathrm{e}^{\mathrm{i}\omega t}\ \mathrm{d}t\ .$$

Taking into account that the vibrational states $|\alpha\rangle$ are eigenvectors of the Hamiltonian $\hat{H}$ such that $\hat{H}|\alpha\rangle = E_\alpha |\alpha\rangle$, the previous expression can be rewritten as:

$$\begin{aligned} S(\omega) =& \frac{1}{2\pi} \sum_{\alpha,\beta} \int_{-\infty}^{\infty} f(E_\alpha)\ \langle \alpha | \mathrm{e}^{\mathrm{i}\hat{H}t/\hbar}\ \hat{A}\ \mathrm{e}^{-\mathrm{i}\hat{H}t/\hbar} | \beta \rangle \langle \beta | \hat{A} | \alpha \rangle\ \mathrm{e}^{\mathrm{i}\omega t}\ \mathrm{d}t \\ =& \frac{1}{2\pi} \sum_{\alpha,\beta} \int_{-\infty}^{\infty} f(E_\alpha)\ \langle \alpha | \mathrm{e}^{\mathrm{i}E_\alpha t/\hbar}\ \hat{A}\ \mathrm{e}^{-\mathrm{i}E_\beta t/\hbar} | \beta \rangle \langle \beta | \hat{A} | \alpha \rangle\ \mathrm{e}^{\mathrm{i}\omega t}\ \mathrm{d}t \\ =& \frac{1}{2\pi} \sum_{\alpha,\beta} \int_{-\infty}^{\infty} f(E_\alpha)\ \langle \alpha | \hat{A} | \beta \rangle \langle \beta | \hat{A} | \alpha \rangle\ \mathrm{e}^{-\mathrm{i}(\omega_\beta - \omega_\alpha)t} \mathrm{e}^{\mathrm{i}\omega t}\ \mathrm{d}t\ , \end{aligned}$$

where in the last step we have considered the time evolution of the operator $\hat{A}$ governed by Equation B.11. If we introduce the Fourier representation of the delta function (Equation E.13), this expression reduces to:

$$S(\omega) = \sum_{\alpha,\beta} f(E_\alpha)\ \langle \alpha | \hat{A} | \beta \rangle \langle \beta | \hat{A} | \alpha \rangle\ \delta(\omega - \omega_{\beta\alpha})\ , \tag{F.26}$$

with the transition frequency $\omega_{\beta\alpha} \equiv \omega_\alpha - \omega_\alpha$. First, notice that, for negative frequencies, this function becomes:

$$S(-\omega) = \sum_{\alpha,\beta} f(E_\alpha)\ \langle \alpha | \hat{A} | \beta \rangle \langle \beta | \hat{A} | \alpha \rangle\ \delta(\omega - \omega_{\alpha\beta})\ , \tag{F.27}$$

since $\delta(-\omega - \omega_{\beta\alpha}) = \delta(\omega + \omega_{\beta\alpha}) = \delta(\omega - \omega_{\alpha\beta})$. Second, the expression of $S(\omega)$ in Equation F.26 is also true if the indeces α and β are interchanged, so:

$$S(\omega) = \sum_{\alpha,\beta} f(E_\beta)\ \langle \beta | \hat{A} | \alpha \rangle \langle \alpha | \hat{A} | \beta \rangle\ \delta(\omega - \omega_{\alpha\beta})\ .$$

Considering just the numerator of $f(E_\beta)$ (whose expression is given in Equation F.9), we can operate as follows:

$$\begin{aligned} \mathrm{e}^{-E_\beta / k_\mathrm{B} T}\, \delta(\omega - \omega_{\alpha\beta}) &= \mathrm{e}^{-\hbar\omega_\beta / k_\mathrm{B} T}\, \delta(\omega - \omega_{\alpha\beta}) \\ &= \mathrm{e}^{-\hbar(\omega_\alpha - \omega)/k_\mathrm{B} T}\, \delta(\omega - \omega_{\alpha\beta}) = \mathrm{e}^{\hbar\omega / k_\mathrm{B} T} \mathrm{e}^{-E_\alpha / k_\mathrm{B} T}\, \delta(\omega - \omega_{\alpha\beta})\ , \end{aligned}$$

since, according to the delta function, $\omega = \omega_{\alpha\beta} = \omega_\alpha - \omega_\beta$ and we can replace the frequency associated with the subindex β as done. From that, we have:

$$f(E_\beta)\ \delta(\omega - \omega_{\alpha\beta}) = \mathrm{e}^{\hbar\omega / k_\mathrm{B} T} f(E_\alpha)\ \delta(\omega - \omega_{\alpha\beta})\ ,$$

and the substitution of this expression into $S(\omega)$ yields:

$$S(\omega) = \mathrm{e}^{\hbar\omega/k_\mathrm{B}T} \sum_{\alpha,\beta} f(E_\alpha)\, \langle\alpha|\hat{A}|\beta\rangle\langle\beta|\hat{A}|\alpha\rangle\, \delta(\omega - \omega_{\alpha\beta}) \,.$$

If we compare this expression with Equation F.27, it is easy to see the relation that obeys the Fourier transform of the correlation function:

$$S(\omega) = \mathrm{e}^{\hbar\omega/k_\mathrm{B}T} S(-\omega) \,. \tag{F.28}$$

Expression for the correlation function

The expressions for the symmetric (S) and antisymmetric (A) parts of the Fourier transform of the correlation function (Equation F.25) can be rewritten by taking into account the relation obtained in Equation F.28:

$$S_\mathrm{S}(\omega) = \frac{1}{2}(S(\omega) + S(-\omega)) = \frac{1}{2}S(\omega)\left(1 + \mathrm{e}^{-\hbar\omega/k_\mathrm{B}T}\right) \,,$$
$$S_\mathrm{A}(\omega) = \frac{1}{2}(S(\omega) - S(-\omega)) = \frac{1}{2}S(\omega)\left(1 - \mathrm{e}^{-\hbar\omega/k_\mathrm{B}T}\right) \,.$$

Therefore, the function $S(\omega)$ can be written in terms of either its symmetric or its antisymmetric part:

$$S(\omega) = \frac{2S_\mathrm{S}(\omega)}{1 + \mathrm{e}^{-\hbar\omega/k_\mathrm{B}T}} = \frac{2S_\mathrm{A}(\omega)}{1 - \mathrm{e}^{-\hbar\omega/k_\mathrm{B}T}} \,.$$

Besides, this Fourier transform can be expressed in terms of the **Bose-Einstein distribution function** $n(\omega)$, given by:

$$n(\omega) = \frac{1}{\mathrm{e}^{\hbar\omega/k_\mathrm{B}T} - 1} \,, \tag{F.29}$$

such that:

$$S(\omega) = 2S_\mathrm{A}(\omega)[1 + n(\omega)] \,. \tag{F.30}$$

Considering Equation F.24 and the inverse Fourier transform, we can obtain an expression for the correlation function $\mathcal{C}(t)$ from the previous form of $S(\omega)$:

$$\mathcal{C}(t) = \int_{-\infty}^{\infty} S(\omega)\, \mathrm{e}^{-\mathrm{i}\omega t}\mathrm{d}\omega = \int_{-\infty}^{\infty} 2S_\mathrm{A}(\omega)[1 + n(\omega)]\, \mathrm{e}^{-\mathrm{i}\omega t}\mathrm{d}\omega \,. \tag{F.31}$$

Since $S_\mathrm{A}(\omega)$ is antisymmetric and $1 + n(-\omega) = -n(\omega)$, the correlation function can be expressed as the following half-sided Fourier integral:

$$\mathcal{C}(t) = \int_{0}^{\infty} 2S_\mathrm{A}(\omega)\left([1 + n(\omega)]\, \mathrm{e}^{-\mathrm{i}\omega t} + n(\omega)\, \mathrm{e}^{\mathrm{i}\omega t}\right)\mathrm{d}\omega \,. \tag{F.32}$$

There, $S(\omega)$ would correspond to the spectral density defined in Equation E.12, since it is just the Fourier transform of the correlation function (Equation F.24). Therefore, $2S_\mathrm{A}(\omega)$ would represent the strength of each Fourier component and gives a measure of the response of the system to different frequencies. In general, the precise expression of the correlation function cannot be computed, and a model for the reservoir and its interaction with the system of interest is required.

F.5.2 Time-correlation function for a harmonic oscillator reservoir

With the aim to evaluate the correlation function, we consider the simple case of a reservoir composed of a collection of harmonic oscillators. This would correspond to the situation discussed in Subsection 2.4.2, where some electronic transition is coupled to a set of vibrational modes. Remember that potential energy surfaces were first approximated by harmonic potentials, such that nuclear movements are described in terms of normal mode oscillations. If the exciton-phonon coupling is sufficiently low, the nuclear degrees of freedom can be then treated as a harmonic oscillator reservoir with which the two-level system (modelling the electronic transition) interacts.

Expression for the spectral density

The reservoir is thus considered to be composed of a collection of harmonic oscillators of frequency ω_κ and associated creation and annihilation operators $\hat{b}_\kappa^\dagger$ and $\hat{b}_\kappa$. The reservoir operator $\hat{\mathcal{R}}$ appearing in the Hamiltonian of Equation 2.8, describing the interaction between system and reservoir, is here given by:

$$\hat{\mathcal{R}} = \sum_\kappa \hbar\lambda_\kappa(\hat{b}_\kappa^\dagger + \hat{b}_\kappa)\,, \tag{F.33}$$

where λ_κ is the coupling strength between the electronic transition and the vibrational mode κ (exciton-phonon coupling). For simplicity, we have considered just one vibrational bath interacting with the system, so that we have just one term in the interaction Hamiltonian. The correlation function of the reservoir operators would we given by Equation F.23, where the general operator $\hat{A}$ is now the operator $\hat{\mathcal{R}}$ in Equation F.33:

$$C(t) = \langle\hat{\mathcal{R}}(t)\hat{\mathcal{R}}(0)\rangle = \sum_\alpha f(E_\alpha)\,\langle\alpha|\hat{\mathcal{R}}(t)\hat{\mathcal{R}}(0)|\alpha\rangle\,,$$

where α labels the vibrational state $|\alpha\rangle$ that is eigenvector of the of the complete Hamiltonian $\hat{H}$ such that $\hat{H}|\alpha\rangle = E_\alpha|\alpha\rangle$. Remember that $f(E_\alpha)$ stands for the probability of the state α, following the thermal distribution of Equation F.9. According to Equation F.26, the Fourier transform of the correlation function can be expressed as:

$$S(\omega) = \sum_{\alpha,\beta} f(E_\alpha)\,\langle\alpha|\hat{\mathcal{R}}|\beta\rangle\langle\beta|\hat{\mathcal{R}}|\alpha\rangle\,\delta\left(\omega-\omega_{\beta\alpha}\right)\,,$$

with the transition frequency $\omega_{\beta\alpha} \equiv (E_\beta - E_\alpha)/\hbar$. By considering the expression for the operators $\hat{\mathcal{R}}$ given in Equation F.33, we have:

$$S(\omega) = \sum_{\kappa,\kappa'}\hbar^2\lambda_\kappa\lambda_{\kappa'}\sum_{\alpha,\beta} f(E_\alpha)\,\langle\alpha|\left(\hat{b}_\kappa^\dagger+\hat{b}_\kappa\right)|\beta\rangle\langle\beta|\left(\hat{b}_{\kappa'}^\dagger+\hat{b}_{\kappa'}\right)|\alpha\rangle\,\delta(\omega-\omega_{\beta\alpha})\,,$$

Only terms with $\kappa = \kappa'$ survives, and the above expression can be finally written as [425]:

$$S(\omega) = \sum_\kappa \hbar^2\lambda_\kappa^2\sum_{\alpha_\kappa,\beta_\kappa} f(E_{\alpha_\kappa})\,|\langle\beta_\kappa|\left(\hat{b}_\kappa^\dagger+\hat{b}_\kappa\right)|\alpha_\kappa\rangle|^2\,\delta(\omega-\omega_{\beta_\kappa\alpha_\kappa})\,, \tag{F.34}$$

where the vibrational state $|\alpha_\kappa\rangle$ present α_κ excitations associated with the harmonic oscillator labelled as κ. Considering the action of the creation and annihilation operators

(Equation D.6), the matrix element becomes:

$$|\langle\beta_\kappa|\left(\hat{b}_\kappa^\dagger+\hat{b}_\kappa\right)|\alpha_\kappa\rangle|^2=\alpha_\kappa\delta_{\beta_\kappa,\alpha_\kappa-1}+(\alpha_\kappa+1)\delta_{\beta_\kappa,\alpha_\kappa+1}\,.$$

If we substitute this expression into Equation F.34, the function $S(\omega)$ reduces to:

$$S(\omega)=\sum_\kappa\hbar^2\lambda_\kappa^2\sum_{\alpha_\kappa}f(E_{\alpha_\kappa})\,\Big[\alpha_\kappa\;\delta(\omega-(E_{\alpha_\kappa-1}-E_{\alpha_\kappa})/\hbar)\\+(\alpha_\kappa+1)\;\delta(\omega-(E_{\alpha_\kappa+1}-E_{\alpha_\kappa})/\hbar)\Big]\,,$$

where $E_{\alpha_\kappa+1}-E_{\alpha_\kappa}=\hbar\omega_\kappa$ corresponds to the energy associated with one vibrational excitation. Taking into account that the mean occupation number of a harmonic oscillator mode is given by the Bose-Einstein distribution function $n(\omega)$ given in Equation F.29, we have: $\sum_{\alpha_\kappa}\alpha_\kappa\;f(E_{\alpha_\kappa})=n(\omega_\kappa)$. Therefore, the Fourier transform of the correlation function can be finally written as:

$$S(\omega)=\sum_\kappa\hbar^2\lambda_\kappa^2\left(n(\omega_\kappa)\;\delta(\omega+\omega_\kappa)+[n(\omega_\kappa)+1]\;\delta(\omega-\omega_\kappa)\right)\,. \tag{F.35}$$

Spectral density as a function of $J(\omega)$

It is convenient to define the function $J(\omega)$—which is also named spectral density itself—as the following sum of delta functions:

$$J(\omega)\equiv\sum_\kappa\hbar^2\lambda_\kappa^2\delta(\omega-\omega_\kappa)=\sum_\kappa\hbar^2\omega_\kappa^2D_\kappa\delta(\omega-\omega_\kappa)\,. \tag{F.36}$$

The Huang-Rhys parameter D_k is related to the exciton-phonon coupling λ_κ according to Equation 2.63, that is: $\lambda_\kappa=\omega_\kappa\sqrt{D_\kappa}$. From Equation F.35, the spectral density $S(\omega)$ can be expressed in terms of $J(\omega)$ as:

$$S(\omega)=n(-\omega)\;J(-\omega)+[1+n(\omega)]\;J(\omega)\,.$$

Since $1+n(-\omega)=-n(\omega)$, we finally have:

$$S(\omega)=[1+n(\omega)][J(\omega)-J(-\omega)]\,. \tag{F.37}$$

According to Equation F.30, the antisymmetric part $S_{\rm A}(\omega)$ of the spectral density is simply given by:

$$2S_{\rm A}(\omega)=J(\omega)-J(-\omega)\,, \tag{F.38}$$

Although $J(\omega)$ has been defined in terms of a sum of delta functions in Equation F.36, real systems present a continuous profile. Depending on the specific configuration, there exist different models for the power spectrum. Generally they are characterized by a power law rise for small frequencies followed by a exponential decay for large frequencies (after reaching the specified cut-off frequency $\omega_{\rm c}$) [425]. Some examples are the Ohmic power spectrum:

$$J_{\rm Ohmic}(\omega)=\Theta(\omega)\;J_0\;\omega\;{\rm e}^{-\omega/\omega_{\rm c}}\,,$$

and the Debye power spectrum:

$$J_{\text{Debye}}(\omega) = \Theta(\omega)\, J_0\, \frac{\omega}{\omega^2 + \omega_{\text{D}}^2}\,,$$

where J_0 is a normalization factor and ω_{D} is the Debye frequency. The step function $\Theta(\omega)$ ensures that the power spectrum is zero for $\omega < 0$.

Expression for the correlation function

Once the spectral density is determined, the time-correlation function $\mathcal{C}(t)$ can be computed from Equation F.32. By substituting the expression of the antisymmetric part of the spectral density given in Equation F.38, we have:

$$\mathcal{C}(t) = \int_0^\infty J(\omega)\left([1 + n(\omega)]\, \mathrm{e}^{-\mathrm{i}\omega t} + n(\omega)\, \mathrm{e}^{\mathrm{i}\omega t}\right)\mathrm{d}\omega\,,$$

where we have removed the $J(-\omega)$ term as the integral runs over positive frequency values. This expression is commonly split into its real and imaginary parts, so the time-correlation function can be finally written as:

$$\mathcal{C}(t) = \int_0^\infty J(\omega)\left(\cos(\omega t)[1 + 2n(\omega)] - \mathrm{i}\sin(\omega t)\right)\mathrm{d}\omega\,.$$

F.6 Absorption spectrum of organic molecules

Luminescence and absorption experiments are used to gain insight into the vibrational structure of organic molecules. In this section we will study the characteristic profile of the absorption spectrum associated with organic molecules, owing to vibronic transitions (that is, transitions between different electronic energy levels implying a change in the vibrational state). Since the displaced harmonic oscillator (DHO) model is often used to describe vibronic spectroscopy, we will also study the imprint left by the different relevant quantities of this model on the absorption spectrum.

F.6.1 Lineshape function within the DHO model

The absorption spectrum depends on the **transition rate** at which the system is promoted from the ground to the excited state due to the absorption of a photon. This rate can be estimated through the Fermi's Golden rule, and expressed in terms of the **lineshape function**. The most relevant expressions related to the absorption rate and its associated lineshape function have been derived in Appendix F, Section F.4. According to Equation F.21,

the lineshape function $\mathcal{A}(\omega)$ is given by:

$$\mathcal{A}(\omega) = \frac{1}{2\pi\hbar} \int_{-\infty}^{\infty} \mathrm{d}t \; \mathrm{e}^{\mathrm{i}\omega t} \; \mathcal{F}(t) \; , \tag{F.39}$$

where the function $\mathcal{F}(t)$ is defined in Equation F.18 as:

$$\mathcal{F}(t) \equiv \langle \mathrm{e}^{\mathrm{i}\hat{H}_{\mathcal{G}} t/\hbar} \mathrm{e}^{-\mathrm{i}\hat{H}_{\mathcal{E}} t/\hbar} \rangle_{\mathrm{g}} \; . \tag{F.40}$$

There, $\hat{H}_{\mathcal{G}}$ and $\hat{H}_{\mathcal{E}}$ are the Hamiltonians corresponding to the molecular states $|\mathcal{G}\rangle$ and $|\mathcal{E}\rangle$, respectively, and the angle brackets stand for the thermal average over the vibrational eigenstates associated with the electronic ground state.

We are interested in evaluating the correlation function $\mathcal{F}(t)$ when considering the DHO model, discussed in the main text in Subsection 2.4.1. Within this model, the Hamiltonians $\hat{H}_{\mathcal{G}}$ and $\hat{H}_{\mathcal{E}}$ would be those coming from the energies in Equation 2.51 after introducing the transformation in Equation 2.54, that is:

$$\begin{aligned} \hat{H}_{\mathcal{G}} &= \hbar\omega_{\mathrm{v}} \hat{b}^{\dagger}\hat{b} \; , \\ \hat{H}_{\mathcal{E}} &= \hbar\omega_{00} + \hbar\omega_{\mathrm{v}} \hat{b}^{\dagger}\hat{b} + \hbar\omega_{\mathrm{v}} D + \hbar\omega_{\mathrm{v}} \sqrt{D} \; (\hat{b} + \hat{b}^{\dagger}) \; , \end{aligned}$$

where we have considered $E_{\mathrm{g}}^{\mathrm{min}} = 0$ and the definition of the energy of the zero-phonon vibronic transition $\hbar\omega_{00}$ is the one given in Equation 2.52. There, ω_{v} is the frequency of the vibrational mode, and $\hat{b}^{\dagger}$ and $\hat{b}$ are the associated creation and annihilation operators. The Huang-Rhys parameter D, defined in Equation 2.55, gives a measure of the strength of the exciton-phonon coupling. If we rewrite the Hamiltonian $\hat{H}_{\mathcal{E}}$ as:

$$\hat{H}_{\mathcal{E}} = \hbar\omega_{00} + \hbar\omega_{\mathrm{v}} \left(\sqrt{D} + \hat{b}^{\dagger}\right)\left(\sqrt{D} + \hat{b}\right) \; ,$$

the correlation function in Equation F.40 becomes:

$$\mathcal{F}(t) = \langle \mathrm{e}^{\mathrm{i}\hbar\omega_{\mathrm{v}}\hat{b}^{\dagger}\hat{b}t/\hbar} \mathrm{e}^{-\mathrm{i}\omega_{00}t} \mathrm{e}^{-\mathrm{i}\hbar\omega_{\mathrm{v}}(\sqrt{D}+\hat{b}^{\dagger})(\sqrt{D}+\hat{b})t/\hbar} \rangle_{\mathrm{g}} \; .$$

It can be shown that this trace can be written as [425, 426]:

$$\mathcal{F}(t) = \exp\left[-\mathrm{i}\omega_{00}t + D\left([1 + n(\omega_{\mathrm{v}})](\mathrm{e}^{-\mathrm{i}\omega_{\mathrm{v}}t} - 1) + n(\omega_{\mathrm{v}})(\mathrm{e}^{\mathrm{i}\omega_{\mathrm{v}}t} - 1)\right)\right] \; , \tag{F.41}$$

where $n(\omega)$ is the Bose-Einstein distribution function (Equation F.29), which encloses the dependence on the temperature T. Notice that $\mathcal{F}(t)$ contains both phonon absorption (positive frequencies) and phonon emission processes (negative frequencies). This function is sometimes expressed as:

$$\mathcal{F}(t) = \mathrm{e}^{-\mathrm{i}\omega_{00}t} \mathrm{e}^{-G(0)+G(t)} \; , \tag{F.42}$$

where:

$$G(t) = D\left([1 + n(\omega_{\mathrm{v}})] \; \mathrm{e}^{-\mathrm{i}\omega_{\mathrm{v}}t} + n(\omega_{\mathrm{v}}) \; \mathrm{e}^{\mathrm{i}\omega_{\mathrm{v}}t}\right) \; . \tag{F.43}$$

By using this last expression for $\mathcal{F}(t)$, the lineshape function of Equation F.39 can be rewritten as:

$$\mathcal{A}(\omega) = \frac{1}{2\pi\hbar} \int_{-\infty}^{\infty} \mathrm{d}t \; \mathrm{e}^{\mathrm{i}(\omega-\omega_{00})t - G(0) + G(t)} \; . \tag{F.44}$$

Notice that for $D = 0$, the absorption spectrum reduces to a line at $\omega = \omega_{00}$.

Two limiting cases

Starting from the general expression for the lineshape function $\mathcal{A}(\omega)$ in Equation F.44, we now study the absorption spectrum profile corresponding to two limiting cases, differing from each other in the relation between the vibrational frequency and the temperature.

High-frequency modes When the temperature T is low compared to the vibrational frequency ω_v (that is, $\hbar\omega_v \gg k_B T$), the average phonon number can be disregarded: $n(\omega_v) \approx 0$. Then, the correlation function $\mathcal{F}(t)$ of Equation F.42 becomes:

$$\mathcal{F}(t) = \exp\left[-i\omega_{00}t + D(e^{-i\omega_v t} - 1)\right] = e^{-i\omega_{00}t} \sum_k \frac{D^k}{k!} e^{-D} e^{-ik\omega_v t} ,$$

where we have considered the expansion of $e^{D(x-1)}$ around $x = 0$, with $x \equiv e^{-i\omega_v t}$, namely:

$$e^{D(x-1)} = \sum_k \frac{D^k}{k!} e^{-D} x^k = \sum_k \frac{D^k}{k!} e^{-D} e^{-ik\omega_v t} .$$

By introducing this expression for $\mathcal{F}(t)$ into Equation F.39, the lineshape function $\mathcal{A}(\omega)$ reads:

$$\mathcal{A}(\omega) = \frac{1}{2\pi\hbar} \int_{-\infty}^{\infty} dt\ e^{i(\omega-\omega_{00})t} \sum_k \frac{D^k}{k!} e^{-D} e^{-ik\omega_v t} .$$

If we consider the integral representation of the delta function (Equation E.13), the previous expression reduces to:

$$\mathcal{A}(\omega) = \frac{1}{\hbar} \sum_k \frac{D^k}{k!} e^{-D}\ \delta(\omega - \omega_{00} - k\omega_v) . \tag{F.45}$$

This corresponds to a sequence of peaks located at frequencies $\omega = \omega_{00} + k\omega_v$ (with $k = 0, 1, 2\ldots$) and whose amplitudes are given by the **Franck–Condon coefficients*** F_{0k}:

$$F_{0k} = \frac{D^k}{k!} e^{-D} . \tag{F.46}$$

*These coefficients represent the overlap of the vibrational components of the two states involved in the transition (Equation F.2), in this case, between the vibrational ground state and the vibrational state k: $F_{0k} = |\langle \chi_g^0 | \chi_e^k \rangle|^2$.

Notice that this expression is nothing but a Poisson distribution, where the parameter D gives the average number of events in an interval (the distribution reaches its maximum at $k = D$). Therefore, the intensities of the absorption peaks are related to the displacement d in terms of the Huang-Rhys parameter D (Equation 2.55) and, in turn, to the coupling strength between nuclear and electronic degrees of freedom Equation 2.57.

The normalized lineshape function $\mathcal{A}(\omega)$ given in Equation F.45 is plotted in Figure F.3 for three different values of the Huang-Rhys parameter D. A small damping is introduced so as to obtain finite linewidths. These plots are accompanied by the respective sketches of the DHO model, representing the harmonic oscillator potentials associated with the molecular ground and excited states as a function of the molecular coordinate q. The energy gap between the minima is $\hbar\omega_{00} = 3$ eV, and the vibrational frequency is taken as $\omega_v = 5$ meV. In general, we can distinguish the following cases:

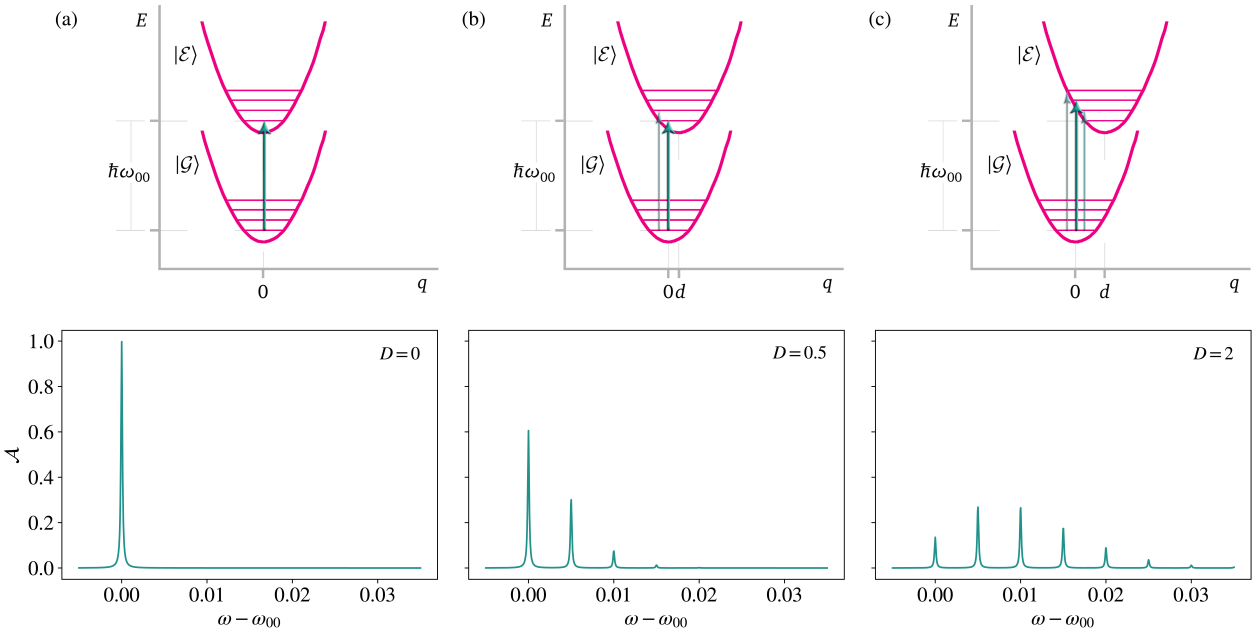

Figure F.3.
Sketch of the DHO model (equivalently to that in Figure 2.3) corresponding to three different values of the displacement d, parametrized in terms of the Huang-Rhys parameter: (a) $D=0$, (b) $D=0.5$, and (c) $D=2.0$. The main transitions are indicated with vertical arrows. Below, the normalized lineshape functions $\mathcal{A}(\omega)$ are depicted for the same cases, with $\omega_{\mathrm{v}}=5$ meV.

- If there is no displacement ($D=0$), as in Figure F.3 (a), the only term that survives is $k=0$, that is, the one with no vibrational excitations involved. Therefore, only the peak associated with the pure electronic transition at $\omega=\omega_{00}$ appears.
- When $D\neq 0$, the peak associated with the electronic transition 0-0 appears followed by a set of peaks involving different vibrational excitations:
  - If the displacement is small ($D<1$), as in Figure F.3 (b), the peak corresponding to $k=0$ is the most intense, while the amplitude of the subsequent transitions shows a continuous decrease.
  - On the contrary, if the displacement is large ($D\gg 1$), as in Figure F.3 (c), the transition with the maximum amplitude is that with $k=D$.

Therefore, the Huang-Rhys parameter D corresponds to the mean number of vibrational quanta that are excited in the electronic excited state on absorption from the ground state (at $q=0$).

All in all, the absorption spectrum associated with organic molecules is composed of a set of peaks each of which represents a transition from the ground state to a different vibrational state in the electronic first-excited state. The starting peak at ω_{00} corresponds to the pure electronic transition (that is, the 0-0 transition, where no phonons are involved), and it is accompanied by a set of other transitions. These peaks are separated by a frequency ω_{v} and their amplitudes, given by the Franck–Condon factors F_{0k} (Equation F.46), follow a Poisson distribution. There, the index k would correspond to the number of vibrational quanta that are excited.

Low frequency modes In the high-temperature limit, the temperature T is high compared to the vibrational frequency ω_{v} (that is, $\hbar\omega_{\mathrm{v}}\ll k_{\mathrm{B}}T$). The time-correlation function $\mathcal{F}(t)$, given in Equation F.41, has peaks at $t=0,\pm 2\pi/\omega_{\mathrm{v}},\ldots$ These sharpen as the tem-

perature increases, as shown in Figure F.4 [Left]. There, we plot the time-correlation function for $k_B T = 1, 5$, and 25 meV. Again, we have taken $\hbar\omega_{00} = 3$ meV and $\hbar\omega_v = 5$ meV. Since the correlation function $\mathcal{F}(t)$ decays quickly, the so-called **short-time approximation** can be performed. Exponentials can be approximated by:

$$e^{-i\omega_v t} \approx 1 - i\omega_v t - \frac{1}{2}\omega_v^2 t^2 ,$$

so that Equation F.41 becomes:

$$\mathcal{F}(t) = \exp\left[-i\omega_{00} t - iD\omega_v t - D\omega_v^2 \left(\frac{1}{2} + n(\omega_v)\right) t^2\right] .$$

The Bose-Einstein distribution function (Equation F.29) can be approximated as: $n(\omega_v) \approx k_B T/(\hbar\omega_v)$, while disregarding the $1/2$ term. By performing this substitution, and considering the expression for the reorganization energy $\Lambda \equiv \hbar\omega_v D$ (Equation 2.58), we have:

$$\mathcal{F}(t) = \exp\left[-i\left(\omega_{00} + \frac{\Lambda}{\hbar}\right) t - \frac{\Lambda k_B T}{\hbar^2} t^2\right] .$$

Additionally, we could introduce the Franck–Condon transition frequency $\omega_{eg} \equiv \omega_{00} + \Lambda/\hbar$ (Equation 2.59). By introducing this expression for $\mathcal{F}(t)$ into Equation F.39, the lineshape function $\mathcal{A}(\omega)$ reads:

$$\mathcal{A}(\omega) = \frac{1}{2\pi\hbar} \int_{-\infty}^{\infty} dt \; e^{i(\omega - \omega_{eg})t} \; e^{-(\Lambda k_B T/\hbar^2) t^2} .$$

The integrand can be written as a Gaussian, and the lineshape function finally becomes:

$$\mathcal{A}(\omega) = \frac{1}{4\pi\Lambda k_B T} \exp\left[-\frac{\hbar^2(\omega - \omega_{eg})^2}{4\Lambda k_B T}\right] .$$

Therefore, the set of vibronic transitions making up the absorption spectrum for high temperatures presents a Gaussian envelope centered at frequency $\omega = \omega_{eg}$ and with variance $\sigma = \sqrt{2\Lambda k_B T}$. This is shown in Figure F.4 [Right], where the lineshape function is plotted for $k_B T = 25$ meV. Notice that the width of the Gaussian profile can be then used to quantify the excited state distortion.

We have considered the case in which only a single vibrational mode with frequency ω_v couples to the electronic transition. Nevertheless, all these expressions are easily generalized when several vibrational modes are involved.

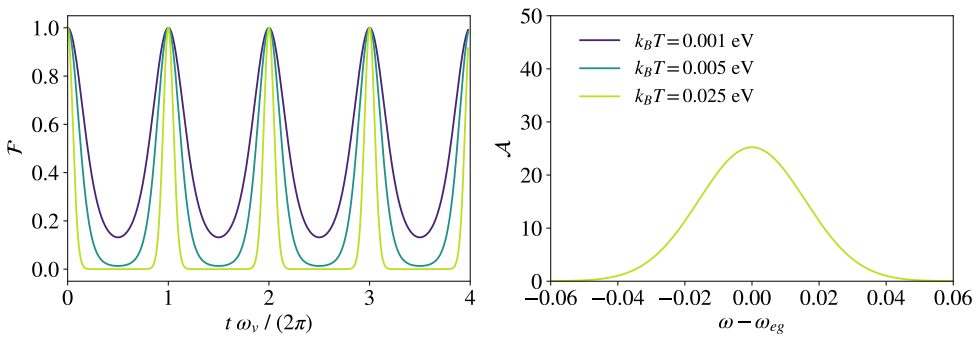

Figure F.4. **[Left]** Time-correlation function $\mathcal{F}(t)$ as a function of time when $\omega_v = 5$ meV and for different values of the temperature, $k_B T = 1$ meV (blue), 5 meV (turquoise), and 25 meV (yellow). **[Right]** Normalized lineshape function $\mathcal{A}(\omega)$ as a function of frequency for $\omega_v = 5$ meV and $k_B T = 25$ meV.

F.6.2 Comparison between absorption and fluorescence spectra

Emission and excitation spectra

Spectrometers devices are provided with both excitation and emission monochromators, that is, optical band-pass filters that allow only a specific narrow band of frequencies to pass from all those coming into them. Depending on the monochromator that is scanned (in such a way that a broad range of frequencies is swept), two kinds of spectra can be obtained:

- The **emission spectra** gives the frequency of the emission for a specific value of the excitation frequency (that is, the emission monochromator is scanned while the excitation one is fixed). Generally, the excitation frequency is chosen at a value where the absorption of the system is important.
- The **excitation spectra** gives the emission of the system as a function of the excitation frequency (that is, the excitation monochromator is scanned while the other is fixed). Notice that the emission is recorded for a specific frequency, that usually coincides with the value of the maximum emission.

Therefore, the excitation spectra would mimic the **absorption spectra**, but the emission usually varies depending on the output frequency. For atoms, both absorption and emission occur at the same wavelength. Nevertheless, for organic molecules the wavelength of the emission is usually longer than the excitation one due to the vibrational structure. As we will see, the comparison between these two spectra provides important information.

Absorption and fluorescence

Absorption from the electronic ground state usually leaves the molecule in a vibrational excited state of the excited potential energy surface, as only vertical transitions are allowed according to the Franck–Condon principle (see Section F.2). This vibrational energy is rapidly dissipated through vibrational relaxation, reaching the lowest vibrational level of the same electronically excited state. The system can then emit a photon and return to the electronically ground state, process known as fluorescence (see Section F.1). Again, when working within the Franck–Condon approximation, these transitions take place without varying the nuclear coordinate. The system usually ends in a vibrational excited state of the ground potential energy surface, and this vibrational energy is eventually dissipated through vibrational relaxation.

Therefore, there exists a difference between the absorption and emission frequencies connected to the vibrational excitation that the molecule acquires in both transitions. This energy difference is known as Stokes shift, and equals the vibrational energy that is dissipated in both the excited and the ground electronic states.

Excited state distortion and Stokes shift

As we have explained in Subsection 2.4.1, the nucleus of an excited molecule is generally displaced with respect to its position for the molecule in its ground state. This displacement, that has been introduced as d in the DHO model, can be of different extent depending on the specific molecule:

- If there is no distortion ($d = 0$), the 0-0 vibronic transition (in which there is no vibrational excitation neither in the initial nor the final states) is the most likely one. Therefore, the most intense peaks in both absorption and emission coincide, since they correspond to the same transition.
- On the contrary, if the distortion is non-zero ($d \neq 0$), there will be some vibronic transition 0-k whose probability is greater than the 0-0 transition. This would happen for both absorption and emission, leading to the so-called **mirror-image rule**.

The **Stokes shift** S is the energy difference between the peaks with maximum emission and absorption corresponding to the same electronic transition. If there is no distortion, the Stokes shift is zero since the most intense peaks in both absorption and emission spectra coincide.

Stokes shift and reorganization energy

According to Equation 2.61, the vibrational energy in the electronic excited state after the absorption from the ground state at $q = 0$ is the **reorganization energy** Λ. In Figure F.5 [Left] this transition is represented with a green arrow. As we have seen, the reorganization energy is related to the Huang-Rhys parameter D through Equation 2.58, that is, $\Lambda \equiv \hbar\omega_v D$. This expression is compatible with the interpretation of D as the mean number of vibrational quanta excited in the electronic state on absorption from the ground state.

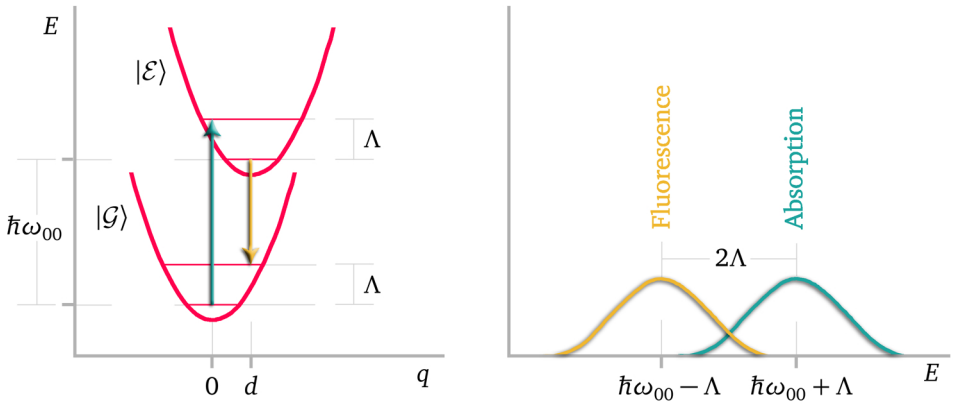

Figure F.5. [Left] Harmonic approximation for the vibrational potentials associated with the ground and first-excited electronic states, where two transitions are depicted: in green, the absorption from the electric ground state with zero phonons to the electronic excited state with vibrational energy Λ; in yellow, the fluorescence from the electronic excited state with no vibrational excitations to the ground state with vibrational energy Λ. [Right] Absorption (green) and emission (yellow) spectra associated with the processes previously indicated.

This reorganization energy acquired as a result of absorption from the ground state will be dissipated through vibrational relaxation until the zero-vibrational level in the excited electronic state is reached. The emission from the electronic excited state thus starts from the state with no vibrational excitations, and ends on the electronic ground state surface in a state with vibrational excitations. The vertical transition takes place at the point

$q = d$, that is, the position of the minimum of the excited state surface. This vibrational energy is also of value Λ, as depicted in Figure F.5 [Left]. Therefore, the absorption and emission maxima are shifted twice this quantity Λ, as shown in Figure F.5 [Right]. The **Stokes shift** S is precisely the energy difference between peaks in the absorption and fluorescence spectra, hence:

$$S = 2\Lambda = 2\hbar\omega_{\mathrm{v}} D$$

Franck–Condon principle and mirror-image rule

The intensity of the peaks of vibronic transitions (the ones that involve a simultaneous change in both electronic and vibrational energy levels) are explained by the **Franck–Condon principle**. It dictates that the probability of a vibronic transition is proportional to the overlap between the vibrational wavefunctions of the different states. In many cases, the maximum overlap between vibrational wavefunctions corresponds to the same vibrational pair for both absorption and emission. Therefore, the peak with strongest intensity would correspond to this specific vibronic transition in both spectra. This correspondence may occur for the different vibrational pairs, so that absorption and emission spectra would follow a mirror symmetry as shown in Figure F.6. This is called the **mirror-image rule** and is usually followed when the excited state distortion is small, but not when this is large.

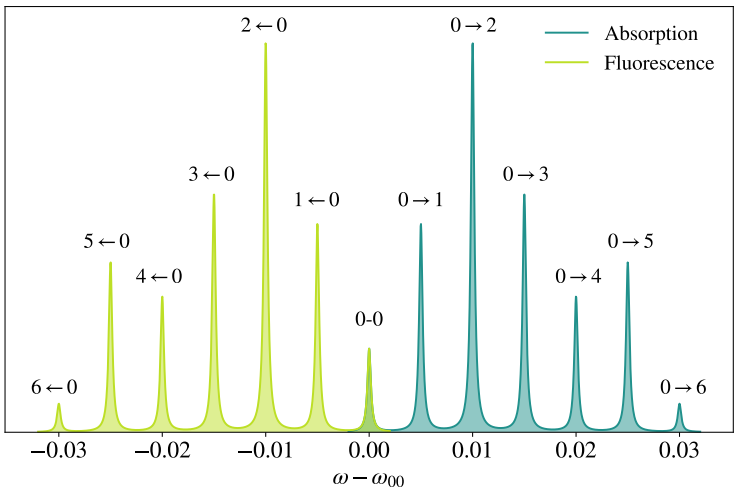

Figure F.6. Absorption (green) and fluorescence (yellow) spectra.

BIBLIOGRAPHY

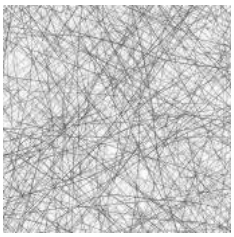

[1] C. Cohen-Tannoudji, J. Dupont-Roc, and G. Grynberg, *Photons and Atoms: Introduction to Quantum Electrodynamics* (Wiley-VCH, 1997).

[2] W. E. Lamb and R. C. Retherford, "Fine structure of the hydrogen atom by a microwave method," Phys. Rev. **72**, 241–243 (1947).

[3] H. B. G. Casimir, "On the Attraction Between Two Perfectly Conducting Plates," Indag. Math. **10**, 261–263 (1948). Kon. Ned. Akad. Wetensch. Proc. **51**, 793–795 (1948).

[4] H. Walther, B. T. H. Varcoe, B.-G. Englert, and T. Becker, "Cavity quantum electrodynamics," Reports on Progress in Physics **69**, 1325–1382 (2006).

[5] E. M. Purcell, H. C. Torrey, and R. V. Pound, "Resonance absorption by nuclear magnetic moments in a solid," Phys. Rev. **69**, 37–38 (1946).

[6] K. Drexhage, "Influence of a dielectric interface on fluorescence decay time," Journal of Luminescence **1–2**, 693 – 701 (1970).

[7] K. J. Vahala, "Optical microcavities," Nature **424**, 839–846 (2003).

[8] A. Kavokin, J. J. Baumberg, G. Malpuech, and F. P. Laussy, *Microcavities* (Oxford University Press, New York, USA, 2008).

[9] D. K. Armani, T. J. Kippenberg, S. M. Spillane, and K. J. Vahala, "Ultra-high-Q toroid microcavity on a chip," Nature **421**, 925–928 (2003).

[10] J. M. Gérard, D. Barrier, J. Y. Marzin, R. Kuszelewicz, L. Manin, E. Costard, V. Thierry-Mieg, and T. Rivera, "Quantum boxes as active probes for photonic microstructures: The pillar microcavity case," Appl. Phys. Lett. **69**, 449–451 (1996).

[11] A. J. Bennett, D. C. Unitt, P. See, A. J. Shields, P. Atkinson, K. Cooper, and D. A. Ritchie, "Microcavity single-photon-emitting diode," Appl. Phys. Lett. **86**, 181102 (2005).

[12] E. Moreau, I. Robert, J. M. Gérard, I. Abram, L. Manin, and V. Thierry-Mieg, "Single-mode solid-state single photon source based on isolated quantum dots in pillar microcavities," Applied Physics Letters **79**, 2865–2867 (2001).

[13] M. Pelton, C. Santori, J. Vučkovič, B. Zhang, G. S. Solomon, J. Plant, and Y. Yamamoto, "Efficient source of single photons: A single quantum dot in a micropost microcavity," Phys. Rev. Lett. **89**, 233602 (2002).

[14] N. G. Stoltz, M. Rakher, S. Strauf, A. Badolato, D. D. Lofgreen, P. M. Petroff, L. A. Coldren, and D. Bouwmeester, "High-quality factor optical microcavities using oxide apertured micropillars," Applied Physics Letters **87**, 031105 (2005).

[15] A. Daraei, A. Tahraoui, D. Sanvitto, J. A. Timpson, P. W. Fry, M. Hopkinson, P. S. S. Guimarães, H. Vinck, D. M. Whittaker, M. S. Skolnick, and A. M. Fox, "Control of polarized single quantum dot emission in high-quality-factor microcavity pillars," Applied Physics Letters **88**, 051113 (2006).

[16] S. Reitzenstein, C. Hofmann, A. Gorbunov, M. Strauß, S. H. Kwon, C. Schneider, A. Löffler, S. Höfling, M. Kamp, and A. Forchel, "AlAs/GaAs micropillar cavities with quality factors exceeding 150.000," Applied Physics Letters **90**, 251109 (2007).

[17] P. Michler, A. Kiraz, C. Becher, W. V. Schoenfeld, P. M. Petroff, L. Zhang, E. Hu, and A. Imamoglu, "A quantum dot single-photon turnstile device," Science **290**, 2282–2285 (2000).

[18] B. Gayral, J. M. Gérard, A. Lemaître, C. Dupuis, L. Manin, and J. L. Pelouard, "High-Q wet-etched GaAs microdisks containing InAs quantum boxes," Applied Physics Letters **75**, 1908–1910 (1999).

[19] Y.-S. Park, A. K. Cook, and H. Wang, "Cavity QED with diamond nanocrystals and silica microspheres," Nano Letters **6**, 2075–2079 (2006).

[20] J. D. Joannopoulos, P. R. Villeneuve, and S. Fan, "Photonic crystals: putting a new twist on light," Nature **386**, 143–149 (1997).

[21] L. Novotny and B. Hecht, *Principles of Nano-Optics* (Cambridge University Press, 2006).

[22] P. R. Villeneuve, S. Fan, and J. D. Joannopoulos, "Microcavities in photonic crystals: Mode symmetry, tunability, and coupling efficiency," Phys. Rev. B **54**, 7837–7842 (1996).

[23] K. Srinivasan, P. E. Barclay, O. Painter, J. Chen, A. Y. Cho, and C. Gmachl, "Experimental demonstration of a high quality factor photonic crystal microcavity," Appl. Phys. Lett. **83**, 1915–1917 (2003).

[24] J. Vučkovič and Y. Yoshihisa, "Photonic crystal microcavities for cavity quantum electrodynamics with a single quantum dot," Appl. Phys. Lett. **82**, 2374–2376 (2003).

[25] Y. Akahane, T. Asano, B. S. Song, and S. Noda, "High-Q photonic nanocavity in a two-dimensional photonic crystal," Nature **425**, 944–947 (2003).

[26] P. Lodahl, A. Floris van Driel, I. S. Nikolaev, A. Irman, K. Overgaag, D. Vanmaekelbergh, and W. L. Vos, "Controlling the dynamics of spontaneous emission from quantum dots by photonic crystals," Nature **430**, 654–657 (2004).

[27] J. S. Fakonas, H. Lee, Y. A. Kelaita, and H. A. Atwater, "Two-plasmon quantum interference," Nature Photonics **8**, 317–320 (2014).

[28] M.-C. Dheur, E. Devaux, T. W. Ebbesen, A. Baron, J.-C. Rodier, J.-P. Hugonin, P. Lalanne, J.-J. Greffet, G. Messin, and F. Marquier, "Single-plasmon interferences," Science Advances **2** (2016).

[29] S. Maier, *Plasmonics: Fundamentals and Applications* (Springer, New York, USA, 2007).

[30] V. G. Kravets, A. V. Kabashin, W. L. Barnes, and A. N. Grigorenko, "Plasmonic surface lattice resonances: A review of properties and applications," Chemical Reviews **118**, 5912–5951 (2018).

[31] E. Kretschmann and H. Raether, "Notizen: Radiative decay of non radiative surface plasmons excited by light," Zeitschrift für Naturforschung A: Phys. Sci. **23**, 2135–2136 (1968).

[32] R. H. Ritchie, E. T. Arakawa, J. J. Cowan, and R. N. Hamm, "Surface-plasmon resonance effect in grating diffraction," Phys. Rev. Lett. **21**, 1530–1533 (1968).

[33] M. Kuttge, F. J. García de Abajo, and A. Polman, "Ultrasmall mode volume plasmonic nanodisk resonators," Nano Letters **10**, 1537–1541 (2010).

[34] J. Bellessa, C. Bonnand, J. C. Plenet, and J. Mugnier, "Strong coupling between surface plasmons and excitons in an organic semiconductor," Phys. Rev. Lett. **93**, 036404 (2004).

[35] J. Dintinger, S. Klein, F. Bustos, W. L. Barnes, and T. W. Ebbesen, "Strong coupling between surface plasmon-polaritons and organic molecules in subwavelength hole arrays," Phys. Rev. B **71**, 035424 (2005).

[36] G. P. Wiederrecht, G. A. Wurtz, and J. Hranisavljevic, "Coherent coupling of molecular excitons to electronic polarizations of noble metal nanoparticles," Nano Letters **4**, 2121–2125 (2004).

[37] S. Zhang, K. Bao, N. J. Halas, H. Xu, and P. Nordlander, "Substrate-induced Fano resonances of a plasmonic nanocube: A route to increased-sensitivity localized surface plasmon resonance sensors revealed," Nano Letters **11**, 1657–1663 (2011).

[38] G. Zengin, M. Wersäll, S. Nilsson, T. J. Antosiewicz, M. Käll, and T. Shegai, "Realizing strong light-matter interactions between single-nanoparticle plasmons and molecular excitons at ambient conditions," Phys. Rev. Lett. **114**, 157401 (2015).

[39] J. J. Mock, R. T. Hill, A. Degiron, S. Zauscher, A. Chilkoti, and D. R. Smith, "Distance-dependent plasmon resonant coupling between a gold nanoparticle and gold film," Nano Letters **8**, 2245–2252 (2008).

[40] D. Y. Lei, A. I. Fernández-Domínguez, Y. Sonnefraud, K. Appavoo, R. F. Haglund, J. B. Pendry, and S. A. Maier, "Revealing plasmonic gap modes in particle-on-film systems using dark-field spectroscopy," ACS Nano **6**, 1380–1386 (2012).

[41] P. J. Schuck, D. P. Fromm, A. Sundaramurthy, G. S. Kino, and W. E. Moerner, "Improving the mismatch between light and nanoscale objects with gold bowtie nanoantennas," Phys. Rev. Lett. **94**, 017402 (2005).

[42] H. Kollmann, X. Piao, M. Esmann, S. F. Becker, D. Hou, C. Huynh, L.-O. Kautschor, G. Bösker, H. Vieker, A. Beyer, A. Gölzhäuser, N. Park, R. Vogelgesang, M. Silies, and C. Lienau, "Toward plasmonics with nanometer precision: Nonlinear optics of Helium-Ion milled gold nanoantennas," Nano Letters **14**, 4778–4784 (2014).

[43] P. Mühlschlegel, H.-J. Eisler, O. J. F. Martin, B. Hecht, and D. W. Pohl, "Resonant optical antennas," Science **308**, 1607–1609 (2005).

[44] B. Metzger, M. Hentschel, T. Schumacher, M. Lippitz, X. Ye, C. B. Murray, B. Knabe, K. Buse, and H. Giessen, "Doubling the efficiency of third harmonic generation by positioning ITO nanocrystals into the hot-spot of plasmonic gap-antennas," Nano Letters **14**, 2867–2872 (2014).

[45] V. G. Kravets, F. Schedin, and A. N. Grigorenko, "Extremely narrow plasmon resonances based on diffraction coupling of localized plasmons in arrays of metallic nanoparticles," Phys. Rev. Lett. **101**, 087403 (2008).

[46] B. Auguié and W. L. Barnes, "Collective resonances in gold nanoparticle arrays," Phys. Rev. Lett. **101**, 143902 (2008).

[47] I. Buluta, S. Ashhab, and F. Nori, "Natural and artificial atoms for quantum computation," Reports on Progress in Physics **74**, 104401 (2011).

[48] P. Michler, *Single Semiconductor Quantum Dots* (Springer-Verlag Berlin Heidelberg, 2009).

[49] M. W. Doherty, N. B. Manson, P. Delaney, F. Jelezko, J. Wrachtrup, and L. C. Hollenberg, "The nitrogen-vacancy colour centre in diamond," Physics Reports **528**, 1 – 45 (2013).

[50] V. Acosta and P. Hemmer, "Nitrogen-vacancy centers: Physics and applications," MRS Bulletin **38**, 127–130 (2013).

[51] M. Atatüre, D. Englund, N. Vamivakas, S.-Y. Lee, and J. Wrachtrup, "Material platforms for spin-based photonic quantum technologies," Nature Reviews Materials **3**, 38–51 (2018).

[52] A. Srivastava, M. Sidler, A. V. Allain, D. S. Lembke, A. Kis, and A. Imamoglu, "Optically active quantum dots in monolayer WSe_2," Nature Nanotechnology **10**, 491–496 (2015).

[53] Y.-M. He, G. Clark, J. R. Schaibley, Y. He, M.-C. Chen, Y.-J. Wei, X. Ding, Q. Zhang, W. Yao, X. Xu, C.-Y. Lu, and J.-W. Pan, "Single quantum emitters in monolayer semiconductors," Nature Nanotechnology **10**, 497–502 (2015).

[54] M. Koperski, K. Nogajewski, A. Arora, V. Cherkez, P. Mallet, J.-Y. Veuillen, J. Marcus, P. Kossacki, and M. Potemski, "Single photon emitters in exfoliated WSe_2 structures," Nature Nanotechnology **10**, 503–506 (2015).

[55] P. Tonndorf, R. Schmidt, R. Schneider, J. Kern, M. Buscema, G. A. Steele, A. Castellanos-Gomez, H. S. J. van der Zant, S. M. de Vasconcellos, and R. Bratschitsch, "Single-photon emission from localized excitons in an atomically thin semiconductor," Optica **2**, 347–352 (2015).

[56] A. Branny, G. Wang, S. Kumar, C. Robert, B. Lassagne, X. Marie, B. D. Gerardot, and B. Urbaszek, "Discrete quantum dot like emitters in monolayer $MoSe_2$: Spatial mapping, magneto-optics, and charge tuning," Applied Physics Letters **108**, 142101 (2016).

[57] C. Palacios-Berraquero, M. Barbone, D. M. Kara, X. Chen, I. Goykhman, D. Yoon, A. K. Ott, J. Beitner, K. Watanabe, T. Taniguchi, A. C. Ferrari, and M. Atatüre, "Atomically thin quantum light-emitting diodes," Nature Communications **7**, 12978 (2016).

[58] S. K. Saikin, E. Alexander, V. Stéphanie, and A.-G. Alán, "Photonics meets excitonics: Natural and artificial molecular aggregates," Nanophotonics **2**, 21 (2013).

[59] E. E. Jelley, "Spectral absorption and fluorescence of dyes in the molecular state," Nature **138**, 1009–1010 (1936).

[60] F. Würthner, T. E. Kaiser, and C. R. Saha-Möller, "J-aggregates: From serendipitous discovery to supramolecular engineering of functional dye materials," Angewandte Chemie International Edition **50**, 3376–3410 (2011).

[61] A. Frisk Kockum, A. Miranowicz, S. De Liberato, S. Savasta, and F. Nori, "Ultrastrong coupling between light and matter," Nature Reviews Physics **1**, 19–40 (2019).

[62] V. Giannini, A. I. Fernández-Domínguez, S. C. Heck, and S. A. Maier, "Plasmonic nanoantennas: Fundamentals and their use in controlling the radiative properties of nanoemitters," Chemical Reviews **111**, 3888–3912 (2011).

[63] D. Kleppner, "Inhibited spontaneous emission," Phys. Rev. Lett. **47**, 233–236 (1981).

[64] P. Goy, J. M. Raimond, M. Gross, and S. Haroche, "Observation of cavity-enhanced single-atom spontaneous emission," Phys. Rev. Lett. **50**, 1903–1906 (1983).

[65] R. G. Hulet, E. S. Hilfer, and D. Kleppner, "Inhibited spontaneous emission by a Rydberg atom," Phys. Rev. Lett. **55**, 2137–2140 (1985).

[66] E. Yablonovitch, "Inhibited spontaneous emission in solid-state physics and electronics," Phys. Rev. Lett. **58**, 2059–2062 (1987).

[67] J.-M. Gerard and B. Gayral, "Strong purcell effect for InAs quantum boxes in three-dimensional solid-state microcavities," J. Lightwave Technol. **17**, 2089 (1999).

[68] G. Björk, S. Machida, Y. Yamamoto, and K. Igeta, "Modification of spontaneous emission rate in planar dielectric microcavity structures," Phys. Rev. A **44**, 669–681 (1991).

[69] Y. Yamamoto, S. Machida, and G. Björk, "Microcavity semiconductor laser with enhanced spontaneous emission," Phys. Rev. A **44**, 657–668 (1991).

[70] J. L. Jewell, J. P. Harbison, A. Scherer, Y. H. Lee, and L. T. Florez, "Vertical-cavity surface-emitting lasers: Design, growth, fabrication, characterization," IEEE Journal of Quantum Electronics **27**, 1332–1346 (1991).

[71] J. M. Gérard, B. Sermage, B. Gayral, B. Legrand, E. Costard, and V. Thierry-Mieg, "Enhanced spontaneous emission by quantum boxes in a monolithic optical microcavity," Phys. Rev. Lett. **81**, 1110–1113 (1998).

[72] S. L. McCall, A. F. J. Levi, R. E. Slusher, S. J. Pearton, and R. A. Logan, "Whispering-gallery mode microdisk lasers," Applied Physics Letters **60**, 289–291 (1992).

[73] O. Painter, R. K. Lee, A. Scherer, A. Yariv, J. D. O'Brien, P. D. Dapkus, and I. Kim, "Two-dimensional photonic band-gap defect mode laser," Science **284**, 1819–1821 (1999).

[74] O. L. Muskens, V. Giannini, J. A. Sánchez-Gil, and J. Gómez Rivas, "Strong enhancement of the radiative decay rate of emitters by single plasmonic nanoantennas," Nano Letters **7**, 2871–2875 (2007).

[75] G. M. Akselrod, C. Argyropoulos, T. B. Hoang, C. Ciracì, C. Fang, J. Huang, D. R. Smith, and M. H. Mikkelsen, "Probing the mechanisms of large purcell enhancement in plasmonic nanoantennas," Nature Photonics **8**, 835–840 (2014).

[76] Y. Xu, R. K. Lee, and A. Yariv, "Quantum analysis and the classical analysis of spontaneous emission in a microcavity," Phys. Rev. A **61**, 033807 (2000).

[77] S. R.-K. Rodriguez, "Classical and quantum distinctions between weak and strong coupling," European Journal of Physics **37**, 025802 (2016).

[78] E. T. Jaynes and F. W. Cummings, "Comparison of quantum and semiclassical radiation theories with application to the beam maser," Proceedings of the IEEE **51**, 89–109 (1963).

[79] J. J. Hopfield, "Theory of the contribution of excitons to the complex dielectric constant of crystals," Phys. Rev. **112**, 1555–1567 (1958).

[80] Y. Kaluzny, P. Goy, M. Gross, J. M. Raimond, and S. Haroche, "Observation of self-induced Rabi oscillations in two-level atoms excited inside a resonant cavity: The ringing regime of superradiance," Phys. Rev. Lett. **51**, 1175–1178 (1983).

[81] F. W. Cummings, "Stimulated emission of radiation in a single mode," Phys. Rev. **140**, A1051–A1056 (1965).

[82] J. H. Eberly, N. B. Narozhny, and J. J. Sanchez-Mondragon, "Periodic spontaneous collapse and revival in a simple quantum model," Phys. Rev. Lett. **44**, 1323–1326 (1980).

[83] S. Haroche and J. M. Raimond, "Radiative properties of Rydberg states in resonant cavities," Advances in Atomic and Molecular Physics **20**, 347–411 (1985).

[84] J. A. C. Gallas, G. Leuchs, H. Walther, and H. Figger, "Rydberg atoms: High-resolution spectroscopy and radiation interaction–Rydberg molecules," Advances in Atomic and Molecular Physics **20**, 413–466 (1985).

[85] G. Rempe, H. Walther, and N. Klein, "Observation of quantum collapse and revival in a one-atom maser," Phys. Rev. Lett. **58**, 353–356 (1987).

[86] M. Brune, J. M. Raimond, P. Goy, L. Davidovich, and S. Haroche, "Realization of a two-photon maser oscillator," Phys. Rev. Lett. **59**, 1899–1902 (1987).

[87] M. G. Raizen, R. J. Thompson, R. J. Brecha, H. J. Kimble, and H. J. Carmichael, "Normal-mode splitting and linewidth averaging for two-state atoms in an optical cavity," Phys. Rev. Lett. **63**, 240–243 (1989).

[88] R. J. Thompson, G. Rempe, and H. J. Kimble, "Observation of normal-mode splitting for an atom in an optical cavity," Phys. Rev. Lett. **68**, 1132–1135 (1992).

[89] J. P. Reithmaier, G. Sęk, A. Löffler, C. Hofmann, S. Kuhn, S. Reitzenstein, L. V. Keldysh, V. D. Kulakovskii, T. L. Reinecke, and A. Forchel, "Strong coupling in a single quantum dot-semiconductor microcavity system," Nature **432**, 197–200 (2004).

[90] T. Yoshie, A. Scherer, J. Hendrickson, G. Khitrova, H. M. Gibbs, G. Rupper, C. Ell, O. B. Shchekin, and D. G. Deppe, "Vacuum Rabi splitting with a single quantum dot in a photonic crystal nanocavity," Nature **432**, 200–203 (2004).

[91] D. G. Lidzey, D. D. C. Bradley, M. S. Skolnick, T. Virgili, S. Walker, and D. M. Whittaker, "Strong exciton–photon coupling in an organic semiconductor microcavity," Nature **395**, 53–55 (1998).

[92] C. Bonnand, J. Bellessa, and J. C. Plenet, "Properties of surface plasmons strongly coupled to excitons in an organic semiconductor near a metallic surface," Phys. Rev. B **73**, 245330 (2006).

[93] K. Santhosh, O. Bitton, L. Chuntonov, and G. Haran, "Vacuum Rabi splitting in a plasmonic cavity at the single quantum emitter limit," Nature Communications **7**, 11823 (2016).

[94] R. Chikkaraddy, B. de Nijs, F. Benz, S. J. Barrow, O. A. Scherman, E. Rosta, A. Demetriadou, P. Fox, O. Hess, and J. J. Baumberg, "Single-molecule strong coupling at room temperature in plasmonic nanocavities," Nature **535**, 127 (2016).

[95] P. G. Savvidis, J. J. Baumberg, R. M. Stevenson, M. S. Skolnick, D. M. Whittaker, and J. S. Roberts, "Angle-resonant stimulated polariton amplifier," Phys. Rev. Lett. **84**, 1547–1550 (2000).

[96] C. Ciuti, P. Schwendimann, B. Deveaud, and A. Quattropani, "Theory of the angle-resonant polariton amplifier," Phys. Rev. B **62**, R4825–R4828 (2000).

[97] R. M. Stevenson, V. N. Astratov, M. S. Skolnick, D. M. Whittaker, M. Emam-Ismail, A. I. Tartakovskii, P. G. Savvidis, J. J. Baumberg, and J. S. Roberts, "Continuous wave observation of massive polariton redistribution by stimulated scattering in semiconductor microcavities," Phys. Rev. Lett. **85**, 3680–3683 (2000).

[98] J. J. Baumberg, P. G. Savvidis, R. M. Stevenson, A. I. Tartakovskii, M. S. Skolnick, D. M. Whittaker, and J. S. Roberts, "Parametric oscillation in a vertical microcavity: A polariton condensate or micro-optical parametric oscillation," Phys. Rev. B **62**, R16247–R16250 (2000).

[99] A. Imamoğlu and R. Ram, "Quantum dynamics of exciton lasers," Physics Letters A **214**, 193 – 198 (1996).

[100] H. Deng, G. Weihs, D. Snoke, J. Bloch, and Y. Yamamoto, "Polariton lasing vs. photon lasing in a semiconductor microcavity," Proceedings of the National Academy of Sciences **100**, 15318–15323 (2003).

[101] J. Kasprzak, M. Richard, S. Kundermann, A. Baas, P. Jeambrun, J. M. J. Keeling, F. M. Marchetti, M. H. Szymańska, R. André, J. L. Staehli, V. Savona, P. B. Littlewood, B. Deveaud, and L. S. Dang, "Bose–Einstein condensation of exciton polaritons," Nature **443**, 409–414 (2006).

[102] R. Balili, V. Hartwell, D. Snoke, L. Pfeiffer, and K. West, "Bose–Einstein condensation of microcavity polaritons in a trap," Science **316**, 1007–1010 (2007).

[103] H. Mabuchi and A. C. Doherty, "Cavity quantum electrodynamics: Coherence in context," Science **298**, 1372–1377 (2002).

[104] H. J. Kimble, "Strong interactions of single atoms and photons in cavity QED," Physica Scripta **T76**, 127 (1998).

[105] J. M. Raimond, M. Brune, and S. Haroche, "Manipulating quantum entanglement with atoms and photons in a cavity," Rev. Mod. Phys. **73**, 565–582 (2001).

[106] Y. G. Rubo, F. P. Laussy, G. Malpuech, A. Kavokin, and P. Bigenwald, "Dynamical theory of polariton amplifiers," Phys. Rev. Lett. **91**, 156403 (2003).

[107] K. R. Patton and U. R. Fischer, "Hybrid of superconducting quantum interference device and atomic Bose–Einstein condensate: An architecture for quantum information processing," Phys. Rev. A **87**, 052303 (2013).

[108] D. Bajoni, E. Semenova, A. Lemaître, S. Bouchoule, E. Wertz, P. Senellart, and J. Bloch, "Polariton light-emitting diode in a GaAs-based microcavity," Phys. Rev. B **77**, 113303 (2008).

[109] S. I. Tsintzos, N. T. Pelekanos, G. Konstantinidis, Z. Hatzopoulos, and P. G. Savvidis, "A GaAs polariton light-emitting diode operating near room temperature," Nature **453**, 372–375 (2008).

[110] A. Amo, T. C. H. Liew, C. Adrados, R. Houdré, E. Giacobino, A. V. Kavokin, and A. Bramati, "Exciton-polariton spin switches," Nature Photonics **4**, 361–366 (2010).

[111] R. Johne, I. A. Shelykh, D. D. Solnyshkov, and G. Malpuech, "Polaritonic analogue of Datta and Das spin transistor," Phys. Rev. B **81**, 125327 (2010).

[112] T. C. H. Liew, A. V. Kavokin, T. Ostatnický, M. Kaliteevski, I. A. Shelykh, and R. A. Abram, "Exciton-polariton integrated circuits," Phys. Rev. B **82**, 033302 (2010).

[113] C. Leyder, T. C. H. Liew, A. V. Kavokin, I. A. Shelykh, M. Romanelli, J. P. Karr, E. Giacobino, and A. Bramati, "Interference of coherent polariton beams in microcavities: Polarization-controlled optical gates," Phys. Rev. Lett. **99**, 196402 (2007).

[114] T. Espinosa-Ortega and T. C. H. Liew, "Complete architecture of integrated photonic circuits based on and and not logic gates of exciton polaritons in semiconductor microcavities," Phys. Rev. B **87**, 195305 (2013).

[115] D. Ballarini, M. De Giorgi, E. Cancellieri, R. Houdré, E. Giacobino, R. Cingolani, A. Bramati, G. Gigli, and D. Sanvitto, "All-optical polariton transistor," Nature Communications **4**, 1778 (2013).

[116] D. Bajoni, E. Semenova, A. Lemaître, S. Bouchoule, E. Wertz, P. Senellart, S. Barbay, R. Kuszelewicz, and J. Bloch, "Optical bistability in a GaAs-based polariton diode," Phys. Rev. Lett. **101**, 266402 (2008).

[117] N. A. Gippius, I. A. Shelykh, D. D. Solnyshkov, S. S. Gavrilov, Y. G. Rubo, A. V. Kavokin, S. G. Tikhodeev, and G. Malpuech, "Polarization multistability of cavity polaritons," Phys. Rev. Lett. **98**, 236401 (2007).

[118] T. C. H. Liew, A. V. Kavokin, and I. A. Shelykh, "Optical circuits based on polariton neurons in semiconductor microcavities," Phys. Rev. Lett. **101**, 016402 (2008).

[119] B. Lounis and M. Orrit, "Single-photon sources," Reports on Progress in Physics **68**, 1129–1179 (2005).

[120] R. Loudon, *The Quantum Theory of Light* (Oxford University Press, 2000), 3rd ed.

[121] H. J. Carmichael and D. F. Walls, "A quantum-mechanical master equation treatment of the dynamical stark effect," Journal of Physics B: Atomic and Molecular Physics **9**, 1199–1219 (1976).

[122] H. J. Kimble and L. Mandel, "Theory of resonance fluorescence," Phys. Rev. A **13**, 2123–2144 (1976).

[123] H. J. Kimble, M. Dagenais, and L. Mandel, "Photon antibunching in resonance fluorescence," Phys. Rev. Lett. **39**, 691–695 (1977).

[124] F. Diedrich and H. Walther, "Nonclassical radiation of a single stored ion," Phys. Rev. Lett. **58**, 203–206 (1987).

[125] K. Brunner, U. Bockelmann, G. Abstreiter, M. Walther, G. Böhm, G. Tränkle, and G. Weimann, "Photoluminescence from a single GaAs/AlGaAs quantum dot," Phys. Rev. Lett. **69**, 3216–3219 (1992).

[126] J. Y. Marzin, J. M. Gérard, A. Izraël, D. Barrier, and G. Bastard, "Photoluminescence of single inas quantum dots obtained by self-organized growth on GaAs," Phys. Rev. Lett. **73**, 716–719 (1994).

[127] T. Basché, W. E. Moerner, M. Orrit, and H. Talon, "Photon antibunching in the fluorescence of a single dye molecule trapped in a solid," Phys. Rev. Lett. **69**, 1516–1519 (1992).

[128] C. Kurtsiefer, S. Mayer, P. Zarda, and H. Weinfurter, "Stable solid-state source of single photons," Phys. Rev. Lett. **85**, 290–293 (2000).

[129] P. Michler, A. Imamoglu, M. D. Mason, P. J. Carson, G. F. Strouse, and S. K. Buratto, "Quantum correlation among photons from a single quantum dot at room temperature," Nature **406**, 968–970 (2000).

[130] H. J. Kimble, "The quantum internet," Nature **453**, 1023–1030 (2008).

[131] C. H. Bennett, G. Brassard, and A. K. Ekert, "Quantum cryptography," Scientific American **267**, 50–57 (1992).

[132] N. Gisin, G. Ribordy, W. Tittel, and H. Zbinden, "Quantum cryptography," Rev. Mod. Phys. **74**, 145–195 (2002).

[133] E. Waks, K. Inoue, C. Santori, D. Fattal, J. Vuckovic, G. S. Solomon, and Y. Yamamoto, "Quantum cryptography with a photon turnstile," Nature **420**, 762–762 (2002).

[134] A. Beveratos, R. Brouri, T. Gacoin, A. Villing, J.-P. Poizat, and P. Grangier, "Single photon quantum cryptography," Phys. Rev. Lett. **89**, 187901 (2002).

[135] C. Marand and P. D. Townsend, "Quantum key distribution over distances as long as 30 km," Opt. Lett. **20**, 1695–1697 (1995).

[136] W. T. Buttler, R. J. Hughes, S. K. Lamoreaux, G. L. Morgan, J. E. Nordholt, and C. G. Peterson, "Daylight quantum key distribution over 1.6 km," Phys. Rev. Lett. **84**, 5652–5655 (2000).

[137] G. Brassard, N. Lütkenhaus, T. Mor, and B. C. Sanders, "Limitations on practical quantum cryptography," Phys. Rev. Lett. **85**, 1330–1333 (2000).

[138] N. Lütkenhaus, "Security against individual attacks for realistic quantum key distribution," Phys. Rev. A **61**, 052304 (2000).

[139] P. Kok, W. J. Munro, K. Nemoto, T. C. Ralph, J. P. Dowling, and G. J. Milburn, "Linear optical quantum computing with photonic qubits," Rev. Mod. Phys. **79**, 135–174 (2007).

[140] E. Knill, R. Laflamme, and G. J. Milburn, "A scheme for efficient quantum computation with linear optics," Nature **409**, 46–52 (2001).

[141] J. L. O'Brien, "Optical quantum computing," Science **318**, 1567–1570 (2007).

[142] X. Maître, E. Hagley, G. Nogues, C. Wunderlich, P. Goy, M. Brune, J. M. Raimond, and S. Haroche, "Quantum memory with a single photon in a cavity," Phys. Rev. Lett. **79**, 769–772 (1997).

[143] Y. Wang, J. Li, S. Zhang, K. Su, Y. Zhou, K. Liao, S. Du, H. Yan, and S.-L. Zhu, "Efficient quantum memory for single-photon polarization qubits," Nature Photonics **13**, 346–351 (2019).

[144] D. Bouwmeester, J.-W. Pan, K. Mattle, M. Eibl, H. Weinfurter, and A. Zeilinger, "Experimental quantum teleportation," Nature **390**, 575–579 (1997).

[145] Y. H. Shih and C. O. Alley, "New type of einstein-podolsky-rosen-bohm experiment using pairs of light quanta produced by optical parametric down conversion," Phys. Rev. Lett. **61**, 2921–2924 (1988).

[146] C. Santori, D. Fattal, J. Vučković, G. S. Solomon, and Y. Yamamoto, "Indistinguishable photons from a single-photon device," Nature **419**, 594–597 (2002).

[147] S. Laurent, S. Varoutsis, L. Le Gratiet, A. Lemaître, I. Sagnes, F. Raineri, A. Levenson, I. Robert-Philip, and I. Abram, "Indistinguishable single photons from a single-quantum dot in a two-dimensional photonic crystal cavity," Applied Physics Letters **87**, 163107 (2005).

[148] D. F. Walls, "Squeezed states of light," Nature **306**, 141–146 (1983).

[149] V. Giovannetti, S. Lloyd, and L. Maccone, "Quantum metrology," Phys. Rev. Lett. **96**, 010401 (2006).

[150] M. Xiao, L.-A. Wu, and H. J. Kimble, "Precision measurement beyond the shot-noise limit," Phys. Rev. Lett. **59**, 278–281 (1987).

[151] V. Giovannetti, S. Lloyd, and L. Maccone, "Quantum-enhanced measurements: Beating the standard quantum limit," Science **306**, 1330–1336 (2004).

[152] V. Giovannetti, S. Lloyd, and L. Maccone, "Quantum-enhanced positioning and clock synchronization," Nature **412**, 417–419 (2001).

[153] A. N. Boto, P. Kok, D. S. Abrams, S. L. Braunstein, C. P. Williams, and J. P. Dowling, "Quantum interferometric optical lithography: Exploiting entanglement to beat the diffraction limit," Phys. Rev. Lett. **85**, 2733–2736 (2000).

[154] A. J. Shields, "Semiconductor quantum light sources," Nature Photonics **1**, 215–223 (2007).

[155] Z. Yuan, B. E. Kardynal, R. M. Stevenson, A. J. Shields, C. J. Lobo, K. Cooper, N. S. Beattie, D. A. Ritchie, and M. Pepper, "Electrically driven single-photon source," Science **295**, 102–105 (2002).

[156] A. Kuhn, M. Hennrich, and G. Rempe, "Deterministic single-photon source for distributed quantum networking," Phys. Rev. Lett. **89**, 067901 (2002).

[157] B. Darquié, M. P. A. Jones, J. Dingjan, J. Beugnon, S. Bergamini, Y. Sortais, G. Messin, A. Browaeys, and P. Grangier, "Controlled single-photon emission from a single trapped two-level atom," Science **309**, 454–456 (2005).

[158] M. Keller, B. Lange, K. Hayasaka, W. Lange, and H. Walther, "Continuous generation of single photons with controlled waveform in an ion-trap cavity system," Nature **431**, 1075–1078 (2004).

[159] C. Brunel, B. Lounis, P. Tamarat, and M. Orrit, "Triggered source of single photons based on controlled single molecule fluorescence," Phys. Rev. Lett. **83**, 2722–2725 (1999).

[160] B. Lounis and W. E. Moerner, "Single photons on demand from a single molecule at room temperature," Nature **407**, 491–493 (2000).

[161] R. Brouri, A. Beveratos, J.-P. Poizat, and P. Grangier, "Photon antibunching in the fluorescence of individual color centers in diamond," Opt. Lett. **25**, 1294–1296 (2000).

[162] A. Beveratos, S. Kühn, R. Brouri, T. Gacoin, J.-P. Poizat, and P. Grangier, "Room temperature stable single-photon source," The European Physical Journal D - Atomic, Molecular, Optical and Plasma Physics **18**, 191–196 (2002).

[163] J. Kim, O. Benson, H. Kan, and Y. Yamamoto, "A single-photon turnstile device," Nature **397**, 500–503 (1999).

[164] C. Santori, M. Pelton, G. Solomon, Y. Dale, and Y. Yamamoto, "Triggered single photons from a quantum dot," Phys. Rev. Lett. **86**, 1502–1505 (2001).

[165] V. Zwiller, H. Blom, P. Jonsson, N. Panev, S. Jeppesen, T. Tsegaye, E. Goobar, M.-E. Pistol, L. Samuelson, and G. Björk, "Single quantum dots emit single photons at a time: Antibunching experiments," Applied Physics Letters **78**, 2476–2478 (2001).

[166] S. Buckley, K. Rivoire, and J. Vučković, "Engineered quantum dot single-photon sources," Reports on Progress in Physics **75**, 126503 (2012).

[167] G. S. Solomon, M. Pelton, and Y. Yamamoto, "Single-mode spontaneous emission from a single quantum dot in a three-dimensional microcavity," Phys. Rev. Lett. **86**, 3903–3906 (2001).

[168] A. Kuhn and D. Ljunggren, "Cavity-based single-photon sources," Contemporary Physics **51**, 289–313 (2010).

[169] I. Aharonovich, S. Castelletto, D. A. Simpson, C.-H. Su, A. D. Greentree, and S. Prawer, "Diamond-based single-photon emitters," Reports on Progress in Physics **74**, 076501 (2011).

[170] C. K. Hong and L. Mandel, "Experimental realization of a localized one-photon state," Phys. Rev. Lett. **56**, 58–60 (1986).

[171] J. Brendel, N. Gisin, W. Tittel, and H. Zbinden, "Pulsed energy-time entangled twin-photon source for quantum communication," Phys. Rev. Lett. **82**, 2594–2597 (1999).

[172] Z. Y. Ou and L. Mandel, "Violation of Bell's inequality and classical probability in a two-photon correlation experiment," Phys. Rev. Lett. **61**, 50–53 (1988).

[173] S. Fasel, O. Alibart, S. Tanzilli, P. Baldi, A. Beveratos, N. Gisin, and H. Zbinden, "High-quality asynchronous heralded single-photon source at telecom wavelength," New Journal of Physics **6**, 163–163 (2004).

[174] A. Faraon, A. Majumdar, and J. Vučković, "Generation of nonclassical states of light via photon blockade in optical nanocavities," Phys. Rev. A **81**, 033838 (2010).

[175] H. Carmichael, R. Brecha, and P. Rice, "Quantum interference and collapse of the wavefunction in cavity QED," Optics Communications **82**, 73 – 79 (1991).

[176] G. Rempe, R. J. Thompson, R. J. Brecha, W. D. Lee, and H. J. Kimble, "Optical bistability and photon statistics in cavity quantum electrodynamics," Phys. Rev. Lett. **67**, 1727–1730 (1991).

[177] J. McKeever, A. Boca, A. D. Boozer, R. Miller, J. R. Buck, A. Kuzmich, and H. J. Kimble, "Deterministic generation of single photons from one atom trapped in a cavity," Science **303**, 1992–1994 (2004).

[178] M. Hijlkema, B. Weber, H. P. Specht, S. C. Webster, A. Kuhn, and G. Rempe, "A single-photon server with just one atom," Nature Physics **3**, 253–255 (2007).

[179] T. A. Fulton and G. J. Dolan, "Observation of single-electron charging effects in small tunnel junctions," Phys. Rev. Lett. **59**, 109–112 (1987).

[180] M. A. Kastner, "The single-electron transistor," Rev. Mod. Phys. **64**, 849–858 (1992).

[181] A. Imamoğlu, H. Schmidt, G. Woods, and M. Deutsch, "Strongly interacting photons in a nonlinear cavity," Phys. Rev. Lett. **79**, 1467–1470 (1997).

[182] L. Tian and H. J. Carmichael, "Quantum trajectory simulations of two-state behavior in an optical cavity containing one atom," Phys. Rev. A **46**, R6801–R6804 (1992).

[183] H. Schmidt and A. Imamoglu, "Giant Kerr nonlinearities obtained by electromagnetically induced transparency," Opt. Lett. **21**, 1936–1938 (1996).

[184] P. Grangier, D. F. Walls, and K. M. Gheri, "Comment on "Strongly interacting photons in a nonlinear cavity"," Phys. Rev. Lett. **81**, 2833–2833 (1998).

[185] M. J. Werner and A. Imamoğlu, "Photon-photon interactions in cavity electromagnetically induced transparency," Phys. Rev. A **61**, 011801 (1999).

[186] S. Rebić, S. M. Tan, A. S. Parkins, and D. F. Walls, "Large Kerr nonlinearity with a single atom," Journal of Optics B: Quantum and Semiclassical Optics **1**, 490–495 (1999).

[187] S. Rebić, A. S. Parkins, and S. M. Tan, "Polariton analysis of a four-level atom strongly coupled to a cavity mode," Phys. Rev. A **65**, 043806 (2002).

[188] I. I. Smolyaninov, A. V. Zayats, A. Gungor, and C. C. Davis, "Single-photon tunneling via localized surface plasmons," Phys. Rev. Lett. **88**, 187402 (2002).

[189] K. M. Birnbaum, A. Boca, R. Miller, A. D. Boozer, T. E. Northup, and H. J. Kimble, "Photon blockade in an optical cavity with one trapped atom," Nature **436**, 87–90 (2005).

[190] B. Dayan, A. S. Parkins, T. Aoki, E. P. Ostby, K. J. Vahala, and H. J. Kimble, "A photon turnstile dynamically regulated by one atom," Science **319**, 1062–1065 (2008).

[191] A. Faraon, I. Fushman, D. Englund, N. Stoltz, P. Petroff, and J. Vučkovič, "Coherent generation of non-classical light on a chip via photon-induced tunnelling and blockade," Nature Physics **4**, 859–863 (2008).

[192] A. Reinhard, T. Volz, M. Winger, A. Badolato, K. J. Hennessy, E. L. Hu, and A. Imamoglu, "Strongly correlated photons on a chip," Nature Photonics **6**, 93–96 (2012).

[193] C. Lang, D. Bozyigit, C. Eichler, L. Steffen, J. M. Fink, A. A. Abdumalikov, M. Baur, S. Filipp, M. P. da Silva, A. Blais, and A. Wallraff, "Observation of resonant photon blockade at microwave frequencies using correlation function measurements," Phys. Rev. Lett. **106**, 243601 (2011).

[194] A. J. Hoffman, S. J. Srinivasan, S. Schmidt, L. Spietz, J. Aumentado, H. E. Türeci, and A. A. Houck, "Dispersive photon blockade in a superconducting circuit," Phys. Rev. Lett. **107**, 053602 (2011).

[195] K. Müller, A. Rundquist, K. A. Fischer, T. Sarmiento, K. G. Lagoudakis, Y. A. Kelaita, C. Sánchez Muñoz, E. del Valle, F. P. Laussy, and J. Vučković, "Coherent generation of nonclassical light on chip via detuned photon blockade," Phys. Rev. Lett. **114**, 233601 (2015).

[196] A. Verger, C. Ciuti, and I. Carusotto, "Polariton quantum blockade in a photonic dot," Phys. Rev. B **73**, 193306 (2006).

[197] H. J. Carmichael, P. Kochan, and B. C. Sanders, "Photon correlation spectroscopy," Phys. Rev. Lett. **77**, 631–634 (1996).

[198] L. Schneebeli, M. Kira, and S. W. Koch, "Characterization of strong light-matter coupling in semiconductor quantum-dot microcavities via photon-statistics spectroscopy," Phys. Rev. Lett. **101**, 097401 (2008).

[199] A. Kubanek, A. Ourjoumtsev, I. Schuster, M. Koch, P. W. H. Pinkse, K. Murr, and G. Rempe, "Two-photon gateway in one-atom cavity quantum electrodynamics," Phys. Rev. Lett. **101**, 203602 (2008).

[200] I. Schuster, A. Kubanek, A. Fuhrmanek, T. Puppe, P. W. H. Pinkse, K. Murr, and G. Rempe, "Nonlinear spectroscopy of photons bound to one atom," Nature Physics **4**, 382–385 (2008).

[201] D. E. Chang, A. S. Sørensen, E. A. Demler, and M. D. Lukin, "A single-photon transistor using nanoscale surface plasmons," Nature Physics **3**, 807–812 (2007).

[202] J. L. O'Brien, A. Furusawa, and J. Vuckovic, "Photonic quantum technologies," Nature Photonics **3**, 687–695 (2009).

[203] D. E. Chang, V. Vuletic, and M. D. Lukin, "Quantum nonlinear optics–photon by photon," Nature Photonics **8**, 685–694 (2014).

[204] D. Gerace, H. E. Türeci, A. Imamoglu, V. Giovannetti, and R. Fazio, "The quantum-optical Josephson interferometer," Nature Physics **5**, 281–284 (2009).

[205] A. D. Greentree, C. Tahan, J. H. Cole, and L. C. L. Hollenberg, "Quantum phase transitions of light," Nature Physics **2**, 856–861 (2006).

[206] D. G. Angelakis, M. F. Santos, and S. Bose, "Photon-blockade-induced mott transitions and xy spin models in coupled cavity arrays," Phys. Rev. A **76**, 031805 (2007).

[207] D. E. Chang, V. Gritsev, G. Morigi, V. Vuletic, M. D. Lukin, and E. A. Demler, "Crystallization of strongly interacting photons in a nonlinear optical fibre," Nature Physics **4**, 884–889 (2008).

[208] M. J. Hartmann, F. G. S. L. Brandão, and M. B. Plenio, "Strongly interacting polaritons in coupled arrays of cavities," Nature Physics **2**, 849–855 (2006).

[209] M. P. A. Fisher, P. B. Weichman, G. Grinstein, and D. S. Fisher, "Boson localization and the superfluid-insulator transition," Phys. Rev. B **40**, 546–570 (1989).

[210] I. Carusotto, D. Gerace, H. E. Tureci, S. De Liberato, C. Ciuti, and A. Imamoğlu, "Fermionized photons in an array of driven dissipative nonlinear cavities," Phys. Rev. Lett. **103**, 033601 (2009).

[211] M. J. Hartmann, "Polariton crystallization in driven arrays of lossy nonlinear resonators," Phys. Rev. Lett. **104**, 113601 (2010).

[212] T. C. H. Liew and V. Savona, "Single photons from coupled quantum modes," Phys. Rev. Lett. **104**, 183601 (2010).

[213] M. Bamba, A. Imamoğlu, I. Carusotto, and C. Ciuti, "Origin of strong photon antibunching in weakly nonlinear photonic molecules," Phys. Rev. A **83**, 021802 (2011).

[214] P. R. Rice and H. J. Carmichael, "Single-atom cavity-enhanced absorption. I. Photon statistics in the bad-cavity limit," IEEE Journal of Quantum Electronics **24**, 1351–1366 (1988).

[215] F. Casagrande and L. A. Lugiato, "Antibunching in absorptive optical bistability," Il Nuovo Cimento B (1971-1996) **55**, 173–190 (1980).

[216] R. J. Brecha, P. R. Rice, and M. Xiao, "N two-level atoms in a driven optical cavity: Quantum dynamics of forward photon scattering for weak incident fields," Phys. Rev. A **59**, 2392–2417 (1999).

[217] S. L. Mielke, G. T. Foster, and L. A. Orozco, "Nonclassical intensity correlations in cavity QED," Phys. Rev. Lett. **80**, 3948–3951 (1998).

[218] G. T. Foster, S. L. Mielke, and L. A. Orozco, "Intensity correlations in cavity QED," Phys. Rev. A **61**, 053821 (2000).

[219] M. Hennrich, A. Kuhn, and G. Rempe, "Transition from antibunching to bunching in cavity QED," Phys. Rev. Lett. **94**, 053604 (2005).

[220] R. E. Slusher, L. W. Hollberg, B. Yurke, J. C. Mertz, and J. F. Valley, "Observation of squeezed states generated by four-wave mixing in an optical cavity," Phys. Rev. Lett. **55**, 2409–2412 (1985).

[221] M. G. Raizen, L. A. Orozco, M. Xiao, T. L. Boyd, and H. J. Kimble, "Squeezed-state generation by the normal modes of a coupled system," Phys. Rev. Lett. **59**, 198–201 (1987).

[222] G. T. Foster, L. A. Orozco, H. M. Castro-Beltran, and H. J. Carmichael, "Quantum state reduction and conditional time evolution of wave-particle correlations in cavity QED," Phys. Rev. Lett. **85**, 3149–3152 (2000).

[223] A. Majumdar, M. Bajcsy, A. Rundquist, and J. Vučković, "Loss-enabled sub-poissonian light generation in a bimodal nanocavity," Phys. Rev. Lett. **108**, 183601 (2012).

[224] B. W. Shore and P. L. Knight, "The Jaynes-Cummings model," Journal of Modern Optics **40**, 1195–1238 (1993).

[225] A. D. Greentree, J. Koch, and J. Larson, "Fifty years of Jaynes-Cummings physics," Journal of Physics B Atomic Molecular Physics **46**, 220201 (2013).

[226] M. Tavis and F. W. Cummings, "Exact solution for an N-molecule–radiation-field Hamiltonian," Phys. Rev. **170**, 379–384 (1968).

[227] B. M. Garraway, "The Dicke model in quantum optics: Dicke model revisited," Philosophical Transactions of the Royal Society A: Mathematical, Physical and Engineering Sciences **369**, 1137–1155 (2011).

[228] P. Kirton, M. M. Roses, J. Keeling, and E. G. Dalla Torre, "Introduction to the dicke model: From equilibrium to nonequilibrium, and vice versa," Advanced Quantum Technologies **2**, 1800043 (2019).

[229] R. H. Dicke, "Coherence in spontaneous radiation processes," Phys. Rev. **93**, 99–110 (1954).

[230] M. Sánchez-Barquilla, R. E. F. Silva, and J. Feist, "Cumulant expansion for the treatment of light–matter interactions in arbitrary material structures," The Journal of Chemical Physics **152**, 034108 (2020).

[231] E. Waks and D. Sridharan, "Cavity QED treatment of interactions between a metal nanoparticle and a dipole emitter," Phys. Rev. A **82**, 043845 (2010).

[232] A. Sipahigil, R. E. Evans, D. D. Sukachev, M. J. Burek, J. Borregaard, M. K. Bhaskar, C. T. Nguyen, J. L. Pacheco, H. A. Atikian, C. Meuwly, R. M. Camacho, F. Jelezko, E. Bielejec, H. Park, M. Lončar, and M. D. Lukin, "An integrated diamond nanophotonics platform for quantum-optical networks," Science **354**, 847–850 (2016).

[233] D. E. Chang, A. S. Sørensen, P. R. Hemmer, and M. D. Lukin, "Quantum optics with surface plasmons," Phys. Rev. Lett. **97**, 053002 (2006).

[234] F. Peyskens and D. Englund, "Quantum photonics model for nonclassical light generation using integrated nanoplasmonic cavity-emitter systems," Phys. Rev. A **97**, 063844 (2018).

[235] K. A. Fischer, Y. A. Kelaita, N. V. Sapra, C. Dory, K. G. Lagoudakis, K. Müller, and J. Vučković, "On-chip architecture for self-homodyned nonclassical light," Phys. Rev. Applied **7**, 044002 (2017).

[236] A. Faraon, E. Waks, D. Englund, I. Fushman, and J. Vučkovič, "Efficient photonic crystal cavity-waveguide couplers," Applied Physics Letters **90**, 073102 (2007).

[237] K. A. Fischer, K. Müller, A. Rundquist, T. Sarmiento, A. Y. Piggott, Y. Kelaita, C. Dory, K. G. Lagoudakis, and J. Vuckovic, "Self-homodyne measurement of a dynamic mollow triplet in the solid state," Nature Photonics **10**, 163–166 (2016).

[238] K. Müller, K. A. Fischer, C. Dory, T. Sarmiento, K. G. Lagoudakis, A. Rundquist, Y. A. Kelaita, and J. Vučković, "Self-homodyne-enabled generation of indistinguishable photons," Optica **3**, 931–936 (2016).

[239] A. Rundquist, M. Bajcsy, A. Majumdar, T. Sarmiento, K. Fischer, K. G. Lagoudakis, S. Buckley, A. Y. Piggott, and J. Vučković, "Nonclassical higher-order photon correlations with a quantum dot strongly coupled to a photonic-crystal nanocavity," Phys. Rev. A **90**, 023846 (2014).

[240] A. Auffèves, D. Gerace, J.-M. Gérard, M. F. m. c. Santos, L. C. Andreani, and J.-P. Poizat, "Controlling the dynamics of a coupled atom-cavity system by pure dephasing," Phys. Rev. B **81**, 245419 (2010).

[241] G. Yeoman and G. M. Meyer, "Two-atom laser," Phys. Rev. A **58**, 2518–2527 (1998).

[242] E. del Valle, F. P. Laussy, F. Troiani, and C. Tejedor, "Entanglement and lasing with two quantum dots in a microcavity," Phys. Rev. B **76**, 235317 (2007).

[243] M. Radulaski, K. A. Fischer, K. G. Lagoudakis, J. L. Zhang, and J. Vučković, "Photon blockade in two-emitter-cavity systems," Phys. Rev. A **96**, 011801 (2017).

[244] A. Auffèves, D. Gerace, S. Portolan, A. Drezet, and M. F. Santos, "Few emitters in a cavity: From cooperative emission to individualization," New Journal of Physics **13**, 093020 (2011).

[245] C. Gies, F. Jahnke, and W. W. Chow, "Photon antibunching from few quantum dots in a cavity," Phys. Rev. A **91**, 061804 (2015).

[246] R. Bonifacio and L. A. Lugiato, "Cooperative radiation processes in two-level systems: Superfluorescence," Phys. Rev. A **11**, 1507–1521 (1975).

[247] R. Bonifacio, P. Schwendimann, and F. Haake, "Quantum statistical theory of superradiance. I," Phys. Rev. A **4**, 302–313 (1971).

[248] M. Gross and S. Haroche, "Superradiance: An essay on the theory of collective spontaneous emission," Physics Reports **93**, 301 – 396 (1982).

[249] J. P. Clemens and H. J. Carmichael, "Stochastic initiation of superradiance in a cavity: An approximation scheme within quantum trajectory theory," Phys. Rev. A **65**, 023815 (2002).

[250] D. Meiser and M. J. Holland, "Steady-state superradiance with alkaline-earth-metal atoms," Phys. Rev. A **81**, 033847 (2010).

[251] D. Meiser and M. J. Holland, "Intensity fluctuations in steady-state superradiance," Phys. Rev. A **81**, 063827 (2010).

[252] V. V. Temnov and U. Woggon, "Photon statistics in the cooperative spontaneous emission," Opt. Express **17**, 5774–5782 (2009).

[253] V. V. Temnov and U. Woggon, "Superradiance and subradiance in an inhomogeneously broadened ensemble of two-level systems coupled to a low-*Q* cavity," Phys. Rev. Lett. **95**, 243602 (2005).

[254] M. Gegg, A. Carmele, A. Knorr, and M. Richter, "Superradiant to subradiant phase transition in the open system Dicke model: Dark state cascades," New Journal of Physics **20**, 013006 (2018).

[255] H. J. Carmichael, "Quantum fluctuations in absorptive bistability without adiabatic elimination," Phys. Rev. A **33**, 3262–3269 (1986).

[256] P. D. Drummond and D. F. Walls, "Quantum theory of optical bistability. II. atomic fluorescence in a high-*Q* cavity," Phys. Rev. A **23**, 2563–2579 (1981).

[257] V. M. Parfenyev and S. S. Vergeles, "Quantum theory of a spaser-based nanolaser," Opt. Express **22**, 13671–13679 (2014).

[258] C. Gies, J. Wiersig, M. Lorke, and F. Jahnke, "Semiconductor model for quantum-dot-based microcavity lasers," Phys. Rev. A **75**, 013803 (2007).

[259] M. Richter, M. Gegg, T. S. Theuerholz, and A. Knorr, "Numerically exact solution of the many emitter–cavity laser problem: Application to the fully quantized spaser emission," Phys. Rev. B **91**, 035306 (2015).

[260] M. Gegg and M. Richter, "Efficient and exact numerical approach for many multi-level systems in open system CQED," New Journal of Physics **18**, 043037 (2016).

[261] A. Grankin, E. Brion, E. Bimbard, R. Boddeda, I. Usmani, A. Ourjoumtsev, and P. Grangier, "Quantum statistics of light transmitted through an intracavity Rydberg medium," New Journal of Physics **16**, 043020 (2014).

[262] A. V. Gorshkov, J. Otterbach, M. Fleischhauer, T. Pohl, and M. D. Lukin, "Photon-photon interactions via Rydberg blockade," Phys. Rev. Lett. **107**, 133602 (2011).

[263] R. Sáez-Blázquez, J. Feist, A. I. Fernández-Domínguez, and F. J. García-Vidal, "Enhancing photon correlations through plasmonic strong coupling," Optica **4**, 1363–1367 (2017).

[264] R. Sáez-Blázquez, J. Feist, F. J. García-Vidal, and A. I. Fernández-Domínguez, "Photon statistics in collective strong coupling: Nanocavities and microcavities," Phys. Rev. A **98**, 013839 (2018).

[265] H. S. Dhar, M. Zens, D. O. Krimer, and S. Rotter, "Variational renormalization group for dissipative spin-cavity systems: Periodic pulses of nonclassical photons from mesoscopic spin ensembles," Phys. Rev. Lett. **121**, 133601 (2018).

[266] R. Trivedi, M. Radulaski, K. A. Fischer, S. Fan, and J. Vučković, "Photon blockade in weakly driven cavity quantum electrodynamics systems with many emitters," Phys. Rev. Lett. **122**, 243602 (2019).

[267] F. Herrera, B. Peropadre, L. A. Pachon, S. K. Saikin, and A. Aspuru-Guzik, "Quantum nonlinear optics with polar J-aggregates in microcavities," The Journal of Physical Chemistry Letters **5**, 3708–3715 (2014).

[268] F. Barachati, S. De Liberato, and S. Kéna-Cohen, "Generation of Rabi-frequency radiation using exciton-polaritons," Phys. Rev. A **92**, 033828 (2015).

[269] J. A. Ćwik, P. Kirton, S. De Liberato, and J. Keeling, "Excitonic spectral features in strongly coupled organic polaritons," Phys. Rev. A **93**, 033840 (2016).

[270] A. Thomas, J. George, A. Shalabney, M. Dryzhakov, S. J. Varma, J. Moran, T. Chervy, X. Zhong, E. Devaux, C. Genet, J. A. Hutchison, and T. W. Ebbesen, "Ground-state chemical reactivity under vibrational coupling to the vacuum electromagnetic field," Angewandte Chemie International Edition **55**, 11462–11466 (2016).

[271] F. Herrera and F. C. Spano, "Cavity-controlled chemistry in molecular ensembles," Phys. Rev. Lett. **116**, 238301 (2016).

[272] B. Munkhbat, M. Wersäll, D. G. Baranov, T. J. Antosiewicz, and T. Shegai, "Suppression of photo-oxidation of organic chromophores by strong coupling to plasmonic nanoantennas," Science Advances **4** (2018).

[273] J. A. Hutchison, T. Schwartz, C. Genet, E. Devaux, and T. W. Ebbesen, "Modifying chemical landscapes by coupling to vacuum fields," Angewandte Chemie International Edition **51**, 1592–1596 (2012).

[274] J. Feist, J. Galego, and F. J. Garcia-Vidal, "Polaritonic chemistry with organic molecules," ACS Photonics **5**, 205–216 (2018).

[275] R. F. Ribeiro, L. A. Martínez-Martínez, M. Du, J. Campos-Gonzalez-Angulo, and J. Yuen-Zhou, "Polariton chemistry: Controlling molecular dynamics with optical cavities," Chem. Sci. **9**, 6325–6339 (2018).

[276] J. Galego, F. J. Garcia-Vidal, and J. Feist, "Cavity-induced modifications of molecular structure in the strong-coupling regime," Phys. Rev. X **5**, 041022 (2015).

[277] J. Galego, F. J. Garcia-Vidal, and J. Feist, "Suppressing photochemical reactions with quantized light fields," Nature Communications **7**, 13841 (2016).

[278] J. A. Hutchison, A. Liscio, T. Schwartz, A. Canaguier-Durand, C. Genet, V. Palermo, P. Samorì, and T. W. Ebbesen, "Tuning the work-function via strong coupling," Advanced Materials **25**, 2481–2485 (2013).

[279] S. Wang, A. Mika, J. A. Hutchison, C. Genet, A. Jouaiti, M. W. Hosseini, and T. W. Ebbesen, "Phase transition of a perovskite strongly coupled to the vacuum field," Nanoscale **6**, 7243–7248 (2014).

[280] J. Flick, M. Ruggenthaler, H. Appel, and A. Rubio, "Atoms and molecules in cavities, from weak to strong coupling in quantum-electrodynamics (QED) chemistry," Proceedings of the National Academy of Sciences **114**, 3026–3034 (2017).

[281] E. Orgiu, J. George, J. A. Hutchison, E. Devaux, J. F. Dayen, B. Doudin, F. Stellacci, C. Genet, J. Schachenmayer, C. Genes, G. Pupillo, P. Samorì, and T. W. Ebbesen, "Conductivity in organic semiconductors hybridized with the vacuum field," Nature Materials **14**, 1123 (2015).

[282] J. Feist and F. J. Garcia-Vidal, "Extraordinary exciton conductance induced by strong coupling," Phys. Rev. Lett. **114**, 196402 (2015).

[283] B. A. Gregg, "Excitonic solar cells," The Journal of Physical Chemistry B **107**, 4688–4698 (2003).

[284] J.-L. Brédas, J. E. Norton, J. Cornil, and V. Coropceanu, "Molecular understanding of organic solar cells: The challenges," Accounts of Chemical Research **42**, 1691–1699 (2009).

[285] S. Hofmann, T. C. Rosenow, M. C. Gather, B. Lüssem, and K. Leo, "Singlet exciton diffusion length in organic light-emitting diodes," Phys. Rev. B **85**, 245209 (2012).

[286] A. A. High, E. E. Novitskaya, L. V. Butov, M. Hanson, and A. C. Gossard, "Control of exciton fluxes in an excitonic integrated circuit," Science **321**, 229–231 (2008).

[287] S. M. Menke, W. A. Luhman, and R. J. Holmes, "Tailored exciton diffusion in organic photovoltaic cells for enhanced power conversion efficiency," Nature Materials **114**, 152–157 (2013).

[288] Z. G. Soos and R. C. Powell, "Generalized random-walk model for singlet-exciton energy transfer," Phys. Rev. B **6**, 4035–4046 (1972).

[289] R. C. Powell and Z. G. Soos, "Singlet exciton energy transfer in organic solids," Journal of Luminescence **11**, 1 – 45 (1975).

[290] R. R. Lunt, N. C. Giebink, A. A. Belak, J. B. Benziger, and S. R. Forrest, "Exciton diffusion lengths of organic semiconductor thin films measured by spectrally resolved photoluminescence quenching," Journal of Applied Physics **105**, 053711 (2009).

[291] T. Förster, "10th spiers memorial lecture. Transfer mechanisms of electronic excitation," Discuss. Faraday Soc. **27**, 7–17 (1959).

[292] D. L. Dexter, "A theory of sensitized luminescence in solids," The Journal of Chemical Physics **21**, 836–850 (1953).

[293] D. Andrews, "A unified theory of radiative and radiationless molecular energy transfer," Chemical Physics **135**, 195 – 201 (1989).

[294] P. Andrew and W. L. Barnes, "Energy transfer across a metal film mediated by surface plasmon polaritons," Science **306**, 1002–1005 (2004).

[295] F. Le Kien, S. D. Gupta, K. P. Nayak, and K. Hakuta, "Nanofiber-mediated radiative transfer between two distant atoms," Phys. Rev. A **72**, 063815 (2005).

[296] T. Förster, "Zwischenmolekulare energiewanderung und fluoreszenz," Annalen der Physik **437**, 55–75 (1948).

[297] L. Stryer and R. P. Haugland, "Energy transfer: A spectroscopic ruler," Proceedings of the National Academy of Sciences **58**, 719–726 (1967).

[298] S. Weiss, "Fluorescence spectroscopy of single biomolecules," Science **283**, 1676–1683 (1999).

[299] J. R. Lakowicz, *Energy Transfer* (Springer US, 1999), pp. 367–394.

[300] D. M. Willard, L. L. Carillo, J. Jung, and A. Van Orden, "CdSe–ZnS quantum dots as resonance energy transfer donors in a model protein–protein binding assay," Nano Letters **1**, 469–474 (2001).

[301] S. Wang, N. Mamedova, N. A. Kotov, W. Chen, and J. Studer, "Antigen/antibody immunocomplex from CdTe nanoparticle bioconjugates," Nano Letters **2**, 817–822 (2002).

[302] B. Schuler, E. A. Lipman, and W. A. Eaton, "Probing the free-energy surface for protein folding with single-molecule fluorescence spectroscopy," Nature **419**, 743–747 (2002).

[303] P. Carriba, G. Navarro, F. Ciruela, S. Ferré, V. Casadó, L. Agnati, A. Cortés, J. Mallol, K. Fuxe, E. I. Canela, C. Lluís, and R. Franco, "Detection of heteromerization of more than two proteins by sequential BRET-FRET," Nature Methods **5**, 727–733 (2008).

[304] S. Weiss, "Measuring conformational dynamics of biomolecules by single molecule fluorescence spectroscopy," Nature Structural Biology **7**, 724–729 (2000).

[305] R. Roy, S. Hohng, and T. Ha, "A practical guide to single-molecule FRET," Nature Methods **5**, 507–516 (2008).

[306] A. Miyawaki, J. Llopis, R. Heim, J. M. McCaffery, J. A. Adams, M. Ikura, and R. Y. Tsien, "Fluorescent indicators for Ca2+based on green fluorescent proteins and calmodulin," Nature **388**, 882–887 (1997).

[307] I. L. Medintz, A. R. Clapp, H. Mattoussi, E. R. Goldman, B. Fisher, and J. M. Mauro, "Self-assembled nanoscale biosensors based on quantum dot FRET donors," Nature Materials **2**, 630–638 (2003).

[308] A. M. Dennis, W. J. Rhee, D. Sotto, S. N. Dublin, and G. Bao, "Quantum dot–fluorescent protein FRET probes for sensing intracellular pH," ACS Nano **6**, 2917–2924 (2012).

[309] M. A. Baldo, M. E. Thompson, and S. R. Forrest, "High-efficiency fluorescent organic light-emitting devices using a phosphorescent sensitizer," Nature **403**, 750–753 (2000).

[310] V. Vohra, G. Calzaferri, S. Destri, M. Pasini, W. Porzio, and C. Botta, "Toward white light emission through efficient two-step energy transfer in hybrid nanofibers," ACS Nano **4**, 1409–1416 (2010).

[311] S. Chanyawadee, P. G. Lagoudakis, R. T. Harley, M. D. B. Charlton, D. V. Talapin, H. W. Huang, and C.-H. Lin, "Increased color-conversion efficiency in hybrid light-emitting diodes utilizing non-radiative energy transfer," Advanced Materials **22**, 602–606 (2010).

[312] N. Cicek, S. Nizamoglu, T. Ozel, E. Mutlugun, D. U. Karatay, V. Lesnyak, T. Otto, N. Gaponik, A. Eychmüller, and H. V. Demir, "Structural tuning of color chromaticity through nonradiative energy transfer by interspacing cdte nanocrystal monolayers," Applied Physics Letters **94**, 061105 (2009).

[313] S. Nizamoglu, E. Sari, J.-H. Baek, I.-H. Lee, and H. V. Demir, "White light generation by resonant nonradiative energy transfer from epitaxial InGaN/GaN quantum wells to colloidal CdSe/ZnS core/shell quantum dots," New Journal of Physics **10**, 123001 (2008).

[314] S. Chanyawadee, R. T. Harley, M. Henini, D. V. Talapin, and P. G. Lagoudakis, "Photocurrent enhancement in hybrid nanocrystal quantum-dot p—i—n photovoltaic devices," Phys. Rev. Lett. **102**, 077402 (2009).

[315] S. Buhbut, S. Itzhakov, E. Tauber, M. Shalom, I. Hod, T. Geiger, Y. Garini, D. Oron, and A. Zaban, "Built-in quantum dot antennas in dye-sensitized solar cells," ACS Nano **4**, 1293–1298 (2010).

[316] J. Lee, A. O. Govorov, and N. A. Kotov, "Bioconjugated superstructures of CdTe nanowires and nanoparticles: Multistep cascade Förster resonance energy transfer and energy channeling," Nano Letters **5**, 2063–2069 (2005).

[317] T. Franzl, T. A. Klar, S. Schietinger, A. L. Rogach, and J. Feldmann, "Exciton recycling in graded gap nanocrystal structures," Nano Letters **4**, 1599–1603 (2004).

[318] S. Bidault, A. Devilez, P. Ghenuche, B. Stout, N. Bonod, and J. Wenger, "Competition between Förster resonance energy transfer and donor photodynamics in plasmonic dimer nanoantennas," ACS Photonics **3**, 895–903 (2016).

[319] J. de Torres, M. Mivelle, S. B. Moparthi, H. Rigneault, N. F. Van Hulst, M. F. García-Parajó, E. Margeat, and J. Wenger, "Plasmonic nanoantennas enable forbidden Förster dipole-dipole energy transfer and enhance the FRET efficiency," Nano Letters **16**, 6222–6230 (2016).

[320] A. Iqbal, S. Arslan, B. Okumus, T. J. Wilson, G. Giraud, D. G. Norman, T. Ha, and D. M. J. Lilley, "Orientation dependence in fluorescent energy transfer between Cy3 and Cy5 terminally attached to double-stranded nucleic acids," Proceedings of the National Academy of Sciences **105**, 11176–11181 (2008).

[321] L. Folan, S. Arnold, and S. Druger, "Enhanced energy transfer within a microparticle," Chemical Physics Letters **118**, 322 – 327 (1985).

[322] S. D. Druger, S. Arnold, and L. M. Folan, "Theory of enhanced energy transfer between molecules embedded in spherical dielectric particles," The Journal of Chemical Physics **87**, 2649–2659 (1987).

[323] T. Kobayashi, Q. Zheng, and T. Sekiguchi, "Resonant dipole-dipole interaction in a cavity," Phys. Rev. A **52**, 2835–2846 (1995).

[324] G. S. Agarwal and S. D. Gupta, "Microcavity-induced modification of the dipole-dipole interaction," Phys. Rev. A **57**, 667–670 (1998).

[325] G. Kurizki and A. Z. Genack, "Suppression of molecular interactions in periodic dielectric structures," Phys. Rev. Lett. **61**, 2269–2271 (1988).

[326] S. John and J. Wang, "Quantum optics of localized light in a photonic band gap," Phys. Rev. B **43**, 12772–12789 (1991).

[327] M. Hopmeier, W. Guss, M. Deussen, E. O. Göbel, and R. F. Mahrt, "Enhanced dipole-dipole interaction in a polymer microcavity," Phys. Rev. Lett. **82**, 4118–4121 (1999).

[328] W. L. Barnes, "Fluorescence near interfaces: The role of photonic mode density," Journal of Modern Optics **45**, 661–699 (1998).

[329] P. Andrew and W. L. Barnes, "Förster energy transfer in an optical microcavity," Science **290**, 785–788 (2000).

[330] S. Götzinger, L. de S. Menezes, A. Mazzei, S. Kühn, V. Sandoghdar, and O. Benson, "Controlled photon transfer between two individual nanoemitters via shared high-Q modes of a microsphere resonator," Nano Letters **6**, 1151–1154 (2006).

[331] A. Konrad, M. Metzger, A. M. Kern, M. Brecht, and A. J. Meixner, "Controlling the dynamics of Förster resonance energy transfer inside a tunable sub-wavelength Fabry–Pérot-resonator," Nanoscale **7**, 10204–10209 (2015).

[332] M. Lunz, V. A. Gerard, Y. K. Gun'ko, V. Lesnyak, N. Gaponik, A. S. Susha, A. L. Rogach, and A. L. Bradley, "Surface plasmon enhanced energy transfer between donor and acceptor CdTe nanocrystal quantum dot monolayers," Nano Letters **11**, 3341–3345 (2011).

[333] X. Zhang, C. A. Marocico, M. Lunz, V. A. Gerard, Y. K. Gun'ko, V. Lesnyak, N. Gaponik, A. S. Susha, A. L. Rogach, and A. L. Bradley, "Wavelength, concentration, and distance dependence of nonradiative energy transfer to a plane of gold nanoparticles," ACS Nano **6**, 9283–9290 (2012).

[334] F. Reil, U. Hohenester, J. R. Krenn, and A. Leitner, "Förster-type resonant energy transfer influenced by metal nanoparticles," Nano Letters **8**, 4128–4133 (2008).

[335] N. Aissaoui, K. Moth-Poulsen, M. Käll, P. Johansson, L. M. Wilhelmsson, and B. Albinsson, "FRET enhancement close to gold nanoparticles positioned in DNA origami constructs," Nanoscale **9**, 673–683 (2017).

[336] P. Ghenuche, M. Mivelle, J. de Torres, S. B. Moparthi, H. Rigneault, N. F. Van Hulst, M. F. García-Parajó, and J. Wenger, "Matching nanoantenna field confinement to FRET distances enhances Förster energy transfer rates," Nano Letters **15**, 6193–6201 (2015).

[337] V. Faessler, C. Hrelescu, A. Lutich, L. Osinkina, S. Mayilo, and F. J "Accelerating fluorescence resonance energy transfer with plasmonic nanoresonators," Chemical Physics Letters **508**, 67 – 70 (2011).

[338] Chris E. Finlayson and David S. Ginger and Neil C. Greenham, "Enhanced Förster energy transfer in organic/inorganic bilayer optical microcavities," Chemical Physics Letters **338**, 83 – 87 (2001).

[339] C. Blum, N. Zijlstra, A. Lagendijk, M. Wubs, A. P. Mosk, V. Subramaniam, and W. L. Vos, "Nanophotonic control of the Förster resonance energy transfer efficiency," Phys. Rev. Lett. **109**, 203601 (2012).

[340] M. J. A. de Dood, J. Knoester, A. Tip, and A. Polman, "Förster transfer and the local optical density of states in erbium-doped silica," Phys. Rev. B **71**, 115102 (2005).

[341] K. Rustomji, M. Dubois, B. Kuhlmey, C. M. de Sterke, S. Enoch, R. Abdeddaim, and J. Wenger, "Direct imaging of the energy-transfer enhancement between two dipoles in a photonic cavity," Phys. Rev. X **9**, 011041 (2019).

[342] C. L. Cortes and Z. Jacob, "Fundamental figures of merit for engineering Förster resonance energy transfer," Opt. Express **26**, 19371–19387 (2018).

[343] J. A. Gonzaga-Galeana and J. R. Zurita-Sánchez, "A revisitation of the Förster energy transfer near a metallic spherical nanoparticle: (1) Efficiency enhancement or reduction? (2) The control of the Förster radius of the unbounded medium. (3) The impact of the local density of states," The Journal of Chemical Physics **139**, 244302 (2013).

[344] M. Wubs and W. L. Vos, "Förster resonance energy transfer rate in any dielectric nanophotonic medium with weak dispersion," New Journal of Physics **18**, 053037 (2016).

[345] C. A. Marocico, X. Zhang, and A. L. Bradley, "A theoretical investigation of the influence of gold nanosphere size on the decay and energy transfer rates and efficiencies of quantum emitters," The Journal of Chemical Physics **144**, 024108 (2016).

[346] H. T. Dung, L. Knöll, and D.-G. Welsch, "Intermolecular energy transfer in the presence of dispersing and absorbing media," Phys. Rev. A **65**, 043813 (2002).

[347] D. Martín-Cano, L. Martín-Moreno, F. J. García-Vidal, and E. Moreno, "Resonance energy transfer and superradiance mediated by plasmonic nanowaveguides," Nano Letters **10**, 3129–3134 (2010).

[348] J. I. Gersten and A. Nitzan, "Accelerated energy transfer between molecules near a solid particle," Chemical Physics Letters **104**, 31 – 37 (1984).

[349] X. M. Hua, J. I. Gersten, and A. Nitzan, "Theory of energy transfer between molecules near solid state particles," The Journal of Chemical Physics **83**, 3650–3659 (1985).

[350] J. Zhang, Y. Fu, and J. R. Lakowicz, "Enhanced Förster resonance energy transfer (FRET) on a single metal particle," The Journal of Physical Chemistry C **111**, 50–56 (2007).

[351] X. Zhang, C. A. Marocico, M. Lunz, V. A. Gerard, Y. K. Gun'ko, V. Lesnyak, N. Gaponik, A. S. Susha, A. L. Rogach, and A. L. Bradley, "Experimental and theoretical investigation of the distance dependence of localized surface plasmon coupled Förster resonance energy transfer," ACS Nano **8**, 1273–1283 (2014).

[352] P. Michetti and G. C. La Rocca, "Polariton states in disordered organic microcavities," Phys. Rev. B **71**, 115320 (2005).

[353] V. M. Agranovich and Y. N. Gartstein, "Nature and dynamics of low-energy exciton polaritons in semiconductor microcavities," Phys. Rev. B **75**, 075302 (2007).

[354] H. Najafov, B. Lee, Q. Zhou, L. C. Feldman, and V. Podzorov, "Observation of long-range exciton diffusion in highly ordered organic semiconductors," Nature Materials **9**, 938–943 (2010).

[355] J. R. Salcedo, A. E. Siegman, D. D. Dlott, and M. D. Fayer, "Dynamics of energy transport in molecular crystals: The picosecond transient-grating method," Phys. Rev. Lett. **41**, 131–134 (1978).

[356] D. Sanvitto, F. Pulizzi, A. J. Shields, P. C. M. Christianen, S. N. Holmes, M. Y. Simmons, D. A. Ritchie, J. C. Maan, and M. Pepper, "Observation of charge transport by negatively charged excitons," Science **294**, 837–839 (2001).

[357] J. Schachenmayer, C. Genes, E. Tignone, and G. Pupillo, "Cavity-enhanced transport of excitons," Phys. Rev. Lett. **114**, 196403 (2015).

[358] D. Hagenmüller, J. Schachenmayer, S. Schütz, C. Genes, and G. Pupillo, "Cavity-enhanced transport of charge," Phys. Rev. Lett. **119**, 223601 (2017).

[359] S. Aberra Guebrou, C. Symonds, E. Homeyer, J. C. Plenet, Y. N. Gartstein, V. M. Agranovich, and J. Bellessa, "Coherent emission from a disordered organic semiconductor induced by strong coupling with surface plasmons," Phys. Rev. Lett. **108**, 066401 (2012).

[360] L. Shi, T. K. Hakala, H. T. Rekola, J.-P. Martikainen, R. J. Moerland, and P. Törmä, "Spatial coherence properties of organic molecules coupled to plasmonic surface lattice resonances in the weak and strong coupling regimes," Phys. Rev. Lett. **112**, 153002 (2014).

[361] J. Wei, F. Zhao, J. Liu, Q. Zhao, N. Wu, and D. Xu, "Enhanced exciton transport in an optical cavity field with spatially varying profile," Phys. Rev. E **100**, 012125 (2019).

[362] J. Liu, Q. Zhao, and N. Wu, "Vibration-assisted exciton transfer in molecular aggregates strongly coupled to confined light fields," The Journal of Chemical Physics **150**, 105102 (2019).

[363] C. Gonzalez-Ballestero, J. Feist, E. Moreno, and F. J. Garcia-Vidal, "Harvesting excitons through plasmonic strong coupling," Phys. Rev. B **92**, 121402 (2015).

[364] V. Agranovich, H. Benisty, and C. Weisbuch, "Organic and inorganic quantum wells in a microcavity: Frenkel-Wannier-Mott excitons hybridization and energy transformation," Solid State Communications **102**, 631–636 (1997).

[365] J. Wainstain, C. Delalande, D. Gendt, M. Voos, J. Bloch, V. Thierry-Mieg, and R. Planel, "Dynamics of polaritons in a semiconductor multiple-quantum-well microcavity," Phys. Rev. B **58**, 7269–7278 (1998).

[366] D. G. Lidzey, D. D. C. Bradley, A. Armitage, S. Walker, and M. S. Skolnick, "Photon-mediated hybridization of frenkel excitons in organic semiconductor microcavities," Science **288**, 1620–1623 (2000).

[367] R. J. Holmes, S. Kéna-Cohen, V. M. Menon, and S. R. Forrest, "Strong coupling and hybridization of Frenkel and Wannier-Mott excitons in an organic-inorganic optical microcavity," Phys. Rev. B **74**, 235211 (2006).

[368] J. Wenus, R. Parashkov, S. Ceccarelli, A. Brehier, J.-S. Lauret, M. S. Skolnick, E. Deleporte, and D. G. Lidzey, "Hybrid organic-inorganic exciton-polaritons in a strongly coupled microcavity," Phys. Rev. B **74**, 235212 (2006).

[369] G. H. Lodden and R. J. Holmes, "Long-range, photon-mediated exciton hybridization in an all-organic, one-dimensional photonic crystal," Phys. Rev. Lett. **109**, 096401 (2012).

[370] D. M. Coles, N. Somaschi, P. Michetti, C. Clark, P. G. Lagoudakis, P. G. Savvidis, and D. G. Lidzey, "Polariton-mediated energy transfer between organic dyes in a strongly coupled optical microcavity," Nature Materials **13**, 712 (2014).

[371] X. Zhong, T. Chervy, S. Wang, J. George, A. Thomas, J. A. Hutchison, E. Devaux, C. Genet, and T. W. Ebbesen, "Non-radiative energy transfer mediated by hybrid light-matter states," Angewandte Chemie International Edition **55**, 6202–6206 (2016).

[372] X. Zhong, T. Chervy, L. Zhang, A. Thomas, J. George, C. Genet, J. A. Hutchison, and T. W. Ebbesen, "Energy transfer between spatially separated entangled molecules," Angewandte Chemie International Edition **56**, 9034–9038 (2017).

[373] F. J. Garcia-Vidal and J. Feist, "Long-distance operator for energy transfer," Science **357**, 1357–1358 (2017).

[374] K. Akulov, D. Bochman, A. Golombek, and T. Schwartz, "Long-distance resonant energy transfer mediated by hybrid plasmonic–photonic modes," The Journal of Physical Chemistry C **122**, 15853–15860 (2018).

[375] R. Sáez-Blázquez, J. Feist, A. I. Fernández-Domínguez, and F. J. García-Vidal, "Organic polaritons enable local vibrations to drive long-range energy transfer," Phys. Rev. B **97**, 241407 (2018).

[376] M. Reitz, F. Mineo, and C. Genes, "Energy transfer and correlations in cavity-embedded donor-acceptor configurations," Scientific Reports **8**, 9050 (2018).

[377] M. Du, L. A. Martínez-Martínez, R. F. Ribeiro, Z. Hu, V. M. Menon, and J. Yuen-Zhou, "Theory for polariton-assisted remote energy transfer," Chem. Sci. **9**, 6659–6669 (2018).

[378] D. J. Gorman, B. Hemmerling, E. Megidish, S. A. Moeller, P. Schindler, M. Sarovar, and H. Haeffner, "Engineering vibrationally assisted energy transfer in a trapped-ion quantum simulator," Phys. Rev. X **8**, 011038 (2018).

[379] G. Groenhof and J. J. Toppari, "Coherent light harvesting through strong coupling to confined light," The Journal of Physical Chemistry Letters **9**, 4848–4851 (2018).

[380] R. van Grondelle and V. I. Novoderezhkin, "Energy transfer in photosynthesis: Experimental insights and quantitative models," Phys. Chem. Chem. Phys. **8**, 793–807 (2006).

[381] G. D. Scholes, G. R. Fleming, A. Olaya-Castro, and R. van Grondelle, "Lessons from nature about solar light harvesting," Nature Chemistry **3**, 763–774 (2011).

[382] P. D. Frischmann, K. Mahata, and F. Würthner, "Powering the future of molecular artificial photosynthesis with light-harvesting metallosupramolecular dye assemblies," Chem. Soc. Rev. **42**, 1847–1870 (2013).

[383] X.-B. Li, C.-H. Tung, and L.-Z. Wu, "Semiconducting quantum dots for artificial photosynthesis," Nature Reviews Chemistry **2**, 160–173 (2018).

[384] J. Barber, "Photosynthetic energy conversion: Natural and artificial," Chem. Soc. Rev. **38**, 185–196 (2009).

[385] G. S. Engel, T. R. Calhoun, E. L. Read, T.-K. Ahn, T. Mančal, Y.-C. Cheng, R. E. Blankenship, and G. R. Fleming, "Evidence for wavelike energy transfer through quantum coherence in photosynthetic systems," Nature **446**, 782–786 (2007).

[386] H. Lee, Y.-C. Cheng, and G. R. Fleming, "Coherence dynamics in photosynthesis: Protein protection of excitonic coherence," Science **316**, 1462–1465 (2007).

[387] E. Wientjes, J. Renger, A. G. Curto, R. Cogdell, and N. F. van Hulst, "Strong antenna-enhanced fluorescence of a single light-harvesting complex shows photon anti-bunching," Nature Communications **5**, 4236 (2014).

[388] F. Caruso, A. W. Chin, A. Datta, S. F. Huelga, and M. B. Plenio, "Highly efficient energy excitation transfer in light-harvesting complexes: The fundamental role of noise-assisted transport," The Journal of Chemical Physics **131**, 105106 (2009).

[389] G. D. Scholes, "Long-range resonance energy transfer in molecular systems," Annual Review of Physical Chemistry **54**, 57–87 (2003).

[390] J. A. Leegwater, "Coherent versus incoherent energy transfer and trapping in photosynthetic antenna complexes," The Journal of Physical Chemistry **100**, 14403–14409 (1996).

[391] H. Sumi, "Theory on rates of excitation-energy transfer between molecular aggregates through distributed transition dipoles with application to the antenna system in bacterial photosynthesis," The Journal of Physical Chemistry B **103**, 252–260 (1999).

[392] H. Sumi, "Bacterial photosynthesis begins with quantum-mechanical coherence," The Chemical Record **1**, 480–493 (2001).

[393] G. D. Scholes and G. R. Fleming, "On the mechanism of light harvesting in photosynthetic purple bacteria: B800 to B850 energy transfer," The Journal of Physical Chemistry B **104**, 1854–1868 (2000).

[394] G. D. Scholes, X. J. Jordanides, and G. R. Fleming, "Adapting the Förster theory of energy transfer for modeling dynamics in aggregated molecular assemblies," The Journal of Physical Chemistry B **105**, 1640–1651 (2001).

[395] S. Jang, Y. Jung, and R. J. Silbey, "Nonequilibrium generalization of Förster–Dexter theory for excitation energy transfer," Chemical Physics **275**, 319–332 (2002). Photoprocesses in Multichromophoric Molecular Assemblies.

[396] S. Jang, M. D. Newton, and R. J. Silbey, "Multichromophoric Förster resonance energy transfer," Phys. Rev. Lett. **92**, 218301 (2004).

[397] Y. C. Cheng and R. J. Silbey, "Coherence in the B800 ring of purple bacteria LH2," Phys. Rev. Lett. **96**, 028103 (2006).

[398] S. Jang, M. D. Newton, and R. J. Silbey, "Multichromophoric Förster resonance energy transfer from B800 to B850 in the light harvesting complex 2: Evidence for subtle energetic optimization by purple bacteria," The Journal of Physical Chemistry B **111**, 6807–6814 (2007).

[399] V. Sundström, "Femtobiology," Annual Review of Physical Chemistry **59**, 53–77 (2008).

[400] F. Bloch, "Generalized theory of relaxation," Phys. Rev. **105**, 1206–1222 (1957).

[401] A. G. Redfield, "On the theory of relaxation processes," IBM Journal of Research and Development **1**, 19–31 (1957).

[402] V. I. Novoderezhkin, M. A. Palacios, H. van Amerongen, and R. van Grondelle, "Energy-transfer dynamics in the LHCII complex of higher plants: Modified Redfield approach," The Journal of Physical Chemistry B **108**, 10363–10375 (2004).

[403] M. Schröder, U. Kleinekathöfer, and M. Schreiber, "Calculation of absorption spectra for light-harvesting systems using non-Markovian approaches as well as modified Redfield theory," The Journal of Chemical Physics **124**, 084903 (2006).

[404] M. Yang and G. R. Fleming, "Influence of phonons on exciton transfer dynamics: comparison of the Redfield, Förster, and modified Redfield equations," Chemical Physics **282**, 163 – 180 (2002).

[405] R. S. Knox, "Electronic excitation transfer in the photosynthetic unit: Reflections on work of william arnold," Photosynthesis Research **48**, 35–39 (1996).

[406] S. Savikhin, D. R. Buck, and W. S. Struve, "Oscillating anisotropies in a bacteriochlorophyll protein: Evidence for quantum beating between exciton levels," Chemical Physics **223**, 303 – 312 (1997).

[407] Y.-C. Cheng and G. R. Fleming, "Dynamics of light harvesting in photosynthesis," Annual Review of Physical Chemistry **60**, 241–262 (2009).

[408] B. P. Krueger, G. D. Scholes, and G. R. Fleming, "Calculation of couplings and energy-transfer pathways between the pigments of LH2 by the ab initio transition density cube method," The Journal of Physical Chemistry B **102**, 5378–5386 (1998).

[409] G. D. Scholes, I. R. Gould, R. J. Cogdell, and G. R. Fleming, "Ab initio molecular orbital calculations of electronic couplings in the LH2 bacterial light-harvesting complex of Rps. acidophila," The Journal of Physical Chemistry B **103**, 2543–2553 (1999).

[410] M. E. Madjet, A. Abdurahman, and T. Renger, "Intermolecular Coulomb couplings from ab initio electrostatic potentials: Application to optical transitions of strongly coupled pigments in photosynthetic antennae and reaction centers," The Journal of Physical Chemistry B **110**, 17268–17281 (2006).

[411] M. F. Iozzi, B. Mennucci, J. Tomasi, and R. Cammi, "Excitation energy transfer (EET) between molecules in condensed matter: A novel application of the polarizable continuum model (PCM)," The Journal of Chemical Physics **120**, 7029–7040 (2004).

[412] J. Adolphs and T. Renger, "How proteins trigger excitation energy transfer in the FMO complex of green sulfur bacteria," Biophysical Journal **91**, 2778–2797 (2006).

[413] G. R. Fleming and M. Cho, "Chromophore-solvent dynamics," Annual Review of Physical Chemistry **47**, 109–134 (1996).

[414] T. Renger, V. May, and O. Kühn, "Ultrafast excitation energy transfer dynamics in photosynthetic pigment-protein complexes," Physics Reports **343**, 137–254 (2001).

[415] R. Sáez-Blázquez, J. Feist, E. Romero, A. I. Fernández-Domínguez, and F. J. García-Vidal, "Cavity-modified exciton dynamics in photosynthetic units," J. Phys. Chem. Lett. **10**, 4252–4258 (2019).

[416] H.-P. Breuer and F. Petruccione, *The Theory of Open Quantum Systems* (Oxford University Press, 2002).

[417] C. Gardiner and P. Zoller, *Quantum Noise* (Springer-Verlag Berlin Heidelberg, 2004).

[418] G. Lindblad, "On the generators of quantum dynamical semigroups," (1976).

[419] V. Gorini, A. Kossakowski, and E. C. G. Sudarshan, "Completely positive dynamical semigroups of N-level systems," Journal of Mathematical Physics **17**, 821–825 (1976).

[420] C. Gerry and P. Knight, *Introductory Quantum Optics* (Cambridge University Press, 2004).

[421] M. O. Scully and M. S. Zubairy, *Quantum Optics* (Cambridge University Press, 1997).

[422] J. J. Sanchez-Mondragon, N. B. Narozhny, and J. H. Eberly, "Theory of spontaneous-emission line shape in an ideal cavity," Phys. Rev. Lett. **51**, 550–553 (1983).

[423] L. Mandel and E. Wolf, *Optical Coherence and Quantum Optics* (Cambridge University Press, 1995).

[424] R. Short and L. Mandel, "Observation of sub-poissonian photon statistics," Phys. Rev. Lett. **51**, 384–387 (1983).

[425] V. May and O. Kühn, *Charge and energy transfer dynamics in molecular systems* (Wiley-VCH, 2011), 3rd ed.

[426] P. O. J. Scherer and S. F. Fischer, *Theoretical molecular biophysics* (Springer-Verlag Berlin Heidelberg, 2017), 2nd ed.

[427] B. R. Mollow, "Power spectrum of light scattered by two-level systems," Phys. Rev. **188**, 1969–1975 (1969).

[428] R. E. Grove, F. Y. Wu, and S. Ezekiel, "Measurement of the spectrum of resonance fluorescence from a two-level atom in an intense monochromatic field," Phys. Rev. A **15**, 227–233 (1977).

[429] P. Lodahl, S. Mahmoodian, and S. Stobbe, "Interfacing single photons and single quantum dots with photonic nanostructures," Rev. Mod. Phys. **87**, 347–400 (2015).

[430] P. Törmä and W. L. Barnes, "Strong coupling between surface plasmon polaritons and emitters: A review," Reports on Progress in Physics **78**, 013901 (2014).

[431] A. N. Poddubny, M. M. Glazov, and N. S. Averkiev, "Nonlinear emission spectra of quantum dots strongly coupled to a photonic mode," Phys. Rev. B **82**, 205330 (2010).

[432] P. M. Visser and G. Nienhuis, "Solution of quantum master equations in terms of a non-Hermitian Hamiltonian," Phys. Rev. A **52**, 4727–4736 (1995).

[433] A. Delga, J. Feist, J. Bravo-Abad, and F. J. Garcia-Vidal, "Quantum emitters near a metal nanoparticle: Strong coupling and quenching," Phys. Rev. Lett. **112**, 253601 (2014).

[434] T. Schwartz, J. A. Hutchison, C. Genet, and T. W. Ebbesen, "Reversible switching of ultrastrong light-molecule coupling," Phys. Rev. Lett. **106**, 196405 (2011).

[435] M. Ramezani, A. Halpin, A. I. Fernández-Domínguez, J. Feist, S. R.-K. Rodriguez, F. J. Garcia-Vidal, and J. G. Rivas, "Plasmon-exciton-polariton lasing," Optica **4**, 31–37 (2017).

[436] W. Zhang, A. O. Govorov, and G. W. Bryant, "Semiconductor-metal nanoparticle molecules: Hybrid excitons and the nonlinear Fano effect," Phys. Rev. Lett. **97**, 146804 (2006).

[437] R. D. Artuso and G. W. Bryant, "Optical response of strongly coupled quantum dot-metal nanoparticle systems: Double peaked Fano structure and bistability," Nano Letters **8**, 2106–2111 (2008).

[438] A. Ridolfo, O. Di Stefano, N. Fina, R. Saija, and S. Savasta, "Quantum plasmonics with quantum dot-metal nanoparticle molecules: Influence of the Fano effect on photon statistics," Phys. Rev. Lett. **105**, 263601 (2010).

[439] R.-Q. Li, D. Hernángomez-Pérez, F. J. García-Vidal, and A. I. Fernández-Domínguez, "Transformation optics approach to plasmon-exciton strong coupling in nanocavities," Phys. Rev. Lett. **117**, 107401 (2016).

[440] M. S. Tame, K. R. McEnery, S. K. Özdemir, J. Lee, S. A. Maier, and M. S. Kim, "Quantum plasmonics," Nature Physics **9**, 329–340 (2013).

[441] S. Savasta, R. Saija, A. Ridolfo, O. Di Stefano, P. Denti, and F. Borghese, "Nanopolaritons: Vacuum Rabi splitting with a single quantum dot in the center of a dimer nanoantenna," ACS Nano **4**, 6369–6376 (2010).

[442] A. Thoma, P. Schnauber, M. Gschrey, M. Seifried, J. Wolters, J.-H. Schulze, A. Strittmatter, S. Rodt, A. Carmele, A. Knorr, T. Heindel, and S. Reitzenstein, "Exploring dephasing of a solid-state quantum emitter via time- and temperature-dependent Hong-Ou-Mandel experiments," Phys. Rev. Lett. **116**, 033601 (2016).

[443] K. D. Rector and M. D. Fayer, "Vibrational dephasing mechanisms in liquids and glasses: Vibrational echo experiments," The Journal of Chemical Physics **108**, 1794–1803 (1998).

[444] T. W. Ebbesen, "Hybrid light-matter states in a molecular and material science perspective," Accounts of Chemical Research **49**, 2403–2412 (2016).

[445] V. M. Agranovich, M. Litinskaia, and D. G. Lidzey, "Cavity polaritons in microcavities containing disordered organic semiconductors," Phys. Rev. B **67**, 085311 (2003).

[446] A. Tsargorodska, M. L. Cartron, C. Vasilev, G. Kodali, O. A. Mass, J. J. Baumberg, P. L. Dutton, C. N. Hunter, P. Törmä, and G. J. Leggett, "Strong coupling of localized surface plasmons to excitons in light-harvesting complexes," Nano Letters **16**, 6850–6856 (2016).

[447] S. Caprasecca, S. Corni, and B. Mennucci, "Shaping excitons in light-harvesting proteins through nanoplasmonics," Chem. Sci. **9**, 6219–6227 (2018).

[448] D. M. Coles, Y. Yang, Y. Wang, R. T. Grant, R. A. Taylor, S. K. Saikin, A. Aspuru-Guzik, D. G. Lidzey, J. K.-H. Tang, and J. M. Smith, "Strong coupling between chlorosomes of photosynthetic bacteria and a confined optical cavity mode," Nature Communications **5**, 5561 (2014).

[449] D. Coles, L. C. Flatten, T. Sydney, E. Hounslow, S. K. Saikin, A. Aspuru-Guzik, V. Vedral, J. K.-H. Tang, R. A. Taylor, J. M. Smith, and D. G. Lidzey, "A nanophotonic structure containing living photosynthetic bacteria," Small **13**, 1701777 (2017).

[450] R. van Grondelle, J. P. Dekker, T. Gillbro, and V. Sundstrom, "Energy transfer and trapping in photosynthesis," Biochimica et Biophysica Acta (BBA) - Bioenergetics **1187**, 1 – 65 (1994).

[451] X. Hu, T. Ritz, A. Damjanović, F. Autenrieth, and K. Schulten, "Photosynthetic apparatus of purple bacteria," Quarterly Reviews of Biophysics **35**, 1–62 (2002).

[452] R. J. Cogdell, A. Gall, and J. Köhler, "The architecture and function of the light-harvesting apparatus of purple bacteria: From single molecules to in vivo membranes," Quarterly Reviews of Biophysics **39**, 227–324 (2006).

[453] R. Fenna, B. Matthews, J. Olson, and E. Shaw, "Structure of a bacteriochlorophyll-protein from the green photosynthetic bacterium chlorobium limicola: Crystallographic evidence for a trimer," Journal of Molecular Biology **84**, 231 – 240 (1974).

[454] R. E. Fenna and B. W. Matthews, "Chlorophyll arrangement in a bacteriochlorophyll protein from chlorobium limicola," Nature **258**, 573–577 (1975).

[455] B. Matthews, R. Fenna, M. Bolognesi, M. Schmid, and J. Olson, "Structure of a bacteriochlorophyll a-protein from the green photosynthetic bacterium prosthecochloris aestuarii," Journal of Molecular Biology **131**, 259 – 285 (1979).

[456] G. McDermott, S. M. Prince, A. A. Freer, A. M. Hawthornthwaite-Lawless, M. Z. Papiz, R. J. Cogdell, and N. W. Isaacs, "Crystal structure of an integral membrane light-harvesting complex from photosynthetic bacteria," Nature **374**, 517–521 (1995).

[457] J. Koepke, X. Hu, C. Muenke, K. Schulten, and H. Michel, "The crystal structure of the light-harvesting complex II (B800–850) from Rhodospirillum molischianum," Structure **4**, 581 – 597 (1996).

[458] S. Karrasch, P. Bullough, and R. Ghosh, "The 8.5 Å projection map of the light-harvesting complex I from Rhodospirillum rubrum reveals a ring composed of 16 subunits." The EMBO Journal **14**, 631–638 (1995).

[459] S. Scheuring, J. Seguin, S. Marco, D. Lévy, B. Robert, and J.-L. Rigaud, "Nanodissection and high-resolution imaging of the Rhodopseudomonas viridis photosynthetic core complex in native membranes by AFM," **100**, 1690–1693 (2003).

[460] A. W. Roszak, T. D. Howard, J. Southall, A. T. Gardiner, C. J. Law, N. W. Isaacs, and R. J. Cogdell, "Crystal structure of the RC-LH1 core complex from Rhodopseudomonas palustris," Science **302**, 1969–1972 (2003).

[461] H. A. Frank and R. J. Cogdell, "Carotenoids in photosynthesis," Photochemistry and Photobiology **63**, 257–264 (1996).

[462] T. Pullerits, M. Chachisvilis, and V. Sundström, "Exciton delocalization length in the B850 antenna of Rhodobacter sphaeroides," The Journal of Physical Chemistry **100**, 10787–10792 (1996).

[463] D. Leupold, H. Stiel, K. Teuchner, F. Nowak, W. Sandner, B. Ücker, and H. Scheer, "Size enhancement of transition dipoles to one- and two-exciton bands in a photosynthetic antenna," Phys. Rev. Lett. **77**, 4675–4678 (1996).

[464] R. Monshouwer, M. Abrahamsson, F. van Mourik, and R. van Grondelle, "Superradiance and exciton delocalization in bacterial photosynthetic light-harvesting systems," The Journal of Physical Chemistry B **101**, 7241–7248 (1997).

[465] M. Dahlbom, T. Pullerits, S. Mukamel, and V. Sundström, "Exciton delocalization in the B850 light-harvesting complex: Comparison of different measures," The Journal of Physical Chemistry B **105**, 5515–5524 (2001).

[466] R. Jimenez, F. van Mourik, J. Y. Yu, and G. R. Fleming, "Three-pulse photon echo measurements on LH1 and LH2 complexes of Rhodobacter sphaeroides: A nonlinear spectroscopic probe of energy transfer," The Journal of Physical Chemistry B **101**, 7350–7359 (1997).

[467] D. Leupold, B. Voigt, M. Pfeiffer, M. Bandilla, and H. Scheer, "Nonlinear polarization spectroscopy (frequency domain) studies of excited state processes: The B800–850 antenna of Rhodobacter sphaeroides," Photochemistry and Photobiology **57**, 24–28 (1993).

[468] K. Sauer, R. J. Cogdell, S. M. Prince, A. Freer, N. W. Isaacs, and H. Scheer, "Structure-based calculations of the optical spectra of the LH2 bacteriochlorophyll-protein complex from Rhodopseudomonas acidophila," Photochemistry and Photobiology **64**, 564–576 (1996).

[469] V. Sundström, T. Pullerits, and R. van Grondelle, "Photosynthetic light-harvesting: Reconciling dynamics and structure of purple bacterial LH2 reveals function of photosynthetic unit," The Journal of Physical Chemistry B **103**, 2327–2346 (1999).

[470] S. Hess, F. Feldchtein, A. Babin, I. Nurgaleev, T. Pullerits, A. Sergeev, and V. Sundström, "Femtosecond energy transfer within the LH2 peripheral antenna of the photosynthetic purple bacteria Rhodobacter sphaeroides and Rhodopseudomonas palustris LL," Chemical Physics Letters **216**, 247–257 (1993).

[471] S. Hess, M. Chachisvilis, K. Timpmann, M. R. Jones, G. J. Fowler, C. N. Hunter, and V. Sundström, "Temporally and spectrally resolved subpicosecond energy transfer within the peripheral antenna complex (LH2) and from LH2 to the core antenna complex in photosynthetic purple bacteria," Proceedings of the National Academy of Sciences **92**, 12333–12337 (1995).

[472] K. Timpmann, F. G. Zhang, A. Freiberg, and V. Sundström, "Detrapping of excitation energy from the reaction centre in the photosynthetic purple bacterium Rhodospirillum rubrum," Biochimica et Biophysica Acta (BBA) - Bioenergetics **1183**, 185–193 (1993).

[473] S. Tretiak, C. Middleton, V. Chernyak, and S. Mukamel, "Bacteriochlorophyll and carotenoid excitonic couplings in the LH2 system of purple bacteria," The Journal of Physical Chemistry B **104**, 9540–9553 (2000).

[474] S. Hu, M. Khater, R. Salas-Montiel, E. Kratschmer, S. Engelmann, W. M. J. Green, and S. M. Weiss, "Experimental realization of deep-subwavelength confinement in dielectric optical resonators," Science Advances **4** (2018).

[475] V. Zazubovich, I. Tibe, and G. J. Small, "Bacteriochlorophyll a Franck–Condon factors for the $S_0 \rightarrow S_1(Q_y)$ transition," The Journal of Physical Chemistry B **105**, 12410–12417 (2001).

[476] C. De Caro, R. W. Visschers, R. van Grondelle, and S. Voelker, "Inter- and intraband energy transfer in LH2-antenna complexes of purple bacteria. A fluorescence line-narrowing and hole-burning study," The Journal of Physical Chemistry **98**, 10584–10590 (1994).

[477] J. Linnanto, J. E. I. Korppi-Tommola, and V. M. Helenius, "Electronic states, absorption spectrum and circular dichroism spectrum of the photosynthetic bacterial LH2 antenna of Rhodopseudomonas acidophila as predicted by exciton theory and semiempirical calculations," The Journal of Physical Chemistry B **103**, 8739–8750 (1999).

[478] A. M. van Oijen, M. Ketelaars, J. Köhler, T. J. Aartsma, and J. Schmidt, "Unraveling the electronic structure of individual photosynthetic pigment-protein complexes," Science **285**, 400–402 (1999).

[479] R. Hildner, D. Brinks, J. B. Nieder, R. J. Cogdell, and N. F. van Hulst, "Quantum coherent energy transfer over varying pathways in single light-harvesting complexes," Science **340**, 1448–1451 (2013).

[480] F. Caycedo-Soler, C. A. Schroeder, C. Autenrieth, A. Pick, R. Ghosh, S. F. Huelga, and M. B. Plenio, "Quantum redirection of antenna absorption to photosynthetic reaction centers," The Journal of Physical Chemistry Letters **8**, 6015–6021 (2017).

[481] T. Ritz, S. Park, and K. Schulten, "Kinetics of excitation migration and trapping in the photosynthetic unit of purple bacteria," The Journal of Physical Chemistry B **105**, 8259–8267 (2001).

[482] T. Mirkovic, E. E. Ostroumov, J. M. Anna, R. van Grondelle, Govindjee, and G. D. Scholes, "Light absorption and energy transfer in the antenna complexes of photosynthetic organisms," Chemical Reviews **117**, 249–293 (2017).

[483] S. Hu, M. Khater, R. Salas-Montiel, E. Kratschmer, S. Engelmann, W. M. J. Green, and S. M. Weiss, "Experimental realization of deep-subwavelength confinement in dielectric optical resonators," Science Advances **4** (2018).

[484] M. S. Skolnick, T. A. Fisher, and D. M. Whittaker, "Strong coupling phenomena in quantum microcavity structures," Semiconductor Science and Technology **13**, 645–669 (1998).

[485] G. Khitrova, H. M. Gibbs, M. Kira, S. W. Koch, and A. Scherer, "Vacuum Rabi splitting in semiconductors," Nature Physics **2**, 81–90 (2006).

[486] D. Meschede, H. Walther, and G. Müller, "One-atom maser," Phys. Rev. Lett. **54**, 551–554 (1985).

[487] Y. Zhu, D. J. Gauthier, S. E. Morin, Q. Wu, H. J. Carmichael, and T. W. Mossberg, "Vacuum Rabi splitting as a feature of linear-dispersion theory: Analysis and experimental observations," Phys. Rev. Lett. **64**, 2499–2502 (1990).

[488] J. Ye, D. W. Vernooy, and H. J. Kimble, "Trapping of single atoms in cavity QED," Phys. Rev. Lett. **83**, 4987–4990 (1999).

[489] J. McKeever, J. R. Buck, A. D. Boozer, A. Kuzmich, H.-C. Nägerl, D. M. Stamper-Kurn, and H. J. Kimble, "State-insensitive cooling and trapping of single atoms in an optical cavity," Phys. Rev. Lett. **90**, 133602 (2003).

[490] C. Weisbuch, M. Nishioka, A. Ishikawa, and Y. Arakawa, "Observation of the coupled exciton-photon mode splitting in a semiconductor quantum microcavity," Phys. Rev. Lett. **69**, 3314–3317 (1992).

[491] R. Houdré, C. Weisbuch, R. P. Stanley, U. Oesterle, P. Pellandini, and M. Ilegems, "Measurement of cavity-polariton dispersion curve from angle-resolved photoluminescence experiments," Phys. Rev. Lett. **73**, 2043–2046 (1994).

[492] T. B. Norris, J.-K. Rhee, C.-Y. Sung, Y. Arakawa, M. Nishioka, and C. Weisbuch, "Time-resolved vacuum Rabi oscillations in a semiconductor quantum microcavity," Phys. Rev. B **50**, 14663–14666 (1994).

[493] R. Houdré, R. P. Stanley, U. Oesterle, M. Ilegems, and C. Weisbuch, "Room-temperature cavity polaritons in a semiconductor microcavity," Phys. Rev. B **49**, 16761–16764 (1994).

[494] E. Peter, P. Senellart, D. Martrou, A. Lemaître, J. Hours, J. M. Gérard, and J. Bloch, "Exciton-photon strong-coupling regime for a single quantum dot embedded in a microcavity," Phys. Rev. Lett. **95**, 067401 (2005).

[495] D. G. Lidzey, D. D. C. Bradley, T. Virgili, A. Armitage, M. S. Skolnick, and S. Walker, "Room temperature polariton emission from strongly coupled organic semiconductor microcavities," Phys. Rev. Lett. **82**, 3316–3319 (1999).

[496] A. I. Tartakovskii, M. Emam-Ismail, D. G. Lidzey, M. S. Skolnick, D. D. C. Bradley, S. Walker, and V. M. Agranovich, "Raman scattering in strongly coupled organic semiconductor microcavities," Phys. Rev. B **63**, 121302 (2001).

[497] S. Kéna-Cohen, M. Davanço, and S. R. Forrest, "Strong exciton-photon coupling in an organic single crystal microcavity," Phys. Rev. Lett. **101**, 116401 (2008).

[498] R. J. Holmes and S. R. Forrest, "Strong exciton-photon coupling and exciton hybridization in a thermally evaporated polycrystalline film of an organic small molecule," Phys. Rev. Lett. **93**, 186404 (2004).

[499] A. Shalabney, J. George, J. Hutchison, G. Pupillo, C. Genet, and T. W. Ebbesen, "Coherent coupling of molecular resonators with a microcavity mode," Nature Communications **6**, 5981 (2015).

[500] J. del Pino, J. Feist, and F. J. Garcia-Vidal, "Quantum theory of collective strong coupling of molecular vibrations with a microcavity mode," New Journal of Physics **17**, 053040 (2015).

[501] S. Kéna-Cohen, S. A. Maier, and D. D. C. Bradley, "Ultrastrongly coupled exciton-polaritons in metal-clad organic semiconductor microcavities," Advanced Optical Materials **1**, 827–833 (2013).

[502] P. A. Hobson, W. L. Barnes, D. G. Lidzey, G. A. Gehring, D. M. Whittaker, M. S. Skolnick, and S. Walker, "Strong exciton–photon coupling in a low-Q all-metal mirror microcavity," Applied Physics Letters **81**, 3519–3521 (2002).

[503] Y. Sugawara, T. A. Kelf, J. J. Baumberg, M. E. Abdelsalam, and P. N. Bartlett, "Strong coupling between localized plasmons and organic excitons in metal nanovoids," Phys. Rev. Lett. **97**, 266808 (2006).

[504] G. A. Wurtz, P. R. Evans, W. Hendren, R. Atkinson, W. Dickson, R. J. Pollard, A. V. Zayats, W. Harrison, and C. Bower, "Molecular plasmonics with tunable exciton–plasmon coupling strength in J-aggregate hybridized Au nanorod assemblies," Nano Letters **7**, 1297–1303 (2007).

[505] P. Vasa, W. Wang, R. Pomraenke, M. Lammers, M. Maiuri, C. Manzoni, G. Cerullo, and C. Lienau, "Real-time observation of ultrafast rabi oscillations between excitons and plasmons in metal nanostructures with J-aggregates," Nature Photonics **7**, 128–132 (2013).

[506] T. K. Hakala, J. J. Toppari, A. Kuzyk, M. Pettersson, H. Tikkanen, H. Kunttu, and P. Törmä, "Vacuum Rabi splitting and strong-coupling dynamics for surface-plasmon polaritons and Rhodamine 6G molecules," Phys. Rev. Lett. **103**, 053602 (2009).

[507] F. Valmorra, M. Bröll, S. Schwaiger, N. Welzel, D. Heitmann, and S. Mendach, "Strong coupling between surface plasmon polariton and laser dye Rhodamine 800," Applied Physics Letters **99**, 051110 (2011).

[508] S. Rodriguez and J. G. Rivas, "Surface lattice resonances strongly coupled to Rhodamine 6G excitons: Tuning the plasmon-exciton-polariton mass and composition," Opt. Express **21**, 27411–27421 (2013).

[509] A. I. Väkeväinen, R. J. Moerland, H. T. Rekola, A.-P. Eskelinen, J.-P. Martikainen, D.-H. Kim, and P. Törmä, "Plasmonic surface lattice resonances at the strong coupling regime," Nano Letters **14**, 1721–1727 (2014).

[510] P. Vasa, R. Pomraenke, S. Schwieger, Y. I. Mazur, V. Kunets, P. Srinivasan, E. Johnson, J. E. Kihm, D. S. Kim, E. Runge, G. Salamo, and C. Lienau, "Coherent exciton–surface-plasmon-polariton interaction in hybrid metal-semiconductor nanostructures," Phys. Rev. Lett. **101**, 116801 (2008).

[511] D. E. Gómez, K. C. Vernon, P. Mulvaney, and T. J. Davis, "Surface plasmon mediated strong exciton–photon coupling in semiconductor nanocrystals," Nano Letters **10**, 274–278 (2010).

[512] N. T. Fofang, T.-H. Park, O. Neumann, N. A. Mirin, P. Nordlander, and N. J. Halas, "Plexcitonic nanoparticles: Plasmon-exciton coupling in nanoshell–J-aggregate complexes," Nano Letters **8**, 3481–3487 (2008).

[513] A. E. Schlather, N. Large, A. S. Urban, P. Nordlander, and N. J. Halas, "Near-field mediated plexcitonic coupling and giant Rabi splitting in individual metallic dimers," Nano Letters **13**, 3281–3286 (2013).

[514] M. Barth, S. Schietinger, S. Fischer, J. Becker, N. Nüsse, T. Aichele, B. Löchel, C. Sönnichsen, and O. Benson, "Nanoassembled plasmonic-photonic hybrid cavity for tailored light-matter coupling," Nano Letters **10**, 891–895 (2010).

[515] M. T. Hill, Y.-S. Oei, B. Smalbrugge, Y. Zhu, T. de Vries, P. J. van Veldhoven, F. W. M. van Otten, T. J. Eijkemans, J. P. Turkiewicz, H. de Waardt, E. J. Geluk, S.-H. Kwon, Y.-H. Lee, R. Nötzel, and M. K. Smit, "Lasing in metallic-coated nanocavities," Nature Photonics **1**, 589–594 (2007).

[516] B. Min, E. Ostby, V. Sorger, E. Ulin-Avila, L. Yang, X. Zhang, and K. Vahala, "High-Q surface-plasmon-polariton whispering-gallery microcavity," Nature **457**, 455–458 (2009).

[517] P. F. Herskind, A. Dantan, J. P. Marler, M. Albert, and M. Drewsen, "Realization of collective strong coupling with ion Coulomb crystals in an optical cavity," Nature Physics **5**, 494–498 (2009).

[518] C. Schneider, M. M. Glazov, T. Korn, S. Höfling, and B. Urbaszek, "Two-dimensional semiconductors in the regime of strong light-matter coupling," Nature Communications **9**, 2695 (2018).

[519] K. He, N. Kumar, L. Zhao, Z. Wang, K. F. Mak, H. Zhao, and J. Shan, "Tightly bound excitons in monolayer WSe_2," Phys. Rev. Lett. **113**, 026803 (2014).

[520] A. Chernikov, T. C. Berkelbach, H. M. Hill, A. Rigosi, Y. Li, O. B. Aslan, D. R. Reichman, M. S. Hybertsen, and T. F. Heinz, "Exciton binding energy and nonhydrogenic Rydberg series in monolayer WS_2," Phys. Rev. Lett. **113**, 076802 (2014).

[521] Y. Li, A. Chernikov, X. Zhang, A. Rigosi, H. M. Hill, A. M. van der Zande, D. A. Chenet, E.-M. Shih, J. Hone, and T. F. Heinz, "Measurement of the optical dielectric function of monolayer transition-metal dichalcogenides: MoS_2, $MoSe_2$, WS_2, and WSe_2," Phys. Rev. B **90**, 205422 (2014).

[522] X. Liu, T. Galfsky, Z. Sun, F. Xia, E.-c. Lin, Y.-H. Lee, S. Kéna-Cohen, and V. M. Menon, "Strong light-matter coupling in two-dimensional atomic crystals," Nature Photonics **9**, 30–34 (2015).

[523] S. Dufferwiel, S. Schwarz, F. Withers, A. A. P. Trichet, F. Li, M. Sich, O. Del Pozo-Zamudio, C. Clark, A. Nalitov, D. D. Solnyshkov, G. Malpuech, K. S. Novoselov, J. M. Smith, M. S. Skolnick, D. N. Krizhanovskii, and A. I. Tartakovskii, "Exciton-polaritons in van der Waals heterostructures embedded in tunable microcavities," Nature Communications **6**, 8579 (2015).

[524] X. Liu, W. Bao, Q. Li, C. Ropp, Y. Wang, and X. Zhang, "Control of coherently coupled exciton polaritons in monolayer tungsten disulphide," Phys. Rev. Lett. **119**, 027403 (2017).

[525] N. Lundt, S. Klembt, E. Cherotchenko, S. Betzold, O. Iff, A. V. Nalitov, M. Klaas, C. P. Dietrich, A. V. Kavokin, S. Höfling, and C. Schneider, "Room-temperature Tamm-plasmon exciton-polaritons with a WSe_2 monolayer," Nature Communications **7**, 13328 (2016).

[526] M. Kaliteevski, I. Iorsh, S. Brand, R. A. Abram, J. M. Chamberlain, A. V. Kavokin, and I. A. Shelykh, "Tamm plasmon-polaritons: Possible electromagnetic states at the interface of a metal and a dielectric Bragg mirror," Phys. Rev. B **76**, 165415 (2007).

[527] M. E. Sasin, R. P. Seisyan, M. A. Kalitteevski, S. Brand, R. A. Abram, J. M. Chamberlain, A. Y. Egorov, A. P. Vasil'ev, V. S. Mikhrin, and A. V. Kavokin, "Tamm plasmon polaritons: Slow and spatially compact light," Applied Physics Letters **92**, 251112 (2008).

[528] L. C. Flatten, Z. He, D. M. Coles, A. A. P. Trichet, A. W. Powell, R. A. Taylor, J. H. Warner, and J. M. Smith, "Room-temperature exciton-polaritons with two-dimensional WS_2," Scientific Reports **6**, 33134 (2016).

[529] S. Wang, S. Li, T. Chervy, A. Shalabney, S. Azzini, E. Orgiu, J. A. Hutchison, C. Genet, P. Samorì, and T. W. Ebbesen, "Coherent coupling of WS_2 monolayers with metallic photonic nanostructures at room temperature," Nano Letters **16**, 4368–4374 (2016).

[530] W. Liu, B. Lee, C. H. Naylor, H.-S. Ee, J. Park, A. T. C. Johnson, and R. Agarwal, "Strong exciton–plasmon coupling in MoS_2 coupled with plasmonic lattice," Nano Letters **16**, 1262–1269 (2016).

[531] J. Cuadra, D. G. Baranov, M. Wersäll, R. Verre, T. J. Antosiewicz, and T. Shegai, "Observation of tunable charged exciton polaritons in hybrid monolayer WS_2–plasmonic nanoantenna system," Nano Letters **18**, 1777–1785 (2018).

[532] M.-E. Kleemann, R. Chikkaraddy, E. M. Alexeev, D. Kos, C. Carnegie, W. Deacon, A. C. de Pury, C. Große, B. de Nijs, J. Mertens, A. I. Tartakovskii, and J. J. Baumberg, "Strong-coupling of WSe_2 in ultra-compact plasmonic nanocavities at room temperature," Nature Communications **8**, 1296 (2017).

[533] J. Twamley and S. D. Barrett, "Superconducting cavity bus for single nitrogen-vacancy defect centers in diamond," Phys. Rev. B **81**, 241202 (2010).

[534] G. Balasubramanian, P. Neumann, D. Twitchen, M. Markham, R. Kolesov, N. Mizuochi, J. Isoya, J. Achard, J. Beck, J. Tissler, V. Jacques, P. R. Hemmer, F. Jelezko, and J. Wrachtrup, "Ultralong spin coherence time in isotopically engineered diamond," Nature Materials **8**, 383–387 (2009).

[535] Y. Kubo, F. R. Ong, P. Bertet, D. Vion, V. Jacques, D. Zheng, A. Dréau, J.-F. Roch, A. Auffeves, F. Jelezko, J. Wrachtrup, M. F. Barthe, P. Bergonzo, and D. Esteve, "Strong coupling of a spin ensemble to a superconducting resonator," Phys. Rev. Lett. **105**, 140502 (2010).

[536] R. Amsüss, C. Koller, T. Nöbauer, S. Putz, S. Rotter, K. Sandner, S. Schneider, M. Schramböck, G. Steinhauser, H. Ritsch, J. Schmiedmayer, and J. Majer, "Cavity QED with magnetically coupled collective spin states," Phys. Rev. Lett. **107**, 060502 (2011).

[537] S. Probst, H. Rotzinger, S. Wünsch, P. Jung, M. Jerger, M. Siegel, A. V. Ustinov, and P. A. Bushev, "Anisotropic rare-earth spin ensemble strongly coupled to a superconducting resonator," Phys. Rev. Lett. **110**, 157001 (2013).

[538] S. Gröblacher, K. Hammerer, M. R. Vanner, and M. Aspelmeyer, "Observation of strong coupling between a micromechanical resonator and an optical cavity field," Nature **460**, 724–727 (2009).

[539] A. Wallraff, D. I. Schuster, A. Blais, L. Frunzio, R.-S. Huang, J. Majer, S. Kumar, S. M. Girvin, and R. J. Schoelkopf, "Strong coupling of a single photon to a superconducting qubit using circuit quantum electrodynamics," Nature **431**, 162–167 (2004).

[540] O. Astafiev, A. M. Zagoskin, A. A. Abdumalikov, Y. A. Pashkin, T. Yamamoto, K. Inomata, Y. Nakamura, and J. S. Tsai, "Resonance fluorescence of a single artificial atom," Science **327**, 840–843 (2010).

[541] M. Combescot and O. Betbeder-Matibet, "Scattering rates and lifetime of exact and boson excitons," Phys. Rev. Lett. **93**, 016403 (2004).

[542] F. P. Laussy, M. M. Glazov, A. Kavokin, D. M. Whittaker, and G. Malpuech, "Statistics of excitons in quantum dots and their effect on the optical emission spectra of microcavities," Phys. Rev. B **73**, 115343 (2006).

[543] M. Combescot, O. Betbeder-Matibet, and R. Combescot, "Exciton-exciton scattering: Composite boson versus elementary boson," Phys. Rev. B **75**, 174305 (2007).

[544] F. Tassone and Y. Yamamoto, "Exciton-exciton scattering dynamics in a semiconductor microcavity and stimulated scattering into polaritons," Phys. Rev. B **59**, 10830–10842 (1999).

[545] M. M. Glazov, H. Ouerdane, L. Pilozzi, G. Malpuech, A. V. Kavokin, and A. D'Andrea, "Polariton-polariton scattering in microcavities: A microscopic theory," Phys. Rev. B **80**, 155306 (2009).

[546] F. Tassone, C. Piermarocchi, V. Savona, A. Quattropani, and P. Schwendimann, "Bottleneck effects in the relaxation and photoluminescence of microcavity polaritons," Phys. Rev. B **56**, 7554–7563 (1997).

[547] Y. Toyozawa, "On the dynamical behavior of an exciton," Progress of Theoretical Physics Supplement **12**, 111–140 (1959).

[548] M. Müller, J. Bleuse, and R. André, "Dynamics of the cavity polariton in CdTe-based semiconductor microcavities: Evidence for a relaxation edge," Phys. Rev. B **62**, 16886–16892 (2000).

[549] A. I. Tartakovskii, M. S. Skolnick, D. N. Krizhanovskii, V. D. Kulakovskii, R. M. Stevenson, R. Butté, J. J. Baumberg, D. M. Whittaker, and J. S. Roberts, "Stimulated polariton scattering in semiconductor microcavities: New physics and potential applications," Advanced Materials **13**, 1725–1730 (2001).

[550] L. S. Dang, D. Heger, R. André, F. Bœuf, and R. Romestain, "Stimulation of polariton photoluminescence in semiconductor microcavity," Phys. Rev. Lett. **81**, 3920–3923 (1998).

[551] P. Senellart and J. Bloch, "Nonlinear emission of microcavity polaritons in the low density regime," Phys. Rev. Lett. **82**, 1233–1236 (1999).

[552] R. Huang, F. Tassone, and Y. Yamamoto, "Experimental evidence of stimulated scattering of excitons into microcavity polaritons," Phys. Rev. B **61**, R7854–R7857 (2000).

[553] P. Senellart, J. Bloch, B. Sermage, and J. Y. Marzin, "Microcavity polariton depopulation as evidence for stimulated scattering," Phys. Rev. B **62**, R16263–R16266 (2000).

[554] M. Saba, C. Ciuti, J. Bloch, V. Thierry-Mieg, R. André, L. S. Dang, S. Kundermann, A. Mura, G. Bongiovanni, J. L. Staehli, and B. Deveaud, "High-temperature ultrafast polariton parametric amplification in semiconductor microcavities," Nature **414**, 731–735 (2001).

[555] C. Ciuti, P. Schwendimann, and A. Quattropani, "Parametric luminescence of microcavity polaritons," Phys. Rev. B **63**, 041303 (2001).

[556] Y. Yamamoto, "Half-matter, half-light amplifier," Nature **405**, 629–630 (2000).

[557] D. M. Whittaker, "Classical treatment of parametric processes in a strong-coupling planar microcavity," Phys. Rev. B **63**, 193305 (2001).

[558] A. Baas, J.-P. Karr, M. Romanelli, A. Bramati, and E. Giacobino, "Optical bistability in semiconductor microcavities in the nondegenerate parametric oscillation regime: Analogy with the optical parametric oscillator," Phys. Rev. B **70**, 161307 (2004).

[559] J. P. Karr, A. Baas, and E. Giacobino, "Twin polaritons in semiconductor microcavities," Phys. Rev. A **69**, 063807 (2004).

[560] A. Kavokin, P. G. Lagoudakis, G. Malpuech, and J. J. Baumberg, "Polarization rotation in parametric scattering of polaritons in semiconductor microcavities," Phys. Rev. B **67**, 195321 (2003).

[561] K. V. Kavokin, I. A. Shelykh, A. V. Kavokin, G. Malpuech, and P. Bigenwald, "Quantum theory of spin dynamics of exciton-polaritons in microcavities," Phys. Rev. Lett. **92**, 017401 (2004).

[562] M. D. Martín, G. Aichmayr, L. Viña, and R. André, "Polarization control of the nonlinear emission of semiconductor microcavities," Phys. Rev. Lett. **89**, 077402 (2002).

[563] P. G. Lagoudakis, P. G. Savvidis, J. J. Baumberg, D. M. Whittaker, P. R. Eastham, M. S. Skolnick, and J. S. Roberts, "Stimulated spin dynamics of polaritons in semiconductor microcavities," Phys. Rev. B **65**, 161310 (2002).

[564] A. Imamoğlu, R. J. Ram, S. Pau, and Y. Yamamoto, "Nonequilibrium condensates and lasers without inversion: Exciton-polariton lasers," Phys. Rev. A **53**, 4250–4253 (1996).

[565] S. Pau, H. Cao, J. Jacobson, G. Björk, Y. Yamamoto, and A. Imamoğlu, "Observation of a laserlike transition in a microcavity exciton polariton system," Phys. Rev. A **54**, R1789–R1792 (1996).

[566] H. Cao, S. Pau, J. M. Jacobson, G. Björk, Y. Yamamoto, and A. Imamoğlu, "Transition from a microcavity exciton polariton to a photon laser," Phys. Rev. A **55**, 4632–4635 (1997).

[567] M. Kira, F. Jahnke, S. W. Koch, J. D. Berger, D. V. Wick, T. R. Nelson, G. Khitrova, and H. M. Gibbs, "Quantum theory of nonlinear semiconductor microcavity luminescence explaining "boser" experiments," Phys. Rev. Lett. **79**, 5170–5173 (1997).

[568] J. J. Baumberg, A. V. Kavokin, S. Christopoulos, A. J. D. Grundy, R. Butté, G. Christmann, D. D. Solnyshkov, G. Malpuech, G. Baldassarri Höger von Högersthal, E. Feltin, J.-F. Carlin, and N. Grandjean, "Spontaneous polarization buildup in a room-temperature polariton laser," Phys. Rev. Lett. **101**, 136409 (2008).

[569] J. Kasprzak, D. D. Solnyshkov, R. André, L. S. Dang, and G. Malpuech, "Formation of an exciton polariton condensate: Thermodynamic versus kinetic regimes," Phys. Rev. Lett. **101**, 146404 (2008).

[570] R. Butté, J. Levrat, G. Christmann, E. Feltin, J.-F. m. c. Carlin, and N. Grandjean, "Phase diagram of a polariton laser from cryogenic to room temperature," Phys. Rev. B **80**, 233301 (2009).

[571] D. Snoke, "Spontaneous bose coherence of excitons and polaritons," Science **298**, 1368–1372 (2002).

[572] M. H. Anderson, J. R. Ensher, M. R. Matthews, C. E. Wieman, and E. A. Cornell, "Observation of Bose-Einstein condensation in a dilute atomic vapor," Science **269**, 198–201 (1995).

[573] H. Deng, G. Weihs, C. Santori, J. Bloch, and Y. Yamamoto, "Condensation of semiconductor microcavity exciton polaritons," Science **298**, 199–202 (2002).

[574] Y. Sun, P. Wen, Y. Yoon, G. Liu, M. Steger, L. N. Pfeiffer, K. West, D. W. Snoke, and K. A. Nelson, "Bose-Einstein condensation of long-lifetime polaritons in thermal equilibrium," Phys. Rev. Lett. **118**, 016602 (2017).

[575] E. Wertz, L. Ferrier, D. D. Solnyshkov, P. Senellart, D. Bajoni, A. Miard, A. Lemaître, G. Malpuech, and J. Bloch, "Spontaneous formation of a polariton condensate in a planar GaAs microcavity," Applied Physics Letters **95**, 051108 (2009).

[576] S. Christopoulos, G. B. H. von Högersthal, A. J. D. Grundy, P. G. Lagoudakis, A. V. Kavokin, J. J. Baumberg, G. Christmann, R. Butté, E. Feltin, J.-F. Carlin, and N. Grandjean, "Room-temperature polariton lasing in semiconductor microcavities," Phys. Rev. Lett. **98**, 126405 (2007).

[577] T. Guillet, M. Mexis, J. Levrat, G. Rossbach, C. Brimont, T. Bretagnon, B. Gil, R. Butté, N. Grandjean, L. Orosz, F. Réveret, J. Leymarie, J. Zúñiga Pérez, M. Leroux, F. Semond, and S. Bouchoule, "Polariton lasing in a hybrid bulk ZnO microcavity," Applied Physics Letters **99**, 161104 (2011).

[578] G. Malpuech, A. Di Carlo, A. Kavokin, J. J. Baumberg, M. Zamfirescu, and P. Lugli, "Room-temperature polariton lasers based on GaN microcavities," Applied Physics Letters **81**, 412–414 (2002).

[579] G. Christmann, R. Butté, E. Feltin, J.-F. Carlin, and N. Grandjean, "Room temperature polariton lasing in a GaN/AlGaN multiple quantum well microcavity," Applied Physics Letters **93**, 051102 (2008).

[580] A. Das, J. Heo, M. Jankowski, W. Guo, L. Zhang, H. Deng, and P. Bhattacharya, "Room temperature ultralow threshold GaN nanowire polariton laser," Phys. Rev. Lett. **107**, 066405 (2011).

[581] A. A. Khalifa, A. P. D. Love, D. N. Krizhanovskii, M. S. Skolnick, and J. S. Roberts, "Electroluminescence emission from polariton states in GaAs-based semiconductor microcavities," Applied Physics Letters **92**, 061107 (2008).

[582] P. Bhattacharya, B. Xiao, A. Das, S. Bhowmick, and J. Heo, "Solid state electrically injected exciton-polariton laser," Phys. Rev. Lett. **110**, 206403 (2013).

[583] C. Schneider, A. Rahimi-Iman, N. Y. Kim, J. Fischer, I. G. Savenko, M. Amthor, M. Lermer, A. Wolf, L. Worschech, V. D. Kulakovskii, I. A. Shelykh, M. Kamp, S. Reitzenstein, A. Forchel, Y. Yamamoto, and S. Höfling, "An electrically pumped polariton laser," Nature **497**, 348–352 (2013).

[584] S. Kéna-Cohen and S. R. Forrest, "Room-temperature polariton lasing in an organic single-crystal microcavity," Nature Photonics **4**, 371–375 (2010).

[585] J. D. Plumhof, T. Stöferle, L. Mai, U. Scherf, and R. F. Mahrt, "Room-temperature bose-einstein condensation of cavity exciton-polaritons in a polymer," Nature Materials **13**, 247–252 (2014).

[586] K. S. Daskalakis, S. A. Maier, R. Murray, and S. Kéna-Cohen, "Nonlinear interactions in an organic polariton condensate," Nature Materials **13**, 271–278 (2014).

[587] T. Cookson, K. Georgiou, A. Zasedatelev, R. T. Grant, T. Virgili, M. Cavazzini, F. Galeotti, C. Clark, N. G. Berloff, D. G. Lidzey, and P. G. Lagoudakis, "A yellow polariton condensate in a dye filled microcavity," Advanced Optical Materials **5**, 1700203 (2017).

[588] T. Byrnes, N. Y. Kim, and Y. Yamamoto, "Exciton-polariton condensates," Nature Physics **10**, 803–813 (2014).

[589] D. Sanvitto and S. Kéna-Cohen, "The road towards polaritonic devices," Nature Materials **15**, 1061–1073 (2016).

[590] A. J. Leggett, "Superfluidity," Rev. Mod. Phys. **71**, S318–S323 (1999).

[591] I. Carusotto and C. Ciuti, "Probing microcavity polariton superfluidity through resonant rayleigh scattering," Phys. Rev. Lett. **93**, 166401 (2004).

[592] G. Malpuech, D. D. Solnyshkov, H. Ouerdane, M. M. Glazov, and I. Shelykh, "Bose glass and superfluid phases of cavity polaritons," Phys. Rev. Lett. **98**, 206402 (2007).

[593] A. Amo, J. Lefrère, S. Pigeon, C. Adrados, C. Ciuti, I. Carusotto, R. Houdré, E. Giacobino, and A. Bramati, "Superfluidity of polaritons in semiconductor microcavities," Nature Physics **11**, 805–810 (2009).

[594] A. Amo, D. Sanvitto, F. P. Laussy, D. Ballarini, E. d. Valle, M. D. Martin, A. Lemaître, J. Bloch, , D. N. Krizhanovskii, M. S. Skolnick, C. Tejedor, and L. Viña, "Collective fluid dynamics of a polariton condensate in a semiconductor microcavity," Nature **457**, 291–295 (2009).

[595] G. Lerario, A. Fieramosca, F. Barachati, D. Ballarini, K. S. Daskalakis, L. Dominici, M. De Giorgi, S. A. Maier, G. Gigli, S. Kéna-Cohen, and D. Sanvitto, "Room-temperature superfluidity in a polariton condensate," Nature Physics **13**, 837–841 (2017).

[596] I. Carusotto and C. Ciuti, "Quantum fluids of light," Rev. Mod. Phys. **85**, 299–366 (2013).

[597] K. G. Lagoudakis, M. Wouters, M. Richard, A. Baas, I. Carusotto, R. André, L. S. Dang, and B. Deveaud-Plédran, "Quantized vortices in an exciton–polariton condensate," Nature Physics **4** (2008).

[598] D. Sanvitto, F. M. Marchetti, M. H. Szymanska, G. Tosi, M. Baudisch, F. P. Laussy, D. N. Krizhanovskii, M. S. Skolnick, L. Marrucci, A. Lemaître, J. Bloch, C. Tejedor, and L. Viña, "Persistent currents and quantized vortices in a polariton superfluid," Nature Physics **6**, 527–533 (2010).

[599] G. Roumpos, M. D. Fraser, A. Löffler, S. Höfling, A. Forchel, and Y. Yamamoto, "Single vortex–antivortex pair in an exciton–polariton condensate," Nature Physics **7**, 129–133 (2011).

[600] F. M. Marchetti, M. H. Szymańska, C. Tejedor, and D. M. Whittaker, "Spontaneous and triggered vortices in polariton optical-parametric-oscillator superfluids," Phys. Rev. Lett. **105**, 063902 (2010).

[601] A. Kavokin, G. Malpuech, and M. Glazov, "Optical spin Hall effect," Phys. Rev. Lett. **95**, 136601 (2005).

[602] C. Leyder, M. Romanelli, J. P. Karr, E. Giacobino, T. C. H. Liew, M. M. Glazov, A. V. Kavokin, G. Malpuech, and A. Bramati, "Observation of the optical spin Hall effect," Nature Physics **3**, 628 – 631 (2007).

[603] J. Keeling, F. M. Marchetti, M. H. Szymańska, and P. B. Littlewood, "Collective coherence in planar semiconductor microcavities," Semiconductor Science and Technology **22**, R1–R26 (2007).

[604] W. H. Nitsche, N. Y. Kim, G. Roumpos, C. Schneider, M. Kamp, S. Höfling, A. Forchel, and Y. Yamamoto, "Algebraic order and the Berezinskii-Kosterlitz-Thouless transition in an exciton-polariton gas," Phys. Rev. B **90**, 205430 (2014).

[605] K. S. Daskalakis, S. A. Maier, and S. Kéna-Cohen, "Spatial coherence and stability in a disordered organic polariton condensate," Phys. Rev. Lett. **115**, 035301 (2015).

[606] J. I. Cirac and P. Zoller, "Quantum computations with cold trapped ions," Phys. Rev. Lett. **74**, 4091–4094 (1995).

[607] Q. A. Turchette, C. J. Hood, W. Lange, H. Mabuchi, and H. J. Kimble, "Measurement of conditional phase shifts for quantum logic," Phys. Rev. Lett. **75**, 4710–4713 (1995).

[608] T. Pellizzari, S. A. Gardiner, J. I. Cirac, and P. Zoller, "Decoherence, continuous observation, and quantum computing: A cavity QED model," Phys. Rev. Lett. **75**, 3788–3791 (1995).

[609] L.-M. Duan and H. J. Kimble, "Scalable photonic quantum computation through cavity-assisted interactions," Phys. Rev. Lett. **92**, 127902 (2004).

[610] D. Loss and D. P. DiVincenzo, "Quantum computation with quantum dots," Phys. Rev. A **57**, 120–126 (1998).

[611] B. E. Kane, "A silicon-based nuclear spin quantum computer," Nature **393**, 133–137 (1998).

[612] K. Hennessy, A. Badolato, M. Winger, D. Gerace, M. Atatüre, S. Gulde, S. Fält, E. L. Hu, and A. Imamoglu, "Quantum nature of a strongly coupled single quantum dot-cavity system," Nature **445**, 896–899 (2007).

[613] J. I. Cirac, P. Zoller, H. J. Kimble, and H. Mabuchi, "Quantum state transfer and entanglement distribution among distant nodes in a quantum network," Phys. Rev. Lett. **78**, 3221–3224 (1997).

[614] H. J. Carmichael, *Statistical Methods in Quantum Optics 1: Master Equations and Fokker-Planck Equations* (Springer-Verlag Berlin Heidelberg, 1999).

[615] J. Jeske and J. H. Cole, "Derivation of markovian master equations for spatially correlated decoherence," Phys. Rev. A **87**, 052138 (2013).

[616] J. Sakurai, *Advanced Quantum Mechanics* (Addison-Wesley, 1967).

[617] E. A. Power and S. Zienau, "Coulomb gauge in non-relativistic quantum electrodynamics and the shape of spectral lines," Phil. Trans. R. Soc. Lond. A **251**, 427–454 (1959).

[618] P. W. Atkins and R. G. Woolley, "The interaction of molecular multipoles with the electromagnetic field in the canonical formulation of non-covariant quantum electrodynamics," Proceedings of the Royal Society of London. A. Mathematical and Physical Sciences **319**, 549–563 (1970).

[619] R. G. Woolley, "Molecular quantum electrodynamics," Proc. R. Soc. Lond. A **321**, 557–572 (1971).

[620] S. A. Gardiner, "Theory and application of dark states in cavity QED," Master of science thesis (1995).

PUBLICATIONS

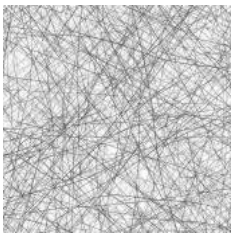

Publications related to the content of this thesis:

- R. Sáez-Blázquez, J. Feist, A. I. Fernández-Domínguez, and F. J. García-Vidal, "Enhancing photon correlations through plasmonic strong coupling," Optica **4**, 1363–1367 (2017)

- R. Sáez-Blázquez, J. Feist, F. J. García-Vidal, and A. I. Fernández-Domínguez, "Photon statistics in collective strong coupling: Nanocavities and microcavities," Phys. Rev. A **98**, 013839 (2018)

- R. Sáez-Blázquez, J. Feist, A. I. Fernández-Domínguez, and F. J. García-Vidal, "Organic polaritons enable local vibrations to drive long-range energy-transfer," Phys. Rev. B **97**, 241407 (2018)

- R. Sáez-Blázquez, J. Feist, E. Romero, A. I. Fernández-Domínguez, and F. J. García-Vidal, "Cavity-modified exciton dynamics in photosynthetic units," J. Phys. Chem. Lett. **10**, 4252–4258 (2019)

AGRADECIMIENTOS

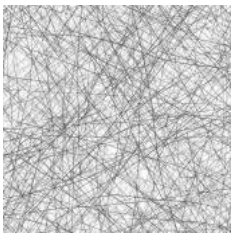

Gracias, Antonio, F. J., mis directores de tesis. Por eso, pero no solo por eso. Gracias, Johannes, casi un tercer director de tesis. Y tampoco solo por eso.

Gracias a todo su grupo entremezclado. Gracias a todos los doctorandos con los que he coincidido a lo largo de estos años. Gracias, Carlos, Javi (Cuerda), Javi (del Pino), Javi (Galego), que habéis terminado antes que yo. Gracias, Álvaro, Mónica, que terminaréis después. Y ahí en medio, yo. Gracias, Diego, a ti también. Gracias, Rui, DongXing.

Gracias a todo el departamento de *Física Teórica de la Materia Condensada*. Planta por planta. A todos.

De entre todos ellos, gracias especialmente a mi grupo de las mesas. Gracias a la formación original. Gracias, Lucía, Jesús, Carlos, Michael. Gracias a los que pronto vinieron después. Gracias, Guillermo, Nerea, Jose. Y gracias también a todos los que han seguido uniéndose más tarde.

Gracias, Clàudia. Clù.

Gracias, Elena. Gracias, Paloma.

Y gracias también al tribunal de esta tesis. Gracias, F. M. Marchetti, F. Prins, P. Törmä, I. De Vega, S. R. K. Rodriguez. Sois parte de esta pequeña historia. Gracias, V. Giannini, R. Esteban.

Realicé una estancia en Trento. Gracias, I. Carusotto. Te agradezco que me acogieras en tu grupo. Gracias, C. Menotti. Gracias, A. Ricatti. Gracias por todo.

Gracias a su grupo. Y a todo el *BEC Center*. Gracias, Albert. Gracias, Aurelian.

Gracias, Alberto. Fuiste todo Trento.

Gracias, Ana, Estefanía, Gabriel. Fuisteis casa.

Y gracias también a mis compañeros en Samba. Gracias a todos los EC3. Gracias, Asma, nuestra Cendrillon. Gracias, YouYou, mi twin sister. Gracias, Burcu, *je suis perdu*. Gracias, Mariglen. Mañana por la mañana.

A mis profesores de física cuando era arquitecta. Gracias, F. González de Posada. Gracias, M. A. Navacerrada Saturio. Fue la física antes de la física. Y gracias, también, D. Gazapo y B. Díaz Urgorri.

Y gracias a mi profesores de física en física. En la Complutense. Gracias, A. López Maroto. Gracias a todos.

Gracias a quienes me dieron la oportunidad de trabajar unos meses en sus grupos mientras estaba en la carrera. Gracias, P. Artal, A. Pérez Canyellas, A. Acín, K. Jansen. Gracias. Y gracias al LOUM, al CSIC, al ICFO y al DESY.

Gracias a mis compañeros. Gracias, Rodrigo, Franco, Álex, Sergio. Siempre en paralelo.

Gracias también a mis profesores del instituto. Y de mi pequeño colegio *Gregorio Canella*. Gracias sobre todo a ellos. Han pasado muchos años, pero fue necesario que esos años pasaran. Gracias, Don Aurelio, Señorita Maribel, Don Jesús, Inés.

Gracias, Sonia, Ana, Daniel. Mis amigos. Madrid.

Gracias, familia. A toda entera, la extensa. Gracias, Abuelo Felipe, Abuela Ángela. Los ventrosinos Felipe Blázquez Romero y Ángela García Valpuesta. Gracias, Abuela María, Tía Jose. Las raparieganas María Amparo Galindo Martín y Josefina Galindo Martín. Gracias, tíos, tías. Gracias, primos, primas. Somos muchos, y no imagináis cómo me gusta daros las gracias a todos.

Gracias a mis padres. Gracias, papi, mami. Gracias, Ruth. Mi hermana. Gracias a ti también, Eriquet.

Y, finalmente, gracias a la educación pública, que es la que me ha permitido llegar aquí. Gracias sobre todo a aquellos que creen en ella y que luchan por ella.

Madrid, 31 de enero de 2020

Rocío Sáez Blázquez

But for now we are young
Let us lay in the sun
And count every beautiful thing we can see
Love to be
In the arms of all I'm keeping here with me

In the aeroplane over the sea,
Neutral Milk Hotel

How strange it is to be anything at all.

UAM Universidad Autónoma de Madrid